

DISSERTATION

**Search for a CP-Odd Higgs Boson Decaying to Zh in
 pp Collisions at $\sqrt{s} = 13$ TeV and Development of a
 b -Jet Tagging Calibration Method for c Jets at the
ATLAS Experiment**

Hannah Arnold



Fakultät für Mathematik und Physik
Albert-Ludwigs-Universität Freiburg

**Search for a CP-Odd Higgs Boson Decaying to Zh in
 pp Collisions at $\sqrt{s} = 13$ TeV and Development of a
 b -Jet Tagging Calibration Method for c Jets at the
ATLAS Experiment**

DISSERTATION

zur Erlangung des Doktorgrades der
Fakultät für Mathematik und Physik der

ALBERT-LUDWIGS-UNIVERSITÄT

Freiburg im Breisgau

vorgelegt von

Hannah Arnold

Dezember 2018

Dekan: Prof. Dr. Gregor Herten
Betreuer der Arbeit: Prof. Dr. Karl Jakobs
Dr. Christian Weiser
Referent: Dr. Christian Weiser
Koreferentin: Prof. Dr. Beate Heinemann
Prüfer: Prof. Dr. Gregor Herten
Prof. Dr. Harald Ita
Dr. Christian Weiser

Datum der mündlichen Prüfung: 22. März 2019

Für meinen Vater.

Contents

Introduction	1
1 Theoretical Preliminaries and Motivation	5
1.1 The Standard Model of Particle Physics	6
1.2 An Extension of the Standard Model: Two-Higgs-Doublet Models	9
1.3 Searching for an Extended Scalar Sector: Higgs-Boson Phenomenology in pp Collisions	14
1.3.1 Introduction: Experimental Constraints and Theoretical Assumptions	14
1.3.2 Higgs-Boson Production in pp Collisions	17
1.3.3 Higgs-Boson Decays	20
1.3.4 Summary and Conclusions	25
1.4 Describing and Simulating pp -Collision Events	25
1.4.1 Implications of the Running of the Strong Coupling	26
1.4.2 Factorisation	26
1.4.3 The Partonic Cross Section	28
1.4.4 Parton Distribution Functions	32
1.4.5 Fragmentation	33
1.4.6 Particle Decays	36
1.4.7 Soft QCD: Minimum-Bias, Underlying Event and Multiple Parton Interactions	37
2 The ATLAS Experiment at the Large Hadron Collider	39
2.1 The Large Hadron Collider	39
2.2 The ATLAS Experiment	41
2.2.1 The Inner Detector	43
2.2.2 The Calorimeter	45
2.2.3 The Muon Spectrometer	47
2.2.4 Forward Detectors	49
2.2.5 Luminosity Determination	50
2.2.6 The Trigger System	52
2.2.7 Detector Simulation	53
2.3 Data-Taking during 2011 and 2015/2016	53
3 Reconstruction and Identification of Physics Objects at the ATLAS Experiment	57
3.1 Track and Vertex Reconstruction	57
3.2 Clustering of Calorimeter Cells	59
3.3 Reconstruction and Classification of Jets	60

3.3.1	Jet Definitions	60
3.3.2	Jet Energy and Mass Scales and Resolutions	62
3.3.3	Pile-up Jet Suppression	70
3.3.4	Jet Quality	71
3.4	Identification of b Jets	71
3.4.1	Introduction	71
3.4.2	Lifetime-based b -tagging algorithms	72
3.4.3	The Soft Muon Tagging algorithm	77
3.4.4	Calibration of the Lifetime-based b -tagging Algorithms	77
3.4.5	Calibration of the Mistag Rate of the SMT Algorithm	83
3.5	Electron Reconstruction and Identification	84
3.6	Muon Reconstruction and Identification	88
3.7	Electron and Muon Isolation Requirements	93
3.8	Reconstruction and Identification of Hadronically Decaying τ Leptons	95
3.9	Reconstruction of Missing Transverse Momentum	96
4	Calibration of the c-Jet Tagging Efficiency Using Events with a W Boson Produced in Association With a Single c Quark	101
4.1	Introduction	101
4.2	Data and Simulated Samples	103
4.3	Object Definitions and Event Selection	105
4.4	Determination of the $W+c$ Yield	107
4.4.1	Strategy	107
4.4.2	Background Determination	108
4.4.3	Results	115
4.5	Measurement of the c -Jet Tagging Efficiency of SMT c Jets	115
4.5.1	Strategy	115
4.5.2	Determination of the Tagging Rates of the Backgrounds	118
4.5.3	Estimation of the Light-Jet Contamination in $W+c$ Candidate Events	120
4.5.4	Results	121
4.6	Calibration of the c -Jet Tagging Efficiency for inclusive c -jet Samples	124
4.6.1	The Extrapolation Procedure	124
4.6.2	Corrections of c -Hadron Production and Decay Properties in Simulation	126
4.6.3	Results: Extrapolation Factors	136
4.7	Results and Discussion	139
5	Search for the Higgs Boson A Decaying to Zh in the $\nu\bar{\nu}b\bar{b}$ and $\ell\bar{\ell}b\bar{b}$ Final States	141
5.1	Introduction	141
5.2	Previous Results	143
5.3	The Data Sample, Signal and Background Modelling	149
5.4	Event Reconstruction and Selection	155
5.4.1	Definition of the Physics Objects	155
5.4.2	Event Reconstruction	157

5.4.3	Event Selection	163
5.5	Event Categorisation	170
5.5.1	Selection of the Kinematic Regime	171
5.5.2	Number of Identified b Jets	174
5.5.3	Signal, Control and Validation Regions	181
5.6	Systematic Uncertainties	184
5.6.1	Experimental Systematic Uncertainties	184
5.6.2	Modelling Systematic Uncertainties	187
5.7	Statistical Analysis	191
5.7.1	Introduction: the $A \rightarrow Zh$ Search as Hypothesis Test	191
5.7.2	Discovery vs. Exclusion Limit	193
5.7.3	The Likelihood Function	194
5.7.4	The $A \rightarrow Zh$ Fit Model	196
5.7.5	Symmetrisation, Smoothing and Pruning of Systematic Uncertainties	201
5.7.6	Expected Results	203
5.7.7	Validation of the Fit Model	211
5.8	Results and Interpretations	225
5.8.1	Results of the $A \rightarrow Zh$ Search	225
5.8.2	2HDM Interpretation of the $A \rightarrow Zh$ Results	231
5.8.3	Additional Results and Interpretations	236
	Conclusion	241
	Bibliography	247
	Acknowledgements	271

Introduction

The enthusiastic celebration of the discovery of a new scalar particle by the ATLAS and CMS collaborations at the Large Hadron Collider (LHC) at CERN in the year 2012 did not only infect the whole physics community, but made headlines around the globe. The particle was identified with the *Higgs boson*, the last missing piece of the Standard Model of particle physics, sought after for almost 50 years since its prediction in the mid-1960s. To date this hypothesis withstood every test carried out with great scrutiny.

As the only fundamental scalar particle, i.e. with spin 0, the Higgs boson is set apart from the other known elementary particles falling into two categories: the fermionic matter particles with spin $1/2$ and the force-mediating vector bosons with spin 1. The Standard Model describes successfully the dynamics and interactions of the fermions via the electromagnetic, weak and strong forces as the exchange of the respective vector bosons based on the concept of *local gauge symmetry*. Since this concept, however, predicts only *massless* force mediators, it is by itself not able to explain the observation that the gauge bosons of the weak interaction, the W^\pm and Z bosons, are very massive and prompted the introduction of the *Brout-Englert-Higgs* (BEH) mechanism. Its key idea is to break the electroweak gauge symmetry *spontaneously*: the W^\pm and Z bosons acquire masses, while the gauge symmetry of the theory is maintained, and the gauge interactions remain unchanged. In a similar manner, through *Yukawa couplings*, also the experimentally observed masses of the charged fermions are accommodated in the theory.

The BEH mechanism implies the existence of a massive, unstable scalar particle, the Higgs boson, that couples to all massive particles proportional to their masses. It was this prediction that allowed the testing of the electroweak symmetry breaking by searching for, and eventually discovering, the Higgs boson via its well defined decay signatures, regardless of its a-priori unknown mass. It led to the Nobel Prize in Physics 2013 being awarded to François Englert and Peter W. Higgs for their “theoretical discovery”.

Despite its many successes, of which the Higgs-boson discovery was only the latest, the Standard Model is not the ultimate theory describing Nature: none of the attempts to incorporate the gravitational force succeeded yet, and it fails to provide explanations for certain observed phenomena. As such, it remains unclear, why there are three generations of fermions differing only regarding their masses, while already the first generation suffices to build the matter of which everything around us is composed of. Also the *baryon asymmetry*, i.e. why there is apparently only matter left in the universe, while antimatter was originally produced with an equal amount, or why ordinary matter only accounts for 20 % of the matter in the universe, and what the unspecified remainder, the *dark matter*, is made of, is left unexplained by the Standard Model. These and other open questions suggest that the Standard Model is a low-energy limit of a more fundamental theory. While several such theories have been developed that based on differing concepts attempt to improve on the shortcomings of the Standard Model, e.g. *Supersymmetry* or *String Theory*, experimental indications that either of them is actually realised in Nature are still pending.

One approach to search for physics beyond the Standard Model, without making assumptions on the details of the underlying theory, is to build up on the well-established Standard Model and modify only a

particular aspect of it. One rather straightforward modification, which only affects the Higgs sector, is the class of *Two-Higgs-Doublet Models* (2HDMs). While in the Standard Model the electroweak symmetry breaking is implemented in its simplest version, leading to one Higgs boson, in the 2HDMs the mechanism is consistently extended and leads, under the assumption of CP and lepton-flavour conservation, to the prediction of five Higgs bosons. One of the Higgs bosons, the light CP-even scalar h , can be identified with the observed Higgs boson with a mass of roughly 125 GeV.¹

If the observed particle was indeed the h boson suggested by the 2HDMs, its couplings to the fermions and bosons would differ from the ones expected in the Standard Model. The degree of expected deviation, however, is not predicted: the modifying factors depend not only on the 2HDM type, but also on two free parameters that need to be determined experimentally. Although the measured couplings of the observed scalar are in good agreement with the Standard Model expectation, they are currently known with a limited precision of 10 – 20 % leaving still room for a modification of the couplings as proposed by the 2HDMs.

In order to elucidate whether the observed Higgs boson is the one predicted by the Standard Model or rather the h boson of the considered 2HDMs, two main and complementary approaches can be pursued: (i) measuring the couplings of the observed Higgs boson with higher precision, and (ii) searching for the other, heavier Higgs bosons expected to exist, in the case of an extended scalar sector. The analysis presented in this thesis follows the second approach: namely, searching for the CP-odd pseudoscalar Higgs boson A in data collected with the ATLAS experiment from proton-proton (pp) collisions at a centre-of-mass energy of 13 TeV in the years 2015 and 2016.

The analysis targets A bosons decaying into a Z boson and an h boson; the Z - and the h -boson candidates are identified via their decays into pairs of leptons (electrons, muons or neutrinos) and bottom (b) quarks, respectively. Using the only fairly recently observed scalar as a probe for new physics makes this decay mode particularly intriguing, especially because at the time of conducting the analysis its decay into b -quark pairs has not been observed yet.

The unprecedented centre-of-mass energy of the analysed pp collisions allow to search for A bosons over a large mass range from 220 GeV up to 2 TeV. To extend the targeted mass range relative to previous searches to such high masses, where the Z and h bosons acquire large transverse momenta, requires reconstruction techniques developed for such *boosted* topologies and strategies to combine them with the more classical approaches employed in the low-mass range. This means in particular that, while the b quarks from the h -boson decay are reconstructed as separate *jets* in the latter case, they are reconstructed jointly as one large jet in the former case; in both cases, *b-tagging* information is used to identify b hadrons inside the jets that emerged from b quarks.

The possibility to identify jets likely originating from b quarks by means of *b-tagging* is heavily exploited in a variety of LHC measurements. On the basis of a number of characteristic properties of the production of b hadrons from b quarks and their subsequent decays, there are several algorithms available at the ATLAS experiment that use information provided by the inner tracking detectors to select b jets and distinguish them from c jets and light jets, which emerge from charm (c) quarks and light quarks as well as gluons, respectively. In order to use *b-tagging* in physics analyses, such as the described search, these algorithms need to be calibrated, i.e. the efficiency with which a b jet is identified as such, as well as the efficiencies of mistakenly identifying c jets and light jets as b jets, need to be measured. A novel method to calibrate the *b-tagging* efficiency for c jets is presented in this thesis.

¹Throughout this thesis mostly natural units are used, i.e. $\hbar = c = 1$.

The calibration method is developed using data collected with the ATLAS experiment in pp collisions at a centre-of-mass energy of 7 TeV during the 2011 data-taking. The key ingredient, a sample of c jets, is obtained from events, where a leptonically decaying W boson is produced in association with a single c quark; the c jet is identified by a muon stemming from the semileptonic decay of the c hadron. The charge correlation of the muon with the electron from the W -boson decay is exploited to subtract background contributions efficiently. The results of the efficiency measurement are presented in the form of data-to-simulation scale factors, i.e. as ratios relative to the efficiencies obtained in simulation. In order for the derived corrections to be applicable to simulated samples with general c -jet topologies, the scale factors are extrapolated using a simulation-based procedure that was developed in the course of this thesis. The method was adopted in other calibrations that also select their samples via exclusive hadron decays.

Organisation of the manuscript and main contributions by the author

Chapter 1 starts with a brief review of the Standard Model mainly focusing on recapping the BEH mechanism and laying the ground work for the extension of the scalar sector in the context of the 2HDMs. After introducing the four CP- and flavour-conserving 2HDMs in whose context the $A \rightarrow Zh$ search results are presented, their phenomenology in pp collisions is discussed based on the SM Higgs-boson phenomenology. Particular focus is given to the production and the decay of the A boson and the decay of h boson motivating the conducted search for $A \rightarrow Zh$ with $h \rightarrow b\bar{b}$. The chapter concludes with a summary of the basics of describing and simulating pp -collision events; both for the $A \rightarrow Zh$ search as well as the calibration, simulated samples constitute a crucial tool.

Chapter 2 introduces the LHC and in particular the ATLAS experiment. It also provides some details on the analysed datasets.

Chapter 3 is a compilation of the techniques used at the ATLAS experiment to reconstruct and identify the physics objects used in the described analyses. Particular attention is given to the reconstruction of the various kinds of jets and the relevant b -tagging algorithms; calibration methods and associated sources of systematic uncertainties are reviewed.

In Chapter 4 the novel method to calibrate the c -jet tagging efficiency using $W+c$ events is presented. Conducted in the context of the most recent $W+c$ cross-section measurement performed by the ATLAS collaboration [1], to which the author contributed to in the course of the Diploma thesis [2], it starts with a review of the common parts leading to the extraction of the $W+c$ sample. After introducing the methodology of the measurement of the c -jet tagging efficiency for c jets with a muon and presenting the intermediary results, the scale-factor extrapolation procedure is discussed comprehensively. The chapter closes with the presentation and discussion of the final results.

All aspects of the calibration were developed and carried out by the author; this particularly applies to the established extrapolation procedure. The author was furthermore the editor of both the internal supporting documentation as well as the preliminary publication of the results in form of a conference note [3]. Most results presented in this chapter have also been published in Ref. [4].

Chapter 5 is dedicated to the search for the A boson via its decay to Zh in the $\nu\bar{\nu}b\bar{b}$ and $\ell\bar{\ell}b\bar{b}$ final states. Starting with a general introduction, it follows a brief recap of previous searches conducted at the LHC in the same decay channels. In this context also the preliminary result [5] obtained using only 2015 data is reviewed, to which the author also contributed. The author in particular developed together with a small team the complete analysis framework that was used by the analysis team for both the preliminary

and the final result.² The author furthermore provided the results for the $\ell\bar{\ell}b\bar{b}$ channel in collaboration with another analyser, performed in a small team studies related to the statistical analysis and was co-editor of the internal supporting documentation, on which the conference note was based. It then follows the detailed description of the analysis leading to the final result.

After introducing the analysed data sample as well as characterising the considered signals and the various background contributions, the reconstruction and selection of the candidate events is discussed, highlighting the specificities of the two targeted kinematic regimes. How to achieve their orthogonality, while maintaining optimal performance is detailed in the context of the event categorisation; here also the subject of classifying the signal regions according to the number of b -tagged jets is discussed, as well as the used control and validation regions. Special focus is given to a number of improvements over the preliminary result, in particular since they were predominantly introduced and developed by the author. This especially applies to (i) the event selection of the $\ell\bar{\ell}b\bar{b}$ channel, (ii) the regime-selection strategy as well as the addition of (iii) categories with additional b -tagged jets, sensitive to a particular production mode of the A boson, in both channels. (i) was carried out together with a bachelor student, supervised by the author, and parts of (ii) were studied in collaboration with a few members of the analysis team.

Systematic uncertainties due to experimental effects and in particular the modelling of the dominant backgrounds are discussed in the following section.

After introducing some general concepts of statistical data analysis, particular room is given to its application in the context of the presented analysis. The described fit model used for both the $\ell\bar{\ell}b\bar{b}$ and $\nu\bar{\nu}b\bar{b}$ channels as well as their combination was developed and intensively studied by the author. Therefore, the treatment of systematic uncertainties and especially the expected results and the validation of the fit model are comprehensively discussed. Most parts of the fit model were furthermore adopted for the alternative interpretation of the analysis results in the search for new heavy vector bosons (W' and Z') using a simplified model describing heavy vector triplets (HVT).

The chapter concludes with a detailed discussion of the results of the $A \rightarrow Zh$ search, including their interpretation in the context of the CP- and flavour-conserving 2HDMs; interpretations of the results in the context of the HVT model as well as a particular supersymmetric model, the $hMSSM$, are presented as well. Most of the shown results have previously been published in Ref. [6].

This thesis concludes with a summary of its most important results.

²The framework, internally referred to as *CxAODFramework*, became necessary because of a new Event Data Model (EDM) introduced for the ATLAS experiment in time for the 2015 data-taking. Exploiting all advantages of the new EDM, it was not only used for the presented analyses, but also by about 30 other analysis teams according to survey results. It was successfully reviewed by the ATLAS Software Group and recognised as one of a few common analysis frameworks used within the collaboration.

This chapter starts with a brief recapitulation of the *Standard Model* (SM) of particle physics, the theoretical framework that categorises all known elementary particles and describes their dynamics as well as interactions which are governed by three of the four known fundamental forces. Completed in the mid-1970s, the SM has demonstrated impressive successes not only in describing known phenomena, but also in providing predictions; its latest being the discovery of a new scalar boson in the year 2012 [7, 8], whose properties are so far consistent with the ones predicted for the *Higgs boson*. Nonetheless the SM is not a complete theory able to describe Nature: it does not incorporate the gravitational force, and it is not able to provide explanations for certain observed phenomena such as the baryon asymmetry in the universe [9], the existence of dark matter [10] or neutrino oscillations [11, 12]. While it therefore seems that the SM is a low-energy limit of a more fundamental, yet to be revealed theory, it serves as an important basis for building and studying more exotic and complex models attempting to improve on its shortcomings.

One rather straightforward extension of the SM is the class of *Two-Higgs-Doublet Models* (2HDMs) introduced in Sec. 1.2. Here the mechanism of electroweak symmetry breaking, introduced in the SM to accommodate particle masses and leading in its simple representation to one Higgs boson, is consistently extended. Particular attention is given to the class of CP- and flavour-conserving 2HDMs, which suggest the existence of five Higgs bosons; one of which, the light CP-even scalar h , can be identified with the observed Higgs boson. In Sec. 1.3 the phenomenology of those 2HDMs is discussed, building up on the well-studied phenomenology of the SM Higgs-boson and in view of the search for the pseudoscalar CP-odd Higgs boson A via its decay to $h \rightarrow b\bar{b}$ in association with a Z boson in proton-proton (pp) collisions described in Chap. 5.

The final section introduces concepts for the theoretical description of pp -collision events and in particular their simulation by means of *Monte-Carlo event generators*, given simulated samples constitute a crucial tool in the analyses presented in this thesis. Some attention is given to the modelling of the fragmentation of quarks into hadrons and the decay of the latter, since this subject plays quite a crucial role in the c -jet tagging efficiency calibration presented in Chap. 4

While the overview of the SM presented in the following is based on standard text books, such as Refs. [13, 14], the rather detailed description of the mechanism of electroweak symmetry breaking follows particularly closely the presentation in Ref. [15]. Both the introduction to the 2HDMs as well as parts of their phenomenological discussion are largely based on Refs. [16, 17]; the SM Higgs-boson phenomenology on Refs. [18, 19]. Section 1.4 is a compilation based on Refs. [20–24].

1.1 The Standard Model of Particle Physics

As a renormalisable gauge theory [25–28] the Standard Model (SM) is a Lorentz-invariant relativistic quantum field theory, where the physical particles are identified with (or with linear combinations of) excited states of the quantum fields, the *field quanta*. Formulated based on a Lagrangian density function, the equations of motion of the fields are derived from the Euler-Lagrange equation. The SM Lagrangian is invariant under local gauge transformations of the $SU(3)_C \otimes SU(2)_L \otimes U(1)_Y$ symmetry group. According to Noether's theorem this invariance entails the conservation of three types of charges to which the respective gauge fields, introduced to achieve the local gauge invariance, couple and thereby mediate the corresponding interaction.

The invariance under transformations of the non-abelian $SU(3)_C$ group leads to the conservation of the *colour* charge and to the theory of *quantum chromodynamics* (QCD) [29–31]. The group of fermionic particles carrying colour charge is referred to as *quarks*; they come in three different states: *red*, *blue* and *green*. Due to the non-abelian structure of the symmetry group (i.e. the group generators do not commute) also the associated gauge bosons, the *gluons*, carry colour (more precisely combinations of colour and anti-colour), leading to a total of eight self-interacting mediators of the *strong force*.

Both quarks and the other group of known fermionic particles, the *leptons*, are subject to the *electromagnetic* and *weak* interactions that are described unified in the *electroweak theory* with $SU(2)_L \otimes U(1)_Y$ gauge symmetry [32–34]. The conserved charge of the non-abelian $SU(2)_L$ group is the *weak isospin* I . Due to the V-A structure of the weak interaction, its gauge bosons W^1 , W^2 and W^3 , building an isospin triplet with $I = 1$, couple only to the left-handed components of the fermions which are thus arranged into doublets with $I = 1/2$; the right-handed components are represented as singlets with $I = 0$. Leptons, whose third component of the weak isospin is $I_3 = -1/2$, have an electrical charge of $Q = +1$ (in units of the elementary electric charge e); those with $I_3 = +1/2$ are electrically neutral and are referred to as *neutrinos*. Up-type quarks with $I_3 = +1/2$ carry an electrical charge of $Q = 2/3$, down-type quarks with $I_3 = -1/2$ have $Q = -1/3$. Both charges are related to each other via the Gell-Mann-Nishijima formula [35, 36]

$$Q = I_3 + \frac{Y}{2}, \quad (1.1)$$

where Y is the *hypercharge*, the conserved charge of the abelian $U(1)_Y$ group. Denoting its single gauge boson B , the following four linear combinations define physical fields

$$W_\mu^\pm = \frac{1}{\sqrt{2}} (W_\mu^1 \mp iW_\mu^2) \quad (1.2)$$

$$Z_\mu = \cos \theta_W \cdot W_\mu^3 - \sin \theta_W \cdot B_\mu \quad (1.3)$$

$$A_\mu = \sin \theta_W \cdot W_\mu^3 + \cos \theta_W \cdot B_\mu. \quad (1.4)$$

whose quanta can in order of appearance be identified with the experimentally observable W^\pm and Z bosons, the electrically charged ($Q = \pm 1$) and neutral mediators of the weak interaction, as well as the *photon* (γ), the gauge boson of the $U(1)_Q$ symmetry group of the electromagnetic interaction. Since the latter does not distinguish between the chiral states of the charged fermions, the electromagnetic charge e can be expressed

	Generation			Quantum Numbers		
	1 st	2 nd	3 rd	Q	I_3	Y
Leptons	$\begin{pmatrix} \nu_e \\ e \end{pmatrix}_L$	$\begin{pmatrix} \nu_\mu \\ \mu \end{pmatrix}_L$	$\begin{pmatrix} \nu_\tau \\ \tau \end{pmatrix}_L$	0	1/2	-1
	e_R	μ_R	τ_R	-1	0	-2
	$\begin{pmatrix} u \\ d' \end{pmatrix}_L$	$\begin{pmatrix} c \\ s' \end{pmatrix}_L$	$\begin{pmatrix} t \\ b' \end{pmatrix}_L$	2/3	1/2	1/3
Quarks	u_R	c_R	t_R	2/3	0	4/3
	d'_R	s'_R	b'_R	-1/3	0	-2/3

Table 1.1: Classification of the three generations of fermionic particles of the SM introduced in the text according to their quantum numbers into left-handed (“L”) isospin doublets and right-handed (“R”) isospin singlets: Q is their electrical charge in units of the elementary electric charge e , I_3 the third component of their weak isospin and Y their hypercharge; they are related via Eq. 1.1. The quarks are colour triplets; the down-type quark eigenstates d' , s' , b' of the weak interaction are related to the mass eigenstates via Eq. 1.6.

in terms of the gauge couplings g and g' of the $SU(2)_L$ and $U(1)_Y$ groups, respectively,

$$e = g \cdot \sin \theta_W = g' \cdot \cos \theta_W, \quad (1.5)$$

where θ_W is the *weak mixing angle*. The non-abelian structure of the $SU(2)_L$ group reflects that electroweak interactions occur not only between the fermions, but also between the vector bosons W^\pm , Z and γ .

Based on the discussed quantum numbers, the fermionic particles of the SM can be classified as shown in Table 1.1, where the quarks need to be considered as actually being colour triplets; for each fermion exists an *anti*-particle with identical properties, except for the charges which are “opposite”, i.e. of opposite sign and anti-colour if applicable. Both quarks and leptons come in three *generations* that are identical copies in terms of the quantum numbers, but differ in their *observed* masses. The *muon* (μ) and the τ -lepton are heavier copies of the *electron* (e); their weak isospin partners, the neutrinos, are considered to be *massless* in the SM (though observed neutrino oscillations indicate otherwise). This is also the reason why only left-handed neutrinos appear in the SM: right-handed ones do not participate in any of the described interactions nor does the Higgs boson introduced below couple to it.

Also in the case of the quarks their masses are increasing from the first to the third generation, even much more considerably. By choosing the eigenstates of the weak interaction of the up-type quarks, the *up quark* (u), the *charm quark* (c) and the *top quark* (t), to coincide with their mass eigenstates, the weak eigenstates (indicated by the “'”) of the down-type quarks, the *down quark* (d), the *strange quark* (s) and the *bottom quark* (b), are related to their mass eigenstates via the unitary Cabbibo-Kobayashi-Maskawa (CKM) matrix V_{CKM} [37, 38]

$$\begin{pmatrix} d' \\ s' \\ b' \end{pmatrix} = V_{\text{CKM}} \cdot \begin{pmatrix} d \\ s \\ b \end{pmatrix}; \quad (1.6)$$

V_{CKM} can be described by four free parameters: three mixing angles and one complex CP-violating phase.

Not only the charged fermions, but also the W^\pm and Z bosons happen to be massive. While the require-

ment of local gauge invariance does not allow “naive” mass terms in the Lagrangian, masses are accounted for by the *spontaneous breaking* of the $SU(2)_L \otimes U(1)_Y$ symmetry [39–41]. Referred to as *Brout-Englert-Higgs mechanism*, this is achieved in the “most economical” [13] way by arranging four real fields in a complex scalar isospin doublet

$$\Phi = \begin{pmatrix} \phi^+ \\ \phi^0 \end{pmatrix} \quad (1.7)$$

with hypercharge $Y = 1$, i.e. ϕ^+ is charged with $Q = +1$ and ϕ^0 is neutral, whose Lagrangian¹

$$\mathcal{L} = (D_\mu \Phi)^\dagger (D^\mu \Phi) - V(\Phi^\dagger \Phi), \quad (1.8)$$

is invariant under the $SU(2)_L \otimes U(1)_Y$ symmetry, but its ground state is chosen such that it is not: that is, the parameter μ^2 in the potential

$$V(\Phi^\dagger \Phi) = \frac{\lambda}{4} (\Phi^\dagger \Phi)^2 - \mu^2 \Phi^\dagger \Phi, \quad (1.9)$$

describing the self-interaction of Φ , is taken positive to obtain a non-vanishing vacuum expectation value for the ground state Φ_0 :

$$\Phi_0^\dagger \Phi_0 = \frac{v^2}{2}, \quad v = 2 \sqrt{\frac{\mu^2}{\lambda}}; \quad (1.10)$$

with $\lambda > 0$ in order to guarantee vacuum stability. Choosing from the degenerate set of possible ground states satisfying this requirement

$$\Phi_0 = \begin{pmatrix} 0 \\ \frac{v}{\sqrt{2}} \end{pmatrix}, \quad (1.11)$$

breaks the $SU(2)_L \otimes U(1)_Y$ symmetry spontaneously down to $U(1)_Q$ invariance. Expanding the scalar doublet around the vacuum expectation value yields:

$$\Phi = \begin{pmatrix} \phi^+ \\ \frac{1}{\sqrt{2}}(v + h + i\chi) \end{pmatrix}; \quad (1.12)$$

ϕ^+ and χ are unphysical fields corresponding to “would-be” Goldstone bosons [42–44] that vanish by choosing an appropriate gauge, the *unitary gauge*, and only one real, physical field, the *Higgs field* h , is left:

$$\Phi = \begin{pmatrix} 0 \\ \frac{1}{\sqrt{2}}(v + h) \end{pmatrix}, \quad (1.13)$$

that is associated with a neutral scalar boson, the *Higgs boson* H , with mass

$$m_H = \sqrt{2\mu^2}. \quad (1.14)$$

Moreover, by inserting Eq. 1.13 in Eq. 1.8 terms appear that can be identified with mass terms for the W^\pm

¹The covariant derivative $D_\mu = \partial_\mu + ig I_W^i W_\mu^i + ig' \frac{Y}{2} B_\mu + ig_s T_c^a G_\mu^a$ of the $SU(3)_C \otimes SU(2)_L \otimes U(1)_Y$ symmetry contains the SM interactions: I_W^i , Y and T_c^a are the generators of the respective gauge groups of the electroweak and strong interactions, g_s and G_μ^a are the gauge coupling and fields of the latter; all other quantities have already been introduced in the text.

and Z bosons with

$$m_{W^\pm} = \frac{gv}{2}, \quad m_Z = \frac{m_{W^\pm}}{\cos \theta_W}, \quad (1.15)$$

as well as terms describing triple and quartic self-interactions of the Higgs boson, scaling with m_H^2/v and m_H^2/v^2 , respectively, and interactions involving one (two) Higgs boson(s) and pairs of vector bosons, $V = W^\pm, Z$, that are proportional to their masses squared: m_V^2/v (m_V^2/v^2). As the $U(1)_Q$ symmetry remains unbroken, its gauge boson, the photon, remains massless and no direct couplings to the Higgs boson occur.

Through interaction with the isospin doublet Φ , and its charge-conjugate $\tilde{\Phi} = (\phi^{0*}, -\bar{\phi})^T$ in the case of up-type quarks, via *Yukawa couplings*, also mass terms for the charged fermions f arise as well as terms describing the interaction of pairs of (oppositely-charged, same-flavoured) fermions with the Higgs boson that are linearly proportional to their masses, i.e. m_f/v . The respective Lagrangian can be written as

$$\mathcal{L}_{\text{Yukawa}} = - \sum_{i,j=1}^3 \left(\bar{\Psi}_{l_L}^i G_l^{ij} \psi_{l_R}^j \Phi + \bar{\Psi}_{q_L}^i G_u^{ij} \psi_{u_R}^j \tilde{\Phi} + \bar{\Psi}_{q_L}^i G_d^{ij} \psi_{d_R}^j \Phi + h.c. \right), \quad (1.16)$$

where Ψ_{f_L} and ψ_{f_R} denote the left-handed isospin doublets and right-handed isospin singlets of leptons, up-type and/or down-type quarks ($f = l, u, d, q$) as listed in Table 1.1, respectively; G_f are 3×3 matrices and i, j the generation indices. By (i) transforming into the mass-eigenstate basis of the fermions (thus diagonalising the matrices $G_f \rightarrow G'_f$), (ii) spontaneously breaking the symmetry and choosing the unitary gauge (thus yielding Φ according to Eq. 1.13 and $\tilde{\Phi} = (\frac{1}{\sqrt{2}}(v+h), 0)^T$) and (iii) identifying $G'_f{}^i{}_i v/\sqrt{2}$ with the fermion masses m_f^i , Eq. 1.16 becomes

$$\mathcal{L}_{\text{Yukawa}} = - \sum_f m_f \left(\bar{\psi}_{f_L} \psi_{f_R} + \bar{\psi}_{f_R} \psi_{f_L} \right) \left(1 + \frac{h}{v} \right), \quad (1.17)$$

where f runs over all fermion flavours *and* generations (replacing i, j) and ψ_{f_L} stands for the charged component of the left-handed isospin doublets.

The SM has in total 19 free parameters that need to be determined from measurements;² depending on the choice of parametrisation these are: the three masses of the Higgs and the weak gauge bosons, m_H and m_V , as well as the nine masses of the charged fermions, m_f , the electromagnetic and the strong coupling constants, $\alpha = e^2/(4\pi)$ and $\alpha_s = g_s^2/(4\pi)$, respectively (where g_s is the gauge coupling of the strong interaction), the vacuum expectation value of the Higgs potential, v , and the four parameters of V_{CKM} .

1.2 An Extension of the Standard Model: Two-Higgs-Doublet Models

It was indicated in the previous section that the choice of introducing a single complex scalar isospin doublet to spontaneously break the $SU(2)_L \otimes U(1)_Y$ symmetry of the Standard Model (SM) to give masses to the weak gauge bosons and the charged fermions was minimal, though “there is really no rational reason why only the lowest Higgs representation would be present”, and thus it is believed that “the Higgs formulation is really something like an effective description of a much more complicated situation” [46].

²Considering further the masses of the three neutrinos as well as the three mixing angles and the one (three) CP-violating phase(s) describing the mixing matrix in the case of Dirac (Majorana) neutrinos, adds seven (nine) more free parameters. [45]

The *custodial symmetry* [47] of the Higgs potential in the SM (cf. Eq. 1.9), where the lowest non-trivial representation of a Higgs multiplet is assumed, leads to the relation between the masses of the neutral and charged vector bosons in Eq. 1.15 and to a prediction of

$$\rho \equiv \frac{m_W^2}{m_Z^2 \cos^2 \theta_W} \quad (1.18)$$

being equal to unity, which is in good agreement with the experimental result of $\rho = 1.00039 \pm 0.00019$ [45] obtained in electroweak precision measurements. Though expressing the parameter ρ (at tree level) as [48]

$$\rho = \frac{\sum_{i=1}^n [I_i(I_i + 1) - \frac{1}{4} Y_i^2] v_i}{\sum_{i=1}^n \frac{1}{2} Y_i^2 v_i}, \quad (1.19)$$

assuming n scalar multiplets ϕ_i with weak isospin I_i , hypercharge Y_i and vacuum expectation value of the neutral components v_i , various extended scalar sectors are compatible with $\rho = 1$ given the scalar multiplets belong to a specific set of isospin representations. The simplest extension of the SM consists in adding scalar $SU(2)$ singlets with $Y = 0$ or $SU(2)$ doublets with $Y = \pm 1$ (in addition to the doublet already present); the extension by one $SU(2)$ doublet leads to a class of models referred to as *Two-Higgs-Doublet Models* (2HDMs). First studied in Ref. [49] they are well motivated given that additional isospin doublets appear in many theories aiming to describe phenomena left unexplained by the SM; famous examples are the Minimal Supersymmetric Standard Model (MSSM) [50] as well as axion models [51, 52]. Though likely not fundamental, by capturing the most important features 2HDMs allow a general search for an extended scalar sector without being restricted by constraints from a specific underlying theory.

Due to the generally very rich vacuum structure - in its most general form the scalar potential contains 14 free parameters (compared to two in the SM) and can have CP-conserving, CP-violating and charge-violating minima - 2HDMs provide an interesting and well studied phenomenology as reviewed e.g. in Ref. [16]; for example, a CP-violating Higgs sector is able to explain baryogenesis and the *inert 2HDM* provides a dark-matter candidate. In most phenomenological studies of 2HDMs however, simplifying assumptions are made in order to reduce the number of free parameters, depending on the choices at the expense of losing solutions to problems as the ones just mentioned. Very common assumptions are (i) that the Higgs sector is CP-conserving and that CP is also not spontaneously broken (thus baryogenesis no longer can be explained), and (ii) that there are no flavour-changing neutral currents (FCNCs) at tree level, which is in agreement with experimental observations (and given in the SM). Under these assumptions the most general scalar potential for two isospin doublets with $Y = 1$ of the form of Eq. 1.7, i.e.

$$\Phi_a = \begin{pmatrix} \phi_a^+ \\ \phi_a^0 \end{pmatrix} \quad \text{with } a = 1, 2, \quad (1.20)$$

is [16]

$$\begin{aligned} V = & m_{11}^2 \Phi_1^\dagger \Phi_1 + m_{22}^2 \Phi_2^\dagger \Phi_2 - m_{12}^2 [\Phi_1^\dagger \Phi_2 + \Phi_2^\dagger \Phi_1] + \frac{\lambda_1}{2} (\Phi_1^\dagger \Phi_1)^2 + \frac{\lambda_2}{2} (\Phi_2^\dagger \Phi_2)^2 \\ & + \lambda_3 (\Phi_1^\dagger \Phi_1) (\Phi_2^\dagger \Phi_2) + \lambda_4 (\Phi_1^\dagger \Phi_2) (\Phi_2^\dagger \Phi_1) + \lambda_5 [(\Phi_1^\dagger \Phi_2)^2 + (\Phi_2^\dagger \Phi_1)^2], \end{aligned} \quad (1.21)$$

where the eight remaining parameters are real³ as well as the vacuum expectation values, v_1 and v_2 , defining the ground states

$$\Phi_a^0 = \begin{pmatrix} 0 \\ \frac{v_a}{\sqrt{2}} \end{pmatrix}, \quad a = 1, 2, \quad (1.22)$$

that are of the same form as Eq. 1.11; furthermore $v_1^2 + v_2^2 = v^2$, where v is defined by Eq. 1.10, and v_1 and v_2 are assumed to be positive without loss of generality.

Having two isospin doublets results in eight fields, of which three are again needed to provide mass to the weak gauge bosons (just as described in the previous section) leaving five physical Higgs fields that are associated with five massive Higgs bosons: two charged scalars H^\pm , two neutral scalars, a lighter h and a heavier H , and one pseudoscalar A . Decomposing the two scalar doublets Φ_a ($a = 1, 2$) as before

$$\Phi_a = \begin{pmatrix} \phi_a^+ \\ \frac{1}{\sqrt{2}}(v_a + \rho_a + i\eta_a) \end{pmatrix} \quad (1.23)$$

and inserting them in Eq. 1.21 allows to identify corresponding mass terms of the form

$$(\chi_1^+, \chi_2^+) M_\chi^2 \begin{pmatrix} \chi_1^- \\ \chi_2^- \end{pmatrix}, \quad (1.24)$$

where $\chi_a = \{\phi_a, \rho_a, \eta_a\}$ and $\chi_a^+ = \chi_a^-$ for the neutral CP-even and CP-odd fields, ρ and η , respectively, and M_χ^2 being non-diagonal mass-squared matrices. Diagonalising them in order to obtain the mass eigenstate basis, in which the fields are free, is achieved through appropriate rotations of the fields; two rotation angles are needed: one to perform the diagonalisation of the mass-squared matrices of the neutral scalars and one for the charged scalars and the pseudoscalar, referred to as α and β , respectively. The latter is defined via the vacuum expectation values

$$\tan \beta \equiv \frac{v_2}{v_1} \quad (1.25)$$

and constitutes ‘‘perhaps the single most important parameter in studies of 2HDMs’’ [16]. Thus, one obtains for the physical fields⁴

$$\begin{aligned} H^\pm &= -\phi_1^\pm \cdot \sin \beta + \phi_2^\pm \cdot \cos \beta, \\ A &= -\eta_1 \cdot \sin \beta + \eta_2 \cdot \cos \beta, \\ H &= \rho_1 \cdot \cos \alpha + \rho_2 \cdot \sin \alpha, \\ h &= -\rho_1 \cdot \sin \alpha + \rho_2 \cdot \cos \alpha, \end{aligned} \quad (1.27)$$

where h and H are orthogonal combinations of ρ_1 and ρ_2 , chosen such that $m_h < m_H$. As the masses of the Higgs bosons depend on the parameters of the potential and the vacuum expectation values, they can be chosen as the free parameters of the theory, and thus need to be determined experimentally; this results

³If and only if the parameters of the potential and the vacuum expectation values are real, independent of the chosen basis, the potential is CP-conserving [53].

⁴And for the three massless Goldstone bosons:

$$\begin{aligned} G^\pm &= \phi_1^\pm \cdot \cos \beta + \phi_2^\pm \cdot \sin \beta, \\ G^0 &= \eta_1 \cdot \cos \beta + \eta_2 \cdot \sin \beta, \end{aligned} \quad (1.26)$$

Model	u_R^i	d_R^i	l_R^i	Obey \mathbb{Z}_2 symmetry
Type I	Φ_2	Φ_2	Φ_2	Φ_1
Type II	Φ_2	Φ_1	Φ_1	Φ_1, d_R^i, l_R^i
Lepton-specific	Φ_2	Φ_2	Φ_1	Φ_1, l_R^i
Flipped	Φ_2	Φ_1	Φ_2	Φ_1, d_R^i

Table 1.2: Summary of the four 2HDM model types with natural flavour conservation obtained by imposing an additional \mathbb{Z}_2 symmetry: all fermions with the same quantum numbers, i.e. right-handed up-type quarks, u_R^i , down-type quarks, d_R^i and charged leptons, l_R^i , couple to the same isospin doublet, either Φ_1 or Φ_2 . The generation index is denoted “ i ”.

together with v , m_{12} (which mixes the doublets), α and $\tan\beta$ in a total of eight free parameters (compared to two related to the Higgs sector in the SM).⁵

A neutral CP-even scalar with the couplings of the SM Higgs-boson (cf. Sec. 1.1), denoted H_{SM} , is described by the following linear combination of the neutral CP-even scalar fields

$$H_{\text{SM}} = \rho_1 \cdot \cos\beta + \rho_2 \cdot \sin\beta \quad (1.28)$$

$$= h \cdot \sin(\beta - \alpha) + H \cdot \cos(\beta - \alpha). \quad (1.29)$$

If $\cos(\beta - \alpha) = 0$, the light CP-even scalar h possesses couplings identical to the SM Higgs-boson, a case that is referred to as *alignment limit*; the two bosons become indistinguishable if they also have the same mass. Thus, in most phenomenological studies and experimental tests of 2HDMs after the discovery of the SM-like Higgs boson in 2012, such as the ones presented in Secs. 1.3 and 5, the observed Higgs boson is identified with the light CP-even scalar. Besides defining its mass, this can also be exploited to restrict the allowed parameter space to $\cos(\beta - \alpha)$ values close to the alignment limit as demonstrated in Sec. 1.3.

Usually, the alignment limit is associated with the *decoupling limit*, where the H , A and H^\pm are much heavier than h , resulting in an SM-like phenomenology with only small corrections to the various couplings due to the presence of the additional, heavy Higgs bosons [54]; in e.g. Ref. [55] though, also the “more interesting case” of alignment without decoupling is reviewed and studied.

Other than in the SM, in 2HDMs the diagonalisation of the fermion mass matrices does not entail the diagonalisation of the Yukawa interactions and the absence of tree-level FCNCs; according to the Paschos–Glashow–Weinberg theorem [56, 57] though flavour conservation can be established by requiring that all fermions with the same quantum numbers couple to the same isospin doublet, i.e. either Φ_1 or Φ_2 , which can be achieved by imposing an additional discrete \mathbb{Z}_2 symmetry.⁶ This allows to distinguish four 2HDM types with natural flavour conservation that are summarised in Table 1.2: (i) the *Type I*, where all charged fermions couple to Φ_2 ,⁷ (ii) the *Type II*, where only up-type quarks couple to Φ_2 , (iii) the *Lepton-specific*, where all the quarks couple to Φ_2 and (iv) the *Flipped Model*, where up-type quarks and

⁵Considering only the masses of the massive gauge bosons to be known, although also $v = (\sqrt{2}G_F)^{-1/2} \approx 246$ GeV, with G_F being the *Fermi constant*, is measured [45].

⁶In the SM the theorem is fulfilled by the right-handed up-type quarks only coupling to $\tilde{\Phi}$, and all other right-handed fermions to Φ (cf. Eq. 1.16). The m_{12} term in Eq. 1.21 breaks the \mathbb{Z}_2 symmetry softly.

⁷It is just convention to chose Φ_2 .

Coupling modifiers	Model			
	Type I	Type II	Lepton-specific	Flipped
ξ_h^u	$\cos \alpha / \sin \beta$	$\cos \alpha / \sin \beta$	$\cos \alpha / \sin \beta$	$\cos \alpha / \sin \beta$
ξ_h^d	$\cos \alpha / \sin \beta$	$-\sin \alpha / \cos \beta$	$\cos \alpha / \sin \beta$	$-\sin \alpha / \cos \beta$
ξ_h^l	$\cos \alpha / \sin \beta$	$-\sin \alpha / \cos \beta$	$-\sin \alpha / \cos \beta$	$\cos \alpha / \sin \beta$
ξ_H^u	$\sin \alpha / \sin \beta$	$\sin \alpha / \sin \beta$	$\sin \alpha / \sin \beta$	$\sin \alpha / \sin \beta$
ξ_H^d	$\sin \alpha / \sin \beta$	$\cos \alpha / \cos \beta$	$\sin \alpha / \sin \beta$	$\cos \alpha / \cos \beta$
ξ_H^l	$\sin \alpha / \sin \beta$	$\cos \alpha / \cos \beta$	$\cos \alpha / \cos \beta$	$\sin \alpha / \sin \beta$
ξ_A^u	$\cot \beta$	$\cot \beta$	$\cot \beta$	$\cot \beta$
ξ_A^d	$-\cot \beta$	$\tan \beta$	$-\cot \beta$	$\tan \beta$
ξ_A^l	$-\cot \beta$	$\tan \beta$	$\tan \beta$	$-\cot \beta$

Table 1.3: Coupling modifiers used to express the Yukawa couplings of the neutral Higgs bosons h , H and A to up-type quarks (u), down-type quarks (d) and charged leptons (l) relative to the Yukawa couplings of the SM Higgs-boson. The modifiers ξ_A^f of the pseudoscalar A appear also in the couplings of the charged scalars H^\pm described by Eq. 1.31.

leptons couple to Φ_2 and the respective non-mentioned class of charged fermions to Φ_1 . While (i) is simply enforced by requiring $\Phi_1 \rightarrow -\Phi_1$ invariance, the other types are obtained by imposing the same symmetry in addition for (ii) the down-type quarks, for (iii) the leptons or for (iv) both down-type quarks and leptons. It is interesting to note, that the Yukawa couplings of the MSSM, which are obtained by imposing *continuous* symmetries, have the same structure as the Type-II Model (at tree-level); given the additional bounds on the allowed parameter space, the MSSM constitutes a special case of the Type-II Model.

The resulting Yukawa couplings for the four models can be expressed relative to the Yukawa couplings of the SM Higgs-boson (cf. Eq. 1.17) by introducing the coupling modifiers $\xi_{h/H/A}^f$, with f referring to up(u)- and down(d)-type quarks as well as charged leptons (l), which are a function of the rotation angles, α and β , and are listed in Table 1.3. The interaction part of the Yukawa Lagrangian then takes the form [58]

$$\mathcal{L}_{\text{Yukawa,int}}^{\text{2HDM}} = - \sum_{f=u,d,l} \frac{m_f}{v} \left(\xi_h^f \bar{\psi}_f \psi_f h + \xi_H^f \bar{\psi}_f \psi_f H - i \xi_A^f \bar{\psi}_f \gamma_5 \psi_f A \right) \quad (1.30)$$

$$- \left[\frac{\sqrt{2} V_{CKM}}{v} \bar{\psi}_u (m_u \xi_A^u P_L + m_d \xi_A^d P_R) \psi_d H^+ + \frac{\sqrt{2} m_l \xi_A^l}{v} \bar{\psi}_{\nu_L} \psi_{l_R} H^+ + h.c. \right]; \quad (1.31)$$

where the sum over the three generations (and chiralities) is implicit; $P_{L/R}$ are the projection operators for left/right-handed fermions, V_{CKM} is the CKM matrix (cf. Eq. 1.6) and the subscript ν_L indicates left-handed neutrinos. The same parameters ξ_A^f that modify the couplings of the pseudoscalar A (with respect to the SM) enter the couplings of H^\pm .

The couplings of the neutral Higgs bosons to pairs of vector bosons V , $V = W, Z$, are the same for all

four model types and are modified with respect to the SM by

$$\xi_h^{VV} = \sin(\beta - \alpha), \quad (1.32)$$

$$\xi_H^{VV} = \cos(\beta - \alpha), \quad (1.33)$$

$$\xi_A^{VV} = 0; \quad (1.34)$$

that the couplings to the pseudoscalar A vanish (at tree level) obeying CP conservation has important implications for its production at hadron colliders as discussed in the following section and is particularly relevant for the search described in Chap. 5.

In addition to the couplings that are also present in the SM, including triple and quartic self-interactions of the various Higgs bosons, tree-level couplings involving *different* Higgs bosons occur as well. While the expressions describing the couplings between more than two Higgs bosons are quite involved, the ones involving only two Higgs bosons and one weak gauge boson instead can be written compactly as

$$g_{hAZ} = \frac{1}{2} \sqrt{g^2 + g'^2} \cos(\beta - \alpha), \quad (1.35)$$

$$g_{HAZ} = \frac{1}{2} \sqrt{g^2 + g'^2} \sin(\beta - \alpha), \quad (1.36)$$

$$g_{AH^\pm W^\mp} = \mp \frac{i}{2} g, \quad (1.37)$$

$$g_{hH^\pm W^\mp} = \mp \frac{i}{2} g \cos(\beta - \alpha), \quad (1.38)$$

$$g_{HH^\pm W^\mp} = \mp \frac{i}{2} g \sin(\beta - \alpha), \quad (1.39)$$

$$(1.40)$$

where g and g' are the gauge couplings of the $SU(2)_L$ and $U(1)_Y$ groups, respectively, and the symmetry between the h and H couplings is evident. As the observed Higgs boson is often identified with h , Eqs. 1.35 and 1.38 are particularly intriguing as the discovered Higgs boson can be used to search for the decays of the heavier Higgs bosons H^\pm and A as e.g. done in the analysis described in Chap. 5.

The phenomenology of the production and the decay of the various Higgs bosons of the introduced four CP- and flavour-conserving 2HDMs is discussed in the next section with an emphasis on $A \rightarrow Zh$ given Chap. 5 is dedicated to the search for it.

1.3 Searching for an Extended Scalar Sector: Higgs-Boson Phenomenology in pp Collisions

1.3.1 Introduction: Experimental Constraints and Theoretical Assumptions

Since its discovery in the year 2012 by the ATLAS and CMS collaborations at the Large Hadron Collider (LHC) [7, 8], the observed production and decay channels as well as the measurements of the spin and CP properties of the Higgs boson with a mass of 125.04 ± 0.24 GeV [59–61] consolidate its compatibility with the predictions for the Higgs boson of the SM [62–64]. Nonetheless, as up to now only its couplings to a number of SM particles are measured with a limited precision of 10 – 20 % [60, 65, 66], the possibility

remains that it is not the SM Higgs-boson, but part of an extended scalar sector predicted by many theories beyond the SM: it can, for example, be identified with the light neutral, CP-even Higgs boson h of the CP- and flavour-conserving 2HDMs introduced in the previous section.⁸ In that case its couplings to SM particles are expected to be modified with respect to the predictions for the SM Higgs boson by factors that vary for the four different 2HDM types and as function of the parameters α and β (cf. Table 1.3 and Eq. 1.32). Naturally, the measurements addressing the couplings of the observed Higgs boson with pp -collision data at centre-of-mass energies of 7 and 8 TeV already constrain quite tightly the allowed 2HDM parameter space: Fig. 1.1 shows the expected and observed exclusion regions at the 95 % confidence limit (CL) in the $\tan\beta$ - $\cos(\beta - \alpha)$ plane of the four different 2HDM types obtained by the ATLAS collaboration [67]. As expected for a SM-like Higgs boson, $\cos(\beta - \alpha)$ values close to the alignment limit ($\cos(\beta - \alpha) = 0$) are strongly favoured, however, (small) modifications of the SM couplings are still allowed: in particular in the Type-I Model (cf. Fig. 1.1(a)), but also in the others especially for small $\cos(\beta - \alpha)$ and low $\tan\beta$ values (around $\tan\beta = 1$).⁹

Thus, as one of the simplest extensions of the SM, the 2HDMs not only allow to search for and study an extended Higgs sector in a rather generic way - without affecting other parts of the SM and making assumptions on an underlying theory -, but they also particularly highlight the complementarity of precise measurements of the couplings of the discovered Higgs boson to SM particles and direct searches for the predicted additional, heavy Higgs bosons H , A and H^\pm . A complementary search for the pseudoscalar A via its decay into the light CP-even scalar h (with mass 125 GeV) and a Z boson, with a subsequent decay of the h into a b -quark pair, using 13 TeV data collected with the ATLAS experiment is presented in Chap. 5. The $A \rightarrow Zh$ decay was discussed as a particular promising decay channel at the LHC in e.g. Refs. [16, 68, 69], also considering the restrictions due to the observed SM-like Higgs boson.

The phenomenology of the production and the decay of the Higgs bosons of the 2HDMs is in general very rich, given there are four different types of Yukawa couplings varying with α and β and at least four of the five Higgs bosons have unknown masses; usually certain assumptions have to be made, e.g. regarding the mass spectrum, in order to obtain a comprehensive review. Therefore, the following description mainly focuses at motivating the search for $A \rightarrow Zh$ and $h \rightarrow bb$ and studying the production of the A boson in pp collisions at 13 TeV and the decay modes of the A and h bosons assuming (i) the latter is the observed Higgs boson, and thus its mass is determined and fixed to 125 GeV, and (ii) the other Higgs bosons are heavier and degenerate in mass, i.e. $m_A = m_H = m_{H^\pm} \geq 200$ GeV. These choices have two important implications: (i) decays of the h involve only SM particles, and thus the possible decay modes are the same as for the SM Higgs-boson (though with modified branching ratios varying with α and β) and (ii) decays of the other scalars involve in addition to SM particles only the h , i.e. for example the decay $A \rightarrow Zh$ is allowed, while $A \rightarrow ZH$ or $A \rightarrow W^\mp H^\pm$ are not. As the couplings of the (neutral) Higgs bosons to SM particles can be readily expressed in terms of modifying factors with respect to the predictions for the SM Higgs boson and the phenomenology of the production and the decay of the SM Higgs boson is well

⁸While 2HDMs are a wide class of models, in the context of this and all following sections 2HDMs always refer to the four types introduced in the previous section emerging from requiring the Higgs sector to be CP-conserving and that no FCNCs occur at tree level.

⁹For all, but the Type-I Model, there is also a narrow region away from $\cos(\beta - \alpha) = 0$ where the parameter space is not excluded. The reason being that these regions correspond to an inverted sign of the coupling to down-type fermions (τ -leptons, b quarks), leptons (τ -lepton, muon) or b quarks in the Type-II, the Lepton-specific and the Flipped Model, respectively, and the couplings to those fermions are only measured with limited precision. The lack of such a region in the Type-I Model is due to all couplings to the charged fermions are the same.

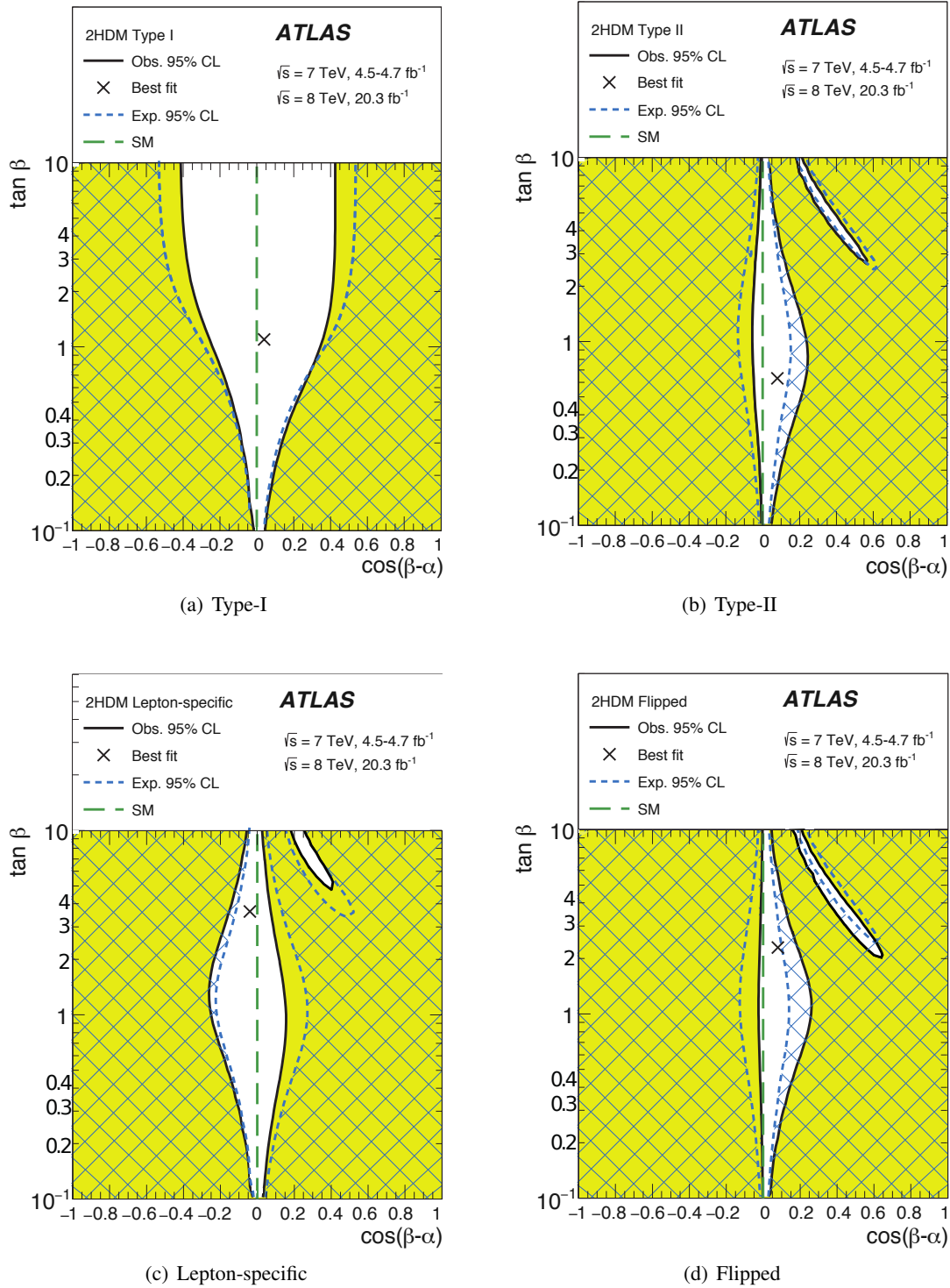


Figure 1.1: Observed and expected exclusion regions at the 95 % CL in the $\cos(\beta - \alpha)$ - $\tan\beta$ plane for the four CP- and flavour-conserving 2HDMs described in Sec. 1.2. The results by the ATLAS collaboration are obtained from fits to the measured rates of the production and the decay of the observed SM-like Higgs boson, which is identified with the light CP-even Higgs boson h , using pp -collision data at centre-of-mass energies of 7 and 8 TeV. The decay modes are assumed to be the same as for the SM Higgs-boson, however the branching ratios are modified according to the 2HDM predictions for couplings to SM particles (cf. Table 1.3 and Eq. 1.32). Also the observed best-fit value is marked by the cross in each plot, close to the SM expectation at $\cos(\beta - \alpha) = 0$. The parameters α and β are assumed to satisfy $0 \leq \beta \leq \pi/2$ and $0 \leq \beta - \alpha \leq \pi$ without loss of generality. Taken from Ref. [67].

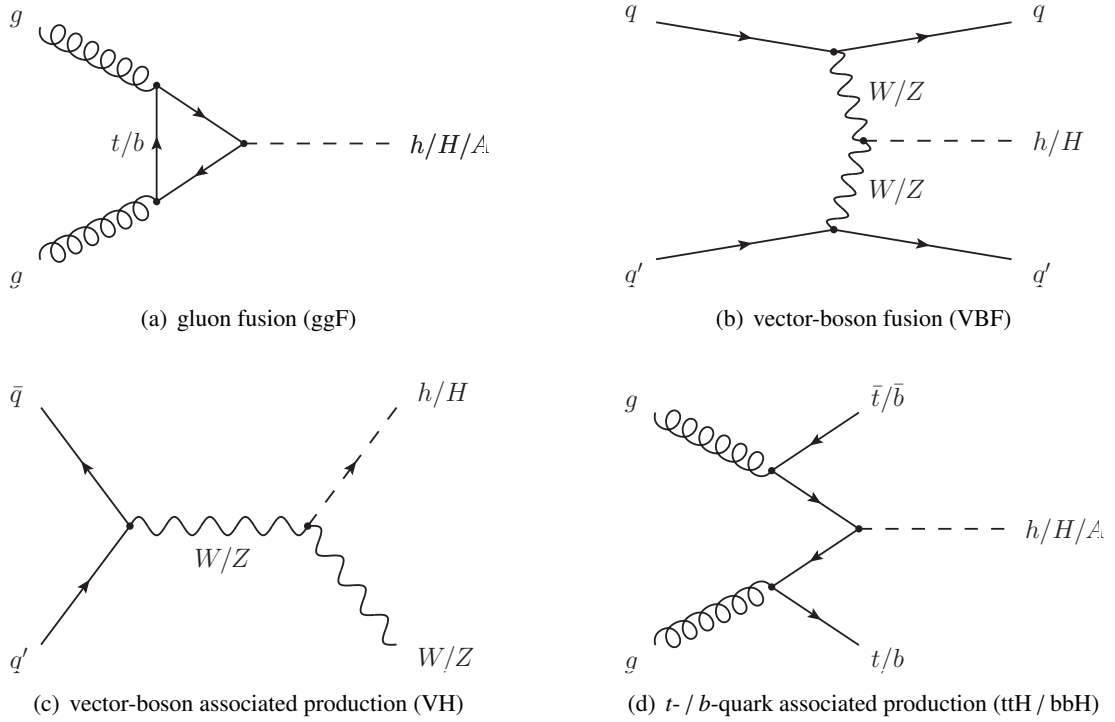


Figure 1.2: Examples of leading-order Feynman diagrams for the main production mechanisms of the SM Higgs-boson as well as the neutral CP-even Higgs bosons h , H and the CP-odd, pseudoscalar A of the CP-conserving 2HDMs in pp collisions: (a) gluon fusion, (b) vector-boson fusion, (c) associated production with a heavy vector boson as well as (d) in association with a heavy quark pair. Since the A does not couple to pairs of vector bosons at tree level (cf. Eq. 1.34), it cannot be produced via (b) and (c).

studied and known, the following presentation of the 2HDM phenomenology builds up on it revealing both commonalities and differences.

1.3.2 Higgs-Boson Production in pp Collisions

In pp collisions, the SM Higgs-boson can be produced via several mechanisms that (might) differ by their cross section. Given its couplings to fermions and vector bosons are proportional to their masses and masses squared, respectively (cf. Sec. 1.1), the dominant production modes involve the heaviest particles of the SM, namely massive gauge bosons as well as top and b quarks. With their Feynman diagrams depicted in Fig. 1.2, these are (a) gluon-fusion production (ggF) via a top- or b -quark loop, (b) vector-boson fusion production (VBF), (c) production in association with a W or Z boson (VH) or (d) with pairs of top or b quarks (ttH / bbH).

From Figure 1.3(a) showing the cross-sections for the main SM Higgs-boson production-modes at a centre-of-mass energy of 13 TeV as a function of the Higgs-boson mass m_H , one can see that ggF is over a wide range by far the dominant production mechanism. Explained by the abundance of gluons with small momentum fractions of the proton (x), it is only replaced as leading mode by the VBF production at very high Higgs-boson masses whose production requires large x values that are mainly carried by the valence

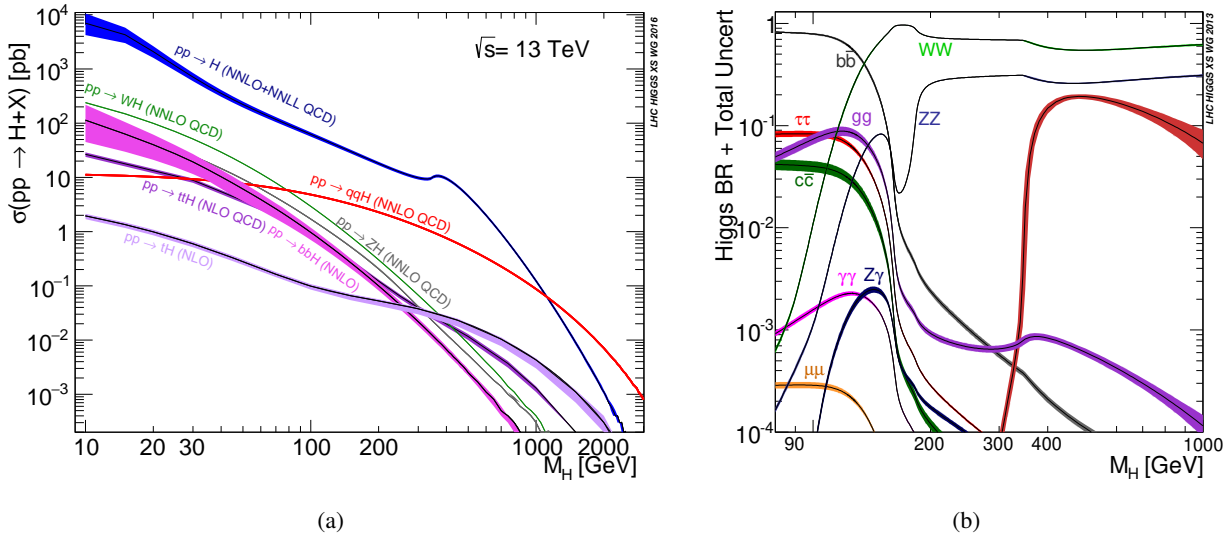


Figure 1.3: (a) Production cross-sections in pp collisions with $\sqrt{s} = 13$ TeV and (b) decay branching ratios of the SM Higgs-boson as function of its mass; uncertainties are indicated by the bands. SM-like couplings as well as narrow-width are assumed; no electroweak corrections are taken into account in Fig. (a). The dark red line in Fig. (b) without a label starting to rise at about 300 GeV is the decay into $t\bar{t}$. Taken from Refs. [70] and [19], respectively.

quarks, as can be seen from Fig. 1.11. For $m_H > 200$ GeV also the production in association with a single top quark (tH) gains in importance, eventually surpassing both VH and ttH/bbH production.

Also the two neutral CP-even Higgs bosons of the 2HDMs are mainly produced via the described mechanisms, but the cross sections vary not just as a function of the considered Higgs-boson mass, but also as function of the parameters α and β that modify their couplings to fermions and vector bosons with respect to the SM (cf. Table 1.3 and Eqs. 1.32-1.33).

Since the A boson does not couple to vector bosons at tree level, it cannot be produced via vector-boson fusion nor in association with vector bosons as the CP-even scalars; this only leaves the associated production with pairs of top and b quarks in addition to the gluon-fusion production. While the associated production with top quarks generally contributes to the total cross section at the sub-percent level, the production in association with b quarks (bbA) can become significant and even dominant for large values of $\tan\beta$: Figure 1.4 shows the cross sections of the gluon-fusion and bbA production modes in the $\cos(\beta-\alpha)$ - $\tan\beta$ plane for a benchmark mass of $m_A = 300$ GeV for the four 2HDM types. Although the cross sections are constant for varying $\cos(\beta-\alpha)$ values, given the A boson coupling modifiers to fermions are only functions of $\tan\beta$, this two-dimensional presentation is chosen to simplify the comparison with the results of the performed search presented in Chap. 5.8 for the same A -boson mass. While the Lepton-specific and the Flipped Models generally differ from the Type I and Type II, respectively, in terms of the modifying factors to the lepton couplings, they here show the same behaviour because the contribution of leptons in the loop of the gluon-fusion production is unaffected by the differences [16]. In the case of the Type-I / Lepton-specific Model both the couplings to up- and down-type quarks are modified with a factor $\cot\beta$, and thus also the cross sections for both production modes decrease rapidly over several orders of magnitude for increasing $\tan\beta$ values, as can be seen from Figs. 1.4(a) and 1.4(c). In the Type-II / Flipped

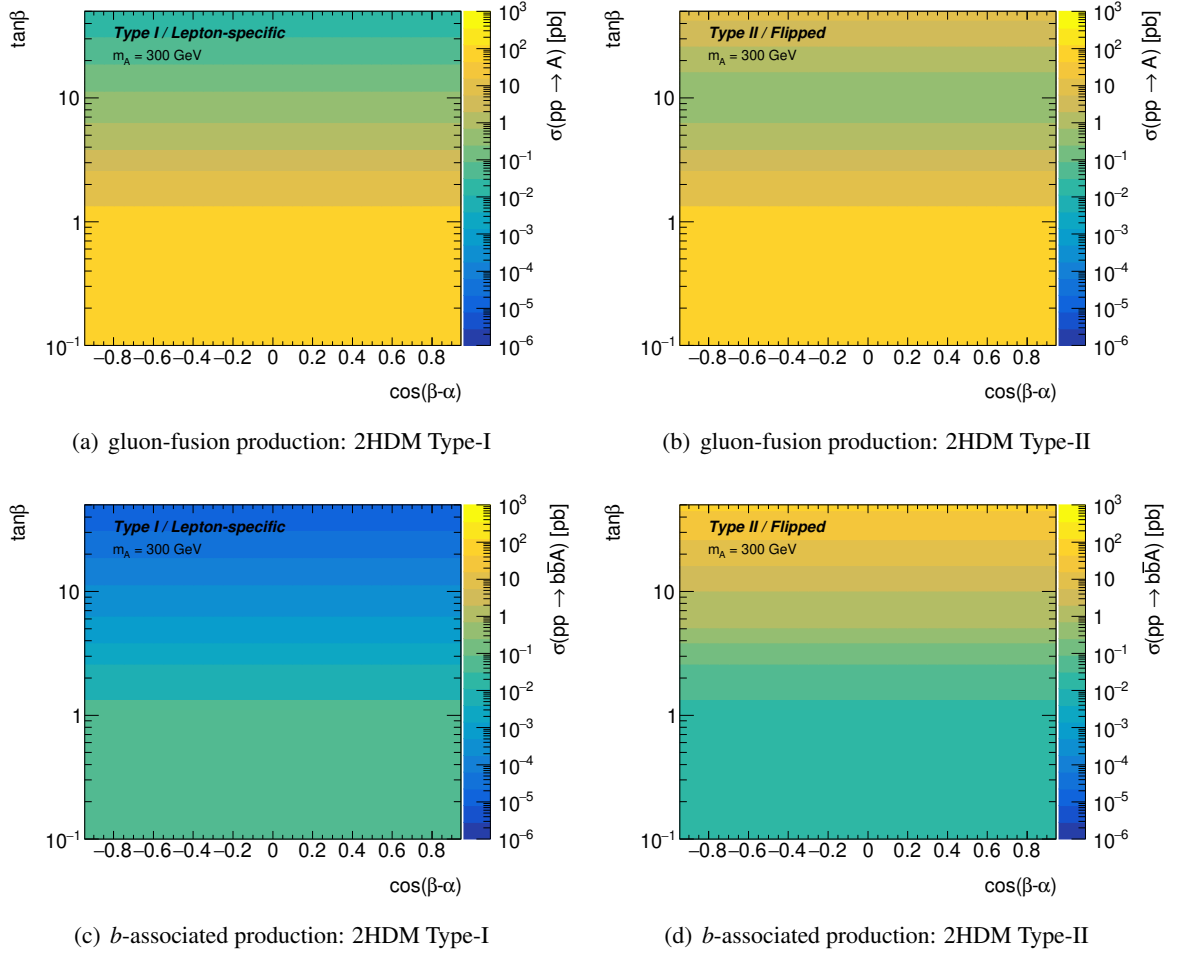


Figure 1.4: Production cross-sections in pp collisions with $\sqrt{s} = 13$ TeV for the pseudoscalar A of the CP- and flavour-conserving 2HDM with a mass of 300 GeV as function of $\cos(\beta - \alpha)$ and $\tan\beta$ for gluon-fusion production in (a) the Type-I / Lepton-specific and (b) the Type-II / Flipped Model and b -associated production in (c) the Type-I / Lepton-specific and (d) the Type-II / Flipped Model. The cross sections are calculated in the five-flavour scheme considering up to next-to-next-to-leading order (NNLO) QCD corrections using SUSHI [71–74]. As explained in the text their size and variation as function of $\cos(\beta - \alpha)$ and $\tan\beta$ is the same in the Type-I and the Lepton-specific Model and the Type-II and the Flipped Model, respectively.

Model the couplings to up-type quarks are also modified with a factor $\cot\beta$, while the modifiers for down-type quarks scale with $\tan\beta$, leading to enhanced couplings with increasing $\tan\beta$ values and the cross section for bbA production increases significantly towards large $\tan\beta$ values as shown in Fig. 1.4(d). The behaviour of the gluon-fusion cross-section in those models is somewhat more complex as can be seen from Fig. 1.4(b), reflecting the opposite trends of the top- and b -quark loop contributions with increasing $\tan\beta$ values: the former decreases, while the latter increases just as expected from the $\tan\beta$ -dependence of the respective coupling modifiers; though the increase of the b -quark loop contribution is smaller compared to the bbA production because of an additional dependence of the loop contribution on the virtual quark mass favouring heavy particles [75, 76]. Therefore, while in the case of the Type-I / Lepton-specific Model the bbA contribution to the total cross section is constantly small across the full $\tan\beta$ range, in the case

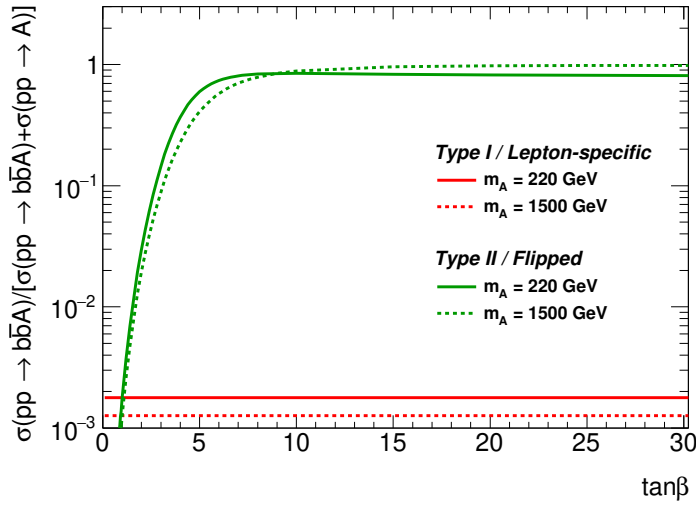


Figure 1.5: Relative contribution of b -associated production to the total A -boson production cross-section as function of $\tan\beta$ for the Type-I / Lepton-specific and Type-II / Flipped 2HDM models for two mass points, $m_A = 200, 1500$ GeV. The total cross section is approximated by the sum of the contributions of the gluon-fusion and b -associated production. The cross sections are calculated in the five-flavour scheme considering up to next-to-next-to-leading order (NNLO) QCD corrections using `SUSHI` [71–74]. As explained in the text they do not depend on $\cos(\beta - \alpha)$, but show the same $\tan\beta$ dependence in the Type-I and the Lepton-specific Model and the Type-II and the Flipped Model, respectively.

of the Type-II and the Flipped Model it grows rapidly with increasing $\tan\beta$ values becoming quickly the dominant contribution: this can be seen from Fig. 1.5, showing the bbA fraction as function of $\tan\beta$ for the different model types and two reference mass points; the behaviour depends only mildly on the A mass. Experimentally, the b -associated production provides a specific signature that can be exploited to better distinguish the signal over an otherwise overwhelming background contribution with respect to the gluon-fusion production as e.g. discussed in more detail in Chap. 5.

Let it be briefly mentioned for completeness, that at the LHC the charged Higgs bosons are produced predominantly either through the decay of or in association with a top quark, depending on whether the considered Higgs-boson mass is below or above the top mass; a complementary production mode is quark annihilation involving c and s quarks [77].

1.3.3 Higgs-Boson Decays

In the SM, the partial decay width of the Higgs boson with a given mass depends only on the square of its couplings to the decay products and the accessible phase space. Given the proportionality of the couplings to fermions and gauge bosons to their masses (squared, in the case of the latter), decays into the heaviest particles (kinematically) allowed are preferred; this is reflected in the branching ratios shown for the dominant Higgs decays as a function of the Higgs-boson mass in Fig. 1.3(b). Decays to massless particles, such as photons and gluons, still occur via loop processes involving heavy, coloured or charged particles, e.g. top quarks or W bosons; in the same way also the decay to a photon and Z boson ($Z\gamma$) is possible. Since these loop-induced decays are suppressed by additional powers of the electroweak or strong coupling constants, their contribution to the total Higgs decay width is only relevant for Higgs-boson masses

below about 130 GeV [18]. At masses above the kinematic threshold, the decays into pairs of real, massive vector bosons become dominant, but already below, where at least one in the pair needs to be off-shell, the contribution is significant. This is also the case for the observed Higgs boson: at a mass of about 125 GeV a number of decay modes have significant contributions, though the by far dominant one is the decay into a b -quark pair (57.7%), followed by the decay into a pair of W bosons (21.5%). The decay into a pair of gluons has the third highest branching ratio (8.6%), but is experimentally hardly accessible (at the LHC); together with the decay into a pair of τ -leptons (6.3%) those four modes are covering 94% of all possible decays. Despite their small branching ratios, the decays into pairs of photons (0.23%) and Z bosons (2.6%) played a crucial role in the Higgs-boson discovery: provided the Z bosons are reconstructed in their decays to electron and muon pairs, both decay modes not only allow a complete reconstruction of the Higgs-boson candidates, but also provide excellent mass resolution (and thus are often referred to as the “golden channels”).

As for the production cross-sections, also the branching ratios for the various decay modes of the Higgs bosons in the 2HDMs do not simply depend on the masses of the Higgs bosons and the possible decay products (which depend on the chosen mass spectrum) as in the SM, but are further functions of the coupling-modifying parameters α and β (cf. Table 1.3 and Eqs. 1.32-1.33).

By identifying the light CP-even Higgs boson with the observed Higgs boson, i.e. fixing its mass to 125 GeV, and given the chosen mass spectrum, also in most of the parameter space of the four 2HDMs h decays preferentially into a pair of b quarks, as can be seen from Fig. 1.6 showing the $h \rightarrow bb$ branching ratio as a function of $\cos(\beta - \alpha)$ and $\tan\beta$. In particular in the Type-II and the Flipped Model, shown in Fig. 1.6(b) and 1.6(d), the branching ratio becomes very large at high $\tan\beta$ values due to the enhanced couplings to down-type quarks. However, there are also regions in all four models, where the decay is strongly suppressed: the narrow regions that are present in all four models and appear at the same $\cos(\beta - \alpha)$ - $\tan\beta$ values in the Type-I and Lepton-specific Model as well as the Type-II and Flipped Models are caused by the couplings to down-type quarks vanishing (in the Type-I Model this case is referred to as *fermiophobic limit*, as not just the couplings to down-type quarks vanish, but also to all other fermions). Although the Lepton-specific Model has the same couplings to down-type quarks as the Type-I Model, the $h \rightarrow bb$ branching ratio is strongly suppressed at high $\tan\beta$ values, except close to the alignment limit (cf. Fig. 1.6(a) vs. Fig. 1.6(c)); this is explained by the enhancement of the couplings to leptons, favouring the decay to pairs of τ -leptons.

Which of the accessible decay modes of the other two neutral Higgs bosons H and A are preferred, depends as in the SM on their masses (and the mass spectrum that is fixed here). In the case of the former, the same decay modes as for the SM Higgs-boson shown in Fig. 1.3(b) are possible, as well as the decay to pairs of light CP-even scalars h ; this mode often dominates over the decay into pairs of vector bosons when kinematically accessible [69], but vanishes in the alignment limit (i.e. $\cos(\beta - \alpha) \rightarrow 0$) due to the coupling g_{Hhh} being proportional to $\cos(\beta - \alpha)$.

In the case of the pseudoscalar A , not all the decay modes of the SM Higgs-boson are allowed, since it does not couple to pairs of vector bosons (at tree level). The decay to Zh thus often dominates when kinematically accessible (i.e. ≥ 200 GeV); even close to the alignment limit, where it eventually vanishes due to the coupling being proportional to $\cos(\beta - \alpha)$. This is in particular true (and well known) below the threshold, where the decay into a top-quark pair becomes kinematically accessible and often dominant

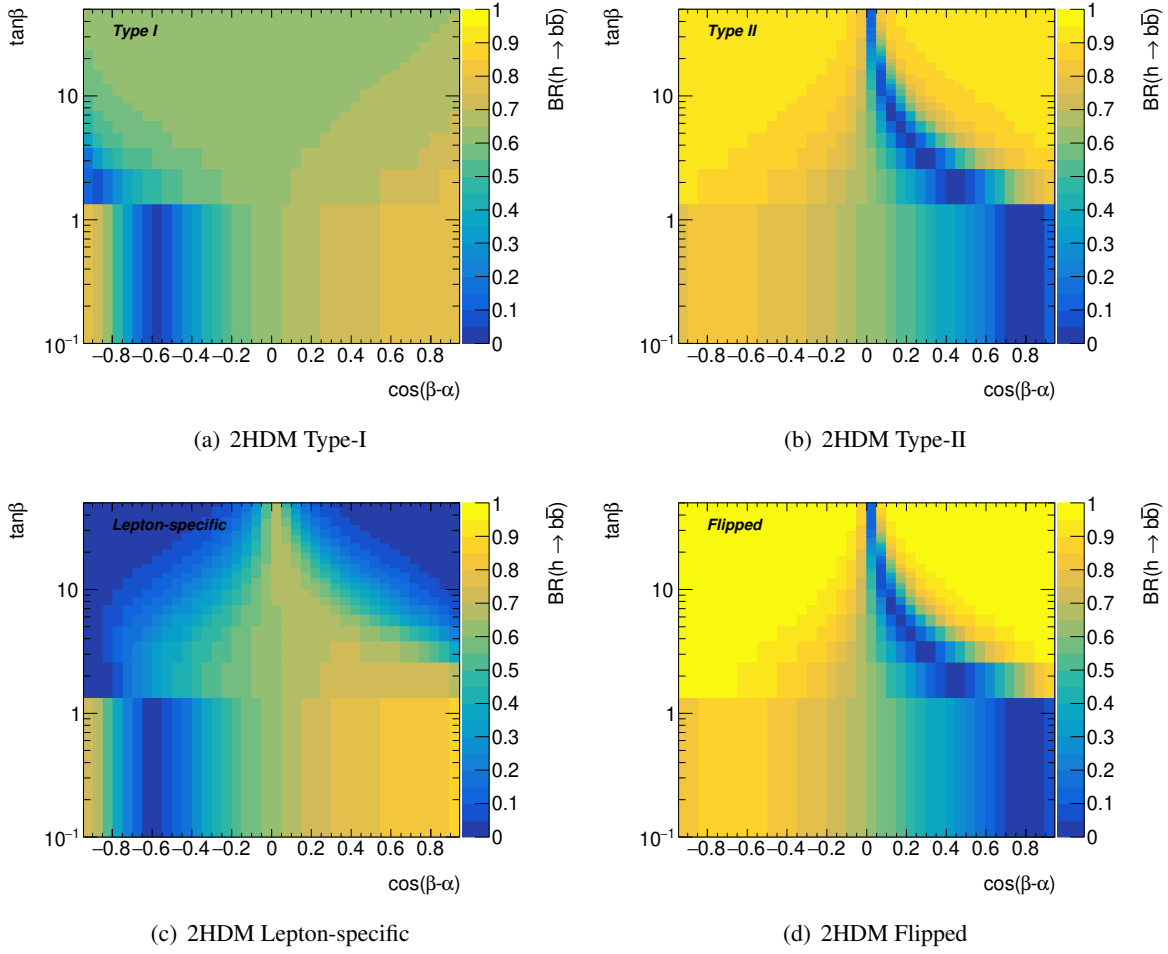


Figure 1.6: Branching ratio of the decay of the light CP-even Higgs boson h to a b -quark pair as function of $\cos(\beta - \alpha)$ and $\tan\beta$ in the (a) Type-I, (b) Type-II, (c) Lepton-specific and (d) Flipped Model. Identified with the observed Higgs boson its mass is fixed to 125 GeV; as $m_A = m_H = m_{H^\pm} \gg 125$ GeV is assumed only decays to SM particles are allowed - the same as for the SM Higgs-boson of the same mass (cf. Fig. 1.3(b)). The branching ratio is calculated with 2HDMC [78, 79].

($m_A \sim 350$ GeV); but not just, as can be seen from Fig. 1.7 showing the branching ratios of the leading and/or realistically measurable decay modes of the A boson in the four model types for two reference values of $\tan\beta$ close to the alignment limit (i.e. for $\cos(\beta - \alpha) = 0.1$).¹⁰ Already at low, but even more so at intermediate and high $\tan\beta$ values, the branching ratio of the decay to Zh is at high A masses either comparable to the one of the decay to $t\bar{t}$ or dominating. This is because (i) the A coupling to up-type quarks is suppressed at high $\tan\beta$ values in all four models (cf. Table 1.3), and (ii) the respective enhancement of the couplings to down-type quarks and/or leptons in the Type-II, Lepton-specific and Flipped Models favouring the decays to $b\bar{b}$ (Type II and Flipped) and $\tau^+\tau^-$ (Lepton-specific) rather affects the low(er)-mass range. Only in the Type-II and Flipped Models is the decay into $b\bar{b}$ already at low $\tan\beta$ values and small A masses, below the $t\bar{t}$ threshold, at least comparable, but mostly dominating over the decay into

¹⁰The decay modes $c\bar{c}$, $Z\gamma$, $\mu^+\mu^-$ and to pairs of gluons (g) are neglected since deemed to either have too small branching ratios or too large backgrounds; the latter in particular applies to the decay into gg .

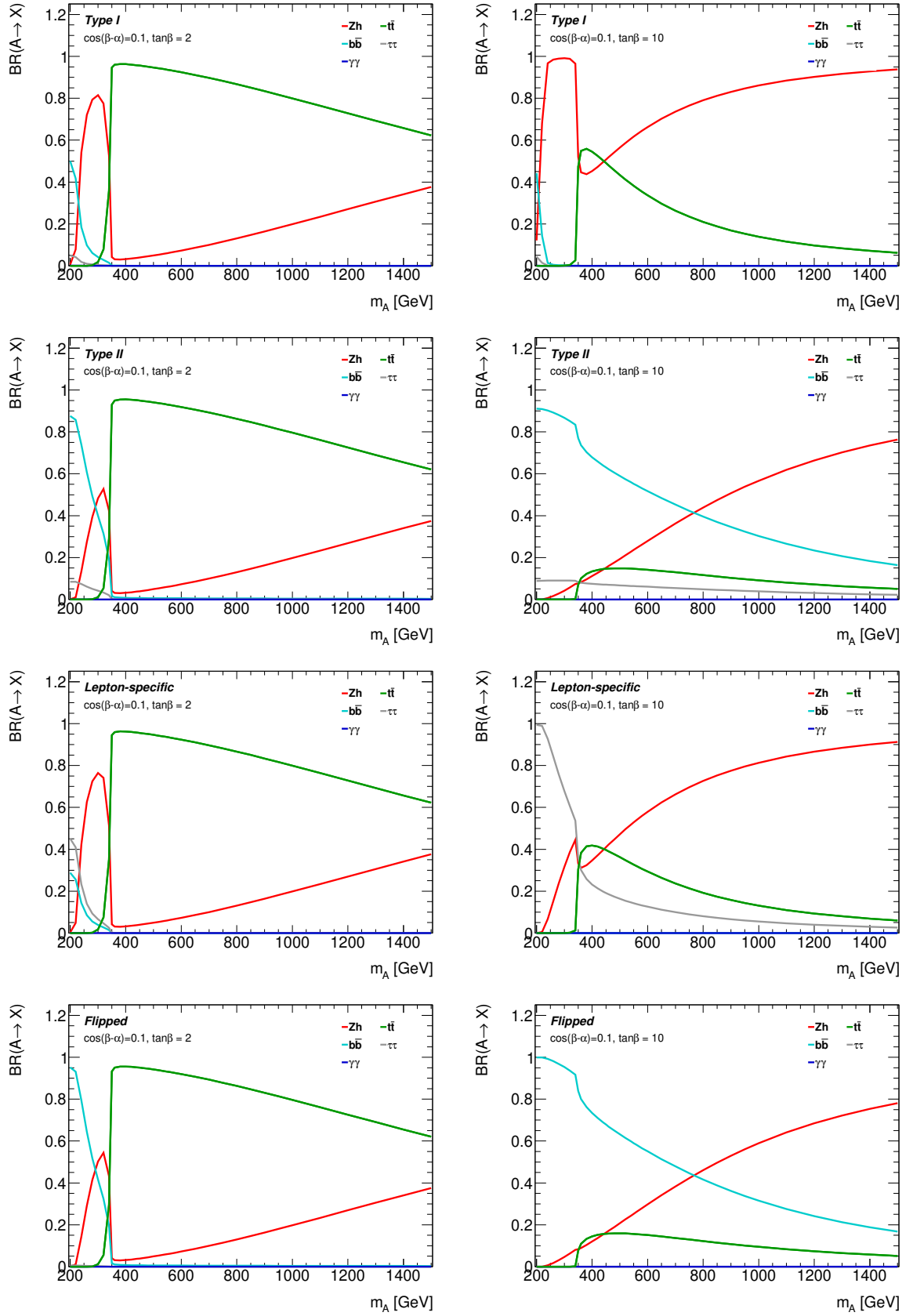


Figure 1.7: Branching ratio of the dominant and/or realistically measurable decays of the pseudoscalar Higgs boson A of the CP- and flavour-conserving 2HDMs as function of its mass for two reference values of $\tan\beta$, $\tan\beta = 2$ (left) and $\tan\beta = 10$ (right), close to the alignment limit (i.e. for $\cos(\beta - \alpha) = 0.1$). Assuming further $m_A = m_H = m_{H^\pm} \gg m_{h_i} = 125$ GeV, only the decays to Zh and pairs of top quarks ($t\bar{t}$), b quarks ($b\bar{b}$), τ -leptons ($\tau\tau$) and photons ($\gamma\gamma$) are considered. The branching ratios are calculated with 2HDMC [78, 79].

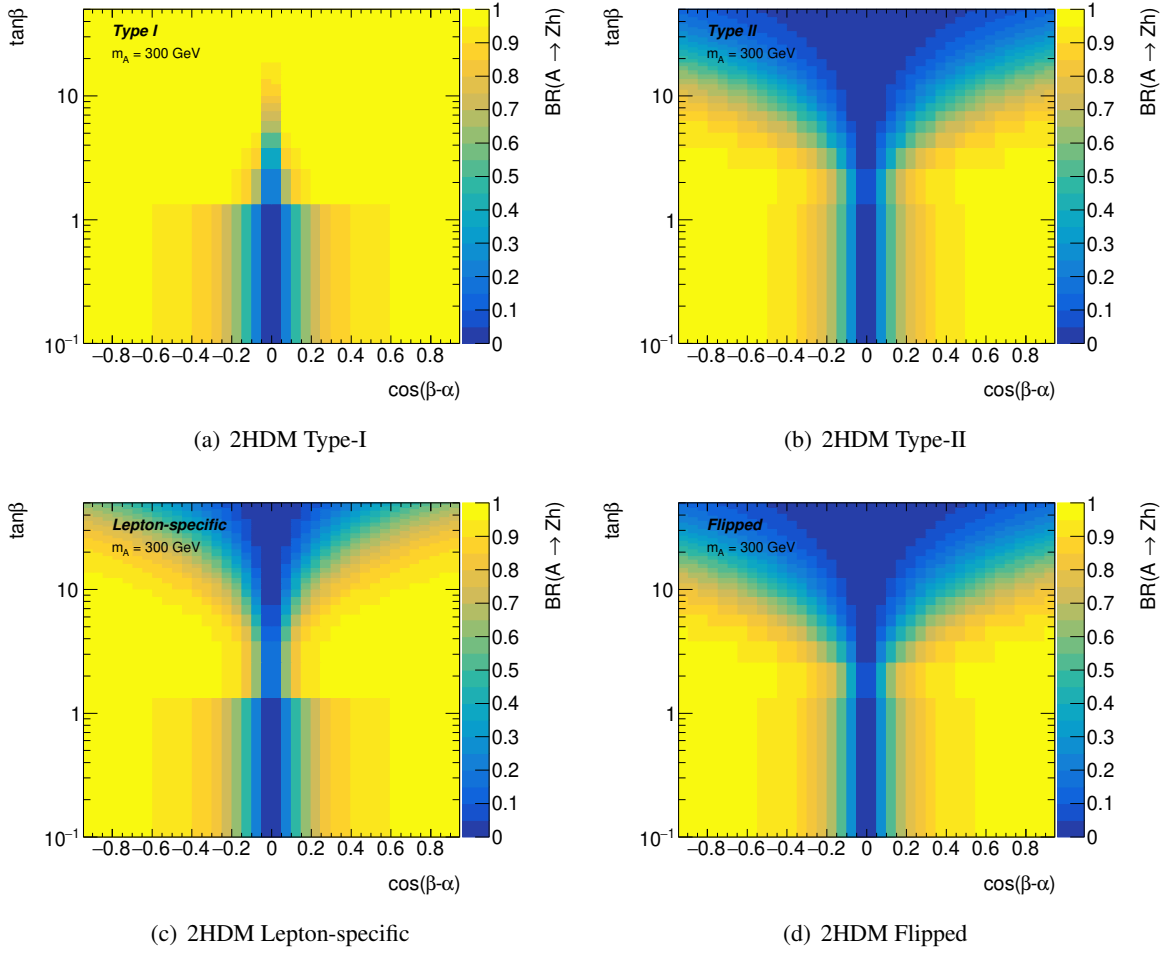


Figure 1.8: Branching ratios of the decay of the pseudoscalar Higgs boson A of the CP- and flavour-conserving 2HDMs into Zh as function of $\cos(\beta - \alpha)$ and $\tan\beta$ in the (a) Type-I, (b) Type-II, (c) Lepton-specific and (d) Flipped Model. In all four models the branching ratio vanishes for $\cos(\beta - \alpha) \rightarrow 0$ (cf. Table 1.3); which is just not properly displayed in (a) due to resolution effects. It is assumed that $m_A = m_H = m_{H^\pm} = 300 \text{ GeV} > m_h = 125 \text{ GeV}$. The branching ratio is calculated with 2HDMC [78, 79].

Zh . While for very low masses this is an expected effect driven by the available phase space, at masses around 300 GeV, where the decay into Zh is generally kinematically preferred, this result is determined by the A coupling to Zh rapidly decreasing towards the alignment limit. This can be seen from Figure 1.8, which shows the branching ratio of the decay to Zh in the $\cos(\beta - \alpha)$ - $\tan\beta$ plane for $m_A = 300 \text{ GeV}$ in the four different models: it mainly becomes small close to the alignment limit, i.e. for $\cos(\beta - \alpha) \leq 0.1$, and, as discussed already before, also at high values of $\tan\beta$, especially in the Type-II and the Flipped Model, but also in the Lepton-specific; in the remaining parameter space on the contrary the branching ratio is large and the decay to Zh clearly dominates the total decay width, in particular in the Type-I Model (cf. Fig. 1.8(a)).

Let it be briefly mentioned, that the possible decay modes of the charged Higgs boson H^\pm involving SM particles are combinations of up- and down-type quarks or charged leptons and neutrinos (i.e. basically the same decay modes as for W bosons with preferred decays to the heavy particles); in the low mass

range below the top mass $H^- \rightarrow \tau\bar{\nu}$ is the preferred decay, above $H^- \rightarrow \bar{t}b$. Also the decay $H^\pm \rightarrow W^\pm h$ involving the light neutral scalar is allowed in the present scenario and interesting in regions where the other decays are parametrically suppressed, though not close to the alignment limit due to vanishing couplings (cf. Eq. 1.38).

1.3.4 Summary and Conclusions

The Higgs-boson production and decay phenomenology in the SM, but even more so in the considered 2HDMs, is very rich. In the case of the latter it does not only depend on the considered Higgs boson and its mass, but also on the chosen mass spectrum of the various Higgs bosons as well as the model type and the parameters α and β , which modify the couplings with respect to the SM. Thus, the sensitivity of a search for a 2HDM Higgs boson in a certain decay mode varies even after fixing the mass spectrum still as function of its mass, for the different model types and across the parameter space: just due to the varying expected signal yield, not even considering various means of SM background suppression. In the case of the search for $A \rightarrow Zh$ with $h \rightarrow b\bar{b}$ presented in Chap. 5, one can see from Figs. 1.4, 1.7 and 1.6 that for example there is no or only very limited sensitivity (i) close to the alignment limit because of the vanishing g_{hAZ} coupling in all of the four 2HDMs, (ii) in narrow regions, mainly at low $\tan\beta$ and far away from the alignment limit, due to the coupling g_{hbb} vanishing, (iii) in the Type-I Model at high $\tan\beta$ values, despite the large branching ratios for the decays $A \rightarrow Zh$ and $h \rightarrow b\bar{b}$ in most of the parameter space, due to the suppressed cross sections both for gluon fusion and b -associated production and (iv) in the Lepton-specific Model at intermediate and high $\tan\beta$ due to the enhanced couplings to (τ -)leptons.

1.4 Describing and Simulating pp -Collision Events

The measurements described in this thesis are based on the analysis of high-energy proton-proton (pp) collision events provided by the Large Hadron Collider and detected by the ATLAS experiment. The understanding and description of the final states occurring in such events is complicated and poses a challenging theoretical problem; even more so given that the colliding protons are not elementary, but composite particles made up of quarks and gluons. Figure 1.9 indicates schematically for the case of multijet production the complexity and various aspects of a pp -collision event: a multitude of particles with momenta ranging over a large range are involved. Even if the *hard-scatter* event is not mediated by the strong force, the description of pp -collision events is determined by the theory and phenomenology of QCD (cf. Sec. 1.1).

Based on the concept of factorisation, the description of such events is broken down according to the scales of momentum transfer Q involved into various parts belonging to two different regimes: hard processes with large Q , such as the *hard-scatter event*, are described by means of perturbation theory; non-perturbative, soft processes with small Q , such as the *parton density* of the proton and the *fragmentation* of the emerging partons, by models, whose parameters need to be determined by the data. Initial- and final state radiation (ISR/FSR) of gluons complicate the description in addition, as does the underlying event evoked by the beam remnants. Finally, also the decays of unstable particles produced in the event needs to be modelled to obtain a complete picture. The exploitation of *Monte-Carlo techniques* to deal with the computation of the various aspects, leads to the concept of *Monte-Carlo event generators* for computer simulation, also for the expected events as a whole.

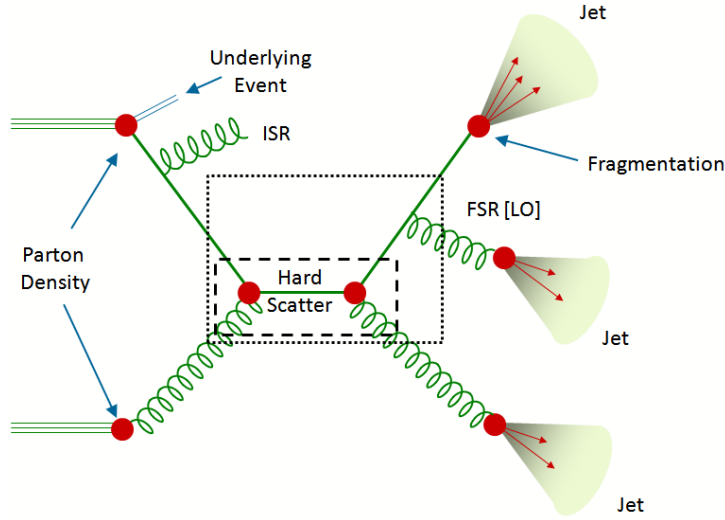


Figure 1.9: Schematic illustration of the complexity of a hard proton-proton collision event: not only the hard-scatter process, but also initial- and final-state radiation lead to jet production via fragmentation; accompanied by the underlying event due to the beam remnants. Taken from Ref. [80].

1.4.1 Implications of the Running of the Strong Coupling

Other than its name suggests, the strong coupling constant α_s in fact varies as a function of the energy scale (or the momentum transfer) Q of the process under consideration; an effect also referred to as *running*.¹¹ While the absolute value of $\alpha_s(Q^2)$ at a certain energy scale Q cannot be predicted, as one of the free parameters of the SM, and needs to be determined from data [81], its evolution with Q is given by the *renormalisation group equation* (RGE) and can be studied using perturbation theory in α_s . The result that the strong coupling decreases with increasing Q is referred to as *asymptotic freedom*, a common feature of non-abelian gauge theories [31, 82]. In contrast, the strong coupling increases with decreasing Q ; however, it is not yet mathematically proven that this behaviour of α_s leads to the phenomenon of *confinement*, i.e. the empiric fact that only colourless *hadrons*, e.g. *protons*, are observed, while coloured quarks and gluons are not.

In particular, by solving the RGE in lowest approximation a constant $\Lambda_{\text{QCD}} \approx 200 \text{ MeV}$ appears that defines the scale, where $\alpha_s(Q^2)$ nominally diverges. Thus, only at high energies with $Q \gg \Lambda_{\text{QCD}}$, where $\alpha_s(Q^2) \ll 1$, the perturbative expansion in $\alpha_s(Q^2)$ constitutes a valid tool for the calculation of observables; consequently for processes with energies $Q \lesssim \Lambda_{\text{QCD}}$ parametric models need to be employed. While Λ_{QCD} is not too well defined, being a non-perturbative quantity itself, the order of its magnitude is still meaningful: it is closely connected to the scale of hadron masses.

1.4.2 Factorisation

In particular when calculating the cross section for a certain process in a hadron-hadron collision, the difficulty arises that different energy scales Q are involved. *Factorisation* allows to break down the calculation into a high-energy part that can be computed using perturbation theory and a low-energy part that is described by tunable models. Thus, according to *collinear factorisation theorems* [83–85] the cross section

¹¹Sometimes “running” is reserved for the effect that α_s depends on the unphysical renormalisation scale μ_R discussed in Sec. 1.4.3.

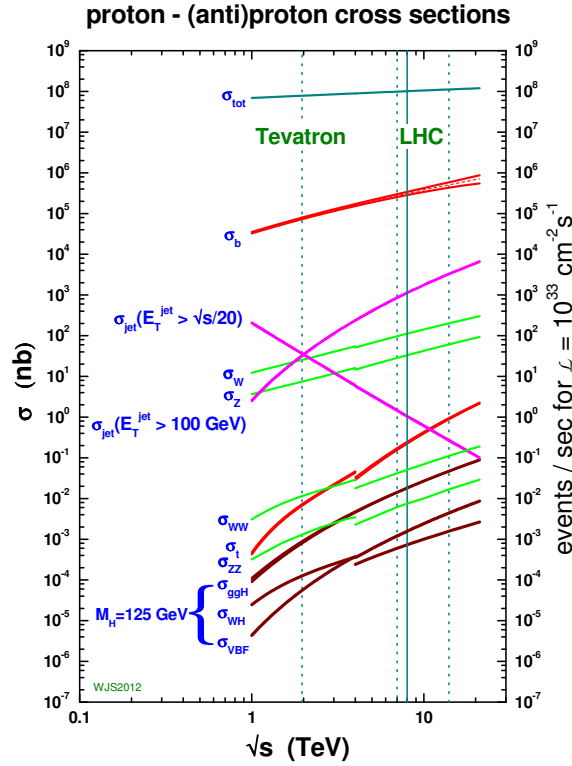


Figure 1.10: Production cross-sections for selected processes occurring in proton-(anti)proton collisions as function of the centre-of-mass energy. Except the total cross section (σ_{tot}) which is computed based on a parametrisation provided by the Particle Data Group, the cross sections are calculated at NLO or NNLO in QCD (using corresponding MSTW2008 parton distribution functions (cf. Sec. 1.4.4)). Switching from proton-antiproton to proton-proton collisions at $\sqrt{s} = 4$ TeV results for some of the cross sections in a discontinuity. Taken from Ref. [86].

for a scattering process $pp \rightarrow n$ (in which only non-coloured particles arise) can be written as

$$\sigma_{pp \rightarrow n} = \sum_{i,j} \int_0^1 \int_0^1 dx_i dx_j f_i(x_i, \mu_F) f_j(x_j, \mu_F) \hat{\sigma}_{ij \rightarrow n}(x_i, x_j, \mu_F), \quad (1.41)$$

where the sums run over all *partonic* constituents, i.e. quarks and gluons, of the protons p and $\hat{\sigma}_{ij \rightarrow n}$ is the partonic cross section for the production of the final state n by partons of type i and j , the hard-scatter event, that is perturbatively calculable (cf. Sec. 1.4.3).¹² The *parton distribution function* (PDF) $f_{i(j)}(x_{i(j)}, \mu_F)$ describes the probability to find a parton of type $i(j)$ carrying a fraction $x_{i(j)}$ of the longitudinal momentum of the proton probed at an energy scale μ_F (cf. Sec. 1.4.4). The PDFs at a certain μ_F are not calculable in perturbation theory and are required to be determined in measurements; however they are considered universal and once determined can be applied to any process. Thus, the non-physical, arbitrary *factorisation scale* μ_F defines the scale at which the high energy, perturbative part is separated from the low energy, non-perturbative one.

Similarly, if in the scattering of partons i and j coloured particles arise, their transition into hadronic

¹²In the context of this section, “final state” also refers to intermediate states which eventually transition into a final state due to the instability of involved particles.

final states is described by the non-perturbative process of *fragmentation* or *hadronisation* (cf. Sec. 1.4.5). In particular, *fragmentation functions* $F_k(z_k, \mu_F)$ parametrise the probability that a parton k hadronises into a hadron h_k carrying a fraction z_k of the parton momentum. As is the case for PDFs also the $F_k(z_k, \mu_F)$ need to be modelled and tuned in dedicated measurements, and are considered universal, i.e. they can be used to calculate any process of interest.

Figure 1.10 shows the production cross-sections for a variety of proton-(anti) proton collision processes, as they occur(ed) at the Tevatron collider or the LHC, as function of the centre-of-mass energy. Based on the described factorisation, they are calculated at next-to-leading (NLO) or next-to-next-to-leading (NNLO) order in perturbation theory using PDFs with matching precision. The only exception is the total cross section, which, involving soft processes, cannot be determined perturbatively. The figure shows drastically the different orders of magnitude between the cross sections of the various processes: in particular between processes initiated by the strong interaction and e.g. Higgs-boson production.

1.4.3 The Partonic Cross Section

As mentioned in the previous section, the partonic cross section $\hat{\sigma}_{ij \rightarrow n}(x_i, x_j, \mu_F)$ can be computed by perturbative expansion in the strong coupling constant provided μ_F is chosen reasonably large, i.e. $\mu_F \gg \Lambda_{\text{QCD}}$, and thus $\alpha_s(\mu_F^2)$ sufficiently small. There are different approaches to perform the actual, non-trivial calculation, two of which, that are also exploited in Monte Carlo generators, are briefly introduced in the following.

Fixed-order calculations: matrix elements

According to *Fermi's golden rule* the partonic cross section for the process $ij \rightarrow n$ can be expressed as

$$\hat{\sigma}_{ij \rightarrow n}(\mu_F) = \int d\Phi_n \frac{1}{2\hat{s}} |\mathcal{M}_{ij \rightarrow n}(\Phi_n; \mu_F)|^2, \quad (1.42)$$

where $\mathcal{M}_{ij \rightarrow n}$ is the matrix element describing the transition, Φ_n is the phase-space element of the final state n , and \hat{s} is the square of the parton centre-of-mass energy ($\hat{s} = x_i x_j s$ with \sqrt{s} being the hadron collider centre-of-mass energy). The matrix element can be calculated perturbatively at fixed order in the strong coupling α_s via summation of *Feynman diagrams* obtained from the QCD Lagrangian using *Feynman rules*. Only for the simplest cases, the phase-space integration can be carried out analytically; usually it is accomplished numerically by employing Monte Carlo sampling techniques.

Each additional order in α_s entails the involvement of one additional parton, either in the form of a *real emission* or in the form of a *virtual contribution*, appearing as a *loop* in Feynman diagrams describing the emission and subsequent absorption of a parton; the latter leads to the same n particle final state as the lower order, and thus to quantum-mechanical interference effects. Already at NLO the calculation becomes complicated because of the occurrence of three types of divergences: (i) *ultraviolet (UV) divergences* arising from the integration of the momentum in the loops up to infinity, (ii) *infrared divergences* from soft virtual or real particles reaching zero momentum, and (iii) *collinear divergences* from collinear emissions of massless partons. The latter two types of divergences reflect the limitations of a truncated fixed-order

perturbative expansion at the corners of the phase space; they motivate the exploitation of the *parton-shower* approach described below.

The UV divergences are treated by regularising the singularities (temporarily), usually using *dimensional regularisation*, and renormalising the parameters and fields of the theory, i.e. absorbing the divergences into their redefinitions. In the process an unphysical, arbitrary scale μ_R , referred to as *renormalisation scale*, arises on which the renormalised quantities depend, that is e.g. $\alpha_s(\mu_F^2, \mu_R^2)$ and $\mathcal{M}_{ij \rightarrow n}(\Phi_n; \mu_F, \mu_R)$.

According to the Bloch-Nordsieck [87] and Kinoshita-Lee-Nauenberg theorems [88, 89] the virtual and real, both infrared and collinear, divergences cancel at each order in perturbation theory when computing inclusive or *infrared- and collinear-safe (IRC)* observables. However, since they are related to different phase spaces (n vs $n + 1$ particle final states), it is not straightforward to arrange this cancellation practically and several strategies have been developed to deal with this difficulty; one common approach is to use *infrared subtraction* methods (e.g. Ref. [90]). An observable is IRC-safe, if it is insensitive to the emission of soft and collinear gluons, such as the momentum of a *jet* reconstructed with the anti- k_r algorithm (cf. Sec. 3.3.1). Exclusive hadronic cross sections, the parton multiplicity or the energy of the hardest particle in an event, however, are not IRC-safe observables. When computing non-IRC observables, only the virtual and real infrared divergences cancel, while the collinear divergences do not. In this case, which always applies to the exclusive initial state, the collinear divergences are treated following a similar strategy as for the UV divergences: they are regularised, using e.g. dimensional regularisation, and then absorbed into a redefinition of the PDFs (and fragmentation functions if applicable), which as a result become dependent of the factorisation scale μ_F that arises in the process. The corresponding renormalisation group equation (cf. Sec. 1.4.1) allowing to describe the scale evolution of the PDFs and fragmentation functions perturbatively is the Dokshitzer–Gribov–Lipatov–Altarelli–Parisi (DGLAP) equation [91–93].

Thus, in order to deal with the UV and collinear divergences, two non-physical scales are introduced. The dependence of observables on the choice of these scales naturally decreases with increasing accuracy of the calculations; it eventually vanishes when all-orders of the perturbative series are considered. A common choice is $\mu_F^2 = \mu_R^2 = Q^2$, where Q^2 represents the hard scale of the process under consideration; e.g. $Q^2 = M^2$ for the production of a resonance with mass M , or $Q^2 = p_T^2$ in the case of the pair-production of massless particles with transverse momentum p_T . The impact of unknown higher-order corrections on the predictions is usually estimated by performing variations of the nominal scales; typically the effect of halving or doubling the nominal scale is assessed.

All multipurpose event generators, such as PYTHIA [22, 94], Herwig++ [95] and SHERPA [96], provide leading-order (LO) matrix elements for a comprehensive list of SM and beyond-the-SM $2 \rightarrow 1/2/3$ processes. Dedicated matrix-element and phase-space generators, such as ALPGEN [97], COMIX [98] or MADGRAPH/MADEVENT [99, 100], provide full tree-level calculation with a high, though fixed number of partons. Also the computation of NLO matrix elements is automatised, e.g. by AMC@NLO [101], POWHEG-Box [102–105] or BLACKHAT [106]. Next-to-next-to leading order (NNLO) calculations exist for total cross sections of a number of processes, e.g. top-quark or diboson production; few processes, such as inclusive Higgs-boson production, are even calculated at NNNLO.

LO matrix elements are usually sufficient to describe the shape of distributions reasonably well; however, absolute normalisations are often corrected with *K-factors* to take higher-order effects into account. Typically, they are a single number computed as the ratio of the NLO and LO total cross section.

All-order approaches: parton showers

As indicated in the previous section, fixed-order calculations are limited to the calculation of inclusive or infrared- and collinear-safe observables and particular phase-space regions, where jets are “hard and well-separated” [20]. One approach to overcome this limitation and provide calculations for non-IRC observables and emissions in soft and collinear regions of phase space is to approximate the effects of all higher orders by means of *parton shower* algorithms. They are based on the finding that the structure for emitting a (softer) collinear parton off a hard parton is universal and independent of the considered hard-scatter process. Assuming a hard-scatter process leading to a final state involving parton i has a cross section σ_0 . Then, in the *collinear limit*, the cross section for the process with an additional parton j with momentum fraction z , can be factorised as

$$d\sigma \approx \sigma_0 \frac{\alpha_s}{2\pi} \frac{d\theta^2}{\theta^2} P_{j\leftarrow i}(z, \phi) dz d\phi, \quad (1.43)$$

namely as the leading-order process with cross section σ_0 and the subsequent emission of parton j with an opening angle θ relative to the direction of parton i . The latter is described by $P_{j\leftarrow i}(z, \phi)$, the universal, but flavour- and spin-dependent (via ϕ) *DGLAP splitting functions*. The LO spin-averaged splitting kernels for the various parton combinations are

$$P_{q\leftarrow q}(z) = C_F \frac{1+z^2}{1-z}, \quad P_{g\leftarrow q}(z) = C_F \frac{1+(1-z)^2}{z}, \quad (1.44)$$

$$P_{q\leftarrow g}(z) = T_R(z^2 + (1-z)^2), \quad P_{g\leftarrow g}(z) = C_A \left(\frac{z}{1-z} + \frac{1-z}{z} + z(1-z) \right), \quad (1.45)$$

with underlying QCD vertices qqg and ggg . That means, while gluons can split both into a quark-antiquark and a gluon-gluon pair, a (anti)quark can only emit a gluon; this implies $P_{q\leftarrow q}(1-z) = P_{g\leftarrow q}(z)$. The *Casimir operators*, $C_F = (N_c^2 - 1)/(2 \cdot N_c)$ and $C_A = N_c$, take for three colours values 4/3 and 3, respectively; i.e. $N_c = 3$, and $T_R = 1/2$.

The ratio $d\sigma/\sigma_0$ defines the probability $d\mathcal{P}_i(\theta, z)$ that the same final state occurs, except that instead of the parton i the almost collinear pair ij appears; thus, the different splitting rules can be combined to describe a successive emission, i.e. a *parton shower*. However, $d\mathcal{P}_i(\theta, z)$ still diverges in the limit of soft and collinear emission, i.e. $z \rightarrow 0$, leading to $P_{g\leftarrow q(g\leftarrow g)} \rightarrow \infty$, and $\theta \rightarrow 0$; the divergences are not yet tamed, but need to be regulated by introducing a cutoff, Q_0 , below which no further branchings are allowed and hadronisation sets in. This cutoff formally represents the factorisation scale of the event as introduced in the previous section. Q_0 can be interpreted as a resolution criterion: above Q_0 , a pair of collinear partons can be resolved as such, below it cannot be distinguished from a single parton by means of a measurement; a commonly chosen variable to assess the resolvability is the relative transverse momentum of the partons.

In order to be able to describe the parton shower as an iterative process of subsequent branchings of partons until no more resolvable emissions above Q_0 are produced, one needs to define the probability for the *first branching* to occur. Requiring unitarity, which entails that the sum of probabilities for a resolvable emission and a non-resolvable emission, or emission and no emission, is unity, allows to describe the probability for the branching to happen for the first time as the product of the probability that the branching happens at all and the probability that it has not happened yet. Taking $1/q^2$, where q is the virtuality of the internal line, as the relevant “time” scale for a parton shower, i.e. evolving towards smaller q^2 instead of

later times, this reads:

$$\frac{d\Delta_i(Q^2, q^2)}{dq^2} = \frac{d\mathcal{P}_i}{dq^2} \Delta_i(Q^2, q^2). \quad (1.46)$$

Here

$$d\mathcal{P}_i = \frac{\alpha_s}{2\pi} \frac{dq^2}{q^2} \int_{Q_0^2/q^2}^{1-Q_0^2/q^2} dz P_{j \leftarrow i}(z) \quad (1.47)$$

is the probability for all resolvable branchings of a parton of type i between q^2 and $q^2 + dq^2$; the resolvability requirement is encoded in the integration limits. In this context q^2 is referred to as *ordering variable*; it is exploited that $d\theta^2/\theta^2 = dq^2/q^2 = dp_{\text{T}}^2/p_{\text{T}}^2$. $\Delta_i(Q^2, q^2)$ is referred to as the *Sudakov form factor*:

$$\Delta_i(Q^2, q^2) = \exp \left\{ - \int_{q^2}^{Q^2} \frac{dq'^2}{q'^2} \frac{\alpha_s}{2\pi} \int_{Q_0^2/q'^2}^{1-Q_0^2/q'^2} dz P_{j \leftarrow i}(z) \right\}; \quad (1.48)$$

describing the probability that no branching occurs above q^2 , it is given by the exponent of the negative of the total branching probability between q^2 and Q^2 , where Q^2 is the maximum possible virtuality and the starting point for the shower. Considering the special case with $q^2 = Q_0^2$, $\Delta_i(Q^2, Q_0^2)$ is the probability for no resolvable branchings

$$\Delta_i(Q^2, Q_0^2) \sim \exp \left\{ -C_F \frac{\alpha_s}{2\pi} \log^2 \frac{Q^2}{Q_0^2} \right\}. \quad (1.49)$$

Thus, by introducing the Sudakov form factor via unitarity arguments, parton-shower algorithms resum all terms with leading logarithms of Q_0^2 correctly to all-orders in perturbation theory.¹³

Although the derivation of the parton-shower algorithm was done in the collinear limit, it can be shown that also soft emissions are taken into account. However, this is only done correctly, if angular or p_{T} ordering is used, which properly consider *colour coherence* effects; in the case of q^2 ordering, soft contributions can be accounted for approximately by imposing the impact of coherence. An alternative approach, which also correctly considers coherence effects, is a p_{T} -ordered *dipole shower* algorithm. The latter is exploited by SHERPA and partially by PYTHIA 8 which still also uses p_{T} -ordering for some final-state radiation; Herwig++ relies on angular ordering.

The description of initial-state radiation is more complicated given that (i) the shower-evoking parton stems from an incoming proton described by the non-perturbative PDFs and (ii) showers develop that do not result in the hard scatter, and thus need to be reconnected with the proton remnant. Therefore, usually a *backwards evolution* approach is taken, where starting from the hard interaction the shower is developed backwards in time or equivalently from a higher scale (lower momentum fraction) to a lower scale (higher momentum fraction). The iteration then stops when a cutoff is reached and the description via PDFs sets in. The evolution proceeds basically as in the final-state case, however the Sudakov form factor is modified with respect to Eq. 1.48 by a factor $x/z f_j(x/z, q'^2)/(x f_i(x, q'^2))$, where $f_{(i)j}$ is the PDF of parton $i(j)$.

¹³Resummation similarly achieves an all-order approximation using analytical methods instead of numerical ones.

Combining matrix elements & parton showers: matching & merging

Both perturbative approaches, fixed-order matrix element (ME) calculations and parton-shower (PS) algorithms, have their strengths and shortcomings; their complementarity makes it desirable to combine them to obtain the optimal description of collision events. In short, while the former is excellent in describing processes, where partons are energetic and widely separated, the latter provides reliable predictions in soft and collinear phase-space regions, is thus able to describe the internal structure of jets and can be easily matched to hadronisation models.

There are in particular two difficulties that make the combination challenging: (i) tree-level MEs describe *inclusive* final states, while PSs generate *exclusive* final states and (ii) overlapping phase-space regions. Several strategies have been developed which can be roughly classified into two groups, referred to as *matching* and *merging* approaches. In particular the MC@NLO [107] and PowHEG [102, 103] approaches belong to the first category: exactly matching NLO calculations to parton showers, they provide predictions for inclusive processes and IRC-safe observables, with full NLO accuracy. However, they lack precision regarding the kinematic description of multijet final states. This is addressed by several algorithms [108–113] following the second approach, where LO MEs with increasing parton multiplicity are merged to PSs; also referred to as MEPs. All of those strategies involve some kind of *merging scale*, typically defined as a jet-resolution scale: above partons are generated with the ME and below with the PS. One Example is the CKKW(-L) [108, 109] approach, which maintains the leading-logarithm accuracy of the parton shower (at least in e^+e^- annihilation) without double-counting of contributions; the MLM approach [111, 114] is a more pragmatic version with approximate PS accuracy.

Attempts are also made to combine matching and merging approaches: MENLOPS [115, 116] combines the MC@NLO strategy with MEPs yielding NLO accuracy for the inclusive cross section; the hardest emissions are corrected with tree-level MEs. The MEPs@NLO method [117, 118], exploited e.g. by SHERPA, achieves to maintain the fixed-order accuracy for multijet final states as well as the leading-logarithm accuracy of the PS by combining the MC@NLO strategy with accordingly modified PSs.

1.4.4 Parton Distribution Functions

As already mentioned in Sec. 1.4.2, *parton distribution functions* (PDFs) describe the momentum distribution of the partons, quarks and gluons, within the proton. As such they reflect that it is a composite particle and represent the probability (number) densities to find a parton carrying a fraction x of the proton's longitudinal momentum when probed at an energy scale Q^2 . Figure 1.11 shows examples for PDFs as function of x at two different Q^2 , namely 10 GeV^2 and 10^4 GeV^2 . At high x values the three valence quarks $2 \times u$ and d , which define the proton's quantum numbers, dominate; and even more so towards lower Q^2 . Sea (anti)quarks of all flavours generated by splittings of the gluons exchanged between the valence quarks and in particular the gluons themselves dominate the low x region; and increasingly with increasing Q^2 . While the transition from one Q^2 value to another one can be perturbatively calculated via the DGLAP equations, the x dependence of the PDFs at a certain Q^2 cannot be computed from first principles (yet) given the non-perturbative nature of the problem and needs to be determined from data. Considered to be universal, they can be extracted in dedicated measurements and used in others.

In order to cover a broad x range as well as to be sensitive to the different flavours in the quark sea, precise data from Deep Inelastic Scattering (DIS) of electrons, muons and neutrinos off nucleons is combined

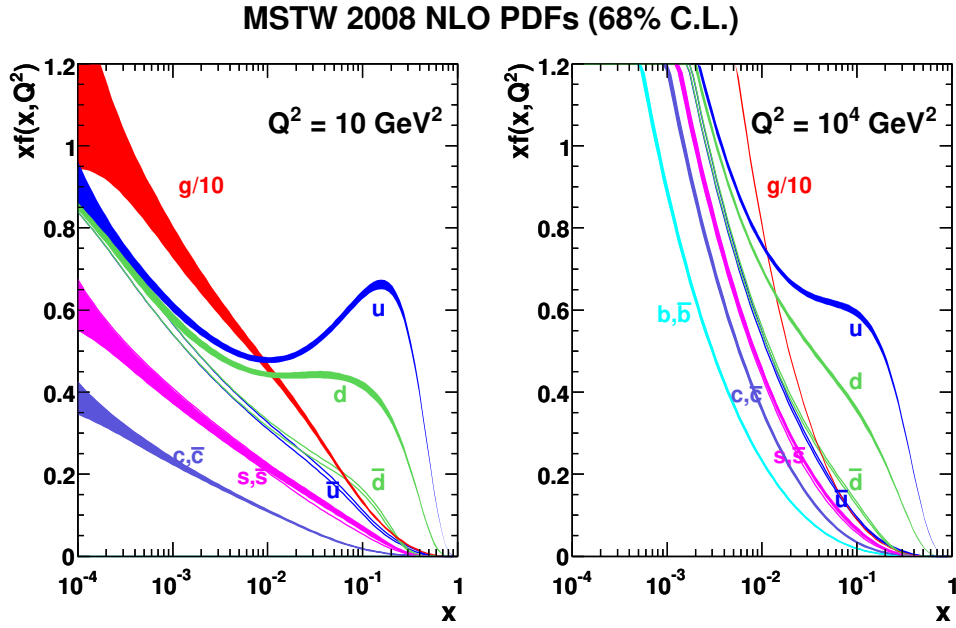


Figure 1.11: Parton distribution functions determined by the MSTW2008 group for two energy scales $Q^2 = 10 \text{ GeV}^2$ and $Q^2 = 10^4 \text{ GeV}^2$. The dependence on the fraction x of the proton longitudinal momentum carried by the partons is obtained in global fits; the Q dependence is given by the DGLAP equation as described in the text. Taken from Ref. [119].

in a global fit with cross-section measurements of e.g. inclusive jet, Drell-Yan and W/Z -boson production performed at colliders; most notable at HERA, but also at the Tevatron and more recently at the LHC (see e.g. Ref. [120]). There are several groups, such as CT10 [121], MSTW2008 [122, 123] and NNPDF 3.0 [124], that perform global fits and provide sets of PDFs and associated uncertainties. The PDF sets differ because of the exploited datasets, but in particular also due to the chosen approaches, i.e. the choice of parametrisation of the PDFs, the treatment of heavy quarks, the value of α_s as well as the treatment and estimation of experimental and theoretical uncertainties.

As the extraction of the PDFs is based on the factorisation theorem (Eq. 1.41), the order of the PDF set is determined by the order of the calculation of the partonic cross section. Since furthermore the PDFs effectively compensate for missing higher-order corrections, it is generally best to use PDFs extracted at the same order as the matrix element they are combined with when computing the cross section of a different process of interest; therefore, the groups also provide sets with lower orders despite higher accuracy being available. While each Monte Carlo generator comes with a default PDF set, they also provide access to other commonly used PDF sets via the LHAPDF interface [125].

1.4.5 Fragmentation

As mentioned before, *fragmentation* or *hadronisation* describes the non-perturbative process of transforming partons into colourless hadrons; it sets in when the energy scale Q is of the order of Λ_{QCD} and the strong coupling becomes large. In the context of parton-shower generators this transition to the non-perturbative regime is governed by the choice of the infrared cutoff Q_0 , which is usually considerably above Λ_{QCD}

(given α_s is required to be small in order perturbation theory to be valid). So far it cannot be described from first principles and instead parametric models are used for its description.

There are in particular two approaches, the *string fragmentation* and the *cluster fragmentation* models, that are currently employed in event generators; many variants, and also hybrid versions, exist and get further refined. Based on certain QCD-inspired principles, they develop in a probabilistic and iterative way a complete picture of the fragmentation process and involve more or less free parameters that are tuned to data; using certain, dedicated measurements under the assumption of universality, they are then used to describe the data in other studies. Given that many of the properties that may influence the observable final state, are “poorly or not at all known, either from theory (lattice QCD) or from experiment [...] it is sometimes more surprising that models can work as well as they do than that they fail to describe everything” [126].

The most prominent string model is the “Lund string model” [127] implemented in the PYTHIA generator [22, 94]. It is based on the assumption of *linear confinement*, a picture that is supported by lattice QCD calculations: the energy stored in the field between a colour charge and a colour anticharge increases linearly with their separation. Considering a quark-antiquark pair $q\bar{q}$, this leads to the picture of a uniform colour-flux tube being stretched between them as they move away from each other; the transverse dimension of the tube is about 1 fm and the string constant κ describing the potential is determined in hadron-mass spectroscopy to be of the order of 1 fm/GeV, corresponding to 0.2 GeV^2 in natural units. With increasing distance the potential energy may reach a threshold for the production of a new $q'\bar{q}'$ pair breaking up the string and splitting it into two colour-singlet systems, $q\bar{q}'$ and $q'\bar{q}$, without any field in between them. The process may repeat itself and continue as long as the invariant masses of the string pieces are sufficiently high; it stops when only on-shell *mesons* remain.

The creation of such $q'\bar{q}'$ pairs from the colour field between the $q\bar{q}$ can be thought of as a quantum-mechanical tunnelling-process with probability

$$\mathcal{P}(m_{q'}^2, p_{\perp q'}^2) \propto \exp\left(\frac{-\pi m_{q'}^2}{\kappa}\right) \exp\left(\frac{-\pi p_{\perp q'}^2}{\kappa}\right), \quad (1.50)$$

where $m_{q'}$ and $p_{\perp q'}$ are the mass and the transverse momentum imparted to the produced quark (antiquark) by the breakup process. The factorisation between $m_{q'}$ and $p_{\perp q'}$ implies a flavour-independent Gaussian distribution of the transverse momentum with expected mean $\langle p_{\perp q'}^2 \rangle = \sigma^2 \approx (250 \text{ MeV})^2$; given the string is assumed to have no transverse excitations the overall transverse momentum is locally compensated by the quark and the antiquark of the pair. Experimentally σ is found to be larger, which can be explained by contributions from unresolved soft-gluon radiation below the chosen shower cutoff; thus, σ is a free parameter that can be tuned. The Gaussian suppression of $m_{q'}$ entails that the heavy c and b quarks are hardly produced in the soft fragmentation process; thus, the rates are expected to scale as: $u : d : s : c : b \approx 1 : 1 : 0.3 : 10^{-11} : 10^{-100}$. Therefore, c hadrons and b hadrons (containing at least one c quark and b quark, respectively) only arise, if heavy-flavour quarks are produced in the hard-scatter event or emerge from gluon splittings; however, measurements suggests that the latter only happens in about 3% (0.3%) for c quarks (b quarks) [45].¹⁴ Although the expected suppression of strange quarks seems to agree well with observations, the factor is a free parameter in PYTHIA.

¹⁴The even heavier top quarks decay before the hadronisation process sets in, which is of the order of $1/\Lambda_{\text{QCD}}$.

There are several approaches to extend the description to also include the production of *baryons*, consisting of three quarks (or antiquarks). The simplest scheme allows besides pairs of quarks also pairs of *diquarks*, loosely bound states of two (anti)quarks with net colour, to be created at a string break. However, neither the relative rate for this to happen nor the probabilities for the flavour and spin states of the individual diquarks can be predicted, and thus are free parameters that need to be constrained by data; measurements of the diquark-to-quark rate from e.g. the proton-to-pion ratio, suggest it to be at the level of 10%.

In the picture of the strings being stretched between quark pairs, additional gluons are represented as transverse kinks and states such as $q\bar{q}g$ can be described without requiring additional free parameters.

Once the string breaking stops the produced (di)quarks need to be assigned to a certain meson or baryon among the different allowed possibilities, in particular between a *pseudoscalar* or a *vector* meson and a spin-1/2 or spin-3/2 baryon, respectively. Unfortunately, the string fragmentation model hardly provides any prediction regarding the multiplet assignment, and since expectations from simple spin-counting arguments are shown to be only approximately in agreement with data in particular cases, a large number of free parameters are needed to describe the *production* or *fragmentation fractions* of primary hadrons. However, constraining them from measurements is also challenging, in particular for lighter hadrons, given that heavier states decay rapidly; assumptions on the various branching ratios need to be made. The production of higher resonances (with angular momentum $L \neq 0$) is assumed to be small and generally neglected; for baryons the flavour-spin states are required to be symmetric.

The constant string tension entails that the different string breaks occur causally independent of each other and do not need to be considered in a certain time-ordered sequence (the only constraint is that the final string pieces are on the mass-shell in order to produce observable hadrons). Therefore, the iterative process can be started at either end of the original $q\bar{q}$ pair and yields the same result; this “left-right symmetry” is reflected in the *fragmentation function*, $f(z)$, that describes the fraction of momentum z carried by the emerging hadron with respect to the string:

$$f(z) \propto \frac{(1-z)^a}{z} \exp\left(-\frac{b \cdot m_{\perp}^2}{z}\right); \quad (1.51)$$

thus, $f(z)$ is known as *Lund symmetric* fragmentation function (normalised to unit area). Here $m_{\perp}^2 = m^2 + p_{\perp}^2$, where m is the mass of the emerging hadron and p_{\perp} its transverse momentum with mean $\langle p_{\perp}^2 \rangle = 2\sigma^2$, given it receives transverse-momentum contributions from two string breaks on either side; a and b are free parameters (a might differ in the case of diquark-pair production).¹⁵ The dependence of $f(z)$ on m implies a harder fragmentation function for heavier hadrons. In fact, it was found to predict a somewhat too hard spectrum for B mesons prompting the modification of $f(z)$ in Eq. 1.51 by a factor $1/z^{r_Q \cdot bm_Q^2}$ for heavy endpoint quarks of mass m_Q , known as the *Bowler fragmentation function* [128]. While the prediction is that the free parameter $r_Q \equiv 1$, and it is also usually set to unity, its introduction allows a smooth transition between the Lund symmetric and the Bowler fragmentation function.

¹⁵This is the simplified version, where the parameter a is assumed to be the same for all flavours. Otherwise $f(z) \propto \frac{1}{z} z^{a\alpha} \left(\frac{1-z}{z}\right)^{a\beta} \exp\left(-\frac{b \cdot m_{\perp}^2}{z}\right)$, where α indicates the parameter of the ‘old’ flavour and β of the new one. [22]

Cluster models [129, 130] are based on the *preconfinement property* of parton showers [131], i.e. that colour singlet combinations of partons, *clusters*, can be formed with an almost process- and scale-independent invariant mass distribution, and reflect the *local parton-hadron duality* hypothesis [132, 133], i.e. distributions of final-state hadrons closely related to those of the partons at Q_0 . They generally describe the fragmentation process in a two-step approach: (i) by enforcing the non-perturbative splitting of gluons produced by the parton shower at the cutoff scale into quark-antiquark (or diquark-antidiquark) pairs and the building of colourless clusters and (ii) by decaying the clusters into hadrons. Two cluster model variants that differ regarding the treatment of the details of the hadronisation process, which are entirely omitted here, are implemented in the HERWIG and SHERPA generators [134, 135].

1.4.6 Particle Decays

Decays of resonances such as the massive gauge bosons or the Higgs boson are described as part of the hard process; their partial decay widths are perturbatively calculable. However, this is not the case for decays of unstable hadrons, arising in the fragmentation of partons involved in the hard scatter, stemming from secondary decays or the underlying event, as well as τ -lepton decays; their branching ratios are considered not to be perturbatively calculable.

In particular the simulation of hadron decays that is required to obtain exclusive final states involves non-trivial modelling and relies on a combination of experimental results and theoretically motivated assumptions. While the Review of Particle Physics by the Particle Data Group [45] provides an impressive amount of information on particle properties, it is still often not sufficient, in particular with regard to excited meson multiplets, excited mesons and any baryons containing heavy quarks and decays with high particle multiplicities. Which hadrons are considered in the simulation varies between the different generators, as it is also closely related to the hadronisation model; generally a large number of mesons is included, while often the number of considered baryon multiplets is rather limited. The generators further differ regarding the choice of considered decay modes as well as their simulation for which there are various approaches of differing sophistication; e.g. the EVTGEN program is specialised on (heavy) hadron decays, and thus provides a more evolved simulation also suited for the study of CP-violating processes.

Since the lifetimes of weakly decaying light hadrons are long with regard to the relevant timescales of the hard-scatter process, their decays are treated in the context of the detector simulation (cf. Sec. 2.2.7). Strong and electromagnetic decays of excited light hadrons, in particular mesons, however need to be considered and are usually simulated using simple matrix elements based on conservation laws.

Although for a large number of decay modes of the weakly decaying heavy mesons, containing a single c or b quark, the branching ratios have been measured, the list is not complete. Thus, in particular in the case of the high-multiplicity hadronic decays, the remaining decay modes need to be generated according to a simple flavour combination scheme based on the *spectator model*: i.e. the heavy quark is decayed neglecting any impact from the light *spectator* quark, followed by hadronisation.

Although a few decay modes of the weakly decaying heavy baryons have been observed, apart from branching ratio of the Λ_c^+ baryon, only ratios thereof are measured; i.e. the majority of the decays are simulated based on the spectator-model approach.

While the strong and electromagnetic decays of excited heavy mesons are generated following the same strategy as for light hadrons, for most of the excited baryons both masses and decay modes are simulated based on theoretical models.

1.4.7 Soft QCD: Minimum-Bias, Underlying Event and Multiple Parton Interactions

The total hadron-hadron cross section can be divided into the cross sections for *elastic* and *inelastic* scattering processes. In reactions of the former type the incoming particles remain intact and the only exchanged quantity is the momentum. The latter type covers all other reactions where the final state particles differ from the incoming ones by one or more quantum numbers being changed and/or additional particles being produced. Based on the final state inelastic processes are further classified into (several) *diffractive* and *non-diffractive* topologies: one criterion is whether the final state resembles the decay of an excitation of the incoming particle or not, another whether there is a large rapidity gap in the final state or not; the latter also includes hard-scatter events. The selection of *minimum-bias* events aims at selecting events from such inelastic processes as inclusively as possible; their simulation is used to model *in-time pile-up* effects (cf. Sec. 2.3).

Provided a hard parton-parton interaction occurs in a hadron-hadron collision, the *underlying event* refers to the activity due to the *beam remnants*, i.e. what is left from the incoming hadrons after the partons involved in the hard scatter are taken out. Comparisons to minimum-bias events at the same energy show that the underlying event is much more active with large fluctuations; an effect referred to as *jet pedestal*.

The partons of the beam remnants may also interact with each other and lead to another hard parton-parton interaction; such *multiple-parton interactions* (MPI) are characterised by jet pairs in a back-to-back topology with little total transverse momentum. Most jets are relatively soft, and thus are not reconstructable; however, they contribute to the total energy in the event, cause colour exchange and thereby increase the number of particles produced during hadronisation.

The single $2 \rightarrow 2$ parton-parton scattering, e.g. via t -channel gluon-exchange, constitutes the basis for the perturbative modelling of both soft inclusive and underlying event processes. Its cross section being proportional to dp_{\perp}^2/p_{\perp}^4 diverges for vanishing transverse momenta; it is regulated by *colour screening* and *saturation* effects which need to be tuned to data. Furthermore, parton showers are also considered as well as *colour (re)connections* to achieve realistic descriptions.

An alternative description chooses the opposite approach and starts from the non-perturbative regime and uses unitarity to relate elastic and inelastic scattering processes through the *optical theorem*. Then the total cross section is dominated by the exchange of *reggeons* and *pomerons*, i.e. colour-singlet fluctuations with leading $q\bar{q}$ and gg content, respectively, between the beam particles.

2 The ATLAS Experiment at the Large Hadron Collider

The ATLAS experiment [136] is one of two general-purpose detectors at the Large Hadron Collider (LHC) [137–140] hosted by CERN, the European Organisation of Nuclear Research, located at the Franco-Swiss border close to Geneva (Switzerland). Taking advantage of the unprecedented energies of the LHC, it is designed to detect a wide range of possible physics signatures in the provided particle collisions, serving in particular the understanding of the electroweak symmetry breaking, the search for the Higgs boson as well as for physics beyond the Standard Model (SM) at the TeV scale. The ATLAS collaboration, consisting currently of more than 3000 scientists and technicians from 182 institutions in 38 countries, developed the detector, operates it since the year 2008 and analyses the collected data in a collaborative effort; its biggest success so far was the co-discovery of the SM-like Higgs boson in July 2012 [7, 8].

The data analysed in the measurements reported in Chaps. 4 and 5 was collected with the ATLAS experiment in proton-proton (pp) collisions at centre-of-mass energies of $\sqrt{s} = 7$ TeV and $\sqrt{s} = 13$ TeV in the years 2011 and 2015/2016, respectively.

In February 2013, after about three years of operation the *Run 1* of the LHC concluded. Two years of scheduled shutdown, the *long shutdown* (LS1), followed, where the accelerator complex, introduced in the next section, as well as the experiments were prepared for the pp collisions at higher centre-of-mass energies. In spring 2015 the LHC *Run 2* started and will last until end of 2018. During LS1 the ATLAS experiment performed a number of subdetector upgrades, most notable the installation of the *insertable b-layer* (IBL), as discussed in the context of Sec. 2.2 providing an overview of the ATLAS detector. The chapter concludes with a summary of the data-taking conditions characterising the datasets on which the work of this thesis is based.

2.1 The Large Hadron Collider

The Large Hadron Collider (LHC) [137–140], which started operation in the year 2008, is the latest and most powerful addition to CERN’s accelerator complex depicted in Fig. 2.1. While mainly designed to provide proton-proton (pp) collisions at centre-of-mass energies of up to $\sqrt{s} = 14$ TeV and instantaneous luminosities of $\mathcal{L} = 10^{34} \text{cm}^{-2} \text{s}^{-1}$, the LHC is also capable of accelerating lead ions (A) and produce AA and pA collisions.

Being hosted in the tunnel of the former LEP collider [141], it lies up to 170 m below the surface and has a circumference of 26.7 km. It is not perfectly circular, but divided into eight arcs and eight straight sections; each straight section is about 528 m long¹ and serves as experimental and/or utility insertion. The two multipurpose experiments ATLAS and CMS [142] are located at Point 1 and Point 5, respectively, diametrically across the ring; the ALICE [143] and LHCb [144] experiments are located at the combined

¹“A proton machine such as LHC does not have the same synchrotron radiation problem and would, ideally, have longer arcs and shorter straight sections for the same circumference.”

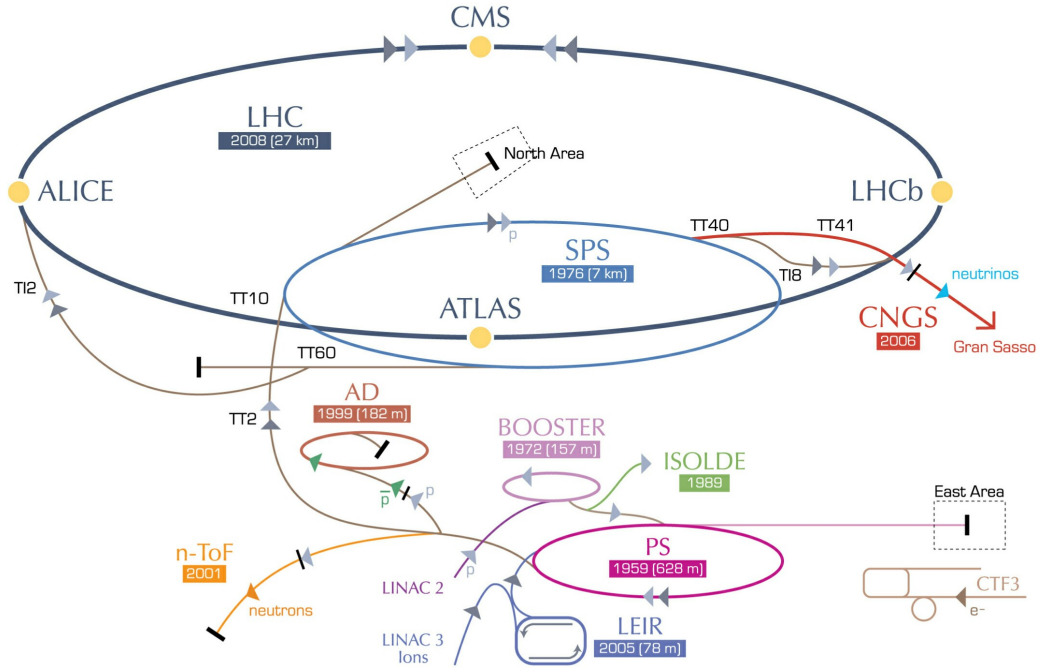


Figure 2.1: Schematic view of the CERN accelerator complex. Protons are pre-accelerated in a chain of smaller accelerators - Linac2, BOOSTER, PS and SPS - before they are accelerated to their final energy and collided in the Large Hadron Collider (LHC). Adapted from Ref. [148].

insertions, Point 2 and Point 8, respectively, where also the beams are injected. Three smaller experiments, LHCf [145], TOTEM [146] and MoEDAL [147], share the caverns with the ATLAS, CMS and LHCb experiments, respectively, while the other four interaction regions are (currently) unequipped and without beam crossings in order to prevent unnecessary disruption of the beams. Since particles with same-signed charges are collided, the beams are counter-rotating in two rings which however are not completely separated due to space-limitations. A “two-in-one” superconducting-magnet design is employed, where twin-bore magnets, consisting of two sets of coils with magnetic flux circulating in the opposite sense through the two evacuated beam pipes, are accommodated within a common mechanical and cooling structure. Thousands of magnets of various kinds are installed to keep the beams focused and on their designated path: (i) 1232 main dipoles, superconducting niobium-titanium magnets cooled to a temperature of 1.9 K using superfluid helium, are used to bend the beams with a field strength of up to 8.33 T, (ii) 392 quadrupole magnets are used to focus the beams, (iii) dedicated *insertion* magnets are used to focus the beams further just before they enter the detectors for collision, and (iii) other magnets are used to e.g. separate the beams again after collision or deflect them for the beam dump.

A superconducting system housing 16 radiofrequency (RF) cavities is operated at 400 MHz to accelerate the beams and keep them at their top energy by compensating energy losses due to synchrotron radiation. At design luminosity, each beam consists of 2808 *bunches* of $1.15 \cdot 10^{11}$ protons that are separated by a gap corresponding to 25 ns. Since the luminosity decays over time, primarily due to beam loss from collisions, with an estimated lifetime of 14.9 h, the operation time per run is limited.

The proton beams are injected into the LHC ring at an energy of 450 GeV and already in the required

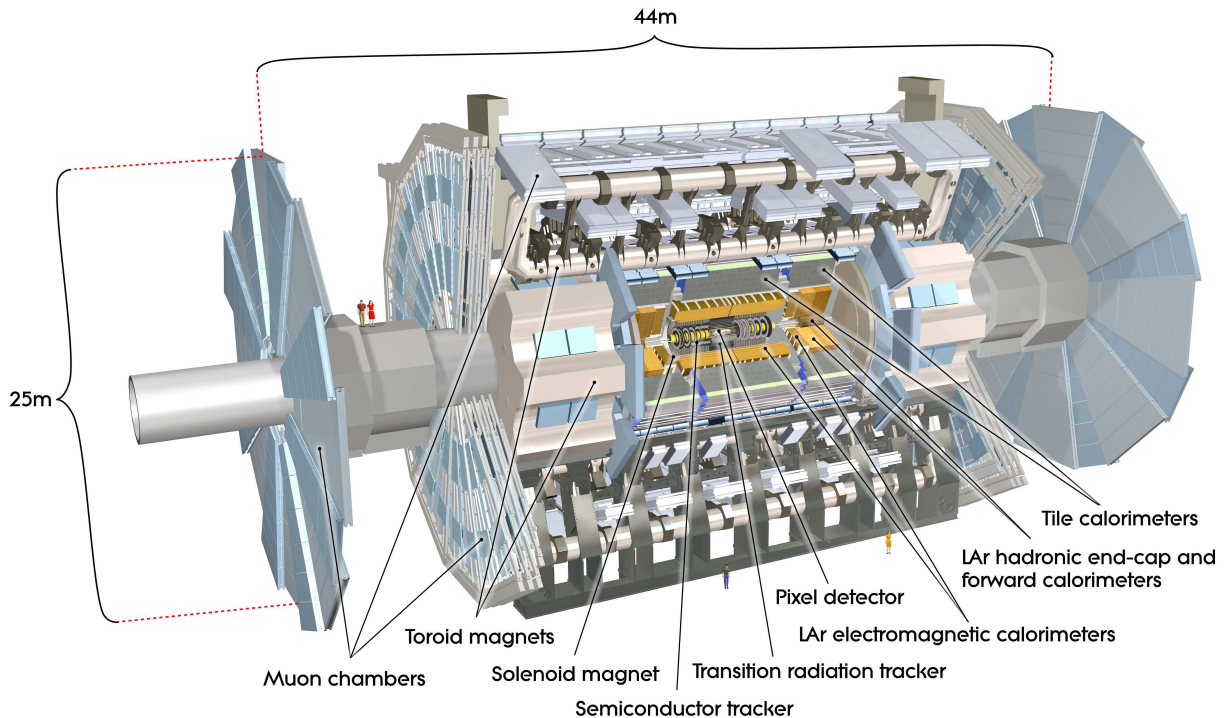


Figure 2.2: Cut-away view of the ATLAS detector, revealing its various subsystems. Taken from Ref. [136].

bunch-train structure after passing through a number of pre-accelerators, as indicated in Fig. 2.1. Protons obtained from ionising hydrogen gas are first accelerated by the linear accelerator *Linac 2* to 50 MeV and grouped into bunches. Their energy is then step-wise increased by three synchrotrons: by the *Proton Synchrotron Booster* to 1.4 GeV, by the *Proton Synchrotron* (PS) to 25 GeV and by the *Super Proton Synchrotron* (SPS) to the injection energy;² the bunch-train structure is generated by the PS. While it requires 39 bunch trains per beam, where each train consists of 72 proton bunches (with 25 ns spacing) and is separated from the next by a gap corresponding to 320 ns, to achieve the design values, the LHC can be operated with a variety of different filling schemes appropriate for certain targeted instantaneous luminosity, amount of pile-up etc. (cf. Sec. 2.3).

2.2 The ATLAS Experiment

The ATLAS detector [136], depicted in Fig. 2.2, is comprised of various subsystems surrounding the beam-line, is cylindrical in shape in order to provide large acceptance and hermetic coverage over most of the solid angle and forward-backward symmetric with respect to the interaction point in its centre; it is about 44 m long and 25 m high and weighs roughly 7 kt. It is designed as a multipurpose detector with the goal of reconstructing and characterising a wide range of physics objects in differing kinematic regimes, from the MeV up to the TeV scale, with high precision, and thus enabling the targeted detection of signatures expected both for the Standard-Model Higgs boson and Beyond-the-Standard Model (BSM) Higgs bosons

²In the case of lead-ion beams, the source is vaporised lead and particles are accelerated via *Linac 3* and the *Low Energy Ion Ring* (LEIR) before they enter the PS and SPS as the proton beams.

(cf. Sec. 1.3) as well as other BSM resonances or supersymmetric particles.

Subdividing the ATLAS detector into three main parts, both the innermost and the outermost part consists of tracking detectors, the *inner detector* (ID) and the *muon spectrometer* (MS), that allow reconstruction of trajectories and provide momentum as well as charge-sign information of charged particles and muons, respectively. The inner detector is embedded in a thin, superconducting solenoid aligned with the beamline producing a 2 T magnetic field that bends particles in the plane perpendicular to the beamline. One barrel and two endcap toroids arranged with an eightfold azimuthal symmetry provide magnetic fields of about 0.5 T and 1 T for the muon spectrometer, respectively, bending particles in the direction parallel to the beamline. Since the inner detector is furthermore required to provide information for the reconstruction of primary and secondary decay vertices serving the location of the origin of the hard-scatter event, the suppression of additional interactions as well as the identification of hadronically decaying τ leptons and b jets, it is placed very closely to the beamline and has a high granularity that somewhat decreases with radial distance. The two independent tracking systems enclose the *calorimeter*; it is divided into the *electromagnetic* (EM) and the *hadronic calorimeter* that provide besides energy measurements of electrons, photons and primary hadrons as well as purely weakly interacting particles by means of missing transverse momentum (cf. Sec. 3.9), also identification and directional information thanks to their high spatial resolution (cf. Chap. 3).

Given the high collision rate and large inelastic cross-section, the ATLAS experiment relies on a staged trigger system employing both hardware- and software-based selection strategies to reduce the input rate by only reading out potentially interesting hard-scatter-like events.

In addition to the main detector system introduced above, the ATLAS experiment is complemented with a number of smaller subsystems dedicated to providing coverage of the very forward region, e.g. for measuring the total (inelastic) cross section or determining the luminosity.

In particular during LS1, the detector was subjected to some changes: besides completing certain subsystems that had been staged, such as the high-level trigger processing farm allowing a higher L1 rate (cf. Sec. 2.2.6) and certain parts of the muon spectrometer, subdetectors were upgraded (as foreseen) to cope with the expected experimental conditions, most notable the inner detector, by installation of the IBL (cf. Sec. 2.2.1), also based on the experiences from Run 1.

To describe the ATLAS detector as well as trajectories of particles emerging from the pp collisions a right-handed Cartesian coordinate system is used: with its origin at the nominal interaction point, the z -axis points along the beamline, the x -axis towards the centre of the LHC ring and the y -axis upwards; the x - y plane being perpendicular to the beamline is referred to as *transverse plane*. Usually, spherical coordinates are preferred; following the common notation θ and ϕ are the polar and azimuthal angles measured from the z - and x -axis, respectively. Often the *pseudorapidity*, defined as $\eta = -\ln[\tan(\theta/2)]$, is used instead of θ ; for massless particles η agrees with the rapidity y and differences are Lorentz-invariant. As $|\eta|$ increases from the y -axis towards the beamline, small $|\eta|$ values describe the central part of the detector, high $|\eta|$ values the forward region. An angular distance in the $\eta - \phi$ space is defined by $\Delta R = \sqrt{(\Delta\eta)^2 + (\Delta\phi)^2}$.

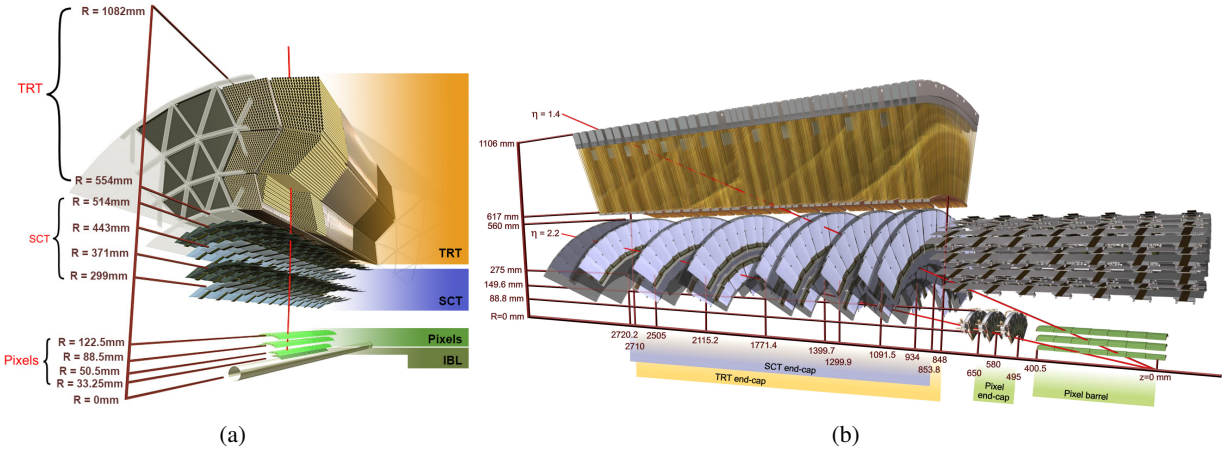


Figure 2.3: Three-dimensional visualisation of the ATLAS inner-detector structure (a) in the barrel and (b) in the endcaps. While in (a) in addition to the layers of the Pixel, SCT and TRT subdetectors, introduced in the text, also the new beampipe and IBL are shown, which were installed during LS1, (b) shows the structure before the upgrade. Taken from Refs. [149] and [136], respectively.

2.2.1 The Inner Detector

The inner detector (ID) [136] is cylindrical in shape, extending about ± 3.5 m from the IP with a radius of ~ 1.2 m, and is composed of three independent subsystems that are based on (somewhat) different technologies. From smaller to larger radii these are: the *pixel* and the *SCT* (semiconductor tracker) detectors that employ silicon pixel and micro-strip sensors to achieve high-resolution track and vertex reconstruction in the pseudorapidity range $|\eta| < 2.5$ as well as the *TRT* (transition radiation tracker) detector. Comprised of several layers of gaseous straw tubes interleaved with transition-radiation material, the TRT provides in addition to tracking information also electron identification, complementing that of the calorimeter, within $|\eta| < 2.0$; despite having the lowest resolution, it significantly improves the precision of the momentum determination due to providing a high number of hit measurements at large radii. By combining the information of the three systems, the ID achieves efficient pattern recognition in both the R - ϕ and z directions as well as precise transverse-momentum measurements for charged particles with transverse momenta (p_T) ranging between about 0.5 GeV and a few TeV; the transverse-momentum resolution scales with p_T according to: $\sigma_{p_T}/p_T = 0.05\% p_T \oplus 1\%$.

Figures 2.3(a) and 2.3(b) show sketches of the arrangement and the structures of the three subsystems in the central and somewhat more forward part, i.e. in the *barrel* and the *endcap*, respectively. As can be seen, each subsystem consists of several layers that are arranged in form of concentric cylinders around the beamline in the barrel region and of disks perpendicular to the beamline in the endcaps. Figure 2.3(a) also shows the *IBL* (insertable B-Layer), that was added during LS1 to become the fourth and innermost pixel layer, together with a new beampipe of smaller radius (23.5 mm instead of previously 58 mm) [150, 151]. The original pixel detector, referred to as pixel detector in the remainder of this section, was the innermost part of the ID during Run 1. It consists of three layers both in the barrel and each of the endcaps, so that a charged particle typically crosses three layers and provides three space points for the track reconstruction; the innermost barrel layer is referred to as *b-layer*, highlighting its importance for the identification of *b* jets

(cf. Sec. 3.4). In total 1744 pixel sensors are used that are of identical design: $250\ \mu\text{m}$ thick with an area of $\sim 2 \times 6.3\ \text{cm}^2$ they accommodate 47232 n^+ -type pixels in n -type bulk material (which becomes effectively p -type after a certain radiation dose); resulting in about 80 million readout channels. The nominal pixel size is $50 \times 400\ \mu\text{m}^2$ in $R\text{-}\phi \times z$ yielding intrinsic accuracies of $10\ \mu\text{m}$ ($R\text{-}\phi$) and $115\ \mu\text{m}$ (z) in the barrel region and $10\ \mu\text{m}$ ($R\text{-}\phi$) and $115\ \mu\text{m}$ (R) in the disks. In the barrel, the pixel modules are mounted on 112 staves which overlap and are tilted by -20° (tangential to the cylinder); in the endcaps, they are mounted on sectors, where eight sectors make up one disk. Each staff carries 13, each sector six modules.

Given the high-radiation the innermost pixel layer is particularly subjected to, it was foreseen to replace the b-layer after few years of operation; however it was decided that inserting the IBL instead was the better and only viable solution [151]. With a nominal size of $50 \times 250\ \mu\text{m}^2$ in $R\text{-}\phi \times z$ the pixel dimension is reduced with respect to the pixel detector. In addition to n -in- n sensors similar to the ones used for the pixel detector, also 3D sensors are employed (for the first time in a tracking detector of a collider experiment). The modules are arranged on 14 staves, where each staff is equipped with 12 planar modules placed in the centre and four 3D sensors at each end; the staves are tilted by 14° and overlap. The IBL adds about 12 million readout channels; with the increased closeness to the beamline, the reduced pixel sizes as well as material budget, it improves the quality of the impact-parameter determination of tracks significantly and thereby the performance of the vertex reconstruction and b -jet identification (cf. Secs. 3.1 and 3.4, respectively).

The SCT consists of four layers of silicon-microstrip sensors in the barrel and nine in form of disks in each of the endcaps. In order to be able to measure both $R\text{-}\phi$ and z coordinates, each layer consists of one set of strips aligned parallel to the beamline (barrel) and radially (endcaps), respectively, and one set of stereo strips at an angle of $40\ \text{mrad}$; i.e. for a charged particle passing through all layers in the barrel four space points are measured. All of the 15912 SCT sensors exploit a single-sided p -in- n technology accommodating 768 active strips of $12\ \text{cm}$ length; they are $\sim 285\ \mu\text{m}$ thick and shaped rectangular in the barrel and trapezoidal in the endcaps with side length of the order of $5.5\text{-}6.5\ \text{cm}$. With a strip pitch of $80\ \mu\text{m}$ (on average in the endcaps), the intrinsic accuracies are $17\ \mu\text{m}$ ($R\text{-}\phi$) and $580\ \mu\text{m}$ (z) in the barrel and $17\ \mu\text{m}$ ($R\text{-}\phi$) and $580\ \mu\text{m}$ (R) in the disks. Each SCT module consists of two stereo pairs of strip sensors; the 2112 modules in the barrel are mounted in rows of 12 on individual brackets, the 1976 modules of the endcaps are arranged in outer, middle and inner rings to form the (sometimes incomplete) disks.³ The SCT has in total ~ 6.3 million readout channels.

Both types of silicon sensors are designed to initially operate at a bias voltage of $\sim 150\ \text{V}$; higher values however might be required to maintain good charge-collection efficiencies after years of operation depending on the radiation exposure. In order to suppress noise after radiation damage, the silicon sensors are kept at low temperatures of approximately $-7^\circ\ \text{C}$.

The TRT, covering $|\eta| < 2.0$, is comprised of 298,304 drift (straw) tubes of $4\ \text{mm}$ diameter: filled with a gas-mixture, the tube wall is made of a multi-layer film with good electrical and mechanical properties, and a gold-plated tungsten wire serves as anode. In the barrel, the $144\ \text{cm}$ long straws are aligned with the beamline and arranged in 73 layers; in each of the endcaps, the $37\ \text{cm}$ long straws are arranged radi-

³Only the middle modules of disk 8 and the modules forming the inner rings, have only one pair of stereo strip sensors.

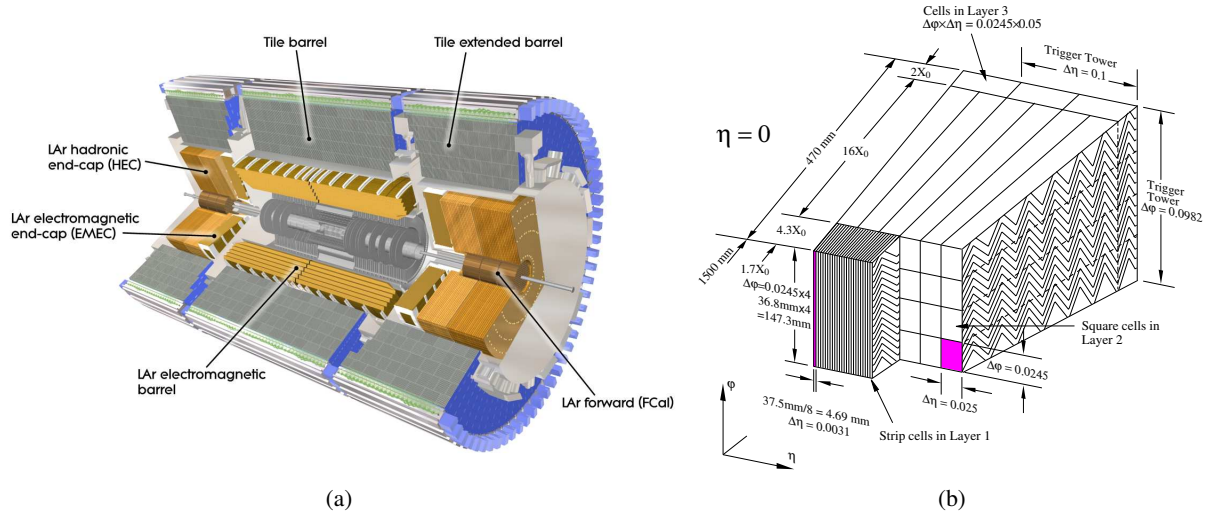


Figure 2.4: (a) Cut-away view of the ATLAS calorimeter revealing the electromagnetic and hadronic calorimeter subsystems. (b) Sketch of a module of the LAr electromagnetic barrel calorimeter. The granularity in η and ϕ of the three layers in depth are shown as well as the accordion structure of the absorbers/electrodes and the dimensions of (trigger) towers. Taken from Ref. [136].

ally in wheels with uniform azimuthal spacing resulting in 160 layers. Only providing R - ϕ information, the intrinsic accuracy is $130 \mu\text{m}$. Charged particles with $p_T > 0.5 \text{ GeV}$ pass through at least 36 straws, with the exception of the barrel-endcap transition region, where at least 22 are traversed. The straws are interleaved with polypropylene fibres (foil) in the barrel (endcaps) serving as transition-radiation material. Low-energy photons stemming from transition radiation cause higher signal amplitudes in the gas-mixture than minimum-ionising particles. Since the probability for the emission of transition radiation only depends on the Lorentz γ -factor of a particle, the number of high-threshold hits due to transition-radiation photons is exploited in the particle identification. It particularly helps the identification of electrons and their distinction from pions in an energy range between 0.5 GeV and 150 GeV .

In order to ensure the stable operation of the TRT straws, the gas mixture is circulated and its quality monitored continuously. At the end of the Run 1 data-taking, several unrepairable leaks in the services pipes occurred. This motivated to operate affected modules in Run 2 no longer with the expensive xenon-based gas-mixture, but with an argon-based one that is significantly less expensive. While no significant degradation of the tracking performance was observed [152], the argon-based mixture is not expected to provide appropriate electron identification due to its inefficient absorption of transition-radiation photons.

Other than the silicon detectors the TRT is operated at room temperature.

2.2.2 The Calorimeter

The calorimeter [136], depicted in a cut-away view in Fig. 2.4(a), is composed of a number of sampling calorimeters that differ (somewhat) regarding the exploited technology and granularity given the various targeted physics processes and the radiation exposure changing over the large covered pseudorapidity range of $|\eta| < 4.9$. Providing full coverage and being symmetric in ϕ , it can be roughly divided into an inner *electromagnetic* (EM) and an outer *hadronic* calorimeter. The depth of each part is chosen such that

electromagnetic and hadronic showers are well contained and *punch-through* into the muon system is minimised. The total radial extension in the barrel measures roughly 3 m; corresponding to a thickness of the EM calorimeter of > 22 radiation lengths (X_0) and 9.7 interaction length (λ) of the hadronic calorimeter at $\eta = 0$. The EM calorimeter is further divided into an EM *barrel* and *endcap* (EMEC) calorimeter covering $|\eta| < 1.475$ and $1.375 < |\eta| < 2.5$, respectively. The hadronic calorimeter consists of the central *tile barrel* and *tile extended barrel* calorimeters, covering $0 < |\eta| < 1.7$; the *hadronic endcap calorimeter* (HEC), located behind the EMEC, and the *forward calorimeter* (FCal), which also provides electromagnetic energy measurements, extend its pseudorapidity coverage to $|\eta| < 4.9$. All, but the tile calorimeters that use scintillating tiles, exploit liquid argon (LAr) as active medium for its intrinsic linear behaviour and radiation-hardness as well as its response stability over time. The LAr calorimeters are housed in three cryostats, the barrel and the two endcaps; i.e. the EMEC, the HEC and the FCal are sharing one on each side. In order to minimise the material in front of the calorimeter, the solenoid is accommodated in the insulating vacuum of the barrel cryostat.

The achieved energy resolution of the EM calorimeter is excellent and improves with increasing energy of the objects E according to $\sigma_E/E = 10\%/\sqrt{E} \oplus 0.7\%$; the energy resolution of the hadronic barrel and endcap calorimeters follows $\sigma_E/E = 50\%/\sqrt{E} \oplus 3\%$ and of the forward calorimeter $\sigma_E/E = 100\%/\sqrt{E} \oplus 10\%$.

The EM Calorimeter

Both the EM barrel as well as each endcap consists of two parts: two identical half-barrels, separated by a small gap at $z = 0$, and two coaxial wheels with a small boundary at $|\eta| = 2.5$, respectively (cf. Fig. 2.4(a)). Each of the half-barrels is about 3.2 m in length and has an inner (outer) radius of 1.4 m (2 m); both wheels at each endcap are ~ 31 cm long and have an inner (outer) radius of 33 cm (~ 2.1 m). The LAr active material is interleaved with accordion-shaped lead absorber plates and kapton electrodes over its full coverage providing complete ϕ symmetry without any cracks. As indicated in Fig. 2.4(b) showing the sketch of a barrel module, the accordion waves are running in ϕ in the barrel and axially in the endcaps; folding angles (and wave amplitudes) vary with the radius in order to provide uniform performance regarding linearity and resolution as a function of ϕ . The thickness of the absorber plates of the order of 1-2 mm decreases with increasing $|\eta|$ in order to limit the decrease of the sampling fraction and energy resolution. The two outer of the three electrode layers are at high-voltage potential, the inner one is used to read out the signal via capacitive coupling; operated at 2000 V the drift time is about 450 ns.

Figure 2.4(b) furthermore shows for the barrel that the EM calorimeter is segmented both in depth and in η , with varying granularity. It consists of three layers in depth with decreasing lateral granularity; except in the inner endcap wheel, where there are only two layers with lower granularity than for the rest. The first layer is finely segmented along η with $\Delta\eta \times \Delta\phi = 0.025/8 \times 0.01$ in the barrel, allowing the identification of $\pi \rightarrow \gamma\gamma$; the granularity in the endcaps and the barrel-endcap transition region is lower. The middle layer is largest in depth corresponding to $16 X_0$ designed to collect the dominant fraction of the energy deposited by an electromagnetic shower. Its typical cell size of $\Delta\eta \times \Delta\phi = 0.025 \times 0.025$ is used to divide the EM calorimeter into 200×256 towers spanning its full depth; it also provides fast information for the L1 trigger as described in Sec. 2.2.6. The granularity of the third layer is coarser in η , it is halved with respect to the second layer, as its main purpose is to collect the tails of the electromagnetic showers; and as such provide also information to distinguish between electromagnetic and hadronic showers.

In front of the first layer a *presampler* is installed within $|\eta| < 1.8$ to account for energy lost by electrons and photons traversing the inner detector and the solenoid; it consists of a thin, instrumented LAr layer.

The Hadronic Calorimeter

The barrel and the extended barrels of the tile calorimeter are 5.8 m and 2.6 m in length, respectively. Being placed directly outside of the EM calorimeter, they have an inner radius of $r \approx 2.3$ m and extend to $r \approx 4.3$ m. Each barrel is composed of 64 wedge-shaped modules of size $\Delta\phi \approx 0.1$; steel plates as absorber alternate almost periodically with the scintillating tiles with a ratio of approximately 4.7:1 in terms of volume. The tiles, being oriented normally to the beamline and arranged in rows running radially, provide almost seamless coverage in ϕ . The scintillators are read out at two sides of the modules by separate photomultiplier tubes located at the top of the wedges via wavelength-shifting fibres. Between the barrel and the extended barrel a gap of about half a meter hosts cabling and services for the ID and the LAr calorimeters; dedicated modules are used to partially recover the energy lost in the uninstrumented regions.

Also the tile calorimeters are segmented into three layers in depth with thicknesses corresponding to 1.4, 4.1 and 1.8 λ in the barrel and 1.5, 2.6, and 3.3 in the extended barrels, respectively. The segmentation in $\Delta\eta \times \Delta\phi$ is considerably coarser than in the EM calorimeters: the cell size of 0.1×0.1 and twice as coarse in $\Delta\eta$ in the third layer is sufficient though to measure the energy and the spatial information of hadronic showers with the required precision; given they tend to be wider than electromagnetic ones.

The HEC covering a pseudorapidity range of $1.5 < |\eta| < 3.2$ overlaps in coverage both with the tile and the forward calorimeters. Each of its endcaps is subdivided into two independent wheels with outer radii of ~ 2 m. The 25 mm (50 mm) thick copper plates serving as absorbers are interleaved with 8.5 mm wide gaps containing LAr as active material; using twice as thick absorber plates in the rear wheels results in a coarser sampling fraction with respect to the inner wheels. For $|\eta| < 2.5$ readout cells of $\Delta\eta \times \Delta\phi = 0.1 \times 0.1$ are used; beyond their granularity is halved. The HEC has the ability to also detect muons and measure any radiative energy loss.

The FCal provides coverage in the very forward region of $3.1 < |\eta| < 4.9$. As can be seen from Fig. 2.4(a), it is recessed by about 1.2 m with respect to the EM calorimeter in order to limit the neutron albedo into the ID. Nonetheless it is exposed to high particle fluxes, prompting very small gaps of active material (LAr). Each endcap is composed of three parts: designed to measure the energy of electromagnetic and hadronic interactions, respectively, the first uses copper and the other two tungsten as absorber material; accounting for the high particle fluxes the FCal is exposed to, the LAr gaps in between are very small.

2.2.3 The Muon Spectrometer

As mentioned in the introduction, three toroid magnets deliver a magnetic field to the outermost detector part, the muon spectrometer [136], which provides tracking and momentum information for particles exiting the calorimeters in the pseudorapidity range $|\eta| < 2.7$. The large barrel toroid bends charged particles (muons) up to $|\eta| < 1.4$ parallel to the beamline (in z direction); between $1.6 < |\eta| < 2.7$ the magnetic field is provided by the two smaller endcap toroids. Their coils are rotated around the beamline such that they fit in between the barrel toroid's coils in terms of their position in ϕ , as indicated in Fig. 2.5(a) showing in

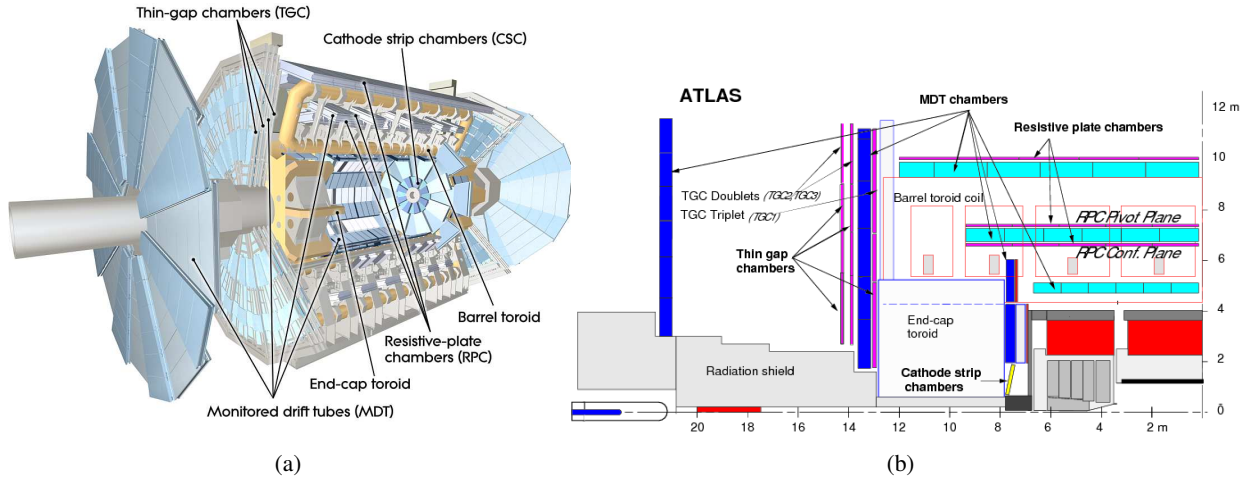


Figure 2.5: (a) Cut-away view of the ATLAS muon spectrometer. The various subsystems as well as the magnets are indicated. (b) Schematic view of the muon-spectrometer structure in the projection onto the bending plane ($|\eta|$). Taken from Refs. [136] and [153], respectively.

a cut-away view the toroid magnets and the muon spectrometer.

Four types of tracking chambers with differing technologies and properties are exploited to provide precise tracking as well as fast trigger information. Both in the barrel as well as in the endcaps the precision-chambers are arranged in three layers, also referred to as *stations*: in form of concentric cylinders around the beamline with radii of about 5 m, 7 m and 9 m and in large wheels perpendicular to the beamline located approximately at ± 7 m, ± 13 m and ± 21 m in z direction [153], respectively. As illustrated in the schematic projection onto the z - y plane in Fig. 2.5(b), the chambers in the endcaps are only located in front and behind the endcap toroids, while in the barrel region chambers are also placed between the coils. Reflecting the symmetry of the magnets, each layer is divided into eight octants in ϕ consisting of two sectors with chambers of slightly differing size; numbered from 1 through 16 running with ϕ , they are arranged such that there is a small overlap in the x - y plane maximising the azimuthal coverage. However, there are gaps in the acceptance: (i) at $\eta = 0$ allowing for services to the inside of the detector and (ii) in sectors 12 and 14, at $\phi = 240^\circ$ and $\phi = 300^\circ$, respectively, due to the feet of the detector support structure.

Precision measurements of the track coordinates in the bending plane are mainly provided by *Monitored Drift Tube* (MDT) chambers, covering $|\eta| < 2.7$; only in the innermost station of the endcap for $2.0 < |\eta| < 2.7$ they are replaced by *Cathode Strip Chambers* (CSCs).

MDT chambers consist of three to eight layers of aluminium drift tubes with a diameter of ~ 30 mm and a central tungsten-rhenium wire at a potential of ~ 3 kV; they are filled with an argon- CO_2 gas-mixture (97:3) operated at 3 bar. The maximum drift time is with approximately 700 ns rather long; the on average achieved intrinsic resolution in the bending plane is with $80 \mu\text{m}$ ($35 \mu\text{m}$) per tube (per chamber) however excellent. Due to the non-linearity of the space-drift time relation of the Ar- CO_2 gas-mixture the spatial resolution of the MDTs degrades at high interaction rates; prompting the usage of CSCs in the innermost layer of the forward region capable of coping with the challenging rate and background conditions. The CSCs are multiwire proportional chambers with the wires oriented in radial direction and both cathode planes segmented into strips, one perpendicular and one parallel to the wires; thus allowing measurements

of both η and ϕ coordinates. Since track coordinates are derived by interpolating between the signals of neighbouring cathode planes (the wire signals are not used) and each chamber contains four CSC planes, four independent measurements of the coordinates of a traversing particle are obtained.

The maximum drift time of about 20 ns is significantly shorter than for the MDTs and smaller than the nominal bunch-spacing. In the bending direction an excellent intrinsic resolution of $60\ \mu\text{m}$ per CSC plane ($40\ \mu\text{m}$ per chamber) is achieved; in the non-bending (ϕ) direction however the resolution is only 5 mm due to the coarser cathode segmentation.

In order to achieve standalone (i.e. without using ID information) a transverse-momentum resolution of $\sigma_{p_T}/p_T = 10\% p_T$ at 1 TeV, the relative alignment of the chambers with respect to each other needs to be of the order of $30\ \mu\text{m}$; for this purpose an optical alignment-monitoring system is employed.

Resistive Plate Chambers (RPCs) and *Thin Gap Chambers* (TGCs) are exploited to provide fast information at the order of 15-25 ns regarding traversing muons to the L1 trigger in the pseudorapidity range of $|\eta| < 2.4$ (cf. Sec. 2.2.6). Furthermore, by also measuring track coordinates in the non-bending plane they complement the MDT measurements (restricted to the bending plane). RPCs are used in the barrel ($|\eta| < 1.05$) and are arranged in concentric cylindrical layers around the beamline, building three *trigger stations*: as can be seen from Fig. 2.5(b), they are placed in front and behind the MDT layer of the middle station as well as behind the MDT layer of the outermost station. Each RPC consists of two detector layers, where one detector consists of two parallel electrode plates separated from each other by a 2 mm insulating spacer; the gap is filled with a $\text{C}_2\text{H}_2\text{F}_4$ -based gas-mixture and is penetrated by an electric field of about 4.9 kV/mm. Two sets of strips are placed orthogonal to each other to provide read-out of the η and ϕ coordinates.

In the endcap regions TGCs are employed for their high-rate capabilities: they are arranged in three disks, where one (two) are located in front (behind) the MDT wheel of the middle station (cf. Fig. 2.5(b)). TGCs exploit the same principle as multiwire proportional chambers.

The MS is one of the detector systems that were staged and completed to its initial design during LS1 by adding missing MDT chambers in the barrel-endcap transition-region [154]. Furthermore, RPC-equipped MDT chambers were mounted inside two elevator shafts, located in sectors 13 on each detector side, to recover a $\sim 1\%$ acceptance gap. Some of the new MDT chambers rely on smaller tube radii with respect to the ones described above providing better rate capabilities.

2.2.4 Forward Detectors

Besides the main detector subsystems described in the previous sections aiming at measuring hard-scatter events with rather centrally produced decay products, the (current) ATLAS experiment also accommodates four smaller subsystems dedicated to providing coverage of the very forward region. All consisting of two identical parts located symmetrically at $\pm z$ from the interaction point (IP), these are sorted according to increasing distance: the LUCID, the ZDC, the AFP and the ALFA detectors, where the AFP detector was installed in two steps during Run 2.

LUCID (LUminosity measurement using Cherenkov Integrating Detector), designed to monitor online the instantaneous luminosity and beam conditions, but also to measure the relative integrated luminosity (cf. Sec. 2.2.5), its primary aim is to detect inelastic pp scattering in the forward direction. It is located at

$z = \pm 17$ m in the ATLAS endcap regions with a radial distance of ~ 10 cm from the beamline, resulting in a pseudorapidity coverage of $5.6 < |\eta| < 6.0$ [136, 155]. As already anticipated, after Run 1 the LUCID system had to be upgraded and was completely replaced, including electronics, by LUCID-2 [156] in order to cope with the more demanding conditions posed by the higher energy and increased luminosity in Run 2. Already during most of the 2011 data-taking, the 20 aluminium tubes, with 15 mm diameter and 1.5 m length, making up each LUCID part were operated under vacuum, instead of being filled with C_4F_{10} gas as originally done, to reduce the sensitivity of the Cherenkov detectors mitigating pile-up effects. Based on the Run 1 experiences, LUCID-2 uses smaller photomultiplier tubes (PMTs) which are located further away from the beamline: they have a diameter of 10 mm and are located at a radial distance of ~ 12.6 cm resulting in a coverage of $5.56 < |\eta| < 5.64$. Furthermore, simply exploiting the thin quartz windows of the PMTs as Cherenkov medium, and thus dispensing the aluminium tubes, the PMTs are placed on a support structure surrounding the beamline.

The main purpose of the ALFA (Absolute Luminosity For ATLAS) detector [136] is to detect elastic pp -scattering events at small angles; and thereby provide the possibility to measure the total cross-section [157, 158] that is related to the elastic-scattering amplitude in the forward direction (i.e. for Mandelstam momentum-transfer $t \rightarrow 0$) via the *optical theorem* as well as the absolute luminosity. This requires special beam optics, where the beam is more parallel and less divergent than usual, and the detector to be located far away from the IP in the z direction and close to the beamline: each AFP arm consists of scintillating-fibre trackers placed inside two *Roman Pots* [159], that allow them to approach the beamline very closely;⁴ positioned at $z = \pm 240$ m their pseudorapidity coverage is $|\eta| > 8.5$.

The AFP (ATLAS Forward Proton Detector) detector [160, 161] is designed to measure elastic or diffractive processes, where one or both protons remain intact and due to moderate energy losses are scattered at small angles, in dedicated pp collisions with low pile-up. Its program is complementary to the ALFA one, given that they target different acceptances in terms of beam optics and Mandelstam momentum-transfer variable t . The AFP is located at $z = \pm 210$ m, combining silicon-tracking sensors with high-resolution Time-of-Flight (ToF) detectors, it is installed in two Roman-Pot stations on each arm, allowing it to be moved close to the beamline. While the first arm without the ToF detector was installed during the winter shutdown in 2016, the full system was completed during the one in 2017.

The ZDC (Zero-Degree Calorimeter) detector [136] is located at $z = \pm 140$ m from the IP, where the beam-pipe is split into two independent ones. Each arm consists of one electromagnetic and three hadronic calorimeter modules. While its primary purpose is to measure neutrons with $|\eta| > 8.3$ in AA collisions, by detecting neutrons and photons in that pseudorapidity range, it increases the acceptance for diffractive processes and provided an additional minimum-bias trigger at the beginning of Run 1.

2.2.5 Luminosity Determination

The luminosity determination done by the ATLAS collaboration proceeds in two steps, based on two expressions of the luminosity [155, 162]. For a circular pp collider operated with n_b bunch pairs colliding per

⁴A Roman Pot is a 'container' in which a detector system can be placed; being connected to the beampipe with bellows, though separated from the vacuum of the collider by a thin window, it can be moved very close to the beam. [136]

revolution with frequency f_r , the instantaneous luminosity can be written as

$$\mathcal{L} = \frac{\mu n_b f_r}{\sigma_{\text{inel}}} = \frac{\mu_{\text{vis}} n_b f_r}{\sigma_{\text{vis}}}, \quad (2.1)$$

where σ_{inel} is the pp inelastic cross-section and μ is the average number of inelastic interactions per bunch crossing.⁵ They are related to their *visible* counterparts, σ_{vis} and μ_{vis} , via the efficiency ε of the detector and algorithm providing the measurement of the observed interaction rate per crossing $\mu_{\text{vis}} = \varepsilon\mu$. In order to obtain the luminosity estimate, the absolute luminosity scale of that particular detector and algorithm combination needs to be calibrated, which is equivalent to measuring $\sigma_{\text{vis}} = \varepsilon\sigma_{\text{inel}}$. This is done by exploiting that the luminosity can also be expressed as function of accelerator parameters:

$$\mathcal{L} = \frac{n_b f_r n_1 n_2}{2\pi \Sigma_x \Sigma_y}, \quad (2.2)$$

where $n_{1(2)}$ is the number of protons per bunch in beam 1 (2) and $\Sigma_{x(y)}$ characterise the horizontal (vertical) beam widths. Combining this expression with Eqs. 2.1 yields

$$\sigma_{\text{vis}} = \mu_{\text{vis}}^{\text{vdM}} \frac{2\pi \Sigma_x \Sigma_y}{n_1 n_2}, \quad (2.3)$$

allowing σ_{vis} to be measured in dedicated *van der Meer* (vdM) scans [163, 164], given the bunch-population product $n_1 n_2$ is determined separately by the LHC Bunch-Current Normalisation Working Group through analysing the LHC beam currents (e.g. see Ref [165]). In the vdM scans, the beam separation is varied in steps, individually in horizontal and vertical direction, and the beam parameters $\Sigma_{x(y)}$ as well as $\mu_{\text{vis}}^{\text{vdM}}$, defined as the maximal visible rate, are extracted; the beam conditions differ from nominal physics runs, there are fewer bunches, no bunch trains and lower bunch intensities.

Several detectors are exploited to determine the luminosity and the associated systematic uncertainty: besides the dedicated systems introduced in the previous section, this also includes the ID or the tile and forward calorimeters, where certain rates sensitive to μ_{vis} are measured. Various algorithms have been developed, ranging from *event counting*, via *hit/particle counting* to *charge integration* [156]; which detectors and algorithms are used, depends also on the μ range. For the 2011 data-taking, the luminosity was determined based on measurements performed with LUCID, the ID as well as the BCM (Beam Conditions Monitor) [136].⁶ Measurements in the calorimeters provided cross-checks to the main luminosity measurement; all results were in good agreement and a total relative uncertainty of 1.8 % was determined.

For the early Run-2 data-taking, the luminosity was solely determined using LUCID-2 (cf. Sec. 2.2.4); at the time it was the only system able to measure the online per-bunch luminosity accurately for each of the colliding bunch pairs [156]. The luminosity was measured (preliminary) with a precision of 2.1 % and 3.4 % for the 2015 and 2016 datasets, respectively; the uncertainty for the 2016 dataset was finally reduced to 2.2 %.

⁵The average is performed over the n_b bunches as well as over one *luminosity block* (LB). An LB constitutes the basic time unit for storing luminosity information and is in general of the order of one minute; the assumption is that during that timespan data is taken under uniform conditions.

⁶The BCM consists of four small diamond sensors located at $z = \pm 184$ cm. Arranged around the beam-pipe it was originally designed to prevent damage of the ID by monitoring beam losses and to trigger a beam-abort, if thresholds are exceeded, but it also provides luminosity signals at $|\eta| = 4.2$.

2.2.6 The Trigger System

Due to limitations regarding the computing resources for readout, storage and offline processing of the data, the ATLAS trigger system [136] is designed to reduce the nominal input rate of 40 MHz to an output rate of about 200 Hz: only potentially interesting events are selected for recording based on rapidly identifying certain signatures or topologies, e.g. of muons, electrons or missing transverse energy.

Several upgrades and changes in the trigger system were performed during LS1 [166]: in particular to cope with the changed LHC conditions, i.e. the increase in centre-of-mass energy and the decrease in the bunch-spacing (cf. Sec. 2.3) leading to expectedly higher trigger rates, but also to be able to make use of the newly installed detector systems, the IBL and the additional RPC chambers (cf. Secs. 2.2.1 and 2.2.3).

In Run 1 the trigger system was composed of three levels of event selection: the hardware-based *Level-1* (L1) and the software-based *Level-2* (L2) and *event filter* (EF) collectively referred to as *High-Level Trigger* (HLT); they use partial and full event information, respectively. In Run 2, L2 and EF were merged, allowing in particular a better sharing of the available resources, but also hardware and software simplification.

The L1 trigger was designed to reduce the input rate to 75 kHz until the HLT processing farm was upgraded to cope with 100 kHz, which happened as foreseen during LS1. Indeed, the L1 rate was always kept below 60 Hz during the 2011 data-taking [167], and did not exceed the nominally allowed rate during Run 2.

In nominal conditions the L2 trigger was supposed to reduce the rate to 3 kHz; in 2011 it was always below 5 kHz. While the design output rate for recording was 200 Hz, it was possible to already increase the limit during Run 1 to 400 Hz and further to 1 kHz in Run 2.

The L1 trigger decision is based on coarse-granularity measurements provided by a limited set of the detector subsystems, i.e. the EM and hadronic calorimeters as well as the muon trigger chambers, RPC and TGC. The L1 calorimeter trigger [168] aims to identify localised energy depositions compatible with high- E_T objects such as electrons, photons, jets, and hadronically decaying τ -leptons or event topologies with large (missing) transverse energy. For this purpose it evaluates the total energy deposited in cells of the EM and hadronic calorimeter within *trigger towers*, i.e. detector regions corresponding to 4×4 the cell area in $\eta \times \phi$ of the middle layer of the EM calorimeter as illustrated in Fig. 2.4(b).

The L1 muon trigger aims to find hit patterns expected for high- p_T muons stemming from the interaction region. This is done by identifying hit coincidences between the various trigger stations: hits are required to lie within *roads*, i.e. envelopes containing the trajectories of muons with a certain p_T from the nominal interaction point. Since this effectively defines a p_T threshold, the system design allows to apply several such thresholds simultaneously.

While the final decision of the L1 trigger is solely based on the multiplicity of objects above predefined E_T / p_T thresholds, it also provides information on the trigger object's location in the detector defining *Regions-of-Interest* (RoIs).

After being accepted by the L1 trigger, events are processed by the HLT exploiting *all* detector subsystems and their full granularity. In Run 1 the L2 trigger decision was based on fast processing partial detector information restricted to the RoIs using custom online algorithms; at the EF the full detector information is available and reconstruction algorithms similar to the *offline* ones, discussed in Chap. 3, are used. In Run 2, where the merging of the L2 and EF farms removes the rate limitation between the two steps, providing higher flexibility of the algorithms to exploit information provided within the RoIs *or* the full detector, most HLT triggers still rely on a very similar two-staged approach in order to reduce the

processing time.

The configuration of the trigger system is done via a collection of *trigger chains* or *triggers* that, defined by a certain event signature, specify the reconstruction sequence and selection steps from the L1 to the HLT. By changing the selection criteria and thresholds applied to the objects, the trigger rates can be controlled. For certain signatures, e.g. jets or missing transverse momentum, this might not be sufficient to ensure a constant rate and the related triggers are *prescaled* by a factor N : only 1 in N events passing the trigger selection are also accepted for readout. However, all of the *single-object triggers* used to collect the data on which the analyses presented in Chaps. 4 and 5 are based, are *unprescaled*; targeting final states with at least one electron, one muon or large missing transverse momentum they are discussed somewhat further in Secs. 3.5, 3.6 and 3.9, respectively.

2.2.7 Detector Simulation

Simulated datasets constitute an important tool for most of the physics analyses and performance studies carried out by the ATLAS collaboration and in particular for the analyses described in this thesis. In order to be able to treat the simulated data in the same way as the real data, regarding object and event reconstruction as well as analysis, the detector and the interaction of the *generated* decay products of a certain physics process with it,⁷ need to be simulated as well. This *simulation* step is followed by the *digitisation* step, where the hits produced in the simulation are converted into detector responses (*digits*).

The simulation of the ATLAS detector (response) [169] is built from databases containing in addition to the detector geometry also information regarding the data conditions as well as detector imperfections etc. and is integrated into the ATHENA framework [170]. A detailed (“full”) simulation exploits the GEANT4 [171] toolkit to describe interactions between particles as well as particles and the detector material. Its precise description of the large and complex detector geometry and the interaction processes, however, requires large computing resources and limits the size of the simulated samples, that can be processed in a timely manner; this prompts the complementary exploitation of fast (and less evolved) simulation programs to provide high statistics datasets. Currently, the ATLFAST-II (AFII) package is employed for this purpose, which uses the *Fast Calorimeter Simulation* (FastCaloSim) [172] for the calorimeter simulation, while GEANT4 is used to simulate the inner detector and the muon spectrometer response. This combination of fast and full simulation reduces the overall simulation time by roughly one order of magnitude while reproducing key features of the reconstructed object properties [173]. FastCaloSim exploits a simplified description of the calorimeter geometry, that is also used by the reconstruction software, as well as parametrisations of the energy responses and distributions in the calorimeter, based on GEANT4 simulations of single photons, electrons and charged pions; while most calorimeter objects are well reproduced, FastCaloSim fails to describe topo-clusters, used to reconstruct hadronic showers, properly (cf. Chap. 3.2).

2.3 Data-Taking during 2011 and 2015/2016

As mentioned in the introduction, the datasets on which the analyses described in Chaps. 4 and 5 are based, were collected with the ATLAS experiment in pp collisions at centre-of-mass energies of $\sqrt{s} = 7$ TeV and $\sqrt{s} = 13$ TeV in the years 2011 and 2015/2016, i.e. during Run 1 and Run 2, respectively. Figure 2.6(a)

⁷For a basic introduction of the generation of pp events, see Sec. 1.4.

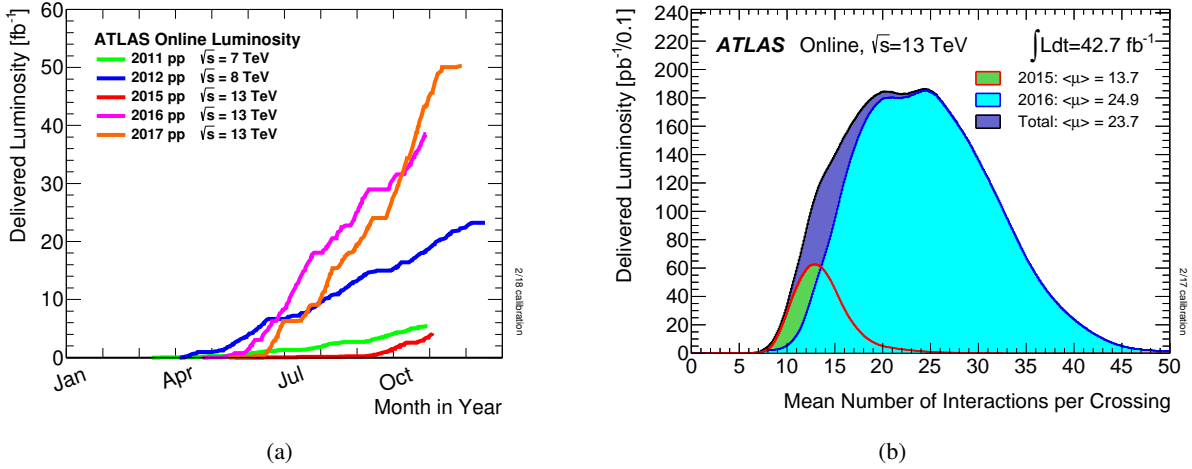


Figure 2.6: (a) Comparison of the cumulative delivered luminosity during stable pp collisions versus the month during data-taking in the years 2011-2017. (b) Luminosity-weighted distribution of the mean number of inelastic interactions per pp bunch-crossing μ in the years 2015 and 2016. It is obtained from the instantaneous per-bunch luminosity via Eq. 2.1 with $\sigma_{\text{inel}} = 80$ mb. Taken from Ref. [174].

shows a comparison of the cumulative luminosity delivered by the LHC as function of the month for the various years of data-taking between 2011 and 2017. While the typical number of protons in the colliding bunches varied only slightly and is close to the design value of $1.15 \cdot 10^{11}$, the number of colliding bunches (n_b) as well as the bunch spacing changed over the years; this together with optimised beam parameters resulted in a change of the peak values of the instantaneous luminosity and the average number of inelastic interactions per bunch crossing μ (cf. Eqs. 2.2 and 2.1).

In 2011, the ATLAS experiment collected data between March and end of October, where the LHC was operated with 50 ns bunch spacing and collided at most 1331 bunch pairs, reaching a peak luminosity of $3.65 \cdot 10^{33} \text{cm}^{-2}\text{s}^{-1}$. In 2015 and 2016, the LHC was nominally running with 25 ns bunch spacing and colliding up to 2232 and 2208 bunch pairs, reaching peak luminosities of $5.0 \cdot 10^{33} \text{cm}^{-2}\text{s}^{-1}$ and $13.8 \cdot 10^{33} \text{cm}^{-2}\text{s}^{-1}$, respectively; the latter being well above the design value. The data-taking period in 2015 was rather short, only from August until November, while it lasted from April until November in 2016.

In all three years, the recorded dataset corresponds to 93 % of the total integrated luminosity delivered by the LHC from the beginning of stable beams until the end of the recording by the ATLAS experiment; the loss is due to an inefficiency of the data-acquisition system as well as the “warm start” of the detector (only once stable beams are reached in the LHC, the high-voltage in the tracking detectors is ramped up and the preamplifiers of the pixel detector are turned on). The data finally analysed by the reported measurements is yet another subset: namely events recorded during times, where all relevant detector components were fully operational, and in which all reconstructed physics objects fulfil certain data quality criteria. The total integrated luminosities correspond to 83 %, 76 % and 85 % of the luminosities delivered during the 2011, 2015 and 2016 data-takings, respectively; the losses in the 2015 and 2016 datasets were, for example, due to neglected runs, where the IBL was not included and the toroid magnet not functional, respectively [175]. The luminosity is determined as described in Sec. 2.2.5 with total relative uncertainties of 1.8 %, 2.1 % and 3.4 % in 2011, 2015 and 2016, respectively.

	2011	2015	2016
Centre-of-mass energy \sqrt{s} [TeV]	7	13	13
Maximum number of colliding bunch pairs (n_b)	1331	2232	2208
Nominal bunch spacing [ns]	50	25	25
Average μ	9.1	13.7	24.9
Peak μ	31.4	36.4	51.8
Peak luminosity [$10^{33} \text{cm}^{-2} \text{s}^{-1}$]	3.65	5.0	13.8
Total integrated luminosity, ready for analyses [fb^{-1}]	4.6	3.2	32.9

Table 2.1: Summary of the parameters characterising the datasets collected in pp collisions during the years 2011, 2015 and 2016. Average μ refers to the bunch-averaged pile-up parameter (cf. Eq. 2.1), and the total integrated luminosity indicates the remaining dataset after requiring basic quality criteria (see text).

As a result of the high instantaneous luminosities, several pp collisions occur per bunch crossing: for the 2015 and 2016 datasets the luminosity-weighted distributions of μ are shown in Fig. 2.6(b); they are obtained via the relation in Eq. 2.1 from the measured per-bunch luminosities and taking $\sigma_{\text{inel}} = 80 \text{ mb}$. While the mean of the average inelastic interactions per bunch crossing in the 2015 and 2016 datasets is 13.7 and 24.9, respectively, there occurred also runs with a μ of up to ~ 36 and ~ 52 .⁸ This is a significant increase with respect to the 2011 data-taking, where the average μ was already 9.1 and a maximum of ~ 31 was observed.

The effect of multiple interactions on the analysis of hard-scatter events is referred to as *pile-up*. In order to distinguish the impact from additional pp collisions in the same and from neighbouring bunch crossings, they are also denoted as *in-time* and *out-of-time* pile-up, respectively. The latter poses an issue to detector systems, where the read-out time is long compared to the bunch-spacing time, e.g. in the LAr calorimeter (cf. Sec. 2.2.2). While μ is used as a measure of the out-of-time pile-up activity, the amount of in-time pile-up is estimated by the number of reconstructed primary vertices in an event (cf. Sec. 3.1).

All discussed characteristic parameters describing the analysed datasets are summarised in Table 2.1.

⁸As defined in Sec. 2.2.5, μ itself is already an average over all bunch-crossings in each LB.

3 Reconstruction and Identification of Physics Objects at the ATLAS Experiment

Particles emerging from the pp collisions traverse the ATLAS detector and, if interacting, lead to hits in the tracking detectors and/or energy deposits in the calorimeters. This raw data is then processed in several steps by various, sophisticated reconstruction and identification algorithms implemented in the ATHENA framework [170] in order to finally identify the measured signals with physics objects, such as electrons or jets, defined by relatively few parameters. Combining all possible information from the various subdetectors results in high identification efficiencies and background rejections as well as optimal four-momentum reconstructions; it even allows to infer the presence of non-interacting particles from a momentum imbalance in the transverse plane.

This chapter gives an overview of the essential reconstruction and identification steps starting from high-level detector information, tracks and clusters, and leading to the definition of the physics objects employed in the physics analyses presented in Chaps. 4 and 5; particular emphasis is given to the reconstruction of three types of jets (Sec. 3.3) and the identification of b jets (Sec. 3.4). While the focus lies on the description of the offline reconstruction and identification, the corresponding approaches exploited by the triggers (cf. Sec. 2.2.6), used to collect the analysed datasets, are also briefly reviewed. Besides introducing the various methods, studies of their performance and the procedures to correct the efficiencies and scales in simulation in order to match the ones observed in data are discussed, as well as the associated systematic uncertainties that need to be considered in the reported analyses.

Given the two analyses are based on the 2011 and 2015+2016 datasets, respectively, the exploited reconstruction methods differ: they got improved and adapted to the changed collision and detector conditions (cf. Chap. 2); the findings of the performance measurements, whose strategies also evolved over time, might also differ. The description concentrates on the commonalities and, where necessary, on the more recent procedures and results used for the 2015+2016 dataset, while significant differences between the years are mentioned explicitly.

3.1 Track and Vertex Reconstruction

The reconstruction of tracks from hits in the tracking detectors¹ caused by traversing charged particles constitutes an important ingredient to their reconstruction and identification as well as the reconstruction of the hard-scatter vertex described in the subsequent sections and below, respectively. The ATLAS detector has two independent tracking systems, the inner detector (ID) and the muon spectrometer (MS) (cf. Secs. 2.2.1 and 2.2.3, respectively). As the latter is only used in the reconstruction of muons, the track reconstruction based on hits in the MS is introduced in the context of the muon reconstruction in Sec. 3.6, and it follows

¹Hits refer to *clusters* in the silicon detectors and *drift circles* in the TRT.

a description of the track reconstruction and vertex finding of the ID.

There are currently two sequences of track-reconstruction algorithms [176, 177] employed, the main *inside-out* and a consecutive *outside-in* track-reconstruction approach.² The former is designed to efficiently reconstruct tracks of *primary* charged particles produced in the hard-scatter interaction or stemming from decays of short-lived particles; it starts in the silicon detectors and performs the track building towards the outer border of the ID. Taking the opposite approach starting from information of the TRT left unused by the inside-out sequence, the latter targets particles emerging from decays of long(er)-lived particles or photon conversions tending to not have sufficient hits in the silicon detectors required by the former.

The inside-out sequence starts by creating three-dimensional measurements, *space-points*, from the hits in the silicon detectors. Sets of three space-points function as seeds for the building of track candidates: based on the seed direction a window search is performed and a combinatorial Kalman filter [178] is exploited to associate hits to emerging track candidates. Generally, a high number of track candidates are found, many of which share measurements, are incomplete or are fake tracks based on measurements originating from several particles. Therefore, before performing the extension into the outer TRT and the track refit employing the full information of all three tracking detectors, ambiguities are resolved by employing a scoring schema [179] based on simple measures of the track quality.

The reverse outside-in sequence starts from track segments in the TRT that are built from candidates identified with a standard Hough transform [180] using also a combinatorial Kalman filter; hits used by the inside-out approach are neglected. By *back-tracking*, i.e. adding subsequently silicon hits, the segments are extended inwards and tracks are built exploiting information missed by the first approach.

Reconstructed tracks are required to have a minimum transverse momentum (p_T) of 400 MeV [181]; additional quality criteria, e.g. regarding the number of hits in the silicon detectors,³ as well as association to the primary vertex (see below), are employed to ensure only well reconstructed tracks are considered. Somewhat depending on the required criteria, the pile-up activity as well as the track transverse momentum and pseudorapidity, the reconstruction efficiency for tracks from primary particles using the inside-out sequence is at the level of 80 % [181, 182].

For Run 2 the ambiguity solving of the inside-out sequence was revised in order to optimise the track-reconstruction performance in dense environments [183], e.g. inside high- p_T jets, as exploited in searches for new heavy resonances such as the one presented in Chap. 5, considering also the additional information provided by the inclusion of the IBL (cf. Sec. 2.2.1). The reconstruction efficiency of tracks in the core of high- p_T light (b) jets is improved at the level of 10 % (14 %); resulting in a relative increase of the b -tagging efficiency by 7-13 % for a given mistag rate of the IP3D algorithm for jets with $p_T > 100$ GeV in simulated Z' events (cf. Sec. 3.4).

Based on tracks fulfilling certain quality criteria the primary interaction point, the *primary vertex*, of

²There is also a third sequence, the *second stage pattern* recognition, which is dedicated to the finding of V0 vertices, kink objects due to bremsstrahlung and their associated tracks.

³In Run 2, standard (loose) quality criteria comprise of: (i) at least seven silicon hits, (ii) no more than one silicon hit shared by multiple tracks, where SCT hits are weighted by a factor 0.5, (iii) no more than one (two) missing hits in the pixel (SCT), where a hit is expected.[182] Tracks employed by the electron and muon reconstruction usually need to fulfil stricter criteria which are optimised individually to yield maximal performance.

the hard-scatter event is reconstructed using an *iterative vertex finding* approach [184]. Due to colliding bunches of protons and the significant inelastic cross-section, several primary vertices are reconstructed in a triggered event: the one with the highest sum of the squared p_T of the associated tracks is identified with the *hard-scatter vertex*; all other vertices are referred to as *pile-up vertices*.

The selection of tracks likely stemming from the hard-scatter vertex is mainly based on two variables, the *transverse* and *longitudinal impact parameters*. Denoted d_0 and z_0 , respectively, they define for a track at its point of closest approach to the centre of the detector in the transverse plane the distance in the transverse plane as well as to the primary vertex in the z direction [184].⁴ Expressing z_0 initially relative to the beam-spot centre [185] the global maximum of its distribution of all considered tracks, serves as seed to the vertex finding. The vertex position is then determined using the *Adaptive Vertex Fitter* [186] that also refits the tracks with the constraint that they originate from that vertex; tracks found to be incompatible by more than seven standard deviations are used to seed a new vertex. The procedure is repeated until either all tracks are associated with vertices or no further vertices can be built which requires at least two associated tracks.

Considering only vertices with at least three (two) associated tracks with $p_T > 400$ MeV as done for the analyses performed using 2011 (2015/16) data described in this thesis (cf. Chaps. 4 and 5), assures reconstruction efficiencies of more than 90 (85) % depending on the number of associated tracks and additional vertices from pile-up interactions [181, 187].

3.2 Clustering of Calorimeter Cells

Electromagnetically and hadronically interacting particles usually deposit their energy in several cells of the calorimeter (cf. Sec. 2.2.2), both in the lateral and the longitudinal direction. Two different algorithms are used at the ATLAS experiment to group associated cells into *clusters*. Each cluster contains at best, but not necessarily, the total deposited energy of one particle: the *sliding-window* [136] and the *topological-clustering* [188] algorithms. Clusters built with the former are of fixed size in $\eta \times \phi$, allowing a very precise cluster energy calibration [189]; they constitute the starting point of the reconstruction of central electrons (and photons) and are thus further discussed in the context of Sec. 3.5. The latter algorithm is particularly efficient regarding noise suppression in clusters with a large numbers of cells; the resulting topological clusters, *topo-clusters*, are used as input to the reconstruction of jets, hadronically decaying τ (τ_{had}) leptons and the missing transverse momentum as described in subsequent sections.

Calorimeter cells are collected into topo-clusters according to a “spatial signal-significance pattern” [188], where the significance is defined as the absolute ratio of the cell energy and the average (expected) noise measured at the electromagnetic (EM) energy scale.⁵ Cells with a significance greater four serve as seeds to the cluster-forming; neighbouring cells in all three dimensions are collected into the *proto-cluster* and, if their significance exceeds two, their neighbours as well. Two proto-clusters are merged if (i) a direct neighbour is a seed cell itself or (ii) two seed cells share a direct neighbouring cell. Applying this procedure iteratively to further neighbours, the cluster formation stops once one set of neighbouring cells with significances less than or equal two are collected.

⁴In Run 2 the beamline served as reference, accounting for the tilt of the beam.

⁵Using the *absolute* significance as measure, also allows cells with negative energies, mainly caused by fluctuations due to pile-up interactions, to serve as seed; in which case often also the total cluster energy becomes negative. For reconstructing physics objects, however, only clusters with a positive net energy are considered.

Since in the cluster formation spatial signal structures are not taken into account explicitly, proto-clusters might be built from signals belonging to two or more particles. This is remedied by splitting proto-clusters with two or more local maxima, i.e. cells with energies above 500 MeV, guided by energy distributions provided by the highly granular electromagnetic calorimeters; cells can only be shared by at most two (highest-energy) proto-clusters. The obtained proto-clusters are the topo-clusters used as input for the object reconstruction.

The EM scale at which the topo-cluster energy is determined, describes correctly the energy deposited by electrons or photons, but not by hadrons, due to the non-compensating character of the ATLAS calorimeters. While therefore the energy-scale calibration of the reconstructed physics objects is particularly important, when there is a significant hadronic component, as is the case for jets or τ_{had} leptons (cf. Secs. 3.3 and 3.8), it is also beneficial to have a calibration scheme that does not make particular assumptions regarding the kind of physics object the topo-cluster might belong to, e.g. for the $E_{\text{T}}^{\text{miss}}$ reconstruction (cf. Sec. 3.9). The *local hadronic cell weighting* (LCW) calibration makes such an attempt [188]: exploring topo-cluster information sensitive to the nature of the shower, they are classified as electromagnetic or hadronic, and topo-cluster moment-dependent calibrations derived using simulations of single pions and tested in situ using test-beam data, are applied to correct the effects of (i) the non-compensating calorimeter response to hadrons, (ii) accidental energy losses due to noise threshold effects inherent to the clustering strategy, and (iii) energy loss due to passive material.

3.3 Reconstruction and Classification of Jets

3.3.1 Jet Definitions

Due to the nature of QCD, coloured objects, quarks and gluons, cannot be observed directly; they fragment and hadronise almost immediately after they are produced, leading to collimated sprays of energetic (colour-neutral) hadrons, referred to as *jets*.⁶ Jet algorithms provide a “jet definition” [190], i.e. a set of rules for grouping particles into jets, involving a *distance measure(s)*, and a *recombination scheme* determining how to assign a momentum to the resulting jet, that reflects the characteristics of the original parton. A good jet definition yields a common representation, if applied to different kinds of inputs, such as experimental measurements and simulated particles. All jets used in this thesis are reconstructed using the *anti- k_t algorithm* [191] implemented in the FASTJET package [192]: it is a *sequential recombination* jet algorithm that, being *infrared* and *collinear safe*, “behaves like an ideal cone algorithm” [193].

Defining the distance d_{ij} between two “particles” i and j as

$$d_{ij} = \min(k_{\text{T}i}^{2p}, k_{\text{T}j}^{2p}) \frac{\Delta R_{ij}^2}{R^2}, \quad (3.1)$$

and the distance d_{iB} between particle i and the beam B

$$d_{iB} = k_{\text{T}i}^{2p}, \quad (3.2)$$

⁶The only exception is the top quark which decays before the process of hadronisation sets in.

where ΔR_{ij} is the angular distance between the two particles, $k_{Ti/j}$ their transverse momenta and R the *radius parameter*, the jet definition of the anti- k_t algorithm is obtained for $p = -1$; the parameter p governs the relative power of the energy versus the geometrical scales, setting $p = 1$ yields the definition of the k_t algorithm [194, 195]. The clustering then proceeds as follows: for each particle i , (i) compute d_{iB} and all d_{ij} , (ii) identify the smallest of the distances, (iii) if it is a d_{ij} recombine i with j into a single new particle, else consider i to be a jet and remove it from the list of particles, (iv) in either case, return to (i) unless no particles are left.

The key property of the anti- k_t algorithm is that the jet shape is resilient with respect to soft radiation, while being flexible with respect to hard radiation.⁷ Whether reconstructed jets reflect in addition to the characteristics of the original (single) parton, also the event topology, depends on the chosen radius parameter R . The optimal value of R poses a trade-off between capturing perturbative (soft) radiation preferring larger radii and excluding contamination from the underlying event and pile-up, favouring smaller radii (cf. e.g. Ref. [196]); partons stemming from the decay of boosted objects, e.g. the Higgs boson, might be too collimated to be resolved individually and rather form a single jet, however, with substructure.

Therefore, there are three different types of jets exploited in the analyses presented in this thesis, jets reconstructed from topo-clusters (cf. Sec. 3.2) (i) at the EM scale with radius parameter $R = 0.4$, also referred to as *small-R jets*, and (ii) at the LCW scale with radius parameter $R = 1.0$, referred to as *large-R jets*, as well as (iii) *track jets* with radius parameter $R = 0.2$ reconstructed from high-quality ID tracks identified to stem from the hard-scatter vertex (cf. Sec. 3.1).⁸ While jets of types (i) and (ii) are exploited to reconstruct single partons and boosted objects decaying to (pairs of) partons, respectively, and thus need to be able to provide good approximations of the original particles properties, i.e. four-momentum, track jets are exclusively used to resolve the substructure of the large-R jets (in particular regarding their heavy-flavour content (cf. Secs. 3.4 and 5.4.2)), relying on their excellent directional resolution and pile-up resilience. They are associated with large-R jets by means of the *ghost-association* technique developed to determine the jet area [197]: “ghosts”, infinitely soft (pseudo-)particles (here corresponding to the track jets with their p_T set to a negligible amount, basically only preserving their direction) are added as input to the jet reconstruction without perturbing its outcome; if clustered inside the jet, they are considered associated.

The impact of soft radiation, stemming from e.g. the underlying event or pile-up interactions, on the measurement of the jet properties is (further) mitigated via two approaches that differ for small-R and large-R jets; techniques to suppress (small-R) pile-up jets are discussed in Sec. 3.3.3. In the case of small-R jets their measured energy is corrected based on the expected contamination as described in more detail below; in the case of large-R jets the (soft) radiation contaminating each jet is individually identified and removed, by resolving the (hard) substructure. This latter approach is generally referred to as *jet grooming* [198]; the large-R jets used in this thesis are groomed with the *trimming algorithm* [193]: here (i) the constituents of a large-R jet are reclustered using the k_t algorithm with radius parameter $R_{\text{sub}} < R$, (ii) the transverse momentum p_T^i of each subjet i is evaluated and (iii) if $p_T^i < f_{\text{cut}} \cdot p_T$, i.e. smaller than

⁷This can be understood by considering three representative distances ΔR_{12} between two *hard* particles 1 and 2, i.e. (i) $\Delta R_{12} \geq 2R$: each of them clusters all soft particles within a circle of radius R , resulting in two perfectly conical jets (with *jet areas* πR^2), (ii) $R < \Delta R_{12} < 2R$: if (a) $k_{T1} \gg k_{T2}$: results in one conical jet 1 and one partly-conical jet 2, if (b) $k_{T1} \approx k_{T2}$: results in two jets both with clipped cones, where the overlapping part is shared according to k_{T1}/k_{T2} , and (iii) $\Delta R_{12} < R$: 1 and 2 (together with all soft particles) cluster into one single jet - they are *merged* -, which (a) for $k_{T1} \gg k_{T2}$: is conical and centred around k_1 , (b) for $k_{T1} \approx k_{T2}$: has a more complex shape.

⁸In fact, the tracks are either required to be a constituent of the hard-scatter vertex or satisfy $|z_0 \sin(\theta)| < 3 \text{ mm}$.

a predefined fraction of a chosen hard scale such as the p_T of the (ungroomed) large-R jet, subjet i is discarded and (iv) the remaining subjets are assembled to form the *trimmed* large-R jet; the used parameters are $R_{\text{sub}} = 0.2$ and $f_{\text{cut}} = 5\%$ [199]. The k_t algorithm is used for the reclustering of the subjets as it also allows soft particles to become jets; other than the anti- k_t algorithm, which, starting to cluster from the hard particles, tends to create an imbalance by allocating most of the energy to one subjet.

3.3.2 Jet Energy and Mass Scales and Resolutions

A calibration procedure is employed aiming to restore the jet energy scale (JES) of small-R and large-R jets, as well as the jet mass scale (JMS) of the latter, to that of jets reconstructed from simulated stable particles, i.e. *particle jets*. The calibrations address not just the calorimeter non-compensation (cf. Secs. 2.2.2 and 3.2), but also several other effects, namely energy lost in inactive detector regions (dead material) or at the outer edge of the calorimeters (leakage), due to the noise threshold and other effects inherent to the topo-clustering strategy, due to energy not captured by the jet clustering (out-of-cone leakage), as well as pile-up effects in the case of small-R jets. Therefore, the JES calibration of small-R jets is quite evolved and comprises of several steps detailed below; in the case of large-R jets the calibration is particularly focused on improving the jet mass both in terms of scale and resolution (JMR) given that the spectrum may be studied in the context of searches for new physics in boosted scenarios (cf. e.g. Chap. 5).

Small-R Jets: JES

The JES calibration of small-R jets proceeds in Run 2 in six steps [200], starting with (i) the *origin correction*: here the η resolution is improved by recalculating the jet four-momenta so that they point to the hard-scatter primary vertex instead to the centre of the detector, without changing the jet energy. It is followed by two corrections addressing the energy contamination due to in-time and out-of-time pile-up [201]: (ii) the *jet area-based correction* [202], which is an event-level jet-by-jet correction based on the jet area A , a measure for the jet's susceptibility to the soft contamination ("diffuse noise") in the event, and ρ , an estimate of the amount of contamination present: using jets reconstructed from topo-clusters with the k_t algorithm with radius parameter $R = 0.4$, ρ is determined in each event as the median of p_T/A of all jets found in the central region and referred to as *pile-up p_T density*. As the corrected p_T still shows some dependence on N_{PV} , the number of reconstructed primary vertices (PV), and μ , the average number of interactions per bunch crossing (cf. Eq. 2.1), which are sensitive to the in-time and out-of-time pile-up activity, respectively, a (iii) *residual pile-up correction* is applied. It is derived by determining the difference between the jet-area corrected, reconstructed p_T and the matched particle jet p_T in simulation not subjected to pile-up contamination; the dependence on N_{PV} and μ is found to be approximately linear and independent of one another. Therefore, the pile-up corrected p_T can be written as

$$p_T^{\text{corr}} = p_T^{\text{reco}} - \rho \cdot A - \alpha \cdot (N_{\text{PV}} - 1) - \beta \cdot \mu. \quad (3.3)$$

The next step, (iv) the *absolute JES and η calibration* [203], corrects the reconstructed (origin- and pile-up corrected) jet four-momenta to the energy scale at particle level and accounts for biases in the η distribution of jets caused by changing energy responses in the transition between calorimeter geometries or technologies. Employing isolated particle jets from a sample of simulated dijet events, the correction

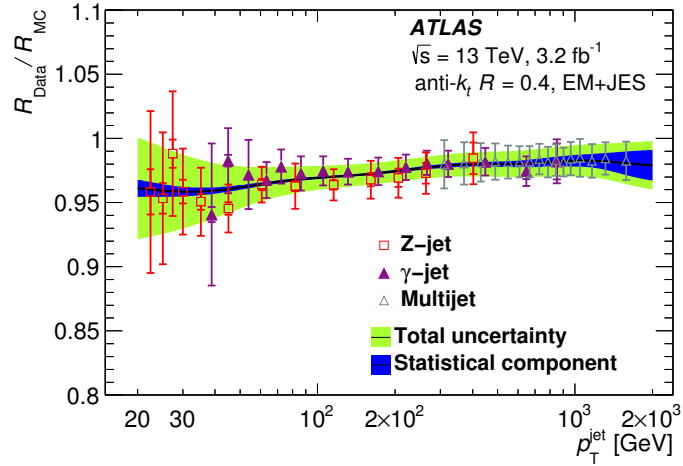


Figure 3.1: Data-to-simulation ratio of the in-situ response of small- R jets as function of the jet transverse momentum determined in Z -jet, γ + jet and multijet events. In addition to the final combined correction with its statistical and total uncertainty, also the results of the individual measurements performed with 2015 data at $\sqrt{s} = 13$ TeV are shown. Taken from Ref. [200].

factors are derived as the inverse of the average energy response⁹ as function of the reconstructed jet energy and the average difference between the true and the origin-corrected jet η in bins of the detector η , respectively. While the latter are very small for most regions of the detector, except in the transition regions, the former can take values of up to 2 for low p_T jets in the central detector region.

A remaining dependence of the JES on jet properties related to the jet's particle composition and internal energy distribution that differ depending on the initiating parton, in particular between quarks and gluons, is addressed by (v) the *global sequential (GS) calibration* [203]. The correction applied sequentially based on five calorimeter, track and muon track-segment observables, without considering correlations, aims at removing the dependence of the average jet- p_T response on them, while conserving the overall JES; i.e. its main effect is to improve the jet energy resolution (JER).

Finally, in a last step differences in the jet response between data and simulation are reduced by (vi) the *in-situ calibration*. Based on comparing the p_T balance of a (probe) jet against other well-measured reference objects in data and simulation, it can be divided in two steps: (a) the η -*intercalibration* [204] exploits dijet events to obtain a residual correction for jets in the forward region by using well-measured central jets as probes; (b) three other in-situ calibrations relying on photons, leptonically decaying Z bosons and a system of well-measured low- p_T jets [204] as probes are statistically combined in order to calibrate central jets over a wide p_T range. The combined data-to-simulation ratio of the in-situ response, defined as the average ratio of the momenta of the probe jet and the reference object, as function of the jet p_T is shown in Fig. 3.1; its inverse is applied as correction to the data: it amounts to about 4 % for low- p_T jets and decreases to 2 % at 2 TeV. The individual results obtained from the three different methods are shown alongside: governing different p_T regimes, they show good agreement in the overlapping regions.

Jets used in the analysis based on 2011 data (cf. Chap. 4) are calibrated with a slightly different, somewhat less evolved procedure [204]: most importantly the steps (ii) and (v) were not present, i.e. the area-based pile-up and the GS correction were not applied, and a pile-up correction similar to the residual

⁹The average jet energy (and similarly p_T) response is defined as $\mathcal{R} = \langle E_{\text{jet}}/E_{\text{truth}} \rangle$ and the corresponding resolution as $\sigma_{\mathcal{R}}/\mathcal{R}$.

correction in Run 2 was used. The in-situ correction was found to be a bit lower; such a difference is not unexpected given changes in the detector (“PMT down-drift” in the tile calorimeter) and its simulation [200].

JES uncertainties On the final calibration a set of systematic uncertainties is assigned that is propagated from the individual calibration steps as well as derived from additional studies. In the context of calibration steps (ii) and/or (iii), three (four) systematic uncertainties are considered to account for mismodelling of N_{PV} , μ , (ρ) and a p_T dependence of the residual terms neglected in Eq. 3.3 in the calibration for 2011 (Run 2) data. While the uncertainty on ρ is evaluated by varying the underlying event contribution by changing the event generator used to simulate the sample, the uncertainties on N_{PV} and μ are determined from the difference between the residual calibration obtained in simulation and in data as observed in in-situ validation studies [203]. Repeating the absolute JES and η calibration, step (iv), for a simulated sample relying on the fast AFII detector simulation (cf. Sec. 2.2.7) a small non-closure is found, most pronounced for forward jets at low p_T ; it is assigned as an additional systematic uncertainty for AFII samples. By resolving the dependence of JES on the number of muon-track segments ghost-associated with the jets in the context of the GSC, step (v), the energy-response distribution of *punch-through jets*, i.e. high- p_T jets that are not fully contained in the calorimeter, is improved. However, an associated uncertainty is derived as the maximum difference between the jet response in simulation and in data determined using a dijet tag-and-probe method [203]. The majority of uncertainties (67 in Run 2) stems from the final step, the in-situ calibration: in addition to statistical uncertainties, for all calibrations the effect of changing the program to simulate the sample as well as the event selection dedicated to obtain the required back-to-back topology is evaluated and assigned as systematic uncertainty. For the η -intercalibration additional uncertainties are considered to cover the impact of pile-up and to account for a non-closure of the method in the $2.0 < \eta_{\text{det}} < 2.6$ region [200]. Affecting only the Z/γ +jets in-situ calibrations, the uncertainties related to the electron, muon and photon reconstruction are propagated (cf. Secs. 3.5 and 3.6).

Furthermore, systematic uncertainties related to the jet flavour and the extrapolation to high- p_T jets are considered. The latter is assigned to jets with p_T greater 2 (1) TeV in Run 2 (2011) data given that even the in-situ method exploiting a system of well-measured low- p_T jets as probes becomes statistically limited in this regime; it is determined from single-hadron response measurements [203]. As the jet response of light quark, b quark and gluon-initiated jets differs an uncertainty on the flavour composition is taken into account. While generally analysis-dependent in Run 2, if not stated otherwise, a 50:50 composition of quarks and gluons is assumed and a conservative uncertainty of 100 % assigned [200]; for 2011 analyses results for representative samples, e.g. an inclusive sample of dijets, are provided as well as related uncertainties obtained from generator comparisons [203]. Also the impact of a mismodelling of the jet response for each of the jet flavours is accounted for by systematic uncertainties derived by comparing the predictions made by different generators, in particular regarding the hadronisation model and parton showering. For 2011 data more sources of uncertainties on the jet response of b jets are considered, namely the b fragmentation, soft radiation and dead material in the detector.

Finally, for 2011 data another systematic uncertainty is considered related to close-by effects; taking into account that the JES determination is only done for isolated jets, the jet response is studied for nearby jet activity as function of the angular distance and an uncertainty is assigned from the comparison to the track-jet response and the differences found in data and simulation [203].

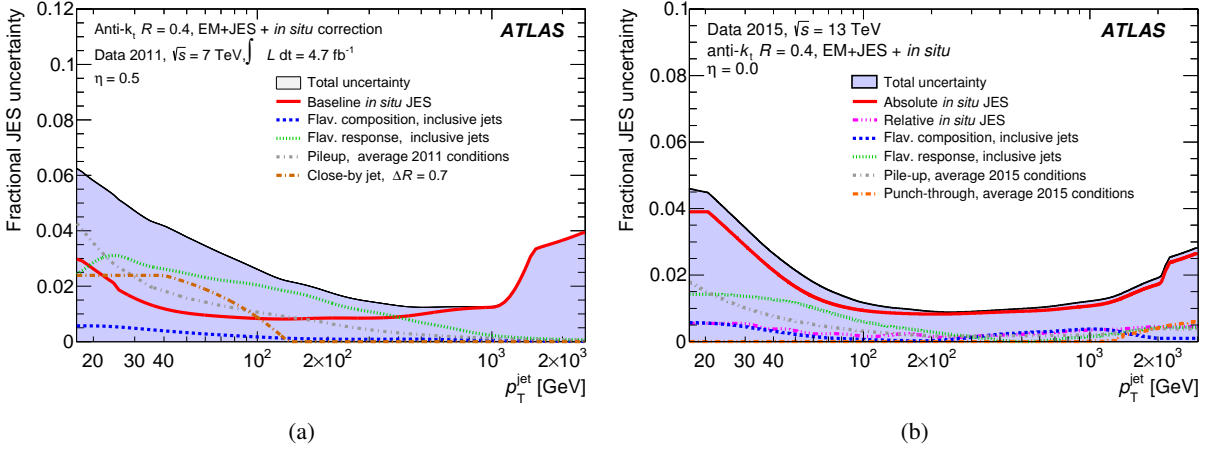


Figure 3.2: Fractional jet energy scale (JES) uncertainty for central small-R jets as function of the jet p_T for (a) 2011 data and (b) 2015+2016 data; the calibration started from the EM scale. The various groups of contributions are introduced in the text and apply to inclusive samples of dijet events. Systematic uncertainties due to the in-situ calibration are referred to as (b) “Baseline *in situ* JES” and (b) “Absolute (Relative) *in situ* JES”, where “Relative” stands for the η -intercalibration. In Fig. (a) the uncertainty on the JES of b jets is not included. Taken from Ref. [204] and [200], respectively.

Figures 3.2(a) and (b) show the relative total JES uncertainty for central jets in inclusive samples of dijet events obtained for 2011 data and in Run 2, respectively, as function of the jet p_T . The contributions from the various discussed sources grouped into certain subsets are shown as well; in Fig. 3.2(a) the uncertainty related to the response of b jets which is at the level of 2% is omitted. The total uncertainty is with 6 (4.5)% largest at low p_T ; it decreases with increasing p_T down to about 2 (1)% before it rises again sharply at 1 (2) TeV due to the large single-hadron response uncertainty in 2011 data (Run 2). With respect to η the uncertainty is fairly constant, except in Run 2 for the range of $2.0 < \eta_{\text{det}} < 2.6$, due to the non-closure uncertainty of the η -intercalibration. Though consistent, the total JES uncertainty in Run 2 is considerably smaller by up to 50% than in 2011 and clearly dominated by the in-situ calibration.

While in the analysis using 2011 data only the overall impact of the total JES uncertainty is evaluated, in the Run 2 analysis a reduced set of 19 of the discussed uncertainties is used, which allows to take almost precisely the correlations across p_T and η between the different sources into account (cf. Sec. 5.6.1). The reduced set is obtained following the global reduction scheme laid out in Ref. [204] through (i) an eigenvalue decomposition of the p_T -dependent uncertainties due to the in-situ calibrations (without the η -intercalibration), (ii) keeping the seven principal components as individual nuisance parameters and (iii) combining all remaining components into a single nuisance parameter while neglecting their correlations.

Small-R Jets: JER

In Run 1, the fractional jet- p_T resolution σ_{p_T}/p_T of small-R jets has been measured in situ in dijet events using two different methods, the *dijet-balance* and the *bisector* methods [205]. As shown in Fig. 3.3(a), the results are in rather good agreement with each other: the fractional resolution decreases with increasing jet p_T and is determined to be at the level of 20 (5)% at low (high) p_T . Furthermore, the measured results agree well with the ones obtained using simulations; generally the agreement is at the level of

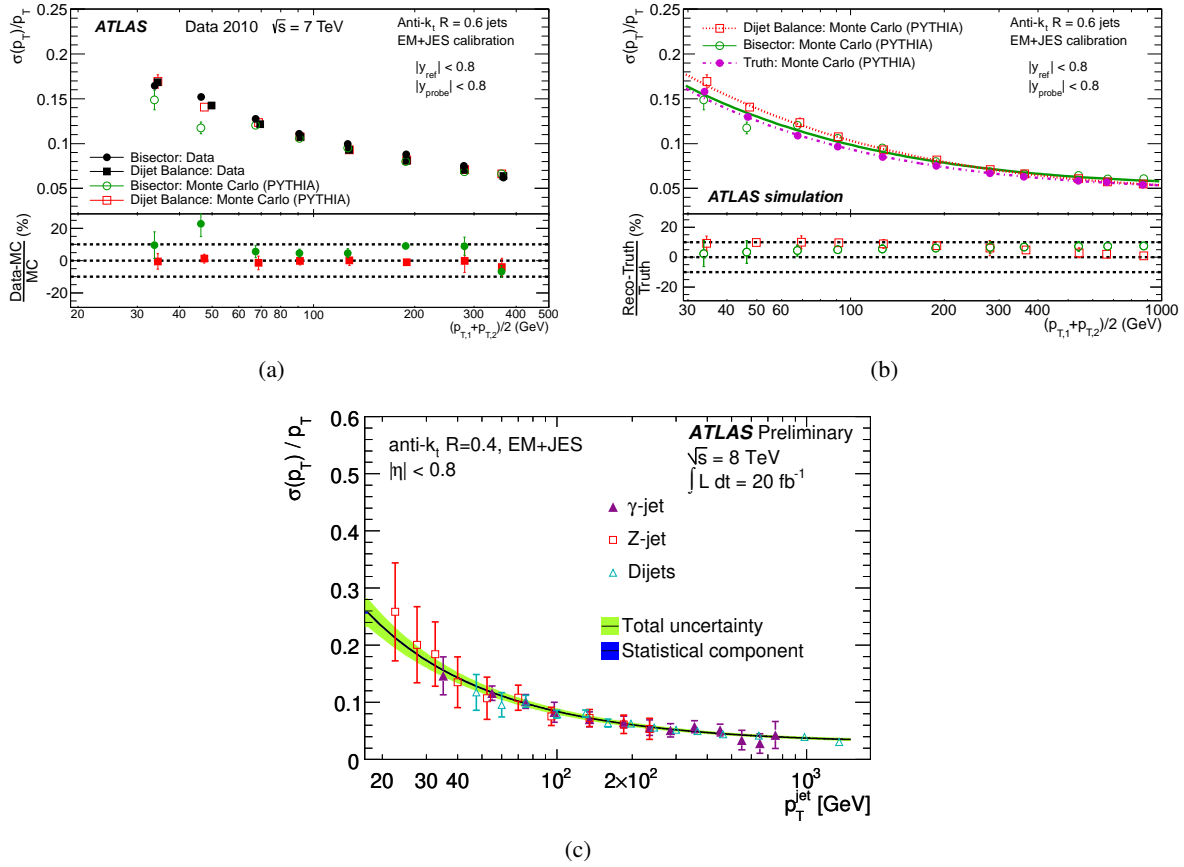


Figure 3.3: Relative jet-momentum resolution as function of the (average) jet p_T . The results of the dijet-balance and bisector methods in simulation for central small- R jets (with $R = 0.6$) are compared to the results obtained (a) for 2010 data at $\sqrt{s} = 7$ TeV and (b) for particle jets; the shown uncertainties are statistical only. (c) In addition to the final result with its statistical and total uncertainty also the individual in-situ results determined in Z+jet, γ + jet and dijet events using 2012 data at $\sqrt{s} = 8$ TeV and to which the fit using the functional form in Eq. 3.4 is performed, are shown. Taken from Refs. [205] and [206], respectively.

10 %, only at low p_T some larger deviation is observed as well as for larger rapidity values (not shown here). That the two methods indeed provide reliable estimates of the true jet- p_T resolution is confirmed by the closure test shown in Fig. 3.3(b): the in-situ methods applied to simulated dijet events reproduce the true jet- p_T resolution at the level of 10 %. Considering both comparisons as systematic uncertainties on the measured resolutions, they are dominating both the total systematic as well as the total uncertainty. Accounting also experimental systematic uncertainties, such as the JES uncertainty, the former amounts to 17-20 % at low p_T (~ 50 GeV), 15-18 % at medium p_T (~ 150 GeV) and 11-18 % at high p_T (~ 400 GeV) and somewhat increases with increasing $|\eta|$. An additional systematic uncertainty is considered related to the event modelling in simulation evaluated by comparing several variations with the default simulation (PYTHIA); it is determined to be at most 5 %.

Other than in Run 1, in Run 2 the jet- p_T resolution in simulation is corrected to match the values obtained in the final Run-1 measurement [206] and extrapolated to the Run-2 conditions. The final Run-1 measurement is based on the fact that the p_T dependence of the fractional calorimeter-based resolution can

be described by the following expression

$$\frac{\sigma(p_T)}{p_T} = \frac{N}{p_T} \oplus \frac{S}{\sqrt{p_T}} \oplus C, \quad (3.4)$$

i.e. made up of three independent contributions, the noise (N), stochastic (S) and constant (C) terms describing effects (i) from electronics and detector noise as well as pile-up, (ii) arising from the sampling nature of the calorimeters, and (iii) due to passive material. The noise term is measured in data using two different methods, *random cones in zero-bias data* and the distribution of soft-jet momenta [206]; with systematic uncertainties arising from the difference of the obtained results and the degree of non-closure of the methods. Then, in the combined measurement of the total resolution obtained by fitting the function of Eq. 3.4 to the fractional resolutions determined using the dijet-balance method [207] and the *direct-balance method* in Z/γ +jet events [208], while the noise term is constrained by the independent measurements. The result is shown in Fig. 3.3(c); the uncertainties related to the various in-situ methods are propagated through the fit and result in relative uncertainties of less than 3 % at 20 GeV and below 1 % above 100 GeV on the total jet energy resolution.

Large-R Jets: JES, JMS and JMR

As mentioned before, in the case of large-R jets the main focus lies on obtaining an accurately reconstructed jet mass with optimal resolution and associated systematic uncertainties. Thus, the calibration of their energy scale only comprises of step (iv) of the six-step procedure described for small-R jets above, i.e. the absolute JES and η calibration based on a sample of simulated multijet events in order to restore the energy scale at particle-level; following that an analogous procedure is used to correct the reconstructed jet-mass scale [198]. This step is particularly important given that other than the transverse momentum the invariant mass is quite susceptible to soft, wide-angle contributions. As a result a uniform mass response is obtained within 3 % across the full energy and $|\eta|$ range [209].

A priori the invariant mass of large-R jets is solely determined from calorimeter information, i.e. the energy and the momentum of all associated with topo-clusters at the LCW scale, and is referred to as *calorimeter-based jet mass* m_{calo} . However, its resolution (quantified as the half of the 68 % interquartile range (IQnR) divided by the median of the response distribution) degrades with increasing jet p_T , as can be seen from Fig. 3.4(a), as the angular separation of the decay products of the boosted particle (here W and Z bosons) falls below the calorimeter granularity. In order to overcome this limitation, tracking information providing excellent directional resolution is exploited and the *track-assisted jet mass* m_{TA} is defined as [209]:

$$m_{\text{TA}} = \frac{p_T^{\text{calo}}}{p_T^{\text{track}}} \times m_{\text{track}}; \quad (3.5)$$

i.e. the invariant mass of the collection of tracks associated with the large-R jet m_{track} is corrected by the ratio of the transverse momenta determined from calorimeter and tracking information, respectively, accounting for the otherwise neglected neutral contributions.¹⁰ Figure 3.4(b) shows the comparison of m_{track} , m_{calo} and m_{TA} both before and after the JES+JMS calibration in a jet- p_T range, where including tracking information is deemed to be beneficial: indeed m_{TA} shows an improved resolution and peak position with

¹⁰For tracks the pion mass is assumed.

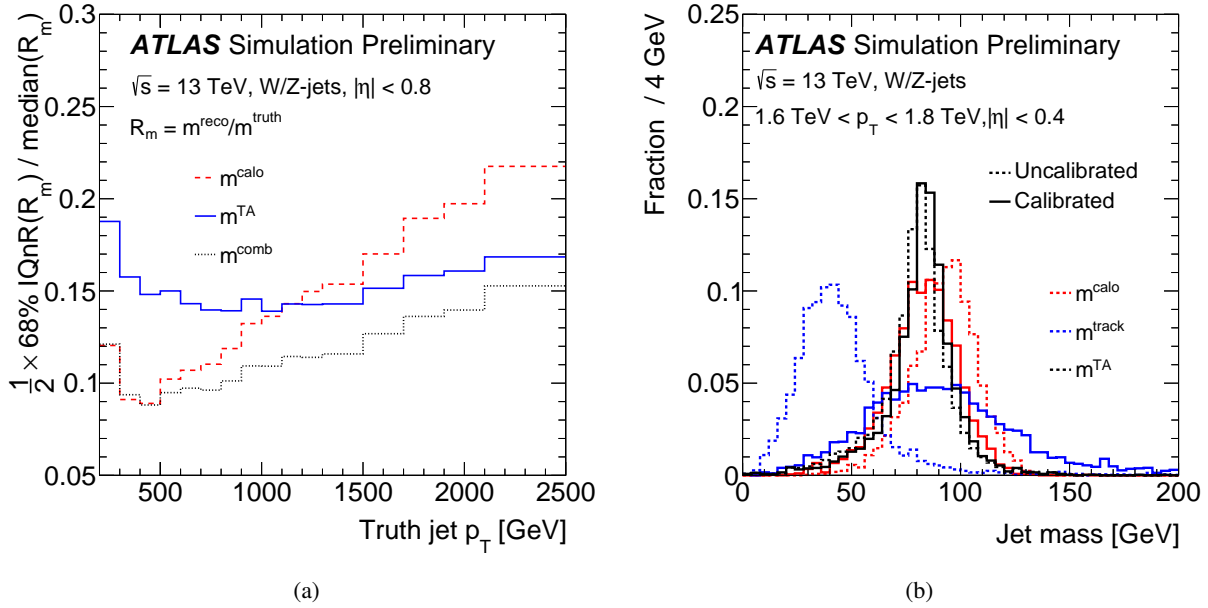


Figure 3.4: Comparison of (a) the mass resolution as function of the true transverse momentum and (b) the (un)calibrated mass distribution of simulated large-R W/Z jets for the calorimeter-based (m_{calo}) and track-assisted (m_{TA}) mass definitions as well as the invariant mass of the collection of tracks associated with the large-R jet (m_{track}) and the combined jet mass (m_{comb}), respectively. Due to the response distributions being non-Gaussian the linear combination of m_{calo} and m_{TA} according to Eq. 3.6 leads to slightly non-optimal resolution results for m_{comb} in the lowest truth jet p_T bins. Taken from Ref. [209].

respect to m_{calo} . Figure 3.4(a) reveals, however, that the resolution of m_{TA} becomes considerably worse than the one of m_{calo} for low jet momenta, i.e. $p_T < 1$ TeV.¹¹ One possibility to obtain a mass definition that does not suffer from this caveat is to combine m_{calo} and m_{TA} ; the former is not explicitly exploited in the definition of the latter and the responses of the calorimeter-based jet p_T and mass are almost independent leading to correlations between m_{calo} and m_{TA} of at most 10%. Thus, the *combined jet mass* m_{comb} is simply defined as [209]:

$$m_{\text{comb}} = a \cdot m_{\text{calo}} + b \cdot m_{\text{TA}}, \quad (3.6)$$

with nearly optimal weights $a = \sigma_{\text{calo}}^{-2} / (\sigma_{\text{calo}}^{-2} + \sigma_{\text{TA}}^{-2})$ and $b = \sigma_{\text{TA}}^{-2} / (\sigma_{\text{calo}}^{-2} + \sigma_{\text{TA}}^{-2})$, where σ_{calo} (σ_{TA}) is the resolution function of m_{calo} (m_{TA}). From Figure 3.4(a) it can be seen that the m_{comb} resolution for W/Z-jets is at most as large as either of the input jet-mass resolutions, bounded by the one of m_{calo} at low jet p_T and the one of m_{TA} at high jet p_T .

Uncertainties related to the JES and JMS corrections are evaluated using the R_{trk} -method [209, 210], i.e. by an in-situ validation in dijet events using track jets; it exploits that the tracking system and the calorimeters have largely uncorrelated systematic uncertainties allowing to disentangle physics and detector

¹¹The point in p_T where the resolution of m_{TA} improves over the one of m_{calo} depends highly on the mass of the decaying particle as well as the subject multiplicity; e.g. over the considered p_T range no improvement is observed in the case of boosted top-quark decays.

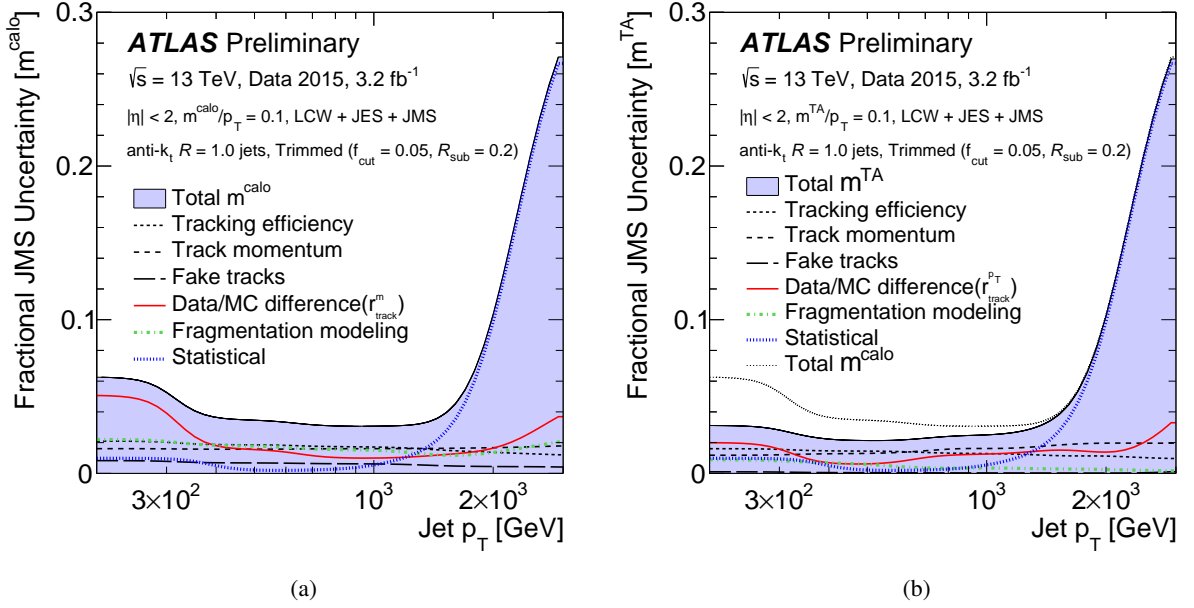


Figure 3.5: Fractional jet mass scale (JMS) uncertainty for the (a) calorimeter-based (m_{calo}) and (b) track-assisted (m_{TA}) large-R jet mass definition as function of the transverse momentum for $m/p_T = 0.1$. The various groups of contributions are introduced in the text; in Fig. (b) the total JMS uncertainty on m_{calo} is shown for comparison. Taken from Ref. [209].

effects. Double ratios are defined to assess the data-simulation agreement

$$R_{\text{trk}} = \frac{r_{\text{trk}}^{\text{data}}}{r_{\text{trk}}^{\text{sim}}} \quad \text{with} \quad r_{\text{trk}} = \frac{X_{\text{calo}}}{X_{\text{track}}}, \quad \text{where } X = \{p_T, m\}; \quad (3.7)$$

and deviations from unity are considered as systematic uncertainty. The uncertainty evaluated for the large-R jet JES also translates into a JMS uncertainty on m_{TA} via Eq. 3.5. Further systematic uncertainties arise from the method itself and are related to the efficiency of the track reconstruction both for isolated tracks and tracks in the core of high- p_T jets, the fake rate due to badly reconstructed tracks and the track-momentum determination; they are treated fully correlated in the propagation to m_{TA} , and thus largely cancel in the $m_{\text{track}}/p_T^{\text{track}}$ ratio in Eq. 3.5. Finally, also an uncertainty related to the fragmentation modelling is considered, estimated from a generator comparison.

Figures 3.5(a) and (b) show the relative total JMS uncertainty for large-R jets in the central region with $m/p_T = 0.1$ for m_{calo} and m_{TA} , respectively, as function of the jet p_T ; the contributions from the various systematic sources are shown alongside. The total uncertainty is smallest in the p_T range of 300 GeV to 1 TeV, at the level of 4(2) % for m_{calo} (m_{TA}); as expected smaller for m_{TA} due to the cancellation of the track-related uncertainties. Although the statistical component due to the limited size of the dataset is expected to increase with increasing p_T , the extreme increase for $p_T > 1.5$ TeV was found to be accidentally highly overestimated (by more than a factor 2) and is much reduced in later versions of the measurement (though direct comparisons are difficult since also the dataset was increased [211]); the impact on the measurement presented in Chap. 5 is nonetheless small given that the targeted p_T range is below, reaching at most up to

~ 2 TeV.

The systematic uncertainties on m_{calo} and m_{TA} are then propagated to m_{comb} via Eq. 3.6, where the track-related uncertainties between the various inputs are treated fully correlated [209].

The total uncertainty on JES is at the level of 3 % over most of the p_{T} range with a similar increase at low and high p_{T} seen for the JMS uncertainty; and comes with the same caveat mentioned before. In the analysis presented in Chap. 5 the various sources of systematic uncertainties are treated fully correlated between the jet mass and the jet p_{T} .

Since the jet-mass resolution (JMR) is dominated by charged-to-neutral fluctuations, its uncertainty cannot be assessed via the R_{trk} -method. In Run 1 it was evaluated using the *subtraction method* [212], where a template fit to the resonance peak of the W boson reconstructed in a sample of single-lepton $t\bar{t}$ events in data and simulation is performed and the difference in the obtained mass resolution is assigned as systematic uncertainty. The obtained relative uncertainty of 20 % is confirmed by a recent Run-2 measurement [211].

Also the preliminary absolute uncertainty on JER for large-R jets of 2 % assumed in the analysis presented in Chap. 5 is confirmed by a recent Run-2 measurement exploiting the dijet-balance method [211]; only at high p_{T} somewhat larger values are found that, however, remain below 5 % up to 1 TeV.

3.3.3 Pile-up Jet Suppression

The pile-up mitigation techniques described above for small-R jets work by correcting the jet energies on average such that the majority of pile-up jets becomes too soft to be selected in analyses; localised fluctuations in the pile-up activity, however, can lead to pile-up jets passing typical p_{T} thresholds. In order to reject such jets further, tracking information is exploited and jets are required to be associated with the hard-scatter vertex.

One variable to identify the primary vertex from which a jet is originating and that was mainly exploited in Run 1 to separate hard-scatter and pile-up jets is the *jet-vertex fraction* [201]. Based on tracks that are ghost-associated with the jet under consideration, it is defined as the ratio of the scalar sum of the p_{T} of all tracks originating from a *particular* primary vertex (PV) and the sum of the p_{T} of all matched tracks (associated with *any* PV). Computing JVF with respect to the PV identified as the hard-scatter vertex (cf. Sec. 3.1), it serves as an estimate of the (charged) fraction of the jet p_{T} that originates from the hard-scatter interaction. Ranging from 0 to unity, pile-up jets tend to have smaller values and peak at 0, hard-scatter jets larger values and peak at unity; to jets without any associated tracks a value of -1 is assigned.

It was shown that requiring $\text{JVF} > 0.75$ results in a flat mean jet multiplicity as function of the average number of interactions per bunch crossing μ (which is sensitive to the out-of-time pile-up activity).

The explicit pile-up dependence of the denominator of JVF, resulting in a shift of hard-scatter jets towards smaller values with increasing number of PVs (N_{PV}), and thus a N_{PV} -dependence of the JVT efficiency, constitutes a limitation in high-luminosity conditions. Therefore, an alternative definition, denoted *corrJVF*, is deployed, in which (i) the N_{PV} -dependence is corrected and (ii) an improved track-to-vertex association is used yielding a large performance gain for b jets.

However, instead of exploiting corrJVF directly in analyses, it is combined with another discriminating variable, R_{p_T} , in a two-dimensional likelihood using a multivariate approach: the *jet-vertex tagger* (JVT) is the standard tool to separate hard-scatter and pile-up jets in Run 2. Being defined as the ratio of the scalar sum of the p_T of all the tracks associated with the jet under consideration originating from the hard-scatter vertex and the calibrated jet p_T (cf. Sec. 3.3.2), the efficiency of R_{p_T} is almost independent of N_{PV} and so is the one of JVT. As for JVF, the JVT values range from 0 to 1, where jets with values close to 1 (0) are signal(pile-up) jet candidates, and to jets without any associated tracks a value of -1 is assigned.

Requiring $JVT > 0.59$ for jets with $20 \text{ GeV} < p_T < 60 \text{ GeV}$ and $|\eta| < 2.4$, selects hard-scatter jets with an efficiency of 92 %, ¹² while having a fake rate of about 1 % [213]. The JVT efficiency was measured in $Z(\rightarrow \mu^+ \mu^-)$ +jets events yielding data-to-simulation scale factors that are compatible with unity within the uncertainties, which are at the level of 1-2 % [213]. Two sources of systematic uncertainties are considered: (i) a disagreement observed regarding the residual contamination from pile-up jets after suppression in data and simulation, and (ii) the impact of the fragmentation model.

3.3.4 Jet Quality

In order to have a handle to suppress (fake) jets arising in the context of non-collision background processes, such as beam-gas and -halo events, cosmic-ray muons and calorimeter electronics noise certain *jet quality criteria* [203, 214] are defined. Jets failing those criteria are referred to as *bad jets*; and in analyses such as the ones described in Chaps. 4 and 5, where missing transverse momentum (cf. Sec. 3.9) is part of the signal signature, events with at least one 'bad' jet (with $p_T > 20 \text{ GeV}$ and passing the JVF/JVT requirements) are rejected to ensure a high-quality dataset.

A number of variables are exploited to distinguish between 'good' and 'bad' jets; they can be roughly separated into three classes [215]: (i) signal shape in the LAr calorimeters, (ii) shower-development via energy ratios and (iii) charged-particle contributions from tracking information (similar to R_{p_T}). Different sets of quality selections are defined with varying 'good' jet selection efficiencies and 'bad' jet rejections: most commonly used is the one providing with $> 99.8(99.5) \%$ for $p_T > 20 \text{ GeV}$ the highest 'good' jet selection efficiency, referred to as the *Looser (Loose)* selection in Run 1 (Run 2) [214, 215]. It rejects most of the fake jets due to calorimeter noise; its overall rejection factor was found to be about 50 % in Run 1. The selection efficiency was measured, and good agreement in data and simulation was found [214].

3.4 Identification of b Jets

3.4.1 Introduction

Several distinct properties of the production and the decay of b hadrons (cf. Secs. 1.4.5 and 1.4.6), i.e. their relatively long lifetime, high mass and (charged) decay multiplicity, semi-leptonic decays involving muons as well as the hard b -quark fragmentation, are exploited in *b-tagging* algorithms in order to identify jets likely containing b hadrons and thus to originate from initial b quarks. Given the importance of such tools for a variety of measurements, including the search for an A of the Two-Higgs-Doublet Model in the $\ell\ell(\nu\nu)bb$ final state described in Sec. 5, and the complexity of the matter, several b -tagging algorithms were and still are developed and constantly refined in order to provide optimal performance for physics

¹²The majority of pile-up jets are found to have $p_T < 60 \text{ GeV}$.

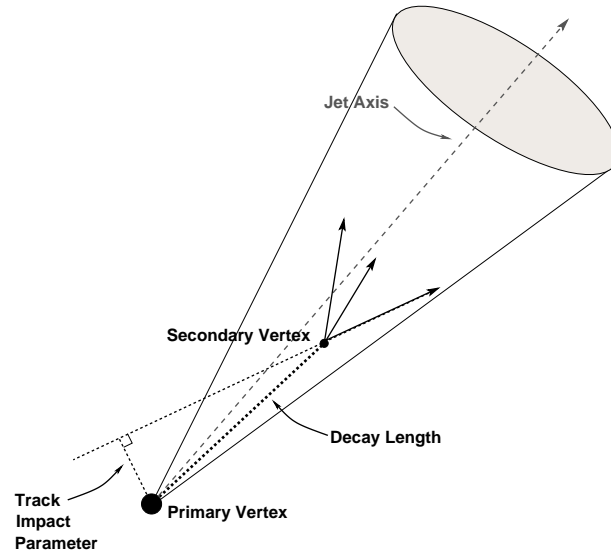


Figure 3.6: Illustration of a jet with a secondary vertex reconstructed from displaced tracks with large impact parameter (significance) and with a significant decay length indicating the decay of a heavy, long-lived particle, i.e. a b or c hadron. Taken from Ref. [218].

analyses; they have in common that they vitally rely on tracking information provided by the inner detector (ID) which entails that only for jets within $|\eta| < 2.5$ b -tagging information is available.

Up to date b -tagging algorithms in ATLAS are solely designed and optimised for small- R jets, referred to as jets in the following. However, in Run 2 they are also applied to track jets providing a possibility to use b -tagging methods also with large- R jets common to substructure techniques [216]; which is achieved by ghost-associating track jets with large- R jets (cf. Sec. 3.3).

Tracks used for b -tagging are associated with jets based on their angular separation, i.e. $\Delta R(\text{track}, \text{jet})$; the maximally allowed separation decreases with increasing jet p_T , accounting for the fact that the decay objects become increasingly collimated. Only tracks satisfying certain quality criteria in order to reject fake tracks, tracks stemming from long-lived particles or material interactions are considered; they further need to fulfil requirements regarding a minimal p_T as well as their association to the primary vertex via transverse and/or longitudinal impact parameter criteria (cf. Sec. 3.1), which are optimised for each b -tagging algorithm individually.

In order to develop a b -tagging algorithm and assess its performance it is vital to be able to *label* jets according to their (true) flavour in simulation [4, 217]. In Run 1 (Run 2) a jet is labelled as a b jet, if a generator-level b quark (weakly-decaying b hadron) with $p_T > 5$ GeV is found in a cone with $R = 0.3$ around the jet axis.¹³ If no b quark (hadron) is matched, the search is repeated first for a c quark (hadron) and, if without success, for a τ lepton; if neither is found, the jet is labelled as light jet.

3.4.2 Lifetime-based b -tagging algorithms

Most of the available (and exploited) b -tagging algorithms belong to the class of *lifetime-based algorithms*. As the name suggests, they exploit the relatively long lifetime of b hadrons which being of the order

¹³A b hadron is only matched to at most one jet, the one closest in ΔR .

of 1.5 ps results in a significant mean decay length of a couple of millimetres before they decay; this is sketched in Fig. 3.6. Thanks to the relatively high mass of b hadrons, tracks stemming from their charged decay products tend to have large impact parameters relative to tracks stemming from the primary vertex (PV). This property is exploited by *impact-parameter based* algorithms, such as the IP2D and IP3D algorithms [4, 219, 220]. While IP3D relies on both the *signed* longitudinal and transverse impact-parameter significances (and their correlations), IP2D only exploits the latter. The positive (negative) sign indicates that the track intersects the jet axis in front of (behind) the PV, as expected given the decay of the b hadron occurs along its flight path. The final jet discriminant is derived using a log-likelihood ratio (LLR) method based on comparing the measured properties for each associated track with probability density functions for the b - and light-jet hypotheses obtained from simulation.

Vertex-based algorithms attempt to reconstruct the secondary vertex (SV) and possibly one or more tertiary vertices (TV) from tracks associated with the jet, but significantly displaced from the PV and thus compatible with stemming from the b -hadron and subsequent c -hadron decays. By combining all tracks belonging to identified two-track vertices using a χ^2 fit, the SV1 algorithm [4, 220] is based on reconstructing a *single* inclusive secondary vertex irrespective of whether the tracks stem from the (charged) decay products of the b -hadron or the subsequent c -hadron decay. Four SV-related properties are exploited, namely (i) the *vertex mass*, computed as the invariant mass of all associated tracks under the pion hypothesis, (ii) the *vertex energy fraction* defined as the ratio of the sum of energies of those tracks in the jet associated with the SV and all tracks in the jet, (iii) the number of two-track vertices from which the SV is formed, as well as (iv) the angular distance between the jet axis and the PV-SV axis, and a final discriminant defined using the LLR method.

The vertex-finding strategy used by the *JetFitter* algorithm [221] exploits the expected topological structure of the b -to- c -hadron decay chain: using a Kalman filter, secondary and tertiary vertices are reconstructed based on the assumption that they lie on a common line with the PV approximating the b -hadron flight direction, allowing also single-track vertices. Six variables describing the decay topology and the vertex properties, namely (i) the number of vertices with at least two tracks, (ii) the number of tracks associated with these vertices, (iii) the number of single-track vertices on the reconstructed b -hadron flight axis, (iv) the invariant mass of all tracks associated with the decay chain, (v) the energy fraction defined as the ratio of the sum of energies of those tracks and all tracks matched to the jet and (vi) the flight-length significance, computed as the weighted average of the decay length divided by the uncertainty of all displaced vertices, as well as the p_T and the $|\eta|$ of the jets, on which the variable's distributions depend,¹⁴ are used as input to an artificial neural network (ANN) [4]. From its three output nodes corresponding to the b -, c - and light-jet hypotheses, p_b , p_c and p_l , respectively, a final discriminant separating b and light jets is defined as $w = \ln(p_b/p_l)$.

While the mistag rates of the vertex-based algorithms for certain b -jet tagging efficiencies are smaller than the impact-parameter ones, the same is true for their b -jet identification efficiency, which is limited by the vertex-finding efficiency; thus, the most powerful and efficient tagging algorithms are obtained by combining the different approaches. Several of such high-level tagging algorithms were and are being

¹⁴To avoid that the p_T and $|\eta|$ distributions that differ for b , c and light jets are used by the neural network to separate between the jet flavours, a two-dimensional reweighting is performed to yield flat kinematic distributions for all three jet flavours prior to their use in the neural network training.

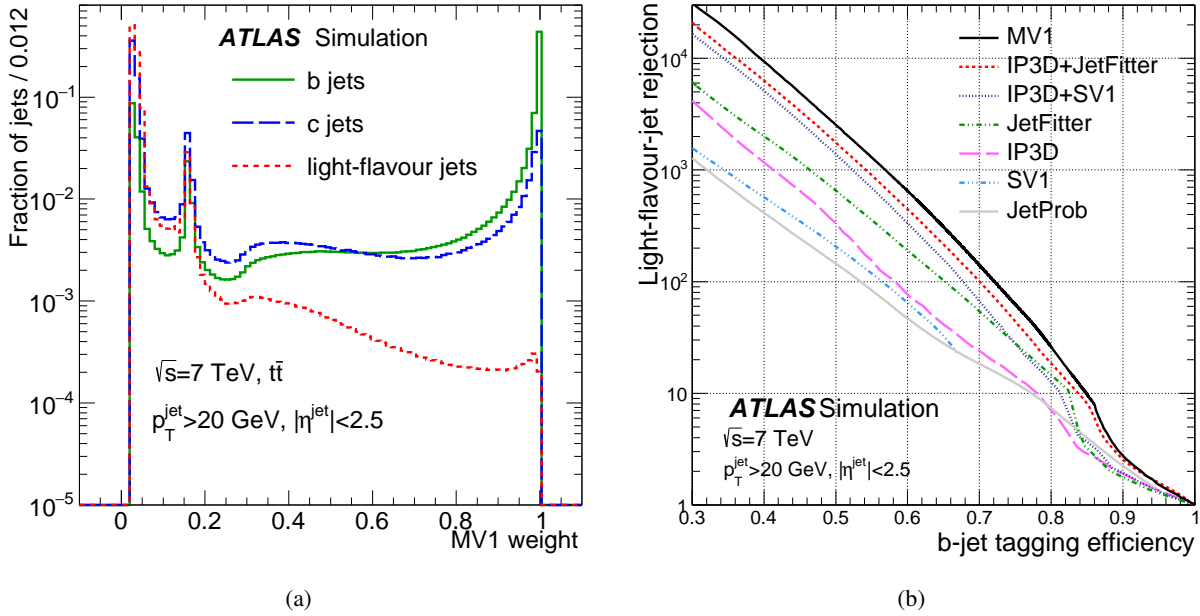


Figure 3.7: (a) Comparison of the output distribution for light, c and b jets and (b) performance in terms of light-jet rejection versus b -tagging efficiency in simulated $t\bar{t}$ events at $\sqrt{s} = 7$ TeV of the MV1 and the various b -tagging algorithm provided for 2011 data analyses as discussed in the text, respectively. The spike around 0.15 in Fig. (a) is caused by jets for which no secondary vertex was found. Taken from Ref. [4].

defined, differing not just by their inputs, but also by the choice of the combination technique; examples are (i) the IP3D+SV1 algorithm [4], which is simply obtained by summation of the individual discriminants, (ii) the IP3D+JetFitter algorithm [4] (also referred to as JetFitterCombNN), which (mainly) differs from the previous JetFitter definition by one additional input, the IP3D discriminant, as well as the somewhat more elaborate (iii) MV1 [4] and (iv) MV2c10 algorithms [217, 219, 220], that rely on multivariate techniques for the combination. The MV1 and MV2c10 algorithm constitute the standard b -tagging tools used in ATLAS physics analyses at the end of Run 1 and based on 2015+2016 data in Run 2, respectively, and in particular also in the analyses reported in Chaps. 4 and 5.

The MV1 algorithm being an ANN with a single output node, the final discriminant, also exploits the correlations between its inputs, namely the IP3D, the SV1 and the IP3D+JetFitter discriminants as well as a *jet category* defined by the jet's p_T and η .¹⁵ While the correlations are small between the IP3D discriminant and the vertex-based ones, they are larger between the SV1 and IP3D+JetFitter weights and different for the various jet flavours. The algorithm is trained to separate b jets from light jets, which are mainly obtained from simulated $t\bar{t}$, but also dijet events in order to populate the high- p_T regime. Figure 3.7(a) shows the distributions of the MV1 output weight for b jets, c jets and light jets in simulated $t\bar{t}$ events: b (light) jets tend to have large (small) values close to unity (zero); the spike around 0.15 is caused by jets for which no SV was found.

Instead of using only the final discriminants of the vertex- and impact-parameter based algorithms, the MV2c10 algorithm takes directly all of their discussed variables (and some more) as inputs which does

¹⁵And jets in the same category receive a common weight to diminish that the ANN exploits the jet kinematic distributions to enhance the tagging performance.

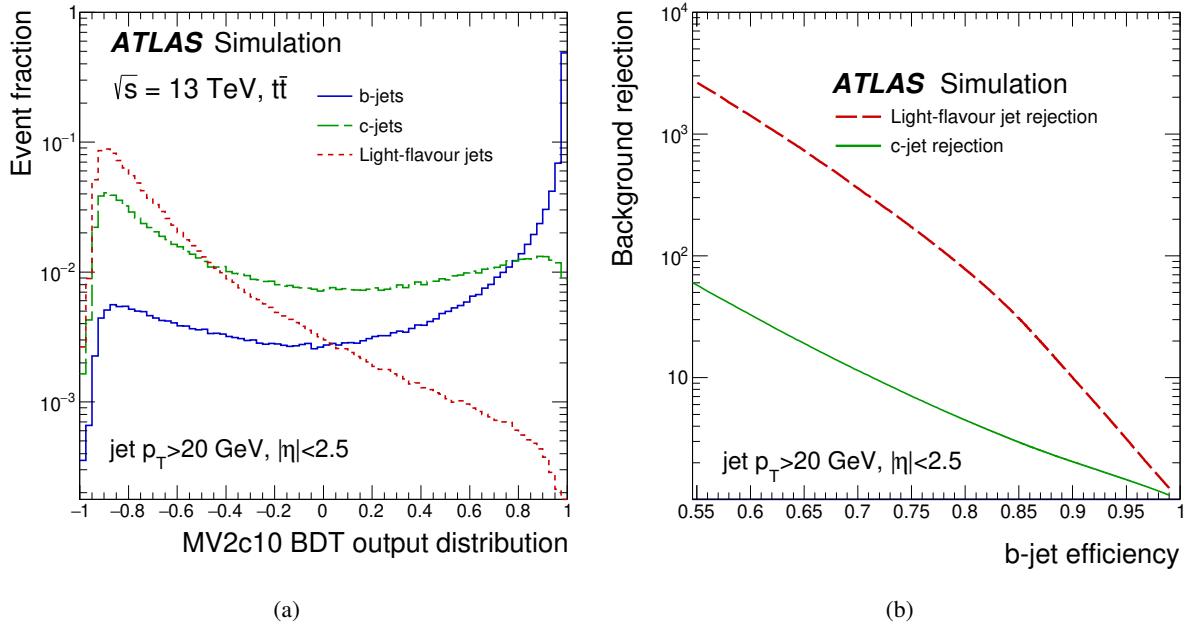


Figure 3.8: (a) Comparison of the output distribution for light, c and b jets and (b) performance in terms of light- and c -jet rejection versus b -tagging efficiency in simulated $t\bar{t}$ events at $\sqrt{s} = 13$ TeV of the MV2 b -tagging algorithm as provided for 2015+2016 data analyses. Taken from Ref. [217].

not only result in a simplified workflow, but also to an improved b -tagging performance. In total 24 variables, 22 related to the IP2D/IP3D, SV1 and JetFitter algorithms as well as the p_T and η of the jets, are used as input to a boosted decision tree (BDT).¹⁶ The training is performed with b jets as signal against a background of 93% light and 7% c jets from simulated $t\bar{t}$ events [217].¹⁷ The distributions of the MV2c10 output weight for b , c and light jets in simulated $t\bar{t}$ events are shown in Fig. 3.8(a): b (light) jets tend to have large (small) values close to +1(-1); c jets show a mixed behaviour, though closer to the one of light jets.

The performance of the b -tagging algorithms is evaluated using simulations by means of their b -tagging efficiency, i.e. the efficiency to b -tag a jet labelled as b jet, as well as their ability to reject jets labelled as c jets or light jets. The rejection is defined as the inverse of the c -jet tagging efficiency and mistag rate, i.e. the efficiency of mistakenly identifying c jets or light jets as b jets, respectively.

Figure 3.7(b) shows the light-jet rejection as function of the b -tagging efficiency estimated in simulated $t\bar{t}$ events at $\sqrt{s} = 7$ TeV, i.e. the expected performance of the discussed b -tagging algorithms provided for analyses based on 2011 data. The observed hierarchy is as expected: the combined b -tagging algorithms provide better light-jet rejections for the same b -tagging efficiency, in particular towards lower efficiencies corresponding to higher b -jet purities. Across most of the considered range the MV1 algorithm clearly provides the best performance with light-jet rejections being a factor 1.3-1.7 higher than the ones of the

¹⁶In order not to exploit the kinematic differences between the various jet flavours, for the training the p_T and η distributions of b jets are reweighted so that they agree with the combined c and light jet spectra [217].

¹⁷In an earlier version of the MV2 algorithm the background was composed of 90% light and 10% c jets motivating the notation "c10" in its name. However, improvements to the algorithms resulted in an increased performance, yielding a better c jet rejection while maintaining the same light-jet rejection despite reducing the c -jet fraction in the training sample. The nomenclature was not adjusted to that change. [217]

(a)			(b)		
MV1 operating points			MV2c10 operating points: small-R (track) jets		
<i>b</i> -tag. eff.	rejection		<i>b</i> -tag. eff.	rejection	
	<i>c</i> jet	light jet		<i>c</i> jet	light jet
60 %	8	635	60 %	35	1539
70 %	5	134	70 %	12 (7)	381 (120)
75 %	4	58	77 %	6 (4)	134 (58)
85 %	2	9	85 %	3	34

Table 3.1: Light and *c* jet rejections for the calibrated operating points of the (a) MV1 and (b) MV2c10 algorithms defined by certain average *b*-tagging efficiencies in simulated $t\bar{t}$ events. For the MV2c10 algorithm also the results for track jets are shown, if available.

second best performing JetFitter+IP3D algorithm for *b*-tagging efficiency between 60-85 %; they show the same *c*-jet rejection indicating that the SV1 and IP3D discriminants do not provide additional information on *c* jets in addition to JetFitter+IP3D.

The light- and *c*-jet rejections as function of the *b*-tagging efficiency of the MV2c10 algorithm estimated in simulated $t\bar{t}$ events at $\sqrt{s} = 13$ TeV, i.e. the expected performance of the standard *b*-tagging algorithms as provided for analyses based on 2015+2016 data, is shown in Fig. 3.8(b). With respect to the MV1 algorithm the light- and *c*-jet rejections are improved by factors of roughly 2-4 and 1.5-4, respectively. Besides the more elaborated approach to combine the information provided by the standalone *b*-tagging algorithms, the improved performance is also due to (i) the installation of the IBL, i.e. the additional innermost layer of the pixel detector providing significantly better impact-parameter resolution, (ii) an optimised track reconstruction providing higher efficiencies in dense environments such as inside high- p_T jets (cf. Sec. 3.1) and (iii) revision of the IP2/3D and SV1 algorithms, adapting also to changes (i) and (ii) as well as harsher pile-up conditions. While the inclusion of the IBL leads to better *b*-tagging performance mainly in the low to medium jet- p_T range, improvements in the high- p_T regime are due to the revision of the various algorithms.

As mentioned earlier, the MV2c10 algorithm is also applied to track jets. Given its optimisation is performed on small-R jets, it is not surprising that the obtained light- and *c*-jet rejections for track jets for the same *b*-tagging efficiencies (in the range between 60-85 %) are significantly lower, i.e. 20-50 % and 40-80 %, respectively.

In Table 3.1 the *c*- and light jet rejections of selected *operating points*, obtained by placing cuts on the MV1 and MV2c10 output distributions corresponding to certain average *b*-tagging efficiencies in simulated $t\bar{t}$ events, for which data-to-simulation scale factors are provided to correct differences between data and simulation are listed; the exploited calibration methods are discussed below. Both for MV1 as well as MV2c10 the operating point at 70 % is the most commonly used one, given it constitutes a good compromise between *b*-tagging efficiency (as well as purity) and background rejection.

3.4.3 The Soft Muon Tagging algorithm

An alternative b -tagging algorithm relies on (soft) muons reconstructed inside jets: the Soft Muon Tagger (SMT) [4]. Instead of being based on the long lifetime of b hadrons, it exploits that about 20% of the b -hadron decays involve muons in the final state, considering both direct and cascade decays. While this fraction intrinsically limits the b -tagging efficiency to values usually lower than the lifetime-based tagging algorithms, its complementarity also in terms of sources of systematic uncertainties makes the SMT algorithm a valuable tool. For example, it is exploited to select a sample of $W+c$ events used to calibrate the c -jet tagging efficiency of the lifetime-based tagging algorithms as described in detail in Chap. 4.

Only combined muons, reconstructed both in the ID and the muon spectrometer (MS) as described in Sec. 3.6, with a minimum p_T of 4 GeV are considered in the SMT algorithm. Their tracks need to satisfy certain quality criteria and to be loosely associated with the PV, thus suppressing signals from light-flavour hadron decays in flight and from pile-up activity or material interactions, respectively. Such SMT-muon candidates are associated with a jet if they are found in a cone with $R = 0.5$ around its axis; in the case of several matches the muon is exclusively associated with the closest jet.

Finally, the decision whether a jet with an associated SMT-muon candidate is considered b -tagged is based on the χ^2_{match} value (normalised by the number of degrees of freedom N_{dof}) of the statistical combination of the muon-track parameters measured in the ID and the MS, respectively: muons stemming from decays of light charged mesons tend to have larger χ^2_{match} values than those from heavy hadron decays; this can be seen from Fig. 3.9(a) showing the $\chi^2_{\text{match}}/N_{\text{dof}}$ distributions for SMT-muon candidates matched to light jets, c jets and b jets, respectively. The reason being that due to the long lifetimes of the light charged mesons, a fraction of the decays occur between the ID and the MS, which implies that the former measures the track parameters of the meson, while the latter the ones of its decay products. The chosen requirement $\chi^2_{\text{match}}/N_{\text{dof}} < 3.2$ selects b jets (c jets) with an average efficiency of 11% (4.4%), the light-jet mistag rate is at the level of 0.2%, as estimated in simulated $t\bar{t}$ and inclusive jet events, respectively. From Figures 3.9(b) and 3.9(c) showing the b -/ c -jet tagging efficiencies and mistag rate as functions of the jet p_T , respectively, one can see that they are increasing with growing p_T and eventually flattening.

3.4.4 Calibration of the Lifetime-based b -tagging Algorithms

As mentioned earlier, the b -tagging efficiency as well as the c -jet tagging efficiency and mistag rate is measured for the discussed operating points of the various b -tagging algorithms and calibrations are provided in terms of data-to-simulation scale factors, usually in bins of jet p_T and $|\eta|$, in order to correct differences in simulation. A key ingredient to precisely measuring the tagging efficiency (or mistag rate) for a certain jet flavour is a sample of jets selected in data that is dominated by that jet flavour. Over the years several approaches to obtain such samples were developed and refined within the ATLAS collaboration; those providing the scale factors for the analyses presented in this thesis are briefly described in the following and in the next section, respectively.

Starting with the b -tagging efficiency calibration methods, they can be categorised into methods based on soft-muon tagging¹⁸ in inclusive jet events and on di- and single-lepton $t\bar{t}$ events to obtain pure samples

¹⁸Not making use of the SMT algorithm, a jet is considered tagged if a muon with $p_T > 4$ GeV is found in a cone with $R = 0.4$

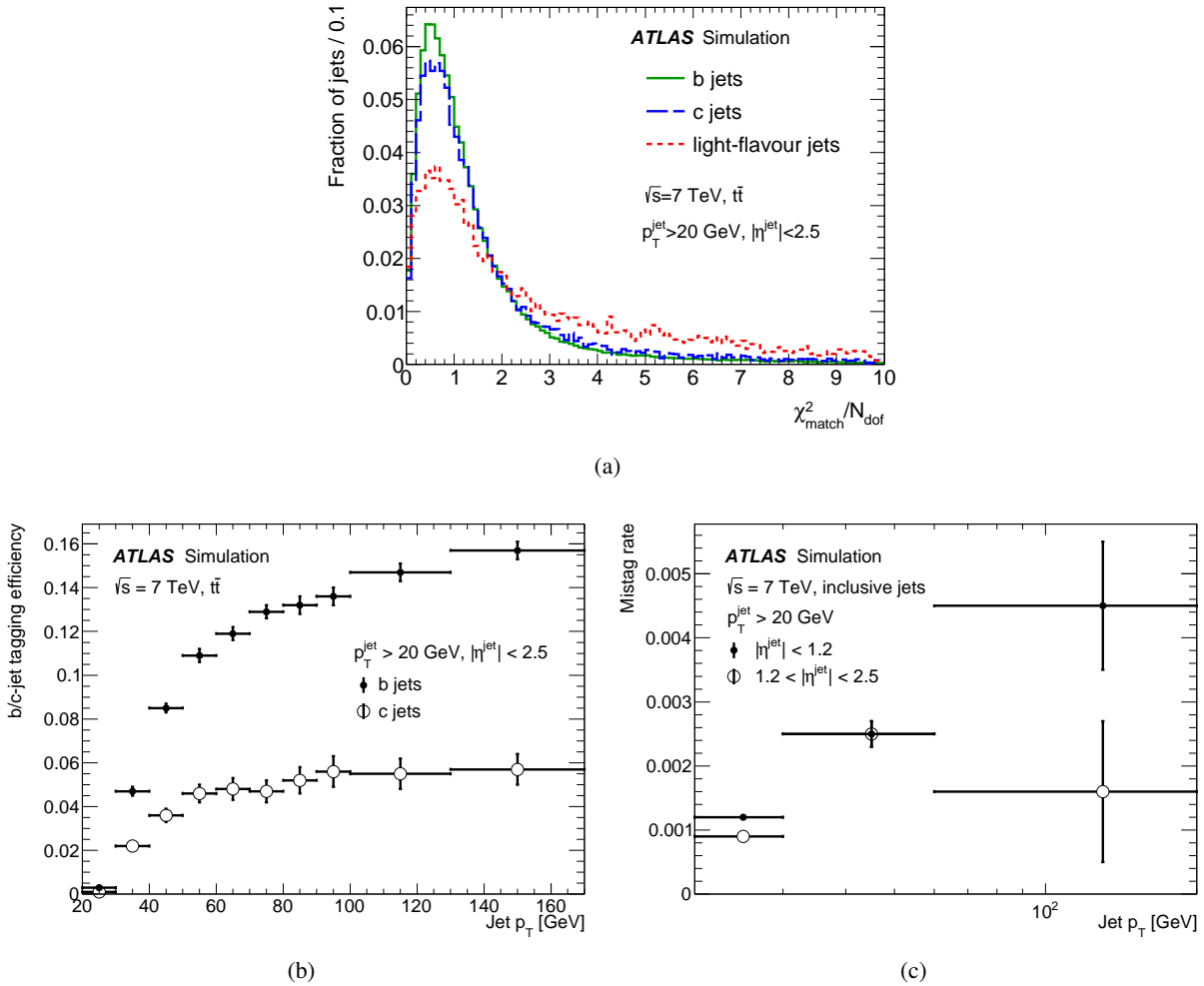


Figure 3.9: (a) Comparison of the distribution of $\chi^2_{\text{match}}/N_{\text{dof}}$ for SMT candidate muons associated with b , c and light jets in simulated $t\bar{t}$ events. (b) b - and c -jet tagging efficiencies as well as (c) the light-jet mistag rate of the SMT algorithm as function of the jet p_T in simulated $t\bar{t}$ and inclusive jet events, respectively. The shown uncertainties are statistical only. Taken from Ref. [4].

of b jets. Two approaches falling into the first category are the p_T^{rel} and *system8* methods [4]; where the latter was developed within the D0 collaboration [222].

The p_T^{rel} distribution, i.e. the distribution of the transverse momentum of the soft muon with respect to the combined muon-plus-jet axis, tends to be harder for muons stemming from b -hadron decays and associated with b jets than for those associated with light and c jets. This is exploited in the p_T^{rel} method by fitting templates for the different jet flavours obtained from simulation to the p_T^{rel} distribution in data and thereby extracting the fraction of b jets before and after applying a b -tagging requirement to derive the corresponding b -tagging efficiency from the ratio.

In the case of the *system8* method the fraction of b jets in the pretag and b -tagged samples are extracted together with six other unknowns from a fully constrained system of eight equations based on the number

around its axis.

of events passing three uncorrelated selection criteria: (i) the studied b -tagging requirement, (ii) a soft-muon tagging requirement ($p_{\text{T}}^{\text{rel}} > 700$ MeV) and (iii) the requirement of at least one additional jet in the event that has a reconstructed secondary vertex with a significant signed decay-length.

Three methods falling into the second category of $t\bar{t}$ -based calibration methods are the *kinematic selection* [4], the *kinematic fit* [4] and the *combinatorial likelihood* [4, 217] approaches. While the kinematic selection method uses both, the kinematic fit and the combinatorial likelihood methods rely solely on single-lepton and dilepton $t\bar{t}$ events, respectively: the purity of $t\bar{t}$ -candidate events passing a characteristic kinematic selection in data is increased by requiring one jet to be b -tagged and/or by restricting the number of jets, respectively.

The kinematic selection approach is based on the assumption that the flavour composition of the $t\bar{t}$ and background samples is known from simulation (or control regions), i.e. the fractions $f_{c|l|fake}$ and mistag efficiencies $\varepsilon_{c|l|fake}$ for c jets, light jets and fakes, as well as the fraction of b jets f_b . The b -jet tagging efficiency ε_b is then obtained from the fraction of b -tagged jets in data: $f_{b\text{-tag}} = \sum_{i=\{b,c,l,fake\}} \varepsilon_i \cdot f_i$.

The kinematic fit method is based on reconstructing the $t\bar{t}$ -decay event topology: the reconstructed physics objects are assigned to the expected decay products by performing a χ^2 minimisation using the masses of the two top quarks and the W bosons as constraints. Only events where the jet identified with the b jet stemming from the hadronic top decay are considered; the b -jet tagging efficiency is then measured as the fraction of jets identified with the b jet stemming from the leptonic top decay that pass the tested b -tagging requirement.

Also relying on the knowledge of the flavour composition in the selected sample from simulation, the combinatorial likelihood method exploits correlations between the jets in the event resulting in an improved precision with respect to the kinematic selection method. A per-event likelihood function is constructed, where all the different jet-pair flavour fractions as well as the probability density functions (PDFs) of the b -tagging discriminant (w) for the different jet flavours and of the jet-pair flavour compositions are estimated from simulation; except the b -tagging discriminant PDF for b jets, $\mathcal{P}_b(w, p_{\text{T}})$, which is extracted from data. The b -jet tagging efficiency is then determined from the integral over $\mathcal{P}_b(w, p_{\text{T}})$ for $w > c$, where c denotes the cut value on the b -tagging discriminant corresponding to the tested operating point.

In order to maximise the precision, the individual measurements of the $p_{\text{T}}^{\text{rel}}$, the system8, the kinematic selection and fit methods, that are afflicted with relative total uncertainties up to 20 % at high p_{T} , are combined to yield the data-to-simulation scale factors applied in measurements based on 2011 data, such as the one presented in Chap. 4; they (mostly) agree with unity within the total uncertainties.¹⁹ The ones used to correct the b -jet tagging efficiency in simulation in analyses based on 2015+2016 data, such as the search discussed in Chap. 5, are solely obtained using the combinatorial likelihood method; which is currently the most precise method that became available only at the end of Run 1. The results for the 70 % operating point of the MV2c10 algorithm are shown in Figs. 3.10(a) and (b) for small-R and track jets, respectively, as function of the jet p_{T} . The scale factors are close to unity; the relative total uncertainties range from 2-12 % depending on the jet p_{T} and are dominated by systematic uncertainties.

Three approaches to calibrate the c -jet tagging efficiency of the lifetime-based algorithms are currently available: the D^{*+} [4], the $W+c$ [4] and the $t\bar{t}$ -based [223] calibration methods. While the $t\bar{t}$ -based method

¹⁹The final data-to-simulation scale factors provided for 2011 analyses were obtained by combining the results from the dijet-based analyses with the combinatorial likelihood approach yielding uncertainties of 2-4 % for most of the p_{T} range. [4]

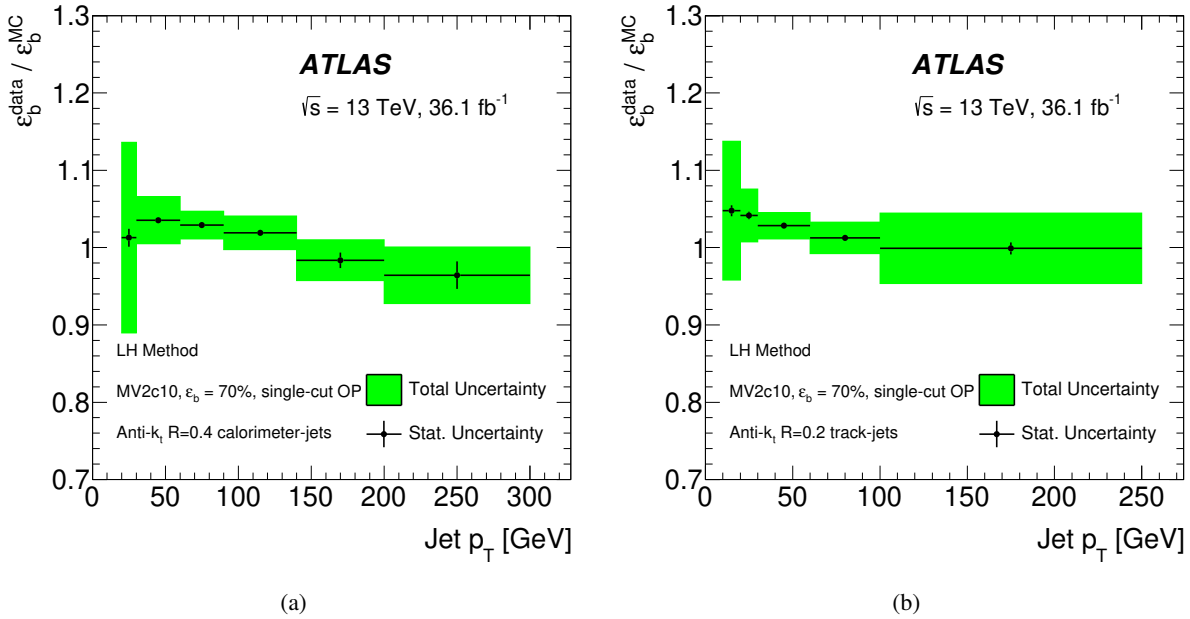


Figure 3.10: Data-to-simulation scale factors for the b -jet tagging efficiency as function of the jet p_T for (a) small-R jets and (b) track jets for the 70% operating point of the MV2c10 algorithm. Determined in 2015+2016 data at a centre-of-mass energy of $\sqrt{s} = 13$ TeV using the combinatorial likelihood method described in the text. Taken from Ref. [217].

measures the c -jet tagging efficiency in an inclusive sample of c jets, the other two are based on samples of c jets associated with more or less exclusive c -hadron decays; thus, in the case of the latter two methods, scale factors applicable to inclusive samples of c jets are obtained by performing a simulation-based extrapolation of the measured scale factors that was developed in the course of this thesis for the $W+c$ method (cf. Sec. 4.6).

The D^{*+} method was the standard approach to calibrate the c -jet tagging efficiency in Run 1; it is based on a sample of jets containing D^{*+} mesons reconstructed in the exclusive decay $D^{*+} \rightarrow D^0(\rightarrow K^-\pi^+)\pi^+$. The D^{*+} -candidate sample is extracted from a fit to the distribution of the mass difference Δm between the reconstructed D^{*+} and D^0 mesons; the fraction of D^{*+} mesons not being prompt, but stemming from b -hadron decays, f_b , is estimated from a fit to the pseudo-proper time distribution of the D^0 candidates. The c -jet tagging efficiency ε_c is then determined from a combined fit of both components to the background-subtracted Δm distribution before and after applying the b -tagging requirement: $\varepsilon_{D^{*+}} = f_b\varepsilon_b + (1 - f_b)\varepsilon_c$; together with the b -tagging efficiency ε_b of b jets with an associated D^{*+} meson.

As described in more detail in Chap. 4, the $W+c$ method is based on selecting a sample of W bosons produced in association with a single c jet, which is identified via the semi-leptonic decay of the c hadron using the SMT algorithm. Exploiting the charge correlation of the soft muon and the electron from the W -boson decay, a very pure sample of $W+c$ events is extracted as the difference between the number of data events with opposite-signed (OS) and same-signed (SS) lepton charges (OS-SS). The c -jet tagging efficiency is computed as the fraction of events in the OS-SS sample passing the studied b -tagging requirement.

The $t\bar{t}$ -based method obtains an inclusive sample of c jets from single-lepton $t\bar{t}$ events, where one of

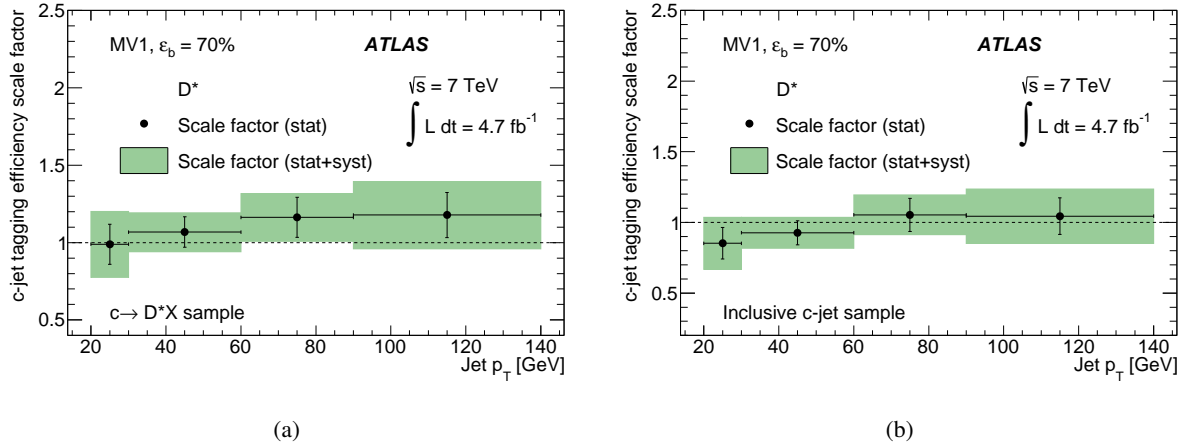


Figure 3.11: Data-to-simulation scale factors for the c -jet tagging efficiency as function of the jet p_T for the 70% operating point of the MV1 algorithm. Determined in 2011 data at a centre-of-mass energy of $\sqrt{s} = 7$ TeV using the D^{*+} method the (a) measured and (b) extrapolated scale factors applicable to inclusive samples of c jets, as described in the text, are shown. Taken from Ref. [4].

the W bosons decays hadronically to one c quark and another (light) quark and the other leptonically to an electron or muon and a neutrino. Similar to the kinematic fit method described above the event topology is reconstructed using a kinematic likelihood fitter, the KLFFitter [224]. The c -jet tagging efficiency is then extracted from the expected and observed numbers of selected jet pairs identified as stemming from hadronic W -boson decays, where exactly zero or one is b -tagged, employing a log-likelihood method. Besides providing scale factors valid for inclusive samples of c jets, this method furthermore benefits from the large $t\bar{t}$ cross-section, in particular at $\sqrt{s} = 13$ TeV, where it was exploited for the first time.

As mentioned earlier the D^{*+} method was the standard approach to provide the data-to-simulation scale factors for analyses in Run 1. Figures 3.11(a) and (b) show the scale factors for the 70% operating point of the MV1 algorithm as function of the jet p_T measured using the exclusive D^{*+} sample in 2011 data and the ones after applying the extrapolation to inclusive c jets, respectively: while both are consistent with unity and with each other (within the uncertainties), the latter are systematically lower. The relative total uncertainties on the inclusive scale factors range between 13-22% depending somewhat on the jet p_T ; statistical and systematic components are contributing almost equally.

Scale factors to correct the c -jet tagging efficiency in simulations used by early Run-2 analyses based on 2015+2016 data, as the search discussed in Chap. 5, were provided by the $W+c$ method adapted for the increased centre-of-mass energy as well as to provide scale factors in bins of jet p_T and $|\eta|$ with respect to the description in Chap. 4. Ranging for the 70% operating point of the MV2c10 algorithm from about 0.8 to 1.2 depending on the jet p_T , they were systematically lower than the corresponding scale factors provided by the novel $t\bar{t}$ -based calibration shown in Fig. 3.12(a), which range between 1.3 and 1.4, indicating that the c -jet tagging efficiency is significantly underestimated in simulation. In order to acknowledge this tension an additional uncertainty was considered covering the difference and leading to relative total uncertainties at the level of 30-60%. Only shortly later the tension was resolved: the $W+c$ method reproduced the scale factors of the $t\bar{t}$ -based calibration; illustrating the importance of having several calibration

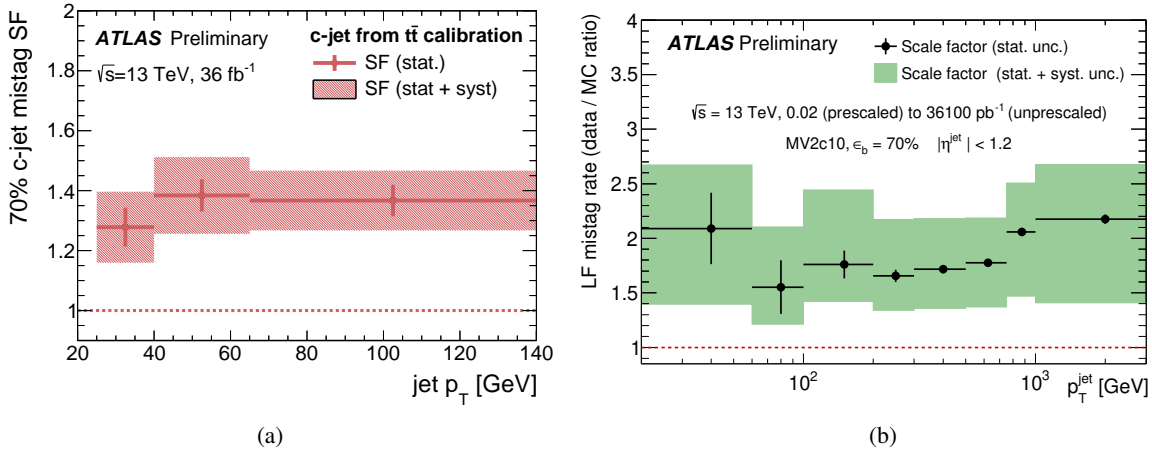


Figure 3.12: Data-to-simulation scale factors for the (a) c -jet tagging efficiency and (b) light-jet mistag rate of the 70% operating point of the MV2c10 algorithm as function of the jet p_T . Based on 2015+2016 data at a centre-of-mass energy of $\sqrt{s} = 13$ TeV they are determined using the $t\bar{t}$ -based and negative tag methods, respectively. Taken from Refs. [223] and [225], respectively.

methods available to perform cross-checks on the obtained results.²⁰

Both in Run 1 and in Run 2 the *negative tag* method [4, 225] constitutes the standard approach for calibrating the light-jet mistag rate. Light jets are mistakenly identified as b jets because of (i) the finite resolution of the track reconstruction in the ID, and (ii) material interactions. The method is based on the assumption that the former results in signed impact-parameter and decay-length distributions that are *symmetric* around zero for light jets; whereas for b and c quarks they tend to be shifted towards positive values (as exploited by the lifetime-based algorithms). Therefore, the mistag rate of the lifetime-based algorithms due to resolution effects is approximated by the *negative tag rate*, i.e. the tag rate measured in an inclusive jet sample that is obtained by applying a modified version of the algorithm, where the selection criteria on the signed impact parameter and decay length are reversed.

Figure 3.12(b) shows the data-to-simulation scale factors for the mistag rate of the 70% operating point of the MV2c10 algorithm determined by means of the *MV2c10Flip* algorithm [225]. The scale factors ranging between 1.5-2 indicate that the mistag rate in simulation is significantly underestimated; the relative total uncertainties between about 20-40% are clearly dominated by the systematic component. The results obtained for the 70% operating point of the MV1 algorithm in 2011 data showed a similar though less dramatic picture: scale factors of about 1.2-1.4 depending on $|\eta|$ with relative total (systematically dominated) uncertainties of 13-30%, and up to 50% at high p_T .

Other than for the b -jet tagging efficiency, the c -jet tagging efficiency and the mistag rate are not measured for track jets; instead their calibrations are estimated from the corresponding small-R jet scale factors and dedicated extrapolation uncertainties are considered.

²⁰After some refinements of the detector simulation implemented in a new release regarding the detector geometry and material interactions affecting the tracking performance in simulation, the c -jet tagging efficiency scale factors reduced to being of the order of unity.

Two further simulation-based extrapolations with corresponding systematic uncertainties are performed: (i) scale factors for the mistag rate of τ leptons are determined based on the ones for the c -jet tagging efficiency, (ii) b -jet and c -jet scale factors at high p_T ($p_T > 300$ GeV and $p_T > 140$ GeV, respectively) estimated based on the last measured p_T -bins.

While in the analysis using 2011 data only the impact of the overall uncertainty on the scale factors for b jets, c jets and light jets are evaluated, in the Run-2 analysis the effect on the result is estimated more accurately by considering a reduced set of systematic uncertainties per jet flavour that still allows to take almost precisely the correlations across p_T and η between the different sources into account (cf. Sec. 5.6.1). Reduced sets of systematic uncertainties are obtained as laid out in Ref. [217] (i) based on an eigenvalue decomposition yielding orthogonal variations while preserving the correct p_T and η dependence, (ii) neglecting those variations that are negligible without impacting the correlations nor the total uncertainty as well as (iii) removing those variations which are below a certain threshold; in the last step a compromise between preserving the correlations and reducing the total uncertainty needs to be made leading to different *reduction schemes*. The one chosen for the analysis described in Chap. 5 is referred to as *Medium* and results into three independent uncertainties for b jets, four for c jets and five for light jets; with a small underestimation of the total uncertainty and a loss of correlations across p_T and η (for b jets the relative difference is at the level of 3 %).

As discussed in some detail in the context of Chap. 4, the b -jet tagging efficiency (c -jet tagging efficiency) predicted in simulation depends on several aspects related to the modelling of the fragmentation and decay of b hadrons (c hadrons) as well as e.g. additional charged particles not stemming from the b hadron, but arising in the fragmentation process, and as such varies for different generators. The use of the EVTGEN program [226] to perform the b - and c -hadron decays for most simulated samples in Run 2 (except those produced with SHERPA) reduces significantly the previously observed spread; in particular regarding the b -jet tagging efficiency. Nonetheless residual differences persist, especially in the case of the c -jet tagging efficiency, and therefore generator-dependent scale factors are used which are determined based on the results obtained using the common reference sample (POWHEG+PYTHIA6) [217].

3.4.5 Calibration of the Mistag Rate of the SMT Algorithm

The light-jet mistag rate of the SMT algorithm is measured in an inclusive jet sample together with two other unknowns from a fully constrained system of three equations based on the number of events passing SMT requirement in two light-jet enriched samples [4]. Using only events with exactly two jets, a single- and a double-veto sample are defined, where one or both jets fail the b -tag criterion of the IP3D+JetFitter algorithm corresponding to the 80 % operating point, respectively.

In a preliminary version of the measurement [227], a straight-line fit was performed to the results yielding a single p_T - and $|\eta|$ -independent scale factor of 1.44 ± 0.20 , which was used in the analysis, described in Chap. 4, to correct the SMT mistag rate in simulation.

3.5 Electron Reconstruction and Identification

Electron reconstruction

Electrons²¹ traversing the central part of the detector leave hits in the inner tracking detectors, from which a track can be reconstructed, before they deposit their energy in several cells of the (electromagnetic) calorimeter. As mentioned already in Sec. 3.2, cluster of calorimeter cells that (supposedly) contain the total deposited electron energy are built using the *sliding-window* algorithm [136]. The electron reconstruction²² [228, 229] starts by searching for cluster seeds using a sliding window with a size corresponding to 3×5 the cell size of the middle layer of the EM calorimeter in $\eta \times \phi$. If the total transverse energy computed from the *towers* within the window, i.e. from every cell within across all EM-calorimeter layers, exceeds 2.5 GeV, a cluster seed is found. Reconstructed tracks are extrapolated to the middle layer of the EM calorimeter; if they can be loosely associated with a cluster, they are considered as electron-track candidates: they are refitted using the *Gaussian Sum Filter* (GSF) [230], which, optimised for electrons, provides better track-parameter estimates by accounting for non-linear bremsstrahlung effects. In case several (refitted) tracks are matched to the same seed cluster, a primary track is selected based on certain quality-criteria and several distance measures. Treating each seed cluster-track match as electron candidate, a cluster is built from cells across all layers within an increased window whose size is optimised to contain (most of) the deposited energy, while limiting the noise; it differs between the barrel and the endcap: 3×7 and 5×5 the cell size of the middle layer, respectively. The electron four-momentum is determined both from tracking and calorimeter information: while the energy is computed from the calibrated energy of the cluster (see below), its angular directions are defined by the corresponding track parameters.

While before the standard track reconstruction described in Sec. 3.1 was used to built tracks belonging to electron candidates, it was adapted for the data-taking in 2012 to improve the electron-reconstruction performance [231]. The key change was to introduce in addition to the standard pion hypothesis an electron hypothesis, which allows higher energy losses due to bremsstrahlung and thereby mitigating its effects on the reconstruction efficiency. The impact on the reconstruction efficiency is mostly at low transverse energy; the overall improvement is at the level of 5 %.

In order to reject objects that are falsely reconstructed as prompt electrons, such as jets and electrons from photon conversions or semileptonic heavy-flavour hadron decays, electron identification algorithms are employed [228, 229]. They are based on a number of discriminating variables (17 in 2011; 20 in 2015/16) related to (i) the longitudinal and lateral shower development, mainly assessed through various energy ratios exploiting the high granularity of the EM calorimeter, (ii) the track quality, such as the number of hits in the tracking detectors, (iii) the track-to-cluster matching as well as (iv) particle identification by the TRT. The particular choice of variables was adapted over the years to cope with changed conditions, such as the increased energy and instantaneous luminosities accompanied with higher pile-up, the installation of the IBL as well as the change in TRT gas (cf. Chap. 2).

Typically three operating points are provided, *Loose*, *Medium* and *Tight*, with increasing (decreasing) background rejection (signal efficiency); they are defined such that the sample selected by the tighter one is

²¹In the context of this thesis “electron” (e) is usually used to refer both to electrons (e^-) and positrons (e^+). The same applies for muons (μ) and τ leptons.

²²Since only central electrons are used in the analyses described in this thesis, the reconstruction of forward electrons which proceeds differently is not discussed, but can be found e.g. in Ref [228].

a subset of the looser one(s). Since the properties of electrons, in particular the shower-shape distributions, depend on the amount of passive material they traverse before they reach the calorimeter, the operating points are optimised in several bins of $|\eta|$ and the transverse energy E_T .²³

While the standard identification algorithm used for 2011 data is *cut-based* and the three operating points are obtained through both considering additional variables and tightening the sequentially applied requirements with respect to the looser definition [228], the baseline used in Run 2 is the *likelihood-based* (LH) method developed for the 2012 data-taking [229, 231]. Here, based on the probability density functions of the discriminating variables the overall signal (S) and background (B) likelihoods \mathcal{L} are determined and combined into a single discriminant: $\mathcal{L}_S/(\mathcal{L}_S + \mathcal{L}_B)$. Using the same full set of discriminating variables, the various operating points are defined by imposing more or less strict requirements on the final discriminant.

None of the exploited discriminating variables explicitly targets the presence of other particles in the vicinity of the identified electrons; dedicated *isolation requirements* that help to further suppress non-isolated electrons, e.g. misidentified jets or electrons stemming from heavy-flavour decays, are discussed in Sec. 3.7.

As mentioned in Sec. 2.2.6, the clean signature of electrons is exploited to trigger the readout of potentially interesting events. Having a common reconstruction sequence from the L1 to the HLT, several electron triggers with differing rates are defined by varying selection criteria and thresholds at the individual steps. At L1 electron RoIs are defined as 2×2 trigger towers in the EM calorimeter, where the sum of the transverse energy of at least one of the four pairs of nearest neighbours within exceeds a pre-defined threshold [136]. The threshold might vary with η to account for varying detector responses; the RoIs might be required to be isolated in the EM and/or the hadronic calorimeters. At HLT, in a first step, fast, custom algorithms are used to (i) reconstruct electron-candidate clusters and tracks from cells and hits within the RoIs, respectively, (ii) identify electrons based on few shower-shape variables, and (iii) match tracks to clusters; in a second step, precise algorithms similar to the offline ones discussed above are exploited and similar identification and isolation criteria defined and applied.

The 2011 dataset used in the analyses described in Chap. 4 was collected with three different lowest unprescaled single-electron triggers with increasing tightness in order to maintain certain rates across the different data-taking periods, where the instantaneous luminosity of the LHC increased; they are defined by requiring at least one online electron passing the E_T and cut-based identification criteria at HLT summarised in Table 3.2(a). At L1 the required E_T threshold is 6 GeV lower; for the trigger marked with (*) it was η dependent, and isolation in the hadronic calorimeter was required.

In Run 2 several unprescaled single-electron triggers were available simultaneously and logical-OR combinations thereof provide optimal selection efficiencies; the E_T , likelihood-based identification and isolation criteria applied at HLT are summarised for the 2015 and 2016 data-taking in Tables 3.2(b) and 3.2(c), respectively. For all triggers the same L1 selection is used, namely: $E_T > 22$ GeV changing with η and isolation both in the EM and hadronic calorimeters; except for the one with the lowest E_T threshold ($E_T > 24$ GeV), here the maximum of the η -dependent threshold was 20 (18) GeV in data (simulation) and only isolation in the hadronic calorimeter was required.

²³Given the electron is assumed to be massless, its transverse momentum (p_T) and transverse energy (E_T) are identical and are used interchangeable throughout this thesis. However, sometimes the notations E_T and p_T for the transverse momentum are used to distinguish between its determination from calorimeter and tracking measurements, respectively.

(a) 2011		(b) 2015		(c) 2016	
E_T	ID & iso.	E_T	ID & iso.	E_T	ID & iso.
> 20 GeV	Medium	> 24 GeV	Medium LH	> 26 GeV	Tight LH [†] ,
> 22 GeV	Medium	> 60 GeV	Medium LH		$p_T^{\text{var-cone}}(0.2)/E_T < 0.1$
> 22 GeV	Medium*	> 120 GeV	Loose LH	> 60 GeV	Medium LH [†]
				> 140 GeV	Loose LH [†]
				> 300 GeV	-

Table 3.2: HLT selection of the single-electron triggers used to collect the dataset the analyses described in Chaps. 4 and 5 are based on, during the (a) 2011, (b) 2015 and (c) 2016 data-taking. The identification (ID) requirements are introduced in the text, where “LH” refers to the likelihood-based variants and “†” indicates an alignment-robust version, where no transverse impact parameter information is used. $p_T^{\text{var-cone}}$ denotes the track-based variable-cone isolation criterion defined in Sec. 3.7. The corresponding L1 requirements are described in the text.

The reconstruction, identification, isolation (cf. Sec. 3.7) and trigger efficiencies are measured using *tag-and-probe* (T&P) methods [232, 233]; correction factors are determined as ratios of the measured efficiencies and the ones in simulation to be applied to simulated samples in order to reproduce the observed efficiencies. While usually being close to unity, deviating scale factors are due to the mismodelling of tracking properties or shower shapes in the calorimeters [231]. Since in particular the latter depend both on the energy of the electron and the traversed material before entering the calorimeters, the efficiencies and scale factors are usually determined in bins of E_T and $|\eta|$.

The efficiencies are defined and measured such that they are expressed with respect to the previous step preserving consistency: the reconstruction efficiency is determined given the presence of the cluster, the identification efficiency with respect to reconstructed electron candidates, the trigger efficiency with respect to electron candidates passing certain identification criteria, as is the isolation efficiency.

Exploiting known resonances, the T&P method aims at selecting a pure and unbiased sample of *probe* electrons by applying strict requirements to other *tag* objects in the event as well as the event topology; the efficiencies are then determined as the fraction of probe electrons passing the tested requirements. While primarily $Z \rightarrow ee$ decays are used, where a well-identified tag electron and the invariant dielectron mass is exploited, $J/\psi \rightarrow ee$ (and $W \rightarrow e\nu$) events are also employed to extend the reach towards lower E_T (and improve the statistical precision, respectively) of the identification-efficiency measurement (in Run 1) and the results are combined in the region of kinematic overlap.

The cluster-reconstruction efficiency in simulation ranges from 97 % (95 %) at $E_T = 7$ GeV to 99 % and more for $E_T \geq 15$ GeV in Run 1 (Run 2) [228, 229]. The efficiency to reconstruct an electron with a high-quality track matched to a cluster increases with E_T reaching a plateau at about 50 GeV and decreases towards high $|\eta|$, except at very high E_T ; lower efficiencies are also found in the calorimeter transition region. The efficiencies measured using 2011 (2015) data range from 85-98 % (95-99 %) and agree well with the ones in simulation. The scale factors derived for analyses based on 2015 data deviate from unity by < 1 %, uncertainties are below 0.5 %, except at very low E_T , where they reach up to 2 %.

Independent of the operating point the identification efficiencies increase with E_T ; while for the Loose criterion the efficiency is fairly flat against $|\eta|$, there is a slight dependence for the tighter operating points:

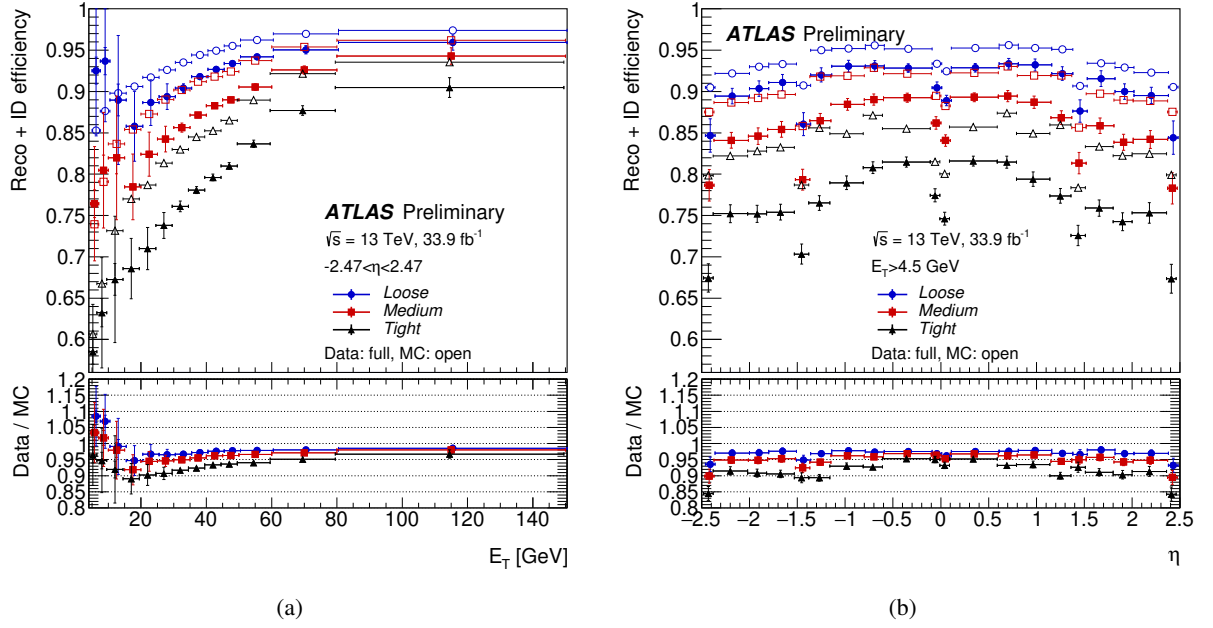


Figure 3.13: Data-simulation comparison of the combined electron reconstruction and identification efficiency as function of (a) the transverse energy and (b) the pseudorapidity in $Z \rightarrow ee$ events for the three likelihood-based identification operating points defined in the text. The data efficiencies are obtained through applying the scale factors measured in 2015+2016 data both using in $Z \rightarrow ee$ and $J\psi \rightarrow ee$ events to a $Z \rightarrow ee$ simulated sample; and shown as the ratio in the bottom pad. Taken from Ref. [234].

the efficiency tends to decrease towards higher $|\eta|$ values. Integrated over the whole η range and for $E_T > 20$ GeV the efficiencies range from 92-99 %, 78-92 % and 65-85 % for the Loose, Medium and Tight operating points used for 2011 analyses and 92-97 %, 87-95 % and 78-91 % for the likelihood-based Loose, Medium and Tight operating points used for 2015 analyses [228, 229]. While for the former good agreement between data and simulation is found resulting in scale factors deviating from unity only within a few percent, at most up to 5 % at high $|\eta|$, for the latter the deviations can be significant and range up to 20 % for the Tight operating point.

The combined reconstruction and identification efficiencies in simulated $Z \rightarrow ee$ events are compared to the ones measured in 2016 data for the three likelihood-based operating points as function of E_T and η in Fig. 3.13; the ratio plot in the bottom pad shows the correction factors. The data efficiencies were obtained by applying the correction factors measured in $Z \rightarrow ee$ and $J\psi \rightarrow ee$ events to simulation [234]. That the efficiencies in simulation are overestimated over a wide range is because in addition to a known mismodelling of the shower shapes by the detector simulation, also the conditions of the TRT in 2016 are not well represented. The total uncertainties are at the percent level, reaching larger values, up to 10 %, at low E_T .

The efficiency of the triggers used in the 2011 data-taking is at the level of 85-90 % for offline E_T values matching the online threshold and reaching a plateau about 10-15 GeV above with values between 95-99 % depending on the trigger when requiring the Medium identification criterion offline [167]. Good agreement between simulation and the measurement is found resulting in scale factors agreeing with unity within 5 %; the uncertainties are typically at the percent level. Similar results are found for the triggers used during the

2015 and 2016 data-taking [229].

A step-wise procedure is employed to calibrate the energy response (and resolution) of reconstructed electrons accounting for various energy losses due to energy deposits in the material in front of the EM calorimeter as well as beyond it and in cells outside the reconstructed cluster, i.e. longitudinal and lateral leakage, respectively [235]. In a first step the results of a data-driven intercalibration of the different LAr calorimeters based on $Z \rightarrow ee$ events are used to equalise the layer scales in data with respect to simulation. Then the cluster energy is corrected to restore the original electron energy in simulation by applying E_T - and $|\eta|$ -dependent calibration factors obtained from simulation using multivariate techniques. Local non-uniformities in the calorimeter response observed in data are corrected based on E/p studies in $W \rightarrow ev$ and measurements of the dielectron invariant mass m_{ee} in Z -boson decays. Finally, the electron response in data and resolution in simulation are calibrated to yield agreement based on an in-situ measurement. The respective correction factors α and C (in bins of E_T and $|\eta|$) are extracted simultaneously from fits to m_{ee} in $Z \rightarrow ee$ events; assuming (i) that the relation between the masses reconstructed in data and simulation can be parametrised in the same way as the energy-response difference, namely $m_{ee}^{\text{data}} = m_{ee}^{\text{sim.}}(1 + \alpha)$, (ii) the mass resolution is described by Eq. 3.4 parametrising the various noise effects and (iii) the sampling term S in Eq. 3.4 is known (at the level of 10%), i.e. the resolution is well modelled up to a Gaussian constant. In 2012, both factors are found to be flat versus $|\eta|$ in the barrel with values at the level of -2% and 0.8%, respectively, and somewhat η -dependent and larger in the endcap region [235]. The relative total uncertainties on the energy scale and resolution are estimated to be below 1% varying with E_T and $|\eta|$ and 10-40% increasing with E_T , respectively. The calibration is validated by performing a data-to-corrected simulation comparison of m_{ee} in $Z \rightarrow ee$ events: the agreement is at the level of 1% at the core of the distribution and decreases slightly towards the tails; the small deviation is covered by the assigned systematic uncertainties [235].

3.6 Muon Reconstruction and Identification

Muons originating from the hard-scatter event and traversing the detector leave hits in the inner tracking detectors, deposit only minimal energy in the calorimeters and reach the outermost part of the detector, specifically designed for their identification, the muon spectrometer (MS) (cf. Sec. 2.2.3). The muon reconstruction and identification is based on independent track reconstruction in the ID and the MS, which proceeds as described in Sec. 3.1 and the following, respectively, and aided by calorimetric information.

The track reconstruction in the MS proceeds in four steps [154, 236]: (i) finding of hit patterns,²⁴ which seed (ii) the making of (track) *segments* in individual chambers, e.g. in the MDTs by fitting straight lines to the hits found in each layer in the bending plane, (iii) building of muon-track candidates by combining hits from segments in different stations and if at least two segments are matched (one high-quality segment is sufficient in the barrel-endcap transition region), (iv) fitting of the muon track using the standard global χ^2 fit, taking into account effects such as the magnetic field (inhomogeneities), multiple scattering or inter-chamber misalignments.

Depending on the detector information exploited in the muon reconstruction four *muon types* with varying purities and efficiencies are distinguished [154, 237]. *Combined* muons are reconstructed if tracks built

²⁴Hit refers to *drift circles* in the MDT and *clusters* in the CSCs, RPCs and TGCs chambers, respectively.

separately in the ID and MS are combined into a single one. Given the tracking volume of the ID, combined muons are limited to $|\eta| < 2.5$. Low- p_T muons or muons entering MS regions with reduced acceptance, i.e. with support structures or service passages, may not traverse enough stations for reconstructing a standalone track and a combined muon. If, however, a track in the ID extrapolated to the MS is matched to at least one track segment in the precision chambers, it is reconstructed as a *segment-tagged* muon. *Standalone* or *extrapolated* muons are reconstructed, if no track in the ID is found, but a standalone MS track is found to be consistent with originating from the interaction point (IP). The muon parameters are expressed at the IP after extrapolating the MS track inward taking the estimated energy loss in the calorimeter into account. Standalone muons can be exploited to increase the $|\eta|$ acceptance to 2.7 with respect to combined muons. Acceptance losses in partially instrumented MS regions, in particular for $|\eta| < 0.1$, can be further recovered with *calorimeter-tagged* muons which are reconstructed from ID tracks matched to energy deposits in the calorimeter expected for minimum-ionising particles.

In Run 1 two slightly differing strategies for the track reconstruction in the MS and the muon reconstruction by combination with ID tracks were exploited [237], referred to as *Chain 1 (Staco/Muonboy)* [238] and *Chain 2 (Muid/Moore)* [239, 240], respectively. One particular difference is that the former obtains the track parameters of combined muons from a statistical combination of the ID and MS tracks, while the latter performs a global refit on the hits in both tracking detectors simultaneously. Here, hits in the MS may be added or neglected to improve the fit quality; most muons are reconstructed with the *outside-in* approach, where tracks reconstructed in the MS are extrapolated inward, taking the expected energy loss in the calorimeters into account, and matched to ID tracks. This latter strategy is also adopted by the *unified chain* (also referred to as *Chain 3*), which was developed in Run 1 aiming to combine the best features of the two chains and eventually replaced them in Run 2 after some further developments [154]; in particular the hit-pattern finding and the estimation of the energy loss in the calorimeters was improved.

Combined muons exploited in the SMT algorithm described in Sec. 3.4 and used in the analysis based on 2011 data reported in Chap. 4 are reconstructed with the Chain 1 algorithm, which was the standard chain in Run 1.

While in Run 1 merely requirements regarding the track quality in terms of the number of hits in the various ID subdetectors were exploited to suppress background contributions mainly from pion and kaon decays, several other track properties are considered additionally in Run 2 and, similar as for electrons, certain identification operating points defined, *Loose*, *Medium*, *Tight* and *High- p_T* , that provide varying background rejections and signal efficiencies (as well as robustness regarding the momentum measurement at high muon p_T) [154]. Besides requirements regarding the standalone track quality in terms of the number of hits in the MS, for combined-muon candidates criteria sensitive to the compatibility between the ID and MS measurements are exploited; given it is expected to be low for muons stemming from light-hadron decays in flight (cf. SMT algorithm in Sec. 3.4). The compatibility is evaluated by means of three variables: (i) the $\Delta(q/p)$ significance, (ii) $\rho' = \Delta p_T / p_T$ and (iii) the normalised χ^2_{match} of the combined track fit, where Δ indicates the difference between the ID and MS measurements.

The standard identification criterion is *Medium*, optimised to minimise the systematic uncertainties associated with the muon reconstruction and calibration, it mainly relies on combined muons; standalone muons are considered only in the $2.5 < |\eta| < 2.7$ region in order to increase the acceptance. In addition to requirements regarding the number of hits and how they are distributed across the MS stations, the ID

and MS measurements of the combined muons need to be loosely compatible: $\Delta(q/p)$ significance < 7 . The analysis reported in Chap. 5, however, exploits Loose muons: designed to maximise the reconstruction efficiency and acceptance, the Loose criterion considers in addition to the muons passing the Medium selection also calorimeter- and segment-tagged muons in the $|\eta| < 0.1$ region.

In order to further suppress background from non-prompt muons stemming from semileptonic heavy flavour hadron decays dedicated *isolation requirements* targeting the detector activity in the vicinity of the muon candidates are defined and discussed in Sec. 3.7.

As mentioned in Sec. 2.2.6, also the very clean signature of muons is exploited to trigger the readout of potentially interesting events. While following the same reconstruction sequence from the L1 to the HLT, various muon triggers with differing rates are defined by requiring individual selection criteria and thresholds at each step, in particular at the HLT level. At L1, the muon candidates are required to pass p_T thresholds that are for the triggers used to collect the datasets analysed in the search reported in Chap. 5 during the 2015 and 2016 data-taking at 20 GeV; except for one low- p_T trigger used in 2015, where it was only at 15 GeV. Similar to the electron triggers, the muon reconstruction at HLT proceeds in two stages using first a fast, custom algorithm and then a precise one which follows closely the offline reconstruction described above [166]. At the first stage, (i) based on including precision information from the MDTs within the L1 muon RoI, muon-track candidates in the MS are built, and (ii) using the offline outside-in approach combined-muon candidates are formed. The reconstruction at the precision stage then starts from the refined RoIs; by employing in addition also the complementary *inside-out* approach (as done offline) recovers about 1-5 % of the muons, mainly at low p_T .²⁵

The 2015+2016 dataset analysed in this thesis is obtained from a logical OR of two or more unprescaled triggers that evolved during the 2016 data-taking in order to cope with the increase in instantaneous luminosity. For the 2015 dataset the logical OR of two unprescaled triggers is used: one which required a higher p_T threshold of 40 GeV at HLT and a second one, where a sufficiently low rate was maintained despite the lower p_T threshold of 20 GeV by requiring a loose track-based isolation: $p_T^{\text{cone}}(0.2)/p_T < 0.12$ (cf. Sec. 3.7). The former was still unprescaled during the early 2016 data-taking, however, it got replaced by one with a higher threshold of $p_T > 50$ GeV for most of the year. The latter could not be supported without prescale from the beginning of the 2016 data-taking; therefore, at first one with an increased p_T threshold of 24 GeV (and 20 GeV at L1) was exploited; then one with a tightened isolation criterion, i.e. $p_T^{\text{var-cone}}(0.3)/p_T < 0.07$, before another one with an even higher p_T threshold of 26 GeV was used.

Also the muon reconstruction/identification, isolation (cf. Sec. 3.7) and trigger efficiencies are measured using T&P methods, introduced in Sec. 3.5, and correction factors to be applied to simulated samples in order to reproduce the observed efficiencies determined. Mainly $Z \rightarrow \mu\mu$ decays are used, where a well-identified tag muon and the invariant dimuon mass is exploited to select a clean sample of probe muons; only in the case of the reconstruction/identification efficiency measurement also $J/\psi \rightarrow \mu\mu$ events are employed to extend the reach towards lower p_T .

The measurement of the reconstruction/identification efficiency is restricted to the ID acceptance; correction factors for standalone muons in the $2.5 < |\eta| < 2.7$ region considered for the Medium and Loose

²⁵Only specialised muon triggers that are not used in the analyses described in this thesis, also rely on standalone-muon candidates.

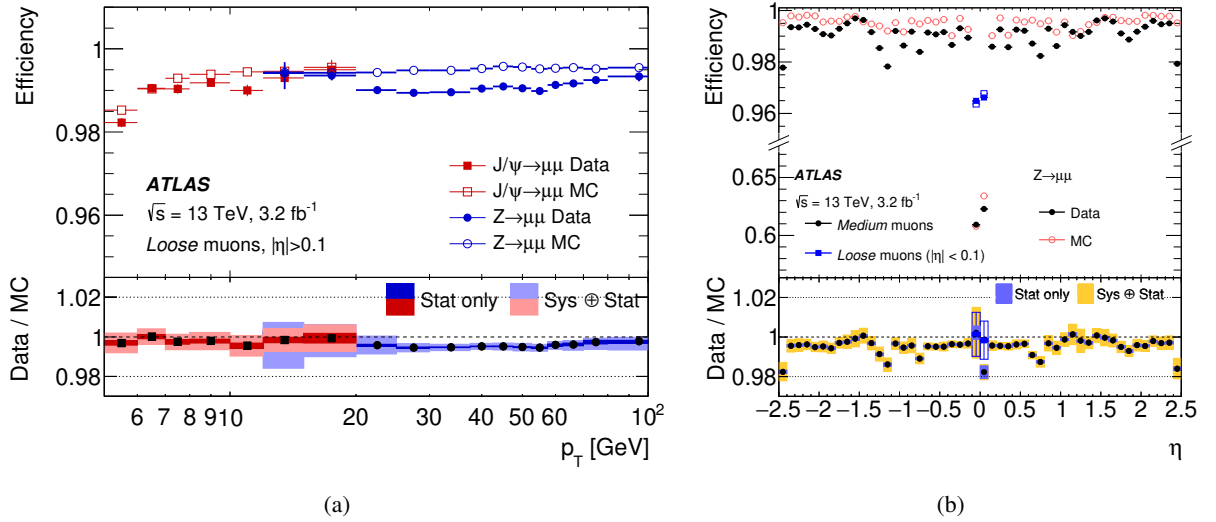


Figure 3.14: Comparison of the reconstruction (and identification) efficiency in $Z(J/\psi) \rightarrow \mu\mu$ in simulation and 2015 data as function of (a) the muon transverse momentum (p_T) for $0.1 < |\eta| < 2.5$ and (b) the muon pseudorapidity (η) for $p_T > 10 \text{ GeV}$ of Loose and Loose as well as Medium muons, respectively. As described in the text for $0.1 < |\eta| < 2.5$ the Medium and Loose definitions are identical. The ratio shown in the bottom pad are the resulting correction factors with their statistical and systematic uncertainties. Taken from Ref. [154].

operating points are then obtained by extrapolation of the results measured in $2.2 < |\eta| < 2.5$ [237]. The efficiency measurement of the Medium (Tight or Hight- p_T) operating point is divided into two steps [154]: (i) measuring the Medium identification efficiency using calorimeter-tagged muons as probes, (ii) measuring the ID-track reconstruction efficiency using standalone muons as probes; based on the assumptions that (a) using calorimeter-tagged muons instead of ID tracks does not affect the Medium identification efficiency and (b) the ID and MS track reconstructions are independent from each other.²⁶ A similar approach is used to measure the Loose identification efficiency for all but the calorimeter-tagged muons in $|\eta| < 0.1$; their measurement is based on using standalone muons as probes. Figure 3.14 shows the reconstruction/identification efficiency of Loose (and Medium) muons as function of the p_T and η for $0.1 < |\eta| < 2.5$ and $p_T > 10 \text{ GeV}$, respectively, measured in 2015 data. The expected efficiency of about 99.5 % for most of the p_T and η range is slightly overestimated, leading to correction factors that are on average around 0.5 %, up to 2 %, below unity; in the low- p_T regime they are still consistent with unity within the somewhat larger uncertainties of the J/ψ -based measurement. Considering also calorimeter- and segment-tagged muons for $|\eta| < 0.1$, increases the efficiency by approximately a factor 1.6; still it is with $\sim 96 \%$ significantly lower than in other η regions. The relative total uncertainty for the Medium operating point is at the level of 0.4 % and 1 % for the Z- and J/ψ -based measurements, respectively; for the latter the statistical uncertainty is the dominant contribution.

For measuring the trigger efficiency only combined muons within the acceptance of the muon triggers, i.e. $|\eta| < 2.4$, are considered [166]. The efficiency of the L1 muon trigger as function of the offline muon p_T is found to be close to 70 % in the barrel and 90 % in the endcaps once reaching a plateau at around the

²⁶In formulas that is $\varepsilon(\text{Medium}) = \varepsilon(\text{Medium}|\text{ID}) \cdot \varepsilon(\text{ID}) = \varepsilon(\text{Medium}|\text{CT}) \cdot \varepsilon(\text{ID}|\text{MS})$, under the assumption that $\varepsilon(\text{Medium}|\text{ID}) = \varepsilon(\text{Medium}|\text{MS})$ and $\varepsilon(\text{ID}) = \varepsilon(\text{ID}|\text{MS})$.

online threshold; relative to that the overall efficiency for a logical-OR of the lowest unscaled triggers is almost 100 % for offline muon- p_T values above the HLT threshold.

The scale and resolution of the muon momentum obtained from the curvature of the muon track in the magnetic field, extracted via the track fit, is measured in data and corrections are extracted to be applied to simulation in order to achieve optimal agreement.

The calibration [154] is based on the assumption that the *corrected* muon momentum determined from ID and standalone tracks, respectively, can be parametrised as function of the p_T in simulation as

$$p_T^{\text{corr}} = \frac{p_T + \sum_{n=0}^1 s_n \cdot (p_T)^n}{1 + \sum_{m=0}^2 r_m \cdot (p_T)^{m-1} \cdot g_m}, \quad (3.8)$$

where the η - and ϕ -dependent parameters s_n and r_m describe the scale and resolution corrections in a certain detector region, respectively; and g_m are Gaussian-distributed random variables with zero mean and unit width. The two scale-related parameters s_0 and s_1 account for a mismodelling of the energy loss of the muon traversing the material before entering the respective tracking detector and the magnetic field integral as well as the radial dimension of the detector, respectively. Since the former is negligible for a track measurement in the ID, s_0^{ID} is set to zero. The same is true for fluctuations of the energy loss affecting the resolution, and not just for the ID, but also the MS; therefore, the related parameter r_0 is also set to zero. The effects of multiple scattering, local field inhomogeneities and local radial displacements are assumed to be independent of the p_T and imperfect knowledge thereof is accounted for by r_1 . Finally, corrections regarding intrinsic resolution effects caused by the spatial resolution of the hit measurements as well as the residual misalignment of the MS are expected to be proportional to the muon p_T , and are parametrised by r_2 . In the case of the MS, r_2^{MS} is obtained from dedicated alignment studies in data.

The remaining parameters are extracted separately for the ID and the MS: binned maximum-likelihood fits are performed to the invariant dimuon mass distribution $m_{\mu\mu}$, as well as $\rho = (p_T^{\text{MS}} - p_T^{\text{corr,ID}})/p_T^{\text{corr,ID}}$ for the latter, reconstructed in $Z \rightarrow \mu\mu$ and $J\psi \rightarrow \mu\mu$ candidate events in data based on measurements from ID and standalone tracks, respectively.

The obtained corrections are propagated to the combined muon momentum assuming that the relation, $p_T^{\text{comb}} = f \cdot p_T^{\text{ID}} + (1 - f) \cdot p_T^{\text{MS}}$, still holds after correction; i.e. that the weight f , with which the individual measurement contributes, remains unchanged and f can be determined from the uncorrected simulation.

The calibration is validated by performing data-to-corrected simulation comparisons of the distribution of $m_{\mu\mu}$ reconstructed from combined muons in $Z \rightarrow \mu\mu$ and $J\psi \rightarrow \mu\mu$ candidate events; an example is shown in Fig. 3.15(a). The applied corrections bring the simulation in very good agreement with the data; residual deviations are within the associated systematic uncertainties of 0.05 % increasing with $|\eta|$ to about 0.1-0.3 % around $|\eta| \approx 2.5$. Also the relative mass resolution, which is well described by the corrected simulation, increases somewhat with $|\eta|$: it is around 1.2-1.6 % at small $|\eta|$ values and increases up to 1.6-1.9 % in the endcaps; corresponding to relative muon momentum resolutions of 1.7-2.3 % and 2.3-2.9 %, respectively. The relative mass resolution also degrades with increasing average momentum of the muons, as can be seen from Fig. 3.15(b); p_T^* denotes an angular-based transverse-momentum definition, exploiting the nominal Z -boson mass, which is uncorrelated with the reconstructed $m_{\mu\mu}$.

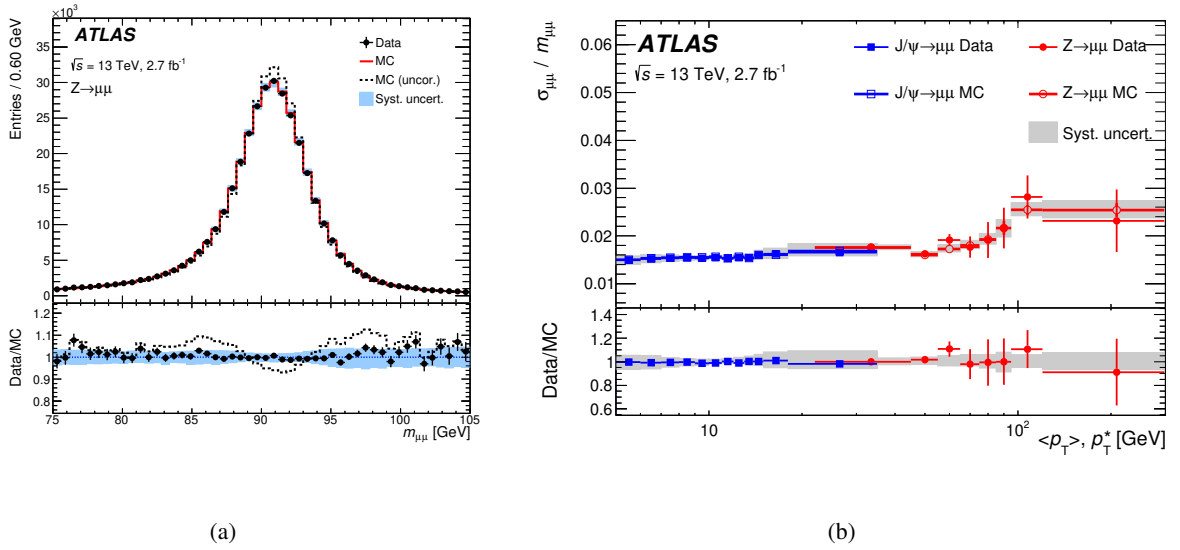


Figure 3.15: (a) Dimuon invariant mass distribution in $Z \rightarrow \mu\mu$ candidate events reconstructed from combined muons. The distribution in data is compared to the combined signal and background prediction, both before (MC(uncor.)) and after (MC) applying the muon momentum scale and resolution corrections described in the text. The bottom pad shows the ratio between data and either of the simulations; after correction the simulation agrees with the data within the systematic uncertainties associated with the procedure. (b) Comparison of the relative dimuon invariant-mass resolution measured as function of the average muon transverse momentum in $J/\psi \rightarrow \mu\mu$ and $Z \rightarrow \mu\mu$ candidate events in 2015 data and simulation after application of the muon momentum scale and resolution corrections described in the text. The bottom pad shows the ratio between data and simulation. Both statistical (error bars) and total systematic (shaded band) uncertainties due to the correction procedure and the extraction method are shown. Taken from Ref. [154].

3.7 Electron and Muon Isolation Requirements

As mentioned in Secs. 3.5 and 3.6, none of the discriminating variables exploited to define the electron and muon identification criteria *explicitly* target the close-by detector activity: the presence of other particles in their vicinity is an indication that they are non-prompt stemming e.g. from semi-leptonic heavy-hadron decays and are reconstructed inside jets or that they are misidentified jets, which is more likely to happen in the case of electrons; therefore, dedicated *isolation requirements* are defined in order to further suppress such background contributions.

Both the *calorimeter-* and *track-based* isolation criteria exploit the total deposited transverse energy and momentum in a region around the identified lepton, respectively, defined by a cone of a certain radius R , excluding the (expected) contribution of the lepton itself. More specifically the analysis described in Chap. 4, selects isolated electrons using a calorimeter-based isolation variable, denoted $E_T^{\text{conc}}(R)$ [231], where the total transverse energy is computed from cells of the EM and hadronic calorimeters in a cone of size $R = 0.3$ around the electron direction. The contribution of cells within $\eta \times \phi = 0.125 \times 0.175$ around the barycentre of the electron cluster is attributed to the electron candidate and subtracted. Corrections regarding (i) the expected leakage of the electron shower outside of the allocated region into the cone as well as (ii) expected pile-up contributions parametrised as function of the number of reconstructed primary vertices (cf. Sec. 3.1) are applied.

Isolated muons in the same analysis are selected relying on a (fixed-cone) track-based isolation variable,

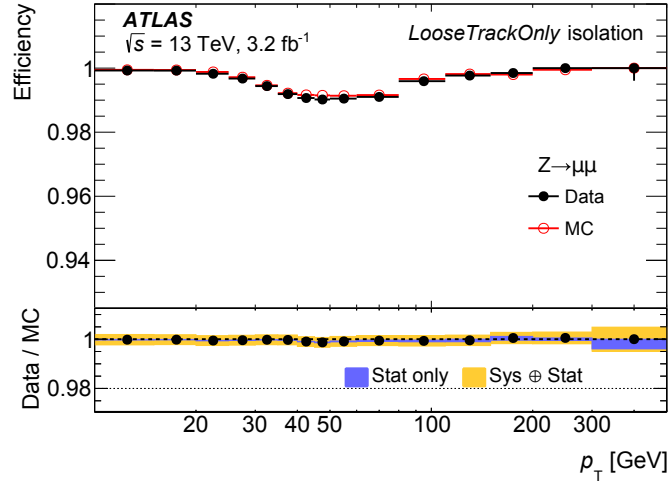


Figure 3.16: Comparison of the efficiency of the LooseTrackOnly isolation operating point as function of the transverse momentum for muons in $Z \rightarrow \mu\mu$ events in simulation and 2015 data. The ratio shown in the bottom pad are the resulting correction factors with their statistical and systematic uncertainties. Taken from Ref. [154].

$p_T^{\text{cone}}(R)$ [236], which is defined as the total transverse momentum computed from all tracks within a cone of size R around the muon direction. In the computation only high-quality tracks with $p_T > 1$ GeV that are compatible with stemming from the primary vertex are considered; while the muon track is excluded.

The Run 2 analysis reported in Chap. 5 completely relies on track-based isolation criteria both for electrons and muons, referred to as *LooseTrackOnly* [154, 229]. It is optimised to provide high signal efficiencies, 99 % on average, (fairly) constant versus η and p_T , and correspondingly low background rejection (at the level of 15). It is based on the *variable-cone* isolation variable, denoted $p_T^{\text{var-cone}}(R_{\text{max}})$, where the cone radius R is shrinking with increasing transverse momentum (energy) of the muon (electron) candidate: $R = \min(R_{\text{max}}, 10 \text{ GeV}/p_T)$, with R_{max} being the maximum cone size reached at low p_T . With respect to its fixed-cone counterpart, p_T^{cone} , it provides a higher signal efficiency for leptons stemming from decays of boosted particles. In the computation the lepton track is excluded; and for electrons also additional tracks from converted bremsstrahlung’s photons. The LooseTrackOnly operating point is then defined by setting R_{max} to 0.3 (0.2) for muons (electrons) and varying requirements imposed to $p_T^{\text{var-cone}}(R_{\text{max}})/p_T$ that provide a constant efficiency versus η and p_T .

The efficiency of the LooseTrackOnly operating point is measured using the T&P approach introduced in Sec. 3.5 for electrons and muons using $Z \rightarrow ee$ and $Z \rightarrow \mu\mu$ events, respectively. For electrons the efficiency rises with E_T reaching at around 15 GeV a plateau with around 99 %, and is flat versus η . For $E_T < 15$ GeV, the efficiency in simulation is slightly overestimated leading to scale factors of up to 1.5 % below unity; above they agree with unity within their relative total uncertainties of less than 0.5 %. The efficiency for muons is shown as function of p_T in Fig. 3.16; it reaches a minimum of about 99 % at around $p_T = 50$ GeV, which is well reproduced in simulation, leading to correction factors compatible with unity within their relative total uncertainties of about 0.2%, increasing maximally to 0.5 % at high p_T .

3.8 Reconstruction and Identification of Hadronically Decaying τ Leptons

With a mass of about 1.8 GeV [45] clearly the heaviest leptons, τ leptons decay weakly, usually before or only briefly after reaching the active regions of the detector. Leptonic decays make up about 35 % of all possible decay modes; they are not specifically targeted, but the decay electrons and muons are reconstructed and identified with the standard methods described in Secs. 3.5 and 3.6, given they are experimentally almost indistinguishable from their prompt versions. Hadronically decaying τ leptons (τ_{had}), however, have a distinct signature that is exploited in their reconstruction and identification. The τ_{had} decays involve an odd number of charged hadrons, possibly accompanied by a small number of neutral hadrons and missing transverse energy; the hadrons are mainly pions, and kaons to a lesser extent. Decays with one charged particle, *1-prong* decays, clearly dominate; while *3-prong* decays contribute by about 15 %, the contribution of decays involving more charged particles is virtually negligible.

The τ_{had} reconstruction [241, 242] starts from jets with radius parameter $R = 0.4$ reconstructed from topo-clusters at the LCW scale as described in Sec. 3.3; only jets with $p_T > 10$ GeV within the acceptance of the ID, excluding the calorimeter transition region ($1.37 < |\eta| < 1.52$), are considered. Due to the relatively high momenta with which τ_{had} leptons emerge from electroweak interactions in comparison to their mass, the τ_{had} -decay products are expected to be highly collimated. This is exploited to define a *core region*, containing most of the reconstructed decay products, and an *isolation region*, used to define jet-discriminating variables, of $\Delta R < 0.2$ and $0.2 < \Delta R < 0.4$ around the seed jet axis (or the τ_{had} direction), respectively.

The primary vertex (PV) from which a τ_{had} candidate is originating, the τ vertex (TV), is identified as the one PV with the highest JVF value computed from tracks²⁷ in the core region of the seed jet (cf. Sec. 3.3.3 for the JVF definition). In order to mitigate pile-up effects and improve the reconstruction efficiency, the TV is used as reference to determine the τ_{had} -candidate direction and transverse momentum, from the topo-clusters in the core region of the seed jet,²⁸ as well as to associate tracks: tracks matched to the TV using impact-parameter requirements are associated with the τ_{had} candidate if they are in its core region. The efficiency for reconstructing the same number of τ_{had} tracks as expected for 1- and 3-prong decays is at the level of 70 %, degrading somewhat for the latter at high τ_{had} -lepton p_T .

The described procedure is quite susceptible to falsely reconstruct jets emerging from quarks and gluons, and to lesser extent electrons, as τ_{had} leptons. Contributions due to the latter are suppressed by a simple overlap-removal: 1-prong τ_{had} candidates are discarded, if they are within $\Delta R = 0.4$ of an electron candidate passing the Loose identification criterion defined in Sec. 3.5.

In order to reject background contributions from jets a τ_{had} -lepton identification algorithm [241, 242] is employed which combines 14 discriminating variables based on tracks and topo-clusters in the τ_{had} core and isolation regions, in particular information regarding (i) the longitudinal and lateral shower development in the hadronic and EM calorimeters, (ii) the EM component of topo-clusters sensitive to the π^0 contribution and (iii) the charged particle content, into a single multivariate classifier; separate Boosted Decision Trees (BDT) are trained for 1-track and 3-track τ_{had} candidates, respectively. Three operating points, *Loose*, *Medium* and *Tight*, with decreasing (increasing) τ_{had} -identification efficiencies (jet rejection) are defined; the requirements on the BDT scores are chosen such that they provide constant efficiencies as function

²⁷Tracks exploited in the τ_{had} reconstruction are reconstructed as described in Sec. 3.1 pass standard quality criteria based on the number of hits in the ID and have $p_T > 1$ GeV.

²⁸Tau candidates are assumed to be massless, so that transverse momentum and energy are the same.

of p_T . The standard operating point, Medium, targets 55 % (40 %) signal efficiency for 1-track (3-track) τ_{had} candidates.

The search reported in Chap. 5 rejects events with Medium τ_{had} candidates as means of background suppression. While scale factors to correct the efficiency in simulation are derived using T&P methods (cf. Sec. 3.5) in $Z \rightarrow \tau\tau$ events [242], no correction regarding the inefficiency to be applied to τ_{had} -vetoed events is foreseen.

The τ_{had} -lepton energy scale (TES) is calibrated in two steps in order to restore the true *visible* energy E_{true} , i.e. the total energy at particle level carried by all τ_{had} -decay products except the neutrinos, in simulation and correct residual differences in the energy response and resolution between data and simulation [243]. In the first step the two classes of effects are corrected [242]: (i) the energy contribution due to pile-up, E_{PU} , and (ii) out-of-cone leakage, topo-cluster threshold effects and decay products not reaching the calorimeter that result in a non-closure of the energy response $\mathcal{R} = \langle (E - E_{\text{PU}})/E_{\text{true}} \rangle$. Extracting both corrections from simulation (in bins of $|\eta|$, the number of primary vertices N_{PV} and n -prong) the corrected τ_{had} -lepton energy is obtained as $E_{\text{corr.}} = (E - E_{\text{PU}})/\mathcal{R}$. Systematic uncertainties computed as the shift on $\langle (E_{\text{corr.}}/E_{\text{true}}) \rangle$ using several simulated samples with (i) an alternative underlying-event tune, (ii) varied topo-cluster noise thresholds, (iii) increased passive material and (iv) an alternative shower model in the detector simulation; the residual non-closure and pile-up dependence are also considered. The total uncertainties vary between 2-6 % depending on p_T , $|\eta|$ and the number of prongs being 1 or 3.

In the second step, the calibration is refined by means of an in-situ measurement using $Z \rightarrow \tau_{\mu}\tau_{\text{had}}$ events, where one τ -lepton decays leptonically into a muon (τ_{μ}) [243]. Assuming the difference between the τ_{had} -lepton energy in data and simulation is described by a mere shift, i.e. $E \rightarrow (1 + \alpha)E$, α is extracted by fitting templates of m_{vis} , the invariant mass of the τ_{had} -muon system, obtained in simulation to the respective distribution in data. Systematic uncertainties related to the background modelling, the muon reconstruction and the τ_{had} -energy resolution. In 2015 data, α was determined to -0.7% (-3.6%) for τ_{had} candidates with 1 (3) associated tracks with total uncertainties of about 1.4 % (3 %).

3.9 Reconstruction of Missing Transverse Momentum

Particles emerging from the hard-scatter interaction that are solely weakly interacting, such as neutrinos, escape direct detection. Their presence can only be inferred from missing transverse momentum $E_{\text{T}}^{\text{miss}}$,²⁹ i.e. a momentum imbalance in the plane transverse to the beam line, where also in pp collisions momentum conservation is expected [244].

Defined as the negative vectorial sum of the momenta of all particles stemming from the hard interaction, its reconstruction requires the most complete and precise event reconstruction involving all detector subsystems; the limited detector acceptance and resolution as well as various sources of fake $E_{\text{T}}^{\text{miss}}$ such as electronics noise and pile-up events pose difficult challenges. Therefore, two terms can be distinguished in the $E_{\text{T}}^{\text{miss}}$ reconstruction, referred to as the *hard* and *soft* term, respectively. The former represents the contributions from fully reconstructed and calibrated (hard) objects identified with electrons, photons, hadronically decaying τ leptons, muons and jets (with $p_T > 20$ GeV passing the JVF/JVT requirements

²⁹ $E_{\text{T}}^{\text{miss}}$ denotes the magnitude of $\vec{E}_{\text{T}}^{\text{miss}} = (E_x^{\text{miss}}, E_y^{\text{miss}})$.

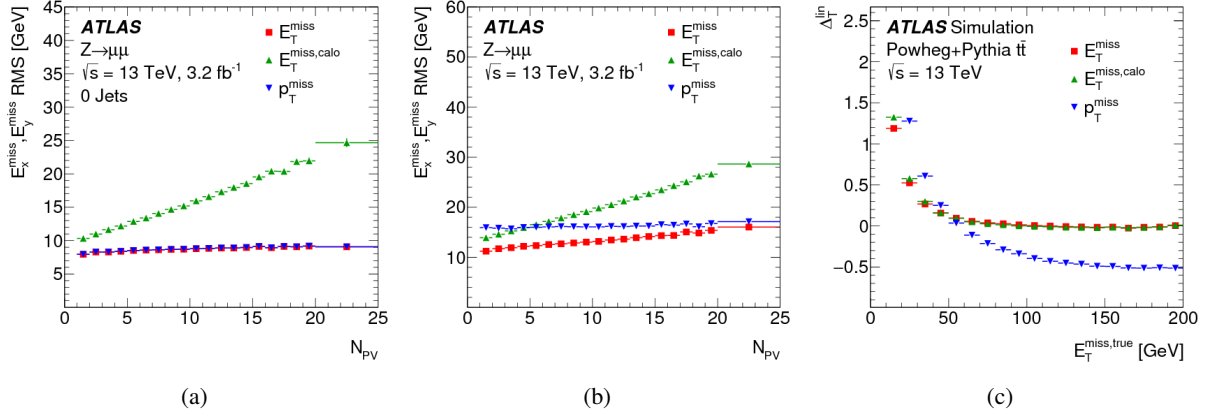


Figure 3.17: Comparison of the three E_T^{miss} estimate variants introduced in the text, E_T^{miss} and $E_T^{\text{miss,calo}}$ relying on the track-based and calorimeter-based soft terms as well as p_T^{miss} , the solely track-based variant denoted $E_{T,\text{trk}}^{\text{miss}}$ in the text, regarding the stability of their resolution against the number of reconstructed primary vertices in the event (N_{PV}), sensitive to in-time pile-up, in (a) exclusive $Z(\rightarrow \mu\mu)$ and (a) inclusive $Z(\rightarrow \mu\mu)$ +jets events selected in data and (c) the linearity of the relative deviation of their estimate from the true E_T^{miss} , i.e. $\Delta_T^{\text{lin}} = (E_T^{\text{miss}} - E_T^{\text{miss,true}}) / E_T^{\text{miss,true}}$, in simulated 1-lepton $t\bar{t}$ events. Taken from Ref. [245].

(cf. Sec. 3.3.3)); the latter, signals identified with stemming from the hard-scatter event, but not associated with any of the beforementioned physics objects.

In order to best describe E_T^{miss} in a specific analysis, generally analysis-dependent preselections are applied to the hard objects; an overlap procedure is employed to avoid multiple consideration of signals arising from the same particle given that the object reconstruction is not mutually exclusive.

Two different soft-term variants are exploited in the Run 1 and Run 2 (standard) E_T^{miss} reconstructions, a *calorimeter-based* version (CST) and a *track-based* version (TST), respectively.

The Run-1 definition of CST [244] involves two components, namely *soft* jets, with $7 \text{ GeV} < p_T < 20 \text{ GeV}$ reconstructed from topo-clusters at the LCW scale, but without JES calibration (cf. Sec. 3.3.2), and topo-clusters at the LCW scale that are not matched to any of the described physics objects, referred to as *cell-out* term. By exploiting tracking information to (i) recover contributions from particles with low p_T that do not reach the calorimeter or do not seed a topo-cluster and (ii) obtain an improved estimate by replacing the energy measurement of topo-clusters by the momentum measurement of matched tracks, the estimate of the cell-out term is improved. In Run 2, CST is solely based on unmatched topo-clusters at the LCW scale [245].

The TST (in Run 2) is computed from high-quality ID tracks identified as emerging from the hard-scatter vertex (cf. Sec. 3.1), that are not associated with any of the objects considered in the hard term.

Despite being oblivious to neutral contributions and limited in the $|\eta|$ coverage, TST is generally favoured over CST due to its excellent pile-up resilience. This can be seen from Fig. 3.17(a) showing the E_T^{miss} resolution³⁰ in exclusive $Z \rightarrow \mu\mu$ events (without jets), where no real E_T^{miss} is expected, selected in 2015 data for the two soft-term variants as function of the number of reconstructed primary vertices

³⁰The E_T^{miss} resolution is estimated from the width of the combined $E_{x(y)}^{\text{miss}}$ distributions in bins of $\sum E_T$, i.e. the scalar sum of the transverse momenta of all objects contributing to the E_T^{miss} reconstruction, obtained from a fit with a Gaussian.

(N_{PV}) .³¹

Although by using the TST definition the soft term is almost pile-up insensitive, in particular the jet term spoils this resilience as can be seen from Fig. 3.17(b) showing the $E_{\text{T}}^{\text{miss}}$ resolution as function of N_{PV} in inclusive $Z(\rightarrow \mu\mu)+\text{jets}$ events in 2015 data; this motivates the definition of a pile-up independent $E_{\text{T}}^{\text{miss}}$ variant that (almost) completely relies on tracking information, denoted $E_{\text{T, trk}}^{\text{miss}}$. Otherwise purely based on high-quality ID tracks associated with the hard-scatter vertex, only the electron and muon momentum estimates are replaced by their superior measurements involving calorimeter and MS information, respectively [246]. While it can be seen from Fig. 3.17(b) that indeed $E_{\text{T, trk}}^{\text{miss}}$ is pile-up independent, it can be seen from Fig. 3.17(c), showing the $E_{\text{T}}^{\text{miss}}$ linearity as function of the true $E_{\text{T}}^{\text{miss}}$ for the three $E_{\text{T}}^{\text{miss}}$ definitions in simulated 1-lepton $t\bar{t}$ events, that it clearly underestimates the true $E_{\text{T}}^{\text{miss}}$ due to neglecting the neutral contributions. However, both of the other $E_{\text{T}}^{\text{miss}}$ estimates relying on TST and CST, respectively, provide an equally good estimate of the true $E_{\text{T}}^{\text{miss}}$ within a few percent; except at small true $E_{\text{T}}^{\text{miss}}$ values due to the *observation bias* [245], i.e. the tendency to reconstruct non-vanishing $E_{\text{T}}^{\text{miss}}$ values also in events without genuine $E_{\text{T}}^{\text{miss}}$ because of the limited detector resolution.

Systematic uncertainties on the $E_{\text{T}}^{\text{miss}}$ scale and resolution arise both from the hard term by propagation of the systematic uncertainties related to the scale and resolution of the hard objects as well as from the soft term. Contributions arising from the latter are estimated from data-to-simulation comparisons of observables in exclusive $Z(\rightarrow \mu\mu)$ events (without jets) sensitive to the soft term.

In Run 1, the distribution of the mean of the $E_{\text{T}}^{\text{miss}}$ projection onto the direction defined by the reconstructed Z -boson p_{T} as function of $\sum E_{\text{T}}$, i.e. the scalar sum of the transverse momenta of all objects contributing to the $E_{\text{T}}^{\text{miss}}$ reconstruction, sensitive to detector resolution and bias, is exploited to estimate a systematic uncertainty on the $E_{\text{T}}^{\text{miss}}$ soft-term scale of 5% [247]. Analogously the data-to-simulation agreement of the $E_{\text{T}}^{\text{miss}}$ resolution as function of $\sum E_{\text{T}}$ is evaluated to define a systematic uncertainty on the $E_{\text{T}}^{\text{miss}}$ soft-term resolution of 2% [247].

Consistent results were obtained with alternative spectra also sensitive to the scale and resolution of the soft term; they are used in Run 2 to estimate the related systematic uncertainties [245]. They are based on the parallel (\mathcal{P}_{\parallel}) and perpendicular (\mathcal{P}_{\perp}) projections of $\vec{p}_{\text{T}}^{\text{soft}}$ onto $\vec{p}_{\text{T}}^{\text{hard}}$, where $\vec{p}_{\text{T}}^{\text{soft}}$ is defined as the negative of the $E_{\text{T}}^{\text{miss}}$ soft-term vector and $\vec{p}_{\text{T}}^{\text{hard}}$ as the sum of the transverse momenta of all hard objects considered in the $E_{\text{T}}^{\text{miss}}$ reconstruction; in exclusive $Z(\rightarrow \mu\mu)$ events without genuine $E_{\text{T}}^{\text{miss}}$ in which the data-simulation comparison is performed, it is expected that $\vec{E}_{\text{T}}^{\text{miss}} = -(\vec{p}_{\text{T}}^{\text{hard}} + \vec{p}_{\text{T}}^{\text{soft}})$. While the average \mathcal{P}_{\parallel} is sensitive to the soft-term scale, the variance of $\mathcal{P}_{\parallel(\perp)}$ is a measure for the fluctuations in the response (transverse angular deflection around the $\vec{p}_{\text{T}}^{\text{hard}}$ axis) of the soft term contributing to the $E_{\text{T}}^{\text{miss}}$ resolution. Systematic uncertainties are evaluated from the comparison of their spectra as function of $p_{\text{T}}^{\text{hard}}$; they are at the level of 10%.

As mentioned in Sec. 2.2.6, the signature of large amounts of $E_{\text{T}}^{\text{miss}}$ is used to trigger the readout of potentially interesting events for analyses targeting final states only containing jets and $E_{\text{T}}^{\text{miss}}$ or highly energetic muons. Other than described above, at trigger level reconstructed muons are not considered and only calorimeter information is used in the $E_{\text{T}}^{\text{miss}}$ calculation. At L1, the $E_{\text{T}}^{\text{miss}}$ reconstruction is based on

³¹The comparison is done with early Run 2 data, where the CST definition deviates slightly from the one in Run 1, in particular no tracking information is exploited to improve the low momentum estimates. [245]

jet elements defined as 2×2 trigger towers extending across both the EM and hadronic calorimeters; E_T^{miss} is then obtained from the total transverse energy computed from jet elements in the full detector volume at the EM scale (cf. Sec. 3.2). The E_T^{miss} triggers exploited to collect the dataset during the 2015/2016 data-taking, on which the analysis reported in Chap. 5 is based, are all unprescaled and seeded by the same L1 trigger; it requires $E_T^{\text{miss}} > 50$ GeV. While the HLT trigger used for the 2015 dataset relies on the *cell algorithm* for E_T^{miss} reconstruction, the two used for the 2016 dataset rely on the *jet-based algorithm* [166]. The former computes E_T^{miss} from summing the momenta of all contributing cells, obtained in the massless approximation from the cell energy at LCW scale; cells with large negative energy, energy below the noise threshold or being non-functioning are neglected. The jet-based algorithm calculates E_T^{miss} based on the total transverse momentum of all jets reconstructed with the jet-trigger algorithm: they are reconstructed and calibrated similarly to the offline small-R jet reconstruction described in Sec. 3.3; though no in-situ correction is applied. The HLT selection of the trigger used for the 2015 dataset requires the reconstructed E_T^{miss} to exceed 70 GeV, the ones used for early and later periods of the 2016 data-taking, 90 GeV and 110 GeV, respectively.

Given that the trigger efficiency is defined as the fraction of events in a sample selected by applying criteria on the offline-reconstructed E_T^{miss} and E_T^{miss} being an event-level quantity, the efficiency of a certain E_T^{miss} trigger depends on the applied offline selection. Therefore, potential correction factors to be applied in simulation in order to match the efficiency in data need to be determined in the context of the analysis in question. However, it is found that for offline E_T^{miss} values greater 200 GeV all the E_T^{miss} triggers are close to fully efficient almost independent of the applied selection; and the L1 trigger efficiency ranges between 95-99%. Thus, only in case analyses chose to apply an offline selection in the trigger turn-on, where data and simulation differences can be large, analysis-dependent correction factors need to be determined. In the case of the analysis described in Chap. 5 the calibration factors obtained in the context of a closely related analysis are used; they are within 5% of unity [248].

4 Calibration of the c -Jet Tagging Efficiency Using Events with a W Boson Produced in Association With a Single c Quark

4.1 Introduction

The possibility to identify jets likely originating from b -quarks, b -tagging, is exploited in many data analyses performed at the LHC. Its application ranges from precision measurements of the Standard Model to searches for new phenomena, such as the search for an A boson of the Two-Higgs-Doublet Model in the $\ell\ell(\nu\nu)bb$ final state described in Sec. 5. As introduced in detail in Sec. 3.4, in order to identify b jets and separate them from c and light jets, b -tagging algorithms exploit several distinct properties of the production and the decay of b hadrons, in particular their relatively long lifetime, of about 1.5 ps. The most commonly used algorithms are therefore referred to as *lifetime-based b -tagging algorithms*.

The performance of the various b -tagging algorithms used within the ATLAS collaboration is generally evaluated in terms of their *b -tagging efficiency*, i.e. the efficiency with which a b jet is identified as such, as well as their c -jet and light-jet rejections using simulated samples of top-quark pair ($t\bar{t}$) events. The rejections are defined as the inverse of the probability to mistakenly identify a c jet or light jet as a b jet, i.e. as the inverse of the *c -jet tagging efficiency* and *mistag rate*, respectively. Because simulations are not expected to describe all effects that impact the performance of b -tagging algorithms accurately, in order to use b -tagging in physics analyses, the b -tagging efficiency, as well as the c -jet tagging efficiency and mistag rate, need to be determined from data and corrected in simulation.

The key to precisely measuring the efficiency of a b -tagging algorithm for a certain jet flavour is to extract a sample of jets from data dominated by that jet flavour. Several strategies to obtain appropriate samples are exploited in the various calibration methods used by the ATLAS collaboration. While several of those methods are briefly introduced in Sec. 3.4.4, this chapter describes in detail the *$W+c$ method* developed to determine the c -jet tagging efficiency of lifetime-based b -tagging algorithms. This method was novel when previously published in Refs. [3, 4]. It is based on a sample, where a single c jet is produced in association with a leptonically decaying W boson and identified by a soft muon stemming from the semileptonic decay of a c hadron.

The calibration method is demonstrated using pp -collision data at $\sqrt{s} = 7$ TeV collected with the ATLAS detector during the year 2011. Only events, where the W boson decays into an electron and a neutrino are targeted.¹

At this centre-of-mass energy, $W+c$ events are with about 80% predominantly produced via s -quark-gluon fusion; the subdominant production mode with a d quark instead of the s quark in the initial state

¹Later versions of the calibration also consider W boson decays into a muon and a neutrino.

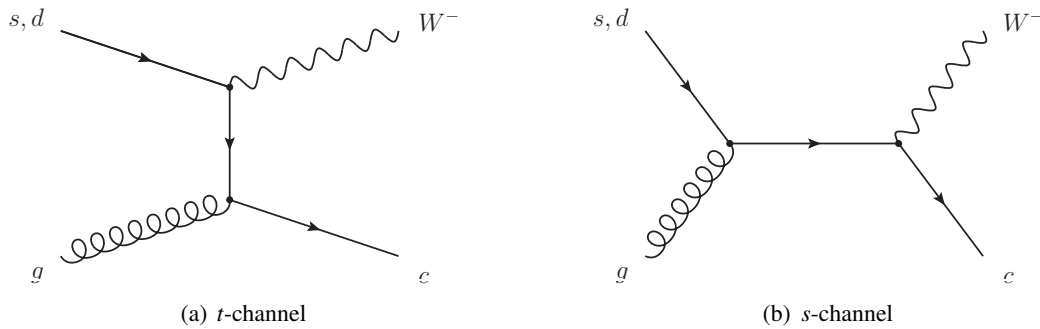


Figure 4.1: Feynman diagrams for the dominant production modes of a single c quark in association with a W boson at leading order.

contributes with about 7%. From Figure 4.1 showing the leading-order Feynman diagrams, it can be seen that the W boson is accompanied by a c quark with an oppositely signed charge, i.e. $sg \rightarrow W^-c$ and $\bar{s}g \rightarrow W^+\bar{c}$.² Furthermore, the soft muon, that emerges in about 10% of the c -hadron decays, carries a charge with the same sign as the original c quark (and consequently with an opposite sign as the W boson). Therefore, requiring that the charges of the soft muon and the electron stemming from the W -boson decay to be of opposite sign, selects $W+c$ events with very high efficiency. As most of the background processes are evenly populated with events, where the charges of the decay leptons are of opposite sign (OS) and of same sign (SS), a statistically very pure sample of c jets is obtained by extracting the number of $W+c$ candidate events as the difference between the number of events with opposite and with same charge (OS-SS). This fundamental strategy was already exploited in several $W+c$ production cross-section measurements [1, 249–252] and in particular also in the most recent one [1], in whose context the presented calibration was conducted.

Jets that are identified to contain a soft muon by the Soft Muon Tagging (SMT) algorithm introduced in Sec. 3.4.3,³ are referred to as SMT jets and a sample composed of such jets, extracted as the number of OS-SS events, is referred to as the SMT-jet sample. Based on such a sample, the c -jet tagging efficiency of the MV1 tagging algorithm, the most commonly used b -tagging algorithm in ATLAS analyses in Run 1, is calibrated for SMT c -jets. In a second step, data-to-simulation scale factors that are applicable to inclusive, unbiased samples of c jets are derived by performing an extrapolation procedure.

The purpose of this simulation-based and data-supported procedure that has been developed in the course of this thesis, is to correct for the bias introduced by selecting c jets via semimuonic c -hadron decays. Since the standard calibration method for the c -jet tagging efficiency used in Run 1 is afflicted with a similar bias, due to selecting a sample of c jets by reconstructing D^{*+} mesons in the exclusive decay $D^{*+} \rightarrow D^0(\rightarrow K^-\pi^+)\pi^+$, it later adopted the extrapolation procedure (cf. Sec. 3.4.4, Ref. [253] vs. Ref. [4]).

Based on what is described in the following, the $W+c$ calibration became the standard calibration method, providing scale factors for early Run-2 analyses. With respect to the D^{*+} method, it has the advantage of smaller statistical uncertainties and a smaller extrapolation. However, it was replaced soon after by yet another, new strategy that measures the c -jet tagging efficiency on an inclusive sample of c jets.

²In the remainder of this chapter, the notation $W+c$ includes both W^-c and $W^+\bar{c}$.

³The SMT b -tagging algorithm uses information complementary to the lifetime-based algorithm(s), and thus can be used for their calibration; especially, because the induced bias is corrected later.

It relies on $t\bar{t}$ events, where one of the W bosons decays hadronically to one c quark and light quark and the other leptonically to an electron or muon and a neutrino. Besides having the advantage of not requiring any extrapolation, it furthermore benefits from the large $t\bar{t}$ cross-section, in particular at $\sqrt{s} = 13$ TeV (cf. Sec. 3.4.4). Nonetheless, the $W+c$ method continues to be used and provides important alternative calibration results.

4.2 Data and Simulated Samples

The presented analysis is based on pp -collision data collected with the ATLAS detector in the year 2011, where the LHC was operated at a centre-of-mass energy of 7 TeV (cf. Sec. 2). Considering only events that were recorded under stable-beam conditions, where all relevant detector components were fully operational and that fulfil standard data-quality requirements, the analysed dataset corresponds to an integrated luminosity of 4.6 fb^{-1} [155].

The dataset used to perform the calibration was collected using single-electron triggers. As described in Sec. 3.5, the trigger decision is based on the transverse momentum (p_T) of the electron candidates as well as on identification and isolation criteria. During the data-taking period the requirements were slightly adjusted reflecting the increase in instantaneous luminosity; in particular the p_T threshold was increased from 20 GeV to 22 GeV (cf. Table 3.2(a)).

Simulated samples are used to model (kinematic) distributions of signal and background processes, to compute selection efficiencies as well as to perform the extrapolation of the scale factors. The normalisation of the signal as well as of the dominant background processes are determined from data, as discussed in detail in Sec. 4.4.

The signal, defined as the production of a W boson in association with a single c quark, is simulated using ALPGEN 2.13 [97] for the matrix element (ME) and PYTHIA 6.423 [22] for parton showering (PS), hadronisation and underlying event. This sample, with respect to which the data-to-simulation scale factors are expressed, is referred to as the PYTHIA-default sample in the following. It needs to be distinguished from a modified version, referred to as PYTHIA-corrected sample, where several c -quark fragmentation and c -hadron decay properties are corrected to improve known shortcomings in the ALPGEN+PYTHIA description. The PYTHIA-corrected sample is used to validate the level of agreement between data and simulation, but foremost to perform the scale-factor extrapolation, in whose context the details of the applied corrections are therefore discussed (cf. Sec. 4.6).

Two alternative signal samples are exploited to obtain (i) corrections for which no measurements in data are available, (ii) assess the validity of the extrapolation procedure, and (iii) determine associated systematic uncertainties. One alternative signal sample is obtained by replacing PYTHIA: the parton showering is done by HERWIG 6.520 [254, 255], the underlying event by JIMMY 4.31 [256]; this sample is referred to as HERWIG sample. In the case of a second alternative signal sample ALPGEN+PYTHIA is interfaced to the EVTGEN [226] program, which is dedicated to modelling c -hadron and b -hadron decays. However, since in Run 1 it was not standard to use EVTGEN to describe heavy-hadron decays, the sample is without detector simulation and can only be used to perform generator level studies.

The MLM [257, 258] matching scheme implemented in ALPGEN is applied to remove overlaps between events with the same parton multiplicity originating from the ME and the PS.

The dominant background contribution stems from W bosons produced in association with light jets. As the production of a W boson in association with a single b quark is generally negligible, contributions from decays of heavy hadrons rather stem from W -boson events, where c - or b -quark pairs arise from gluon splittings, denoted $W+bb$ and $W+cc$, respectively. However, they are suppressed because (i) only events with one jet are considered in the analysis, and (ii) the OS and SS contributions are expected to be equal, as soft muons arise similarly from the decay of the hadron containing the quark or the one containing the antiquark, and thus the contribution to the OS-SS sample is negligible.

Events with W bosons produced in association with light jets, referred to as W +light events, are considered as candidate events, if the light jet is falsely identified as a c jet. This happens, due to the presence of a soft-muon candidate which is either a track mimicking a muon or a *decay-in-flight* muon stemming from the decay of a light meson, such as a pion or kaon, emerging from the fragmentation process. As W bosons in association with u/d -quarks are primarily produced in d/u quark-gluon fusion, the same charge correlation between the W boson and accompanying light quark exists as in the case of the signal process. However, the correlation is strongly diluted given the soft fragmentation of light hadrons, due to which the hardest particles tracks in the jets (which have the highest probability to fake the soft muon) do not necessarily stem from the decay of the hadron containing the initial quark. Nonetheless, it is important to determine the residual OS/SS asymmetry and contribution to the OS-SS sample precisely in data, as described in Sec. 4.4.2, given the relatively large cross-section of W +jets production.

Simulated events of W bosons produced in association with c jets, b jets and light jets are generated separately, using ALPGEN interfaced to HERWIG+JIMMY, as for the alternative signal sample. As exclusive samples for $W+bb$ and $W+cc$ production with zero to four additional partons and an inclusive sample with five or more additional partons are used, several overlaps need to be removed: (i) between events with the same parton multiplicity originating from the ME and the PS, using the MLM matching scheme, (ii) between events with heavy-flavour quark pairs originating from the ME and the PS, and (iii) with the $W+c$ sample.

The other important background contribution is due to multijet production, in particular dijet production originating from pairs of c quarks or b quarks. Events are considered as candidate events, if in addition to a c -jet candidate identified by the presence of a soft muon, a signal electron is mimicked by (i) a true (soft) electron from a c -/ b -hadron decay, or by (ii) a jet, while the (soft) neutrinos from the semileptonic hadron decays and mismeasurements of the jet energies lead to a large amount of missing transverse momentum (E_T^{miss}). In particular in the case of (i) for initial c -quark pairs, the candidate leptons are expected to have opposite charges. However, events of type (ii) and those of type (i) in the case of an initial b -quark pair, where the candidate leptons can stem either from the b - or the subsequent c -hadron decays dilute the OS/SS asymmetry strongly and limit the multijet contribution in the SMT-jet sample. The asymmetry, the normalisation as well as the various distributions are obtained in a data-driven manner, as described in Sec. 4.4.2.

Smaller background contributions arise from single and pair-produced top-quarks as well as diboson and Z +jets events. In particular events from single top-quark production contribute to the SMT-jet sample. Single-top events mimic the signal signature, if the W boson from the top-quark decay (or one of the

W bosons in the Wt -channel) decays leptonically, the b -jet is identified as candidate jet and additional objects, mainly jets, are missed in the reconstruction. Depending on the provenance of the electron and the soft-muon candidates, events contribute either to the OS or the SS sample. For example, if both lepton candidates stem from the top-quark decay, their charges are of opposite sign; if only one of the lepton candidates originates from the top-quark decay, their charges are of same sign. As the events appear to be somewhat more likely OS events, the single-top background exhibits an asymmetry.

In single- and dilepton $t\bar{t}$ events, where already the decay of one of the top quarks suffices to mimic the signal signature, several objects need to be missed in the reconstruction, and therefore the overall $t\bar{t}$ contribution is small. While the W boson and the b quark from the same top decay are of opposite sign, $t\bar{t}$ events are almost equally classified as OS and SS events. This is due to events, where the candidate leptons either stem from different top decays or the soft-muon candidate emerges from a subsequent c -hadron decay, leading to the candidate leptons having same-signed charges. All top-background samples are simulated using MC@NLO 4.01 [107] interfaced to HERWIG for parton showering, except in the case of single-top production in the t -channel, where ACERMC 3.7 [259] interfaced to PYTHIA is used.

The main contribution from diboson production arises from WV , $V = W, Z$, where $W \rightarrow e\nu$ and the other vector boson V decays hadronically, with one jet being identified as c jet and one lost. WW -candidate events likely contribute to the OS sample, while WZ and ZZ events dilute the OS/SS asymmetry. Simulated diboson events are obtained using the HERWIG program.

Background from Z +jets production has a nearly negligible contribution to the SMT-jet sample, given only differently flavoured leptons are considered here. Z +jets events are simulated with ALPGEN interfaced to HERWIG+JIMMY, just as in the case of W +jets events.

While the CTEQ6L1 [260] parton distribution function (PDF) set is used for all leading order (LO) MC generators, for the next-to-leading order (NLO) ME programs the CT10 [121] PDF set is used and CTEQ6L1 only for the interfaced PS generators.

The cross sections of inclusive W -boson, Z -boson and $t\bar{t}$ production are known with NNLO accuracy [261, 262]; the ones of the single-top and diboson production with NLO [263, 264] accuracy.

PYTHIA and HERWIG are both interfaced to the TAUOLA [265] and PHOTOS [266] programs, which model the decay of τ -leptons and the QED final-state radiation of photons, respectively.

For all simulated samples the effect of additional pp interactions in the same bunch crossing (pile-up) is modelled by overlaying minimum-bias events, generated with PYTHIA, with the hard-scatter process (cf. Sec. 1.4).

All simulated events are processed through a detailed simulation of the ATLAS detector (cf. Sec. 2.2.7), and physics objects are similarly reconstructed in both data and simulated events, as described in Sec. 3.

4.3 Object Definitions and Event Selection

In this analysis, W -boson decays into an electron and a neutrino are targeted, the presence of the neutrino is inferred by a substantial amount of missing transverse momentum ($E_{\text{T}}^{\text{miss}}$). The c -jet candidate is identified by an associated soft muon that stems from the semileptonic decay of the c hadron using the Soft Muon Tagger (SMT) described in Sec. 3.4.3. Before detailing the criteria aimed at efficiently selecting signal events and suppressing contributions from background processes mimicking the signal signature, the

physics objects involved are defined based on the reconstruction and identification strategies introduced in detail in Sec. 3. The strategy to exploit the charge asymmetry of the signal process to finally obtain a statistically very pure sample of $W+c$ events is discussed in the next section.

Only electrons built from clusters unaffected by calorimeter imperfections and within $|\eta| = 2.47$, excluding the calorimeter transition region $1.37 < |\eta| < 1.52$, are considered. Two types of electrons are used in this analysis that are referred to as *veto* and *signal electrons*. In addition to the differing requirement regarding their transverse momentum (p_T^e), they also differ regarding the criteria identifying them as prompt, i.e. not stemming from decays in flight, photon conversions or additional pp interactions, and to used to reduce the contribution of misidentified jets. While veto electrons are expected to pass the *Medium* cut-based identification requirement and $p_T^e > 20$ GeV, signal electrons need to satisfy the *Tight* operating point and have $p_T^e > 25$ GeV. The latter, furthermore, need to fulfil $E_T^{\text{cone}}(0.3) < 3$ GeV, where E_T^{cone} is the calorimeter-based isolation, and satisfy the criterion regarding the longitudinal impact parameter significance: $|\sigma_{d_0}/d_0| < 10$.

Two types of *combined* muons are exploited in the analysis: *soft muons*, used by the SMT algorithm to identify the c -jet candidate (see below), and isolated, high- p_T *veto muons*. While the selection of the former is detailed in Sec. 3.4.3, the latter need to fulfil basic track-quality criteria and to be compatible with stemming from the hard-scatter vertex, i.e. satisfy $|z_0| < 10$ mm, have $p_T^\mu > 20$ GeV and satisfy the requirement on the fixed-cone track-based isolation variable: $p_T^{\text{cone}}(0.2)/p_T < 0.1$.

Jets are reconstructed from calorimeter information using the anti- k_t algorithm with radius parameter $R = 0.4$. They are required to have $p_T > 25$ GeV and are within $|\eta| = 2.5$. In order to suppress jets originating from in-time pile-up activity, they further need to pass a requirement on the jet-vertex fraction: $JVF > 0.75$.

Among the selected jets, a c -jet candidate is identified by the presence of a soft muon within a cone of radius $\Delta R = 0.5$ around the jet axis. This is done using the SMT algorithm which has an average c -jet tagging efficiency across p_T and $|\eta|$ of about 4.4 % in simulated $t\bar{t}$ events. The b -jet tagging efficiency is about 11 % and the light-jet misidentification rate is around 0.2 % (in simulated multijet events).

The presence of neutrinos in an event can be inferred from the momentum imbalance in the transverse plane, described by the missing transverse momentum (E_T^{miss}). The analysis exploits a variant with a calorimeter-based *soft term* (CST E_T^{miss}).

As the different object reconstruction and identification algorithms exploit the same or similar detector information independently, it is not guaranteed that only a single physics object is reconstructed from it. As this applies in particular to electrons and jets, jets that are found within a cone of radius $R = 0.2$ around the signal electron direction are discarded.

Only high-quality events are considered that fulfil standard data-quality criteria, have a primary vertex compatible with a vertex from a hard-scatter event and are free of *Loose bad* jets, in order to suppress fake jets.

Events are required to have exactly one signal electron, $E_T^{\text{miss}} > 25$ GeV and a transverse mass of the W -boson candidate m_T^W , defined as

$$m_T^W = \sqrt{2p_T^e E_T^{\text{miss}} (1 - \cos \Delta\phi(\vec{E}_T^{\text{miss}}, \vec{p}_T^e))}, \quad (4.1)$$

greater 40 GeV; $\Delta\phi(\vec{E}_T^{\text{miss}}, \vec{p}_T^e)$ is the azimuthal angle between the E_T^{miss} and electron directions. As the data is collected using single-electron triggers, the electron is required to match the one that has triggered the event readout. Events with additional veto electrons or muons are discarded to suppress background from $t\bar{t}$ and Z +jets events.

Events are further required to have exactly one high-quality jet, and that this jet is identified as a c -jet candidate by the SMT algorithm. The few events, where more than one soft muon is associated with the candidate jet, are rejected; as are those, where the jet is found to be closer than $\Delta R = 0.5$ to the signal electron.

Systematic uncertainties related to the event reconstruction due to the basic detector response and its description in simulations are taken into account wherever relevant as discussed throughout the subsequent sections. The trigger, reconstruction, identification and isolation efficiencies as well as the energy scale and resolution of electrons were measured in 2011 data and are corrected accordingly in simulation; the corresponding uncertainties are propagated to the analysis. The same applies to the systematic uncertainties related to the reconstruction efficiency and the energy resolution of muons.

Uncertainties related to jets mainly arise from their energy scale (JES) and resolution (JER) determinations. The JES uncertainty ranges between 2-7 %, falling with increasing jet p_T and relatively constant versus η . Sources are the in-situ analyses (based on 2011 data), the non-closure of the η -intercalibration, pile-up effects, the flavour composition and response covering differences between quark and gluon jets, and the different responses of high- p_T jets. An additional uncertainty is considered for c jets and b jets, which is at the level of 2 %. The JER uncertainty is at the level of 15-20 % slightly varying with p_T and η .

In addition to the uncertainties on the energy scale and resolution of the leptons and jets that are propagated when calculating E_T^{miss} , extra uncertainties related to its soft term from soft jets, calorimeter cells not associated with any reconstructed object and tracks are considered.

Also the SMT mistag rate is determined in data and the corresponding uncertainty of about 15 % is taken into account.

4.4 Determination of the $W+c$ Yield

As mentioned in the introduction, the calibration described here was developed in the context of the latest $W+c$ cross-section measurement and the extraction of the signal sample described in the next sections follows very closely what was done in Ref. [1]. Minor differences in the results are due to a few refinements in the cross-section analysis that were not propagated to the c -jet tagging efficiency measurement [3, 4], because of their negligible impact.

4.4.1 Strategy

As motivated before, the final $W+c$ candidate samples is constructed as the difference between those events passing the event selection, where the charges of the decay leptons, the signal electron and the soft muon, are of opposite sign (OS) and where they are of same sign (SS): $N_{\text{data}}^{\text{OS-SS}}$, i.e. the SMT-jet sample. Although $N_{\text{data}}^{\text{OS-SS}}$ is already a good estimator for the $W+c$ yield, given that most background processes are evenly populating the OS and SS subsamples, still a small correction is needed to account for residual asymmetries:

$$N_{W+c}^{\text{OS-SS}} = N_{\text{data}}^{\text{OS-SS}} - \sum_{\text{bkg}} N_{\text{bkg}}^{\text{OS-SS}}. \quad (4.2)$$

The $W+cc$ and $W+bb$ processes are found to be OS/SS symmetric as expected and therefore neglected, i.e. $N^{\text{SS}} = N^{\text{OS}}$ and $N^{\text{OS-SS}} = 0$. While $N_{\text{bkg}}^{\text{OS-SS}}$ in the case of the other small background contributions, from top-quark, diboson and Z +jets processes, are estimated using simulations (cf. Sec. 4.2), the contributions of the two dominant W +light and multijet backgrounds are determined with data-driven methods.

The W +light and multijet estimates, detailed in the following sections, exploit the fact that the number of OS-SS events can be expressed as

$$N_{\text{bkg}}^{\text{OS-SS}} = \frac{2 \cdot A_{\text{bkg}}}{1 - A_{\text{bkg}}} \cdot N_{\text{bkg}}^{\text{SS}}, \quad (4.3)$$

i.e. in terms of the OS/SS asymmetry A_{bkg} defined as

$$A_{\text{bkg}} = \frac{N_{\text{bkg}}^{\text{OS}} - N_{\text{bkg}}^{\text{SS}}}{N_{\text{bkg}}^{\text{OS}} + N_{\text{bkg}}^{\text{SS}}}, \quad (4.4)$$

and the number of events in the SS subsample $N_{\text{bkg}}^{\text{SS}}$; with $N_{\text{bkg}}^{\text{OS}}$ being the number of events in the OS subsample. Thus, the asymmetries, A_{mj} and $A_{W+\text{light}}$, are measured individually in dedicated data regions. Initial estimates of $N_{W+\text{light}}^{\text{SS}}$ and $N_{\text{mj}}^{\text{SS}}$ are taken from simulation and are obtained in a data-driven manner in the course of the A_{mj} determination, respectively. They are refined together in a common fit to the number of SS events in the data, exploiting that the SS sample is approximately signal-free, thus providing a constraint on the total background normalisation, which is dominated by the multijet and W +light contributions.

4.4.2 Background Determination

Determination of the Multijet Asymmetry

As basically two types of multijet events pass the event selection, namely when in addition to a c -jet candidate (i) a soft electron from a semileptonic c -/ b -hadron decay or (ii) a (light) jet is mimicking the signal electron, the asymmetry of the multijet background depends on its flavour composition. Only for $c\bar{c}$ events of type (i) the lepton charges are expected to be of opposite sign; $b\bar{b}$ events, where the soft leptons might originate from the subsequent c -hadron decays, and events of type (ii) dilute the asymmetry (cf. Sec. 4.2). The flavour composition in turn depends on the respective efficiencies of the event selection for the various sources of fake candidates, in particular the identification and isolation criteria defining the signal electron. Both the modelling of the appropriate flavour composition and the response of fake signal electrons as well as simulating sufficiently large samples, given the small selection efficiencies for fake leptons, is difficult. Therefore, the asymmetry, an initial estimate of the SS normalisation as well as the shape of various kinematic distributions of the multijet background are determined with a data-driven technique that was validated previously for inclusive W -boson measurements using simulations [267].

The multijet contribution in the OS and SS subsamples is estimated from binned maximum-likelihood fits [268] of two templates to the $E_{\text{T}}^{\text{miss}}$ distribution in data. One template represents the contributions from

electroweak and top-quark processes (including the $W+c$ signal), which, containing genuine neutrinos from W and Z boson decays, exhibit substantial amounts of E_T^{miss} . The other template represents the contribution from multijet production with a rather soft spectrum, given that E_T^{miss} is due to (soft) neutrinos from semileptonic b -/ c -hadron decays and mismeasurements of the jet energy. In order to maximise the discriminating power of the E_T^{miss} distribution towards multijet production, the E_T^{miss} requirement applied in the event selection is lifted for the purpose of the fit, and the multijet yields are obtained from the adjusted templates in the signal region, i.e. for $E_T^{\text{miss}} > 25$ GeV.

While the templates describing the combined electroweak and top-quark spectra are taken from simulations, where the relative contributions of the individual processes are fixed (according to their respective cross-section predictions and selection efficiencies), the multijet templates are extracted from a dedicated data sample. This sample dominated by fake electrons is obtained by applying the event selection described in the previous section, but without the E_T^{miss} requirement and with a modified electron definition: (i) at least one of the requirements of the Tight identification criterion are asked to be failed, either the one on the number of hits in the TRT or the one identifying electrons from photon conversions, and (ii) the isolation requirement is inverted, not just to enhance the contribution of non-isolated leptons, but to also reduce the contamination from electroweak and top-quark processes, i.e. $E_T^{\text{cone}}(0.3) \geq 3$ GeV.⁴ Although the selected sample is dominated by multijet events, there are small residual contaminations from electroweak and top-quark processes of the order of 2%. They are estimated using simulations and are subtracted to obtain the multijet templates.

Since the multijet templates derived in the respective OS and SS subsamples are found to be in good agreement with each other (within the given statistical precision), the multijet template extracted from the OS+SS sample, which is less afflicted with statistical uncertainties, is used in the OS/SS fits. The OS and SS templates representing all other processes differ, however, reflecting that the E_T^{miss} distributions of the individual components and their relative contributions to the two subsamples are different, in particular for the $W+c$ signal.

The obtained fit results are shown in Fig. 4.2: the adjusted and stacked templates are in good agreement with the data both in the OS and the SS subsamples, despite the different relative multijet contributions. The multijet yields extracted from the signal region, i.e. with $E_T^{\text{miss}} > 25$ GeV, are $N_{\text{mj}}^{\text{OS}} = 1034 \pm 93$ and $N_{\text{mj}}^{\text{SS}} = 990 \pm 64$, respectively.⁵ This corresponds according to Eq. 4.4 to an asymmetry of $A_{\text{mj}} = 0.02 \pm 0.06$ consistent with zero.

In addition to the statistical uncertainties which are taken into account in the fit procedure and are propagated to the asymmetry, five sources of systematic uncertainties are considered: (i) the statistical uncertainties on the templates due to the limited samples sizes, (ii) the chosen fit range in the E_T^{miss} distribution, (iii) the choice to use the same OS+SS multijet template for the fits in the OS and SS samples, (iv) the normalisations of the non-multijet processes affecting the template shapes, and (v) the definition of the dedicated region in data from which the multijet template is extracted.

In order to evaluate (i) the templates are randomly varied within their statistical uncertainties, the

⁴The number of identification requirements asked to be failed is minimal with respect to other analyses. It is limited by the fact that the multijet template is extracted from the nominal data sample which is collected using single-electron triggers relying on most of the Tight criteria which thus should not be inverted.

⁵As a cross-check, the $N_{\text{mj}}^{\text{OS+SS}}$ and $N_{\text{mj}}^{\text{OS-SS}}$ numbers, resulting from their summation and subtraction, respectively, are compared to the results obtained from fits to the OS+SS and OS-SS samples and good agreement is found.

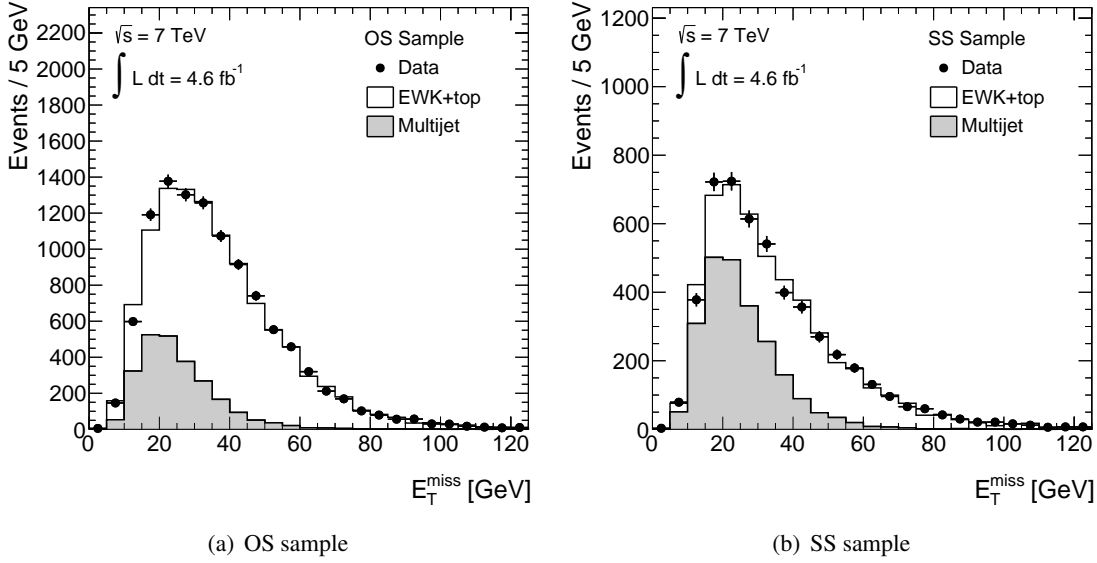


Figure 4.2: Results of the template fits to the E_T^{miss} distribution in data for the (a) OS and (b) SS subsample. The two components, representing top-quark and electroweak processes, including the $W+c$ signal, and multijet production, respectively, are normalised according to the fit results and are drawn stacked as filled histograms. The multijet contributions in the signal regions are determined from the adjusted templates for $E_T^{\text{miss}} > 25$ GeV.

OS and SS template fits are repeated, and the asymmetry computed. The distribution obtained for the asymmetry after a larger number of repetitions is fit with a Gaussian distribution and the uncertainty is determined as its width σ .

The effect of (ii) is evaluated by varying the lower and upper bounds of the nominal fit range of 10-90 GeV, the effects of (iii-v) by variation of the templates, for each variation the fit procedure is repeated, the asymmetry computed, and compared to the nominal result. The impact of (iii) is tested by using the OS and SS templates in the OS and SS fits, respectively. In order to evaluate (iv) the normalisation of each of the electroweak and top-quark processes is changed independently by $\pm 20\%$.

The shape of the multijet template depends on the composition of the dedicated region from which it is extracted: a sample dominated by electrons stemming from heavy flavour decays, which are thus accompanied by neutrinos, has on average a larger amount of E_T^{miss} than a sample that is mainly composed of electrons from photon conversions or fake electrons. In order to evaluate the effect on the template shape and the fit result, various alternative region definitions are tested by (a) changing the isolation requirement ($E_T^{\text{cone}(0.3)} \geq 1$ GeV, ≥ 5 GeV or ≥ 7 GeV) and (b) varying combinations of requiring the two before-mentioned identification criteria to pass or fail; this also includes requiring the Tight identification criterion used in the nominal event selection to be passed. Although for (b) the isolation requirement is inverted with respect to the nominal event selection, for certain variations especially when using the Tight identification requirement, there are rather large contaminations by non-multijet events. They are with 20-25% about a factor of 10 higher than for the nominal case; they are subtracted using simulations. Despite the apparently large variations in the composition of the samples used to extract the alternative multijet templates, the effect on the asymmetry is within the statistical uncertainties of the fit.

The total uncertainty on the asymmetry is chosen such that it covers all discussed variations as well as

the statistical uncertainty of the fit which is dominating. Thus, the final asymmetry estimate for the multijet background remains $A_{mj} = 0.02 \pm 0.06$.

The obtained estimate of N_{mj}^{SS} is refined as described below. For this purpose, an uncertainty of 50% is assigned to it ad hoc, covering the effect of the systematic variations and accounting for the fact that the extraction method was not specifically validated.

Determination of the W +light Asymmetry

W +light events pass the event selection if a light jet is mistagged as a c jet due to the presence of a soft-muon candidate; which is either a track mimicking a muon or a decay-in-flight muon (cf. Sec. 4.2). Thus, the W +light asymmetry is determined from a dedicated region in data, based on the assumption that every track associated with the candidate jet, that satisfies the track-quality, impact-parameter and kinematic requirements of the SMT algorithm, has the same probability to mimic the soft muon.

The dedicated sample is selected by applying the event selection described in the previous section, but replacing the requirement of a c -jet candidate by the requirement of a jet with at least one track fulfilling the SMT-track criteria: it is referred to as *pre-SMT sample*. As on average 1.5 candidate tracks are found, the lepton-charge product (and thus the asymmetry) is computed between the selected electron and *each* of the track candidates. The result is shown in Fig. 4.3(a), where the multijet estimate is obtained from a template fit to the E_T^{miss} distribution in the pre-SMT sample, following the same procedure described in the previous section, and all other contributions are taken from simulation. Although dominated by W +light production, there are substantial contributions of other processes, mainly by multijet and $W+c$ production. They are subtracted from the OS and SS yields in data, when computing the asymmetry $A_{W+light}^{\text{data,tracks}}$ according to Eq. 4.4. The resulting value is $A_{W+light}^{\text{data,tracks}} = 0.12$ (with a negligible statistical uncertainty).

The clear excess of data relative to the expectations in Fig. 4.3(a) is covered by the systematic uncertainties on the background estimates; however, they are not displayed here. In any case, $A_{W+light}^{\text{data,tracks}}$ is independent from the absolute background normalisation and only depends on the relative contributions of the various backgrounds and their different asymmetries, whose impact is evaluated and considered as a systematic uncertainty as further described below.

Accounting for residual differences with respect to W +light events with an SMT jet candidate, a simulation-based correction factor is applied to $A_{W+light}^{\text{data,tracks}}$ to obtain the final estimate of the W +light asymmetry:

$$A_{W+light} = \frac{A_{W+light}^{\text{MC}}}{A_{W+light}^{\text{MC,tracks}}} \times A_{W+light}^{\text{data,tracks}}. \quad (4.5)$$

$A_{W+light}^{\text{MC}}$ and $A_{W+light}^{\text{MC,tracks}}$ are the OS/SS asymmetries of simulated W +light events passing the nominal and the pre-SMT event selections, respectively. They are estimated to be $A_{W+light}^{\text{MC}} = 0.11 \pm 0.03$ and $A_{W+light}^{\text{MC,tracks}} = 0.1442 \pm 0.0010$. Therefore, their ratio of 0.8 ± 0.2 is compatible with unity within the statistical uncertainty due to the limited simulated sample size; which is affecting in particular the precision of $A_{W+light}^{\text{MC}}$. This result confirms the validity of the assumption underlying the derivation of $A_{W+light}^{\text{data,tracks}}$ and

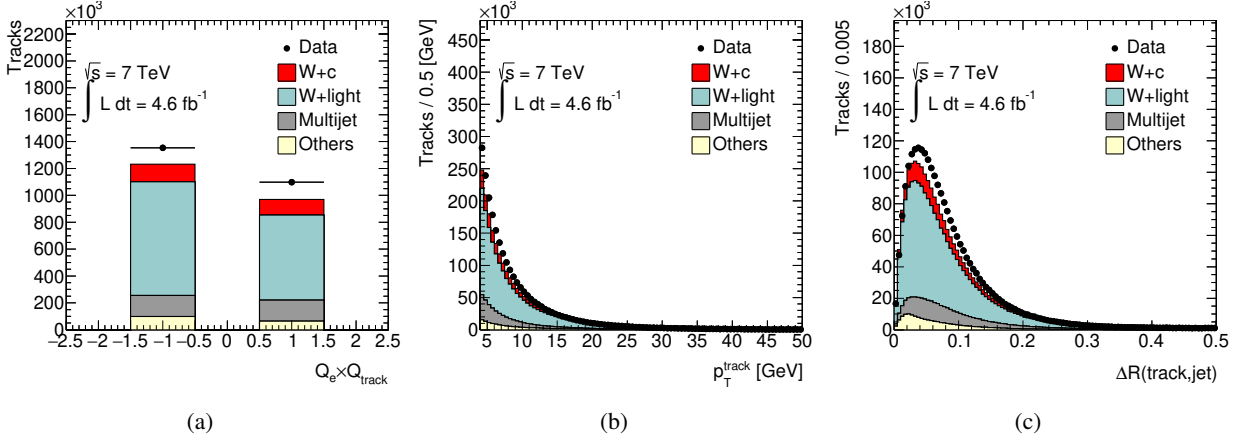


Figure 4.3: Distributions in the pre-SMT sample defined in the text: (a) the charge product between the signal electron and all candidate tracks associated with the jet candidate, (b) the p_T of all candidate tracks and (c) the ΔR between all candidate tracks and the jet candidate. The signal and the various background components are drawn stacked as coloured, filled histograms. Except for the multijet background which is obtained with the data-driven technique described in the previous section, all other processes are taken from simulation. In the case of $W+c$, the ALPGEN+PYTHIA-corrected sample is used. “Other” combines background contributions from top-quark, diboson, Z +jets as well as $W+cc/bb$ processes.

using it as an estimate for $A_{W+light}$.

A number of sources of systematic uncertainties both for $A_{W+light}^{data,tracks}$ as well as for the correction factor are considered and propagated to $A_{W+light}$. For $A_{W+light}^{data,tracks}$ systematic uncertainties arise from estimating the contributions of the various background processes, in particular their relative contributions to the OS and SS subsamples. They are assessed separately for the multijet, the $W+c$ and all remaining processes. In the case of the multijet background, both its contribution to the SS sample as well as its asymmetry are varied independently within the assigned and estimated uncertainties, respectively.

Naively, one could expect that at pre-SMT level the $W+c$ process exhibits the same asymmetry as $W+light$ given that the fraction of events with true soft muons stemming from the c -hadron decay is small. However, the found $W+c$ asymmetry differs quite significantly from $A_{W+light}^{MC,tracks}$. Attributing this to the fragmentation and hadronisation differences between c quarks and light quarks, when computing the nominal result of $A_{W+light}^{data,tracks}$, $W+c$ is treated as a background. The impact of considering it as part of the W +jets signal instead, is evaluated and taken into account as a systematic uncertainty.

An uncertainty on the contribution of the other background processes is estimated by varying their combined normalisation in the OS+SS sample by $\pm 20\%$, covering uncertainties both from cross-section predictions and detector effects, and assessing the impact on $A_{W+light}^{data,tracks}$.

As the simulation-based correction factor is introduced to correct residual differences between soft muons and tracks mimicking soft muons, deviations in simulation from said differences in data need to be assessed. Particularly relevant are differences in the kinematic distributions of candidate tracks and soft muons as well as in their association to jets. Figures 4.3(b) and 4.3(c) show the p_T distribution of candidate tracks and their angular distance (ΔR) to the candidate jet of the pre-SMT sample, respectively. Besides the previously discussed excess, the data also shows different spectra than expected from the simulations: the track p_T

tends to be softer and the ΔR to be larger. The effect of this mismodelling on the correction factor and $A_{W+\text{light}}$ is evaluated by reweighting the overall shapes of the spectra in simulations, so that they match the ones of the multijet-subtracted data. The resulting systematic uncertainty is likely somewhat overestimating the effect, since the corresponding spectra in the SMT sample are kept unchanged (and thus is $A_{W+\text{light}}^{\text{MC}}$), neglecting the correlation with the pre-SMT sample.

The final asymmetry of the $W+\text{light}$ background is computed according to Eq. 4.5: $\text{asym}_{W+\text{light}} = 0.09 \pm 0.03$. The total uncertainty is clearly dominated by the statistical uncertainty due to the limited simulated sample size entering via the correction factor. This suggests that the $W+\text{light}$ asymmetry in data is slightly lower than predicted by simulation. While the values agree within the large uncertainties, it needs to be considered that they are correlated.

Determination of the Multijet and $W+\text{light}$ Normalisations in the SS Sample

Given the signal contribution in the SS subsample is predicted to be small, at the level of 10 %, the number of data events $N_{\text{data}}^{\text{SS}}$ can be exploited to constrain the total background contribution. Thus, considering the signal contamination and the contributions by the subdominant background processes as known, the number of $W+\text{light}$ and multijet events, $N_{W+\text{light}}^{\text{SS}}$ and $N_{\text{mj}}^{\text{SS}}$, are obtained from a constrained fit to $N_{\text{data}}^{\text{SS}}$. The following χ^2 function

$$\chi^2 = \frac{(N_{\text{mj}}^{\text{SS}} - N_{\text{mj,init}}^{\text{SS}})^2}{\sigma(N_{\text{mj,init}}^{\text{SS}})} + \frac{(N_{W+\text{light}}^{\text{SS}} - N_{W+\text{light,MC}}^{\text{SS}})^2}{\sigma(N_{W+\text{light,MC}}^{\text{SS}})}, \quad (4.6)$$

is used, where $N_{\text{mj}}^{\text{SS}}$ is the only free parameter given that

$$N_{W+\text{light}}^{\text{SS}} = N_{\text{data}}^{\text{SS}} - N_{\text{mj}}^{\text{SS}} - N_{\text{other}}^{\text{SS}}, \quad (4.7)$$

with $N_{\text{other}}^{\text{SS}}$ being the combined contribution of the $W+c$ signal and the smaller background processes, which are fixed to their predictions from simulations.⁶ The initial multijet and $W+\text{light}$ estimates, $N_{\text{mj,init}}^{\text{SS}} \pm \sigma(N_{\text{mj,init}}^{\text{SS}}) = 990 \pm 495$ and $N_{W+\text{light,MC}}^{\text{SS}} \pm \sigma(N_{W+\text{light,MC}}^{\text{SS}}) = 1189 \pm 357$, are obtained from the $E_{\text{T}}^{\text{miss}}$ template fit used to derive A_{multijet} and taken from simulation, respectively. The relative uncertainty of 30 % on $N_{W+\text{light,MC}}^{\text{SS}}$ is chosen conservatively to cover both theoretical and detector-related effects (already the uncertainty of the SMT mistag rate is at the level of 15 %, cf. Sec. 4.3).

Performing the minimisation of the χ^2 function yields: $N_{\text{mj}}^{\text{SS}} = 1011 \pm 293$ and $N_{W+\text{light}}^{\text{SS}} = 1208 \pm 293$, in good agreement with the initial estimates. The associated uncertainties are significantly reduced; they have the same absolute value, and are fully anti-correlated, as a consequence of Eq. 4.7.

Estimation of the Residual Background Contributions

The OS-SS contributions of the $t\bar{t}$, single-top, diboson and $Z+\text{jets}$ processes are expected to be small, and thus are estimated using simulations. The $W+cc$ and $W+bb$ backgrounds are assumed to be perfectly OS/SS symmetric and to not contribute to the OS-SS sample.

⁶The choice that $N_{\text{mj}}^{\text{SS}}$ is the free parameter and $N_{W+\text{light}}^{\text{SS}}$ is expressed as a function of it is arbitrary, the roles could also be inverted.

Number of events $N^{\text{OS-SS}}$	
W +light	240 ± 110
Multijet	50 ± 130
$t\bar{t}$	13 ± 5
Single top	62 ± 10
Diboson	35 ± 5
Z +jets	6 ± 14
Total background	410 ± 160
$W+c$ (meas.)	3910 ± 190
Data	4320 ± 100

Table 4.1: Number of data events, measured signal and estimated background yields in the SMT-jet sample. The combined statistical and systematic uncertainties are shown; in the computation of the total background uncertainty the correlations of the uncertainties on the various components due to exploiting the constraint in the SS sample are taken into account.

While for the estimation of the W +light and multijet contributions in the SS sample, the contributions of these smaller backgrounds are regarded fixed, uncertainties on their OS-SS predictions affecting the $W+c$ yield are still considered. As the overall background contribution in the SS sample is constrained by the number of data events and every variation in the contribution of a certain process implies a corresponding change in the contributions of all other processes (see above), the impact of deviations from their expected SS normalisations and asymmetries is evaluated separately. The expected variations, $\delta_{\text{bkg}}^{\text{SS}}$ and $\delta_{\text{bkg}}^{\text{A}}$, are estimated from the uncertainties related to reconstruction effects and statistical fluctuations of the simulated sample as well as the cross-section prediction, in the case of the former; they are, nonetheless, considered to be uncorrelated.

Thus, the impact of uncertainties on the predicted SS normalisation of the various background processes on the $W+c$ yield is evaluated by (i) changing $N_{\text{bkg}}^{\text{SS}}$ of background “bkg” by $\delta_{\text{bkg}}^{\text{SS}}$, (ii) rescaling the sum of all other background contributions correspondingly such that the overall normalisation still matches the number of SS events in data, (iii) recomputing the total number of events in the OS-SS sample using the nominal asymmetries according to Eqs. 4.2 and 4.3, and (iv) deriving the difference with respect to the nominal $W+c$ yield; repeated for each of the considered background processes, the total uncertainty is derived as the squared sum of the obtained differences disregarding any correlations.

While the $W+cc$ and $W+bb$ backgrounds do not contribute to the OS-SS sample, their normalisations in the SS sample still affect the total background contribution in the OS-SS sample indirectly, given they impact the SS normalisations of the other processes. Therefore, an uncertainty on their SS normalisations is taken into account as well.

The impact of uncertainties on the predicted asymmetries is assessed analogously, where A_{bkg} is changed by $\delta_{\text{bkg}}^{\text{A}}$ and the total number of events in the OS-SS sample is recomputed using the nominal contribution in the SS sample.

Source	Uncertainty
Multijet (or W +light) background SS normalisation	1.1%
Multijet background asymmetry	3.3%
W +light background asymmetry	2.3%
Other backgrounds SS normalisations	0.3%
Other backgrounds asymmetries	0.4%
Total	4%

Table 4.2: Breakdown of the systematic uncertainty on the measured $W+c$ yield.

4.4.3 Results

Applying the event selection yields 7445 OS and 3125 SS events in data, resulting in 4320 ± 100 OS-SS events in the SMT-jet sample, dominated by $W+c$ events. The signal yield of 3910 ± 100 (stat.) ± 160 (syst.) is obtained by subtracting the total background contribution according to Eq. 4.2. In Table 4.1 the numbers are summarised together with the individual contributions of the various background processes and their systematic uncertainties. The systematic uncertainties stated for the total background as well as for the $W+c$ signal yield take the correlations between the OS and SS samples into account, between the multijet and W +light as well as the other smaller backgrounds due to the common determination of the normalisation in the SS sample. Table 4.2 shows the breakdown of the total systematic uncertainty on the measured $W+c$ yield: the estimates of the W +light and multijet asymmetries dominate; the uncertainties on the estimates of the smaller backgrounds are almost negligible.

Figure 4.4 shows a number of selected distributions in the SMT-jet sample: the p_T distributions of (a) the c -jet and (b) the soft-muon candidates, (c) the number of tracks associated with the c -jet candidate as well as (d) those tracks that are furthermore associated with a secondary vertex (SV) reconstructed with the SV1 tagging algorithm (cf. Sec. 3.4), compatible with a b - or c -hadron decay,⁷ and (e) the output weight of the MV1 tagging algorithm, for which the c -jet tagging efficiency is calibrated as described in the following sections. The signal and the various background components are drawn stacked as coloured, filled histograms: their contributions are normalised to the yields presented in Table 4.1. Except the shapes of the multijet background, which are obtained from the dedicated data sample used to extract the E_T^{miss} fit templates for the asymmetry determination, all distributions are taken from simulation; in the case of the $W+c$ signal, the PYTHIA-corrected sample is used. The predictions are in reasonable agreement with the data.

4.5 Measurement of the c -Jet Tagging Efficiency of SMT c Jets

4.5.1 Strategy

The SMT-jet sample that has a statistically high c -jet purity of approximately 90%, is used to perform a measurement of the c -jet tagging efficiency of the MV1 tagging algorithm. Figure 4.4(e) shows the output weight of the MV1 tagging algorithm: the $W+c$ signal contribution is normalised to the measured yield

⁷ $N_{\text{trk}}^{\text{SV}} = 0$ corresponds to events, where no SV is reconstructed, including events with 1-track vertices which can only be exploited with the JetFitter algorithm.

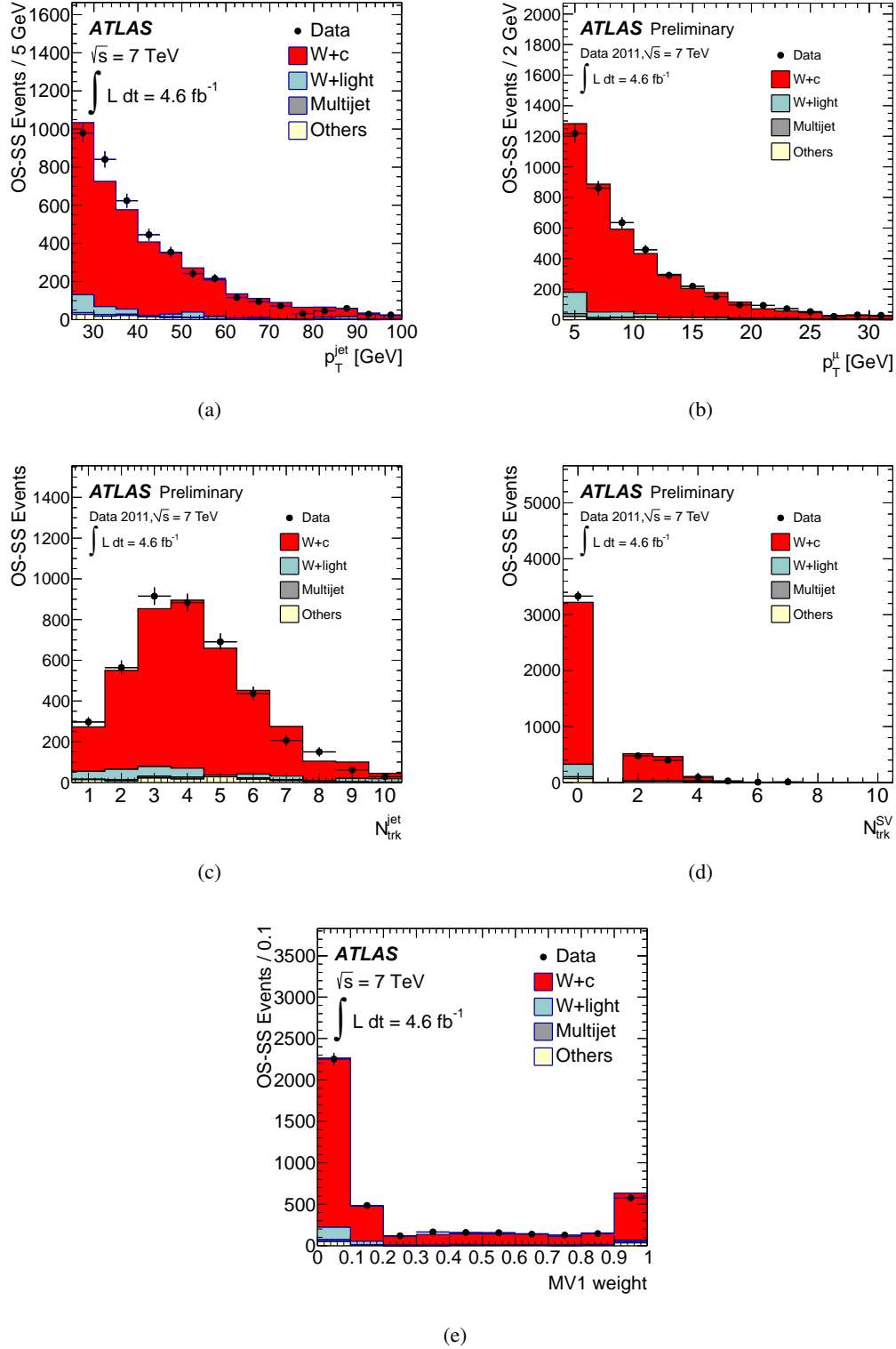


Figure 4.4: Distributions in the SMT-jet sample: the p_T distributions of (a) the c -jet and (b) the soft-muon candidates, (c) the number of tracks associated with the c -jet candidate as well as (d) those tracks that are furthermore associated with a secondary vertex (SV) reconstructed with the SV1 tagging algorithm (cf. Sec. 3.4), where events with zero tracks correspond to the case of no SV being reconstructed, and (e) the output of the MV1 tagging algorithm. The signal and the various background components are drawn stacked as coloured, filled histograms: their contributions are normalised to the yields presented in Table 4.1. Except the shapes of the multijet background which are obtained from the dedicated data sample used to extract the E_T^{miss} fit templates for the asymmetry determination, the distributions are taken from simulation; in the case of the signal using the PYTHIA-corrected sample. “Other” represents the background contributions from top-quark, diboson and Z+jets processes. Previously published in Refs. [3] and [4], respectively.

(cf. Table 4.1) while its shape is extracted from the PYTHIA-corrected sample. The MV1 algorithm is designed such that real b jets tend to have high output-weight values close to one and light jets low values close to zero, as illustrated in Fig. 3.7(a). The MV1 operating points that are calibrated are listed in Table 3.1(a). They correspond to cuts on the MV1 weight distribution at approximate values of 0.07, 0.40, 0.60 and 0.91, yielding b -jet tagging efficiencies of 85 %, 75 %, 70 % and 60 % in simulated $t\bar{t}$ events, respectively.⁸ The most commonly exploited operating point in physics analyses in Run 1, is the 70 % operating point with a c -jet tagging efficiency of about 20 % and a light jet mistag rate of about 0.7 %, in simulated $t\bar{t}$ events. It is used for demonstrative purposes in the following.

The c -jet tagging efficiency of SMT c -jets for a certain operating point in data, $\varepsilon_{c(\mu)}^{\text{data}}$, is derived as the fraction of $W+c$ events⁹ that pass the corresponding b -tagging requirement, i.e.

$$\varepsilon_{c(\mu)}^{\text{data}} = \frac{N_{W+c}^{b\text{-tag}}}{N_{W+c}}. \quad (4.8)$$

N_{W+c} is the $W+c$ yield before applying b -tagging, i.e. at *pretag* level, corrected for the estimated contribution of $W+c$ events, where the c -jet candidate is not a c jet, $N_{W+c,\text{non-}c}^{\text{OS-SS}}$. Expressing $N_{W+c,\text{non-}c}^{\text{OS-SS}}$ in terms of the expected fraction of such events in the pretag sample, f_{W+c}^{light} , N_{W+c} can be computed as

$$N_{W+c} = N_{W+c}^{\text{OS-SS}} - N_{W+c,\text{non-}c}^{\text{OS-SS}} = \left(1 - f_{W+c}^{\text{light}}\right) \cdot N_{W+c}^{\text{OS-SS}}, \quad (4.9)$$

from the $W+c$ yield measured in the OS-SS sample. $N_{W+c}^{b\text{-tag}}$ is the subset of N_{W+c} events that pass the b -tagging requirement:

$$N_{W+c}^{b\text{-tag}} = N_{W+c}^{\text{OS-SS},b\text{-tag}} - N_{W+c,\text{non-}c}^{\text{OS-SS},b\text{-tag}}, \quad (4.10)$$

$$= N_{\text{data}}^{\text{OS-SS},b\text{-tag}} - \sum_{\text{bkg}} \varepsilon_{\text{bkg}} \cdot N_{\text{bkg}}^{\text{OS-SS}} - \varepsilon_{W+c,\text{light}} \cdot f_{W+c}^{\text{light}} \cdot N_{W+c}^{\text{OS-SS}}. \quad (4.11)$$

It is derived from the number of b -tagged events in the SMT-jet sample in data, $N_{\text{data}}^{\text{OS-SS},b\text{-tag}}$, by (i) subtracting all expected background contributions, expressed as the product of the individual tagging rate, ε_{bkg} , and the normalisation in the pretag SMT-jet sample, $N_{\text{bkg}}^{\text{OS-SS}}$ (cf. Table 4.1), and (ii) correcting for the expected contribution of $W+c$ events, where the b -tagged c -jet candidate is not a c jet, formulated as the estimated mistag rate of such events, $\varepsilon_{W+c,\text{light}}$, times their contribution in the pretag sample.

Expressing the various terms in this way, i.e. by separating the tagging rate determinations and the pretag-normalisation estimates, simplifies the propagation of the results and uncertainties derived in the previous section and to take the correlations between the pretag samples and the tagged subsamples into account. This is particularly relevant for the W +light and multijet contributions that are estimated in a data-driven way.

In summary, in order to calculate $\varepsilon_{c(\mu)}^{\text{data}}$, besides $N_{\text{data}}^{\text{OS-SS},b\text{-tag}}$, estimates of f_{W+c}^{light} , $\varepsilon_{W+c,\text{light}}$, and ε_{bkg} , for each of the considered background processes, need to be determined. As described in more detail in the

⁸The exact values are 0.0714225, 0.404219, 0.601713, 0.905363 defined by the 85 %, 75 %, 70 % and 60 % efficiencies in simulated $t\bar{t}$ events, respectively.

⁹Given that only events with one jet are considered, the number of $W+c$ events and the number of c jets agree.

following sections, ε_{mj} is obtained with the same data-driven method used for the asymmetry estimate (cf. Sec. 4.4.2), while f_{W+c}^{light} and the various (mis)tagging rates are derived using simulations.

4.5.2 Determination of the Tagging Rates of the Backgrounds

The tagging rate of a certain background is defined as the fraction of background events in the SMT-jet sample that pass the applied b -tagging requirement

$$\varepsilon_{\text{bkg}} = \frac{N_{\text{bkg}}^{\text{OS-SS},b\text{-tag}}}{N_{\text{bkg}}^{\text{OS-SS}}} = \frac{N_{\text{bkg}}^{\text{OS},b\text{-tag}} - N_{\text{bkg}}^{\text{SS},b\text{-tag}}}{N_{\text{bkg}}^{\text{OS}} - N_{\text{bkg}}^{\text{SS}}}, \quad (4.12)$$

which depends on the individual flavour composition given the differing tagging efficiencies for b jets, c jets and light jets.¹⁰ Since both the numerator and denominator is computed as the difference of (b -tagged) events in the OS and SS subsamples, ε_{bkg} is not an efficiency in the sense that the sample of OS-SS b -tagged events is not a subsample of the pretag OS-SS sample. Therefore, ε_{bkg} is referred to as *tagging rate*.

Determination of the multijet tagging rate

The multijet tagging rate ε_{mj} , or more precisely $N_{mj}^{\text{OS/SS}}$ and $N_{mj}^{\text{OS/SS},b\text{-tag}}$, are determined using the same data-driven technique as used for the asymmetry estimate. They are obtained from template fits to the E_T^{miss} distribution in data at pretag level and after applying the different b -tagging requirements, respectively.

The extracted number of multijet events in the OS and SS subsamples are found to be in good agreement both at pretag level and after applying b -tagging, considering the statistical uncertainties of the fit; and so are the respective tagging rates. Therefore, the final multijet tagging rates are derived from fits to the OS+SS samples in order to minimise the statistical uncertainties, i.e. $\varepsilon_{mj} = N_{mj}^{\text{OS+SS},b\text{-tag}} / N_{mj}^{\text{OS+SS}}$. In Figure 4.5 the fit results obtained (a) at pretag level and (b) after applying the criterion for the 70% operating point are shown. The adjusted, stacked templates are in good agreement with the data.

In addition to the statistical uncertainties, three sources for systematic uncertainties related to the fit procedure are considered that were also discussed in the context of the asymmetry estimate, namely: (i) the chosen fit range in the E_T^{miss} distribution, (ii) the normalisations of the non-multijet processes affecting the template shape, and (iii) the definition of the dedicated region from which the multijet template is extracted; the statistical uncertainties on the templates due to the limited (simulated) sample sizes are neglected. The effects of the different sources are evaluated as before (cf. Sec. 4.4.2): the tagging rates are computed for each variation and compared to the nominal result. The total uncertainties are chosen to cover all discussed variations as well as the statistical uncertainties from the fits which is dominating again.

In order to increase the confidence in the results, one additional consistency check is done. Template fits are performed in the subsamples of events that *fail* the considered b -tagging criteria, the extracted number of multijet events, $N_{mj}^{\text{OS+SS},\text{non-}b\text{-tag}}$, is added to the number determined in the b -tagged subsample, $N_{mj}^{\text{OS+SS},b\text{-tag}}$, and compared to the results found in the pretag sample $N_{mj}^{\text{OS+SS}}$. For all operating points ex-

¹⁰That is: $N_{\text{bkg}}^{\text{OS-SS},b\text{-tag}} = \varepsilon_{\text{bkg}} \cdot N_{\text{bkg}}^{\text{OS-SS}} = \sum_{x=b,c,\text{light}} \varepsilon_x \cdot N_{\text{bkg}}^{\text{OS-SS},x}$, where $\varepsilon_{b/c/\text{light}}$ is the b -tagging and c -jet tagging efficiencies and mistag rate, and $N_{\text{bkg}}^{\text{OS-SS},b/c/\text{light}}$ the subset of events, where the c -jet candidate is a b jet, c jet and light jet.

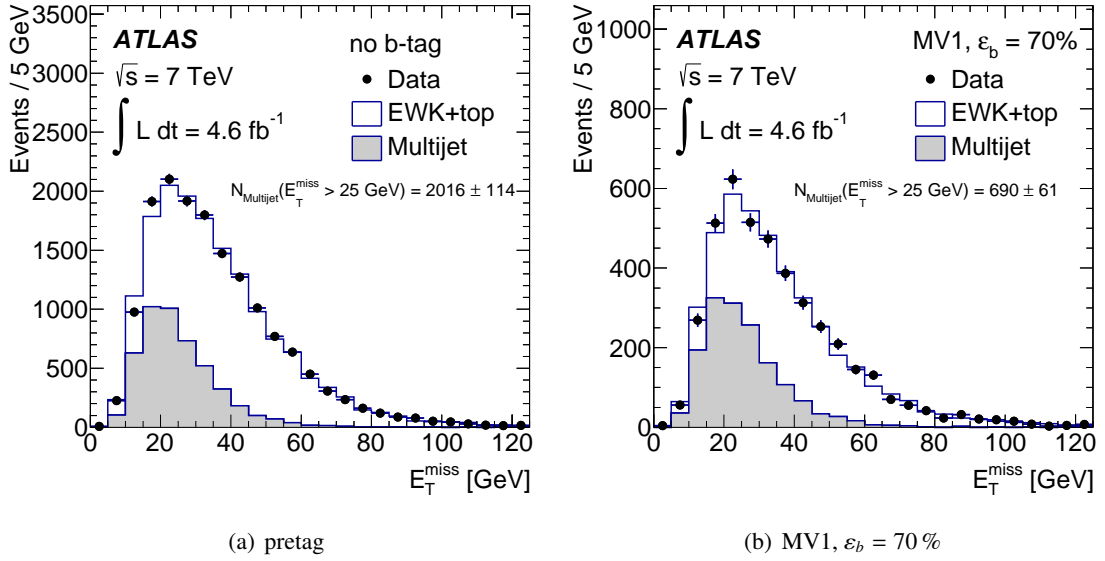


Figure 4.5: Results of the template fits to the E_T^{miss} distributions in the OS+SS data samples (a) at pretag level and (b) after requiring the MV1 criterion corresponding to $\varepsilon_b = 70\%$ to be passed. The two components representing electroweak and top-quark processes, including the $W+c$ signal, and multijet production, respectively, are normalised according to the fit results and are drawn stacked as filled histograms. The multijet contributions are determined from the adjusted templates for $E_T^{\text{miss}} > 25$ GeV. Previously published in Ref. [4].

cellent agreement is found.

The multijet tagging rates, together with their total uncertainties, are summarised for the different operating points in Table 4.3. They range from 26% to 55% depending on the operating point. These results indicate that the pretag multijet sample has a significant heavy flavour component, as suspected. For example, the multijet tagging rate for the 70% operating is 34%, which is significantly higher than the average c -jet tagging efficiency in simulated $t\bar{t}$ events of about $\sim 20\%$.

Determination of the tagging rates of the electroweak and top-quark backgrounds

The tagging rates of the electroweak and top-quark backgrounds are obtained according to Eq. 4.12 using simulation. Besides statistical uncertainties due to the limited simulated sample sizes, systematic uncertainties related to reconstruction effects are considered. In addition to the ones detailed in Sec. 4.3, which are treated coherently in the pretag sample and after applying b -tagging, for the latter also uncertainties related to the calibrations of the b -tagging and c -jet tagging efficiencies as well as the light-jet mistag rates, discussed in Sec. 3.4, are considered. For the 70% operating point of the MV1 algorithm these are at the level of 2-4%, 13-22% and 13-30%, respectively, depending on the jet p_T . Given the limited sizes of the simulated OS and SS subsamples all systematic variations are afflicted with large statistical fluctuations. Therefore, in order to derive reliable estimates, the impact of certain, dominant systematic uncertainties on the tagging rates is evaluated on the OS+SS sample, e.g. the uncertainties on the jet energy scale and resolution. The total uncertainties are computed as the squared sum of the individual contributions and range for the 70% operating point from 6-26% depending on the background component.

Background tagging rates				
Background	Operating point of the MV1 tagging algorithm			
	85 %	75 %	70 %	60 %
multijet	0.55 ± 0.08 (tot.)	0.41 ± 0.08 (tot.)	0.34 ± 0.06 (tot.)	0.26 ± 0.06 (tot.)
W +light	$0.40 \pm 0.12 \pm 0.05$	$0.19 \pm 0.09 \pm 0.03$	$0.14 \pm 0.08 \pm 0.03$	$0.09 \pm 0.04 \pm 0.02$
$t\bar{t}$	$0.60 \pm 0.10 \pm 0.04$	$0.41 \pm 0.13 \pm 0.04$	$0.34 \pm 0.14 \pm 0.03$	$0.25 \pm 0.14 \pm 0.04$
single top	$0.74 \pm 0.02 \pm 0.03$	$0.61 \pm 0.03 \pm 0.04$	$0.55 \pm 0.03 \pm 0.04$	$0.43 \pm 0.03 \pm 0.04$
diboson	$0.37 \pm 0.02 \pm 0.05$	$0.18 \pm 0.02 \pm 0.03$	$0.12 \pm 0.02 \pm 0.03$	$0.05 \pm 0.02 \pm 0.02$
Z +jets	$0.75 \pm 0.86 \pm 0.08$	$1.19 \pm 1.49 \pm 0.17$	$0.53 \pm 0.74 \pm 0.14$	$-0.18 \pm 0.56 \pm 0.04$

Table 4.3: Background tagging rates for the MV1 tagging algorithm. For the multijet background they are extracted with a data-driven technique described in the text; for all other backgrounds they are obtained from simulations. While for the former the total uncertainty is given, for the latter the statistical and the systematic uncertainties due to reconstruction effects are given separately, in order of appearance.

The tagging rates of the various backgrounds with their statistical and systematic uncertainties are summarised in Table 4.3. As a consequence of their definition according to Eq. 4.12, the tagging rates take also values both below zero and larger than one, and may have relative uncertainties larger than 100 % (other than efficiencies).

The high tagging rates of the top backgrounds reflect that their c -jet candidates in the pretag sample are in fact to a significant extend b jets, as expected. However, the W +light tagging rates ranging between 9-40 % are (significantly) higher than naively expected; even considering the large relative total uncertainties of the order of 50 %. Similar results are also found in the OS and SS subsamples which are determined with better precision. For a sample of pure light jets, the average tagging efficiencies of the MV1 algorithm range between 0.1 % and 10 % in simulated $t\bar{t}$ events (cf. Table 3.1(a)). Therefore, it appears the mistag rate of the MV1 tagging algorithm is biased towards higher values for SMT-tagged light jets.

4.5.3 Estimation of the Light-Jet Contamination in $W+c$ Candidate Events

Investigating the flavour composition of simulated $W+c$ events in the SMT-jet sample, confirms that the overwhelming fraction of the c -jet candidates are indeed c jets and only a tiny fraction of $f_{W+c}^{\text{light}} = 0.012 \pm 0.003$ (stat.) \pm 0.002 (syst.) are mistagged light jets.¹¹ The quoted statistical uncertainty arises from the limited number of simulated signal events, the systematic uncertainty is due to reconstruction effects and clearly driven by the uncertainty on the SMT mistag rate (cf. Sec. 4.3).

Applying (additional) b -tagging requirements reduces the already small contribution of non- c jets further. The remaining fraction in the tagged subsample depends on the mistag rate of the MV1 algorithm for light jets in this specific environment. Given the limited simulated sample size, computing $\varepsilon_{W+c,\text{light}}$ according to Eq. 4.12, where “bkg” is the non- c jet contribution of the $W+c$ sample, in the OS-SS sample leads to large statistical uncertainties. Therefore, it is derived from the OS+SS sample based on the assumption that the mistag rate is not charge dependent, and thus does not differ for the OS and SS subsamples; and indeed, the results obtained in the OS-SS and OS+SS samples are in good agreement.

¹¹Jets are labelled as c jets or other according to the labelling scheme introduced in Sec. 3.4.1.

Mistag rate of non- c jets in $W+c$ events			
Operating point of the MV1 tagging algorithm			
85 %	75 %	70 %	60 %
$0.16 \pm 0.03 \pm 0.04$	$0.031 \pm 0.013 \pm 0.011$	$0.027 \pm 0.012 \pm 0.008$	$0.006 \pm 0.006 \pm 0.004$

Table 4.4: Mistag rate of non- c jets in $W+c$ events for the MV1 tagging algorithm. The first uncertainty is the statistical uncertainty due to the limited simulated sample size, the second is the systematic uncertainty due to reconstruction effects.

The results for $\varepsilon_{W+c,\text{light}}$ extracted with the OS+SS sample for the different operating points of the MV1 tagging algorithm are listed in Table 4.4. Two sources of uncertainties are distinguished: the statistical uncertainties due to the limited simulated sample size and the systematic uncertainties due to reconstruction effects; the former generally dominates. The latter is driven by the uncertainties on the mistag rate of the MV1 algorithm and the jet energy scale and resolution.

While the obtained $\varepsilon_{W+c,\text{light}}$ values are compatible with the average mistag rate of the MV1 algorithm, ranging between 0.1-10 %, within the large relative total uncertainties of $\sim 30 - 100$ %, they are systematically larger. This is consistent with the findings of the previous section, supporting the conclusion that the mistag rate of SMT-tagged light jets is biased towards higher values.

4.5.4 Results

The c -jet tagging efficiencies of SMT c -jets in data, $\varepsilon_{c(\mu)}^{\text{data}}$, for the various operating points of the MV1 tagging algorithm are derived according to Eqs. 4.8-4.11. The $W+c$ yield at pretag level is $N_{W+c} = 3910 \pm 100$ (stat.) ± 160 (syst.) (cf. Sec. 4.4.3). For each operating point, $N_{W+c}^{b\text{-tag}}$ is computed from the number of data events in the SMT-jet sample passing the corresponding b -tagging criteria

$$85 \% : 2151 \pm 71, \quad 75 \% : 1292 \pm 58, \quad 70 \% : 983 \pm 52, \quad 60 \% : 563 \pm 43;$$

and the results of the previous section: the ε_{bkg} and $\varepsilon_{W+c,\text{light}}$ values summarised in Tables 4.3 and 4.4, respectively, and $f_{W+c}^{\text{light}} = 0.012 \pm 0.003$ (stat.) ± 0.002 (syst.).

The resulting c -jet tagging efficiencies are shown in Fig. 4.6(a) as function of the operating point and are also listed in Table 4.5. $\varepsilon_{c(\mu)}^{\text{data}}$ decreases from 50 % to 13 % with increasing tightness of the operating point, corresponding to increasing c rejection; the relative total uncertainties on the contrary increase from 3 % to 10 %. Since the statistical uncertainties are of the same order as the total systematic uncertainties, no attempt was made to provide the results in bins of jet p_T (and $|\eta|$).

The breakdown of the systematic uncertainties can be found in Table 4.6. Two sources are dominating the total uncertainty: (i) the yield estimates of the W +light and multijet backgrounds in the SMT-jet sample at pretag level (cf. Table 4.2), and (ii) the tagging-rate estimate of the dominant W +light background (cf. Table 4.3).

The results are compared to the expected c -jet tagging efficiency, $\varepsilon_{c(\mu)}^{\text{sim}}$, defined as the fraction of SMT c -jets in $W+c$ events simulated using PYTHIA-default that pass the MV1 b -tagging requirements, both in

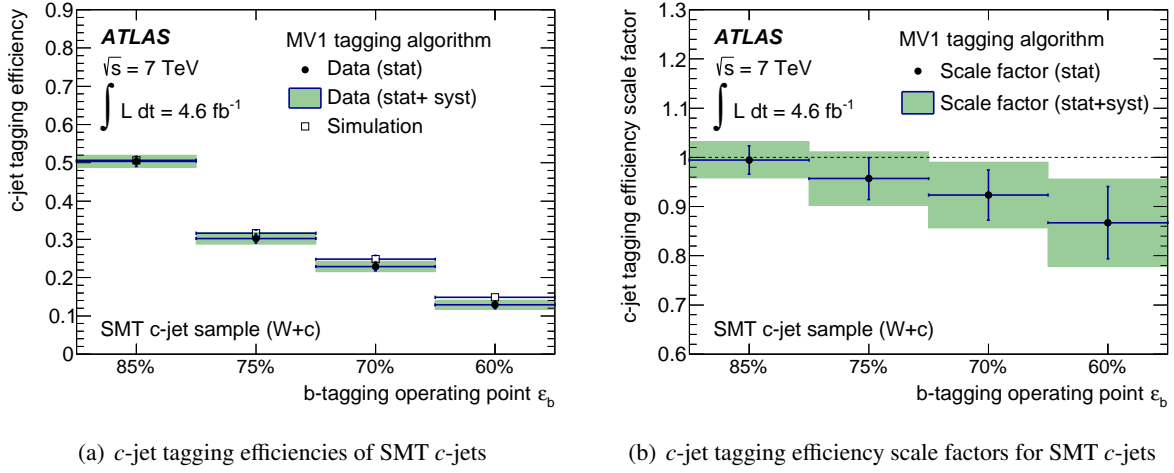


Figure 4.6: (a) Comparison between c -jet tagging efficiencies of SMT c -jets derived using a sample of $W+c$ events selected in data and simulated with PYTHIA-default and (b) data-to-simulation c -jet tagging efficiency scale factors for SMT c -jets for several operating points of the MV1 tagging algorithm. Previously published in Ref. [4].

Efficiencies and data-to-simulation scale factors for SMT c -jets				
Operating points of the MV1 tagging algorithm				
	85 %	75 %	70 %	60 %
$\epsilon_{c(\mu)}^{\text{data}}$	$0.504 \pm 0.013 \pm 0.009$	$0.302 \pm 0.012 \pm 0.009$	$0.229 \pm 0.012 \pm 0.007$	$0.129 \pm 0.010 \pm 0.006$
$\epsilon_{c(\mu)}^{\text{sim}}$	$0.507 \pm 0.006 \pm 0.007$	$0.316 \pm 0.006 \pm 0.006$	$0.248 \pm 0.005 \pm 0.008$	$0.148 \pm 0.004 \pm 0.005$
$\kappa_{c(\mu)}$	$0.99 \pm 0.03 \pm 0.03$	$0.96 \pm 0.04 \pm 0.04$	$0.92 \pm 0.05 \pm 0.05$	$0.87 \pm 0.07 \pm 0.06$

Table 4.5: Measured and expected c -jet tagging efficiencies of SMT c -jets derived using a sample of $W+c$ events selected in data and simulated with PYTHIA-default, $\epsilon_{c(\mu)}^{\text{data}}$ and $\epsilon_{c(\mu)}^{\text{sim}}$, respectively, as well as data-to-simulation c -jet tagging efficiency scale factors for SMT c -jets, $\kappa_{c(\mu)}$, for several operating points of the MV1 tagging algorithm. The first uncertainty is the statistical uncertainty (in the case of $\epsilon_{c(\mu)}^{\text{sim}}$ due to the limited simulated sample size), the second is the systematic uncertainty.

Fig. 4.6(a) and in Table 4.5.¹² Two sources of uncertainties on $\epsilon_{c(\mu)}^{\text{sim}}$ are considered: statistical uncertainties due to the limited simulated sample size and systematic uncertainties due to reconstruction effects. Their contributions are of the same order, as can be seen from the summary in Table 4.5; they are shown combined as total uncertainty in Fig. 4.6(a). The breakdown in Table 4.7 reveals that the uncertainties on the jet energy scale and resolution are dominating the systematic uncertainties.

The level of agreement between the measured and expected c -jet tagging efficiencies can be easily assessed from their ratio, $\kappa_{c(\mu)} = \epsilon_{c(\mu)}^{\text{data}} / \epsilon_{c(\mu)}^{\text{sim}}$, the data-to-simulation scale factors for SMT c -jets. They are shown for the different MV1 operating points in Fig. 4.6(b) and are also listed in Table 4.5. The quoted systematic uncertainties are of the same order as the statistical uncertainties; they combine the systematic uncertainties on $\epsilon_{c(\mu)}^{\text{data}}$, related to the background determinations, as well as the total uncertainty on $\epsilon_{c(\mu)}^{\text{sim}}$, due to the limited simulated sample size and reconstruction effects. The scale factors range from 0.87 to 0.99 with relative total uncertainties between 4-10 %; both the deviation from unity as well as the corresponding

¹²SMT c -jets are those c -jet candidates in the OS-SS sample labelled as c jet (cf. Sec. 3.4.1).

Breakdown of uncertainties on $\varepsilon_{c(\mu)}^{\text{data}}$ [%]				
Source	Operating points of the MV1 tagging algorithm			
	85 %	75 %	70 %	60 %
Background pretag yields	0.7	2.1	2.2	3.9
Background tagging rates	1.6	1.9	2.2	2.4
\leftrightarrow W +light	1.6	1.9	2.2	2.3
\leftrightarrow Multijet	0.2	0.4	0.4	0.6
Light-jet contamination	0.3	0.4	0.4	0.4
Simulated sample size	0.4	0.6	0.6	0.9
Total systematic uncertainty	1.8	2.9	3.2	4.7
Statistical uncertainty	2.2	3.5	4.9	8.0
Total uncertainty	2.8	4.5	5.8	9.3

Table 4.6: Breakdown of the contributions of groups of systematic uncertainties on the c -jet tagging efficiency of SMT c -jets measured in a $W+c$ sample given in percent. Details regarding the systematic uncertainties related to the background normalisation at pretag level can be found in Sec. 4.4.

Breakdown of uncertainties on $\varepsilon_{c(\mu)}^{\text{sim}}$ [%]				
Source	Operating points of the MV1 tagging algorithm			
	85 %	75 %	70 %	60 %
W boson reconstruction	0.5	0.4	0.5	1.0
\leftrightarrow Electron scale	0.2	0.2	0.4	0.5
\leftrightarrow $E_{\text{T}}^{\text{miss}}$ soft term	0.4	0.3	0.2	0.7
Jet energy scale	1.1	1.7	2.4	2.6
Jet energy resolution	0.6	1.1	2.3	1.9
Soft-muon tagging	< 0.1	< 0.1	< 0.1	< 0.1
Event reconstruction	1.4	2.1	3.4	3.4
Simulated sample size	1.2	1.9	2.0	2.7
Total uncertainty	1.8	2.8	3.9	4.3

Table 4.7: Breakdown of the contributions of groups of systematic uncertainties on the c -jet tagging efficiency of SMT c -jets determined in a $W+c$ sample simulated with ALPGEN+PYTHIA-default given in percent. Details regarding the systematic uncertainties related to the event reconstruction can be found in Sec. 4.3.

uncertainty increase systematically with the tightness of the operating point. While for the looser operating points $\kappa_{c(\mu)}$ is compatible with unity (within the uncertainties), this is not the case for the tighter ones. Thus, the PYTHIA-default simulation overestimates the c -jet tagging efficiency of SMT c -jets for operating points of the MV1 tagging algorithm with high(er) c -jet rejection.

This mismodelling in the simulation could be corrected in other analyses by applying the derived data-to-simulation scale factors to SMT c -jets. However, in order to obtain scale factors that are applicable to inclusive, unbiased samples of c jets, $\kappa_{c(\mu)}$ needs to be extrapolated as described in the following section.

4.6 Calibration of the c -Jet Tagging Efficiency for inclusive c -jet Samples

4.6.1 The Extrapolation Procedure

Due to several differences between samples of SMT c -jets and inclusive, unbiased samples of c jets that are elaborated below, the c -jet tagging efficiency scale factors measured on the former are not directly applicable to the latter. However, scale factors appropriate to correct the c -jet tagging efficiency of inclusive samples of c jets are obtained by means of an simulation-based and data-supported extrapolation of the results, discussed in the following.

There are in particular two main differences between an SMT c -jet sample and an inclusive c -jets sample that are introduced by selecting c jets via semimuonic decays of the associated c hadrons: (i) the sample admixture regarding the different c -hadron types, due to their differing semileptonic branching fractions, and (ii) the track multiplicity of the c jets, due to requiring at least one well reconstructed track (stemming from the soft muon). The sample composition is relevant, because the various c -hadron types differ, besides in the semileptonic branching fraction, also regarding other properties that impact the b -tagging performance. In particular, their different lifetimes (which are correlated with the semileptonic branching fractions), but also differences regarding the charged decay multiplicity cause the average c -jet tagging efficiency of c jets to differ depending on the type of the associated c -hadron. For example, for the 70 % operating point of the MV1 algorithm, the c -jet tagging efficiencies of jets associated with the four most prominent weakly decaying c hadrons in an inclusive $W+c$ sample, simulated with PYTHIA-default, are

$$D^0 : 0.174 \pm 0.001, \quad D^+ : 0.305 \pm 0.002, \quad D_s : 0.167 \pm 0.003, \quad \Lambda_c^+ : 0.041 \pm 0.002,$$

where the quoted uncertainties are due to the limited simulated sample size.¹³ Thus, jets associated with a D^+ meson have on average an almost factor of two higher c -jet tagging efficiency than jets associated with D^0 or D_s mesons; the c -jet tagging efficiency of jets associated with Λ_c^+ baryons is particularly small.

The average c -jet tagging efficiency of an inclusive sample of c jets for a certain operating point, ε_c , can be expressed as the c -jet tagging efficiency of an SMT c -jet sample, $\varepsilon_{c(\mu)}$, times an extrapolation factor α

$$\varepsilon_c = \alpha \cdot \varepsilon_{c(\mu)}. \quad (4.13)$$

¹³In the remainder of this chapter the introduced notation is used to also refer to the charge-conjugated states, i.e. \bar{D}^0 , D^- , \bar{D}_s , L_c^+ etc.

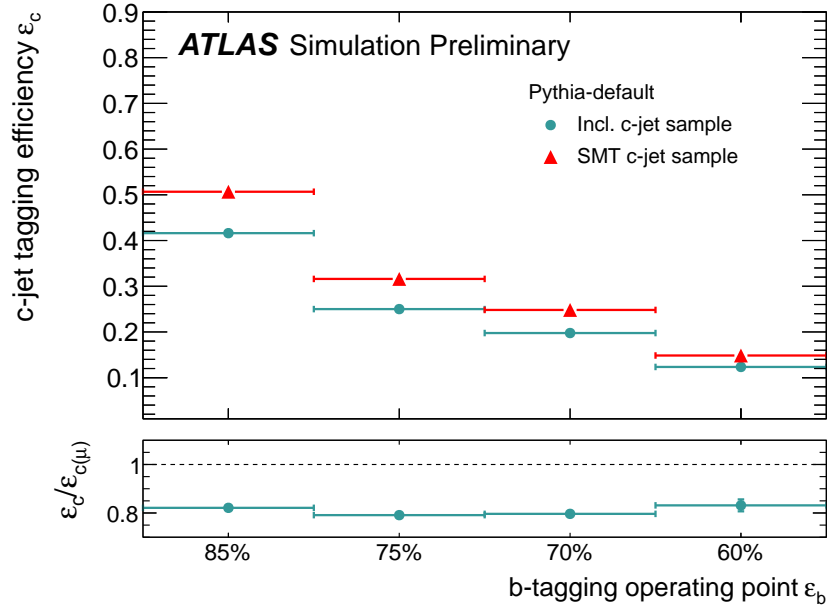


Figure 4.7: Comparison between the c -jet tagging efficiency of c -jets in an SMT c -jet sample and an inclusive sample, simulated using ALPGEN +PYTHIA-default. Their ratio $\varepsilon_c^{\text{sim}}/\varepsilon_{c(\mu)}^{\text{sim}}$ defines the efficiency-extrapolation factor α_{sim} . Only statistical uncertainties due to the limited simulated sample size are considered. Previously published in Ref. [3].

Figure 4.7 shows a comparison of the expected efficiencies, $\varepsilon_c^{\text{sim}}$ and $\varepsilon_{c(\mu)}^{\text{sim}}$, in $W+c$ events simulated with PYTHIA-default for several operating points of the MV1 tagging algorithm.¹⁴ $\varepsilon_c^{\text{sim}}$ is systematically about 20 % lower than $\varepsilon_{c(\mu)}^{\text{sim}}$, resulting in a correction factor α_{sim} below unity across all operating points, as can be seen from their ratio in the bottom pad.

If the extrapolation factor for data, α_{data} , deviates from α_{sim} , which is the case if the simulation does not describe the differences between the inclusive and the SMT c -jet sample correctly, the scale factors $\kappa_{c(\mu)}$, derived for the latter, are not able to correct the c -jet tagging efficiencies of the former so that they match the ones in data. Scale factors κ_c appropriate for inclusive samples of c jets are instead obtained from $\kappa_{c(\mu)}$ by extrapolation

$$\kappa_c = \frac{\varepsilon_c^{\text{data}}}{\varepsilon_c^{\text{sim}}} \stackrel{\text{Eq. 4.13}}{=} \frac{\alpha_{\text{data}} \cdot \varepsilon_{c(\mu)}^{\text{data}}}{\alpha_{\text{sim}} \cdot \varepsilon_{c(\mu)}^{\text{sim}}} = \frac{\alpha_{\text{data}}}{\alpha_{\text{sim}}} \cdot \kappa_{c(\mu)} = \delta \cdot \kappa_{c(\mu)}, \quad (4.14)$$

i.e. by applying extrapolation factors δ , with $\delta \neq 1$. Defined as the ratio of the efficiency-extrapolation factors in data and simulation, α_{data} and α_{sim} , respectively, δ is approximated as

$$\delta \approx \frac{\alpha_{\text{sim}}^{\text{corr}}}{\alpha_{\text{sim}}}, \quad (4.15)$$

where α_{data} is estimated from $\alpha_{\text{sim}}^{\text{corr}}$. $\alpha_{\text{sim}}^{\text{corr}}$ is determined using the PYTHIA-corrected sample, where several c -quark fragmentation and c -hadron decay properties are corrected to best knowledge, as explained in detail in the next section.

¹⁴ $\varepsilon_c^{\text{sim}}$ is computed using c jets from a sample of $W+c$ events selected according to the event selection described in Sec. 4.3 except the SMT requirement used to identify the candidate c jet.

4.6.2 Corrections of c -Hadron Production and Decay Properties in Simulation

In order to obtain with $\alpha_{\text{sim}}^{\text{corr}}$ a reliable estimate of the efficiency-extrapolation factor, α_{data} , several corrections are applied to the PYTHIA-default sample with the aim to improve the description of those c -quark fragmentation and c -hadron decay properties that affect the c -jet tagging efficiencies in both the inclusive and the SMT c -jet samples. In particular, the following quantities, or somewhat related ones, are studied for the most prominent c -hadron types and corrected to best knowledge, defining the PYTHIA-corrected sample:

- the fragmentation fractions,
- the fragmentation functions,
- the total branching ratio of the semileptonic c -hadron decays,
- the branching fractions of certain exclusive semileptonic c -hadron decays,
- the topological branching ratios of hadronic n -prong c -hadron decays, as well as
- the momentum distribution of the soft muon (in the rest frame of the c hadrons).

As described in detail in the following, the corrections are derived where possible from results of dedicated measurements; otherwise the improved ALPGEN+PYTHIA+EVTGEN simulation is employed (Sec. 4.2). The overall effect of the applied corrections is evaluated and validated.

Correction of c -quark fragmentation fractions

The fragmentation fractions, the fraction with which the various c -hadron types emerge from the fragmentation of c quarks, as implemented in PYTHIA-default are compared to the combination of the results obtained from measurements in e^+e^- and $e^\pm p$ collisions [269] for the four predominant weakly decaying c -hadron types in Fig. 4.8(a); the values implemented in HERWIG are also shown (cf. Sec. 4.2). The D^0 meson is with about 56 % the most frequently produced c hadron, followed by the D^+ meson with about 23 %; together with the D_s meson (8 %) and the Λ_c^+ baryon these four types make up 98 % of all possible c -hadrons. While the D^0 - and D_s -meson fractions implemented in PYTHIA-default are in very good agreement with the measurements, the D^+ -meson fraction is overestimated; the situation is inverted for the Λ_c^+ baryon. Thus, in order to correctly describe the c -hadron composition of the inclusive c -jet sample (to lesser extent of the SMT c -jet sample), the fractions in the PYTHIA-default sample are reweighted to match the measured values. Corresponding systematic uncertainties are evaluated for each of the considered c -hadron types separately: their nominal fractions are changed within the uncertainties of the measurements, while maintaining the overall normalisation.

Correction of the total semileptonic branching ratio of c hadrons

The c -hadron composition in the SMT c -jet sample is furthermore determined by the semimuonic branching fractions that differ for the various c -hadron types, as can be seen from Fig. 4.8(b): the values implemented in PYTHIA-default (and HERWIG) are compared to the world average values [270] for the four previously discussed c -hadron types.¹⁵ Because of the relatively large semimuonic branching ratio of D^+ mesons of

¹⁵ Assuming lepton universality in W -boson decays, the branching ratios measured in c -hadron decays involving electrons are shown for all, but the D_s meson: in the case of the D mesons they are measured with higher precision, in the case of Λ_c^+ no measurements

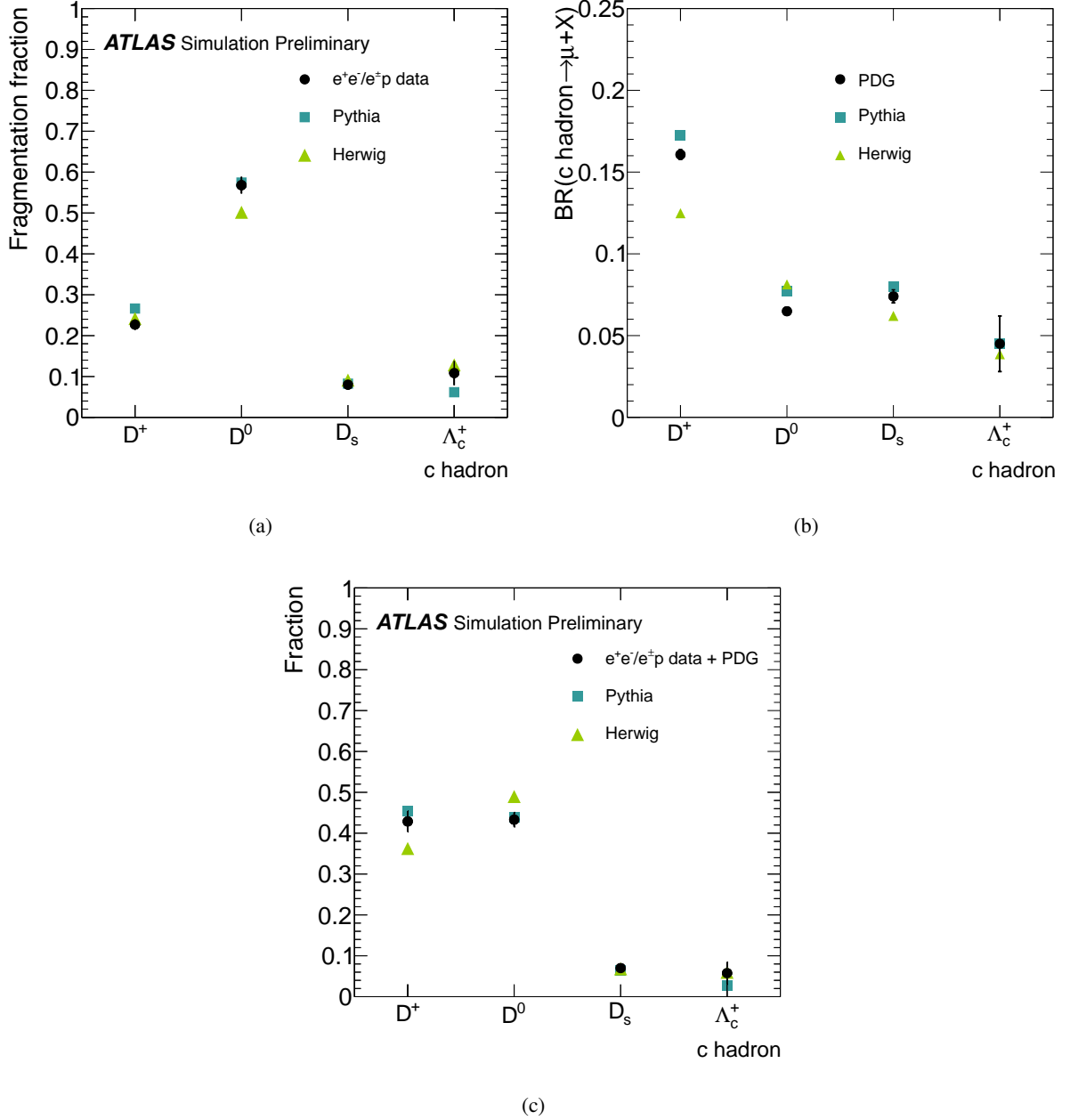


Figure 4.8: For the most relevant weakly decaying c hadrons (a) the fragmentation fractions implemented in the PYTHIA-default and HERWIG samples are compared to combined results of e^+e^- and $e^\pm p$ measurements [269], (b) the predicted branching ratios of their semileptonic decays involving muons are compared to the world average values (“PDG”) [270] and (c) their fraction in a sample of c jets associated with semileptonically decaying c hadrons for which the results in data are obtained from combining the measured fragmentation fractions with the world average values of the semileptonic branching ratios. Figures (a) and (c) were previously published in Ref. [3].

about 16 %, the fraction of D^+ mesons is enhanced in the SMT c -jet sample with respect to the inclusive one. Thus, it is composed of almost equal amounts of D^0 and D^+ mesons, namely of about 43 % each. This can be seen from Fig. 4.8(c) showing the fractions of the four predominant weakly decaying c -hadron types in the SMT c -jet sample as predicted by PYTHIA-default (and HERWIG). They are compared to the results obtained by combining the measured semimuonic branching ratios with the measured fragmentation fractions [269]. Although the semimuonic branching ratios of the D^+ and D^0 mesons implemented in PYTHIA-default are too high (cf. Fig. 4.8(b)), the predicted sample composition is in good agreement with the measurements due to some cancellation effects with the mismodelling of the fragmentation fractions (cf. Fig. 4.8(a)). In the case of the D_s meson and the Λ_c^+ baryon, both the predicted semimuonic branching ratios as well as their fractions in the SMT c -jet sample agree rather well with the measurements. The semileptonic branching ratios of those four c -hadron types are reweighted in PYTHIA-default to match the world average values.

Furthermore, while the semileptonic branching ratios (BR_{sl}) of the subdominant Ξ_c^0 , Ξ_c^+ and Ω_c^0 baryons are not measured, they are corrected based on: (i) the assumption that their BR_{sl} are proportional to their lifetimes τ ,¹⁶ which are measured [270], and (ii) the $\text{BR}_{sl}(\Lambda_c^+)$ results available for the Λ_c^+ baryon, i.e. according to: $\text{BR}_{sl}(B) = \tau_B/\tau_{\Lambda_c^+} \cdot \text{BR}_{sl}(\Lambda_c^+)$, with $B = \{\Xi_c^0, \Xi_c^+, \Omega_c^0\}$.

In order to conserve the overall normalisation in the inclusive c -jet sample, the total hadronic branching ratios of all c -hadron types, whose semileptonic branching ratios were adapted, are adjusted accordingly. Systematic uncertainties are evaluated individually for each of the considered c -hadron types by varying their branching ratios and, in the case of the subdominant baryons, the Λ_c^+ branching ratio and their lifetimes within the uncertainties reported by the measurements.

Correction of the branching fractions of semileptonic and hadronic c -hadron decays

As b -tagging algorithms rely on specific track and vertex properties characteristic for the decays of heavy hadrons, it is crucial that these are well described in simulation. In particular the track multiplicity at the secondary vertex is determined by the charged decay multiplicity of c -hadron decays. However, only in the case of the D^0 meson, the inclusive charged decay multiplicity, referred to as inclusive topological branching fractions, is measured, and can be used to correct the PYTHIA-default sample. For the two most prominent weakly decaying c -hadron types, the branching fractions of an impressive number of particular decay modes are measured (cf. Ref. [45]). This is exploited to improve the charged decay multiplicity of semileptonic D^0 - and D^+ -meson decays indirectly. In addition, an improved simulation, ALPGEN+PYTHIA+EVTGEN (Sec. 4.2), is employed to derive corrections, where no measurements are available.

The corrections are derived separately for semileptonic and hadronic decays. Besides acknowledging that the charged decay multiplicity of the former rather affects the SMT c -jet sample and of the latter rather the inclusive c -jet sample, this allows to correlate the corresponding uncertainties related to the corrections of the semileptonic decays between the two samples.

For improving the charged decay multiplicity of semileptonic decays, only the two dominant c -hadron

with decays to muons exist. In the case of the D_s meson also those decays are considered in the branching ratio where the muons stem from an intermediate τ -lepton decay.

¹⁶More precisely: $\text{BR}_{sl} = \Gamma_c^{sl} \times \tau$, where the semileptonic decay width Γ_c^{sl} is assumed to be universal in the spectator model (cf. Sec. 1.4.6).

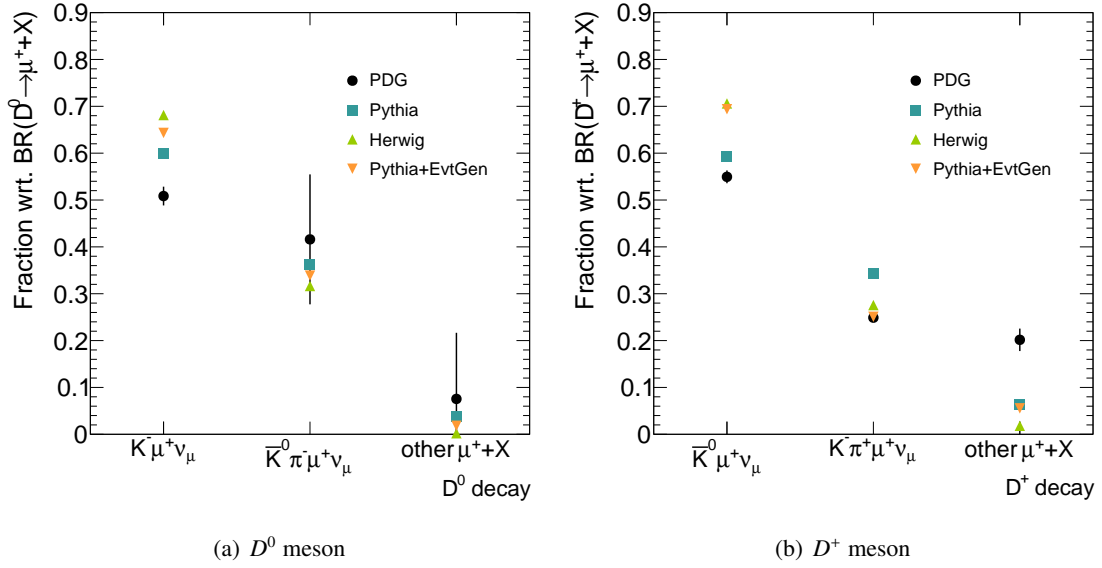


Figure 4.9: Comparison of the relative contributions of certain semimuonic decay modes to the total semimuonic branching ratio of the (a) D^0 and (b) D^+ mesons implemented in the PYTHIA-default, HERWIG and PYTHIA+EVTGEN simulations with the world average values (“PDG”) [270]. The bin in Fig. (b) labelled $D^+ \rightarrow \bar{K}^0 \mu^+ \nu_\mu$ includes contributions from $D^+ \rightarrow \pi^0 \mu^+ \nu_\mu$.

types, D^0 and D^+ , are considered (which make up 86 % of the SMT c -jet sample).

It is exploited that for both mesons the semimuonic decays (and the semielectronic ones alike) proceed mostly via only two modes, namely

$$D^0 \rightarrow K^- \mu^+ \nu_\mu \quad \text{or} \quad D^0 \rightarrow \bar{K}^0 \pi^- \mu^+ \nu_\mu \quad \text{and} \quad D^+ \rightarrow \bar{K}^0 \mu^+ \nu_\mu \quad \text{or} \quad D^+ \rightarrow K^- \pi^+ \mu^+ \nu_\mu,$$

whose branching ratios are measured [270]. The relative contributions of those decay modes to the total semimuonic branching ratio are compared in Fig. 4.9 to the predictions of the PYTHIA-default (and HERWIG) simulation. PYTHIA-default is significantly overestimating the branching ratios of the most frequent decay modes of both the D^0 and the D^+ meson. While the branching ratio of the second most prominent decay mode of the D^+ meson is well described, the contributions from the remaining modes are correspondingly underestimated. The less frequent and well known modes are grouped together as “other $\mu+X$ ” in the histograms and their values are obtained by requiring the overall normalisation, i.e. the total semimuonic branching ratio, to be maintained.¹⁷

The impact of the significant mismodelling of the D^0 -meson branching fractions in PYTHIA-default on the decay multiplicity and the c -jet tagging efficiency is expected to be small, because both of the dominant decay modes involve two charged decay products ($K^- \mu^+$, $\pi^- \mu^+$), and their fractions deviate in opposite direction.

In the case of the D^+ meson the situation is more complex: the dominant decay mode only involves one charged decay product (μ^+), the second dominant three ($K^- \pi^+ \mu^+$) and most of the smaller decay modes involve also three, or more, charged decay products. Since the aim is to improve the charged

¹⁷In the case of the “PDG” this implies that the large uncertainty on the second D^0 -meson decay mode is propagated to the last bin.

decay multiplicity, it is beneficial to group the decay modes not only according to their dominance, but also according to their multiplicity and the precision with which their branching ratios are measured. Therefore, the $D^+ \rightarrow \pi^0 \mu^+ \nu_\mu$ decay with one charged decay product is considered together with the $D^+ \rightarrow \bar{K}^0 \mu^+ \nu_\mu$ decay in the first bin. As a result, mainly decay modes with more than three charged decay products, and small and/or not measured branching fractions, are grouped in the last bin.

The relative branching fractions of each of the considered semileptonic decay modes (or class thereof) are corrected in the PYTHIA-default sample to match the world average values [270], while maintaining the overall normalisation by adjusting the collective contribution of the less frequent modes. Systematic uncertainties are evaluated individually by varying the relative contributions within the uncertainties reported on the measured branching ratios.

The overwhelming fraction of possible decay modes of the four prominent weakly decaying c hadrons is hadronic. Other than for the semileptonic decays the total hadronic branching ratio is not dominated by a limited number of modes, but their number is abundant and only the branching ratios of a relatively small subset are measured. This means that the approach taken to correct the charged decay multiplicities of the semileptonic decays of the dominant c -hadrons types is not feasible. However, as mentioned above, at least for the D^0 meson, which is the dominant weakly decaying c -hadron type in the inclusive sample (cf. Fig. 4.8(a)), the inclusive topological branching fractions are measured, from which the hadronic ones can be deduced as reasoned below.

The branching fraction of the inclusive topological D^0 -meson decay modes are [270]:

$$0\text{-prong: } (15 \pm 6) \%, \quad 2\text{-prong: } (70 \pm 6) \%, \quad 4\text{-prong: } (14.5 \pm 0.5) \%, \quad 6\text{-prong: } (6.4 \pm 1.3) \times 10^{-4},$$

where (i) the 0-prong fraction is obtained from subtracting the 2-,4- and 6-prong results from unity and (ii) the 4-prong (6-prong) results are determined from measuring the branching fractions of eight (two) exclusive *hadronic* decays. Therefore, the *hadronic* topological branching fractions can be inferred assuming that all semileptonic D^0 decays are only contributing to the 2-prong fraction and correspondingly that all other n -prong fractions are carried by hadronic decays. This assumption is supported by the fact that the three dominant semileptonic D^0 -decay modes are 2-prong decays (cf. also Fig. 4.9(a)) and that the sum of their exclusively measured branching fractions makes up the measured total semileptonic branching ratio of $(13.2 \pm 0.6) \%$.¹⁸ Subtracting the semileptonic contribution from the inclusive result, yields a hadronic 2-prong branching fraction of $(57 \pm 6) \%$.

Expressing all results with respect to the total hadronic branching ratio of $(86.8 \pm 0.6) \%$,¹⁹ the relative hadronic n -prong branching fractions are compared to the predictions of the PYTHIA-default, HERWIG and PYTHIA+EVTGEN simulations in Fig. 4.10(a). In particular for the 0-prong and 2-prong fractions relatively large differences between the inferred values and all predictions are found. Nonetheless, they agree within about two standard deviations, given the large uncertainties on the inferred results. While all predictions are quite close to each other, PYTHIA+EVTGEN shows a tendency to agree best with the measurements; this

¹⁸In fact, the sum of the measured branching ratios of the three dominant semileptonic D^0 -decay modes $D^0 \rightarrow K^- \mu^+ \nu_\mu$, $D^0 \rightarrow \bar{K}^0 \pi^- \mu^+ \nu_\mu$ and $D^0 \rightarrow K^- \mu^+ \nu_\mu \pi_0$ is with $(16 \pm 3) \%$ even higher than the measured total semileptonic branching ratio. However, they still agree within uncertainties given the branching ratio of $D^0 \rightarrow K^- \mu^+ \nu_\mu \pi_0$ is measured with very low precision.

¹⁹The total hadronic branching ratio is obtained from the measured total semileptonic branching ratio assuming that their sum adds up to 100 %.

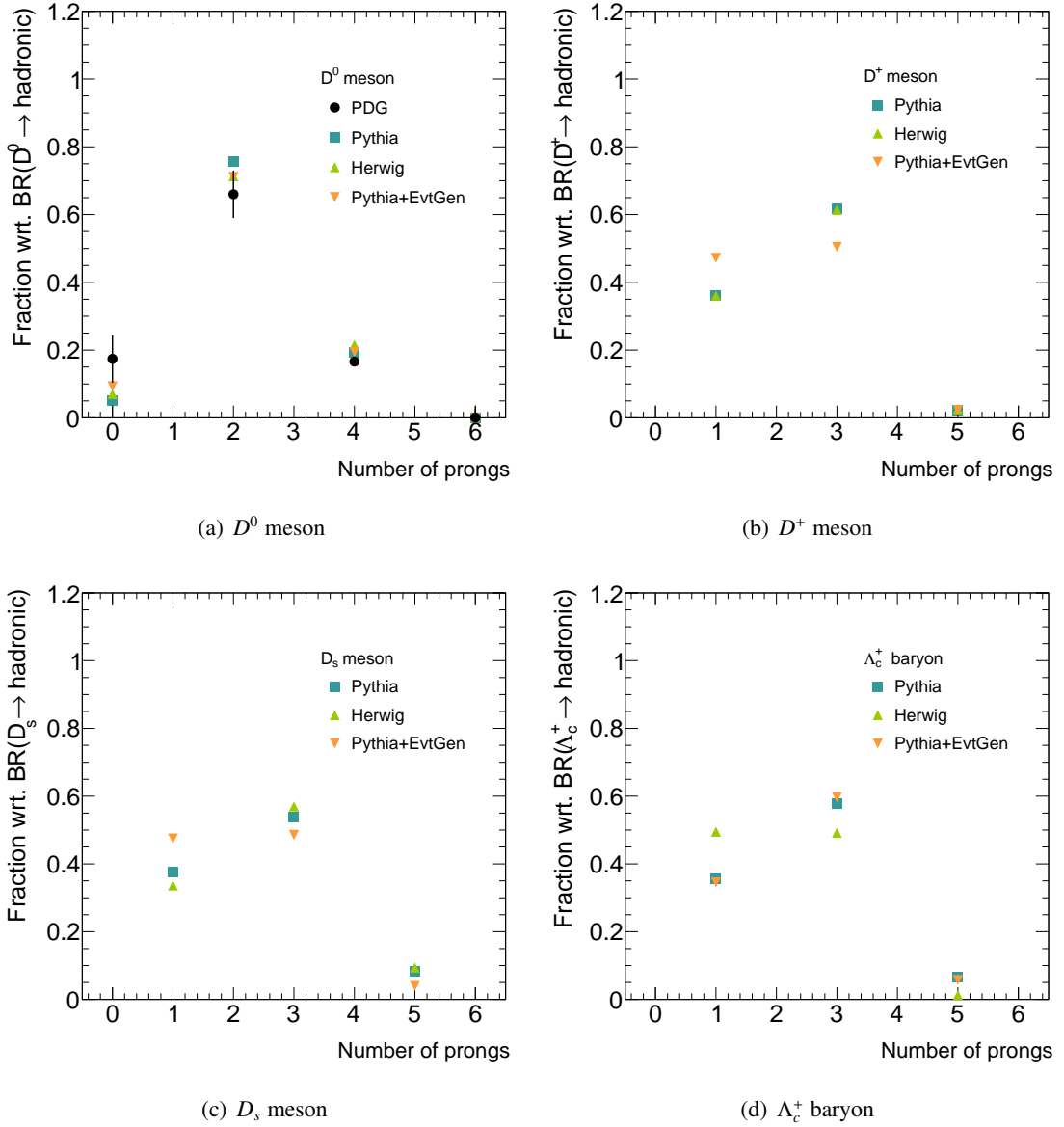


Figure 4.10: Comparison of the topological hadronic branching fractions of the (a) D^0 , (b) D^+ and (c) D_s mesons as well as the (d) Λ_c^+ baryon as implemented in the PYTHIA-default, HERWIG and PYTHIA+EVTGEN simulations. In the case of the D^0 meson the predictions are further compared to results inferred from the measured inclusive n -prong branching fractions [270] as described in the text.

is expected given EVTGEN is dedicated to the description of heavy hadron decays.

Large differences between the predictions are found when repeating the comparison for the D^+ , D_s and Λ_c^+ hadrons, as done in Figs. 4.10(b)-(d); it is solely done for the simulations, given the lack of suitable measurements. Particularly relevant for the c -jet tagging efficiency of inclusive samples of c -jets are the (relative) differences between the 1- and 3-prong fractions. This is because only the JetFitter algorithm is able to exploit 1-track vertices, single tracks can easily be missed in reconstruction and the contributions of higher decay multiplicities are very small.

Given the discussion above, there is good reason to assume that PYTHIA+EVTGEN is describing the situation in data best. Still an attempt is made to use the very limited input from measurements to support this assumption. The n -prongness of the four dominant hadronic decay modes of the D^+ meson, whose branching fractions add up to about 40% [270], is evaluated. More precisely, their overall 3-to-1-prong ratio is compared to the predictions of the three different simulations: the value suggested by the measurements (1.4) is rather well reproduced by PYTHIA+EVTGEN (1.3), while both PYTHIA-default and HERWIG are far off (2.3).²⁰

Therefore, the topological hadronic branching fractions of the D^0 meson are corrected in PYTHIA-default such that they match the values inferred from the measurements. Due to the lack thereof, the ones of the D^+ , D_s and Λ_c^+ hadrons are corrected to match the predictions made by PYTHIA+EVTGEN; the maximum differences with respect to the PYTHIA-default and HERWIG predictions are assigned as uncertainties. The uncertainties, in the case of the D^0 meson from the measurements, are propagated maintaining the overall normalisation.

Study and correction of kinematic distributions

The performance of the b -tagging algorithms depends also on the kinematic distributions of the c hadron and its decay products, in particular on their transverse momentum spectra.

Therefore, the impact of any mismodelling of the fragmentation function, which determines the fraction of the energy of the initial c quark carried by the c hadron, is evaluated. Since no measurements of fragmentation functions at hadron colliders exist, simulations are used to assess the impact of a mismodelling. For this purpose the distributions of a related quantity is studied, namely the ratio of the momenta of the c hadron and the c jet, $p_T^{c \text{ hadron}}/p_T^{c \text{ jet}}$, where the p_T of the c jet at particle level approximates the c -quark p_T . The comparison is done between the PYTHIA-default and HERWIG simulations which rely on different fragmentation models, i.e. the string and the cluster fragmentation model, respectively (cf. Sec. 1.4.5). Figure 4.11(a) shows the $p_T^{c \text{ hadron}}/p_T^{c \text{ jet}}$ distributions for D^+ mesons: the spectrum in PYTHIA-default is softer than in HERWIG; the effect of this difference is taken into account as a systematic uncertainty.

Given that soft muons are used to identify the c -jet candidates and that their reconstruction and selection depends on their kinematic distributions, the momentum distribution of the muon stemming from the c -hadron decay is studied as well. In order to investigate it independently of the description of the c -hadron kinematics, which is already accounted for, the muon momentum is expressed in the rest frame of the

²⁰Only the ratio is compared since the branching fractions of the two classes of decays are not very well described in the simulation, since they have to account for non-implemented decay modes. The considered decays are: $D^+ \rightarrow K^0 \pi^+ (\pi^0)$, $D^+ \rightarrow K^- 2\pi^+ (\pi^0)$, $D^+ \rightarrow K^0 2\pi^+ \pi^-$ and $D^+ \rightarrow 2\pi^+ \pi^- (\pi^0)$.

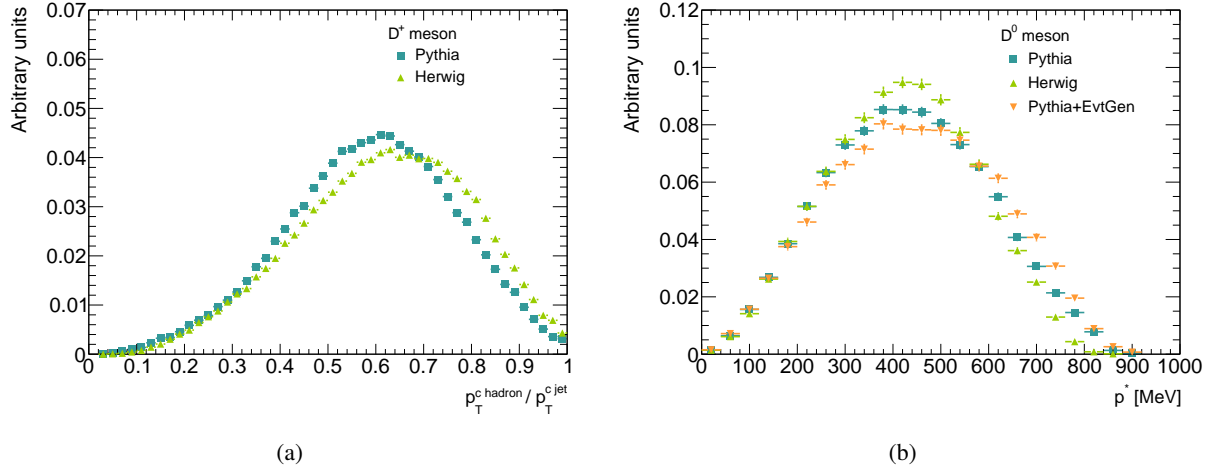


Figure 4.11: Comparison of (a) the distribution of the relative p_T fraction of a c hadron with respect to the associated c jets, sensitive to the fragmentation function, and (b) the momentum spectrum of the decay muon in the rest frame of the c hadron it is stemming from as predicted by the PYTHIA-default, HERWIG and, in the case of the latter, PYTHIA+EVTGEN simulations. The distributions are normalised to unit area.

c hadron and denoted p^* . The p^* distributions of soft muons stemming from D^0 decays as predicted by the PYTHIA-default, HERWIG and PYTHIA+EVTGEN simulations are compared in Fig. 4.11(b). The one predicted by PYTHIA+EVTGEN, which is expected to describe the data best, is the hardest; the one in PYTHIA-default is corrected such that it agrees with it and the full difference is considered as systematic uncertainty, individually for each c -hadron type.

Assessment and validation of the applied corrections

The collective effect of applying all discussed corrections to the PYTHIA-default signal sample, yielding PYTHIA-corrected, is illustrated in Fig. 4.12. The MV1 output weight distributions are compared separately for (a) the SMT c -jet sample and (b) the inclusive c -jet sample. Only statistical uncertainties due to the limited simulated sample size are considered and treated uncorrelated in the ratio, despite the correlation of the predictions given the same events, with different weights, are used.

In the SMT c -jet sample, the effect of the corrections on the MV1 weight is very small: PYTHIA-corrected predicts slightly less events at high values than PYTHIA-default, which translates into an about 2 % lower c -jet tagging efficiency for the 70 % operating point. The small impact is due to competing effects: while the c -jet tagging efficiency for SMT c -jets associated with a certain c -hadron type is somewhat increased (mainly due to the harder p^* spectra), the changed admixture regarding the various c -hadron types in the SMT c -jet sample leads overall to a small decrease of the c -jet tagging efficiency. This is because the Λ_c^+ -baryon contribution is slightly increased in favour of the D^+ meson (cf. Fig. 4.8(c)) and c jets associated with the former (latter) have by far the lowest (highest) c -jet tagging efficiency.²¹

While the c -jet tagging efficiencies of SMT c -jets in the PYTHIA-corrected sample are still higher than the ones measured in data (cf. Table 4.5), the corrections seem to yield a trend into the right direction.

²¹The estimates of the c -jet tagging efficiency of jets associated with a particular c -hadron type are fairly consistent between the PYTHIA-default and PYTHIA-corrected samples.

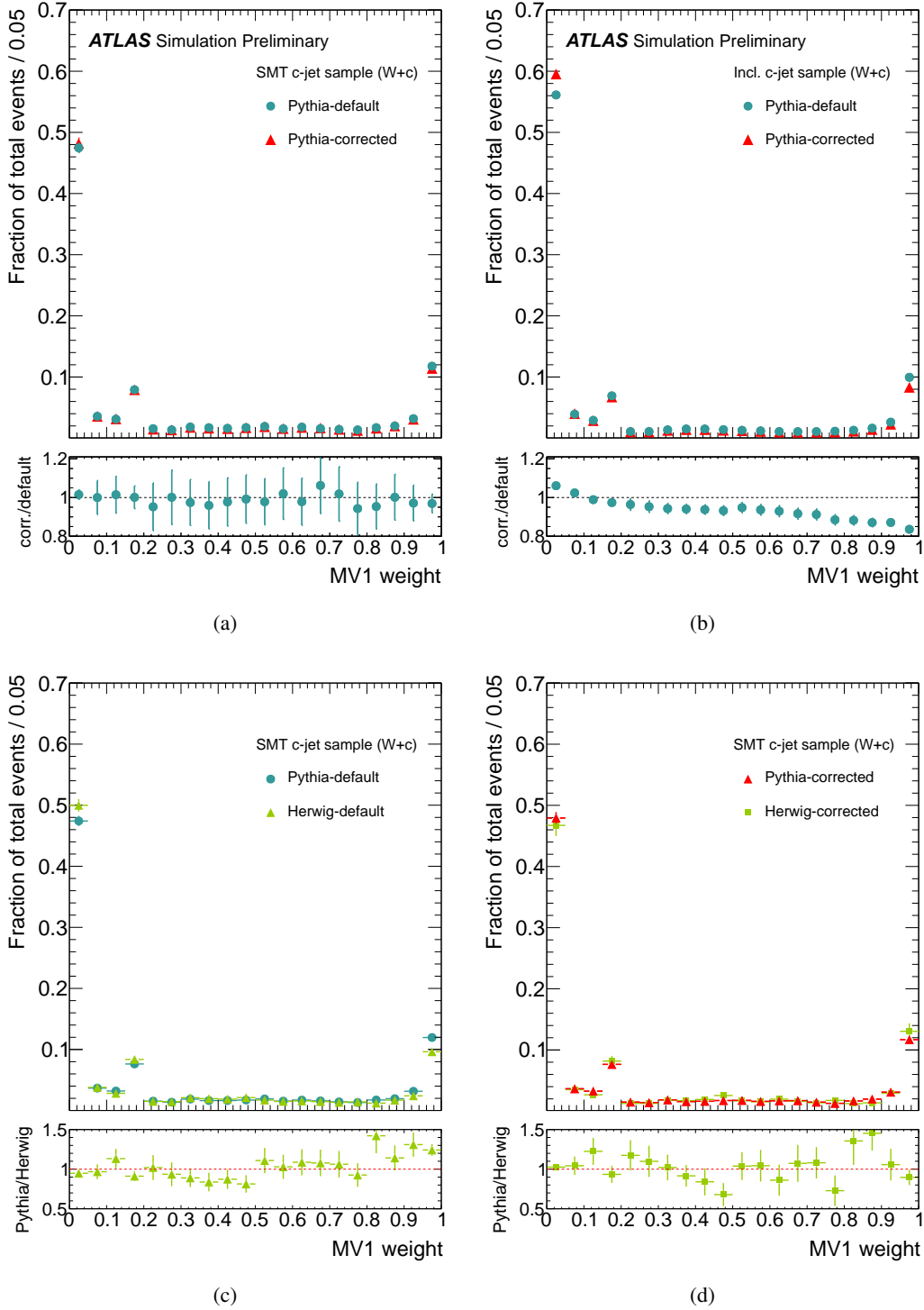


Figure 4.12: Comparisons of the output weight of the MV1 tagging algorithm. Comparison between the PYTHIA-default and the PYTHIA-corrected predictions for (a) an SMT c -jet sample and (b) an inclusive c -jet sample. Comparison between the PYTHIA and HERWIG predictions for SMT c -jets (c) before and (d) after applying all corrections regarding the c -quark fragmentation and c -hadron decay properties described in the text. In the case of the HERWIG simulation, this includes a correction of the fragmentation functions to match the ones in PYTHIA. Figs. (a) and (b) have been previously published in Ref. [3].

In the inclusive c -jet sample, the impact of the corrections on the MV1 weight distribution is quite pronounced, as can be seen from Fig. 4.12(b), in particular from the ratio in the bottom pad. Relative to PYTHIA-default, there is a systematic shift of the MV1 weight distribution in PYTHIA-corrected towards smaller values; corresponding to reduced c -jet tagging efficiencies for all operating points. For example, for the 70 % operating point, ε_c is 14 % lower in PYTHIA-corrected than in PYTHIA-default. This is almost exclusively due to the smaller charged decay multiplicities of all hadronic D -meson decays (cf. Fig. 4.10), resulting in reduced c -jet tagging efficiencies of the associated c jets. For the 70 % operating point, the reduction is approximately 9 %. This trend is further pronounced by the same change in admixture regarding the various c -hadron types also in the inclusive c -jet sample (cf. Fig. 4.8(a)): the Λ_c^+ -baryon component is enhanced in favour of the D^+ -meson one.

One indication that the corrections affecting the SMT c -jet sample are valid, is the reasonable agreement between the data and the PYTHIA-corrected simulation that was demonstrated in Fig. 4.4. To further consolidate the confidence into the validity of the applied corrections as well as to demonstrate that the most important properties affecting the c -jet tagging efficiency are addressed, their combined effect on the alternative signal sample, HERWIG, is evaluated.

As mentioned previously, HERWIG relies on a different fragmentation model than PYTHIA; moreover, the comparisons in Figs. 4.8-4.11 show that there are large differences in their predictions regarding the c -hadron production and decay properties, in particular regarding the ones affecting the SMT c -jet sample. These differences are reflected in the differing MV1 weight distributions shown in Fig. 4.12(c) for SMT c -jets. Due to predicting less events with high MV1 weights, the c -jet tagging efficiencies of SMT c -jets in HERWIG are significantly lower than in PYTHIA-default, by about 16 % for the 70 % operating point.

The HERWIG-corrected sample is obtained by applying all of the previously discussed corrections, and by reweighting in addition the $p_T^{c \text{ hadron}}/p_T^{c \text{ jet}}$ distributions of the four dominant weakly decaying c hadrons to match the ones in PYTHIA. Thus, HERWIG-corrected is defined such that it agrees regarding all the studied c -hadron production and decay properties with PYTHIA-corrected.

Figure 4.12(d) shows the comparison of the MV1 weight distributions of the HERWIG-corrected and the PYTHIA-corrected predictions for SMT c -jets. Overall there is reasonable agreement, considering the large uncertainties. In particular, the agreement at high MV1 values is improved, thus reducing the difference of the c -jet tagging efficiencies at the 70 % operating point to ~ 3 %.

The corresponding comparison of the MV1 weight distributions for inclusive samples of c jets (not shown), reveals that the two simulations agree both before and after the applied corrections at the level of a few percent. This is expected, given the HERWIG and PYTHIA-default simulations predict similar charged decay multiplicities for hadronic decays (cf. Fig. 4.10); i.e. they agree regarding the properties that have the strongest impact on the MV1 weight distribution in inclusive c jet samples.

Nonetheless, that good agreement persists also after applying all corrections, gives confidence that no important properties are left unaddressed nor that the application of the corrections leads to some unintended side effects.

Efficiency and scale-factor extrapolation factors				
Operating points of the MV1 tagging algorithm				
	85 %	75 %	70 %	60 %
α_{sim}	0.82 ± 0.01	0.79 ± 0.01	0.80 ± 0.02	0.83 ± 0.02
$\alpha_{\text{sim}}^{\text{corr}}$	0.76 ± 0.01	0.70 ± 0.01	0.69 ± 0.02	0.72 ± 0.02
δ	0.93 ± 0.03	0.89 ± 0.05	0.87 ± 0.06	0.86 ± 0.07

Table 4.8: Efficiency-extrapolation factors for SMT c -jets, α_{sim} and $\alpha_{\text{sim}}^{\text{corr}}$, obtained using the PYTHIA-default and PYTHIA-corrected simulations, respectively, as well as the scale-factor extrapolation factors, δ , for several operating points of the MV1 tagging algorithm. For α_{sim} and $\alpha_{\text{sim}}^{\text{corr}}$ only statistical uncertainties due to the limited simulated sample size are quoted. For δ only systematic uncertainties due to the corrections regarding the c -quark fragmentation and c -hadron decay properties, described in the text, are considered. Statistical uncertainties are neglected, since the numerator and denominator of δ is computed using approximately the same simulated events.

Breakdown of systematic uncertainties on δ [%]				
Source	Operating points of the MV1 tagging algorithm			
	85 %	75 %	70 %	60 %
Fragmentation fractions	0.5	0.8	0.9	1.1
↔ Λ_c^+ baryon	0.5	0.7	0.9	1.0
Fragmentation functions	0.5	< 0.1	0.14	0.19
Total semileptonic branching ratios	1.4	1.7	1.7	1.8
↔ Λ_c^+ baryon	1.3	1.8	1.7	1.8
Exclusive semileptonic branching ratios	1.5	2.2	1.4	2.2
↔ D^0 meson	1.4	2.2	1.4	2.0
Topological hadronic branching ratios	2.1	3.7	4.8	6.3
↔ D^0 meson	1.9	2.5	2.7	2.8
↔ D^+ meson	0.9	2.6	3.8	5.5
p^*	0.4	0.13	0.8	1.6
Total	3.0	4.7	5.4	7.2

Table 4.9: Breakdown of the contributions of groups of systematic uncertainties on the scale-factor extrapolation factor δ for several operating points of the MV1 tagging algorithm in percent. A further breakdown of certain sources of systematic uncertainties are indicated by “↔”.

4.6.3 Results: Extrapolation Factors

As discussed in detail in the previous section, the corrections applied to the PYTHIA-default sample regarding c -quark fragmentation and c -hadron decay properties hardly affect the c -jet tagging efficiencies of SMT c -jets, $\varepsilon_{c(\mu)}^{\text{sim}}$. However, relative to the PYTHIA-default sample, they lead to significantly reduced c -jet tagging efficiencies of inclusive c -jet samples, $\varepsilon_c^{\text{sim}}$. Therefore, using the PYTHIA-corrected sample to compute the efficiency-extrapolation factor $\alpha_{\text{sim}}^{\text{corr}}$, according to Eq. 4.13, results in values that are systematically lower than α_{sim} determined using the PYTHIA-default sample. This can be seen from their comparison in Table 4.8, for all considered operating points of the MV1 tagging algorithm. Since the $\alpha_{\text{sim}}^{\text{corr}}$ are also further away

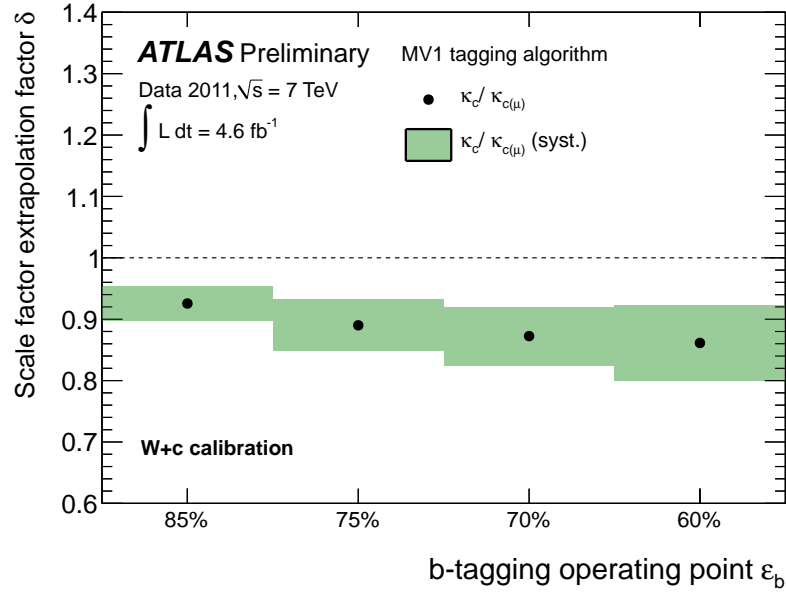


Figure 4.13: Extrapolation factor δ between the c -jet tagging efficiency scale factors applicable to SMT c -jet samples and inclusive c -jet samples for several operating points of the MV1 tagging algorithm. Only systematic uncertainties due to the corrections regarding the c -quark fragmentation and c -hadron decay properties, described in the text, are indicated by the error bands. Statistical uncertainties are neglected, since the numerator and denominator of δ is computed using approximately the same simulated events. Previously published in Ref. [3].

from unity, this result suggests that the c -jet tagging efficiency of the two samples differ more strongly than suggested by PYTHIA-default and that a larger extrapolation is needed.

This difference in the efficiency-extrapolation factors is naturally reflected in the scale-factor extrapolation factors δ , shown in Fig. 4.13 as function of the MV1 operating points and summarised in Table 4.8: δ ranges between 0.86-0.93, and thus is systematically below unity, with a decreasing trend towards tighter operating points.

Given the efficiency-extrapolation factors are computed using approximately the same simulated events, their statistical uncertainties due to the limited sample sizes are neglected. Thus, only the systematic uncertainties discussed in the context of the modelling studies and corrections, in the previous section, are taken into account. Adding the various contributions in quadrature, results in relative total uncertainties between 3% and 7%, increasing with the tightness of the operating points.

From the breakdown of the various groups of systematic uncertainties in Table 4.9, it can be seen that for all operating points, the uncertainties related to the modelling of the topological hadronic branching ratios are dominating. They are driven by the contributions related to the most frequent D^0 meson and the D^+ meson, whose associated jets exhibit the largest tagging efficiencies.

Other, subdominant contributions arise from the systematic uncertainties related to (i) the total semileptonic branching ratios, driven by the large uncertainties on the Λ_c^+ -baryon branching ratio (cf. Fig. 4.8(b)) affecting the c -hadron composition of the SMT c -jet sample, and (ii) the branching ratios of the exclusive semileptonic D^0 - and D^+ -meson decays, which are driven by the large uncertainties on the subdominant semileptonic D^0 decay mode (cf. Fig. 4.9(a)).

The impact of the uncertainties related to the correction of the topological hadronic branching ratios is

Data-to-simulation scale factors for inclusive c -jet samples			
Operating points (ϵ_b) of the MV1 tagging algorithm			
85 %	75 %	70 %	60 %
$0.92 \pm 0.02 \pm 0.02 \pm 0.03$	$0.85 \pm 0.03 \pm 0.03 \pm 0.04$	$0.81 \pm 0.04 \pm 0.04 \pm 0.04$	$0.75 \pm 0.06 \pm 0.05 \pm 0.05$

Table 4.10: Data-to-simulation c -jet tagging efficiency scale factors for inclusive c -jet samples for several operating points of the MV1 tagging algorithm. They are derived with respect to a $W+c$ sample simulated with ALPGEN+PYTHIA-default. The given uncertainties are in order of appearance: the statistical uncertainty, the systematic uncertainty on the measured scale factors for SMT c -jets (cf. Sec. 4.5) and the systematic uncertainty due to the simulation-based extrapolation procedure (cf. Sec. 4.6).

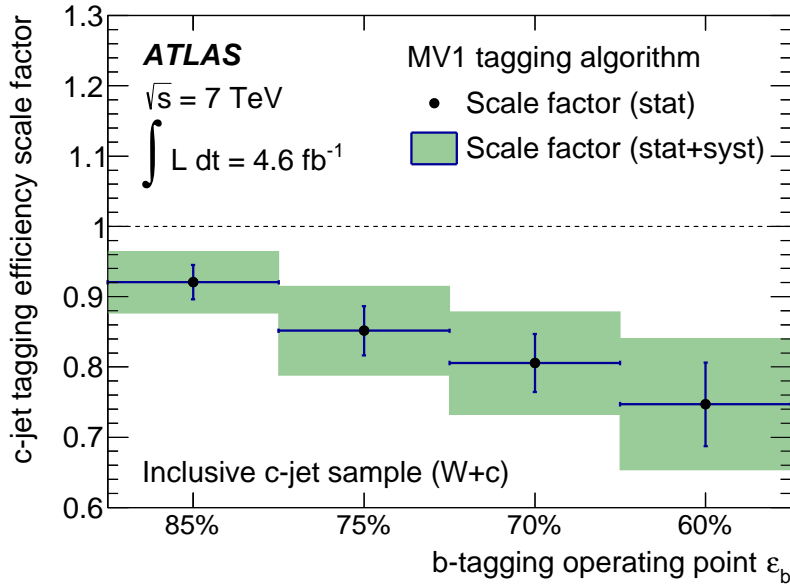


Figure 4.14: Data-to-simulation c -jet tagging efficiency scale factors for inclusive c -jet samples for several operating points of the MV1 tagging algorithm. They are derived with respect to a $W+c$ sample simulated with ALPGEN+PYTHIA-default. Previously published in Ref. [4].

particularly large, because, in addition to being estimated conservatively, they only enter via the numerator in the definition of the efficiency-extrapolation factors. This is different for all the other uncertainties related to the corrections that are applied to both the SMT c -jets and inclusive c -jet samples: they enter the numerator and the denominator, and thus partially cancel.

The scale-factor extrapolation factors being below unity implies that the scale factors measured for SMT c -jets, shown in Fig. 4.5, are not applicable for inclusive samples of c jets. Instead (even) lower scale factors are necessary to bring the c -jet tagging efficiency in simulation closer to the one in data; i.e. the c -jet tagging efficiency of inclusive c -jet samples is overestimated in PYTHIA-default.

Breakdown of uncertainties on κ_c [%]				
Source	Operating points of the MV1 tagging algorithm			
	85 %	75 %	70 %	60 %
Event reconstruction	1.4	2.1	3.4	3.4
Background pretag yields	0.8	2.1	2.3	4.0
Background tagging rates	1.6	1.9	2.2	2.4
c -quark fragmentation	0.7	0.7	0.9	1.0
Hadronic c -hadron decays	2.1	3.7	4.8	6.3
Semileptonic c -hadron decays	2.1	2.9	2.5	3.3
Simulated sample size	1.2	1.9	2.0	2.7
Total systematic uncertainty	4.0	6.2	7.4	9.6
Statistical uncertainty	2.2	3.5	4.9	8.0
Total uncertainty	4.6	7.1	8.9	12

Table 4.11: Breakdown of the contributions of groups of uncertainties on the c -jet tagging efficiency scale factors for inclusive c -jet samples, κ_c , for several operating points of the MV1 tagging algorithm in percent. Details regarding the various groups of systematic uncertainties can be found in Tables 4.6, 4.7 and 4.9.

4.7 Results and Discussion

The data-to-simulation scale factors for the c -jet tagging efficiency of several operating points of the MV1 tagging algorithm are presented in Fig. 4.14 and in Table 4.10. They are expressed relative to a $W+c$ sample simulated with ALPGEN+PYTHIA-default. Derived from the measured c -jet tagging efficiency scale factors for SMT c -jets, they are valid for inclusive samples of c jets due to the simulation-based extrapolation procedure described in detail in the previous section. The values of the final scale factors range between 0.75 and 0.92, decreasing with increasing tightness of the operating points; the relative total uncertainties are instead increasing, from about 5 % to 13 %. This suggests that the PYTHIA-default simulation systematically overestimates the c -jet tagging efficiency of inclusive c -jet samples with respect to the one in the data; the disagreement increases with increasing c -jet rejection.

Three main sources of uncertainties can be distinguished, which are of the same order, as can be seen from Table 4.10: (i) statistical uncertainties, (ii) systematic uncertainties on the measured scale factors for SMT c -jets (cf. Table 4.6), and (iii) systematic uncertainties due to the extrapolation procedure (cf. Table 4.9); the dominant contributions are summarised in Table 4.11. While there are several groups of systematic uncertainties contributing at a similar level, the limited knowledge of the charged particle multiplicity of (hadronic) c -hadron decays, affecting the scale-factor extrapolation, has a quite significant impact.

Since it is not trivial to improve the modelling of the c -hadron properties in the simulations - it needs dedicated measurements and tuning of the event generators-, the required extrapolation constitutes a clear limitation of the presented calibration method. This applies as well to any other method that exploits c hadron characteristics to select the c -jets sample used for the calibration, such as the D^* calibration method which adopted the presented approach. In fact, given that the D^* calibration method relies on reconstructing D^{*+} mesons in a single exclusive decay mode, $D^{*+} \rightarrow D^0(\rightarrow K^-\pi^+)\pi^+$, the extrapolation to

an inclusive sample of c -jets is even larger than for the $W+c$ calibration method. In this regard, the rather new $t\bar{t}$ -based method that measures the c -jet tagging efficiency directly on an inclusive sample of c jets is clearly superior.

Nonetheless, it is beneficial to have several calibration methods for the c -jet tagging efficiency available; as it is also the case for the b -tagging efficiency calibrations (cf. Sec. 3.4.4). Besides providing the possibility to cross-check the various results (which proved important), it also allows analyses to choose among the sets of scale factors those that are determined using independent datasets and are afflicted with different systematic uncertainties. For example, for an analysis studying 1-lepton $t\bar{t}$ events, it might be preferable to use $W+c$ -based scale factors. Furthermore, the different scale-factor results may be combined to achieve optimal precision, in particular in certain phase-space regions; for instance, at small or high jet p_T .

Finally, the $W+c$ calibration method may have an advantage over the $t\bar{t}$ -based calibration method, when it comes to measuring the c -jet tagging efficiency of track jets (cf. Sec. 3.3), in particular at very low jet p_T . This is because the $t\bar{t}$ -based calibration exploits a kinematic likelihood fit in order to assign the physics objects to the top-quark decay products requiring jets to reflect the kinematics of the original quarks. Track jets, however, miss the information on the neutral components. While there are possibilities to handle this difficulty, it does constitute a current limitation of the method.

In summary, the demonstrated $W+c$ method constitutes an important alternative to other c -jet tagging efficiency calibration approaches and established to one of the standard calibration methods used by the ATLAS collaboration in Run 2.

5 Search for the Higgs Boson A Decaying to Zh in the $\nu\bar{\nu}b\bar{b}$ and $\ell\bar{\ell}b\bar{b}$ Final States

5.1 Introduction

All test carried out after the discovery of a Higgs boson in the year 2012 by the ATLAS and CMS collaborations [7, 8], so far confirm its compatibility with the predictions of the Standard Model (SM). Nonetheless, the question remains whether the Higgs boson is part of an extended scalar sector suggested by many theories beyond the SM. To date, its couplings have been only measured for a number of SM particles and with a limited precision that still leaves room for deviations from the SM expectation.

Two-Higgs-Doublet Models (2HDMs), introduced in Sec. 1.2, allow to search for such an extended Higgs sector in a rather generic way, as they do not make assumptions on a particular underlying theory. Assuming that the scalar sector is CP and lepton-flavour conserving, they suggest the existence of five Higgs bosons - two CP-even, one pseudoscalar and two charged Higgs bosons - and four model types - the Type-I, Type-II, Lepton-specific and Flipped Model - that differ regarding the couplings of the Higgs bosons to the *charged* SM fermions.¹ The couplings of the scalars to SM particles can be readily expressed relative to the couplings of the SM Higgs boson by factors that depend on two free parameters (in addition to the Higgs-boson mass): α and β . In the *alignment limit*, i.e. $\cos(\beta - \alpha) = 0$, the couplings of the light CP-even scalar h become identical to the ones of the SM Higgs boson. Therefore, the observed Higgs boson is typically identified with the h boson, whose mass is determined by the measured value of ~ 125 GeV. That the couplings of the observed scalar are so far found to be SM-like, constraints the allowed 2HDM parameter space already considerably, and in particular to $\cos(\beta - \alpha) \rightarrow 0$, as discussed in Sec. 1.3. Hence, one approach to elucidate whether the observed Higgs boson is the one predicted by the SM or part of an extended scalar sector is to measure the couplings of the observed Higgs boson with higher precision.

In this chapter a complementary approach is presented, where the observed scalar is used to search for the CP-odd Higgs boson A by targeting its decay into a Z boson and an h boson.² As shown in Sec. 1.3, the branching ratio for $A \rightarrow Zh$ is large in most of the parameter space and may even dominate the decay width; not only for A -boson masses, $m_A \leq 350$ GeV, i.e. below the threshold, where the decay into a top-quark pair ($t\bar{t}$) becomes kinematically accessible. Although it vanishes for $\cos(\beta - \alpha) = 0$, the decay rate is still significant close to the alignment limit.

The analysis considers those events, where the Z boson decays leptonically into an electron or muon pair, $Z \rightarrow \ell\ell$, or into two neutrinos, $Z \rightarrow \nu\nu$, and the Higgs boson into a b -quark pair, $h \rightarrow b\bar{b}$, as depicted

¹While 2HDMs are a wide class of models, in the context of this chapter, 2HDMs always refer to the four 2HDM types: Type-I, Type-II, Lepton-specific and Flipped Model.

²Throughout this chapter, “the Higgs boson” refers to the CP-even Higgs boson, h , while the CP-odd Higgs boson, A , is usually referred to as “the A boson”.

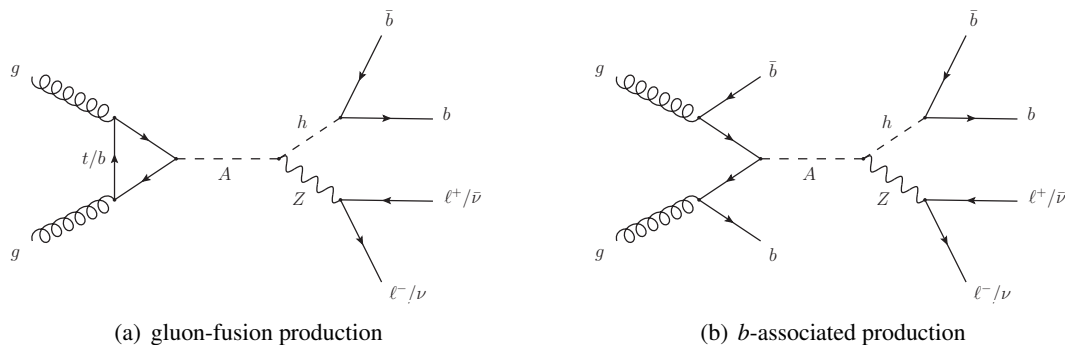


Figure 5.1: Feynman diagrams for the production of the A boson via (a) gluon fusion and (b) b -associated production and its decay via Zh into the $\ell\bar{\ell}b\bar{b}$ and $\nu\bar{\nu}b\bar{b}$ final states in the CP-conserving 2HDMs (cf. Sec. 1.2).

in the Feynman diagrams in Fig. 5.1.³ Similarly to the situation in the SM, at a mass of ~ 125 GeV, the $h \rightarrow bb$ decay is dominant in most of the parameter space. In the Type-II and the Flipped Model, the branching ratio can become especially large due to the $\tan\beta$ -enhanced couplings to down-type quarks.

The leptonic Z -boson decays provide good trigger efficiencies and means to suppress background contributions; the $h \rightarrow bb$ decay mode allows the full reconstruction of the Higgs-boson kinematics. The invariant mass or transverse mass, in the case of $Z \rightarrow \nu\nu$, of the Zh system is used to search for an A -boson signal with masses between 220 GeV (approximately the threshold for on-shell Zh decays) and 2 TeV. With increasing A -boson mass, m_A , the Z and Higgs bosons tend to acquire larger transverse momenta and their decay products become collimated. In order to efficiently reconstruct A -boson candidates with $m_A \geq \text{TeV}$, techniques adapted to such *boosted* topologies are required. Since this applies especially to the reconstruction of the Higgs-boson candidates, the strategy used to reconstruct them changes over the considered m_A range: once the b quarks become too close to be reconstructed as two individual jets (with small radius), the b -quark pair is jointly reconstructed as one jet with larger radius. The two reconstruction methods are associated with two different kinematic regimes, referred to as *resolved regime* and *merged regime*, respectively. While in an intermediate mass range a transition region occurs, where both reconstruction techniques can be exploited, to obtain orthogonal analysis regions, events are exclusively assigned to either regime. In both regimes, jets containing b hadrons that emerge from the b quarks are identified by means of b -tagging.

In most of the parameter space of the four considered 2HDMs, the A boson is mainly produced in gluon fusion via a top-quark loop (ggF), as indicated in the Feynman diagram in Fig. 5.1(a). However, in the Type-II and the Flipped Models, also the contribution of the b -quark associated production (bbA), depicted in Fig. 5.1(b), becomes significant and even dominant at high $\tan\beta$ values due to the enhanced couplings to down-type quarks. The signature of the latter, involving further b quarks in addition to the ones stemming from the Higgs-boson decay, is addressed with dedicated analysis regions containing additional b -tagged jets.

The analysis discussed in the following uses pp -collision data at a centre-of-mass energy of 13 TeV collected with the ATLAS experiment in the years 2015 and 2016. It has been previously published in

³In this chapter, the notation $Z \rightarrow \ell\bar{\ell}$, $Z \rightarrow \nu\bar{\nu}$ and $h \rightarrow b\bar{b}$ is used for $Z \rightarrow \ell^+\ell^-$, $Z \rightarrow \nu\bar{\nu}$ and $h \rightarrow b\bar{b}$, respectively.

Ref. [6],⁴ with several changes to an earlier version based on the 2015 dataset alone [5]. Since a significant part of the improvements and additions were developed in the course of this thesis, their impact is demonstrated with respect to the strategies used to obtain this preliminary result.

While this chapter focuses on the description of the search for an A boson of the 2HDM in the $Zh \rightarrow \ell\ell(\nu\nu)bb$ decay channels, two additional results are presented.

First of all, the results of a search for new heavy vector bosons, $V' = W', Z'$, with masses between 500 GeV and 5 TeV in their decays $Z' \rightarrow Zh \rightarrow \ell\ell(\nu\nu)bb$ and $W' \rightarrow Wh \rightarrow \ell\nu bb$ are presented. Given this analysis targets the same and similar final states, respectively, the general search strategy is very similar to the one of the $A \rightarrow Zh$ analysis. In fact, the Z' search is based on a subset of the $\ell\ell(\nu\nu)bb$ analysis regions of the $A \rightarrow Zh$ search. Since the $\nu\nu bb$ channel has also some sensitivity to a W' signal, it is combined with the $\ell\nu bb$ channel to search for a W' boson. As the latter channel is not considered in the search for the A boson, it is not further discussed; details can be found in Ref. [6].

Such heavy versions of the SM Z and W bosons are predicted by various models that attempt to solve the naturalness problem of the Higgs-boson mass by introducing a new strong interaction at a higher energy scale, e.g. Minimal Walking Technicolour [272–274] or composite Higgs models [275, 276]. In order to be able to interpret the results in the context of a range of models with heavy vector triplets (HVT), they are presented using a simplified model [277, 278]. Searches for V' bosons received some particular attention after two W' searches conducted by the ATLAS and CMS collaborations in Run 1 observed an excess over the SM background expectation at a similar mass of about 2 TeV [279, 280].

Second of all, the results of the $A \rightarrow Zh$ search are also interpreted in the context of the hMSSM [281, 282]. As a simplified version of the Minimal Supersymmetric Standard Model (MSSM), where the mass of the lightest CP-even Higgs boson h is fixed to the mass of the observed Higgs boson, the hMSSM is a concrete realisation of a Type-II 2HDM (cf. Sec. 1.2).

5.2 Previous Results

This section briefly summarises the results of a number of searches published by the ATLAS and CMS collaborations addressing the same final states and interpretations as the analysis described in the following.

The ATLAS collaboration presented a first search for a pseudoscalar Higgs boson A decaying to Zh in the $\nu\nu bb$ and $\ell\ell bb$ final states (where $\ell = e$ or μ) using pp -collision data at a centre-of-mass energy of $\sqrt{s} = 8$ TeV corresponding to an integrated luminosity of 20.3 fb^{-1} [283]. Targeting A -boson masses up to 1 TeV, the analysis restricted to what was introduced as the resolved regime: only events with exactly two b -tagged jets are considered. The resolution of the final discriminants, the invariant and transverse masses of the Zh system, respectively, is improved by employing the observed Higgs-boson mass, i.e. scaling each candidate jet four-momentum such that the reconstructed Higgs-boson mass agrees with 125 GeV.

The analysis did not find any significant deviation from the SM expectation. The significance of the largest local excess at $m_A = 220$ GeV was estimated to be about two standard deviations (2σ). Figure 5.2(a) shows the obtained upper limit on the A -boson production cross-section (in gluon fusion) times the branching ratios of the $A \rightarrow Zh$ and $h \rightarrow bb$ decays at the 95 % confidence level (CL) as function of the A -boson

⁴Ref. [6] supersedes Ref. [271] describing the same results in a slightly different presentation.

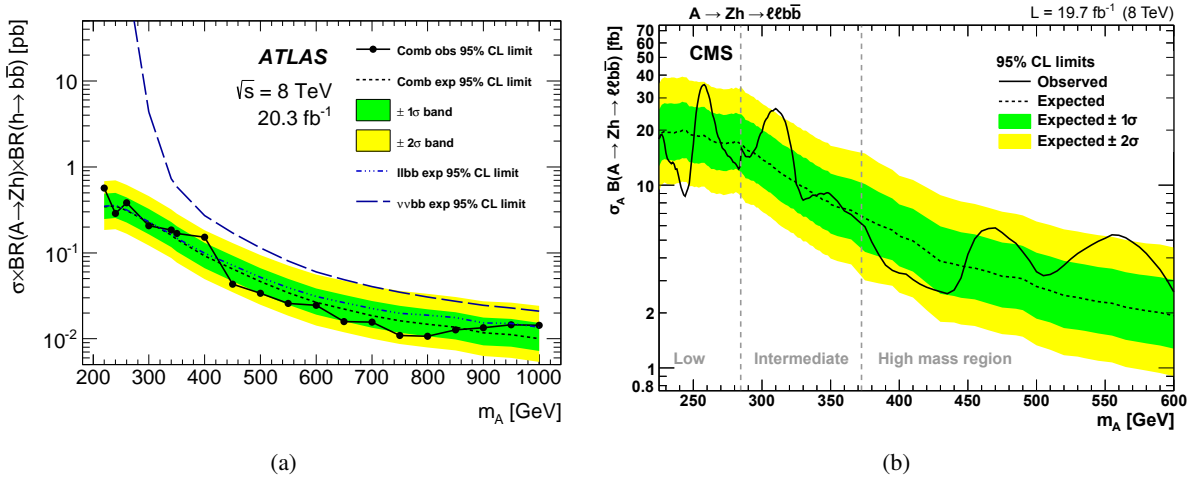


Figure 5.2: Observed and expected upper limits at the 95 % CL on the cross section for A -boson production in gluon fusion times the branching ratios of $A \rightarrow Zh$ and $h \rightarrow b\bar{b}$ (a) obtained by the ATLAS collaboration from the combination of the $\ell\bar{\ell}b\bar{b}$ and $\nu\bar{\nu}b\bar{b}$ channels [283] and (b) as well as the branching ratio $Z \rightarrow \ell\bar{\ell}$, where $\ell = e, \mu$, obtained by the CMS collaboration [284], as function of the A boson mass in the narrow-width approximation using 8 TeV pp collision data.

mass m_A ; it ranges between $0.57 - 0.014$ pb for m_A of $220 - 1000$ GeV. The sensitivity is driven by the $\ell\bar{\ell}b\bar{b}$ final state, in particular at low A -boson masses.

The results are combined with those obtained in an analysis targeting the $Z \rightarrow \ell\bar{\ell}$ and $h \rightarrow \tau\tau$ decays and interpreted in the context of the four before-mentioned 2HDMs. The obtained exclusion regions are shown in Figs. 5.3(a)-(d) for $m_A = 300$ GeV in the $\tan\beta$ versus $\cos(\beta - \alpha)$ plane and in Figs. 5.3(e)-(h) for $\cos(\beta - \alpha) = 0.1$ in the $\tan\beta$ versus m_A plane. Given b -associated production dominates over gluon fusion for large $\tan\beta$ values in the Type-II and Flipped models, the relative selection efficiency and the expected cross-section ratio with respect to gluon fusion are accounted for. While in most of the parameter space the $h \rightarrow b\bar{b}$ decay dominates, and thus the constraints are driven by the respective analysis, in the Lepton-specific model the $h \rightarrow \tau\tau$ decay becomes dominant at large $\tan\beta$ values (cf. Table 1.3) and mainly determines the exclusion limit shown in Figs. 5.3(c) and 5.3(g). Vanishing branching ratios for the $h \rightarrow b\bar{b}$ and/or $h \rightarrow \tau\tau$ decays cause the narrow regions without any exclusion power far from $\cos(\beta - \alpha) = 0$ in Figs. 5.3(a)-(d).

Although the natural width (Γ_A) of the A boson is generally small, justifying the used narrow-width approximation, it may be larger than the experimental mass resolution in certain regions of the 2HDM parameter space, and thus is taken into account in the exclusion regions in Fig. 5.3 for Γ_A/m_A up to 5% (cf. Sec. 5.3).

The results of a search for a heavy Higgs boson decaying into a τ -lepton pair [285] are re-interpreted as an $A \rightarrow \tau\tau$ decay, where the A boson is produced exclusively in gluon fusion or b -associated production, and the regions of parameter space excluded at 95 % CL are overlaid in Fig. 5.3. They are providing complementary information in particular in the alignment limit ($\cos(\beta - \alpha) \rightarrow 0$) and at large $\tan\beta$ values in the Lepton-specific model, where the branching ratio for the $A \rightarrow Zh$ decay vanishes and becomes small, respectively (cf. Eq. 1.35 and Fig. 1.7).

The results of the $\nu\bar{\nu}b\bar{b}$ and $\ell\bar{\ell}b\bar{b}$ channels were further interpreted in the context of the hMSSM. Its

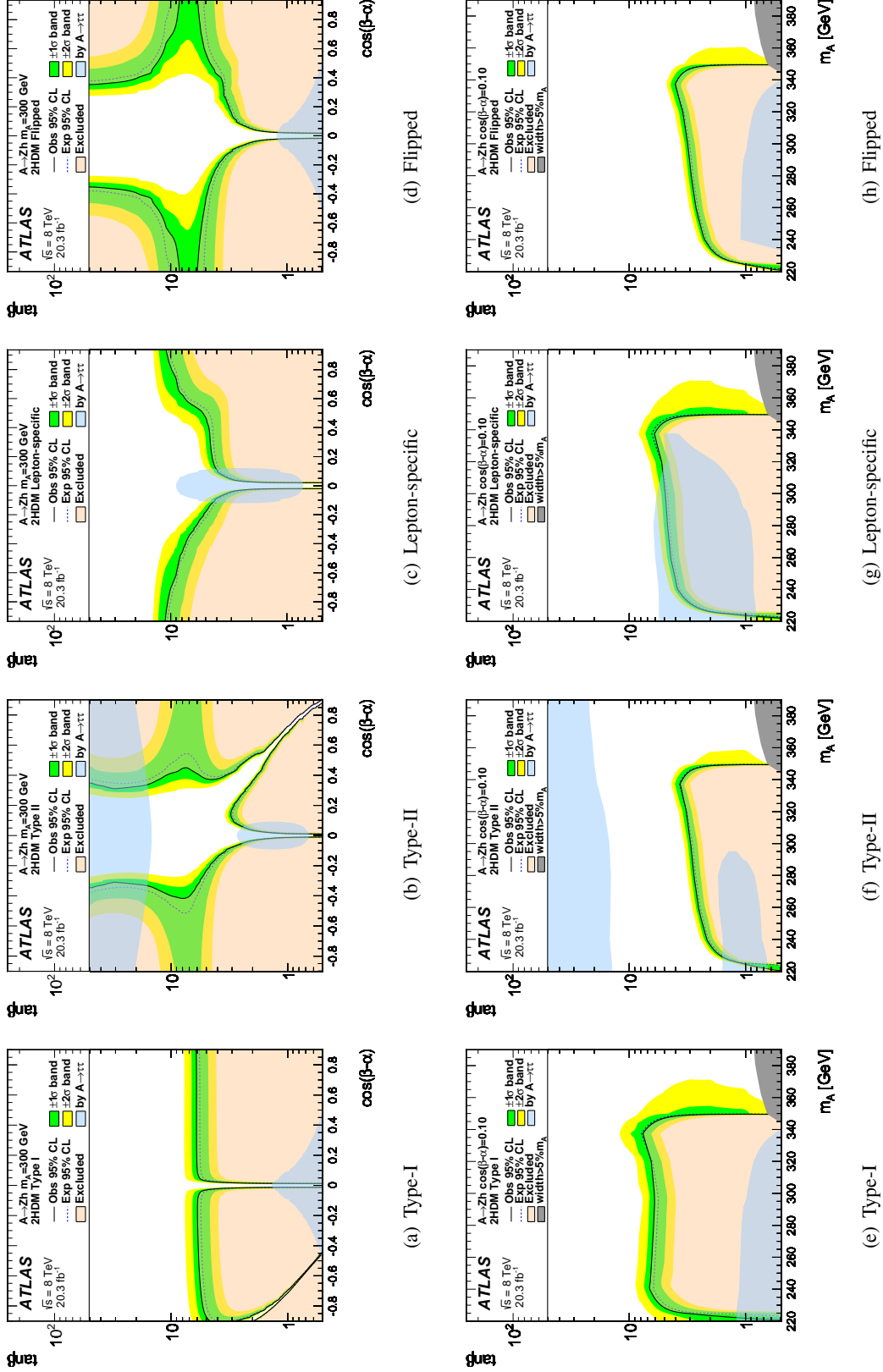


Figure 5.3: Observed and expected exclusion regions at the 95% CL in the context of the four 2HDMs described in the text as function of the (a) – (d) $\tan\beta$ and $\cos(\beta - \alpha)$ parameters for $m_A = 300$ GeV and (e) – (h) $\tan\beta$ and m_A for $\cos(\beta - \alpha) = 0.1$, obtained by the ATLAS collaboration from combining the results of the $A \rightarrow Zh \rightarrow \ell\ell(\nu\nu)bb$ and $A \rightarrow Zh \rightarrow \ell\ell\tau\tau$ analyses using pp -collision data at 8 TeV. In the case of the Type-II and the Flipped models, also the b -associated production mode is taken into account. The variation of the natural width in the parameter space is considered up to $\Gamma_A/m_A = 5\%$; regions with larger values are indicated by the grey solid area. Exclusion obtained from re-interpreting the results in Ref. [285] as $A \rightarrow \tau\tau$ decay mode is displayed as blue shaded area. Taken from Ref. [283].

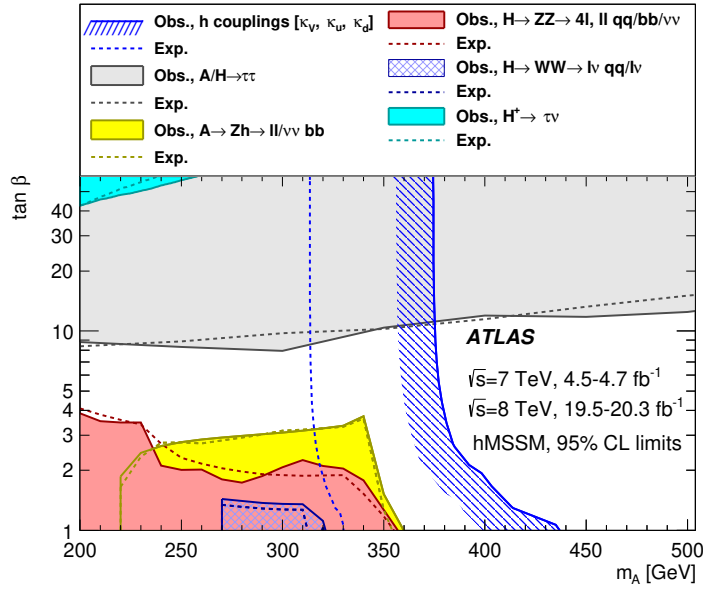


Figure 5.4: Observed and expected exclusion regions at the 95 % CL in the context of the hMSSM model as function of m_A and $\tan\beta$ obtained from several direct searches for heavy Higgs bosons, including $A \rightarrow Zh \rightarrow \ell\ell(\nu\nu)bb$, and fits to the measured production and decay rates of the observed Higgs boson performed by the ATLAS collaboration using pp -collision data at 7 and 8 TeV. Taken from Ref. [67].

Higgs sector is (to good approximation) described by only two free parameters, $\tan\beta$ and m_A ; i.e. with respect to the general Type-II 2HDM, the parameter α is not a free parameter, but determined by $\tan\beta$ and the masses of the Z and A bosons. Figure 5.4 shows the obtained exclusion region in the $\tan\beta$ versus m_A plane [67]. The results from various other direct searches for heavy Higgs bosons as well as from fits to the measured rates of the production and decay of the observed Higgs boson are overlaid. At low $\tan\beta$ values the latter is providing stronger constraints than the direct searches; only at high $\tan\beta$ the direct searches, in particular the search for $A/H \rightarrow \tau\tau$, extends the excluded space significantly to higher m_A values.

In addition, the CMS collaboration published a search for $A \rightarrow Zh$ based on pp -collision data at $\sqrt{s} = 8$ TeV corresponding to 19.7 fb^{-1} [284]. While considering only the $\ell\ell b\bar{b}$ final state and A -boson masses up to 600 GeV, the analysis sensitivity and conclusions in this range are similar to those of the ATLAS results. The analysis exploits as final discriminant the two-dimensional distribution of the Zh invariant mass, which is improved by means of a kinematic fit constraining the mass of the reconstructed Higgs boson to 125 GeV, and the discriminants of multivariate analyses, used to define signal regions in three mass intervals.

No significant excess in the data over the SM background expectation is observed; the largest excess with a significance of 2.6σ is found for $m_A = 560$ GeV. Figure 5.2(b) shows the exclusion limit at the 95 % CL on the A -boson production cross-section times the branching ratio of the $A \rightarrow Zh$, $h \rightarrow b\bar{b}$ and $Z \rightarrow \ell\ell$ (with $\ell = e$ or μ) decays as function of m_A . Considering $\text{BR}(Z \rightarrow ee \text{ or } \mu\mu) = 0.067$ the limits ranging from 17.9 – 1.93 pb for $m_A = 225 - 600$ GeV compare well with the results of the ATLAS collaboration, and so do the exclusion regions in the $\tan\beta$ versus $\cos(\beta - \alpha)$ plane derived for the Type-I and Type-II models and $m_A = 300$ GeV (not shown here).

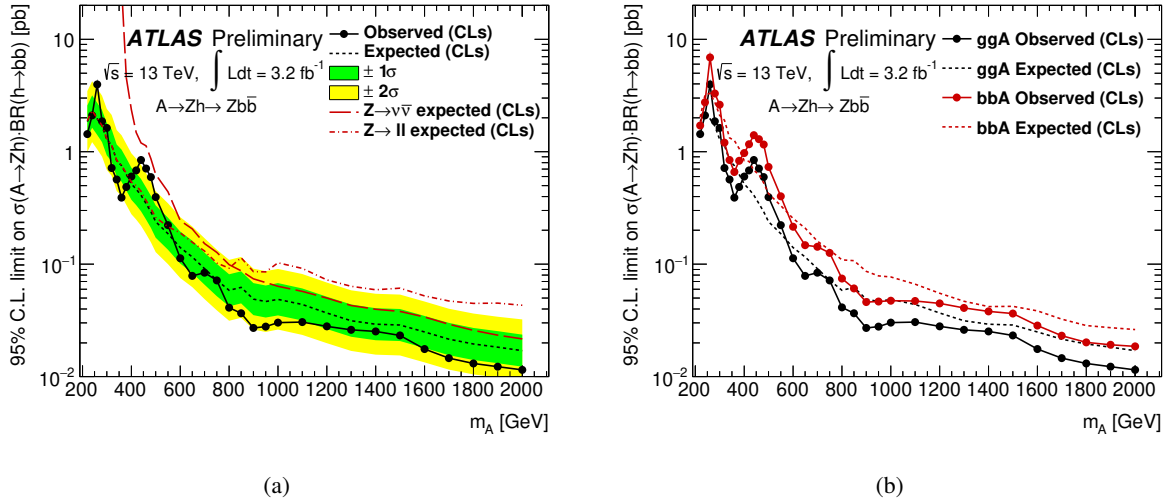


Figure 5.5: (a) Combined observed and expected upper limits at the 95% CL on the cross section for A -boson production in gluon fusion times the branching ratios of the $A \rightarrow Zh$ and $h \rightarrow bb$ decays as function of the A -boson mass, using pp -collision data at 13 TeV collected with the ATLAS experiment. The expected upper limits considering only the $\ell\ell bb$ and $\nu\nu bb$ channel, respectively, are also shown. (b) Comparison of the combined upper limits for pure gluon-fusion and pure b -associated A -boson production. Previously published in Ref. [5].

The ATLAS collaboration presented a preliminary update of the search for $A \rightarrow Zh$ using 3.2 fb^{-1} of pp -collision data at $\sqrt{s} = 13 \text{ TeV}$ [5]. Since in particular cross sections of predicted high-mass resonances were expected to experience a boost from the increase of centre-of-mass energy with respect to $\sqrt{s} = 8 \text{ TeV}$ (cf. Sec. 1.4), the analysis mainly focused on increasing the mass reach of the search up to 2 TeV. This was achieved by introducing additional analysis regions in the merged regime, where the $h \rightarrow bb$ candidates are reconstructed from one large-radius jet.

The analysis did not observe any significant deviation from the SM expectation. The two largest observed excesses have local significances of about 2σ and occur at $m_A = 260 \text{ GeV}$ and $m_A = 440 \text{ GeV}$. Figure 5.5(a) shows the upper limit on the A -boson production cross-section times the branching ratio of the $A \rightarrow Zh$ and $h \rightarrow bb$ decays at the 95% CL as function of m_A considering pure gluon-fusion production; Figure 5.5(b) shows the comparison with considering pure b -associated production, to which the analysis was not optimised. The 95% CL upper limits range from 4.0 – 0.017 pb (6.9 – 0.026 pb) for $m_A = 220 - 2000 \text{ GeV}$ assuming pure gluon-fusion (b -associated) production.

As mentioned before, the choices of this preliminary analysis served as a baseline for the analysis presented in the following sections, and comparisons are drawn wherever relevant in order to motivate deviating approaches.

Several HVT searches in the same intermediary (Vh) and also the same final states have been presented previously by the ATLAS and CMS collaborations using both pp -collision data at $\sqrt{s} = 8$ and 13 TeV. They typically considered two benchmark models: *Model A*, where the coupling of the new heavy vector bosons to fermions and bosons is of comparable strength, as predicted by some models with an extended gauge symmetry [287], and *Model B*, where the couplings to fermions are strongly suppressed, as required

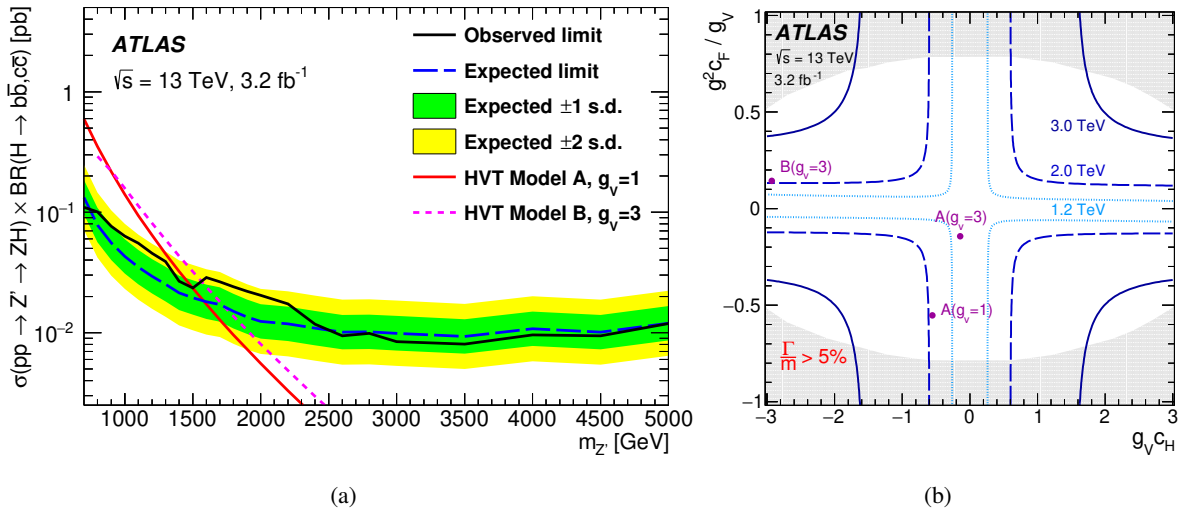


Figure 5.6: (a) Combined observed and expected upper limits at the 95 % CL on the Z' -boson production cross-section times the branching ratios for the $Z' \rightarrow Zh$ and $h \rightarrow b\bar{b}/c\bar{c}$ decays. The predictions for the benchmark *Model A* ($g_V = 1$) and *Model B* ($g_V = 3$) are shown for comparison. (b) Combined observed 95 % CL exclusion contour in the HVT parameter space $[g_V c_H, (g^2/g_V) c_F]$ for V' bosons of mass 1.2 TeV, 2.0 TeV and 3.0 TeV. The parameter space outside of the contours, i.e. towards larger parameter values, is excluded for a resonance with corresponding mass. The parameters of the benchmark *Model A* ($g_V = 1$), *Model A* ($g_V = 3$) and *Model B* ($g_V = 3$) are also shown. Taken from Ref. [286].

by e.g. the Minimal Composite Higgs Model [288]. By fixing the model parameters c_H and c_F that modify the coupling to the SM Higgs boson and the fermions, respectively, they leave g_V , representing the strength of the new interaction, the only free parameter in addition to the masses of the new resonances (m'_V).

The ATLAS analyses [286, 289] based on the $\nu\bar{\nu}b\bar{b}$, $\ell\nu b\bar{b}$ and $\ell\bar{\ell}b\bar{b}$ final states exclude at the 95 % CL W' (Z') bosons with masses below 1.75 (1.49) TeV and 2.22 (1.58) TeV for the benchmark *Model A* ($g_V = 1$) and *Model B* ($g_V = 3$), respectively. Combining all three channels assuming the Z' and W' boson have equal masses ($m_{Z'} = m_{W'}$), allows to exclude V' bosons with $m'_V < 1.73$ (2.31) TeV at the 95 % CL for *Model A* (*Model B*) with coupling constant $g_V = 1$ ($g_V = 3$).

Figure 5.6(a) shows as an example the upper limit at the 95 % CL on the Z' -boson production cross-section times the branching ratios for the decays to Zh and $h \rightarrow b\bar{b}/c\bar{c}$ as a function of $m_{Z'}$ obtained by the latest ATLAS search based on 13 TeV data. This search focused on resonances with masses between 700 GeV and 5 TeV and considered exclusively the merged regime.

Figure 5.6(b) shows the observed exclusion contours in the HVT parameter space $[g_V c_H, (g^2/g_V) c_F]$ for resonances of mass 1.2 TeV, 2.0 TeV and 3.0 TeV obtained when combining all three channels and assuming $m_{W'} = m_{Z'}$. The parameter combination $g_V c_H$ describes the couplings of the new resonances to the Higgs and gauge bosons, the combination $(g^2/g_V) c_F$ the couplings to the fermions, where g is the $SU(2)_L$ gauge coupling (cf. Sec. 1.1). The areas outside of the contours, i.e. towards larger parameter values, are excluded for a V' resonance with corresponding mass.

The CMS search [290], similarly targeting new, heavy resonances with masses between 800 GeV and 4 TeV and exploiting the merged-regime reconstruction, excludes V' bosons with masses below 2.0 TeV for

Model B ($g_V = 3$).

Analyses considering the hadronic decays of the vector bosons have also been performed with 13 TeV data and exclude W' (Z') resonances with masses below 3.15 (2.6) TeV for benchmark *Model B* ($g_V = 3$) [291, 292].

Other searches with Vh intermediate states, but where the h decays to pairs of τ leptons, vector bosons or photons, and targeting either HVT or 2HDMs interpretations, were also presented by both collaborations using 8 TeV data [283, 293, 294].

5.3 The Data Sample, Signal and Background Modelling

The Data Sample

The pp -collision data searched by this analysis was collected with the ATLAS detector in the years 2015 and 2016, where the LHC was operated at a centre-of-mass energy of 13 TeV (cf. Sec. 2). Considering only events that were recorded under stable-beam conditions, where all relevant detector components were fully operational and that fulfil standard data-quality requirements, the analysed dataset corresponds to an integrated luminosity of 36.1 fb^{-1} [162].

The data used in the analysis channel targeting the $\ell\ell bb$ final state was recorded using a combination of lowest, unprescaled single-electron and single-muon triggers, respectively.⁵ As described in Secs. 3.5 and 3.6, the trigger decision is based on the transverse momentum (p_T) of the objects as well as on identification and isolation criteria; varying thresholds and combinations of these requirements are exploited to provide high trigger efficiencies. In order to cope with the increasing instantaneous luminosity throughout the data-taking periods the requirements were occasionally adjusted and tightened. In particular the lowest p_T threshold of the single-muon (single-electron) trigger was increased from 20 (24) GeV used in the 2015 data taking to 24-26 (26) GeV in the 2016 one.

The data used in the analysis channel targeting the $\nu\bar{\nu} bb$ final state was recorded with missing transverse momentum (E_T^{miss}) triggers with thresholds of 70 GeV in the 2015 and 90–110 GeV in the 2016 data-taking periods (cf. Sec. 3.9).

Signal and Background Modelling

For this analysis the various simulated samples used to model the potential signal and several background processes are crucial. Based on the expected signal and background distributions strategies are defined to maximise the signal sensitivity by optimising the signal selection efficiency and the suppression of background contributions. But more importantly even, they are relied on to finally test the different signal and background hypotheses against the data as discussed in Sec. 5.7. While all background processes are normalised to theoretical cross-section predictions, their contributions to the analysis phase space are adjusted in the fit to the data.

⁵The acceptance gain by also considering dilepton triggers was found to be marginal.

The $A \rightarrow Zh$ Signal

Matrix elements for signal events with A bosons decaying to Zh with $h \rightarrow bb$ and $Z \rightarrow \ell\ell$ and $Z \rightarrow \nu\nu$, where $\ell = e, \mu, \tau$, are generated with MADGRAPH5_aMC@NLO 2.2.2 [295] at leading order (LO) accuracy using the NNPDF 2.3 LO [296] set of parton density functions (PDF) for the gluon-fusion production mode and with MADGRAPH5_aMC@NLO 2.2.3 at next-to-leading order (NLO) with massive b quarks using the CT10F4 NLO [121] PDF set for b -associated production. Parton showering and hadronisation are performed with PYTHIA 8 [94] using the NNPDF 2.3 LO [296] PDF set where parameters have been tuned according to the ‘‘A14’’ [297] set. Events are simulated for varying A -boson masses, m_A , ranging between 220 GeV and 2 TeV at different intervals, assuming zero natural width (Γ_A). Since this assumption is deviating from the 2HDM predictions, where the width is a function of the model parameters and exceeds the experimental resolution in certain parts of the parameter space (cf. Sec. 1.3), for the interpretation of the results a procedure is employed, where the reconstructed invariant (transverse) mass of the Zh system is smeared according to a Breit-Wigner function. This approach has been verified to produce at generator level line-shapes that are in agreement with the ones obtained considering a more complete model, which takes non-resonant and interference effects into account, for widths $\Gamma_A/m_A < 10\%$.

As the Higgs boson h is identified with the observed SM-like Higgs boson, its mass, m_h , is fixed to 125 GeV and its width is assumed to be narrow with respect to the limited resolution of the reconstruction in the $h \rightarrow bb$ decay mode. For the interpretation of the results the masses of the other Higgs bosons, H and H^\pm , are assumed to be equal to the mass of the A boson and their natural width to be zero.

For developing the analysis strategy the product of A -boson production cross-section and the branching ratios for the $A \rightarrow Zh$ and $h \rightarrow bb$ decays, $\sigma(gg \rightarrow (bb)A) \times \text{BR}(A \rightarrow Zh) \times \text{BR}(h \rightarrow bb)$, is set to an value of 0.5 pb independent of the A -boson mass. The value corresponds to the expected upper limit at the 95 % confidence level (CL) set on $\sigma(gg \rightarrow (bb)A) \times \text{BR}(A \rightarrow Zh) \times \text{BR}(h \rightarrow bb)$ for an intermediate mass point by the analysis based on 8 TeV data (cf. Sec. 5.2). However, when interpreting the results in terms of 2HDMs, it is considered that the cross sections and the branching ratios of the Higgs bosons are in fact functions of the masses as well as the model parameters with dependencies that are different for each of the considered models (cf. Secs. 1.2 and 1.3). The particular choice of the 2HDM parameters as well as the procedure for the calculation of the cross sections and the branching ratios follows the suggestions laid out in Ref. [70]. Therefore the cross sections for A -boson production both in gluon fusion and b -quark associated production are calculated in the five-flavour scheme as implemented in SUSHI [71–74] considering up to next-to-next-to-leading order (NNLO) QCD corrections.⁶ The results for the b -quark associated production are then combined with calculations performed in the four-flavour scheme [298, 299], following a prescription reported in Ref. [300], referred to as ‘‘Santander matching’’. The calculation of the A -boson width and the branching ratios for the $A \rightarrow Zh$ and $h \rightarrow bb$ decays was done using 2HDMC [78, 79].

Background Processes

The level of background contribution and composition due to different SM processes is different for the analysis channels targeting the $\ell\bar{\ell}b\bar{b}$ and the $\nu\bar{\nu}b\bar{b}$ final states and also varies between the resolved and

⁶The five- and four-flavour schemes refer to whether or not b quarks are considered being part of the initial state when computing hard-processes involving them. Both schemes have (dis)advantages, the latter scheme allows to correctly consider the b -quark mass.

merged regimes as well as the categories targeting the different A -boson production modes. Still, two processes clearly dominate all regions, namely Z -boson production in association with quarks or gluons, in particular with pairs of c quarks and b quarks, and top-quark pair production ($t\bar{t}$). Smaller background contributions arise from various other sources foremost single top-quark and diboson processes. All processes, how they act as a background contribution for the $A \rightarrow Zh$ signal and their modelling is described in the following.

$Z(W)$ +jets With the Z boson decaying to pairs of charged leptons and neutrinos and being produced in association with a b -quark pair, denoted $Z + bb$, the former process exhibits a signature identical to the signal, only few kinematic differences can be exploited to reduce its contribution. Also events where the Z boson is produced in association with a single b quark, single or several c quark(s) and/or light quarks or gluons need to be considered as a background source at reconstruction level, where c jets and light jets happen to be misidentified as b jets; they will be referred to as $Z + cc/bc/bl/cl/l$, respectively, according to the flavour of the jets building the Higgs-boson candidate as discussed in more detail in Sec. 5.4.2.

The corresponding processes where the vector boson is a W boson decaying leptonically to $\ell\nu$ contributes only little to the overall background contribution as there are either additional or missing objects with respect to the signal signature. Events are passing the $\nu\nu bb$ and $\ell\ell bb$ selections at reconstruction level when the lepton is lost or jets are misidentified as a second lepton, respectively.

Events with W or Z bosons decaying to $\ell\nu$ and $\nu\nu$ or $\ell\ell$, respectively, where $\ell = e, \mu, \tau$, and produced in association with partons are simulated with SHERPA 2.2.1 [96]. Using the COMIX [98] and OPENLOOPS [301] generators, matrix elements are calculated at NLO in QCD for up to two and at LO for three or four additional partons. Higher parton multiplicities are modelled with the SHERPA parton shower [302], where double counting is avoided by following the matching and merging procedure of the MEPS@NLO [118] prescription. Since SHERPA 2.2.1 adopts the five-flavour scheme, b and c quarks are treated massless in the matrix element, but massive in the parton shower. The NNPDF 3.0 NNLO [124] PDF set is used with a dedicated parton shower tuning developed by the SHERPA authors in order to improve the description of the LHC data. SHERPA 2.2.1 provides a model for multiple-parton interactions (MPI), and b and c quarks can be produced directly in the hard-scatter process of the underlying event (UE).

In order to ensure that the simulated sample sizes across the full phase space studied in this analysis (and others) are comparable with the expected statistical precision in data, the simulated W and Z samples are split at generation level according to the maximum of the transverse momentum of the vector boson (p_T^V) and the scalar sum of the transverse momenta of all objects (H_T) in the event, obtaining six intervals with the following boundaries: [0, 70, 140, 280, 500, 1000, > 1000] GeV. To further provide simulated samples with sufficient statistical precision also in the specific b - and c -quark-enriched phase space of the analysis, they are also sliced according to the flavour of the hadrons evolving from the partons produced in association with the vector bosons; an exception are the samples of the highest $\max(H_T, p_T^V)$ category, they are inclusive in the flavour of the accompanying hadrons. Events are categorised into three classes containing either at least one b hadron within $|\eta| < 4.0$ or at least one c hadron with $p_T > 4$ GeV and $|\eta| < 3.0$ or no identified b and c hadrons. All simulated $Z \rightarrow \ell\ell$ events moreover satisfy that the invariant mass of the dilepton system ($m_{\ell\ell}$) at generation level is greater than 40 GeV.

The normalisations of the individual simulated samples are such that the sum of all contributions cor-

responds to the total cross section of W or Z production in association with partons calculated with NNLO accuracy in QCD [303].

In order to assess systematic uncertainties related to the modelling of the V +jets processes, as discussed in somewhat more detail in Sec. 5.6.2, an alternative simulation is used. MADGRAPH5_aMC@NLO is used to generate matrix elements up to four additional partons in LO, based on the five-flavour scheme, thus treating b and c quarks as massless, as well as the NNPDF v2.3 LO PDF set. Higher parton multiplicities are modelled by the parton shower which is provided by the PYTHIA 8 generator, using the same PDF set and the “A14” tune. Here b and c quarks are treated as massive.

Top-quark pairs Although decays of $t\bar{t}$ pairs, where each top quark almost exclusively decays to a W boson and a b quark, exhibit additional objects (or is missing some) with regard to the final states of the signal processes, they constitute an important background source in particular for the $\nu\bar{\nu}b\bar{b}$ final state due to the large cross-section of $t\bar{t}$ production. With the W bosons decaying either hadronically into pairs of quarks or leptonically into $\ell\nu$, with $\ell = e, \mu, \tau$, three different final states can be distinguished, where the fully hadronic one can be neglected in this analysis due to leptons missing to mimic the signal signatures. While in the analysis channel targeting the $\ell\bar{\ell}b\bar{b}$ final state, background mainly originates from the fully leptonic $t\bar{t}$ decay, in the channel targeting the $\nu\bar{\nu}b\bar{b}$ final state background arises from $t\bar{t}$ decays where one W boson decays leptonically and the other one hadronically. The $t\bar{t}$ contribution in the channel targeting the $\ell\bar{\ell}b\bar{b}$ final state can be reduced efficiently given the presence of neutrinos that are missing in the signal signature, but even more so kinematic differences. In particular requiring leptons with Z -decay-like features, namely being of the same family and that $m_{\ell\ell}$ is compatible with the nominal Z mass, allows to strongly diminish the $t\bar{t}$ contribution. Missing those handles at reconstruction level in the analysis channel targeting the $\nu\bar{\nu}b\bar{b}$ final state, here the $t\bar{t}$ contamination can only be reduced by vetoing additional leptons with respect to the signal final state, making $t\bar{t}$ production the dominant background process.

Matrix elements for the production and decay of $t\bar{t}$ events are generated at NLO with POWHEG-Box (Version v2) [102–105], using the CT10 [121] PDF sets and preserving the top-quark spin correlations. For parton showering as well as for modelling the fragmentation and the UE, PYTHIA 6 [22] is used with the CTEQ6L1 [260] PDF set and the corresponding Perugia 2012 tune (P2012) [304]. The resummation damping factor h_{damp} that controls the matching between matrix element and parton shower is chosen to be equal to the top-quark mass, which is set to 172.5 GeV. As it determines the transverse momentum of the first additional emission beyond Born level, it effectively regulates the scale of the hard emission against which the $t\bar{t}$ system is recoiling. The particular choice of h_{damp} to be equal to the top-quark mass was shown to yield a good description of the LHC data collected at 7 TeV, also at large p_{T} of the top quarks and the $t\bar{t}$ system [305]. In order to obtain a better agreement with data collected at 13 TeV, the predicted p_{T} spectra of the top quarks and the $t\bar{t}$ system are reweighted sequentially to agree with the corresponding NNLO parton-level spectra [306], referred to as *NNLO reweighting* in the following. Since, as reasoned above, the fully hadronic decay of the $t\bar{t}$ system can be neglected in this analysis, already at generation level at least one W boson is required to decay leptonically.

The normalisation of the simulated events is such that it agrees with the cross sections for $t\bar{t}$ production calculated with NNLO accuracy, including the resummation of next-to-next-to leading logarithm (NNLL) soft gluon terms with `top++ 2.0` (cf. Ref. [307] and references therein).

As described in more detail in Sec. 5.6.2, in the case of the $t\bar{t}$ process related modelling uncertainties are

assessed by comparisons of the nominal predictions to those obtained with both the same generators, but different settings than described above, or using two alternative simulations. In the case of both alternative samples the parton showering, hadronisation and UE are modelled by the Herwig++ [95] generator using the CTEQ6L1 PDF set and the “UE-EE-5” [308] tune, provided by the authors to better describe UE and the effective cross-section of double-parton interactions (DPI). While for one of them also the PowHEG-Box v2 is used to generate the matrix elements, the other relies on the MadGraph5_aMC@NLO generator equally using the CT10 PDF sets.

Single top Also the production of single top quarks constitutes a background for this analysis, in particular when produced in the Wt -channel in association with a W boson. While exhibiting the same or similar final state objects as the decay of the before discussed $t\bar{t}$ process, due to the smaller cross section and differences in the event topology its contribution to the total background contamination is very small and almost negligible in both the analysis channel targeting the $\nu b b$ and $\ell b b$ final states.

Events for single-top processes are simulated separately for the different production modes, s -, t - and Wt -channel, as well as for top and anti-top quarks. Similarly as for the production of $t\bar{t}$ events, Pythia 6 is interfaced to PowHEG-Box which is an earlier version (Version v1). PowHEG-Box v1 bases the NLO matrix elements calculations on the four-flavour scheme together with the fixed four-flavour CT10F4 [121] PDF set. Preservation of the top-quark spin correlations is achieved here by using MadSpin [309] to decay the top quarks. For simulating single-top events produced in the s - and t -channels, the W boson is required to decay leptonically at generation level; in the case of the simulation of the Wt -channel production used in the analysis channel targeting the $\ell b b$ final state this requirement is applied to both W bosons in the event, while no such requirement exists for the simulation of this channel used in the analysis targeting the $\nu b b$ final state. Event samples for s - and t -channel production are normalised such that the assumed cross sections match those calculated at NLO in QCD with the Hathor v2.1 [310, 311] program for a top-quark mass of 172.5 GeV. The cross section used as reference for the Wt -channel production is obtained from an approximate NNLO calculation [312, 313] for the same top-quark mass using the MSTW2008 NNLO [122, 123] PDF set.

Diboson Another background source with a rather small contribution arises from diboson production, i.e. WW , WZ and ZZ , where one of the vector bosons decays leptonically, $Z \rightarrow \ell\ell$, $Z \rightarrow \nu\nu$ or $W \rightarrow \ell\nu$, and one hadronically, $W/Z \rightarrow qq$. In particular $ZZ \rightarrow \ell\ell(\nu\nu)bb$ mimics the signal signature in the considered decay channels; smaller contributions arise at reconstruction level from misidentification of non- b jets as b jets or failing to identify leptons from W boson decays, e.g. from $WZ \rightarrow \ell\ell(\nu\nu)qq$ or $WZ \rightarrow \ell\nu b b$.

Diboson production in those particular final states (i.e. leptonic-hadronic) is simulated using the Sherpa 2.1.1 generator. It provides matrix elements calculated at NLO for up to one parton in the case of ZZ production and for no additional partons in the case of WW and WZ production as well as LO matrix elements for up to three additional partons via the Comix and OpenLoops generators. Also here, higher parton multiplicities are modelled with the Sherpa parton shower and double counting is avoided following the ME+PS@NLO prescription. Using the CT10 PDF set, an improved description of data is obtained by a dedicated parton shower tuning provided by the Sherpa developers. The normalisations of the simulated samples are as

predicted by cross-section calculations with NLO accuracy.⁷

Other processes Also the production of a Higgs boson h with a mass of 125 GeV in association with a Z (W) boson as expected in the Standard Model is considered as a background source, exhibiting the same final state objects as the searched for decay modes of the A boson. Events are simulated at LO with PYTHIA 8 using the NNPDF 2.3 LO PDF set, except for the gluon-initiated Zh production where PYTHIA 8 with the CTEQ6L1 PDF set is only used for parton showering as well as UE and MPI modelling and the matrix elements are calculated at NLO with POWHEG-Box v2 using the CT10 NLO PDF set. In both setups parton shower (and MPI) tunes were applied, namely the “A14” and the “AZNLO”[314] tunes, respectively. The normalisations of the simulated samples is such that the Wh and the *total* Zh contributions correspond to the respective cross sections calculated with NNLO accuracy in QCD and considering NLO EW corrections [19].

Despite the very small cross section it is necessary to also consider contributions from $t\bar{t}$ production in association with a vector boson or a SM Higgs boson h ; in particular in analysis categories targeting the b -associated A -boson production their contribution is not negligible. Both the $t\bar{t}V$ and the $t\bar{t}h$ processes are simulated with MADGRAPH5_aMC@NLO 2.2.2 interfaced to PYTHIA 8 as for the signal, using also the same settings as described above. The mass of the Higgs boson is set to 125 GeV, and all decay modes allowed in the Standard Model are considered with the predicted branching fractions. The provided normalisations correspond to cross sections calculated at NLO.

Given the large cross section, multijet production via strong interactions potentially contributes to the overall background despite lacking prompt leptons. Charged leptons stemming from b and c hadron decays or misidentified jets generally fail to mimic leptons compatible with coming from a Z -boson decay as expected for the $\ell\bar{\ell}b\bar{b}$ final state: they are usually not isolated and the lepton pair only exhibits by chance the same flavour and an invariant mass that is in agreement with the nominal Z mass. This assumption was confirmed by a data-driven estimate performed in the context of the analysis searching for the SM Higgs boson in the decay to a b -quark pair and produced in association with a vector boson [248], thus targeting the same final state.

In the channel targeting the $\nu\bar{\nu}b\bar{b}$ final state multijet contamination mainly arises due to mismeasurements of the jet energy at reconstruction level leading to missing transverse momentum expected from the presence of (prompt) neutrinos in the final state. Kinematic differences with respect to the signal are exploited as detailed in Sec. 5.4.3 to suppress this background source sufficiently so that it can be neglected afterwards. Both for deploying the kinematic selection as well as estimating the remaining, negligible multijet contribution, events are simulated with PYTHIA 8 using the NNPDF2.3LO PDF set and the “A14” tune. The result was furthermore confirmed by a data-driven estimate performed as well in the context of the SM Vh analysis targeting the same $\nu\bar{\nu}b\bar{b}$ final state.

Interfaced Generators and Detector Simulation

Acknowledging the importance of an improved modelling of b - and c -hadron decays with respect to what most parton showers have implemented so far, as well as to ensure a consistent treatment across simulations obtained using different event generators [315], b - and c -hadron decays are commonly described

⁷The cross sections are directly computed with the SHERPA 2.1.1 generator, but since a set of slightly outdated electroweak parameters was used a correction factor of 0.91 needs to be applied taking this difference into account.

exploiting an interface to the EVTGEN [226] program. Only simulations provided by the SHERPA generator are exceptions; mainly because of technical reasons, but great effort was made by the SHERPA authors to reach a similar level of describing b - and c -hadron decays as with EVTGEN.

In the case the PYTHIA 6 generator is used, PHOTOS [266] is interfaced for modelling QED final-state radiation and TAUOLA [265] for simulating τ -lepton decays.

In all simulated event samples the effect of additional pp interactions in the same and neighbouring bunch crossings (pile-up) is taken into account by overlaying minimum-bias events with the single-, double- and non-diffractive pp processes simulated by the PYTHIA 8 generator using the MSTW2008 LO PDF set with the “A2” tune.

All simulated events are processed through a full ATLAS detector simulation; only in the case of the signal samples for b -associated production AFII is exploited (cf. Sec. 2.2.7).

5.4 Event Reconstruction and Selection

A -boson candidates are reconstructed via their decay to a Z boson and a Higgs boson h , where the former decays leptonically to a pair of charged leptons or neutrinos and the latter to a pair of b quarks, defining two final states, $\ell\ell bb$ and $\nu\nu bb$, respectively. In the analysis channel targeting the $\ell\ell bb$ final state Z -boson candidates are fully reconstructed from pairs of electrons or muons, while in the analysis channel targeting the $\nu\nu bb$ final state the decay of Z -boson candidates can only be inferred by the presence of large amounts of missing transverse momentum. As the aim of the analysis is to search for A bosons in a wide mass range from 220 GeV to 2 TeV, different strategies are employed to efficiently reconstruct the Higgs-boson candidate in the different event topologies. They define two kinematic regimes: the resolved and the merged regime.

The physics objects used in the analysis are defined in Section 5.4.1 based on the reconstruction and identification techniques laid out in Chap. 3.

Section 5.4.2 details the event reconstruction, in particular of the Higgs-boson and the A -boson candidates, and the related regime definitions. The final discriminants of the analysis, the reconstructed invariant and transverse mass of the A -boson candidates, are defined and strategies to improve their resolutions are discussed.

In Section 5.4.3, the event selections for the two analyses channels are described, which somewhat differ for the resolved and merged regimes. The impact of an optimised selection in the channel targeting the $\ell\ell bb$ final state is assessed with respect to the previous result.

5.4.1 Definition of the Physics Objects

This section defines the physics objects used to reconstruct A -boson candidates in the targeted $\ell\ell bb$ and $\nu\nu bb$ final states or to suppress background contributions: muons, electrons, missing transverse momentum, jets - identified as originating from b -quarks-, as well as τ_{had} leptons (cf. Chap. 3).

In order to only consider muons of good quality, while maximising the selection efficiency, muons are required to pass the *Loose* identification criterion. Muons likely stemming from secondary processes (e.g. b/c -hadron decays) or pile-up interactions are discarded by (i) requirements on the transverse and longitudinal impact parameters d_0 and z_0 (cf. Sec. 3.1): $|\sigma_{d_0}/d_0| < 3$, with σ_{d_0} being the uncertainty on d_0 ,

and $|\Delta z_0 \sin(\theta)| < 0.5$ mm, as well as (ii) considering only candidates which pass the variable-cone track-based isolation criterion *LooseTrackOnly* that provides a constantly high signal efficiency also for high- p_T muons. Muon candidates with $p_T^\mu > 7$ GeV and $|\eta| < 2.7$ satisfying the above criteria are referred to as *loose* muons in the following; those with $p_T^\mu > 25$ GeV and $|\eta| < 2.5$ as *medium* muons.

Only electrons built from clusters unaffected by calorimeter imperfections that are within $|\eta| = 2.47$ are considered. They are required to fulfil criteria identifying them as prompt, i.e. not stemming from decays in flight, photon conversions or additional pp interactions, and isolated, in order to reduce the probability of having them incorrectly identified as jets. They are similar to the ones for muons described above: in addition to passing the *Loose* likelihood-based identification and *LooseTrackOnly* isolation criteria, their tracks need to satisfy $|\sigma_{d_0}/d_0| < 5$ and $|\Delta z_0 \sin(\theta)| < 0.5$ mm. Electron candidates fulfilling such characteristics with $p_T^e > 7$ (25) GeV are referred to as *loose (medium)* electrons.

Since the analysis is not targeting the Z -boson decay to τ leptons, hadronically decaying τ leptons, τ_{had} , are identified to (i) disentangle them from jets and thereby improve the jet-multiplicity estimate and (ii) to suppress contributions from background processes in the analysis channel targeting the $\nu b\bar{b}$ final state. Focusing on 1- or 3-prong τ_{had} -leptons, candidates are required to have exactly one or three associated tracks. In order to reject jets being incorrectly identified as τ_{had} objects, candidates need to pass the *Medium* identification criterion. Only τ_{had} leptons with $p_T > 20$ GeV and within $|\eta| = 2.5$, excluding the transition region ($1.37 < |\eta| < 1.52$), are considered.

This analysis makes use of three types of jets that are all reconstructed with the anti- k_r algorithm, but differ regarding the used input information and radius parameter (R), as described in detail in Sec. 3.3. The first type are calorimeter-based jets with $R = 0.4$, also referred to as *small-R jets*. Central small-R jets ($|\eta| < 2.5$) with a minimum p_T of 20 GeV, for which b -tagging information is available, are distinguished from *forward* small-R jets which fulfil $2.5 < |\eta| < 4.5$ and have a minimum p_T of 30 GeV. In order to suppress jets originating from in-time pile-up activity, small-R jets with $p_T < 60$ GeV and $|\eta| < 2.4$ need to pass a requirement on the jet-vertex tagger: $\text{JVT} \geq 0.59$.

Jets, referred to as *large-R jets*, are also reconstructed from calorimeter information, but with a larger radius parameter of $R = 1.0$. In order to remove contaminations from energy deposits that originate from initial-state radiation, pile-up interactions or underlying event, they are *trimmed* as described in Sec. 3.3.1. Only large-R jets with $p_T > 250$ GeV and $|\eta| < 2.0$ are selected. In order to exploit the optimal jet-mass resolution over the full p_T range the *combined jet mass* definition is used.

The third type of jet utilised in this analysis are *track jets* built from high-quality ID tracks with radius parameter $R = 0.2$. Only track jets with at least two track constituents, $p_T > 10$ GeV and $|\eta| < 2.5$ are considered. While track jets are lacking information on neutral components, also emerging in the hadronisation process, they are pile-up resistant and provide excellent directional resolution. This is exploited to resolve the substructure of large-R jets and/or to obtain b -tagging information, as discussed in some more detail in Secs. 5.4.2 and 5.5.2.

The presence of neutrinos in an event can be inferred from a momentum imbalance in the transverse plane, the missing transverse momentum (E_T^{miss}): computed as described in Sec. 3.9, the analysis relies on a variant with a track-based *soft term* which is pile-up resistant (TST E_T^{miss}). In addition a (almost) completely track-based missing transverse momentum, denoted $E_{T,\text{trk}}^{\text{miss}}$, is exploited in the analysis; oblivious to any neutral contributions, and thus not able to provide a reliable estimate of the total missing transverse momentum in the event, it is used because of its pile-up independence.

As the different object reconstruction and identification algorithms exploit the same or similar detector information independently, it is not guaranteed that only a single physics object is reconstructed from it. Potential ambiguities are removed by following an *overlap-removal* prescription which was optimised for boosted topologies, where different physics objects happen to be very close to each other. In particular the overlap between loose electrons or muons, τ_{had} candidates and jets, as defined above, is resolved with the following step-wise procedure, where in a certain step only those objects are considered that were not already discarded in previous ones.

Thus, any τ_{had} object is removed, if a loose electron or muon is found with $\Delta R(\tau_{\text{had}}, e/\mu) < 0.2$, where ΔR is the angular distance defined in Sec. 2.2. If a loose electron is sharing an inner-detector track with a loose muon, it is removed; unless the muon is of type *Calorimeter-tagged*, in which case the muon is removed instead. If a small-R (large-R) jet is found closer to an electron than $\Delta R = 0.2$ (1.2), the jet is removed; since energy deposits in the calorimeter stemming from an electron are expected to be clustered as a jet as well. If an electron with transverse momentum p_{T}^e is reconstructed within $\Delta R = \min[0.04 + 10 \text{ GeV}/p_{\text{T}}^e, 0.4]$ to the axis of a small-R jet, it is removed; it likely stems from a semi-leptonic heavy flavour decay. Similarly, if a small-R jet is found closer to a loose muon than $\Delta R = 0.2$, it is removed; unless the jet has at least three associated tracks and the muon energy contributes only little to the total jet energy,⁸ making it unlikely that the jet is actually a muon, in which case the muon is removed instead. Muon candidates likely originating from semi-leptonic heavy flavour decays are removed based on the same criterion as electron candidates. Finally, small-R jets found within $\Delta R = 0.2$ to a τ_{had} object are discarded. Overlap between small-R and large-R jets is not resolved at this stage, but rather as part of the analysis strategy described in detail in Sec. 5.5.1.

As indicated before, *b*-tagging information is only available for small-R and track jets in the central region. In this analysis, the MV2c10 discriminant is exploited and jets passing the criterion of the 70% operating point are referred to as being *b-tagged*. This operating point provides in simulated $t\bar{t}$ events on average a *b*-jet tagging efficiency of 70% with a light-jet mistag rate and a *c*-jet tagging efficiency of 0.26% (0.84%) and 8.2% (14.1%) for small-R jets (track jets), respectively.

5.4.2 Event Reconstruction

This section details the reconstruction of $A \rightarrow Zh$ candidates in the $\ell\ell bb$ and $\nu\nu bb$ final states using the physics objects defined in the previous section. In particular the two strategies that are used to efficiently reconstruct the $h \rightarrow bb$ candidates across the searched *A*-boson mass range are discussed, and the corresponding resolved and merged analysis regimes are defined.

The reconstructed invariant and transverse mass of the *A*-boson candidates are introduced as final discriminants in the analysis channel targeting the $\ell\ell bb$ and $\nu\nu bb$ final state, respectively.

Since the Higgs-boson reconstruction involving jets in general and *b* jets in particular results in a limited resolution of the candidates' mass, several dedicated corrections are employed to improve especially the mass resolution of the *A*-boson candidates.

⁸More precisely it is required that less than 30% of the sum of the p_{T} of the tracks associated with the jet and less than 50% of the jet p_{T} is contributed by the muon.

Higgs-boson candidate reconstruction: the resolved and merged regimes

If the b -quarks stemming from the Higgs-boson decay are separated, each of them can be reconstructed, or *resolved*, by one small-R jet, defining the *resolved regime*. Since the small-R jets are built using the anti- k_t algorithm with a distance parameter $R = 0.4$, the minimum distance between the b quarks, in order to be identified as two individual jets, is approximately of the same order: $\Delta R(b_1, b_2) = 0.4$.

The angular separation between the decay products is closely related to the transverse momentum of the mother particle: is the Higgs boson produced at rest, or with low p_T^h , the b quarks are emitted in opposite directions, or at least far away from each other; with increasing boost of the Higgs boson, the angular separation of the b quarks gets reduced, up to the point, where it falls below the before-mentioned threshold and the previously individual jets “merge”. For large Higgs-boson transverse momentum $p_T^h \gg m_h$ and assuming that the energy of the Higgs boson is equally distributed to the two b quarks, their angular separation can be approximated via

$$\Delta R(b_1, b_2) \approx \frac{2 \cdot m_h}{p_T^h}, \quad (5.1)$$

suggesting that the point of merging is reached, when $p_T^h \approx 625$ GeV (assuming $m_h = 125$ GeV).

Such boosted topologies are addressed by using another strategy to reconstruct the Higgs-boson candidate: it is identified with a large-R jet (and its substructure is resolved using track jets); this scenario is referred to as *merged regime*. Since the large-R jets are built with a radius parameter $R = 1.0$, Eq. 5.1 indicates that the b -quark pair starts to be captured by a single large-R jet for $p_T^h \approx 250$ GeV; motivating the p_T threshold for large-R jets of the same value as discussed in the previous section. It was shown in simulation that the efficiency to reconstruct a Higgs boson decaying to a b -quark pair in this way, increases rapidly with the transverse momentum and is above 95 % for $p_T^h > 400$ GeV (and $|\eta| < 2.0$) [316].

While it happens only in about 10 % of the simulated signal events that more than one large-R jet is found - in which case the leading large-R jet is identified with the Higgs-boson candidate-, in the resolved regime there are on average three to four small-R jets expected, from which two candidate jets need to be selected for reconstructing the Higgs-boson candidate.

Considering also the available b -tagging information, several strategies were tested and the following one was found to perform best, when taking the impact on the background contribution into account as well. In events, where at least two b -tagged jets are found, the two (leading ones, i.e. with highest p_T) are identified as stemming from the Higgs-boson decay. While this choice is obvious for events with exactly two b -tagged jets, this is not necessarily the case in events with more than two b -tagged jets, as expected for b -associated A -boson production. However, basic studies considering (in addition) spatial information did not indicate there was a better assignment strategy.

Due to the limited b -tagging efficiency, in a large fraction of signal events only one small-R jet is identified as containing a b hadron (independent of the considered A -boson production mode, cf. Sec. 5.5.2). In this case, the Higgs-boson candidate is reconstructed from the b -tagged jet and the leading non- b -tagged jet. In events, where none of the jets are b -tagged, the leading two small-R jets are selected for the Higgs-boson reconstruction.

While in the merged regime the Higgs-boson candidate is selected without making use of the available b -tagging information, it is exploited to define similar b -tag categories as in the resolved regime, as discussed in more detail in Sec. 5.5.2.

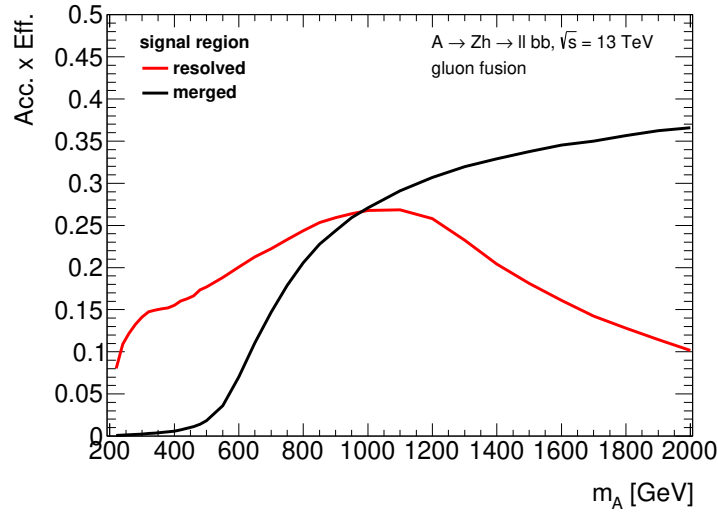


Figure 5.7: Comparison of the expected acceptance times efficiency of $A \rightarrow Zh \rightarrow \ell\ell bb$ as function of the A -boson mass m_A between the resolved and merged regimes, as defined in the text, after the event selection targeting this final state described in Sec. 5.4.3.

Since b -tagging information is not available for large- R jets, whether or not they are likely to contain b hadrons is identified by means of track jets. In a first step, track jets are matched to large- R jets using the ghost-association technique described in Sec. 3.3. According to Eq. 5.1, this procedure allows to resolve the substructure of Higgs-boson candidates with (at least) two track jets with radius parameter $R = 0.2$ up to $p_T^h \approx 1.2$ TeV; beyond that, it is expected that the b -quark pair gets captured by a single track jet. Although this extreme phase space is only probed by the HVT search, the candidate large- R jet is commonly required to have *at least one* associated track jet; especially since no loss in sensitivity was observed for the presented analysis. In a second step, the b -tagging information available for the track jets is used for the event categorisation. In the case, that there are more than two track jets associated to the candidate large- R jet, only the two leading ones are considered for b -tagging; following the strategy proposed in Ref. [317].

Given the close linear relation between the transverse momentum of the Higgs (and Z) boson and the mass of the A boson, which of the described reconstruction strategies is more appropriate and provides a better signal efficiency, depends strongly on the considered A -boson mass and, to a lesser extent, on the required selection criteria that are somewhat tailored to the topology of each regime (cf. Sec. 5.4.3). Figure 5.7 shows for the analysis channel targeting the $\ell\ell bb$ final state a comparison of the product of the expected signal acceptance and reconstruction efficiency in the resolved and merged regimes, after applying event selections detailed in the next section, as a function of the true A -boson mass m_A . As expected, the resolved regime clearly dominates at low A -boson masses, corresponding to low Higgs-boson transverse-momenta and widely separated decay products; the merged regime has a turn-on at $m_A \approx 500$ GeV, reflecting the required minimum p_T of the large- R jets of 250 GeV. At $m_A \approx 1$ TeV, the merged regime starts to be dominant; Higgs-boson transverse-momenta are reached that cause the b quarks to become collimated and no longer reconstructable as two separate small- R jets. Nonetheless, the contribution by the resolved

regime stays significant up to the highest considered masses. As a consequence, over a wide m_A range, there are events that can be successfully reconstructed with both strategies, and thus are considered in Fig. 5.7 in both the resolved and the merged regime; their fraction reaches a maximum of about 60 % in the transition region at $m_A \approx 1$ TeV. Several different approaches were tested to avoid such a double-counting and to define orthogonal analysis categories by assigning events exclusively to one regime; they are extensively discussed in Sec. 5.5.1.

The final discriminants: m_{Vh} and $m_{T,Vh}$

The information on the Higgs-boson candidate is combined with the available knowledge on the Z -boson decay in order to build the final discriminants of the analysis that approximate the A -boson mass. In the analysis channel targeting the $\ell\bar{\ell}b\bar{b}$ final state, the A -boson candidate mass can be fully reconstructed as the invariant mass of the two leptons and the Higgs-boson candidate, and is denoted m_{Vh} . As this is not possible in the $\nu\bar{\nu}b\bar{b}$ final state due to the presence of neutrinos, the transverse mass defined as

$$m_{T,Vh} = \sqrt{(E_T^h + E_T^{\text{miss}})^2 - (\vec{p}_T^h + \vec{E}_T^{\text{miss}})^2}, \quad (5.2)$$

is used as a final discriminant; where E_T^h is the transverse energy and \vec{p}_T^h is the transverse-momentum vector of the Higgs-boson candidate. The m_{Vh} and $m_{T,Vh}$ distributions are used to search for a signal as described in Sec. 5.7.

Corrections to the candidate-mass resolution

Since the mass of the Higgs-boson candidate is not only entering the definition of the final discriminants, but is also an important kinematic quantity to discriminate between the signal and the dominant, non-resonant background processes, $t\bar{t}$ and V +jets, a good resolution is beneficial both in terms of signal acceptance and sensitivity. Therefore, it is improved by means of dedicated corrections applied sequentially to the jet(s) it is reconstructed from. Originally developed for the SM Vh ($h \rightarrow b\bar{b}$) analysis [318], the methods were revisited for the resolved regime of this analysis and partially adapted in order to be applicable in the merged regime as well [317].

The peculiarities of jets emerging from b quarks (and to a lesser extent c quarks) demand corrections beyond the standard jet calibration which, as discussed in Sec. 3.3, is designed to improve the response of a sample inclusive in the jet flavour, and thus dominated by light jets. Since b hadrons in the ground state decay via the weak interaction, about 40% of their decays involve neutrinos and about 20 % also muons; the former completely escape detection and the latter are not contained in the calorimeter, leading to a jet response for b jets away from unity.

However, since soft muons ($p_T > 5$ GeV) can be reconstructed efficiently from tracking information, the latter effect can be mitigated with the *muon-in-jet* correction: if a non-isolated, soft muon is found inside a b -tagged small-R or track jet (i.e. $\Delta R(\text{jet}, \mu) < 0.4$ and 0.2 , respectively), its four-momentum is added to that of the small-R jet, or the large-R jet with which the track jet is ghost-associated; the energy expected to be deposited by the muon in the calorimeter is removed. In the case that more than one soft muon is found inside the b -tagged small-R or track jet, only the one closest to the jet axis is taken into account.

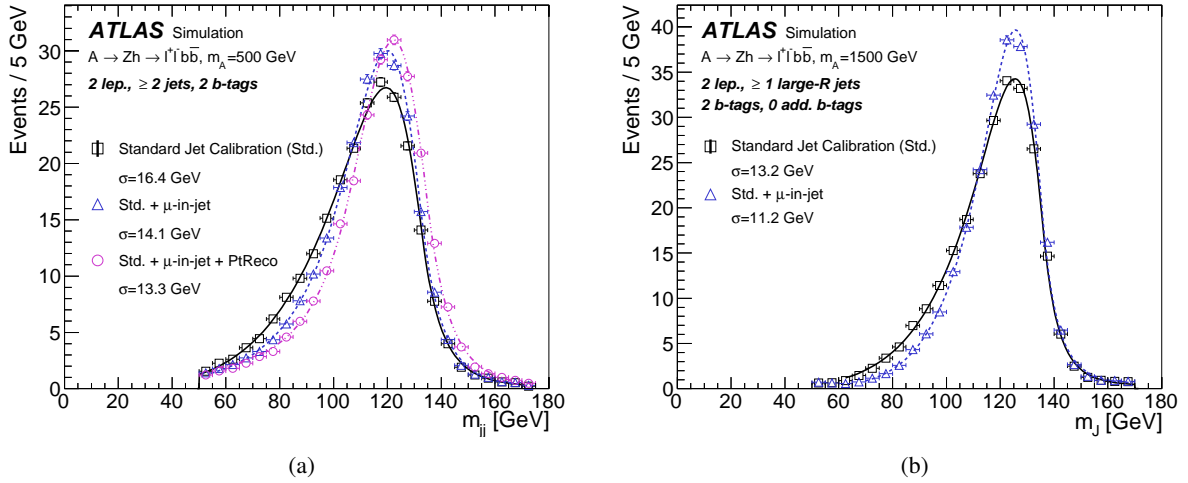


Figure 5.8: Reconstructed Higgs-boson candidate mass in the (a) resolved regime and (b) merged regime in simulated $A \rightarrow Zh \rightarrow \ell\ell b\bar{b}$ events with A -boson masses of $m_A = 500$ GeV and $m_A = 1500$ GeV, respectively. Compared are the spectra after the sequential application of the different b -jet energy corrections described in the text and after the event selections targeting this final state (except the Higgs-boson-mass requirement) described in Sec. 5.4.3. The shown resolution parameter σ is obtained from a fit of an asymmetric function described in Ref. [319]. Previously published in Ref. [6].

The impact of this correction on the reconstructed Higgs-boson mass in simulated signal events is shown for the analysis channel targeting the $\ell\ell b\bar{b}$ final state in Fig. 5.8, separately in the resolved and merged regimes for representative A -boson masses of $m_A = 500$ GeV and 1.5 TeV. Relative to the standard jet calibration, the resolution of the Higgs-boson-candidate mass improves by 14(15)% in the resolved (merged) regime. The magnitude of the improvement varies with the considered A -boson mass and also depends on the regime: it ranges from about 9% at very low m_A in the resolved regime to almost 20% at high m_A in the merged regime. The improvement also translates into a better resolution of the invariant mass of the Zh system by about 5-10%. (Also the $m_{T,Vh}$ resolution is improved, however to a lesser extent given the generally limited resolution.)

In the resolved regime, a second dedicated correction is applied that improves the jet response, and thus the m_h and m_{Vh} ($m_{T,Vh}$) resolutions, denoted *PtReco*. It is derived from the jet response determined in a simulated SM Vh ($h \rightarrow b\bar{b}$) sample as the difference between the transverse momentum of reconstructed b -tagged small-R jets, after muon-in-jet correction, and small-R jets built from the simulated final state particles including muons and neutrinos. This procedure corrects both for energy that is deposited outside the jet cone, which happens more frequently for b jets compared to light jets, as the decay products are emitted under a wider angle due to the larger b -hadron mass, and the energy carried away undetected by neutrinos. The magnitude of the correction depends not only on the p_T of the small-R jets, but also on whether soft muons or electrons are found inside them; in that case the correction is higher, accounting for an on average larger missing momentum fraction from the accompanying neutrinos.

After applying the *PtReco* correction, the transverse momentum of b -tagged small-R jets (containing soft muons or electrons) is increased by up to 12(24)% at low p_T and by up to 1.0(10)% for $p_T > 100$ GeV.

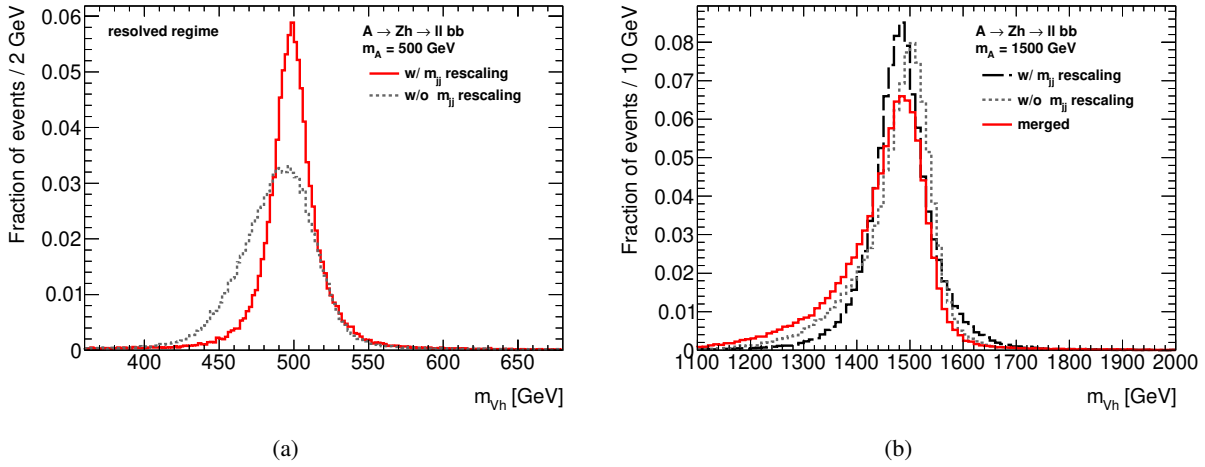


Figure 5.9: Impact of the m_{jj} -rescaling in the resolved regime on the reconstructed mass of the A -boson candidate m_{Vh} in simulated $A \rightarrow Zh \rightarrow \ell\bar{\ell}b\bar{b}$ events with A -boson masses (a) $m_A = 500$ GeV and (b) $m_A = 1500$ GeV. In Figure (b), the m_{Vh} distribution obtained in the merged regime is overlaid for illustration.

While the resolution of the reconstructed Higgs-boson mass is only slightly further improved, by 3 to 6 % depending on the considered m_A , the maximum of the spectrum is shifted closer to the target value of $m_h \approx 125$ GeV, as can be seen from Fig. 5.8(a). The improvement is propagated almost undiminished to the m_{Vh} resolution.

A per-event kinematic likelihood fit, constraining the $\ell\bar{\ell}b\bar{b}$ system to be balanced in the transverse plane (in events with zero or one additional (large- R) jet), as used instead of the PtReco correction in the SM Vh ($h \rightarrow b\bar{b}$) analysis, was investigated. However, the achieved improvement beyond the PtReco correction was considered not sufficient (at the time).⁹

The largest improvement of the m_{Vh} and $m_{T,Vh}$ resolutions is obtained by employing the measured nominal values of the Higgs- and Z -boson masses in their calculation. In the signal regions of the resolved regime, where the Higgs-boson-candidate mass is required to be compatible with the nominal value of 125 GeV (cf. Sec. 5.4.3), the four-momentum of the dijet system is scaled by $125 \text{ GeV}/m_{jj}$, where m_{jj} is the dijet invariant mass. In addition, in all regions of the $\ell\bar{\ell}b\bar{b}$ analysis channel, the four-momentum of the dimuon system is scaled by $91 \text{ GeV}/m_{\mu\mu}$, with $m_{\mu\mu}$ being the dimuon invariant mass. Given that the energy and momentum resolution of the calorimeter improves with increasing energy/momentum and the momentum resolution of the tracking systems decreases with increasing momentum, the m_{jj} -rescaling particularly helps to improve the m_{Vh} (an $m_{T,Vh}$) resolution at small m_A , while the $m_{\mu\mu}$ -rescaling shows its rather small effect only for (very) large m_A . Evaluating the effect of the rescalings on the m_{Vh} resolution in simulated $\ell\bar{\ell}b\bar{b}$ signal events shows that the improvement indeed decrease with increasing A -boson mass: it is as high as 60 % at (very) low m_A and up to 15 % at (very) high m_A .¹⁰

Figure 5.9 demonstrates the impact of the m_{jj} -rescaling on the m_{Vh} distribution in simulated $\ell\bar{\ell}b\bar{b}$

⁹There are indications that a dedicated optimisation of the Higgs-boson-mass window would help to reveal a stronger impact on m_{Vh} .

¹⁰A corresponding rescaling of the dielectron invariant mass, that would also address the limited energy resolution of the calorimeter for small energies, is omitted since its impact on the m_{Vh} resolution is negligible with respect to the m_{jj} -rescaling.

signal events. The comparison of the m_{Vh} distribution before and after the m_{jj} -rescaling in Fig. 5.9(a), clearly illustrates the significant improvement of the m_{Vh} resolution and peak position for an hypothesised A boson with $m_A = 500$ GeV. The same comparison shown in Fig. 5.9(b) for a signal with $m_A = 1.5$ TeV, conveys a much smaller effect on the m_{Vh} resolution; while the tail towards low mass gets reduced, a slight shift of the maximum away from the true m_A can be observed. For illustration, in Fig. 5.9(b) also the m_{Vh} distribution is overlaid that is obtained in the merged regime, where only the $m_{\mu\mu}$ rescaling is performed: it is broader and exhibits in particular a tail towards low m_{Vh} values relative to the m_{Vh} shape in the resolved regime. However, a corresponding rescaling of the large-R jet mass was not considered, given that no gain in sensitivity was found when studied in the context of Ref. [286].

5.4.3 Event Selection

The event selection described in the following aims not only at efficiently selecting high-quality events matching the $A \rightarrow Zh$ signature in the $\ell\ell bb$ and $\nu\nu bb$ final states, but also at suppressing background contributions mimicking the signal signature (cf. Sec. 5.3). The signal selection is completed, and independent regions with varying signal fractions and signal-to-background ratios are defined, by further categorising the events passing the selection, as discussed in Sec. 5.5.

Only high-quality events are considered that (i) fulfil standard data-quality criteria, (ii) have a primary vertex compatible with a vertex from a hard-scattering event (cf. Sec. 3.1), and (iii) are free of *Loose bad* small-R jets to suppress fake jets (cf. Sec. 3.3.4).

In order to be able to reconstruct a Higgs-boson candidate as described in the previous section, only events containing either at least two small-R jets or at least one large-R jet with one ghost-associated track jet are selected. In addition, the leading small-R jet of the pair building the Higgs-boson candidate is required to have $p_T > 45$ GeV. While the two reconstruction schemes in principle define two analysis categories - to which dedicated selection criteria are applied-, they do not constitute independent regions at this point: there is a rather large fraction of events that end up in both the resolved and merged regimes. Thus, the orthogonality of the kinematic regimes needs to be enforced by defining a strategy according to which events are assigned exclusively to one regime; this is the topic of Sec. 5.5.1.

The orthogonality between the channels targeting the $\nu\nu bb$ and $\ell\ell bb$ final states is established by requiring events to have exactly zero or two charged leptons of type *loose* electron or *loose* muon, as defined in the previous section. These channels are therefore referred to as *0-lepton* and *2-lepton channel*, respectively.¹¹ Additional selections are tailored specifically to the two different final states and background compositions. They are summarised together with the common selection in Table 5.1 and are discussed separately in the following.

0-Lepton Channel

Inferring the presence of neutrinos in the $\nu\nu bb$ final state, only events with a large amount of missing transverse momentum are considered for the 0-lepton channel. As the analysed data was collected using E_T^{miss} triggers with thresholds ranging from 70 to 110 GeV (cf. Sec. 5.3), E_T^{miss} is required to be larger

¹¹Other than expected for the signal, at this point the pair is not required to have the same flavour. This ensures that the 0-lepton channel is also orthogonal to the dedicated $t\bar{t}$ control region of the 2-lepton channel defined in Sec. 5.5.3.

Variable	Regime	
	Resolved	Merged
	Common selection	
Number of jets	≥ 2 small- R jets	≥ 1 large- R jet
Leading-jet p_T [GeV]	> 45	> 250
m_h [GeV]	[110,140] (0-lep.), [100,145] (2-lep.)	[75,145]
	0-lepton selection	
E_T^{miss} [GeV]	> 150	> 200
S_T [GeV]	> 150 (120*)	–
$\Delta\phi(j_1, j_2)$	$< 7\pi/9$	–
$E_{T,\text{trk}}^{\text{miss}}$ [GeV]		$> 30^\ddagger$
$\Delta\phi(E_T^{\text{miss}}, E_{T,\text{trk}}^{\text{miss}})$		$< \pi/2$
$\Delta\phi(E_T^{\text{miss}}, h)$		$> 2\pi/3$
$ \min(\Delta\phi(E_T^{\text{miss}}, j)) $		$> \pi/9$ (2 or 3 jets), $> \pi/6$ (≥ 4 jets)
Number of τ_{had}		0^{**}
	2-lepton selection	
Number of <i>medium</i> leptons	≥ 1	2
$E_T^{\text{miss}} / \sqrt{H_T}$ [$\sqrt{\text{GeV}}$]		$< 1.15 + 8 \times 10^{-3} \cdot m_{Vh}$
p_T^V [GeV]		$> 20 + 9 \cdot \sqrt{m_{Vh} - 320}^{\dagger\dagger}$
$m_{\ell\ell}$ [GeV]		$[\max[40 \text{ GeV}, 87 - 0.030 \cdot m_{Vh}], 97 + 0.013 \cdot m_{Vh}]$

Table 5.1: Topological and kinematic selections for the 0- and 2-lepton channels as described in the text. For the kinematic selection in the 2-lepton channel, m_{Vh} is in GeV. * In the case of 2 small-R jets. \ddagger Dropped in events with at least two b -tagged jets. ** Dropped for the W' and V' search. $\dagger\dagger$ Applied if $m_{Vh} > 320$ GeV.

than 150 GeV. Since even at this value the trigger efficiencies are not yet saturated, but are at the level of 80-90 %, correction factors are applied to simulation. They were obtained in a dedicated measurement performed in the context of the SM Vh ($h \rightarrow b\bar{b}$) analysis [248], and are within 5 % of unity. In the merged regime, the E_T^{miss} threshold is raised to 200 GeV, in accordance with the p_T requirement on the large-R jet; at this value the efficiency plateau is reached.

Since at least in the past a mismodelling in simulation due to a non-trivial dependence of the trigger efficiency on the jet activity was observed [318], the affected region of phase space is removed in the resolved regime. This is done by placing a requirement on the scalar sum of the transverse momenta of up to three (forward) small-R jets, denoted S_T . For events containing exactly two small-R jets, $S_T > 120$ GeV is required. In the case an event has additional jet activity, the threshold is raised to 150 GeV, and S_T is calculated including either the third leading small-R jet or the leading forward small-R jet.¹²

¹²While there are indications that the mismodelling is no longer present in Run 2, there was no need to drop the requirement given that the signal efficiency is high.

In order to remove non-collision background mimicking jets, mainly muons from the beam halo, $E_{T,\text{trk}}^{\text{miss}} > 30 \text{ GeV}$ is required; except in events where both candidate small-R jets are b -tagged and the fraction of fake jets is found to be very small.

While the E_T^{miss} requirements already eliminate a large fraction of the multijet background (in particular in the merged regime), exploiting kinematic differences with respect to the signal signature allow to suppress it sufficiently so that it can be neglected in the rest of the analysis. Since the multijet contamination mainly arises from mismeasurements of the jet energy leading to (large) E_T^{miss} , other than for the signal signature expected, the jets and E_T^{miss} tend to be aligned, while the (candidate) jets are rather separated from each other, as are E_T^{miss} and $E_{T,\text{trk}}^{\text{miss}}$. These differences are exploited and reflected in the following selection requirements:

- $|\min(\Delta\phi(E_T^{\text{miss}}, j))| > 20^\circ$ (40°), for $<$ (\geq) 4 small-R jets, including forward small-R jets,
- $\Delta\phi(E_T^{\text{miss}}, h) > 120^\circ$,
- $\Delta\phi(j_1, j_2) < 140^\circ$,
- $\Delta\phi(E_T^{\text{miss}}, E_{T,\text{trk}}^{\text{miss}}) < 90^\circ$,

where j refers to the two leading small-R jets and the third leading (forward) small-R jet in the resolved regime and any (forward) small-R jet in the merged regime. Depending on the regime, h stands for the Higgs-boson candidate either reconstructed from the two candidate small-R jets (j_1, j_2) or the candidate large-R jet. After applying these requirements the remaining multijet background contamination was estimated to be at the level of 1 % of the total background contribution using simulation.

While events containing two *loose* leptons, electrons or muons, are vetoed to establish the orthogonality with the 2-lepton channel, this requirement also significantly reduces the contamination by backgrounds involving leptonically decaying W bosons. Hence, by also discarding events containing hadronically decaying τ leptons, the same background processes are suppressed further: in the resolved regime, the total W +jets ($t\bar{t}$) background contribution is reduced by 9 (14) %, and in the merged regime, even by 22 (21) %, leading to a decrease of the total background contribution of 6 % and 13 %, respectively. Since on the other hand, the signal acceptance over the full considered mass range is hardly affected (< 1 %), this requirement leads to a better sensitivity by 5 % at low and up to 15 % at high A -boson masses.¹³

Finally, the signal region is defined by requiring the reconstructed Higgs-boson mass to be compatible with the mass of the observed Higgs boson of 125 GeV, i.e. to be within the range of 110 (75) GeV and 140 (145) GeV in the resolved (merged) regime. While the mass window in the resolved regime was optimised to yield a high sensitivity over the entire considered mass range, the mass window in the merged regime was adopted from Refs. [286, 317] to yield a high signal efficiency of about 90 %.

2-Lepton Channel

In order to be in agreement with the expectation of a Z -boson decay, only events where the two *loose* leptons are of the same flavour, i.e. electron or muons, are considered. In the resolved regime the muons in the pair are also required to be of opposite charge; neither muons in the merged regime nor electrons need

¹³Due to leptons missed in the reconstruction, the 0-lepton channel has some sensitivity to the $\ell\nu b\bar{b}$ final state of the $W' \rightarrow Wh$ search. In order to increase the Wh acceptance, for this particular interpretation as well as the V' combination, the τ -lepton veto is dropped.

to fulfil this criterion due to the higher charge misidentification rate. In the resolved (merged) regime, one (both) of the leptons needs to fulfil the *medium* criterion (cf. Sec. 5.4.1).

As the data is collected using varying combinations of single-lepton triggers (cf. Sec. 5.3), one lepton is required to match the one that has triggered the event readout and to have a transverse momentum greater than 27 GeV; the latter requirement ensures that the trigger with the highest threshold was operated fully efficiently.

The kinematic selection, discussed in the following, has been optimised regarding both sensitivity and efficiency with respect to the one used in the previous analysis. The latter acting as a baseline and reference,¹⁴ was based on choices made in the Run-1 analysis [283] (resolved regime), the early Run 2 HVT analysis [286] (merged regime), as well as in the 0-lepton channel. The aim of the optimisation was to find a selection that is suitable (i) across the whole A -boson (and Z') mass range, (ii) for the two different production modes (gluon fusion vs. b -associated production), as well as (ii) for both the resolved and merged regimes.

In the end, four kinematic distributions are exploited to suppress the background contaminations for the various signal signatures efficiently: (i) the dilepton invariant mass, $m_{\ell\ell}$, (ii) the Higgs-boson candidate mass, m_h , (iii) $E_T^{\text{miss}} / \sqrt{H_T}$ (defined below), and (iv) the transverse momentum of the Z -boson candidate, p_T^V ; several additional variables were tested, but no further improvement was found (which is in agreement with the findings of the Run-1 analysis). Figures 5.10(a)-(d) show the expected distributions of the discriminating variables for the total ($t\bar{t}$) background and two benchmark signals with masses $m_A = 500$ GeV and $m_A = 1.5$ TeV. Apart from the latter signal, all distributions are obtained in the resolved regime.

From Figure 5.10(a) it can be seen, that requiring $m_{\ell\ell}$ to be compatible with the nominal Z -boson mass of about 91 GeV, allows to suppress in particular the dominant $t\bar{t}$ background; but in general any background process without on-shell Z -boson production.

The $t\bar{t}$ background, and other processes involving leptonically decaying W bosons, can be further reduced by exploiting that they exhibit prompt neutrinos in addition to the objects expected from the considered A -boson decay. However, instead of applying criteria on E_T^{miss} directly, the related quantity $E_T^{\text{miss}} / \sqrt{H_T}$ is employed which shows for the same level of rejection a better acceptance at high A -boson masses (it was already used in the Run-1 analysis). Since H_T is computed from the scalar sum of the p_T of the two leptons and all small-R jets (including forward jets), H_T is proportional to the E_T^{miss} resolution, and thus $E_T^{\text{miss}} / \sqrt{H_T}$ can be seen as an estimate of the E_T^{miss} significance. In events lacking prompt neutrinos (as is the case for the signal process), E_T^{miss} arises from mismeasurements of jet energies as well as from semileptonic b -hadron decays; the dedicated b -jet corrections, discussed in Sec. 5.4.2, are not applied to the jets entering the $E_T^{\text{miss}} / \sqrt{H_T}$ computation, since dedicated systematic uncertainties were not available. Thus, the signal and the total background, dominated by Z +jets production, tend to exhibit small $E_T^{\text{miss}} / \sqrt{H_T}$ values, while the expected distribution for $t\bar{t}$ production is broader and peaking at higher $E_T^{\text{miss}} / \sqrt{H_T}$ values, as can be seen from Fig. 5.10(b).

Since only a few, rare background processes involve a Higgs boson, h , the m_h distribution of the total background is rather peaking at low values and falls off smoothly, as can be seen from Fig. 5.10(c). Therefore, selecting events, where m_h is compatible with the nominal mass of 125 GeV, strongly diminishes almost all background processes. While for both benchmark signal masses the m_h distribution exhibits a

¹⁴Starting as a supervised bachelor project [320], the results were finalised in the course of this thesis.

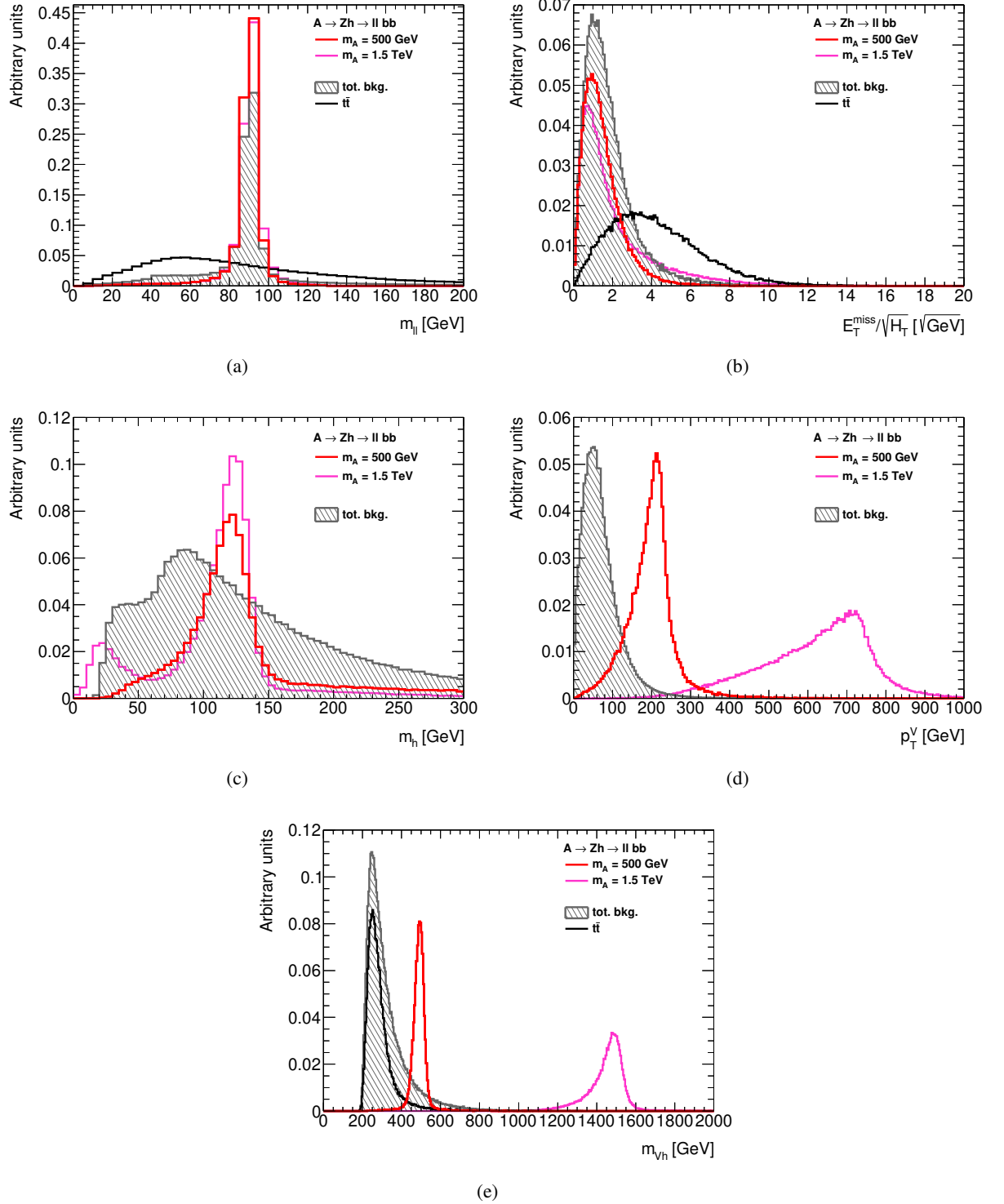


Figure 5.10: Comparison of the simulated distributions for (a) the invariant dilepton mass, $m_{\ell\ell}$, (b) $E_T^{\text{miss}}/\sqrt{H_T}$ approximating the E_T^{miss} significance, (c) the Higgs-candidate mass, m_h , (d) the transverse momentum of the Z -boson candidate, p_T^V , and (e) the invariant mass of the Zh system, m_{Vh} , in the 2-lepton channel. Shown are two A -boson signals produced in gluon fusion with benchmark masses $m_A = 500$ GeV and 1.5 TeV and the total background as well as $t\bar{t}$ production (where relevant). Except the distributions of the 1.5 TeV signal, which are determined in the merged regime, all other distributions are obtained in the resolved regime. From the kinematic selections described in the text only the $m_{\ell\ell}$ and m_h windows are applied; which are also respectively dropped to obtain the distributions in Figs. (a) and (c).

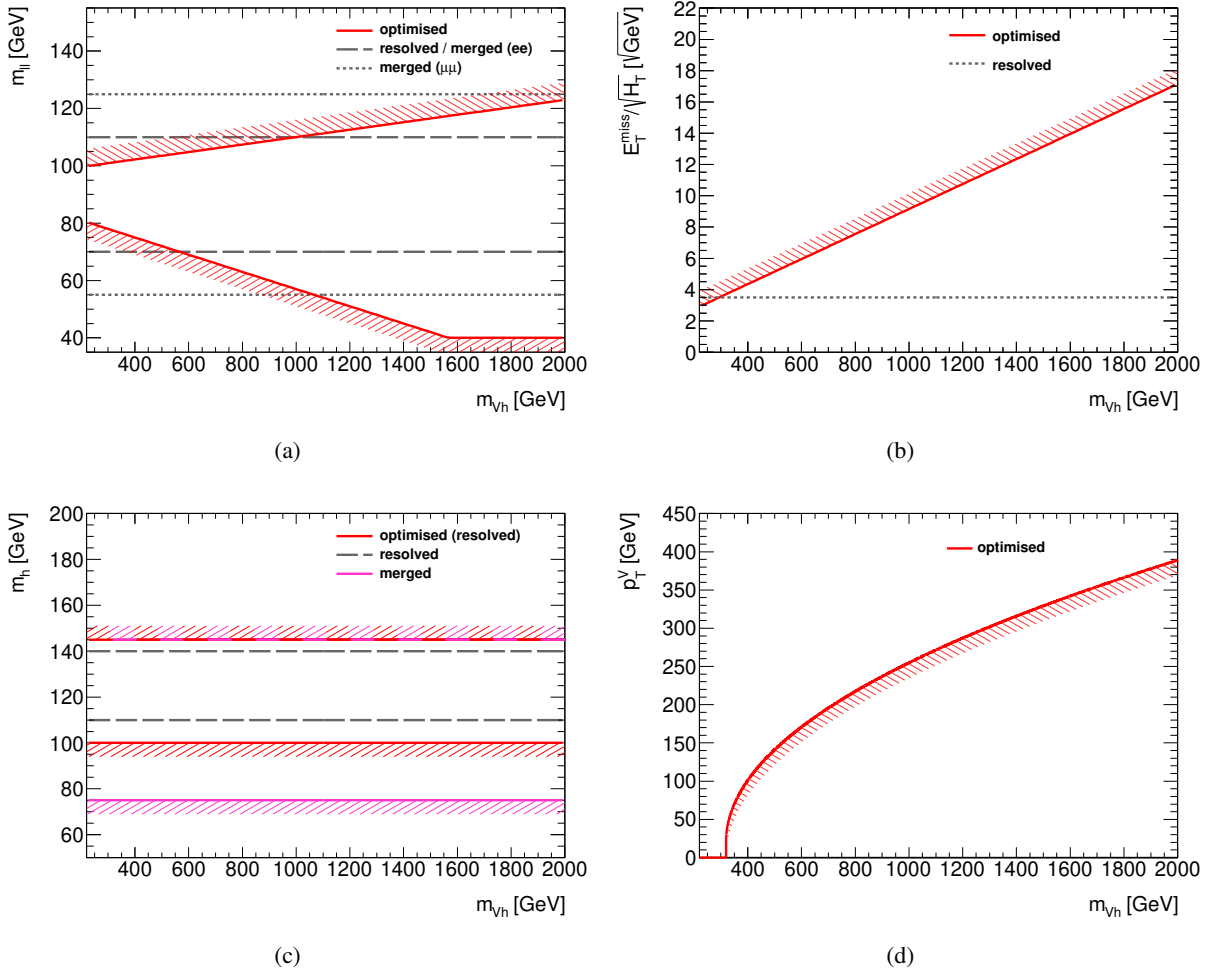


Figure 5.11: Illustration of the m_{Vh} -dependence of the kinematic selection applied to (a) the invariant dilepton mass, $m_{\ell\ell}$, (b) $E_T^{\text{miss}}/\sqrt{H_T}$ approximating the E_T^{miss} significance, (c) the Higgs-candidate mass, m_h , and (d) the transverse momentum of the Z-boson candidate, p_T^V , in the 2-lepton channel, as described in the text and summarised in Table 5.1. Apart from Fig. (c), the same selection is used in the resolved and merged regimes. The hashed bands indicate the rejected phase space.

tail towards low values, in the case of the signal with $m_A = 1.5$ TeV a second peak at very low m_h is observed. It is caused by events, where either the wrong large-R jet is considered as Higgs-boson candidate or where the signal is not fully contained. It can be removed almost completely by increasing the required number of track jets associated to the candidate large-R jet to two.

Figure 5.10(d), showing the expected p_T^V spectra, illustrates the effect that with increasing A -boson mass the Z boson acquires large transverse momenta. It also shows that the p_T^V distribution provides good separation power, in particular for intermediate and high m_A , given that the distribution of the total background contribution is exhibiting a soft spectrum.

While it is therefore clear that the optimal p_T^V cut depends on the targeted A -boson mass, the same is true for the requirements on the other variables. However, the trend is the opposite: while the optimal

p_T^V threshold increases with m_A , the preferred $E_T^{\text{miss}}/\sqrt{H_T}$ and $m_{\ell\ell}$ criteria become looser. This can be understood from the expected distributions of the reconstructed invariant mass of the Zh system m_{Vh} , shown in Fig. 5.10(e). The total background spectrum peaks at rather low values of about $m_{Vh} \approx 250$ GeV, with a long tail towards high masses. The signal, however, appears as a narrow peak at around $m_{Vh} \approx m_A$, even though only the previously discussed muon-in-jet correction is applied. Therefore, with increasing m_A , the signal moves towards higher m_{Vh} values with reduced background contributions. Furthermore, not only the total background contribution is decreasing, the background composition is changing as well. Peaking roughly at the same value, the distribution of the $Z+bb$ background has a relatively long tail towards high m_{Vh} , while the distribution of the $t\bar{t}$ -background drops off rather rapidly. Thus, towards high m_A values looser selection criteria suffice to keep the ($t\bar{t}$) background contribution small than required at small m_A .

While the optimal selection criteria depend on the targeted A -boson mass, it is found that they are very similar for the two production modes and also for the two regimes, where they can be compared, i.e. in the transition region of the intermediate mass regime. The only exception constitutes the Higgs-boson mass window at high A -boson masses, where the resolved and merged regimes prefer different requirements. Thus, the same selection criteria are used irrespective of the production mode or the regime, except for the Higgs-boson mass window.

The m_A -dependence of the optimal selection criteria is acknowledged for the p_T^V , $m_{\ell\ell}$ and $E_T^{\text{miss}}/\sqrt{H_T}$ selection criteria by allowing them to change across the mass range: they are expressed as a function of m_{Vh} , which constitutes a good estimate of the true A -boson mass.¹⁵ The obtained functional forms are summarised in Table 5.1 and illustrated in Fig. 5.11. While they are the same in the resolved and merged regimes, the actual selection requirements are slightly different. This is because of the different Higgs-boson candidate reconstruction and b -jet energy corrections (cf. Sec. 5.4.2). Nonetheless, the correlation between the two m_{Vh} values for events that fall into both the resolved and merged regimes is at the level of 85 (55) % for the signal (background) processes (after the basic event selection). That the functional forms are monotonous, ensures a smooth m_{Vh} distribution regardless of the dependence of the selection criteria on m_{Vh} which is crucial for using it as a final discriminant. The only exception is the lower $m_{\ell\ell}$ cut: it is limited to ≥ 40 GeV for $m_A \gtrsim 1.5$ TeV, because a corresponding criterion is applied in the generation of the simulated Z +jets samples. Since the Z' signal was considered in the optimisation, the trends towards high m_A values are determined by the results obtained with hypothesised masses beyond the m_A range (> 2 TeV).

The Higgs-boson mass window is chosen to be constant across m_{Vh} , both in the resolved and in the merged regimes, despite an observed m_A -dependence of the optimal selection. The main reason for this a clearer definition of an m_h -sideband region to be used as control or validation region, as discussed in Sec. 5.5.3. While the requirement in the resolved regime reflects the result of the optimisation studies up to intermediate m_A values, the window chosen in the merged regime is the same as in the 0-lepton channel and as such adopted from Refs. [286, 317]. As can be seen from e.g. Fig. 5.11(c), the m_h window in the merged regime is considerably extended towards low m_h values compare to the m_h window used in the resolved regime. It therefore provides insufficient background rejection at low/intermediate m_{Vh} values and yields lower sensitivities for A bosons with low/intermediate m_A than the resolved regime. This difference is relevant for the choice of a particular regime-selection strategy as discussed in the next section.

The performance of the optimised kinematic selection can be assessed by comparing the obtained signal

¹⁵For this purpose the m_{jj} -rescaling is not applied (cf. Sec. 5.4.2).

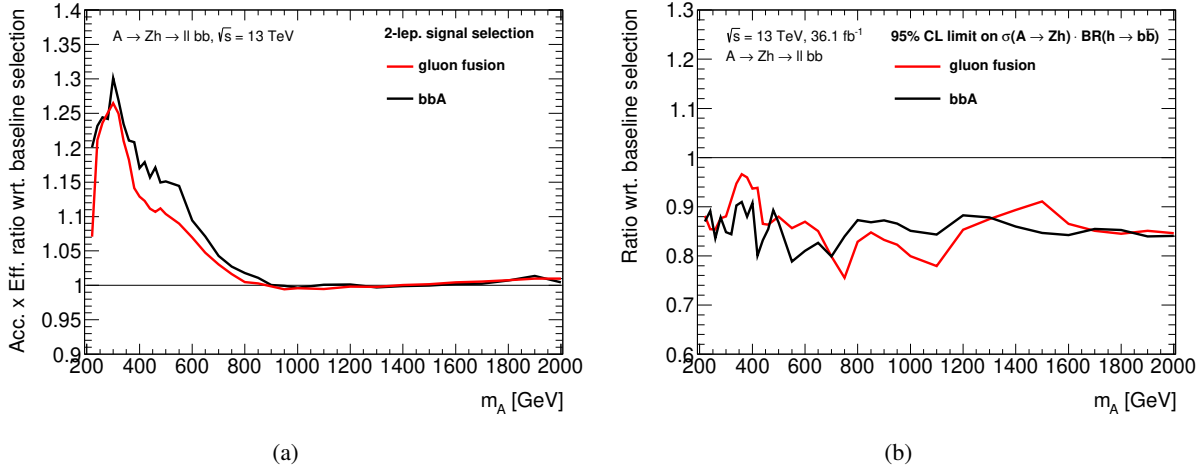


Figure 5.12: Impact of the optimised event selection in the 2-lepton channel on (a) the expected signal acceptance times efficiency and (b) the expected upper limit at the 95 % CL on the cross section for A -boson production times the branching ratios for the $A \rightarrow Zh$ and $h \rightarrow b\bar{b}$ decays, separately for pure gluon-fusion and pure b -associated production (bbA). The results are shown relative to the baseline selection, adopted from the previous analysis, as function of the A -boson mass. Figure 5.12(b) is obtained as described in Sec. 5.7, considering statistical uncertainties only.

efficiency and sensitivity with the one of the baseline selection. The differences between the two selections are illustrated in Fig. 5.11. Figures 5.12(a) and 5.12(b) show, separately for the two production modes, the signal acceptance times efficiency and the expected upper limit on the product of the cross section for A -boson production and the branching ratios for the decays $A \rightarrow Zh$ and $h \rightarrow b\bar{b}$ at the 95 % confidence level (CL), considering only statistical uncertainties, as function of m_A , respectively.¹⁶ The results are similar for the two production modes: there is an efficiency gain at $m_A \leq 800$ GeV up to 25-30 %; the expected limit improves across the whole m_A at the level of 15 %.

5.5 Event Categorisation

The event selection described in the previous section aiming at selecting $A \rightarrow Zh$ events in the $\ell\ell b\bar{b}$ and $\nu\bar{\nu}b\bar{b}$ final states is completed by a further categorisation of the selected events into orthogonal regions with varying signal fractions and signal-to-background ratios.

As discussed earlier, a priori, the two Higgs-boson reconstruction strategies are used such that the same events may be considered in both regimes; the potential double-counting is only slightly reduced by the event selection. In order to eliminate it completely and to obtain independent analysis regions, events that pass the event selection of both regimes need to be assigned to one regime exclusively. Several strategies to achieve orthogonality are discussed in Sec. 5.5.1 motivating the final choice.

The described event selection does not specifically target the prominent signal feature of two b quarks stemming from the Higgs-boson decay, and neither the additional ones from the b -associated production

¹⁶For both the expected signal acceptance as well as the upper limit the overlap between the resolved and merged regimes is removed with the PriorityResolvedSR selection strategy discussed in Sec. 5.5.1. The upper limit is obtained in all cases with the fit model described in Sec. 5.7.

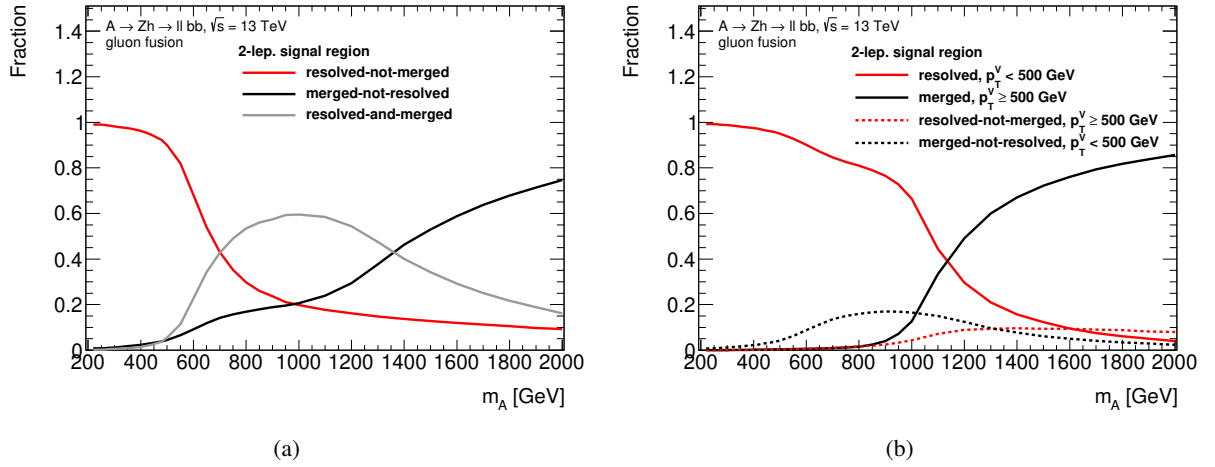


Figure 5.13: Comparison of the fraction of signal events passing the event selection of the 2-lepton channel (a) that are entering exclusively the resolved regime (resolved-not-merged), exclusively the merged regime (merged-not-resolved) or both regimes (resolved-and-merged) as defined in Secs. 5.4.2 and 5.4.3, and (b) that are entering the resolved regime and have $p_T^V < 500$ GeV, the merged regime and have $p_T^V \geq 500$ GeV, entering exclusively the resolved regime and have $p_T^V \geq 500$ GeV, or entering exclusively the merged regime and have $p_T^V < 500$ GeV, as function of the A -boson mass. All categories are defined such that there is no overlap between the different categories (within one comparison). Pure A -boson production in gluon fusion is assumed.

mode. Instead, as described in Sec. 5.5.2, the available b -tagging information is used to define several signal regions in the (orthogonal) resolved and merged regimes by categorising candidate events according to the number of b -tagged jets. The various resulting b -tag categories are discussed regarding both the background contributions and compositions as well as the signal acceptance times efficiencies for the two considered production modes.

The signal regions are complemented with dedicated control and validation regions that are defined in Sec. 5.5.3. They are introduced to help improve and verify the modelling of the background simulations in the signal regions.

5.5.1 Selection of the Kinematic Regime

As mentioned before, the two Higgs-boson reconstruction strategies, are not exploited exclusively, and a given event might be reconstructed in both ways and also pass each of the slightly different event selections of the resolved and merged regimes. This is especially the case in the regime-transition region around $m_A = 1$ TeV, where the merged reconstruction starts to become more efficient (cf. Fig. 5.7); up to 60% of the events are considered both in the resolved and merged signal regions. This can be seen from Fig. 5.13(a), where the fraction of selected signal events in the 2-lepton channel is shown, which enter (i) exclusively the resolved regime, (ii) exclusively the merged regime, and (iii) both regimes, as function of the true A -boson mass. The distributions in Fig. 5.13(a) also confirm the expectation that the exclusive resolved and merged regimes dominate at the low and high m_A , respectively; however, the fraction of events entering exclusively in the resolved regime at high m_A , at the level of 10%, might surprise. It can be explained by the fact that even at high m_A , the p_T spectrum of the Higgs boson has a long tail towards low values; similarly as the closely related p_T spectrum of the Z -boson candidate, shown in Fig. 5.10(d).

There are several possible strategies to assign events exclusively to one regime and to obtain independent analysis regions which can be combined in the final fit described in Sec. 5.7. Only three of the studied options are discussed in the following.

A rather simple approach is to assign events to the resolved or the merged regimes depending on whether or not they are considered to be *boosted*, based on the value of a simple discriminating variable. This strategy, that was first used in the previous analysis and adopted by Ref. [321], is also studied in the present analysis and serves as a reference for the other options discussed below.

Relying on the close relation between the transverse momenta of the Higgs and Z bosons and the reconstruction strategy, the reconstructed Z -boson p_T is exploited as discriminating variable. In the 2-lepton channel, it is identified with the transverse momentum of the Z -boson candidate, p_T^V , reconstructed as the invariant dilepton mass, in the 0-lepton channel, E_T^{miss} is used to approximate the Z -boson p_T . If the estimated Z -boson p_T exceeds 500 GeV, events are considered to be boosted and enter the merged regime; otherwise they are assigned to the resolved regime. This strategy is therefore referred to as ‘‘SimpleMerge500’’. While the chosen threshold was determined in an optimisation procedure, it can be reasoned as follows: for an A boson with mass m_A , the most likely value for p_T^V is $m_A/2$, as can be also seen from Fig. 5.10(d); thus, $p_T^V = 500$ GeV corresponds to $m_A = 1$ TeV, the point in the m_A range, where the overlap between the resolved and merged regimes is largest (cf. Fig. 5.13(a)).

The fraction of selected signal events in the 2-lepton channel entering the resolved (merged) sub-regime with $p_T^V < (\geq) 500$ GeV is shown in Fig. 5.13(b); they dominate - as intended - the low (high) mass regime. However, while this approach provides a straightforward procedure to obtain independent analysis regions, the acceptance loss is substantial, given that resolved (merged) events passing the event selection with $p_T^V \geq (<) 500$ GeV are not considered at all. The fraction of events entering exclusively in these categories is also shown in Fig. 5.13(b): it amounts to as much as $\sim 20\%$.

The losses found with the SimpleMerge500 strategy can be avoided by assigning events entering both regimes exclusively to one, by *prioritising* one regime over the other. This means, if an event passes the event selection of the prioritised regime, it gets assigned to it irrespective of whether or not it also passes the event selection of the other regime. Which regime is tested first could depend on the kinematic topology of the event; for example, the resolved (merged) regime selection could be prioritised in the low (high)- p_T^V regime. However, in the following, only two approaches are discussed, namely where either the resolved or the merged regime is prioritised across the whole m_A range, referred to as the ‘‘PriorityResolvedSR’’ and ‘‘PriorityMergedSR’’ strategies, respectively.¹⁷

Since the b -tagging performance is different in the two regimes (cf. Sec. 3.4), using b -tagging may change the outcome of the prioritisation of the regimes relative to considering kinematic information alone. However, the impact on the most sensitive signal region with two b -tags (cf. Sec. 5.5.2) is found to be small: the PriorityResolvedSR (PriorityMergedSR) strategy leads to a higher signal acceptance of the order of 4% below (above) the transition point at around 1 TeV. Therefore, it is refrained from using b -tagging information to prioritise the regimes, which has the advantage that the regime selection is kept separately from the b -tag categorisation.

¹⁷The ‘‘SR’’ in the name emphasises the fact that events are only considered for one regime, if they pass the corresponding signal region selection, described in Sec. 5.4.3.

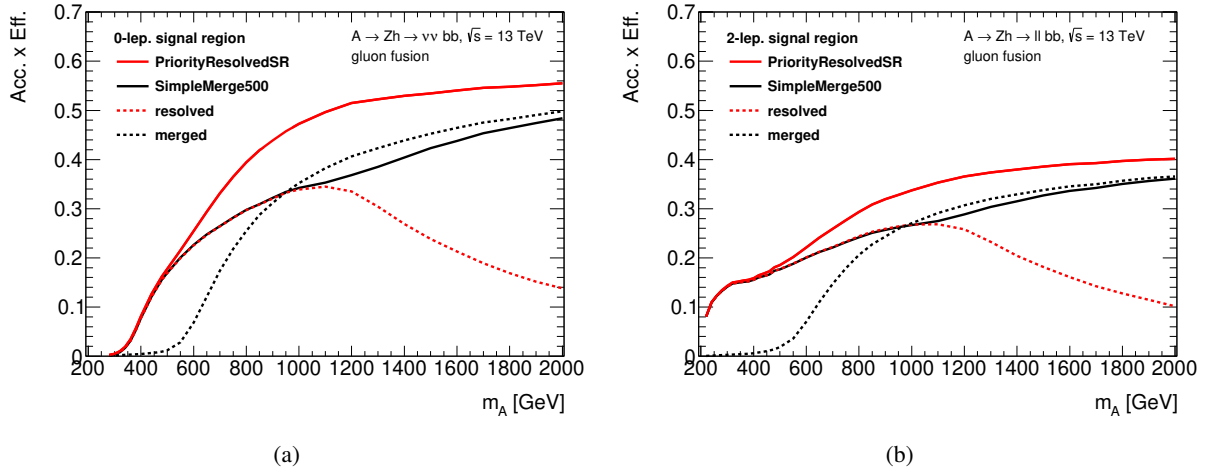


Figure 5.14: Comparison of the impact of the different regime-selection strategies introduced in the text, PriorityResolvedSR and SimpleMerge500, on the signal acceptance times efficiency in the signal region of (a) the 0-lepton channel and (b) the 2-lepton channel, as function of the A -boson mass. Pure A -boson production in gluon fusion is assumed. PriorityMergedSR is not shown since the results are per definition the same as for the PriorityResolvedSR strategy. The results for the resolved and merged regimes are shown as well.

Figure 5.14 shows a comparison of the signal acceptance times efficiency between the PriorityResolvedSR and the SimpleMerge500 strategy as function of m_A ; the results for the PriorityMergedSR are identical with the former. It visualises the significant acceptance gain due to the prioritisation over the SimpleMerge500 scenario in both the 0-lepton and 2-lepton channels: it amounts up to $\sim 40\%$ and 30% in the transition region, respectively. The comparison with the resolved and merged regimes is shown as well for illustration.

While the PriorityResolvedSR and PriorityMergedSR strategies perform (almost) equivalently regarding the signal acceptance (when also considering b -tag categories), this is not the case regarding the sensitivity, where also the signal-to-background ratio as well as the signal resolution in the two regimes matter. This can be seen from Fig. 5.15 showing the expected upper limits on the cross section for A -boson production in gluon fusion times the branching ratios for the $A \rightarrow Zh$ and $h \rightarrow bb$ decays at 95% CL relative to the SimpleMerge500 strategy as function of m_A , separately for the 0-lepton and 2-lepton channels; only statistical uncertainties are considered.¹⁸ The trends in the two channels are comparable and largely as expected. Over a wide m_A range, the PriorityResolvedSR performs similar as the SimpleMerge500 strategy, however, in the regime-transition region, where the acceptance gain is largest: the expected limit in the 0-lepton (2-lepton) channel is up to 20 (15)% better for the former.

While the PriorityMergedSR strategy yields comparable and slightly better results than the PriorityResolvedSR at high m_A , it performs clearly worse below $m_A \lesssim 1$ TeV, where the resolved reconstruction is dominating. This can be mainly attributed to the suboptimal Higgs-boson mass window of the merged

¹⁸The upper limit is obtained in all cases with the fit model, described in Sec. 5.7. Only the binning of the final discriminants, m_{Vh} and $m_{T,Vh}$ is adapted for each of the three strategies to ensure reasonable choices. This mainly addresses the fact that the change of priorities leads to the categories being differently populated with (simulated) events; in particular, when using the SimpleMerge500 strategy, the high p_T^V cut almost eliminates all background contributions in the merged regimes, thus making a reliable estimate difficult.

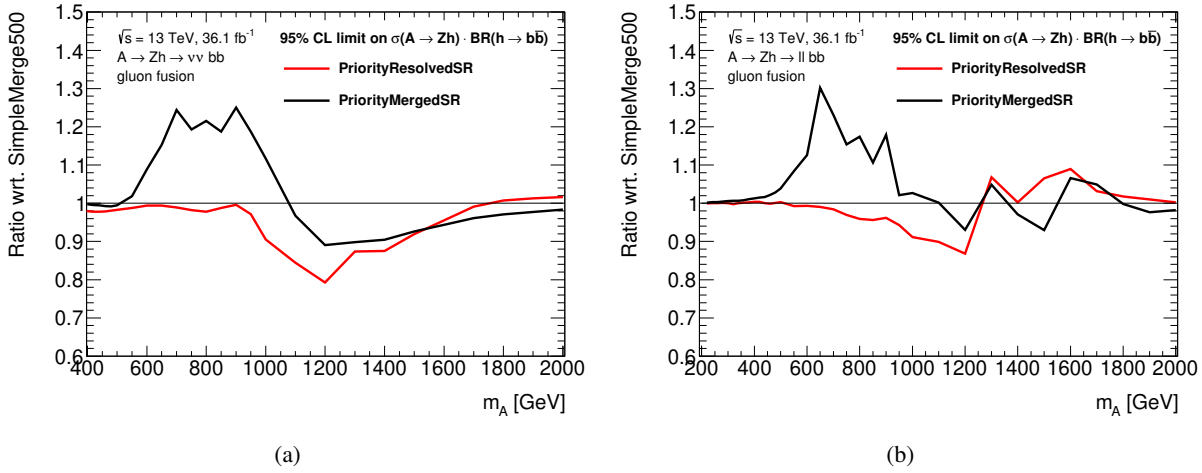


Figure 5.15: Comparison of the impact of the different regime-selection strategies introduced in the text, PriorityResolvedSR and PriorityMergedSR, on the expected upper limit at 95 % CL on the product of the cross section for A -boson production in gluon fusion and the branching ratios for $A \rightarrow Zh$ and $h \rightarrow bb$ decays in (a) the 0-lepton and (b) the 2-lepton channel. The results are presented relative to the SimpleMerge500 strategy and as function of the A -boson mass. Only statistical uncertainties are considered (cf. Sec. 5.7).

regime selection: optimised to yield a high signal acceptance, it extends significantly to lower m_h values compared to the resolved regime, and thus does not sufficiently reject background contributions that peak at the low $m_{Vh}/m_{T,Vh}$ values. The optimisation studies performed in the 2-lepton channel (cf. Sec. 5.4.3) showed that to target A -boson signals with small m_A , similarly tight m_h windows are optimal in the merged regime as in the resolved regime. Therefore, it is expected that the PriorityMergedSR would perform similar to the PriorityResolvedSR strategy, also at smaller m_A , if a correspondingly optimised m_h window was used in the merged regime. However, small differences might still remain given the different $m_{Vh}/m_{T,Vh}$ resolutions in the two regimes (cf. Fig. 5.9).

In conclusion, the PriorityResolvedSR strategy shows overall the best performance across the considered m_A range, both in terms of acceptance times efficiency as well as sensitivity. It is therefore used to obtain orthogonal resolved and merged analysis regions. Thus, while the resolved-regime definition is unchanged with respect to previous sections, the merged regime refers in the following to regions, in which events are *exclusively* reconstructed with the merged strategy.

5.5.2 Number of Identified b Jets

Since the studied signal signature features two b quarks stemming from the Higgs-boson decay and additional b quarks are expected, when considering the b -associated production mode, the signal selection is completed by categorising candidate events according to the number of b -tagged jets, or b -tags. Several analysis regions with varying signal-to-background ratios and sensitivities regarding the considered production mechanisms are defined, as discussed below.

As introduced before (cf. Secs. 5.4.1 and 5.4.2), small-R and track jets are considered for b -tagging in the resolved and merged regimes, respectively. More precisely, two classes of track jets are distin-

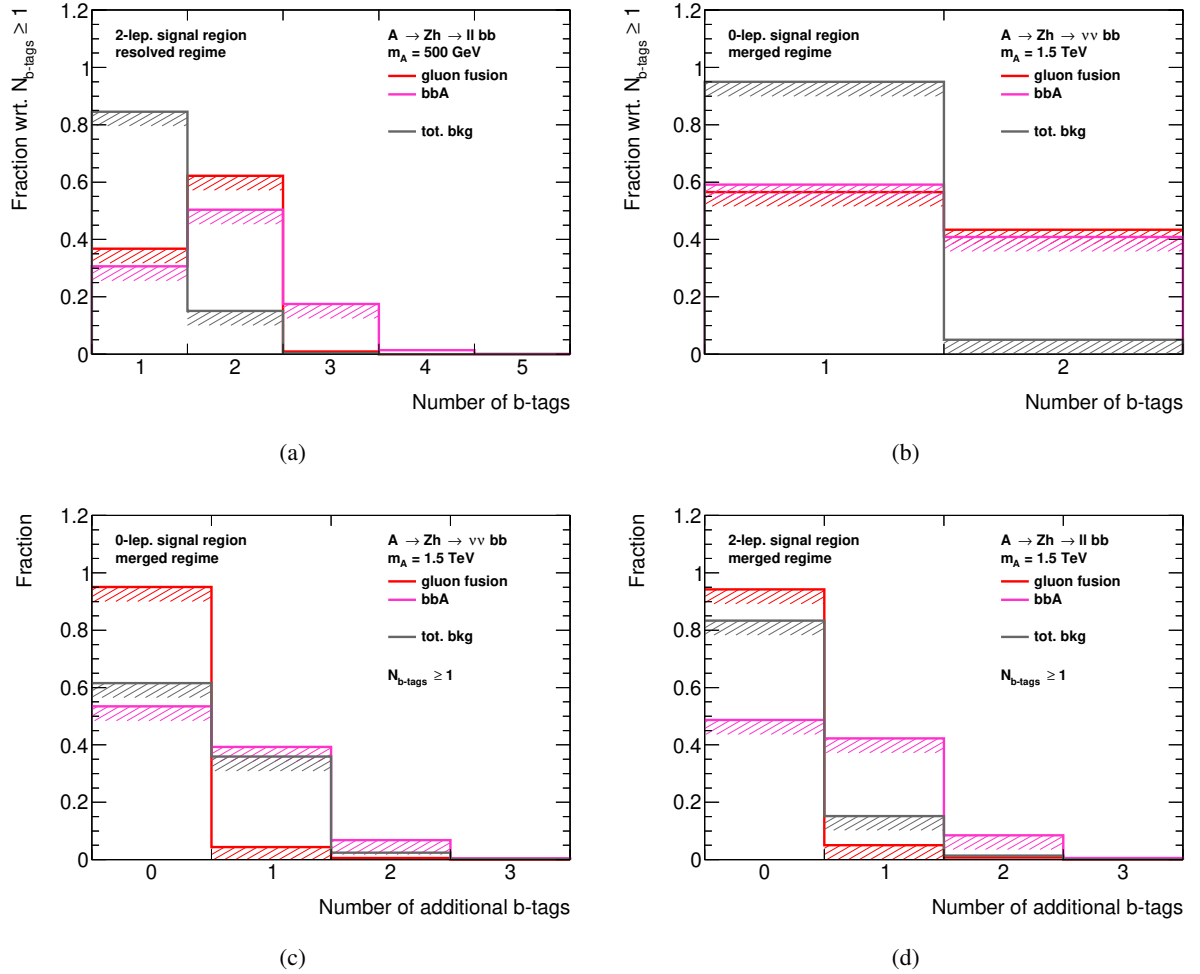


Figure 5.16: Comparison of the predicted b -tag multiplicities in the signal regions of the resolved (merged) regimes between an A boson of mass 500 GeV (1.5 TeV) purely produced in gluon fusion and b -associated production, respectively, and the total background. The number of (a) b -tagged small-R jets in the 2-lepton channel and (b) b -tagged track jets associated with the candidate large-R jet in the 0-lepton channel are expressed relative to the respective number of signal and background events with at least one b -tag. The fraction of events with additional b -tagged track jets not associated with the candidate large-R jet in the merged regime is shown for events with at least one b -tagged track jet associated with the candidate large-R jet in the (c) 0-lepton and (d) 2-lepton channels.

guished: (i) the leading (two) track jets associated with the candidate large-R jet, that are meant to resolve the substructure expected for the targeted $h \rightarrow bb$ decay, and (ii) track jets *not* associated with the candidate large-R jet, addressing the signature of the b -associated production mode with b quarks emitted rather forward and somewhat softer than the ones stemming from the Higgs-boson decay. Therefore, while the number of b -tagged small-R jets defines the number of b -tags in the resolved regime, in an merged regime the number of b -tagged track jets of type (i) determines the number of b -tags and the ones of type (ii) the number of *additional* b -tags.

Figure 5.16 shows the expected (additional) b -tag multiplicities for A -boson signals with $m_A = 500$ GeV (1.5 TeV) in the resolved (merged) regime, separately for pure gluon-fusion and b -associated production, in

events with at least one b -tag.¹⁹ The expected distribution of the total background is also shown. While the b -tag multiplicities of the signal are (largely) independent of the considered lepton channel, the different background contributions and compositions in the two channels may result in different b -tag multiplicities in the case of the total background. The differences are pointed out in the following discussion, where relevant.

From Figures 5.16(a) and (c), it can be seen that, as intended, the two A -boson production modes can be distinguished by the number of b -tags in the resolved regime and the number of additional b -tags in the merged regime: for the b -associated mode a non-negligible fraction of events with more than two b -tags is expected in the resolved regime and with at least one additional b -tag in the merged regime. Therefore, the “3+” b -tags and “1+” additional b -tags categories are particularly sensitive to the b -associated production mode. Events falling into the latter category can be further divided according to the number of b -tags, i.e. the number of b -tagged track jets associated with the Higgs-boson decay. As can be seen from Fig. 5.16(b), there are no differences between the two production modes. It can be noticed however, that the 2-to-1 b -tags ratio is expected to be below unity, and thus significantly lower than in the resolved regime.

Thus, considering also events with zero b -tags, four b -tag categories can be distinguished in the resolved regime and six in the merged regime. The relative signal fractions in the various regions are shown separately for the two production modes in Fig. 5.17 as function of the A -boson mass: they vary not only with the production mode, but also with m_A .

Only events with at least one b -tag are considered for further analysis, i.e. the 0 b -tags categories are not exploited in the following. This discards an overwhelming fraction of background events at the expense of moderate signal losses of at most 10 (15) % in the resolved (merged) regime, across almost the full considered m_A range. Only for signals with $m_A < 600$ GeV produced in gluon fusion, the fraction in the 0 b -tags, 1+ additional (add.) b -tags category of the merged regime is not small, as can be seen from Fig. 5.17(c); it appears that in most of these cases the candidate large- R jet is wrongly identified with the Higgs boson or at least does not completely capture its decay products.

In the resolved regime, over a wide m_A range, most signal events end up in the 2 b -tags category with fractions up to 60 (50) % for gluon fusion (b -associated) production; only for $m_A \gtrsim 1.3$ (1.4) TeV, the 1 b -tag category starts to dominate. In contrast, in the merged regime, the signal predominantly populates the 1 b -tag category with fractions at the level of 50 % over the full considered mass range; where the contributions from the 0 and 1+ add. b -tag categories are considered together. This behaviour reflects the dependence of the b -tagging efficiency on the jet p_T , which is similar for small- R and track jets. The chosen operating point provides an average 70% b -jet tagging efficiency across jet p_T in simulated $t\bar{t}$ events, showing a broad maximum of a slightly higher value around 100 GeV and decreasing fairly steeply for $p_T > 200$ GeV, resulting in b -jet tagging efficiencies of 60 % and lower. In the merged regime, no crossing point of the 1 and 2 b -tags categories is observed, because the chosen regime-selection strategy, PriorityResolvedSR, prioritises the resolved regime, and thus biases the jet p_T spectra in the merged regime, in particular at low m_A , towards larger values.²⁰

The signal fraction in the 3+ b -tag category varies only slightly as a function of m_A : it is consistently

¹⁹The merged regime is defined as containing only events, where the Higgs-boson candidate is exclusively reconstructed with the merged strategy, as discussed in the previous section.

²⁰The same argument explains the higher fraction of signal events in the 0 b -tag category in the merged regime with respect to the resolved regime.

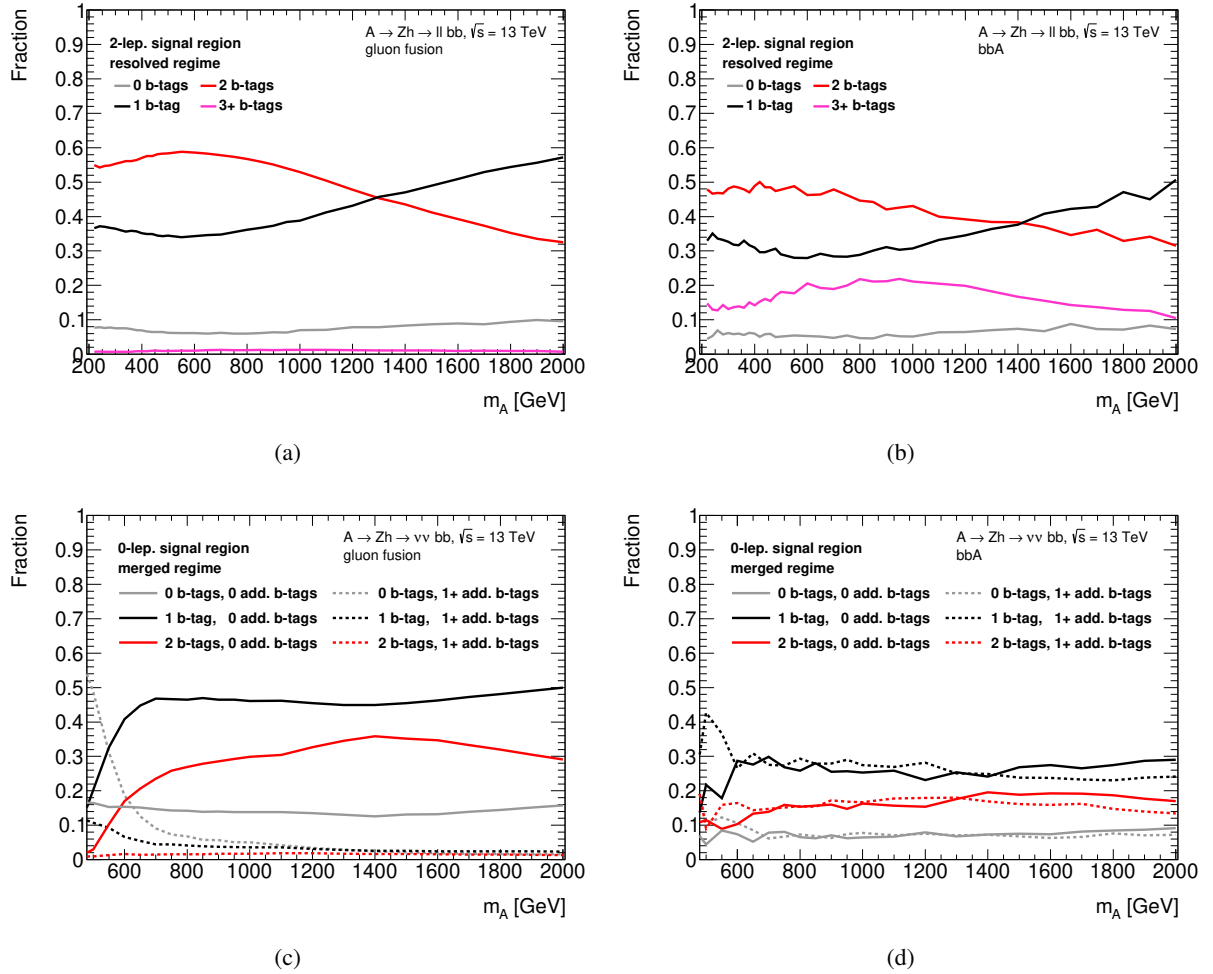


Figure 5.17: Expected signal fractions in the different b -tag categories in the resolved regions of the 2-lepton channel (top) and the merged signal regions of the 0-lepton channel (bottom). They are shown separately for gluon-fusion (left) and b -associated A -boson production (right).

negligible for gluon-fusion production, and at the level of 15-20% for b -associated production (bbA). These numbers are possibly lower than naively expected for the bbA signature. However, it needs to be considered that b -tagging information is only available for jets within the acceptance of the inner detector, i.e. $|\eta| < 2.5$, and with $p_T > 20$ GeV; and b jets stemming from the production mechanism are expected to be rather forward and somewhat softer than the ones from the Higgs-boson decay.

The picture is similar in the categories of the merged regime sensitive to b -associated production with 1+ add. b -tags. The signal fractions for gluon-fusion production are generally small; for b -associated production they are comparable to the ones in the 0 add. b -tags categories with the same number of b -tags and almost independent of the considered A -boson mass: they range between 20-30% in the 1 b -tag category and are at the level of 15% in the 2 b -tags category.

The signal sensitivity of the different categories is not only determined by the signal fractions, but also by the respective background contributions and compositions that vary quite considerably. Figure 5.16

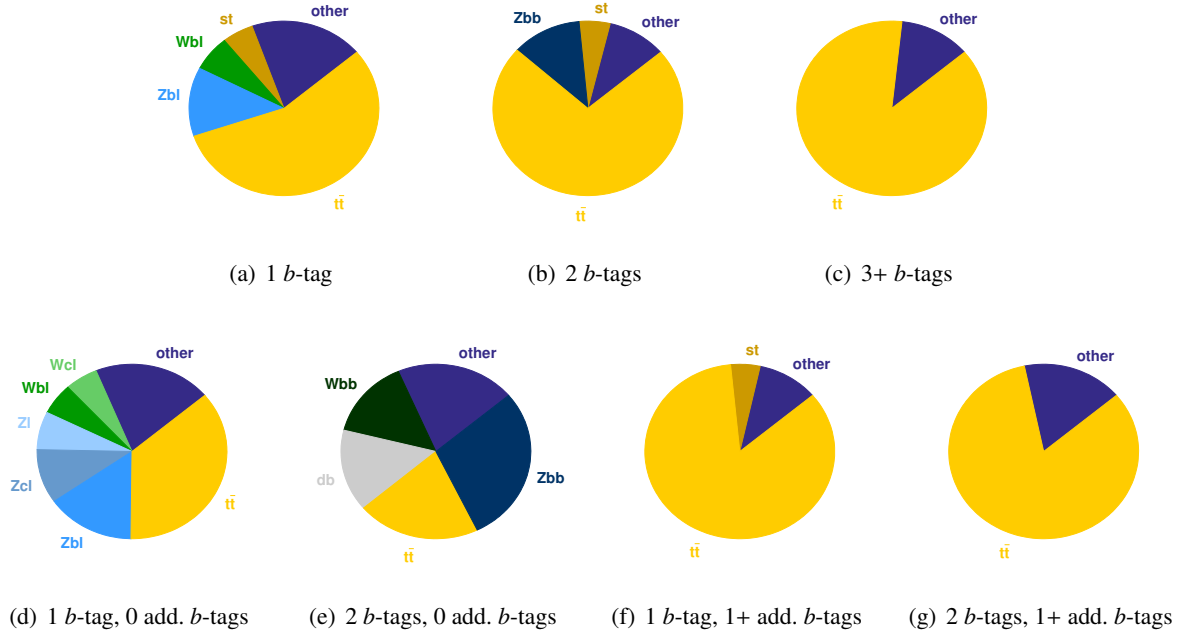


Figure 5.18: Background composition in the b -tag categories of the (a)-(c) resolved and (d)-(g) merged signal regions of the 0-lepton channel. The background processes are as defined in Sec. 5.3; “st” stands for single-top production, “db” for diboson production and “other” for the sum of backgrounds with contributions to the total background below 5%.

shows the contribution of the total background across the different b -tag categories. From Fig. 5.16(a) it can be seen, that in the resolved regime of the 2-lepton channel, about 80-85 % of the background events exhibit only one b -tagged small-R jet, less than 20 % two, and a negligible fraction more; i.e. the signal-to-background ratio clearly improves with the number of b -tags. The situation in the 0-lepton channel is almost the same, despite the quite different background compositions which are visualised for the two channels in Figs. 5.18(a)-(c) and Figs. 5.19(a)-(c), respectively. The V +jets backgrounds are split into various components according to the flavour of the jets used for b -tagging; if none of the considered jets is a heavy flavour jet, the component is labelled $V+l$.²¹

In the 0-lepton channel, $t\bar{t}$ production is by far the dominant background contribution in all of the three b -tag categories, followed by $Z+bl$ and $Z+bb$ in the 1 b -tag and 2 b -tags categories, respectively. In the 3+ b -tags category the $t\bar{t}$ contamination arises mainly from misidentifying c jets and/or a light jets as b jets. In fact, the fraction of events, where one of the b jets from the top-quark decays is missed and the three jets from the hadronic top decay are b -tagged, amounts to about 40 %. Thus, despite the small mistag rates, the $t\bar{t}$ contribution in the 3+ b -tags category is sizeable due to the large $t\bar{t}$ production cross-section.

In the 2-lepton channel, Z +jets production constitutes the largest background process in all resolved b -tag categories: $Z+bl$ and $Z+cl$ events dominate the 1 b -tag category, $Z+bb$ the 2 and 3+ b -tags categories; in the latter two categories also $t\bar{t}$ production has a significant contribution. Since in the 2-lepton channel

²¹Following the jet labelling scheme described in Sec. 3.4, it is also possible that more than one heavy hadron is associated with a single jet. This is exploited in the rare case that only one track jet is associated with the selected large-R jet in order to still obtain a double label as in two-jet events.

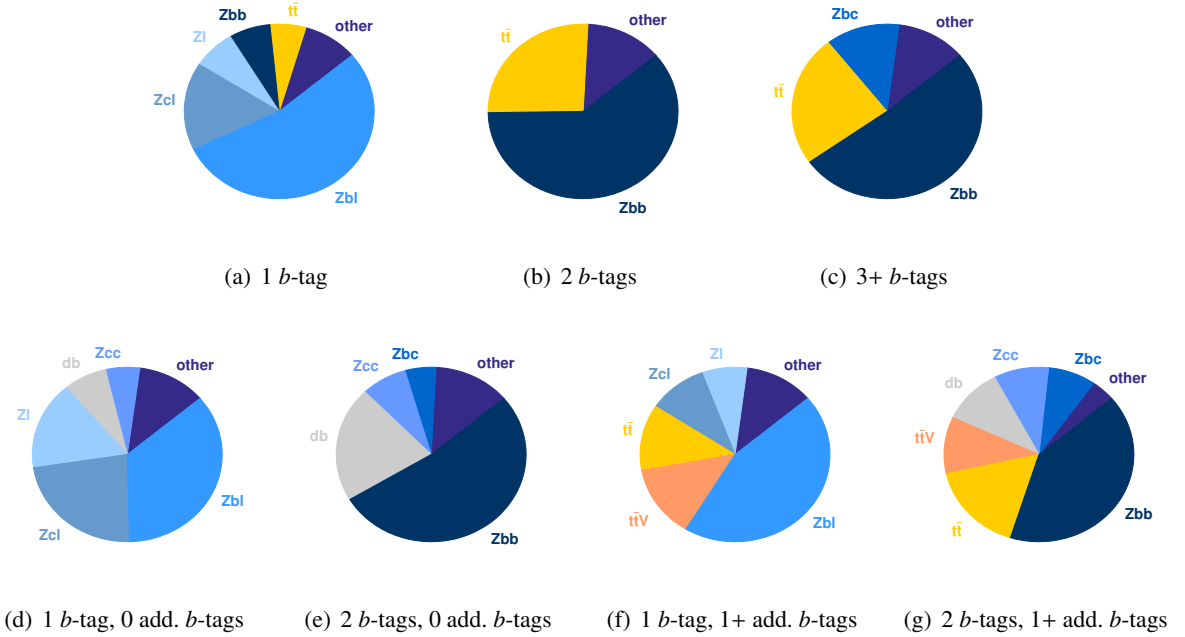


Figure 5.19: Background composition in the b -tag categories of the (a)-(c) resolved and (d)-(g) merged signal regions of the 2-lepton channel. The background processes are as defined in Sec. 5.3; “st” stands for single-top production, “db” for diboson production and “other” for the sum of backgrounds with contributions to the total background below 5%.

generally both top quarks need to decay leptonically in order to meet the signal selection criteria, the $t\bar{t}$ contamination in the 3+ b -tags category mainly arises from events with additional b -(c -)quarks from gluon splittings, despite the small cross section for $t\bar{t}+hf$ production. Additional $t\bar{t}$ contamination is due to misidentifying light jets from initial and final state radiation as b jets.

Also the dominant $Z+bb$ background enters the 3+ b -tags category because of additional radiation, where the overwhelming fraction involves gluon splittings into heavy flavour quark pairs. This also explains the rather large contribution of $Z+bc$ events in the 3+ b -tags category with respect to the 2+ b -tags category: in $Z+bb$ events with additional gluons splitting into c -quark pairs, $Z+bc$ differs from $Z+bb$ only regarding the flavour of the jets used to build the Higgs-boson candidate (cf. Sec. 5.4.2).

In the merged regime, the signal-to-background ratio improves even more drastically with the number of b -tags, as can be seen for the 2-lepton channel in Fig. 5.16(b): only about 5% of the background events passing the event selection exhibit two b -tags; the findings for the 0-lepton channel are similar.

In both channels, the background composition in the different merged b -tag categories generally resemble the corresponding ones in the resolved regime. In particular the 1 b -tag, 0 add. b -tag categories are similarly composed as the 1 b -tag categories, and the 2 b -tag, 1+ add. b -tag categories compared to the 3+ b -tag categories. Besides kinematic differences, implicit requirements on the angular separation of the b -tagged track jets by requiring them to be either associated with the large- R jet (with $R = 1.0$) or not, cause the compositions to differ from the resolved regime and between categories in the merged regime with the same number of b -tagged track jets. Thus, in both the 0-lepton and 2-lepton channel, the contami-

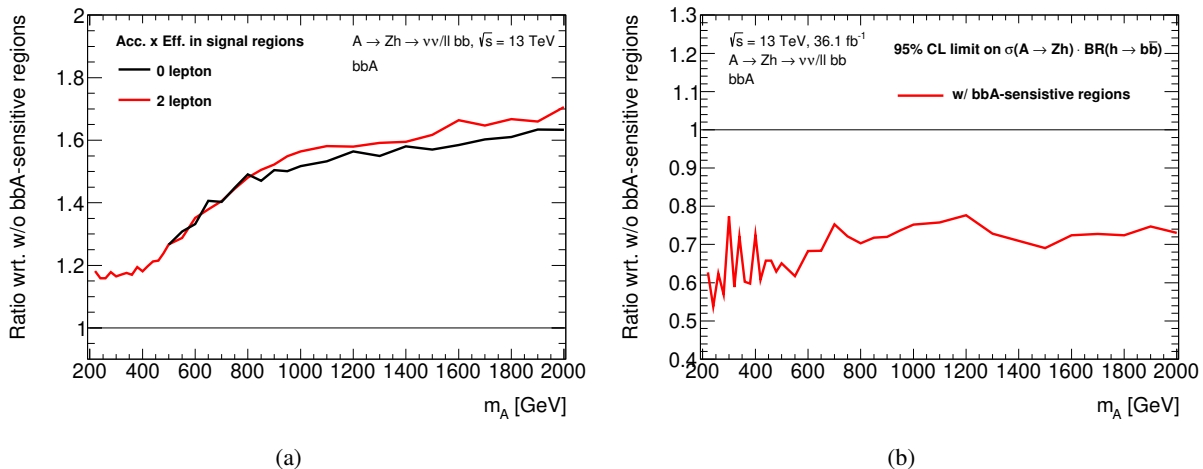


Figure 5.20: Relative impact of the b -tag categories sensitive to b -associated production (bbA), the 3+ b -tags categories in the resolved regime and the 1+ add. b -tag categories in the merged regime, on (a) the signal acceptance times efficiency and (b) on the expected upper limit on the cross-section for bbA production times the branching ratios for the $A \rightarrow Zh$ and $h \rightarrow bb$ decays at the 95 % CL. All considered signal regions of the 0-lepton and 2-lepton channels are combined. Both statistical and systematic uncertainties are considered; nuisance parameters are profiled to the data (cf. Sec. 5.7).

nation due to $t\bar{t}$ production, where the b quarks tend to be emitted far away from each other, is higher in the 1 (2) b -tag (s), 1+ add. b -tags categories than in the 2 b -tags, 0 add. b -tags categories; the opposite trend is observed for $Z+bb$ events.

While the 1+ add. b -tag categories in the 0-lepton channel are abundantly populated with $t\bar{t}$ events (cf. Fig. 5.16(c) and Figs. 5.19(f),(g)), in the 2-lepton channel the background contributions are expected to be very small (cf. 5.16(d)), in particular in the 2 b -tags, 1+ add. b -tags category. In combination with limited simulated sample sizes, this results in large statistical uncertainties on the background predictions. Thus, in order to allow shape information to be exploited in the statistical analysis (Sec. 5.7), the 1 and 2 b -tags categories with 1+ add. b -tags are considered combined in the 2-lepton channel.

Thus, considering the signal fractions and background contributions in the different b -tag categories, it becomes clear that the 1 b -tag regions contribute only little to the overall signal sensitivity; however, they help to constrain background normalisations as discussed further in the next sections. Independent of the considered A -boson production mode, the 2 b -tags (0 add. b -tags) regions are the most sensitive regions. Nonetheless, the bbA -sensitive regions, the 3+ b -tags category in the resolved regime and the 1+ add. b -tags categories in the merged regime, significantly enhance the sensitivity to this production mode. At the same time, neither the acceptance nor the sensitivity for gluon-fusion production are affected by the inclusion of the dedicated regions.

Since these bbA -sensitive signal regions are considered for the first time in the present analysis, their impact on the expected acceptance and sensitivity for A -boson signals produced in b -associated production is demonstrated in Fig. 5.20. As can be seen from Fig. 5.20(a), by including the dedicated regions, the signal acceptance increases in both lepton channels by about 20 % for (very) small m_A and up to 60-70 % for large m_A . Figure 5.20(b) shows the respective change in the expected combined upper limit on the cross

section for A -boson production in b -associated production times the branching ratios for the $A \rightarrow Zh$ and $h \rightarrow bb$ decays at 95 % CL, where all statistical and systematic uncertainties entering the final result are considered (in the form of nuisance parameters which have been profiled to the data; cf. Sec. 5.7): the limit improves by up to 40 % for small m_A , and by about 30 % for $m_A > 600$ GeV.

In summary, the b -tag categorisation finalises the signal selection and yields 13 signal regions, seven in the 0-lepton channel and six in the 2-lepton channel, with varying signal fractions and sensitivities: the 1, 2 and 3+ b -tag(s) categories in the resolved regimes, 1 and 2 b -tag(s) (1+2 b -tags) categories with 0 or 1+ add. b -tags in the merged regimes of the 0-lepton (2-lepton) channel.

Figure 5.21 shows the signal acceptance times efficiency as function of the A -boson mass in the different signal regions of the two channels either assuming pure gluon fusion or b -associated A -boson production. In addition to what was already discussed above, it can be observed that for most of the m_A range the 0-lepton channel is dominating, as expected due to the higher branching ratio for the decay of the Z boson to neutrinos. Only for $m_A \lesssim 500$ GeV the 2-lepton channel is dominant as the 0-lepton channel acceptance is limited by the E_T^{miss} trigger efficiency.

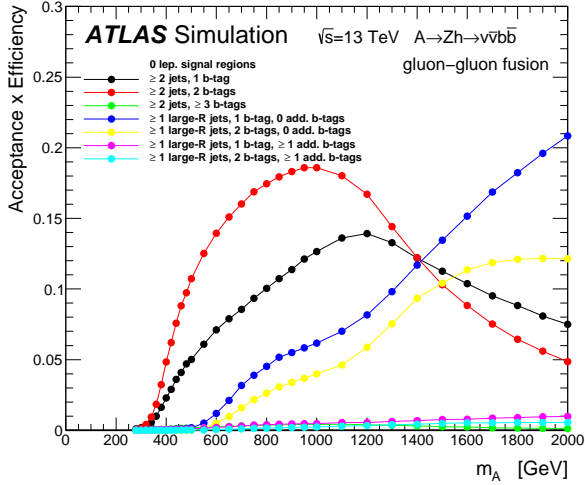
5.5.3 Signal, Control and Validation Regions

As mentioned before, in this analysis all considered background processes are estimated using simulated samples. However, the normalisations of the dominant background processes are determined in the final fit from the data (cf. Sec. 5.7.4), and dedicated modelling systematic uncertainties related to the shape description of the final discriminants and acceptance differences between the analysis regions are considered (cf. Sec. 5.6.2). In addition, systematic uncertainties on the normalisations of the subdominant background processes are taken into account.

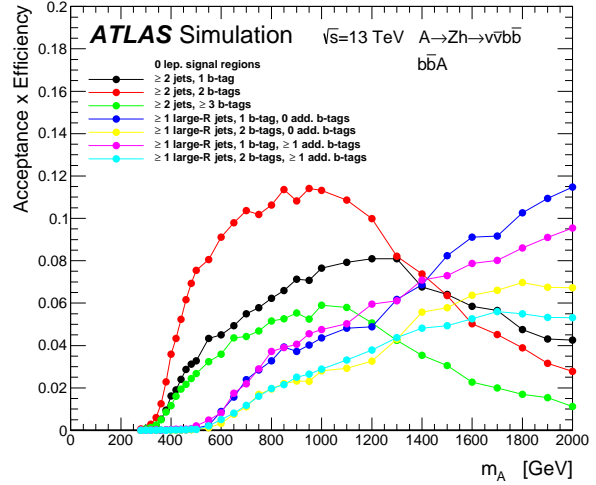
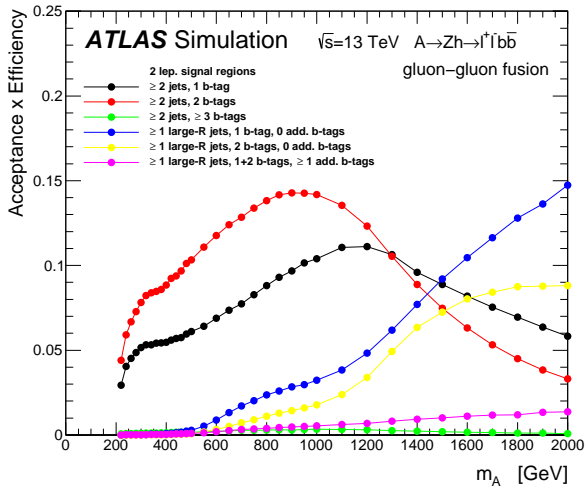
Since an A -boson signal is expected to appear as a narrow resonance on a broad background spectrum in the distributions of the final discriminants, m_{Vh} and $m_{T,Vh}$, in the signal regions, the m_{Vh} and $m_{T,Vh}$ “sidebands” provide good control on the normalisation and shape of the dominant background processes. In the most sensitive 2 b -tags and bbA -sensitive regions, this is in particular the case for the $t\bar{t}$ background in the 0-lepton channel and the $Z+bb$ background in the 2-lepton channel. Since the signal-to-background ratio in the 1 b -tag categories is very low, they contribute rather indirectly to the signal sensitivity by constraining certain background processes (and systematic uncertainties), and thus can be rather considered as control regions. In the 0-lepton channel, they help to better control the $t\bar{t}$ background, and in the 2-lepton channel, the $Z+bl$ and $Z+cl$ components.

The dominance of different Z +jets components in the different b -tag categories allows to control their normalisation and shape with the data. However, the relative contributions of components within the same category, e.g. the $Z+bl/Z+cl$ ratio, cannot be determined; unless the component is controlled by a different category. Consequently, the $Z+bl$ and $Z+cl$ components are grouped together in the final fit, and referred to as $Z+hl$ component, the $Z+bc$ and $Z+cc$ components are treated jointly as a single component together with the dominant $Z+bb$ background, and referred to as $Z+hf$; the $Z+l$ component is kept separately. The same scheme is used to group the W +jets components.

In addition to the signal regions, dedicated regions are exploited to (i) further improve the control on certain background processes by including them in the fit to the data, and to (ii) validate the fit results by



(a) 0-lepton, pure gluon-fusion production

(b) 0-lepton, pure b -associated production

(c) 2-lepton, pure gluon-fusion production

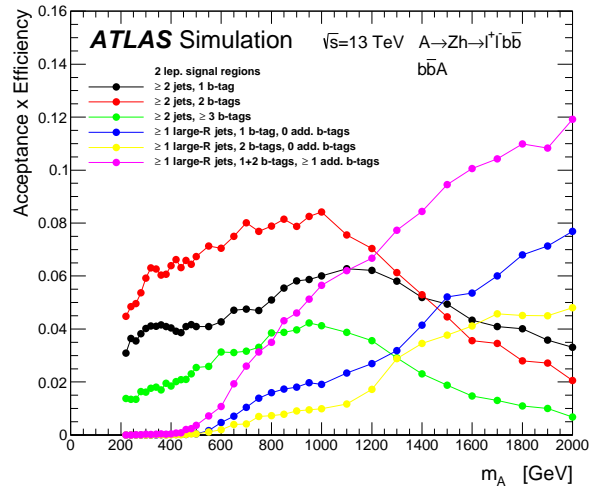
(d) 2-lepton, pure b -associated production

Figure 5.21: Acceptance times efficiency for $A \rightarrow Zh \rightarrow \nu\bar{\nu}b\bar{b}$ and $A \rightarrow Zh \rightarrow \ell\bar{\ell}b\bar{b}$, respectively, in the 0-lepton channel (top) and in the 2-lepton channel (bottom) for pure gluon-fusion (left) and pure b -associated A -boson production (right). Previously published in Ref. [6].

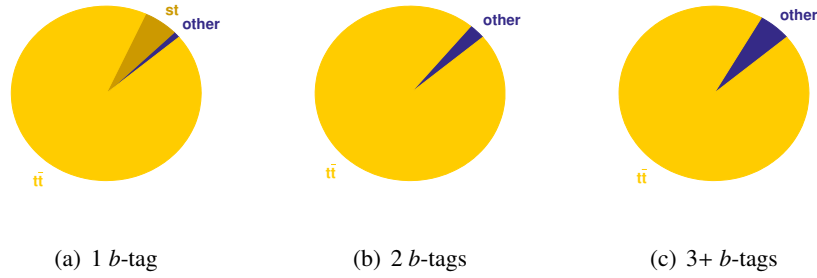


Figure 5.22: Background composition in the b -tag categories of the resolved $e\mu$ region. The background processes are as defined in Sec. 5.3; “st” stands for single-top production and “other” for the sum of backgrounds with contributions to the total background below 5%.

verifying that the adjusted background simulations describe the data well; these are the $e\mu$ (*control*) regions and the m_h -sideband (*validation*) regions or short *sideband regions*, respectively.

The $e\mu$ control regions are introduced in the resolved regime of the 2-lepton channel to improve the control of the $t\bar{t}$ background, whose contribution is sizeable in the 2 b -tags and 3+ b -tags signal regions. The $e\mu$ regions are readily obtained through two small modifications of the event selection used to define the 2-lepton signal regions: (i) instead of requiring the lepton pair to be of same flavour ($ee/\mu\mu$), a mixed-flavour pair ($e\mu$) is selected - giving the region its name-, and (ii) the $E_T^{\text{miss}}/\sqrt{H_T}$ requirement, designed to reduce the $t\bar{t}$ background contribution in the signal region, is dropped.

Figure 5.22 shows the background composition of the $e\mu$ regions, illustrating that they are very pure in $t\bar{t}$ events: their fraction ranges between 93-97% depending on the b -tag category. Although being rather limited in terms of statistical precision, the 3+ b -tags $e\mu$ region provides crucial information on the difficult to model $t\bar{t}$ production in association with additional b jets ($t\bar{t}+hf$).

The ratio of $t\bar{t}$ events entering the 1 and 2 b -tags $e\mu$ regions is sensitive to the b -tagging efficiency for b jets; in fact, a very similar approach is used to calibrate the b -tagging efficiency for b jets, as described in Sec. 3.4. Therefore, in order to minimise the power to constrain the related uncertainties in the final fit, the two regions are combined into the 1+2 b -tags $e\mu$ control region.

While similar $e\mu$ regions can be defined in the merged regime, they are not considered in the final fit given that the $t\bar{t}$ contribution is rather limited in the 2-lepton signal regions of the merged regime. Instead it is assumed that adjustments to the simulation in the resolved regime are also applicable to the merged regime; potential deviations are taken into account by dedicated systematic uncertainties (cf. Sec. 5.6.2).

The m_h -sideband regions are defined for both channels and regimes, mirroring the signal regions. Events enter the respective regions if they pass the whole event selections *with the exception of* the Higgs-mass window requirements, which instead they need to fail. They are still required to fulfil $m_h > 50$ GeV and $m_h < 200$ GeV, in order to ensure that the events in the sideband regions are similar to those in the signal regions; thus making them ideal to control and verify the modelling of the dominant background contributions, given the reduced expected signal fractions.²² At most 35 (50)% of the total signal contri-

²²The $m_h > 50$ GeV requirement, furthermore removes a region at low large-R jet mass in the merged regime that is known to be not well described by simulation and where the applied calibrations are not necessarily valid.

bution ends up in the low sideband regions (below the m_h window), and up to 10 % in the high sideband regions of the 2 (0)-lepton channel; in the case of b -associated A -boson production, the contributions are about 15-20 (10) % higher.

Adopting the PriorityResolvedSR regime-selection strategy also for the sideband regions, events that fail both the resolved and merged signal-region selections, are first tested for entering the resolved and then the merged sideband regions; if they fail the additional m_h selection, they get discarded.

The sideband regions are divided into the same b -tag categories as the signal regions. As intended, the background contributions and compositions are very similar to the signal regions; (small) differences persist due to the altered kinematic selection. Since the total background contributions are limited in the low and high sideband regions, they are merged into a single one for the validation of the fit to data (cf. Sec. 5.7.7).²³

5.6 Systematic Uncertainties

There are several sources of systematic uncertainties that need to be considered in this analysis. They can be roughly grouped into two categories, experimental and modelling systematic uncertainties, which will be discussed separately in the following.

The former group of systematic uncertainties, discussed in Sec. 5.6.1, is related to the detector performance, the characterisation of the collected data and in particular the reconstruction, identification and calibration of the physics objects. As they are determined in dedicated measurements and provided to physics analyses, as described in e.g. Secs. 2.2.5 and 3, their impact on the analysis is assessed by varying the affected properties in the signal and background simulations within the given uncertainties; for example, the transverse momenta of leptons and jets within the energy scale uncertainties. The effect on the normalisations and distributions of the final discriminants in the different analysis regions is taken into account in the fit to the data by means of *nuisance parameters*, as described in more detail in Sec. 5.7.

The impact of systematic uncertainties related to the modelling of the signal and background processes in simulation is evaluated and considered similarly. The uncertainties are derived by means of alternative simulated samples or variations of the generator settings used to obtain the nominal simulations, as described in Sec. 5.6.2.

5.6.1 Experimental Systematic Uncertainties

All experimental uncertainties considered in this analysis are summarised in Table 5.2 and discussed in the following.

The uncertainty on the luminosity determination which amounts to 2.1 % and 3.4 % for the 2015 and 2016 data, respectively, and 3.2 % for the combined dataset, needs to be taken into account for the signal and all (subdominant) background processes, whose normalisations are not determined from the fit to data (cf. Sec. 5.7). Following a methodology similar to the one described in Sec. 2.2.5, it was derived from a preliminary calibration of the luminosity scale using x - y beam-separation scans performed in August 2015 and May 2016. The average number of additional interactions per bunch-crossing μ , which is proportional to the pile-up activity, is corrected in simulation by increasing it by 9 %, and an uncertainty of the same

²³However, for a better validation of the signal regions it would be preferable to keep them separately.

Systematic uncertainty name	Description
Event	
LUMI_201516	uncertainty on total integrated luminosity
PRW_DATASF	uncertainty on pile-up modelling
Electrons	
EL_EFF_Trigger	trigger efficiency uncertainty
EL_EFF_Reco	reconstruction (reco.) efficiency uncertainty
EL_EFF_ID	identification (id.) efficiency uncertainty
EL_EFF_Iso	isolation efficiency uncertainty
EG_SCALE	energy scale uncertainty
EG_RESOLUTION	energy resolution uncertainty
Muons	
MUON_EFF_TrigStat(Syst)	trigger efficiency uncertainty
MUON_EFF_STAT(SYS)	reco. and id. efficiency uncertainty for muons with $p_T > 15$ GeV
MUON_EFF_STAT(SYS)_LPT	reco. and id. efficiency uncertainty for muons with $p_T < 15$ GeV
MUON_ISO_STAT(SYS)	isolation efficiency uncertainty
MUON_TTVA_STAT(SYS)	track-to-vertex association efficiency uncertainty
MUON_SCALE	energy scale uncertainty
MUON_SAGITTA(_RHO)	energy scale uncertainty to cover charge-dependent local misalignment effects
MUON_ID(MS)	energy resolution uncertainty of the inner detector (muon spectrometer)
τ_{had} leptons	
TAUS_MODEL_MODEL	energy scale uncertainty due to modelling and non-closure
TAUS_MODEL_INSITU	energy scale uncertainty due to in-situ calibration
TAUS_MODEL_DETECTOR	energy scale uncertainty due to detector simulation
Small-R jets	
JET_EffNP_{1-7,8restTerm}	energy scale uncertainties due to in-situ calibration
JET_EtaICal_{Modelling,NonClosure,TotalStat}	energy scale uncertainties to cover η -intercalibration non-closure
JET_FlavComp(Flavor_Response)	energy scale uncertainty related to flavour composition (response)
JET_PU_{OffsetMu(NPV),PtTerm,RhoTopology}	energy scale uncertainties due to pile-up effects
JET_{PunchThroughMC,HighPt,BJES_Response}	energy scale uncertainties for 'punch-through', high- p_T and b jets
JET_AFII	energy scale uncertainty for the parametrised calorimeter simulation
JER	energy resolution uncertainty
JET_JvtEfficiency	JVT efficiency uncertainty
Large-R jets	
FATJET_Baseline_Kin	energy and mass scale uncertainty due to basic data-simulation differences
FATJET_Modelling_Kin	energy and mass scale uncertainty due to simulation differences
FATJET_Tracking_Kin	energy and mass scale uncertainty on reference tracks
FATJET_TotalStat_Kin	energy and mass scale uncertainty from stat. unc. on the measurement
FATJET_JER	energy resolution uncertainty
FATJET_JMR	mass resolution uncertainty
b -tagging: small-R and track jets	
FT_EFF_B_{0-2}_{smallR,track}	b -tagging efficiency uncertainties for b jets
FT_EFF_C_{0-3}_{smallR,track}	b -tagging efficiency uncertainties for c jets
FT_EFF_Light_{0-4}_{smallR,track}	b -tagging efficiency uncertainties for light jets
FT_EFF_extrap_{smallR,track}	b -tagging efficiency uncertainty for high- p_T b and c jets
FT_EFF_extrapFromC_{smallR,track}	b -tagging efficiency uncertainty on τ -lepton jets
E_T^{miss} and $E_{T,\text{trk}}^{\text{miss}}$	
METTrigStat	E_T^{miss} trigger efficiency uncertainty due to stat. unc. of the measurement
METTrigTop(Z)	E_T^{miss} trigger efficiency uncertainty due to sample dependence
MET_SoftTrk_ResoPara(Perp)	'soft term'-related longitudinal(transverse) resolution uncertainty
MET_SoftTrk_Scale	'soft term'-related scale uncertainty
MET_JetTrk_Scale	$E_{T,\text{trk}}^{\text{miss}}$ scale uncertainty

Table 5.2: Summary of the experimental systematic uncertainties discussed in the text.

amount is assigned which covers the difference between the measured and predicted inelastic cross section (in a fiducial volume) [322].

The efficiency of the reconstruction and identification of electrons and muons, of their isolation definitions and of the single-lepton triggers was measured in 13 TeV data as described in Secs. 3.5 and 3.6, and the corresponding uncertainties are taken into account in the 2-lepton channel. As can be seen from Table 5.2, for muons dedicated uncertainties are also considered for the track-to-vertex association as well as the identification of muons with low transverse momenta ($p_T < 15$ GeV), and it is differentiated between statistical and systematic sources.

Uncertainties on the lepton energy scales (and resolutions) were also determined using 13 TeV data, as described in Secs. 3.5, 3.6 and 3.8, and are considered not only for electrons and muons, but in the 0-lepton channel also for τ_{had} leptons (due to the various lepton vetoes). For muons two additional uncertainties on the energy scale are included. They cover local charge-dependent effects observed in the data due to misalignments especially in the inner detector, but also in the muon spectrometer; independent uncertainties are provided for their resolutions in the ID and the MS. Three sources of uncertainties on the tau energy scale (TES) are considered: related to the modelling of hadronic τ -lepton decays and the material distribution in the detector in simulation, as well as the in-situ calibration.

As described in Sec. 3.3, the jet energy scale of small-R jets was determined using 2016 data with a precision of about 4.5 % for jets with low p_T and about 1 % for $p_T \approx 200$ GeV, fairly constant versus η . Uncertainties related to the in-situ analyses, the non-closure of the η -intercalibration, pile-up effects, the flavour composition and response (covering differences between quark and gluon jets), the different responses of high- p_T , punch-through and b jets as well as the non-closure of the AFII detector simulation are considered. Taking into account the many sources of uncertainties, they are decomposed and reduced to 21 uncorrelated components that are listed in Table 5.2. For the jet energy resolution of small-R jets one uncertainty is included that is of the order of 1-3 %, decreasing with increasing jet p_T .

The energy and mass scales of large-R jets were also determined in 2016 data with total uncertainties at the level of 3 % and 5 %, respectively. Four sources are distinguished related to (i) basic data-simulation differences, (ii) differences between alternative simulations, (iii) uncertainties on the reference tracks used in the calibrations, as well as (iv) statistical uncertainties. They are treated correlated between the energy and the mass of the large-R jets in this analysis, resulting in four independent scale uncertainties. On the large-R jet energy resolution an uncertainty of 2 % is assumed, independent of the large-R jet p_T ; on the jet mass resolution a relative uncertainty of 20 %.

In this analysis both small-R and track jets are considered for b -tagging. For the former type, the b -jet tagging efficiency as well as the c -jet tagging efficiency and light-jet mistag rate were calibrated with 2016 data, as described in Secs. 3.4 and 4. For track jets, only the b -jet tagging efficiency is calibrated, using the same methods and dataset; corrections for the c -jet tagging efficiency and mistag rate in simulation and the related uncertainties are propagated from the results obtained for small-R jets. The uncertainties considered in this analysis are at the level of 2-12 % for b jets, 40 % for c jets and 30 % for light jets, depending on the jet p_T and $|\eta|$; the latter two uncertainties are even slightly larger for track jets due to the additional extrapolation uncertainty. As already discussed in Secs. 3.4, the unusually large uncertainty for c jets is because a preliminary calibration result is used, where the tension between the scale factors of the baseline $W+c$ calibration and the alternative $t\bar{t}$ calibration is taken into account by assigning the difference as additional uncertainty. The tension got resolved later and it was confirmed that the scale factors, and thus

the b -tagging efficiency, for c jets used in the present analysis was underestimated by 20-40%. However, it was refrained from updating the calibration results due to the timescale of the analysis and the fact that the large assigned uncertainty allowed the corresponding nuisance parameter to be pulled in the fit and somewhat correct the c -jet tagging efficiency in simulation towards the measured result (cf. Sec. 5.7.7).

The uncertainties related to the b -tagging efficiency measurements are also decomposed into uncorrelated components. According to the used scheme, this results into three independent uncertainties for b jets, four for c jets and five for light jets. Further uncertainties are considered that are related to two simulation-based scale-factor extrapolations, similarly applied to small-R and track jets, namely: (i) for b and c jets to high transverse momenta ($p_T > 300$ GeV and $p_T > 140$ GeV, respectively), based on the highest- p_T bins measured, and (ii) for the misidentification of hadronic τ -lepton decays, estimated based on the c jet tagging efficiency; uncertainties related to the first are treated correlated between b and c jets. The uncertainties listed in Table 5.2 apply both to small-R and track jets; however, they are treated uncorrelated in the final fit as recommended.²⁴

In addition to the uncertainties on the energy scale and resolution of the small-R jets and the leptons that are propagated to the E_T^{miss} calculation, extra uncertainties related to the scale and resolution of the E_T^{miss} soft term, are considered; they were determined in 2016 data as described in Sec. 3.9. The uncertainties of the soft term also enter via $E_{T,\text{trk}}^{\text{miss}}$ and are treated fully correlated with E_T^{miss} . An additional uncertainty on $E_{T,\text{trk}}^{\text{miss}}$ is considered for tracks in jets, covering differences observed between data and simulation.

Furthermore, three uncertainties regarding the E_T^{miss} trigger efficiency are taken into account: the statistical uncertainty on the nominal measurement as well as the uncertainties assigned to cover the differences of the results obtained using two alternative samples, i.e. $t\bar{t}$ and Z +jets instead of W +jets; each is at the level of 2%.

5.6.2 Modelling Systematic Uncertainties

In this analysis, the signal and all background processes are estimated from simulations, described in Sec. 5.3, and uncertainties related to their description are taken into account. While for the signal and the subdominant backgrounds only uncertainties regarding their normalisation are considered, for the dominant $t\bar{t}$ and V +jets processes, whose normalisation is extracted from the final fit to data (cf. Sec. 5.7), acceptance uncertainties on the relative normalisation between analysis regions and uncertainties on the shape of the final discriminant (m_{Vh} , $m_{T,Vh}$) are included; all considered modelling uncertainties are summarised in Tables 5.3-5.6 and are discussed in the following.

The uncertainties on the signal normalisation are derived from particle-level comparisons between samples generated with the nominal setup described in Sec. 5.3 and after systematic variations of certain parameters using the RIVET [323] framework. In particular the impact of (i) varying the factorisation and renormalisation scales independently by a factor two, (ii) using an alternative PDF set, namely MSTW2008LO (instead of NNPDF2.3LO), and (iii) changing the parton shower and underlying event tune is evaluated on signal samples for seven representative mass hypotheses, where the A boson is produced in gluon fusion and decays to the $\ell\ell b\bar{b}$ final state. A basic event selection similar to the one described in Sec. 5.4.3 for the resolved regime was applied to define the fiducial region. While the first set of variations results in an ac-

²⁴In any case, the difference between whether or not the b -tagging related uncertainties on small-R and track jets (fully) are treated correlated was found to be negligible in studies for the earlier version of analysis.

Normalisation uncertainties		
Name	Description / source	Value
AZhTheory	Signal acceptance	2-8 % (depending on mass point)
ZlNorm	$Z+l$ normalisation	19 %
WhfNorm	$W+hf$ normalisation	26 %
WhlNorm	$W+hl$ normalisation	23 %
WlNorm	$W+l$ normalisation	20 %
VVNorm	Diboson normalisation	11 %
StopNorm	Single-top normalisation	19 %
ttVNorm	$t\bar{t}V$ normalisation	50 %
ttHNorm	$t\bar{t}h$ normalisation	50 %
HiggsNorm	SM Vh ($h \rightarrow b\bar{b}$) normalisation	50 %

Table 5.3: Summary of the systematic uncertainties on the signal acceptance and normalisation of the background processes obtained from theoretical predictions (cf. Sec. 5.3).

ceptance change at the level of 1 % for all considered mass points, the impact of the other two depend on the A -boson mass, and thus are parametrised as function of m_A . Adding all contributions in quadrature leads to an uncertainty of up to 8 % at low m_A , it decreases towards higher m_A down to about 2 % (cf. Table 5.3). The same uncertainties are applied in the 0-lepton channel and in case b -associated A -boson production is considered.

The impact of certain choices in the simulations on the predicted acceptance and the shape of the final discriminants are assessed for the dominant $t\bar{t}$ and V +jets backgrounds. This is done by comparing various predictions made by a number of alternative simulated samples generated using different programs or different generator settings with respect to the nominal simulations. The comparisons are done at reconstruction level and individually for each channel, in the respective fiducial spaces defined by the event selections described in Sec. 5.4.3. In order to derive acceptance uncertainties, all studied samples are normalised to the same production cross-sections mentioned in Sec. 5.3. When shape uncertainties are evaluated, the samples are normalised to unity, individually in each considered analysis region.²⁵

In the case of the $t\bar{t}$ process, the impact due to the choice of model for parton shower, hadronisation, underlying event (UE) and multi-parton interaction (MPI) is evaluated by comparing the nominal sample (POWHEG+PYTHIA6) to one generated with POWHEG+HERWIG++ (cf. Sec. 5.3). In order to test the impact of a different hard-scatter description, the POWHEG+HERWIG++ sample is compared to the MADGRAPH5_aMC@NLO+HERWIG++ sample, where a different matrix-element generator is exploited. The impact of an increase or decrease of radiation is assessed by comparing the nominal sample to two variations obtained by changing the generator settings: (i) where the renormalisation and factorisation scales are halved while the value of the h_{damp} factor is doubled, and (ii) where the renormalisation and factorisation scales are doubled. By averaging the impact of these two variations, three independent shape uncertainties

²⁵In order to reduce the impact of statistical fluctuations, shape uncertainties are obtained by first parametrising the difference found in each comparison by fitting an n^{th} -order polynomial to the ratio of the alternative over the nominal prediction, and then deriving the systematically varied shape by reweighting the nominal distribution accordingly.

Shape uncertainties	
Name	Description / source
$t\bar{t}$	
TTbar_Herwig_L{0,2}	shower, hadronisation etc. modelling uncertainty
TTbar_aMcAtNlo_L{0,2}	hard-scatter modelling uncertainty
TTbar_rad_L{0,2}	extra radiation uncertainty
NNLORW_L{0,2}	'NNLO reweighting' uncertainty
V +jets	
Vjets_MG_{hf,hl,1}	general modelling uncertainty (SHERPA 2.2.1-vs-MADGRAPH5_aMC@NLO+PYTHIA8 comparison)
Vjets_ShRenorm_{hf,hl,1}	renormalisation scale uncertainty
Vjets_ShFac_{hf,hl,1}	factorisation scale uncertainty
Vjets_ShAlphaPDF_{hf,hl,1}	uncertainty related to the α_S value used in the PDF

Table 5.4: Summary of the modelling systematic uncertainties affecting only the shape of the m_{Vh} distribution of the $t\bar{t}$ and W or Z backgrounds. The uncertainties are derived for each lepton channel (0, 2) separately, also for the W or Z boson backgrounds commonly denoted V , and different flavour components: hf , hl and l . The chosen naming convention is in view of the treatment of the systematic uncertainties in the statistical analysis (cf. Sec. 5.7.4).

are obtained for each of the 0- and 2-lepton analysis regions, listed in Table 5.4.

Acceptance uncertainties on the relative normalisation between analysis regions, namely (i) between the resolved and merged regimes, (ii) between the signal and sideband regions, separately in the resolved and merged regimes, and, in the case of the 2-lepton channel, (iii) between the resolved signal (and sideband) regions and the $e\mu$ control region are obtained by adding the differences due to the discussed variations in quadrature; where, instead of averaging over the impact of the change in radiation, the maximum is considered. The results are summarised in Table 5.5.

In addition to considering the discussed three sources of modelling uncertainties on the $t\bar{t}$ background following the prescription in Ref. [324], one extra shape uncertainty is included, which is related to the applied 'NNLO reweighting', introduced in Sec. 5.3. Its full impact on the shape of the final discriminants is symmetrised and considered as systematic uncertainty (cf. Table 5.4).

Given the significant difference regarding the probed phase-space regions in the 0- and 2-lepton channels, the $t\bar{t}$ background is regarded as independent in the two channels, meaning separate normalisations are allowed in the fit to data and both the acceptance and shape uncertainties are treated uncorrelated (cf. also Sec. 5.7.4).

To derive modelling uncertainties for the V +jets processes two sets of comparisons are considered. For the first, the nominal simulation (SHERPA 2.2.1) is compared to an alternative one obtained with MADGRAPH5_aMC@NLO+PYTHIA8 (cf. Sec. 5.3 for details). By doing so, the combined impact of the choice of hard-scatter description as well as parton-shower, hadronisation and UE model is evaluated, defining a rather *general modelling* uncertainty. For the second comparison, variations of the setup of the nominal simulation are studied, namely (i) factorisation and renormalisation scales are varied independently and coherently by factors 0.5 and 2, (ii) the α_S value used by the nominal PDF set (NNPDF 3.0 NNLO) is var-

Acceptance uncertainties			Value	
Name	Description / source	0 lepton	2 lepton	
<u>$t\bar{t}$</u>				
$ttbar_rmRatio_L\{0,2\}$	merged-to-resolved regime ratio	15 %	46 %	
$ttbar_emuRatio_L2$	SR-to-' $e\mu$ CR' ratio	-	2.4 %	
$ttbar_srcrRatio_L\{0,2\}$	sideband-to-SR ratio			
	\hookrightarrow resolved regime	6 %	3.4 %	
	\hookrightarrow merged regime	11 %	22 %	
<u>Single top</u>				
$Stop_rmRatio_L\{0,2\}$	merged-to-resolved regime ratio		24 %	
$Stop_srcrRatio_L\{0,2\}$	sideband-to-SR ratio			
	\hookrightarrow resolved regime		7 %	
	\hookrightarrow merged regime		5 %	

Table 5.5: Summary of the modelling systematic uncertainties on the acceptance differences between analysis regions for the $t\bar{t}$ and single-top backgrounds as introduced in the text.

ied corresponding to a variation of the renormalisation scale by factors 0.5 and 2, and (iii) variations of the PDF set. Since variation (iii) was found to be of very small size and without impact on the discriminants' shape, it is not further considered. Therefore, three shape uncertainties are included from the second set: two due to the individual renormalisation- and factorisation-scale variations, and one from the α_S (PDF) variation, where the scaling by factors 0.5 and 2 is interpreted as up/down variation of the same source. Thus, in total four shape uncertainties are considered, as listed in Table 5.4.

Acceptance uncertainties are obtained by first adding in quadrature the largest difference to nominal from the variations under (i) and (ii), respectively, then comparing the result to the one from the generator comparison, and assigning whichever is largest as uncertainty.

Although the discussed acceptance and shape effects are determined individually for the two channels, the resulting shape uncertainties are treated correlated and the acceptance uncertainties are harmonised: (i) in the case of the Z +jets background the larger uncertainty is applied to both channels, and (ii) the acceptance uncertainty derived for the W +jets background in the 0-lepton channel, is also used in the 2-lepton channel. In the case of the dominant Z +jets background, remaining differences between the 0- and 2-lepton channel phase-spaces are accounted for by an additional acceptance uncertainty on the ratio of their overall normalisations; the same variations as discussed above are considered.

Since the V +jets background is in fact treated as three independent background contributions, $V+hf$, $V+hl$ and $V+l$, as discussed in Sec. 5.5.3, both the acceptance and shape uncertainties are derived separately for each component. The resulting values in the case of the former are listed in Table 5.6. While the $Z+hf$ and $Z+hl$ normalisations are obtained from the fit to data (cf. Sec. 5.7.4), the normalisations of all other components are estimated from simulation and corresponding uncertainties are derived in the same manner as for the acceptance uncertainties; they are summarised in Table 5.3.

Despite the rather small contribution of the single top-quark background in the 0- and 2-lepton channels,

Acceptance uncertainties					
Name	Description / source	Value			
		hf	hl	l	
<u>Z+jets</u>					
$Z\{hf,hl,l\}_{rmRatio}$	merged-to-resolved regime ratio	19 %	28 %	23 %	
$Z\{hf,hl,l\}_{lepRatio}$	0-to-2-lepton channel ratio	15 %	22 %	8 %	
$Z\{hf,hl,l\}_{srcrRatio}$	sideband-to-SR ratio				
	\hookrightarrow resolved regime	6 %	4 %	6 %	
	\hookrightarrow merged regime	8 %	14 %	5 %	
<u>W+jets</u>					
$W\{hf,hl,l\}_{rmRatio}$	merged-to-resolved regime ratio	43 %	35 %	20 %	
$W\{hf,hl,l\}_{srcrRatio}$	sideband-to-SR ratio				
	\hookrightarrow resolved regime	6 %	5 %	2 %	
	\hookrightarrow merged regime	15 %	2 %	3 %	

Table 5.6: Summary of the modelling systematic uncertainties on the acceptance differences between analysis regions for the W and Z backgrounds as introduced in the text. They are common for the two lepton channels, except for $Z\{hf,hl,l\}_{lepRatio}$ which is only applied to the 0-lepton channel.

not only a normalisation uncertainty, but also acceptance uncertainties regarding the merged-to-resolved regime ratio as well as the sideband-to-signal region ratio are considered, for consistency with the HVT search. All uncertainties are derived in the additional 1-lepton channel, where the single-top contribution is quite significant in certain regions. The same generator variations are studied as described for the $t\bar{t}$ background; for the Wt -channel also the impact of the method used to remove the interference with the $t\bar{t}$ process is taken into account (*diagram subtraction* versus *diagram removal*).

The normalisations and acceptance ratios between the analysis regions are taken from simulation for the remaining background processes with small contribution. Only uncertainties on their overall normalisations are considered: 11 % for the diboson background [325], 50 % for the SM Vh ($h \rightarrow bb$), $t\bar{t}V$ and $t\bar{t}h$ backgrounds, covering the uncertainties on the cross sections; they are also listed in Table 5.3.

5.7 Statistical Analysis

5.7.1 Introduction: the $A \rightarrow Zh$ Search as Hypothesis Test

The search for a new signal, such as the A boson, can be formulated as a frequentist statistical hypothesis test, i.e. the test whether the data is rather described by known (SM) processes alone, the *background-only hypothesis*, or by a combination of known processes *and* the new signal, the *signal-plus-background hypothesis*. By introducing a *signal strength parameter* μ that scales the signal contribution, the signal-plus-background hypothesis turns into the background-only hypothesis for $\mu = 0$. Thus, the signal strength is the *parameter of interest (POI)*, which is estimated in the present analysis from a binned *profile likelihood fit* to the data. The fit is performed in the m_{Vh} and $m_{T,Vh}$ distributions simultaneously in the various analysis regions of the 0- and 2-lepton channels, using the HISTFACTORY tool [326] and the RooSTATS/ RooFIT

framework [327, 328].

As the likelihood L is a (probability) function of the parameters of the statistical model *given the data*, the model is improved by including additional parameters, *nuisance parameters* θ , that are not directly of interest. Their a priori unknown values need to be estimated either directly from the fit to the data or by external, prior measurements; in which case they still may be adjusted in the fit to the data. For most nuisance parameters such *subsidiary measurements* are available with uncertainties, as the ones discussed in Sec. 5.6; they act as constraints in the form of penalty terms in the likelihood and result in a loss of information about μ . In the former case, the nuisance parameters are referred to as being *freely floating*, since they are completely determined from the data, without any constraints or penalties regarding the values they may take; examples are the normalisations of the dominant background processes.

In the case the sensitivity of the analysis to the nuisance parameters is small, this approach mainly propagates the systematic uncertainties on the discriminants into uncertainties on μ . If, on the other hand, the likelihood provides a stronger constraint than the subsidiary measurement, the resulting inference on μ reflects systematic uncertainties that are smaller than the input values: this marginalisation of systematic uncertainties is referred to as *profiling*.

Whether the outcome of the fit results into rejecting the background-only hypothesis or the signal-plus-background hypothesis is then evaluated based on the *test statistic*

$$t_\mu = -2 \ln \lambda(\mu), \quad (5.3)$$

which, in the present analysis, is constructed from the *profile likelihood ratio* (cf. e.g. Ref. [329]):

$$\lambda(\mu) = \frac{L(\mu, \hat{\theta})}{L(\hat{\mu}, \hat{\theta})}, \quad (5.4)$$

for a hypothesised value of μ . Here $\hat{\theta}$ denotes the *conditional* estimate of the nuisance parameters that maximise the likelihood for the *hypothesised* μ , while $\hat{\mu}$ and $\hat{\theta}$ are the *unconditional* estimates of the signal strength and the nuisance parameters, respectively. Thus, the profile likelihood ratio takes values $0 \leq \lambda(\mu) \leq 1$, where large values close to unity imply good agreement between the hypothesised signal strength μ and the observed data.

The following section introduces common measures quantifying the level of disagreement between the data and a tested hypothesis that ultimately allow to claim the discovery of a new signal or to exclude its presence with a certain confidence, as is also done in Sec. 5.8. Section 5.7.3 discusses in detail the general form of the likelihood function $L(\mu, \theta)$, and in particular the inclusion of the various constraints on the fit parameters provided by subsidiary measurements; the description is mainly based on Ref. [330]. Section 5.7.4 describes the *fit model* used to derive the final results of the $A \rightarrow Zh$ analysis, with special emphasis on the considered nuisance parameters and their correlations across the analysis regions and fit components. Section 5.7.5 details a number of “grooming” techniques applied to the list of considered systematic uncertainties, aiming to improve the fit stability. In Section 5.7.6 the expected results are evaluated that are obtained using the *Asimov dataset* introduced in Sec. 5.7.2, and discussed in particular regarding their limitations. While the described nuisance-parameter approach is considered the best way to incorporate systematic uncertainties in a maximum likelihood method and to estimate their impact on the fit

result, it critically depends on the fit model describing all effects due to the various sources of systematic uncertainties properly. Therefore, the validation of the fit model is an integral part of an analysis relying on this approach, and Sec. 5.7.7 is dedicated to it for the present analysis.

5.7.2 Discovery vs. Exclusion Limit

One measure for the level of disagreement between the observed data and a given hypothesis, determined by the value of μ , is the *p-value*, defined as

$$p_\mu = \int_{t_{\mu,obs}}^{\infty} f(t_\mu | \mu) dt_\mu, \quad (5.5)$$

where f denotes the probability density function of the test statistic t_μ , assuming data distributed according to the tested hypothesis, and $t_{\mu,obs}$ is the actually observed value. As the *p-value* describes the probability of finding data of equal or greater *incompatibility* with the prediction, the tested hypothesis is regarded as excluded, if the observed *p-value* is *below* a specified threshold. It is convention, to claim the discovery of a new signal, if the background-only hypothesis ($\mu = 0$) is rejected with a value of $p_0 \leq 2.87 \cdot 10^{-7}$, which corresponds to a *significance* of 5 standard deviations (σ).²⁶ If it is not possible to reject the background-only hypothesis at this level, often upper limits on the signal strength μ or related quantities, such as the signal yield, are set, based on the measure defined by the CL_s method [331, 332]. Defining CL_s according to Ref. [333] as

$$CL_s = \frac{p_\mu}{1 - p_b}, \quad (5.6)$$

where p_μ is defined as in Eq. 5.5, with $t_{\mu,obs} = t_{\mu,limit}$, and

$$p_b = 1 - \int_{t_{\mu,limit}}^{\infty} f(t_\mu | 0) dt_\mu, \quad (5.7)$$

allows to consider signal-plus-background hypotheses with signal strengths greater or equal to μ_{limit} , i.e. $\mu \geq \mu_{limit}$, as excluded at the confidence level CL for

$$CL_s \leq 1 - CL, \quad (5.8)$$

where typically $CL = 95\%$. The advantage of basing the decision whether or not to exclude a signal-plus-background hypothesis on CL_s , instead of p_μ alone, prevents to exclude models to which the analysis has only little or no sensitivity; which is reflected in large values of p_b , penalising the denominator in Eq. 5.6.

When designing an analysis, the *expected (median) significance* with which a hypothesis can be rejected is an often exploited, useful quantity. In order to obtain it, the value of the test statistic in data, $t_{\mu,obs}$, is estimated as the median $\text{med}[t_\mu | \mu']$ of the distribution $f(t_\mu | \mu')$, i.e. the distribution of the test statistic for a hypothesis with signal strength μ , under the assumption that the data is distributed according to a *different* signal strength $\mu' \neq \mu$. Thus, in the case of aiming to determine an expected upper limit, the value of the test statistic in data, $t_{\mu,limit}$, is estimated as the median $\text{med}[t_\mu | 0]$ of the distribution $f(t_\mu | 0)$, where the

²⁶The significance is obtained from $Z_\mu = \Phi^{-1}(1 - p_\mu)$, where Φ^{-1} is the inverse of the cumulative normal distribution and p is defined according to Eq. 5.5.

data is assumed to agree with the background-only hypothesis, i.e. $\mu' = 0$, while a signal-plus-background hypothesis with $\mu \neq 0$ is tested.

In order to be able to compute the p -value for any hypothesis, the distribution of the used test statistic f is required. This can be achieved by sampling the distribution employing the Monte Carlo method [334]. However, this computationally expensive procedure can be bypassed by exploiting approximations based on the results derived by Wald and Wilks, as described in Ref. [335]. Thus, in the large-sample limit, $f(t_\mu | \mu)$ can be described (exactly) by a *non-central χ^2 -distribution* for one degree of freedom with non-centrality parameter $\Lambda = (\mu - \mu')^2 / \sigma^2$ (given μ is the only POI); the approximation also yields reasonably accurate results for fairly small datasets. In this context, a procedure receives justification that is particularly useful when determining the expected (median) significances: an ensemble of simulated datasets is replaced by a single, representative one, the *Asimov dataset*. It is an artificial dataset defined such that the estimators obtained with the profile likelihood fit are the true parameter values, i.e. $\hat{\mu} = \mu$ and $\hat{\theta} = \theta$. In practice, the Asimov dataset is obtained from the simulated predictions for the considered background processes, as well as the signal, in the case the signal-plus-background hypothesis is assumed to be realised in data. Furthermore, using the Asimov dataset also allows to estimate the expected deviations of the median significance due to (expected) statistical fluctuations in the data.

The p -value discussed so far is also referred to as the *local p -value*, in order to be able to distinguish it from the *global p -value*; a distinction that is relevant, if more than one signal hypothesis is tested. This is for example the case in the present analysis, where the m_{Vh} ($m_{T,Vh}$) spectra are searched for an A -boson signal of unknown mass by testing various m_A hypotheses. In that case, it must be taken into account that in the searched range any excess of events above the background-only hypothesis will equally be considered as a potential signal. Considering this “look elsewhere” effect [336], usually results in a reduction of the significance of a certain excess relative to its *local* significance. Building up on the idea of using an asymptotic approximation [337] to obtain the *trial factor* relating the local and global p -values, Ref. [338] suggests that the global p -value p_{glob} of an excess with local p -value p_0 can be estimated from $p_0(m)$, the distribution of the observed local p -values as function of the tested masses m , as

$$p_{glob} \approx p_0 + N(Z_{ref}) \cdot e^{-(Z_0^2 - Z_{ref}^2)/2}, \quad (5.9)$$

where Z_0 is the local significance of the excess of interest, and $N(Z_{ref})$ is the number of downcrossings of $p_0(m)$ below a threshold defined by the reference significance $Z_{ref} \ll Z_0$. Since the uncertainty on the p_{glob} estimate decreases with the number of down-crossings, as $\sigma(N) = \sqrt{N}$, Z_{ref} should be chosen as low as possible; also $Z_{ref} = 0$ is a valid choice [339].

5.7.3 The Likelihood Function

The likelihood function involved in the performed profile likelihood fit is of the form

$$L(\mu, \theta) = L_{\text{EML}}(\mu, \alpha, \gamma, \tau) \cdot L_{\text{Syst}}(\alpha) \cdot L_{\text{Stat}}(\gamma). \quad (5.10)$$

$L_{\text{EML}}(\mu, \alpha, \gamma, \tau)$ is the likelihood employed in the extended maximum likelihood method [268] to estimate the parameters μ , α , γ and τ from N observed data events (without any further external constraints), which reads for a distribution with n_{bins} bins:

$$L_{\text{EML}}(\mu, \alpha, \gamma, \tau) = \prod_{i=1}^{n_{\text{bins}}} \text{Poisson}(N_i | \mu \cdot s_i(\alpha) + b_i(\alpha, \gamma, \tau)) \quad (5.11)$$

where N_i is the number of data events in bin i , i.e. $N = \sum_{i=1}^{n_{\text{bins}}} N_i$; $s_i(\alpha)$ and $b_i(\alpha, \gamma, \tau)$ are the expected number of signal and background events, respectively, that depend on a number of nuisance parameters, and μ is the POI, the signal strength.

Only the n_{sys} nuisance parameters $\alpha = \{\alpha_j\}_{j=1}^{n_{\text{sys}}}$ affect both the signal and background predictions. They are defined such that for $\alpha_j = 0$ the nominal predictions are obtained, and for $\alpha_j = \pm 1$ the ones for the $\pm 1\sigma$ variations of the systematic uncertainty j . To enforce the knowledge of the nominal values (and uncertainties) obtained by the subsidiary measurements, the nuisance parameters are constrained in the likelihood by the term

$$L_{\text{sys}}(\alpha) = \prod_{j=1}^{n_{\text{sys}}} \text{Gauss}(\alpha_j | 0, 1), \quad (5.12)$$

assuming that the α_j follow a standard normal distribution. This approach requires a continuous parametrisation of the likelihood as function of α . However, this is usually not readily available, given the external measurements provide their results in a condensed form as nominal values with the $\pm 1\sigma$ variations (cf. Secs. 5.6 and 3). Thus, the continuous parametrisation of each prediction is approximated by *inter-* and *extrapolating* from the available nominal prediction and the ones for the $\pm 1\sigma$ variations. The impact of each systematic variation can be separated into one part only affecting the normalisation and one only affecting the shape of the discriminating distribution,²⁷ typically, different functional forms are used for inter- and extrapolating the two different effects.²⁸

The expected background contribution depends further on two other sets of nuisance parameters, denoted γ and τ above. The former is related to the fact that the background predictions obtained by means of simulated samples (cf. Sec. 5.3) are afflicted with statistical uncertainties due to the limited number of simulated events; which can be large in certain phase space regions. Following an approach by Barlow and Beeston [340], they can be taken into account by assigning to each bin of every background distribution a nuisance parameter, reflecting the statistical fluctuation about the predicted event yield in each bin. In the used 'lightweight' version, described in Ref. [326], the number of nuisance parameters that needs to be considered is reduced to the number of bins n_{bins} in the distribution by treating the sum of all background processes as a single background contribution. The prediction provided by the simulated samples can be viewed as a subsidiary measurement and a constraint term of the following form can be constructed

$$\prod_{i=1}^{n_{\text{bins}}} \text{Poisson}(n_i | \gamma_i m_i). \quad (5.13)$$

²⁷As discussed in Sec. 5.6 there are also uncertainties that have by design only a normalisation or shape effect.

²⁸The used HISTFACTORY package provides several default inter- and extrapolation functions. In the present analysis, a 6th order polynomial is used to interpolate both the normalisation and shape effects; an exponential function is used to extrapolate the normalisation part, while a linear function is used for the shape part.

	Resolved regime			Merged regime		# add. b -Tags	
	0 lepton	2 lepton		0 lepton	2 lepton		
	SR	SR	$e\mu$ CR	SR	SR		
# b -Tags	1	$m_{T,Vh}$	m_{Vh}	} m_{Vh}	$m_{T,Vh}$	m_{Vh}	0
	2	$m_{T,Vh}$	m_{Vh}		$m_{T,Vh}$	m_{Vh}	1+
							1+
	3+	$m_{T,Vh}$	m_{Vh}	m_{Vh}	-	-	0
							1+

Table 5.7: Summary of the analysis regions, signal regions (SR) and control regions ($e\mu$ CR), included in the fit to data that were introduced in Sec. 5.5.2 and of the different discriminants used in the 0- and 2-lepton channels, the transverse mass ($m_{T,Vh}$) and invariant mass (m_{Vh}) of the Zh system, respectively (cf. Sec. 5.4.2). The 1 and 2 b -tag(s) $e\mu$ CR as well as the 1 b -tag 1+ add. b -tags and 2 b -tags 1+ add. b -tags SRs are combined to the 1+2 b -tags $e\mu$ CR and 1+2 b -tags 1+ add. b -tags SRs, respectively.

It describes the probability to obtain n_i events in bin i from a Poisson process with mean $\gamma_i m_i$; γ_i is the respective nuisance parameter, and m_i is estimated from the predicted background contribution b_i with statistical uncertainty σ_{b_i} : $\sigma_{b_i}/b_i = 1/\sqrt{m_i}$. Thus, the nominal prediction corresponds to $\gamma_i = 1$ and the $\pm 1\sigma$ variations to $\gamma_i = 1 \pm \sigma_{b_i}/b_i$. However, since the m_i might not be of integer value, instead of the Poissonian constraint, a penalty term involving a Gamma distribution is added to the likelihood function

$$L_{\text{stat}}(\boldsymbol{\gamma}) = \prod_{i=1}^{n_{\text{bins}}} \text{Gamma}(\gamma_i | (\sigma_{b_i}/b_i)^{-2}, n_i - 1), \quad (5.14)$$

with $\text{Gamma}(x | A, B) = A(Ax)^B e^{-Ax} / \Gamma(B)$, where $\Gamma(B)$ is the Gamma function.

As can be seen from Eq. 5.10, the parameter set $\boldsymbol{\tau}$ does not appear anywhere else in the likelihood product, i.e. there is no corresponding penalty term encoding prior knowledge from external measurements. The use of these *freely floating parameters* allows to obtain the normalisations of the dominant background processes either in certain analysis regions or coherently across analysis regions solely from the data in the present analysis. They are further discussed in Sec. 5.7.5.

5.7.4 The $A \rightarrow Zh$ Fit Model

With the aim to extract a common normalisation for a hypothesised A boson, a binned profile likelihood fit is performed simultaneously in the 0- and 2-lepton channels in the invariant and transverse mass of the Zh system, m_{Vh} and $m_{T,Vh}$, respectively. The fit is performed several times with varying m_A hypotheses and admixtures of the gluon-fusion and b -associated A -boson production modes, using the same *fit model*. The fit model is defined by the included analysis regions, final discriminants (m_{Vh} and $m_{T,Vh}$) and their binning, the considered background processes as well as the considered nuisance parameters and their correlations across the various fit regions; it completely determines the different terms in the likelihood function.

Table 5.7 summarises the 15 fit regions that comprise of 13 orthogonal signal regions (SR) of the 0- and

2-lepton channels and 2 control regions (CR) for the 2-lepton channel. These are in the resolved regime the 1, 2 or 3+ b -tags signal regions and in the merged regime the 1 and 2 b -tags signal regions with either 0 or 1+ additional b -tags. In the 2-lepton channel, the 1 and 2 b -tags signal regions with 1+ add. b -tags are combined into the 1+2 b -tags, 1+ add. b -tags SR, accounting for the limited simulated sample sizes leading to large statistical fluctuations, in particular in the 2 b -tags, 1+ add. b -tags SR.

For the 2-lepton channel, two $e\mu$ regions in the resolved regime are included in the fit. The 1+2 b -tags and the 3+ b -tags $e\mu$ CR help to control the $t\bar{t}$ background in the respective signal regions. As discussed, in Sec. 5.5.3, the 1 and 2 b -tags $e\mu$ regions are combined to minimise the power to constrain the b -tagging uncertainties. In order to determine not only the $t\bar{t}$ normalisation, but also provide shape information, also in the $e\mu$ CRs the equivalent to the m_{Vh} distribution is fit; it is similarly reconstructed as the invariant mass of the dilepton pair and the small-R jet candidates (cf. Sec. 5.4.2).

As mentioned before, the m_h -sideband regions are not included as control regions in the fit, but are instead used to validate the fit results, as discussed in Sec. 5.7.7. This is motivated by the fact that the signal regions supplemented by the $e\mu$ regions provide already good control of the dominant background processes and that including the sideband regions would only add little to that. Studies showed an improved precision of the background normalisations only by up to 30 %, hardly affecting the sensitivity. Only in the case of the statistically limited 3+ b -tags regions, it would be beneficial to incorporate the sideband regions in the fit. However, it was chosen not to include them given differences in the background compositions between the signal and sideband regions that are not well described by the simulations and difficult to assess using data, as laid out in Sec. 5.7.7.

Given the various fit regions differ significantly regarding their topology, population and purpose, the binning chosen for the fit discriminants in the different regions is optimised individually and varies quite drastically among (and within) them. This can be seen from Table 5.8, showing the number of bins of the m_{Vh} and $m_{T,Vh}$ distributions in the different fit regions. They are the result of attempting to find a trade-off between the following guiding principles, namely to (i) optimally resolve the A -boson signal, (ii) keep the number of bins as small as possible to ease the fit convergence, (iii) provide enough shape information to allow good control on the various background components, and (iv) keep the relative statistical uncertainty on the total background estimate in each bin below ~ 20 %.²⁹ In order to satisfy, in particular, points (i) and (iv), the bin width varies across the m_{Vh} and $m_{T,Vh}$ ranges; it increases from 200 GeV to 2 TeV. The change in bin width is especially drastic in the resolved regions of the 2-lepton channel, where the resolution of the reconstructed signal mass is as low as 2.5 % of the true A -boson mass, across the full mass range.³⁰ However, the available number of simulated events decreases towards high m_{Vh} and is generally rather limited in the 3+ b -tags SR. Therefore, only in the resolved 2 b -tags SR for $m_{Vh} \lesssim 800$ GeV the chosen binning reflects the excellent signal resolution: it is of the order of 1 – 2 times the resolution. Given the 1 b -tag SR adds only little to the sensitivity, and rather acts as a control region for the $Z+hl$ background, a coarser binning is sufficient and preferred, accommodating points (ii) and (iii). The binning in all other

²⁹This rather stringent requirement is adopted from the SM Vh analysis in Run 2. Studies have shown that larger relative statistical uncertainties on the total background prediction can lead to strong biases of the estimate of the signal strength. While something similar could in principle also be caused by other nuisance parameters, the situation seems to be less critical because they are treated correlated across bins; other than the gamma parameters.

³⁰The resolution is determined from a fit to the predicted m_{Vh} distribution of the signal with a Bukin function [319]. It corresponds to e.g. 5 GeV at $m_A = 200$ GeV, 10 GeV at $m_A = 400$ GeV and 20 GeV at $m_A = 800$ GeV.

Region	Number of Bins	
	0 lepton	2 lepton
<u>Signal regions</u>		
1 b -tag	14	28
2 b -tags	14	51
3+ b -tags	8	9
1 b -tag, 0 add. tag	9	16
2 b -tags, 0 add. tag	8	6
1 b -tag, 1+ add. tag	8	}10
2 b -tags, 1+ add. tag	4	
<u>$e\mu$ control regions</u>		
1+2 b -tags	-	7
3+ b -tags	-	4
Total	196	

Table 5.8: Number of bins between 200 GeV and 2200 GeV in the $m_{T,Vh}$ and m_{Vh} distributions in the different analysis regions of the 0- and 2-lepton channels used in the fit to data.

2-lepton channel SRs is mainly determined by point (iv).

Since the signal resolution in the 0-lepton channel is considerably worse, given only the reconstructed transverse mass can be used as a discriminant, the binning in the resolved 1 and 2 b -tags regions is chosen significantly coarser than in 2-lepton channel; the bin width does not go below 50 GeV. However, its larger acceptance allows a finer binning in the merged regime.

The binning in the $e\mu$ CRs, is chosen according to points (iii) and (ii), as well as the limited population in the 1+2 and 3+ b -tags categories, respectively.

The various background processes entering in this analysis, as described in Sec. 5.3, are grouped into the following 12 independent components

- $t\bar{t}$
- Z +jets: $Z+hf$, $Z+hl$, $Z+l$,
- W +jets: $W+hf$, $W+hl$, $W+l$,
- diboson,
- single top,
- SM Vh , $h \rightarrow bb$,
- $t\bar{t}V$, $t\bar{t}h$,

where the V +jets processes are split into the different jet-flavour components as motivated in Sec. 5.5.2. A priori, all background predictions are obtained from simulations, and dedicated systematic uncertainties regarding their modelling are taken into account (cf. Sec. 5.6.2).

In general, each of the systematic uncertainties, both modelling and experimental ones that are listed in Tables 5.2-5.6, is considered as one nuisance parameter in the fit. All the nuisance parameters encoding the experimental systematic uncertainties are considered for all fit regions and are treated fully correlated across them. The only exception are the b -tagging related uncertainties on small- R and track jets, which are per

Floating normalisation factors		
Name	Description	Value
<u>Z+jets</u>		
norm_Zhf	$Z+hf$ normalisation in all regions, but 3+ b -tags	1.19 ± 0.10
norm_Zhl	$Z+hl$ normalisation in all regions, but 3+ b -tags	1.08 ± 0.07
norm_Zjets_T3	$Z+hf/hl$ normalisation in all 3+ b -tags regions	1.12 ± 0.20
<u>$t\bar{t}$</u>		
norm_ttbar_L0	$t\bar{t}$ normalisation in all 0-lepton regions	1.11 ± 0.08
norm_ttbar_L2	$t\bar{t}$ normalisation in all 2-lepton regions, but 3+ b -tags	1.00 ± 0.03
norm_ttbar_L2_T3	$t\bar{t}$ normalisation in 3+ b -tags 2-lepton regions	1.20 ± 0.21

Table 5.9: Summary of the freely floating parameters used to scale the initial normalisations of the various Z +jets and $t\bar{t}$ components obtained from theory predictions (cf. Sec. 5.3) in the fit to data. The shown values are retrieved from a background-only fit as discussed in Sec. 5.7.7.

definition only considered for and correlated across the resolved and merged regime regions, respectively. While also the nuisance parameters for the normalisation-related modelling uncertainties (cf. Table 5.3) are treated coherently across all regions, there are several that are only considered for certain regions and/or are decorrelated for certain regions. The former is the case for all nuisance parameters related to acceptance effects between the different analysis regions, i.e. (i) between the resolved and merged regimes, (ii) between the 0- and 2-lepton channel, (iii) between the signal and sideband regions, and (iv) between the $e\mu$ CR and the signal (sideband) region (cf. Tables 5.5 and 5.6); they are applied to the regions for which they act as an extrapolation from the regions driving the constraint on the normalisations, e.g. to the merged regimes in the case of the merged-to-resolved regime ratio nuisance parameters (“_rmRatio_”).³¹ The latter case, that nuisance parameters are treated decorrelated between certain regions is discussed in the following; it may result in more nuisance parameters than uncertainties listed in Tables 5.2-5.6.

As mentioned before, the (overall) normalisations of the dominant background processes, Z +jets and $t\bar{t}$, are determined in the fit to data. This is done by means of ‘freely floating’ parameters, referred to as *floating normalisations factors*, that scale the initial estimates obtained from the simulated samples with cross sections from higher-order calculations (cf. Sec. 5.3). They are summarised in Table 5.9 and motivated in the following; their values as extracted from the fit are discussed in the context of the fit validation (cf. Sec. 5.7.7).

Related to the Z +jets background, three floating normalisation factors are introduced to determine the normalisations of the $Z+hl$ and $Z+hf$ components. The `norm_Zhf` and `norm_Zhl` factors parametrise their respective normalisations in all of the fit regions, with the exception of the 3+ b -tags regions. In particular the resolved 1 and 2 b -tag(s) regions of the 2-lepton channel, provide good constraints on the $Z+hl$ and $Z+hf$ normalisations, respectively; they can be determined at the level of 10%.

Separating the determination of the normalisation of the $Z+hf$ (and $Z+hl$) component in the 3+ b -tags

³¹This also means that the sideband-to-SR acceptance ratio nuisance parameters are not considered in the nominal fit, but are propagated without marginalisation to the total uncertainties considered in the fit validation.

regions, acknowledges the fact that the third b -tagged jet is in the overwhelming fraction of events another b jet or c jet and the extra challenge related to the modelling of several gluons splitting into b - and c -pairs in the same event. Since, the $Z+hl$ component has a negligible contribution in the 3+ b -tags regions and is afflicted with large statistical uncertainties due to the limited simulated sample size, its normalisation is adjusted together with the $Z+hf$ component using a single floating normalisation, `norm_Zjets_T3`. Despite the limited number of data events in that region, the common normalisation can still be determined at the level of 20 %.

Following this line of reasoning, also the nuisance parameters related to the V +jets shape modelling uncertainties are treated uncorrelated between the 3+ b -tags regions and all other regions; thus, the nuisance parameter names in Table 5.4 are appended “_T3” in the case of the former; the $V+hf$ and $V+hl$ components are treated separately, also in the 3+ b -tags regions.³²

Since the 1+ add. b -tags regions of the merged regime, in particular the 2 b -tags regions, target the same signature as the 3+ b -tags region, only in a different phase space, the background composition is similar, and so are the modelling challenges. This is addressed by treating the nuisance parameters for the merged-to-resolved regime ratio of the V +jets components decorrelated between the 0 and 1+ add. b -tag regions. Thereby allowing different levels of deviation from the normalisations foremost determined in the 1 and 2 b -tags regions of the resolved regime for the different topologies in the merged regime, e.g. `Zhf_rmRatio_0AddTag` vs. `Zhf_rmRatio_1pAddTag`. Given the very limited number of V +jets events in the 1+ add. b -tags regions, it is refrained from decorrelating the nuisance parameters for the V +jets shape modelling uncertainties.

Furthermore, the 0-to-2-lepton channel-acceptance ratios of the various Z +jets components are allowed to deviate from the ones predicted in simulation via respective nuisance parameters that are treated correlated across all regions (e.g. `Zhf_lepRatio`, cf. Table 5.6).

The other three floating normalisations are related to the $t\bar{t}$ normalisation in different analysis regions. In particular, separate nuisance parameters are introduced for the two channels, `norm_ttbar_L0` and `norm_ttbar_L2(_T3)`. Given there is enough constraining power to determine the normalisations with good precision separately in each channel, this acknowledges that the two channels are probing somewhat different phase-space regions, and avoids an additional uncertainty on the channel-acceptance ratio.

As discussed in Sec. 5.5.2, in most of the 0-lepton regions the $t\bar{t}$ background constitutes the dominant contribution, and its normalisation can be constrained at the level of 10 %. The 1+2 b -tags $e\mu$ CR considerably improves the constraining power in the 2-lepton channel, allowing the $t\bar{t}$ normalisation to be determined at the level of a few percent; an uncertainty for the extrapolation to the signal regions is taken into account by means of the SR-to- $e\mu$ CR’ ratio nuisance parameter `ttbar_emuRatio_L2`. The nuisance parameters for the shape-related modelling uncertainties are consistently treated decorrelated between the two channels.

The $t\bar{t}$ contribution in the 0-lepton 3+ b -tags region (as well as in the 2 b -tags merged 1+ add. b -tags) mainly arises from mistagging c jets and light jets as b jets. In the 2-lepton channel, however, a good fraction of the contamination is due to $t\bar{t}+hf$ events, i.e. $t\bar{t}$ events with additional b and c jets from gluon splittings, a process that is difficult to model. Therefore, it is justified that in the 0-lepton channel a com-

³²All (shape-related) modelling uncertainties described in Sec. 5.6.2 are derived inclusively in the number of b -tags in order to (i) best exploit the limited simulated samples sizes, (ii) take into account that uncertainties related to the modelling of the b -tagging efficiencies are considered via dedicated experimental uncertainties, described in Sec. 5.6.1

mon $t\bar{t}$ floating normalisation is used in all regions and the shape-related modelling nuisance parameters are treated correlated across them. In the 2-lepton channel, on the other hand, a dedicated floating normalisation for the 2-lepton 3+ b -tags regions, that is independent from the one used in all other 2-lepton regions, is more appropriate: `norm_ttbar_L2_T3`. Although the $t\bar{t}(+hf)$ contribution is not small in the 3+ b -tags SR, the precision with which the $t\bar{t}(+hf)$ normalisation can be determined, is again clearly improved by the 3+ b -tags $e\mu$ CR. Its relative uncertainty is below 20 %, despite the very limited number of events in either of the 2-lepton 3+ b -tags regions. The nuisance parameter for the normalisation extrapolation from the $e\mu$ CR to the SR is consistently decorrelated for the 3+ b -tags; as are all the nuisance parameters related to the shape-modelling uncertainties. To their respective names a “_T3” is appended for differentiation from the ones used in all other regions, e.g. `TTbar_Herwig_L2_T3`.

Given the very small contribution of $t\bar{t}$ events in the 2-lepton merged regions, it is refrained from treating the 0 and 1+ add. b -tag regions differently, despite their different topologies. Therefore, both in the 0- and the 2-lepton channels, one nuisance parameter is considered for the merged-to-resolved regime extrapolation: `ttbar_rmRatio_L{0,2}`.

Finally, also the statistical uncertainty on the predicted total background contribution due to the limited simulated samples sizes is taken into account. This is done individually per bin, by assigning to each one of them a γ nuisance parameter. Often γ parameters are only considered for bins with a relative statistical uncertainty above a certain threshold, e.g. 1 % or 5 %; assuming the statistical precision for the simulated events is much better than for the data. In the present analysis, however, such a pruning approach is dismissed given that the statistical uncertainty on the background prediction at low discriminant values is at best of the same order than what is expected for the data.

In total, 340 parameters are included in the described fit model: 6 floating normalisations, 196 γ nuisance parameters and 138 other nuisance parameters, considering that a certain fraction of the total number is pruned as described in Sec. 5.7.5. This complex fit model is the result of extensive studies and its validation is, summarised in Sec. 5.7.7, after presenting the expected results in Sec. 5.7.6.

5.7.5 Symmetrisation, Smoothing and Pruning of Systematic Uncertainties

In practice, the impact of all experimental uncertainties and those modelling uncertainties affecting the shape of the m_{Vh} and $m_{T,Vh}$ discriminants are provided as individual histograms and the $\pm 1\sigma$ variations are obtained relative to the nominal templates. There are in particular two aspects of this approach that need to be considered: (i) systematic uncertainties that lead only to a $+(-)1\sigma$ variation, and (ii) that the systematic uncertainties themselves are afflicted with statistical uncertainties given the limited size of the simulated samples used to estimate their impact; both are addressed as described in the following.

There are a few cases, where a systematic variation leads only to a $+(-)1\sigma$ effect (the sign is an arbitrary choice). This is the case for the jet-energy/mass and E_T^{miss} resolutions, e.g. `FATJET_JER/JMR`, and the shape modelling uncertainties derived from generator comparisons, e.g. `TTbar_Herwig`, as well as the ‘NNLO reweighting’. The corresponding $-(+)1\sigma$ variation also needed by the profile likelihood fit, is simply obtained from *symmetrising* the $+(-)1\sigma$ effect.

In general, the systematic $\pm 1\sigma$ variations lead to correspondingly well defined and smooth $\pm 1\sigma$ varia-

tions of the normalisation and the shape of the m_{Vh} and $m_{T,Vh}$ templates. However, statistical fluctuations in the templates due to the limited size of the simulated samples can cause that the $\pm 1\sigma$ variations are irregular, asymmetric or show an effect in the same direction, i.e. they have a “same-sided” effect. These issues occur in particular for those systematic uncertainties that lead to changes of the event kinematic distributions, such as the jet-energy scale uncertainties, because they may cause migrations of events between the bins of the m_{Vh} and $m_{T,Vh}$ distributions or even between analysis regions. Extreme phase-space regions and subdominant processes are more likely affected. Such distorted $\pm 1\sigma$ variations may interfere with the fit convergence and lead to artificial constraints or *pulls* (cf. Eq. 5.15) of the corresponding nuisance parameters. Thus, the effects of the limited simulated sample sizes on the evaluated $\pm 1\sigma$ variations are mitigated by subjecting the templates to a special treatment before they enter the profile likelihood fit.

As such, a dedicated *smoothing* technique is applied to remove residual statistical fluctuations between neighbouring bins for the systematic variations of the energy scales of the physics objects, the scale and resolution of E_T^{miss} , the b -jet tagging efficiencies as well as PRW_DATASF. It is based on the assumption that the considered systematic uncertainties can only lead to well defined variations of the nominal distribution with smooth bin-to-bin transitions. Such a shift or a broadening of the discriminant distribution is reflected in a ratio between the nominal and varied templates that follows a straight line or a parabolic function, respectively. Practically, this is enforced by merging bins in the template ratio in an iterative procedure. Considering the expected statistical fluctuation, the iteration stops when the desired shape is obtained and the relative statistical uncertainty in each bin computed in the nominal distribution is smaller than 5%.³³ The smoothed systematic variation is then derived from applying the smoothed ratio to the nominal distribution.

Furthermore, the templates corresponding to the $\pm 1\sigma$ systematic effects are *averaged* and *symmetrised* such that they symmetrically enclose the nominal case. This is done for all the templates that have been smoothed, as well as the ones corresponding to the modelling uncertainties derived using SHERPA (Vjets_) and related to the in/decrease of the radiation in the $t\bar{t}$ simulation (TTbar_rad).

Finally, given the large number of systematic sources that are (a priori) considered in the analysis, it helps both the performance as well as the stability of the fit, if those that show a very small variation and negligible impact on the fit result are neglected, i.e. *pruned*. More precisely, normalisation and shape uncertainties that are considered to have a negligible impact on a certain process (or groups of processes) in a certain region are not incorporated into the likelihood function. A systematic uncertainty is only completely disregarded, if its effect is negligible for *all* samples and regions.

Thus, the normalisation effect of a systematic uncertainty is pruned, if it is less than $\pm 0.5\%$, or, if both $\pm 1\sigma$ variations lead to either an increase or a decrease of the nominal normalisation, i.e. if the effect is “same-sided”. It is verified that the latter case only happens as the result of statistical fluctuations in the templates and that there is no actual impact on the normalisation.

The shape effect of a systematic uncertainty is neglected, if there are less than two bins deviating from the nominal distribution by at least 1%. If this pruning criterion removes the $+(-)1\sigma$ variation, the corresponding $-(+)1\sigma$ variation is pruned as well. This is done under the assumption that the latter

³³To be precise the (intended) strategy is to merge bins in the ratio that are most compatible with each other, based on a χ^2 fit, until up to three extrema are left. However, due to a mistake found only after publication of the results, always the two extrema at the highest m_{Vh} values were merged independent of their χ^2 values. The impact on the expect and observed limits was evaluated: with the intended strategy they are up to 5% weaker in particular at low A -boson masses, where the effect of systematic uncertainties is the strongest (cf. Sec. 5.7.6).

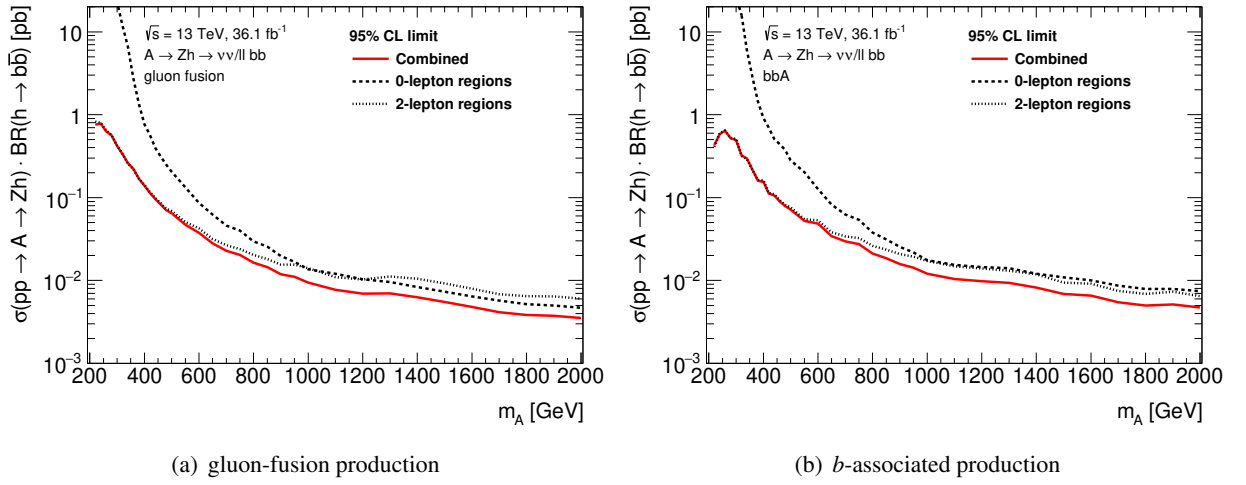


Figure 5.23: Expected upper limits at the 95 % CL on the cross section for A -boson production times the branching ratios for the $A \rightarrow Zh$ and $h \rightarrow bb$ decays for (a) pure gluon-fusion and (b) pure b -associated production, as function of the A -boson mass. In addition to the combined results also the results obtained considering only the 0-lepton and 2-lepton regions, respectively, are shown. To do so the fit model described in Sec. 5.7.4 is not modified besides dropping the respective regions and associated nuisance parameters. The nuisance parameters are profiled to the data (cf. Sec. 5.7.1).

variation only passes the initial pruning step due to statistical fluctuations.

Rather than considering each and every background process individually, potentially afflicted with large statistical uncertainties due to the limited sample sizes, the grouped backgrounds listed in the previous section are treated as single components regarding the described procedures.

5.7.6 Expected Results

In this section expected results obtained with the fit model described in the previous sections using an Asimov dataset are discussed. In particular, two aspects are studied, namely the impact of different analysis regions on the expected upper limits on the cross section for A -boson production times the branching ratios for the $A \rightarrow Zh$ and $h \rightarrow bb$ decays and the limitations expected from the various sources of uncertainties.

Expect upper limits

In the context of the A -boson search, the signal-strength parameter μ scales the cross section for A -boson production times the branching ratios for the $A \rightarrow Zh$ and $h \rightarrow bb$ decays, $\sigma(gg \rightarrow (bb)A) \times \text{BR}(A \rightarrow Zh) \times \text{BR}(h \rightarrow bb)$, assumed for the simulated signal samples (0.5 pb, cf. Sec. 5.3). Therefore, the expected upper limit obtained on $\hat{\mu}$, as described in Sec. 5.7.2, can be expressed as an upper limit on $\sigma(gg \rightarrow (bb)A) \times \text{BR}(A \rightarrow Zh) \times \text{BR}(h \rightarrow bb)$.

In Figure 5.23 the expected upper limit on $\sigma(gg \rightarrow (bb)A) \times \text{BR}(A \rightarrow Zh) \times \text{BR}(h \rightarrow bb)$ at 95 % CL is shown separately for pure gluon-fusion and pure b -associated production as function of the A -boson mass. In order to yield results as close as possible to what is expected for data, an Asimov dataset is used, where the nuisance parameters were profiled to the data; i.e. it is constructed from simulations that were adjusted

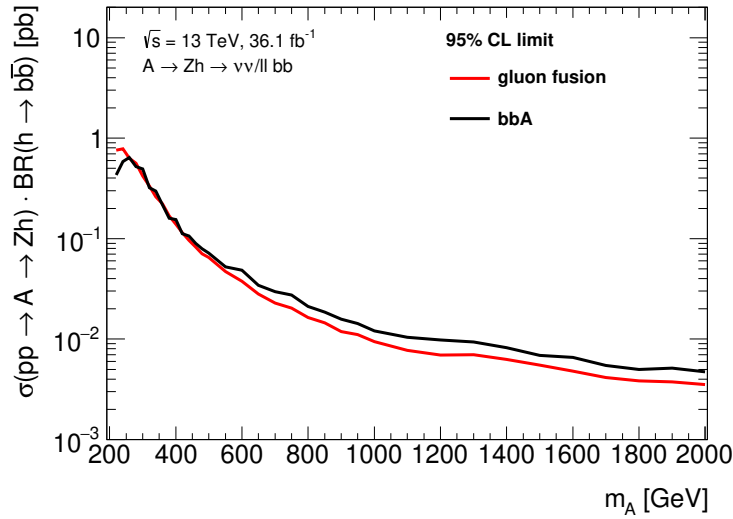


Figure 5.24: Comparison between the expected upper limits at the 95 % CL on the cross section for A -boson production times the branching ratios for the $A \rightarrow Zh$ and $h \rightarrow bb$ decays assuming pure gluon-fusion and pure b -associated production (bbA), as function of the A -boson mass. The nuisance parameters in the fit are profiled to the data (cf. Sec. 5.7.1).

according to the results from a fit to data. The impact of the adjustments on the expected limits relative to the ones obtained with an Asimov dataset built from the default simulations is discussed in Sec. 5.7.7.

The expected upper limits range from 0.8 pb at $m_A = 220$ GeV to 0.003 pb at $m_A = 2$ TeV for pure gluon-fusion production; for pure b -associated A -boson production the results are comparable at low masses and only about 20 % weaker for $m_A > 550$ GeV, as can be seen from their comparison in Fig. 5.24. That the results for the two production modes are so close, is a great improvement over the previous results (cf. Fig. 5.5(b)) and is mainly due to the consideration of the bbA -sensitive analysis regions. That the limit for the bbA mode is still somewhat weaker at intermediate and high m_A can be attributed to (i) the fact that the binning of the discriminants in the 3+ b -tags regions is too coarse (only a single bin above 700 GeV), and (ii) the 1 and 2 b -tags 1+ add. b -tags regions are combined in the 2-lepton channel; choices made in order to reduce the statistical uncertainty on the total background prediction due to the limited simulated sample sizes per bin, particularly affecting these particular phase-space regions.

The impact of different analysis regions on the expected upper limits, besides what was already discussed in earlier sections, is assessed by comparing the results obtained with the nominal fit model and a modified version, where certain regions are neglected (as well as the associated nuisance parameters). Without modifying other aspects of the nominal fit model, in particular the impact of (i) the 0- and 2-lepton channel regions, respectively, and (ii) the merged regime is evaluated.

In Figure 5.23 in addition to the nominal result, also the expected upper limits obtained when only considering the 0- and 2-lepton channel, respectively, are shown. The comparison reveals that for $m_A < 900$ GeV, the limits are driven by the 2-lepton channel; the impact of the 0-lepton channel sets in at about $m_A = 500$ GeV. At higher m_A , both channels are almost equally contributing with a slight dominance of the 0-lepton channel for gluon-fusion production (at the level of 15 %). In particular the trends at low m_A reflect the signal acceptance times efficiency distribution as function of the A -boson mass, shown in

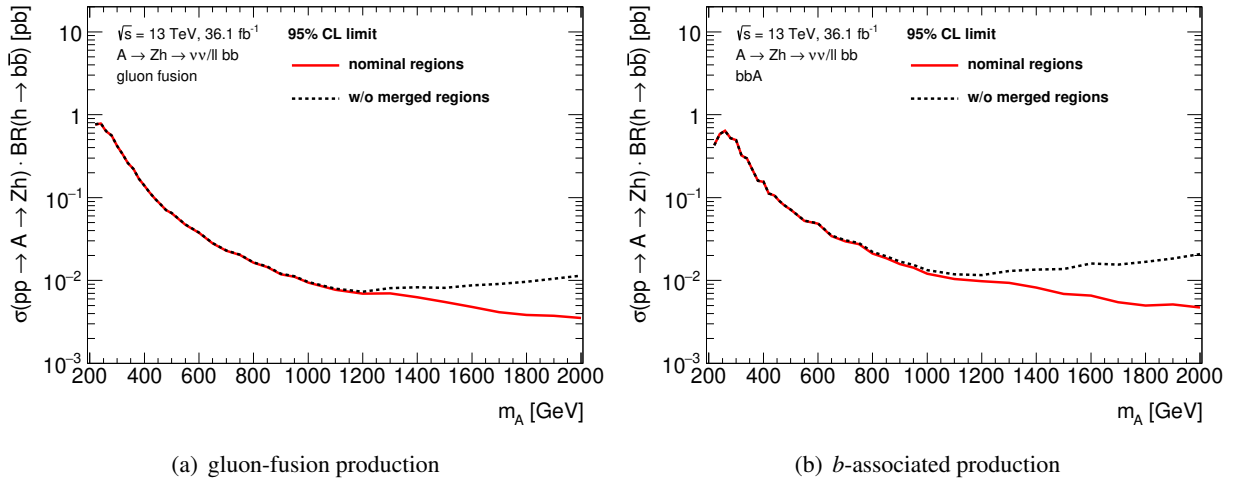


Figure 5.25: Impact of the merged analysis regions on the expected upper limits at the 95 % CL on the cross section for A -boson production times the branching ratios for the $A \rightarrow Zh$ and $h \rightarrow bb$ decays for (a) pure gluon-fusion and (b) pure b -associated production, as function of the A -boson mass. To obtain the results labelled “w/o merged regions” the fit model (cf. Sec. 5.7.4) is not changed besides dropping the merged regions and related nuisance parameters. The nuisance parameters are profiled to the data (cf. Sec. 5.7.1).

Fig. 5.21: it is mainly carried by the 2-lepton channel with a slow turn-on of the 0-lepton channel. The larger acceptance of the 0-lepton channel at higher m_A , however, seems to be balanced by the significantly better mass resolution and signal-to-background ratio in the 2-lepton channel, leading to comparable limits.

The comparison of the nominal expected upper limits and those obtained when only considering the resolved regime, is shown in Figure 5.25. It conveys that the regions of the merged regime help to improve the results for $m_A \gtrsim 1.2$ TeV in the case of gluon-fusion production and somewhat earlier in the case of b -associated production. The observed transition point is determined by the chosen regime-selection strategy, PriorityResolvedSR (cf. Sec. 5.5.1): by prioritising the resolved regions of the merged ones, the point where the latter show an impact is pushed towards higher masses compared to the other discussed strategies. At $m_A = 2$ TeV, where the acceptance of the resolved regime is small and the inclusion of the merged regions is expected to show the largest effect (cf. 5.13(a)), the expected limits are improved by about 60 % (70 %) for gluon-fusion (b -associated) production, respectively.

In summary, the resolved regions of the 2-lepton channel dominate the expected limits at low A -boson masses, the merged regime regions of both channels at high A -boson masses. The sensitivities to the two production modes are similar, however, slightly better for gluon-fusion production.

Expected impact of uncertainties on the signal strength

The expected impact of the statistical and various systematic uncertainties can be evaluated by studying their effect on the estimated signal strength $\hat{\mu}$ of an A -boson signal using an Asimov dataset, i.e. $\hat{\mu} = 1$ per definition. For this purpose, $\sigma(gg \rightarrow (bb)A) \times \text{BR}(A \rightarrow Zh) \times \text{BR}(h \rightarrow bb)$ is assumed to have the value at the expected upper limit shown in Fig. 5.23.

The contribution to the total uncertainty on $\hat{\mu}$ by a group of uncertainties is determined from $\sqrt{\sigma_{\hat{\mu}}^2 - \sigma_{\hat{\mu}'}^2}$,

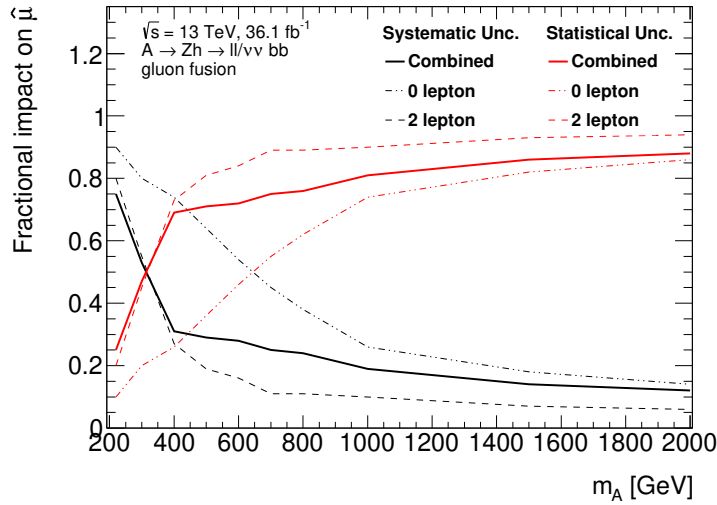


Figure 5.26: Fractional impact of the expected statistical and systematic uncertainties on the signal strength $\hat{\mu}$ obtained using Asimov datasets (i.e. $\hat{\mu} = 1$ per definition) as function of the A -boson mass. Pure gluon-fusion production is assumed as well as signal cross-sections corresponding to the expected upper limits at the 95 % CL.

where $\sigma_{\hat{\mu}}$ is the total uncertainty on $\hat{\mu}$ obtained in the nominal fit, and $\sigma_{\hat{\mu}'}$ the uncertainty on $\hat{\mu}'$ obtained in a fit, where the group of uncertainties under study *does not contribute*. Generally, this is achieved by fixing the related nuisance parameters to their values obtained in the nominal fit, while all other parameters are re-fit. While this potentially leads to asymmetric contributions, they are averaged in the following for simplicity.

Figure 5.26 shows the fractional contribution of the expected statistical and systematic uncertainties to the total uncertainty on $\hat{\mu}$ for A -boson signals produced in pure gluon fusion as function of the A -boson mass: for $m_A < 300$ GeV the systematic uncertainties are dominating, above the statistical uncertainty due to the limited size of the analysed dataset. The breakdown obtained considering only 0- and 2-lepton regions, respectively, is shown as well. It reveals that the transition point is determined by the 2-lepton channel which is driving the sensitivity at low masses; however, it is limited by the branching ratio already at intermediate m_A . The transition point in the 0-lepton channel occurs at higher masses, at about $m_A = 650$ GeV. Therefore, while for $m_A > 300$ GeV the sensitivity of the analysis can still be improved by analysing an even larger dataset, in order to achieve the same at low m_A the systematic uncertainties need to be reduced.

In the case of considering pure b -associated production, the transition point is somewhat shifted to higher m_A . This can be seen from Table 5.10, where the breakdown is listed for both pure gluon-fusion and b -associated production for two benchmark masses, $m_A = 300$ GeV and 1.5 TeV. For b -associated production the systematic uncertainty is larger than the expected statistical uncertainty at $m_A = 300$ GeV, which corresponds to a transition point at a higher mass. This result seems counterintuitive, given the limited number of events entering the 3+ b -tags region which contributes significantly to the bbA sensitivity. The reason is that the uncertainties on the dominant background normalisations obtained from the fit to the data, the floating normalisations, are considered as systematic uncertainties, while in fact they are determined by the size of the analysed dataset. From the table it can be seen that the relative contribution

Source	Uncertainty on $\hat{\mu}$			
	$m_A = 300 \text{ GeV}$		$m_A = 1.5 \text{ TeV}$	
	ggF	bbA	ggF	bbA
Statistical	0.32	0.30	0.49	0.47
Systematic	0.34	0.38	0.20	0.22
Total	0.47	0.48	0.53	0.52
Breakdown of Systematic Uncertainties				
All normalisations	0.10	0.23	0.06	0.05
↔ Floating norm.	0.08	0.23	0.04	0.04
All, but normalisations	0.31	0.30	0.18	0.20
<u>Experimental</u>				
Luminosity & PU	0.03	0.03	0.05	0.05
Leptons	0.01	0.01	0.02	0.02
E_T^{miss}	0.00	0.00	0.00	0.00
Jets	0.05	0.04	0.06	0.06
b -tagging	0.10	0.10	0.08	0.08
↔ b jets	0.10	0.08	0.07	0.05
↔ c jets	0.02	0.04	0.03	0.01
↔ light jets & extrap.	0.00	0.00	0.03	0.02
<u>Modelling</u>				
Z +jets	0.07	0.19	0.05	0.05
W +jets	0.03	0.03	0.02	0.02
$t\bar{t}$	0.08	0.08	0.04	0.05
Other bkgs.	0.04	0.04	0.04	0.05
Signal	0.06	0.06	0.03	0.04
Stat. unc. on sim.	0.27	0.26	0.12	0.15

Table 5.10: Breakdown of the contributions of groups of uncertainties on the expected signal strength $\hat{\mu}$ obtained using Asimov datasets (i.e. $\hat{\mu} = 1$ per definition) for A bosons of benchmark masses 300 GeV and 1.5 TeV produced purely in either gluon fusion (ggF) or b -associated production (bbA). Signal cross-sections corresponding to the expected upper limits at the 95 % CL are assumed. Although the groups in the three breakdown versions are defined exclusively - besides the subgroups indicated by “↔” - the sum of quadrature of the groups differ from the total uncertainty due to correlations. Modelling uncertainties related to the Z +jets and $t\bar{t}$ processes include uncertainties on the floating normalisations; the statistical uncertainty due to the limited simulated samples sizes is considered as separate source of systematic uncertainty.

of the uncertainties on the floating normalisations is almost twice as big for b -associated production than for gluon-fusion production and that it is driven by the uncertainty on the Z +jets normalisation which is consistent with the dominance of the 2-lepton channel. While the modelling uncertainties in the table comprise both normalisation and shape effects, they are dominated by the normalisation uncertainties; the shape uncertainties are rather well constrained (cf. Sec. 5.7.7). Thus, also at low masses, a larger dataset can still somewhat help to improve the analysis sensitivity by means of improving the uncertainties on the floating normalisations, for both the Z +jets and $t\bar{t}$ contributions.

At high m_A , neither the signal nor the background modelling uncertainties have a significant contribution to the uncertainty on $\hat{\mu}$. This is expected given that a signal with a large mass, such $m_A = 1.5$ TeV, is peaking in the tails of the m_{Vh} and $m_{T,Vh}$ background distribution (cf. Fig. 5.10(e)). Instead, there are several sources contributing almost equally, in particular from the experimental uncertainties. The comparison with the lower mass point shows, that here the situation is quite similar in both regimes, namely the dominant contribution is from the b -tagging uncertainty on b -jets, followed by the one on the jet energy (and mass) scale and resolution. Which is as expected, given that both directly impact the signal acceptance and in the case of the resolutions also the discriminants' distributions. It is interesting to note that at $m_A = 300$ GeV, the b -tagging uncertainty on c jets is twice as large for the b -associated than for gluon-fusion production. This is because of the $t\bar{t}$ contamination in the 3+ b -tags region of the 0-lepton channel, where the c jet from one of the W -boson decays is misidentified as a third b -jet (cf. Sec. 5.5.2 and below).

Consistency between the two regimes and targeted production modes is found regarding the single most dominant systematic uncertainty: the statistical uncertainty on the total background prediction due to the limited simulated sample sizes; it clearly dominates with up to 80 % at very low m_A , and even at the highest mass point the contribution is still at the level of 60 %.

An imminent improvement of this very unsatisfactory situation would result from exploiting a method known as *truth tagging*, or *tag rate function* approach, that is used both in the SM Vh analysis and also in the search for the SM Higgs boson produced in association with top quarks and decaying into a pair of b quarks [341] (referred to as $t\bar{t}h$ analysis in the following). Instead of removing simulated events that fail the required b -tagging criterion, such events are kept, however, weighted by their probability of passing the considered requirement. The b -tagging efficiencies of the different jet flavours which are measured in data in bins of the jet p_T and η , as described in Sec. 3.4, define the per-jet probability to pass a certain b -tagging requirement; the corresponding event weight is obtained from considering all possible permutations to build the Higgs candidate from the jets in the event. While this approach would certainly improve the current situation, other measures must be clearly taken as well: despite exploring truth tagging, the statistical uncertainty due to the limited simulated sample sizes is the second dominant systematic uncertainty, closely behind the signal modelling uncertainty, in the systematically limited SM Vh analysis [248].³⁴ Discussions about possible solutions are ongoing within the ATLAS collaboration and also with theorists. Improving the filters at generator level used in the production of V +jets samples, as mentioned in Sec. 5.3, could be one way of obtaining higher efficiencies and better acceptances at reconstruction level. In addition, analysis strategies need to be developed that rely less extensively on the estimation of background processes from simulation.

³⁴Clearly the situation is much different from Run 1: also there the SM Vh analysis exploited truth tagging which lead to a contribution of the statistical uncertainty due to the limited simulated sample size of less than one percent.

The importance of certain, individual systematic uncertainties can be further studied by ranking them according to their impact on the expected signal strength. Assuming in the nominal fit the signal strength $\hat{\mu}$ and the postfit value $\hat{\theta}$ of the nuisance parameter θ with postfit uncertainty $\sigma_{\hat{\theta}}$ is found, then the impact of θ on $\hat{\mu}$ is evaluated by (i) repeating the fit twice with θ being fixed to $\hat{\theta} \pm \sigma_{\hat{\theta}}$, and (ii) computing the difference of the obtained signal strength $\Delta\hat{\mu}$ with respect to $\hat{\mu}$; the procedure is repeated for all nuisance parameters.

Figure 5.27 shows the 15 systematic uncertainties with the largest postfit impact on $\hat{\mu}$ sorted according to decreasing values of $\Delta\hat{\mu}$ for the same benchmark signal hypotheses discussed before; the statistical uncertainties on the total background prediction encoded in gamma parameters are not considered. In addition to the postfit impact, also the prefit impact of the various uncertainties on $\hat{\mu}$ is shown. They deviate from each other, if the fit model is able to extract information from the (Asimov) data on the systematic effect with higher precision than the auxiliary measurement, i.e. the uncertainty is *constrained*. This is reflected by the error bars on the “Pull” being less than one as indicated on the x -axis and discussed in more detail in the next section. The impact of the floating normalisations centred at one (per definition given the fit is performed to the Asimov dataset) can only be evaluated at postfit level given that they are without prior and completely determined by the fit to the (Asimov) data.

Whereas for $m_A = 300$ GeV, where the resolved regime dominates, the ranking is quite clear for both production modes, at $m_A = 1.5$ TeV, where the merged regime dominates, there are several systematic uncertainties that have a similar impact on the signal strength; a pattern that is consistent with the results from the breakdown. Nonetheless, the different rankings are rather consistent regarding the systematic uncertainties that show a strong impact on $\hat{\mu}$. In both regimes, somewhat more pronounced in the resolved regime, the uncertainties regarding the modelling of the dominant Z +jets and $t\bar{t}$ backgrounds rank high. As discussed before, in particular their normalisations have a strong effect on $\hat{\mu}$ (e.g. `norm_ttbar_L0/2`); but also their shapes (e.g. `Vjets_ShRenor_Zhf`) and the extrapolations between the different analysis regions (e.g. `ttbar_emuRatio_L2`) are important. In fact the $Z + hf/hl$ normalisation in the $3+ b$ -tags region, `norm_Zjets_T3`, has not only the strongest impact on $\hat{\mu}$ for the signal with $m_A = 300$ GeV produced in b -association, but it has the largest impact of all systematic uncertainties considered here. This is explained by the fact that, while the $3+ b$ -tags region of the 2-lepton channel is contributing significantly to the signal sensitivity, the region is only sparsely populated, and thus not able to sufficiently constrain the dominant $Z+hf$ background. Moreover, the assumption, discussed in Sec. 5.5.3, that the signal is located in a small number of bins compared to the full m_{Vh} distribution allowing to estimate the background almost independently, does not hold well in this region: the limited event yield and simulated sample size requires coarse binning (cf. Fig. 5.32(j)).

As expected, and consistent with the observations discussed in the context of the breakdown, several of the systematic uncertainties related to b -tagging appear highly ranked in both regimes, for small- R jets in the resolved regime and for track jets in the merged regime. In particular, `FT_B_0_smallR` is ranked first and second for gluon-fusion and b -associated production, respectively, in the resolved regime. This is not surprising given it is the dominant component of the uncertainties related to the b -tagging efficiency for b -jets; encoding the normalisation effect, it directly impacts the signal efficiency. `FT_B_0_smallR` is also one example, where the prior uncertainty is constrained and the impact on $\hat{\mu}$ reduced with respect to the prefit impact. This is not unexpected given that several regions with different number of b -tags are included in the fit and variations of `FT_B_0_smallR` result in migrations between those regions.

The constraint of `FT_C_0_smallR` in the case of the b -associated production mode is especially strik-

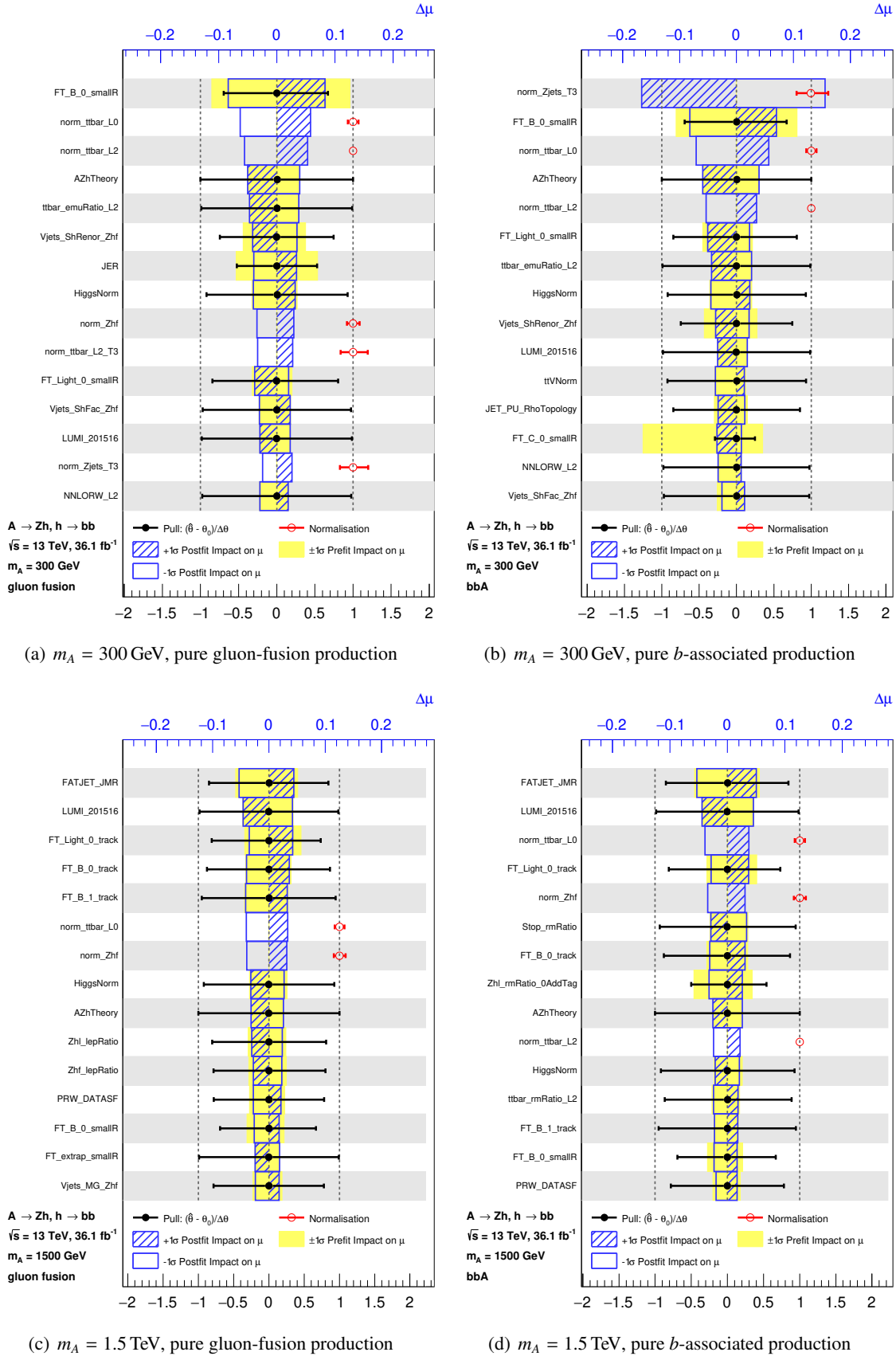


Figure 5.27: Ranking of modelling and experimental systematic uncertainties (cf. Secs. 5.6 and 5.7.4) according to their postfit impact on the expected signal strength $\hat{\mu}$ obtained using Asimov datasets (i.e. $\hat{\mu} = 1$ per definition) for A bosons of benchmark masses 300 GeV (top) and 1.5 TeV (bottom) purely produced in either gluon fusion (left) or b -associated production (right). Signal cross-sections corresponding to the expected upper limits at the 95 % CL are assumed.

ing. The prior of this uncertainty related to the normalisation effect of the c -jet tagging efficiency is with 20-40 % quite large (cf. Sec. 5.6.1); and it is propagated almost undiminished to the $t\bar{t}$ -dominated 3+ b -tags region of the 0-lepton channel. As mentioned above, in this region, the $t\bar{t}$ contamination mainly arises from misidentifying c jets from hadronic top-quark decays. Because the common $t\bar{t}$ normalisation in this channel is determined by the resolved 1 and 2 b -tags regions with high precision, the 3+ b -tags region provides excellent control on the c -jet tagging efficiency and the prefit uncertainty is reduced by about a factor three.

In the merged regime, the uncertainty on the jet mass resolution, FATJET_JMR, corresponding to the resolution of the reconstructed Higgs-boson mass shows the largest impact on the signal strength independent of the signal production mode; as discussed above, variations of it lead not only to migrations into and out of the signal region, but also to differences in the m_{Vh} and $m_{T,Vh}$ distributions. Also, the uncertainty with the same effect in the resolved regime, the jet energy resolution JER, is ranked rather high for gluon-fusion production, and the constraint reflects the sensitivity of the fit model to it.

The uncertainty associated with the luminosity, LUMI_201516, moves up to the second rank in the merged regime. It affects both the signal as well as the subdominant background processes, for which both the shapes and normalisations are estimated from simulation, such as W +jets and diboson, but also $t\bar{t}V$. Their relative contribution is much higher in the merged regime than in the resolved regime.

Further aspects of the systematic uncertainties and their impact on the signal strength are discussed in the following section in the context of the fit validation.

In summary, the modelling uncertainties related to the dominant background processes as well as uncertainties related to b -tagging and the jet-energy/mass scale and resolution have a strong impact on the signal strength. However, the by far dominant systematic uncertainty is the statistical uncertainty on the background estimates due to the limited simulated samples sizes. It needs to be addressed in order to be able to improve the results for $m_A < 300$ GeV; for higher masses, the analysis can still profit from a larger dataset.

5.7.7 Validation of the Fit Model

As mentioned previously, the approach to incorporate systematic uncertainties in a maximum likelihood fit, and evaluate their impact on the results via nuisance parameters, requires thorough validation of the fit model, ensuring all effects due to the various sources of systematic uncertainties are properly described. Besides reasoning the impact of certain systematic uncertainties as done in the previous section, the behaviour of the nuisance parameters in the fit and in particular potential differences arising in the fit to data with respect to the fit to the Asimov dataset need to be understood and are discussed in the following.

Adjustments of the background predictions

The expected upper limits at the 95 % CL on the A -boson production cross-section times the branching ratios for the $A \rightarrow Zh$ and $h \rightarrow bb$ decays as function of m_A , presented in Figs. 5.23-5.25, are obtained from an Asimov dataset, where the predictions are adjusted according to the results of the fit to the data. As mentioned, this is done in order to yield an estimate as close as possible to the results expected in the data. And indeed, the impact from profiling the nuisance parameters to the data is not small: compared to the results computed using the default Asimov dataset, the limits are up to 15 % weaker at low m_A , independent

	Resolved regime			Merged regime			
	1 b -tag	2 b -tags	3+ b -tags	1 b -tag 0 add. b -tags	2 b -tags	1 b -tag 1+ add. b -tags	2 b -tags
0 lepton							
$t\bar{t}$	1.09	1.15	1.56	1.00	1.33	1.08	1.28
$Z+hl$	1.26	1.73	1.50	1.04	-	1.07	-
$Z+hf$	1.38	1.29	1.21	1.22	1.23	1.39	1.52
Total Bkg.	1.15	1.16	1.52	1.05	1.12	1.09	1.28
2 lepton							
$t\bar{t}$	1.00	0.98	1.29	1.03	1.00		0.91
$Z+hl$	1.20	1.37	-	0.99	0.84		1.03
$Z+hf$	1.32	1.25	1.27	1.18	1.20		1.28
Total Bkg.	1.21	1.17	1.28	0.97	1.10		1.00

Table 5.11: Scale factors on the prefit normalisations of the dominant $t\bar{t}$, $Z+hf$ and $Z+hl$ background processes as well as the total background contribution in the various signal regions of the 0- and 2-lepton channel obtained from a background-only fit to the data.

of the considered production mode. The reason for this is an underestimation of the contributions of the dominant background processes, in particular in the resolved regime, by the exploited simulations.

This can be seen from Figs. 5.28 and 5.29 showing the $m_{T,Vh}$ or m_{Vh} postfit distributions in the fit regions of the 0- and 2-lepton channel, respectively. The background predictions are adjusted according to the results of a background-only fit to the data, i.e. the floating normalisations and the other nuisance parameters are taken at their postfit values obtained in a conditional fit assuming $\mu = 0$.³⁵ In addition to the various adjusted background components drawn stacked as coloured, filled histograms, the total background prediction prior to the fit (i.e. *prefit*) is also indicated as dotted blue line. Whereas the post-fit prediction of the total background shows reasonable agreement with the data in all regions, the prefit prediction does not, with only two exceptions: Figs. 5.29(d) and 5.29(g). Generally, the prefit prediction undershoots the data significantly; particularly striking are the needed adjustments in the 3+ b -tags regions.

The factors, by which the prefit normalisations of the dominant background processes, as well as the total background contribution, are scaled in order to obtain the postfit normalisations in the different signal regions are listed in Table 5.11. For example, it can be seen that the data suggests that the $t\bar{t}$ contribution in the 3+ b -tags regions of the 0-lepton (2-lepton) channel is about 60 (30)%, higher than anticipated by the simulation; on the contrary the prediction seems perfectly accurate in the case of the 1- and 2- b -tags regions of the 2-lepton channel, resulting in scale factors close to unity. Also the contributions of the Z +jets components are underestimated at the level of 20-30 %, consistently across the various regions (considering

³⁵It is mainly for practical reasons that a conditional background-only fit is performed; choosing a *certain* signal-mass hypothesis is as good as not considering any signal at all. This is done under the assumption that, in any case, $\hat{\mu}$ is floated almost decorrelated from all other parameters of the fit, and that independent of the hypothesised mass the adjustment of the nuisance parameters affecting mainly the background modelling is little affected by the presence of a potential signal. While this assumption generally holds, motivating also that in this analysis only few control regions are used, there is the exception of the 3+ b -tags resolved region (cf. Sec. 5.7.6).

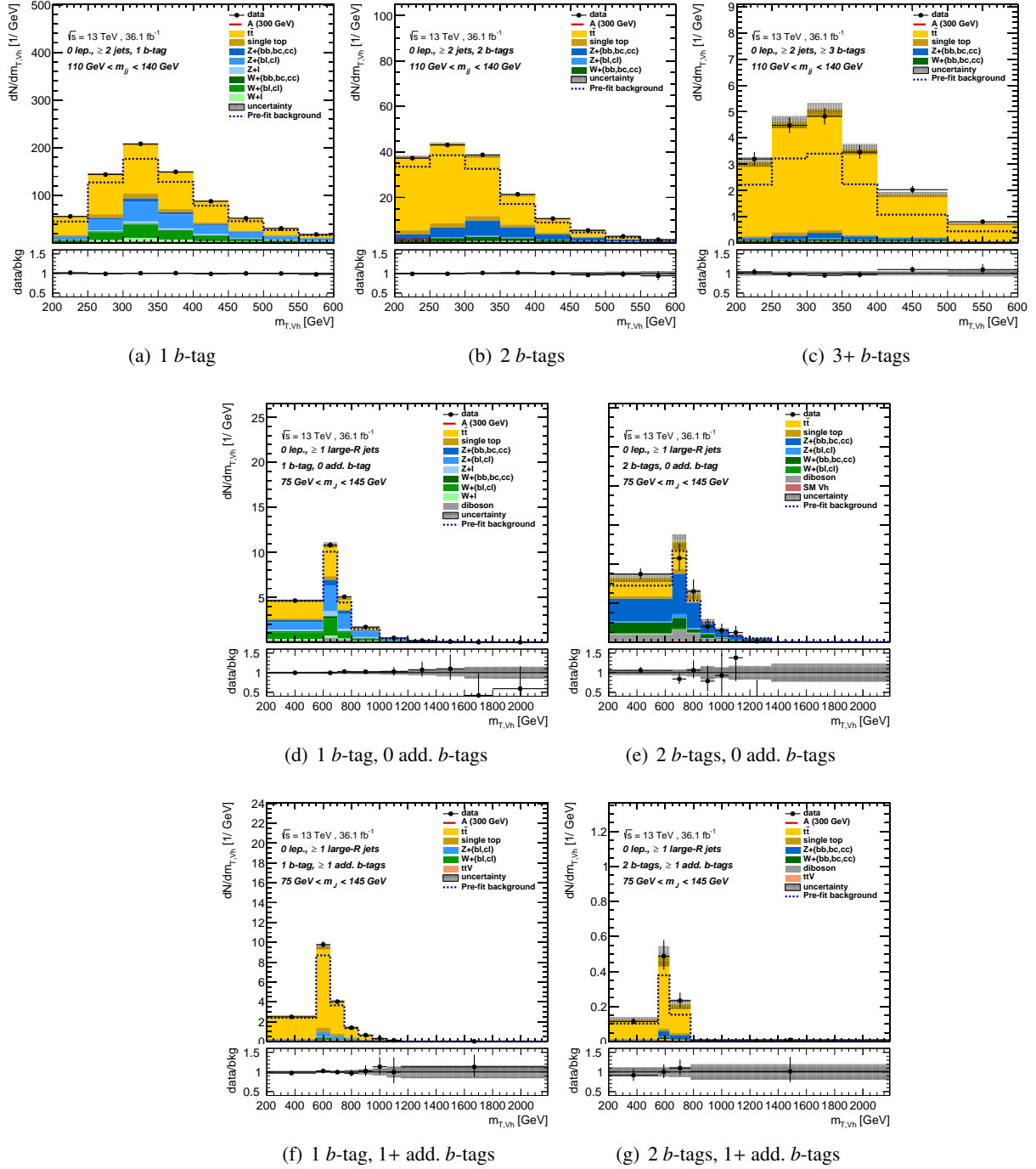


Figure 5.28: Postfit distributions of $m_{T,Vh}$ in the (a)-(c) resolved and (d)-(g) merged signal regions of the 0-lepton channel after a combined background-only fit to the data including the 2-lepton regions (cf. Fig. 5.29). The y-axis shows the number of events divided by the bin width in GeV. The various background components as obtained from the fit are drawn stacked as coloured, filled histograms; the total background prediction given by the prefit simulations is indicated as dotted blue histogram. The combined statistical and systematic uncertainties on the fitted, total background distribution are shown as hatched band. The distribution expected for a hypothesised A boson with $m_A = 300$ GeV produced purely in gluon fusion with an assumed cross section of 5 pb is overlaid as dashed red histogram. The ratio of the data and the fitted, total background distribution is shown in the lower panel. In Figures (a)-(c) a reduced x -axis range is shown with respect to the fitted range; the overflow is not taken into account.

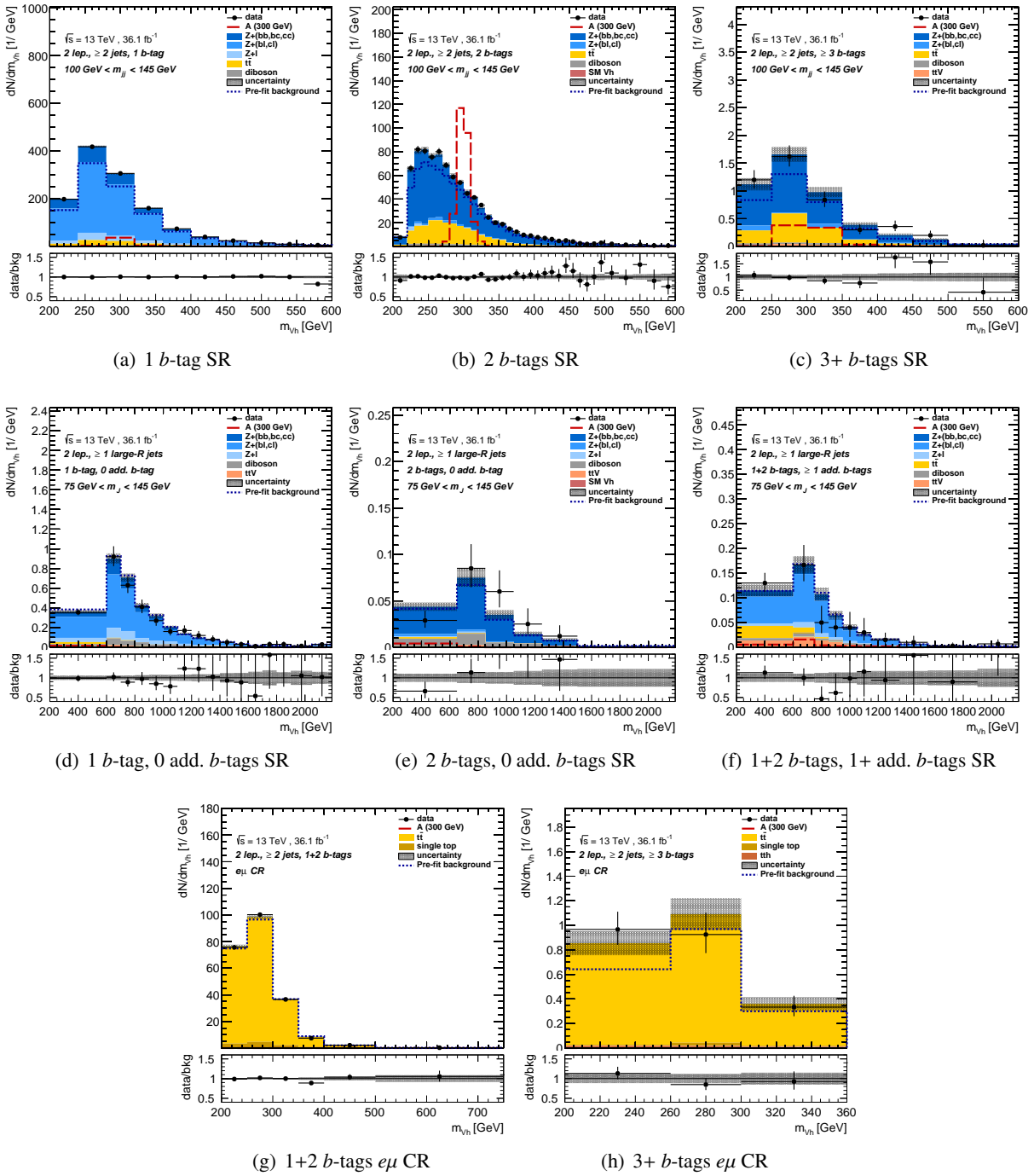


Figure 5.29: Postfit distributions of m_{Vh} in the (a)-(c) resolved and (d)-(f) merged signal regions of the 2-lepton channel as well as the (g)-(h) $e\mu$ control regions after a combined background-only fit to the data including the 0-lepton signal regions (cf. Fig. 5.28). The y-axis shows the number of events divided by the bin width in GeV. The various background components as obtained from the fit are drawn stacked as coloured, filled histograms; the total background prediction given by the prefit simulations is indicated as dotted blue histogram. The combined statistical and systematic uncertainties on the fitted, total background distribution are shown as hatched band. The distribution expected for a hypothesised A boson with $m_A = 300$ GeV produced purely in gluon fusion with an assumed cross section of 5 pb is overlaid as dashed red histogram. The ratio of the data and the fitted, total background distribution is shown in the lower panel. In Figures (a)-(c), (g) and (h) a reduced x -axis range is shown with respect to the fitted range; the overflow is not taken into account.

only those regions which have a reasonable statistical precision).

While these numbers are the result of a complex interplay between all the nuisance parameters that affect either the global normalisation (i.e. across regions, such as the floating normalisations) or the “regional” normalisations (i.e. affecting certain regions, such as the ones related to the b -tagging efficiencies), they can still be reasoned by studying the *pulls* of the nuisance parameters that reflect the individual adjustment (or shift) of each parameter in the fit to the data, as well as the correlations between the different nuisance parameters that arise in the process (initially all sources of systematic uncertainties, and thus the nuisance parameters are treated as uncorrelated).³⁶

Nuisance parameter pulls

The pull of an adjusted nuisance parameter, $\hat{\theta}$, is defined as

$$pull = \frac{\hat{\theta} - \theta}{\sigma_{\theta}} = \frac{\hat{\theta}}{\sigma_{\theta}} \quad (5.15)$$

where θ denotes its prefit value with uncertainty σ_{θ} as propagated from the auxiliary measurement; $\theta \equiv 0$ and $\sigma_{\theta} \equiv 1$ by construction of the likelihood function (cf. Sec. 5.7.3). The postfit uncertainty on a nuisance parameter as well as the correlations between two different nuisance parameters are obtained from the covariance matrix of the estimators of all the parameters, $V_{i,j} = \text{cov}(\hat{\theta}_i, \hat{\theta}_j)$, which is estimated from the inverse of the second derivatives of the log-likelihood function [335]

$$\text{cov}(\theta_i, \theta_j) = \left[-\frac{\partial^2 \log L(\boldsymbol{\theta})}{\partial \theta_i \partial \theta_j} \right]^{-1} \quad (5.16)$$

evaluated at $\hat{\boldsymbol{\mu}}$ and $\hat{\boldsymbol{\theta}}$.³⁷ As already discussed earlier, the postfit uncertainty on the nuisance parameter, $\sigma_{\hat{\theta}_i} = (V_{i,i})^{1/2}$, might be reduced with respect to the prefit uncertainty σ_{θ_i} , if the fit model is able to extract information on the parameter from the data with higher precision than the auxiliary measurement; i.e. the present measurement is able to constrain the nuisance parameter.

Figure 5.30 shows the pulls and postfit uncertainties obtained in a fit to data for the most relevant nuisance parameters, according to the discussion in the previous section, omitting the gamma parameters. The postfit uncertainties can be compared to the ones obtained in a fit to an Asimov dataset, where for the hypothesised A -boson signal with $m_A = 300$ GeV, produced solely via gluon fusion, $\sigma(gg \rightarrow A) \times \text{BR}(A \rightarrow Zh) \times \text{BR}(h \rightarrow bb)$ is assumed to have the value at the expected upper limit at the 95 % CL (cf. Fig. 5.23(a)). The pulls of the Asimov fit are centred at zero, as the estimators agree with the nominal (prefit) values; an exception constitute the floating normalisations in Fig. 5.30(a). They have a nominal value of unity, since in the absence of prefit uncertainties they are expressed in absolute terms.

Generally, the observed constraints as well as the uncertainties on the floating normalisations are in good agreement with the expectation. In addition, most of the pulls from the fit to data are very small; there are only a few more significant ones, such as `Vjets_MG_Zh1` (cf. Fig. 5.30(c)). Only one nuisance parameter is pulled more than one standard deviation (σ_{θ}): `FT_C_0_small1R`; the strong constraint, already

³⁶Clearly, this statement does not only apply to the normalisations, but also the shapes of the background predictions.

³⁷Where here $\hat{\theta}$ stands for both $\hat{\boldsymbol{\mu}}$ as well as the nuisance parameters; and $\sigma_{\hat{\theta}_i} = (V_{i,i})^{1/2}$ and $\text{corr}(\hat{\theta}_i, \hat{\theta}_j) = V_{i,j}/(\sigma_{\hat{\theta}_i}\sigma_{\hat{\theta}_j})$

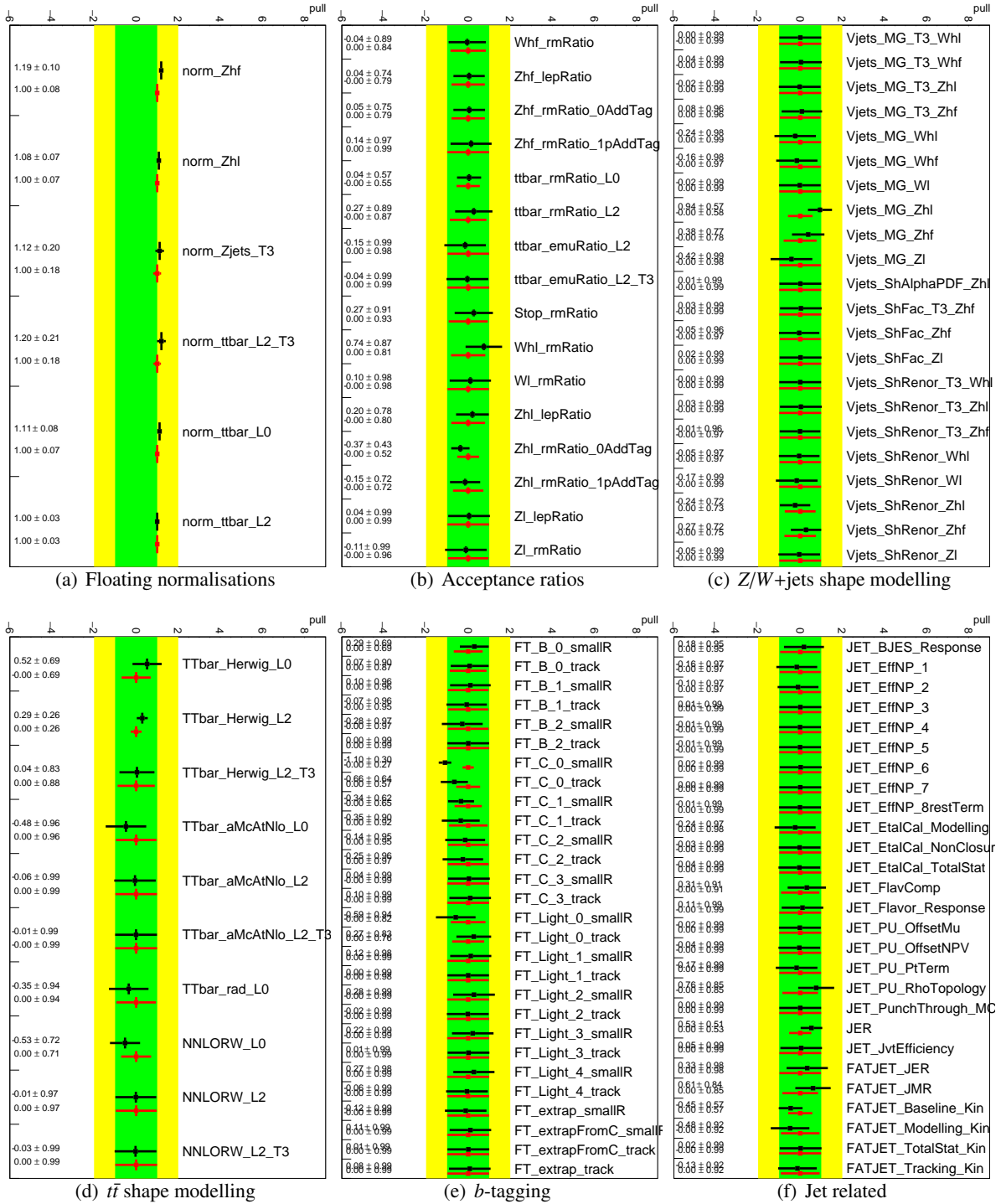


Figure 5.30: Comparison of the nuisance parameter pulls from a fit to data (black) and to an Asimov dataset (red) for the most relevant systematic uncertainties. The cross section of the hypothesised signal produced in pure gluon fusion with a mass of 300 GeV is assumed to have the value at the 95 % CL expected upper limit (cf. Fig. 5.23(a)). The pulls from the Asimov fit are zero, as the estimators agree with the nominal (prefit) values; an exception constitute the floating normalisations in Fig. (a), where the nominal value corresponds to unity, as in the absence of prefit uncertainties they are expressed in absolute terms. The nuisance parameter names are defined in Secs. 5.6 and 5.7.4.

discussed in the previous section, indicates the high sensitivity of the fit model to it.

The floating normalisations, shown in Fig. 5.30(a) and also listed in Table 5.9, deviate 10-20 % from unity, and thus from the prefit prediction. The only exception is the $t\bar{t}$ normalisation the 1 and 2 b -tags regions of the 2-lepton channel, `norm_ttbar_L2`: it is in perfect agreement with the nominal simulation. While it is mainly determined from the dedicated 1+2 b -tags $e\mu$ CR, which shows excellent modelling as can be seen from Fig. 5.29(g), this apparently applies as well to the signal region. The nuisance parameter allowing for potential differences, `ttbar_emuRatio_L2` (cf. Fig. 5.30(b)), is hardly pulled; thus, the corresponding scale factors in Table 5.11 are close to unity as well. The small difference between the scale factors of the 1 and 2 b -tags SRs can be explained by the slight upward pull of `FT_B_0_smallR` (cf. Fig. 5.30(e)). Corresponding to a slight decrease of the b -tagging efficiency with respect to what is assumed in simulation, it causes a migration of events out of the 2 b -tags regions.

In the 0-lepton channel, the floating normalisation for the $t\bar{t}$ background, `norm_ttbar_L0`, indicates that the data generally prefers an about 10 % higher $t\bar{t}$ contribution in the considered phase space. While this is reflected by the $t\bar{t}$ scale factors in Table 5.11 for some of the 0-lepton regions, the ones for the 3+ b -tags and merged 2 b -tags regions are significantly higher. Given that in those regions the $t\bar{t}$ contamination mainly arises from misidentification of c jets (cf. Sec. 5.5.2), this can be explained by the pulls of the nuisance parameters related to the normalisation impact of the c -jet tagging efficiency uncertainties, `FT_C_0_smallR` and `FT_C_0_track`, in the resolved and merged regimes, respectively. The downwards pull of `FT_C_0_smallR` by about 1σ indicates that the c -jet tagging efficiency (for small-R jets) in data is with up to 40 % significantly higher than suggested by the exploited default calibration. Thus, the present analysis is able to confirm the results of the (at the time) alternative $t\bar{t}$ -calibration method (cf. Sec. 5.6.1), demonstrating impressively the power of a *profile* likelihood fit.³⁸

Similarly, the scale factors for the merged 2 b -tags regions of the 0-lepton channel can be explained. `FT_C_0_track` is pulled in the same direction, suggesting an about 30 % higher c -jet tagging efficiency for track jets in the data than anticipated. However, the 2 b -tags, 1+ add. b -tags region (cf. Fig. 5.28(g)), which is driving this result, does not have the constraining power of the resolved regime given it is only sparsely populated.³⁹ Because, at the time of writing, no dedicated calibration for the c -jet tagging efficiency of track jets is available, the results found here cannot be confirmed independently.

As discussed previously, the $t\bar{t}$ contamination of the 3+ b -tags region of the 2-lepton channel has a significant contribution by $t\bar{t}+hf$ production. Thus, while the higher c -jet tagging efficiency in data also affects the measured $t\bar{t}(+hf)$ normalisation, the main reason for the needed adjustment by a scale factor of almost 1.3, is the underestimation of the $t\bar{t}+hf$ normalisation by current simulations in general and by POWHEG +PYTHIA 6 in particular. This mismodelling is also observed by several other analyses, such as the $t\bar{t}h$ analysis which also considers regions with more than three b -tagged small-R jets; not only by the one of the ATLAS collaboration [341], but also by the one of the CMS collaboration [342]. Therefore, at the time of writing, there are ongoing efforts across the collaborations and involving also theorists to find the cause and resolve the underlying issue. Until then, a common approach is to adjust the normalisation in a fit to the data, which justifies the different $t\bar{t}$ floating normalisation in the 3+ b -tags region of the 2-lepton channel, `norm_ttbar_L2_T3`. The value of $1.2(\pm 0.2)$ is predominantly determined in the dedicated 3+ b -tags $e\mu$

³⁸This result is indeed independent as the calibration analysis relies on $t\bar{t}$ events with exactly one well-identified lepton.

³⁹Given the additional uncertainty on the c -jet tagging efficiency of track jets accounting for potential differences when extrapolating the calibration results from small-R jets (cf. Sec. 5.6), the smaller pull of `FT_C_0_track` with respect to `FT_C_0_smallR` still results in a similar increase of the c -jet tagging efficiency.

region, shown in Fig. 5.29(h), and is in agreement with what is found elsewhere.

Given the rather limited statistical precision and the reasonable agreement between the data and the simulation after adjusting the parameters according to the fit, it seems justified that in this analysis it was not considered to apply any corrections regarding the shape of the m_{Vh} distribution of $t\bar{t}(+hf)$ at *prefit* level, as it was done in $t\bar{t}h$ analysis. After all, several shape-related modelling uncertainties are included in the fit, and the chosen decorrelation scheme prevents an unjustified propagation of constraints from the 1 and 2 b -tags regions with high statistical precision and different $t\bar{t}$ composition. For example, the constraint on the uncertainty regarding the parton-shower model, TTbar_Herwig_L2 in Fig. 5.30(d) is not propagated to the 3+ b -tags region, given TTbar_Herwig_L2_T3 is treated decorrelated.⁴⁰

In a similar way the results for the different Z +jets components can be understood. However, the situation is somewhat more complex given the large number of nuisance parameters associated with their description and the correlation across the two lepton channels. The floating normalisations suggest that SHERPA 2.1 underestimates the $Z+hl$ and $Z+hf$ components at the level of 10-20 %, although the corresponding uncertainties are at the same level.⁴¹

While they are mainly determined from the resolved 1 and 2 b -tags regions of the 2-lepton channel, the estimates seem to also describe the contributions in the 0-lepton channel well. The $Zhf/Zhl_lepRatio$ nuisance parameters, accounting for potential differences regarding the acceptances in the two lepton channels, are almost centred at zero, while the slight constraint reflects some sensitivity.

Nonetheless, the $Z+hl$ and $Z+hf$ scale factors in Table 5.11 deviate quite strongly from the floating normalisations in all regions; in particular in the resolved regime they are somewhat higher. This can be mainly attributed to the previously discussed adjustments of the b -tagging related nuisance parameters. For example, the scale factor for the $Z+hl$ component in the 2 b -tags region of the 2-lepton channel of about 1.4 can be explained by the combined effect of the pulls of FT_C_0_smallR and FT_Light_0_smallR. The *prefit* impact of the latter on the $Z+hl$ normalisation is as high as ~ 43 % and the pull by about 0.5σ , results in an increase of about 20 %; the former adds another 7 %. However, a detailed understanding how the various nuisance parameters lead to the background scale factors is difficult, given the degeneracy in particular between the b -tagging related nuisance parameters, affecting the normalisations in the various b -tag regions, and the floating normalisations; their correlations are somewhat discussed below.

Nuisance parameter correlations

Figure 5.31 shows the reduced version of the full correlation matrix obtained from a fit to data, where the hypothesised A -boson signal with $m_A = 300$ GeV is assumed to be produced purely in gluon fusion and $\sigma(gg \rightarrow A) \times BR(A \rightarrow Zh) \times BR(h \rightarrow bb)$ to have the value at the 95 % CL expected upper limit.

It only shows those nuisance parameters that exhibit with at least one other parameter a correlation of ≥ 25 %. While there are only a few stronger correlations between certain nuisance parameters related to

⁴⁰Generally, it should be avoided that shape-related modelling uncertainties get constrained, or (worse) pulled, by not profiling them at all. This is because, in their case the extrapolation between the available $\pm 1\sigma$ variations is even less well defined than for other nuisance parameters. Nonetheless, at the time of the analysis this was still a rather common approach to have these two-point modelling uncertainties, but discussions with both theorists and statisticians started to develop better strategies to estimate modelling uncertainties than by generator comparisons.

⁴¹This result is a clear improvement with respect to SHERPA 2.2.1, where the deviations were rather at the 30 % level.

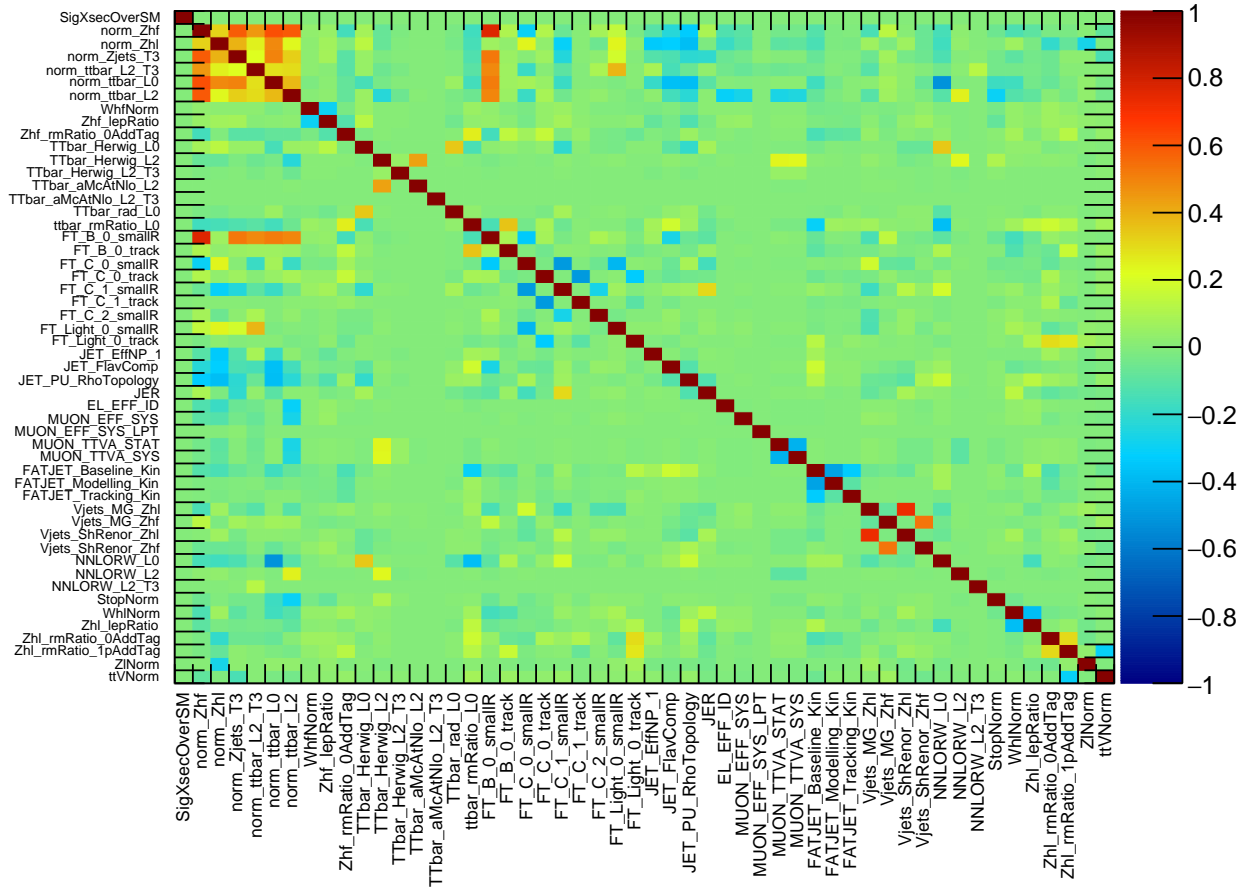


Figure 5.31: Correlation matrix of nuisance parameters from a fit to data. The hypothesised A -boson signal with $m_A = 300$ GeV is assumed to be produced purely in gluon fusion and $\sigma(gg \rightarrow A) \times \text{BR}(A \rightarrow Zh) \times \text{BR}(h \rightarrow bb)$ to have the value at the 95 % CL expected upper limit (cf. Fig. 5.23(a)). Only those nuisance parameters are shown that exhibit at least a 25 % correlation with any other parameter. The nuisance parameter names are defined in Secs. 5.6 and 5.7.4.

experimental and modelling uncertainties, the correlations between all the floating normalisations and with the b -tagging related nuisance parameters `FT_B_0_smallR` are striking.

It might surprise that there are *positive* correlations between the different floating normalisations. A priori, one would rather expect an anti-correlation between the different background components in a certain region, e.g. between `norm_ttbar_L2` and `norm_Zhf`, and no correlation between the floating normalisations of background components that are treated, independently in the two channels, such as `norm_ttbar_L2` and `norm_ttbar_L0`. However, the shown correlations can be understood from the (positive) correlations of the floating normalisations with `FT_B_0_smallR`.

As indicated before, `FT_B_0_smallR` is defined such that an *upwards* (*downwards*) pull corresponds to a decrease (increase) of the prior b -tagging efficiency and, thus to a *decrease* (*increase*) of the number of b -jet events in the considered regions. The same effect can be achieved via a *decrease* (*increase*) of the respective floating normalisations. Therefore, the observed *positive* correlations between the floating normalisations and `FT_B_0_smallR` of at least 50 %, except for the $Z+hl$ background, is just as expected.

The positive correlations among the various floating normalisations arise then indirectly from this when inverting the second derivatives of the log-likelihood function (Eq. 5.16).

In any case, the correlations observed for the fit in data are very well reproduced by a corresponding fit to the Asimov dataset (not shown here), despite the few rather strong pulls occurring in the fit to data, resulting in an evaluation of the correlations for different parameter values than in the Asimov dataset via Eq. 5.16. In the case of the fit to the Asimov dataset, however, also a few correlations with the signal-strength parameter can be observed; the strongest is with FT_B_0_smallR. While this is certainly due to the choice of the hypothesised m_A , as well as the considered production mode, this result is consistent with the findings discussed in the previous section, where FT_B_0_smallR showed the strongest impact on $\hat{\mu}$ for the considered mass point and production mode (cf. Fig. 5.27(a)).

Validation of the fit results

As mentioned earlier, the m_h -sideband regions defined in Sec. 5.5.3 are used to further validate the fit model. Figure 5.32 shows the m_{Vh} and $m_{T,Vh}$ distributions in the various b -tag categories of the resolved and merged sideband regions of the 0- and 2-lepton channel; the same binning as for the signal regions shown in Figs. 5.28 and 5.29 is used. As previously for the signal regions, the background predictions are adjusted according to the postfit values of the nuisance parameters obtained in the *nominal* fit. In addition to the systematic uncertainties considered in the nominal fit, dedicated ones on the acceptance differences between the signal and sideband regions are considered for the dominant background components $t\bar{t}$ and V +jets (as well as single-top), listed in Tables 5.5 and 5.6. For those additional uncertainties, the same (de)correlation scheme is used that was discussed for the signal regions in Sec. 5.7.4; e.g. the $t\bar{t}$ -related nuisance parameters are treated decorrelated between the two lepton channels. Since the adjustments are simply extrapolated from the nominal fit result, the additional uncertainties are not profiled and their prior values are considered.

Generally, there is good agreement between the data and the adjusted simulations, in particular when considering the statistical limitations. There are only three exceptions, where some rather systematic deviations occur: in the 3+ b -tags regions of both lepton channels, and in the 1 b -tag, 0 add. b -tags region of the 0-lepton channel.

In this last, fairly-well populated region, the postfit expectation is systematically undershooting the data, with exception of the first bin, as can be seen from Fig. 5.32(d). As described in Sec. 5.5.3, in the sideband regions events from the low and the high sideband regions are combined. This means that in the sideband region of the merged regime events with Higgs-candidate masses of $50 \text{ GeV} < m_J < 75 \text{ GeV}$ and $145 \text{ GeV} < m_J < 200 \text{ GeV}$, respectively, are combined, although they have quite different event topologies and background compositions. This can be seen from Fig. 5.33(c) which shows the postfit distribution of the Higgs-candidate mass in the full considered range of $50 \text{ GeV} < m_J < 200 \text{ GeV}$, i.e. the signal and sideband regions are merged. The discontinuities at the transition points between the signal and sideband regions, i.e. at $m_J = 75 \text{ GeV}$ and 145 GeV , are a result of the chosen regime-selection strategy, PriorityResolvedSR (cf. Sec. 5.5.1): events are only tested whether they enter the merged sideband-regions after they failed both the resolved and merged signal-region selections as well as the resolved sideband-regions selection.

The $t\bar{t}$ -dominated high-sideband region shows reasonable agreement between the data and the adjusted simulation, which hardly differs from the prefit prediction. In the low-sideband region on the other hand,

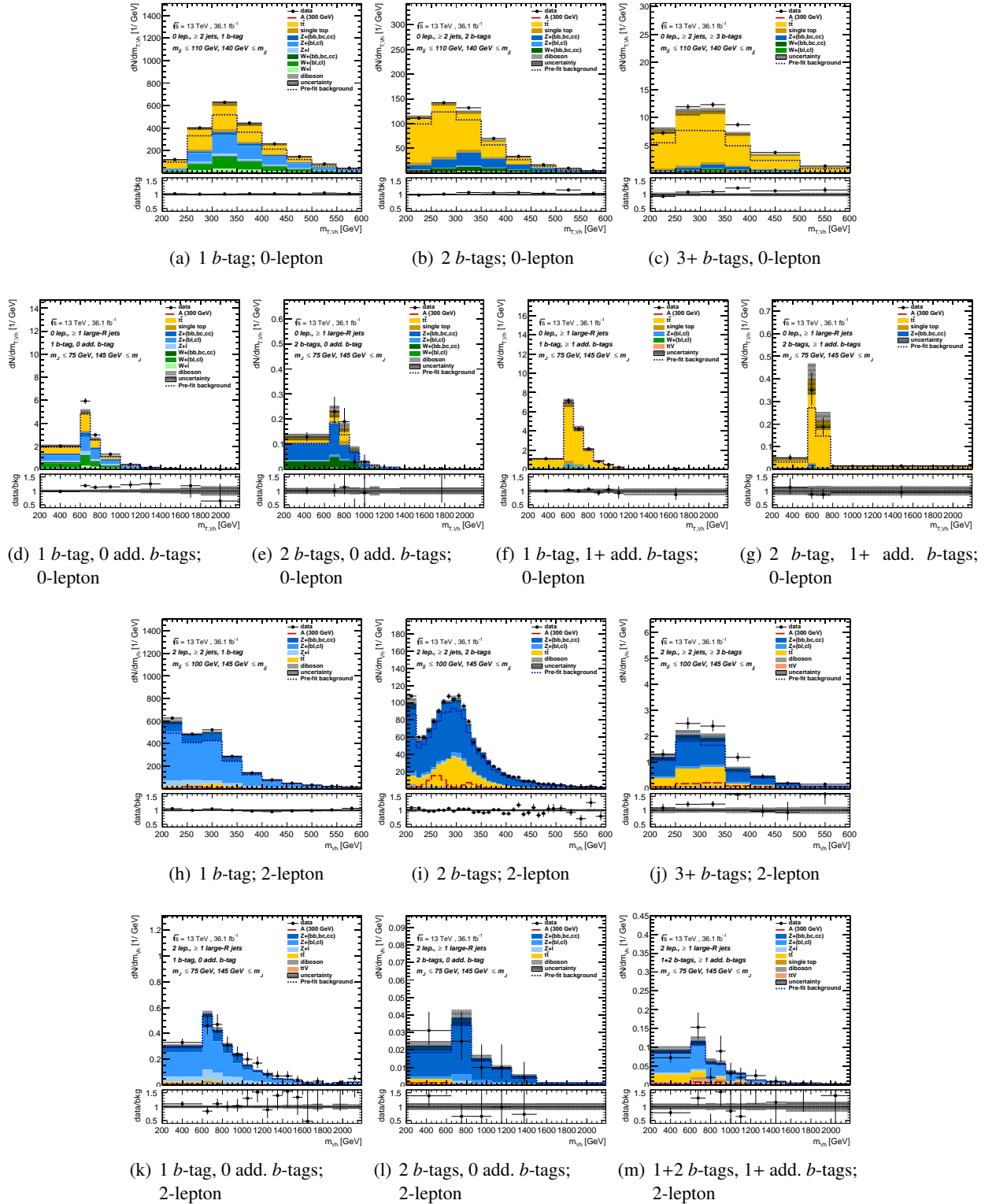


Figure 5.32: Postfit distributions of $m_{T,Vh}$ and m_{Vh} in the resolved and merged sideband regions of the (a)-(g) 0-lepton and (h)-(m) 2-lepton channel after the nominal combined background-only fit to the data in the signal regions (cf. Figs. 5.28 and 5.29). The y -axis shows the number of events divided by the bin width in GeV. The various background components adjusted to the results obtained from the fit are drawn stacked as coloured, filled histograms; the total background prediction given by the prefit simulations is indicated as dotted blue histogram. The combined statistical and systematic uncertainties on the adjusted, total background distribution are shown as hatched band, including additional uncertainties accounting for acceptance differences of the sideband regions with respect to the fit regions. The distribution expected for a hypothesised A boson with $m_A = 300$ GeV produced purely in gluon fusion with an assumed cross section of 5 pb is overlaid as dashed red histogram. The ratio of the data and the fitted, total background distribution is shown in the lower panel.

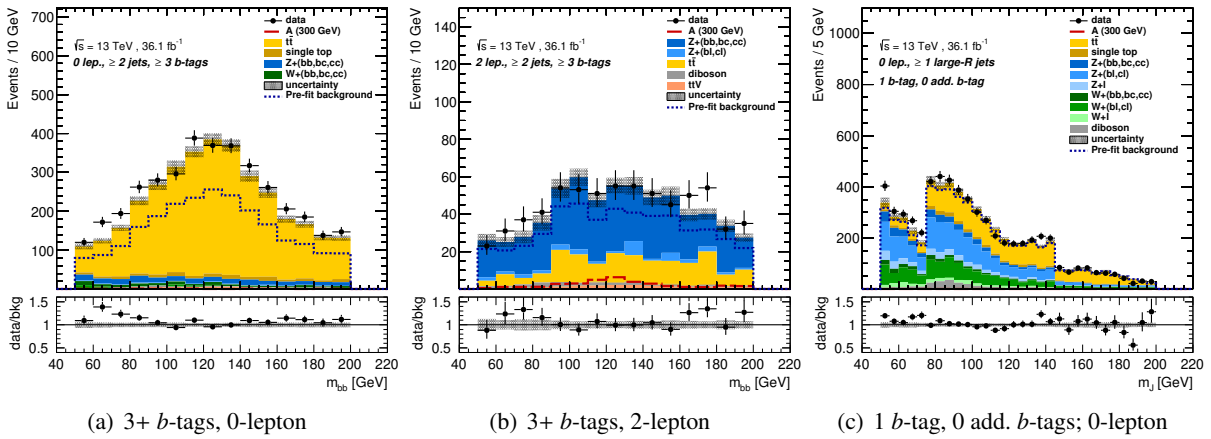


Figure 5.33: Postfit distributions of the Higgs-candidate mass in signal and sideband regions: in the 3+ b -tags regions of (a) the 0-lepton channel, (b) the 2-lepton channel as well as (c) in the 1 b -tag, 0 add. b -tags regions of the 0-lepton channel, after the nominal combined background-only fit to the data in the fit regions (cf. Figs. 5.28 and 5.29). The various background components adjusted to the results obtained from the fit are drawn stacked as coloured, filled histograms; the total background prediction given by the prefit simulations is indicated as dotted blue histogram. The combined statistical and systematic uncertainties on the adjusted, total background distribution are shown as hatched band; additional uncertainties accounting for acceptance differences of the sideband regions with respect to the fit regions are considered. The distribution expected for a hypothesised A boson with $m_A = 300$ GeV produced purely in gluon fusion with an assumed cross section of 5 pb is overlaid as dashed red histogram. The ratio of the data and the fitted, total background distribution is shown in the lower panel.

the total background prediction systematically undershoots the data, causing the mismatch observed in the $m_{T,Vh}$ distribution in the combined sideband region. Given that in this region only one b -tag is required, there is a contribution of events with only one track jet associated with the candidate large- R jet; and this fraction is significantly higher in the low-sideband region than in the signal or the high-sideband regions. This difference can explain why an adjustment of the simulation derived in the signal region is not appropriate for the low-sideband region, while it is for the high-sideband region. The m_J distribution at even lower values, where the fraction of events with only one track jet associated with the candidate large- R jet dominates, are known to be not very well modelled by simulations; this motivated the restriction of the sideband region to $m_J > 50$ GeV.

Similarly, the mismodelling in the 3+ b -tags region of the 0-lepton channel, shown in Fig. 5.32(c), can be explained by the fact that the type of events entering the signal and the sideband regions differ, making the adjustments derived in the signal region not well suited for correcting the simulations in the sideband region. From Figure 5.33(a), showing the full postfit distribution of the Higgs-candidate mass m_{jj} , one can see that again the mismodelling is mainly concentrated in the low sideband region, i.e. $50 \text{ GeV} < m_{jj} < 110 \text{ GeV}$. As discussed before, in the signal region, the main source for the $t\bar{t}$ -background contribution is the misidentification of c jets stemming from one of the W -boson decays, while the fraction of $t\bar{t}+hf$ events is small - justifying the common $t\bar{t}$ normalisation across all 0-lepton regions. In the sideband regions, however, $t\bar{t}+hf$ contribution appears to be significantly higher, in particular in the low-sideband region. This explains the mismodelling, as the underestimation of the $t\bar{t}+hf$ contribution by the exploited simulation is not addressed by the corrections to the $t\bar{t}$ normalisation obtained in the 0-lepton signal region. Considering

that low m_{jj} values rather correspond to small opening angles between the jet candidates, as expected for quark pairs stemming from gluon splittings, it is consistent that the contribution of $t\bar{t}+hf$ events increases towards low m_{jj} values. Accordingly, intermediate and high m_{jj} correspond rather to larger opening angles expected for b -jets and c jets stemming from the same and different top-quark decays, respectively.

In the 3+ b -tags region of the 2-lepton channel, shown in Fig. 5.32(j), the mismodelling is more pronounced than in the other discussed regions; the rather large uncertainties are not able to cover the differences between data and the adjusted simulation. Other than before, the level of disagreement is similar in the low- and high-sideband regions, as can be seen from Fig. 5.33(b). Also here the extrapolation of the adjustments regarding the $t\bar{t}(+hf)$ background from the signal region to the sideband region is not valid and causes the observed disagreement; this can be demonstrated by means of the dedicated $e\mu$ control region.

For this purpose, its definition is slightly adapted. As described in Sec. 5.5.3, the $e\mu$ control region, entering the fit, differs from the signal region only by (i) requiring opposite-flavoured leptons, and (ii) omitting the $E_T^{\text{miss}}/\sqrt{H_T}$ requirement, designed to suppress the $t\bar{t}$ contamination in the signal region. However, in order to obtain $e\mu$ validation regions that mimic the signal and sideband regions as close as possible, the $E_T^{\text{miss}}/\sqrt{H_T}$ requirement is applied. This defines the “signal region-like” $e\mu$ validation region; by replacing the m_h -window requirement by selecting events with $50 \text{ GeV} < m_{jj} < 100 \text{ GeV}$ and $145 \text{ GeV} < m_{jj} < 200 \text{ GeV}$, the “sideband region-like” $e\mu$ validation region is obtained. Thus, only remaining difference between the two $e\mu$ validation regions and the signal and sideband regions, respectively, is the requirement regarding the lepton flavours (opposite vs. same). Therefore, it is expected that the distribution of the $t\bar{t}$ background is very similar in the corresponding regions.

Figure 5.34 shows the m_{vh} distributions in both $e\mu$ validation regions for the 2 b -tags and the 3+ b -tags categories after adjusting the predictions according to the postfit values of the nuisance parameters obtained in the nominal fit. In the case of the 2 b -tags category, for both the “signal region-like” and the “sideband region-like” $e\mu$ regions there is good agreement between data and the adjusted simulation. In particular for the former, this is rather expected given the excellent agreement in the $e\mu$ control region and the minimal adjustments needed (cf. Fig. 5.29(g)).

Also in the case of the 3+ b -tags category of the “signal region-like” $e\mu$ region, shown in Fig. 5.34(c), the modelling of the data distribution is quite reasonable, considering the large uncertainties both on the background prediction as well as the data; the agreement is at the same level as in the case of the nominal $e\mu$ control region (cf. Fig. 5.29(h)). However, in the 3+ b -tags category of the “sideband region-like” $e\mu$ region, shown in Figs. 5.34(d), the adjusted prediction deviates considerably from the data: the simulation is not only underestimating the $t\bar{t}(+hf)$ contribution, but the predicted m_{vh} distribution is also shifted towards lower values. Thus, the adjustments derived in the nominal fit, mainly from the 3+ b -tags $e\mu$ control region, are not suited to describe the $t\bar{t}+hf$ component in the sideband region. Since the observed trend agrees with the discrepancy seen in Fig. 5.32(j), this apparent mismodelling of the $t\bar{t}(+hf)$ prediction seems to be the cause for it. While this suggests, that the observed level of disagreement in the sideband region is expected, the cause for it remains unknown. However, further studies go beyond the scope and the needs of this analysis.

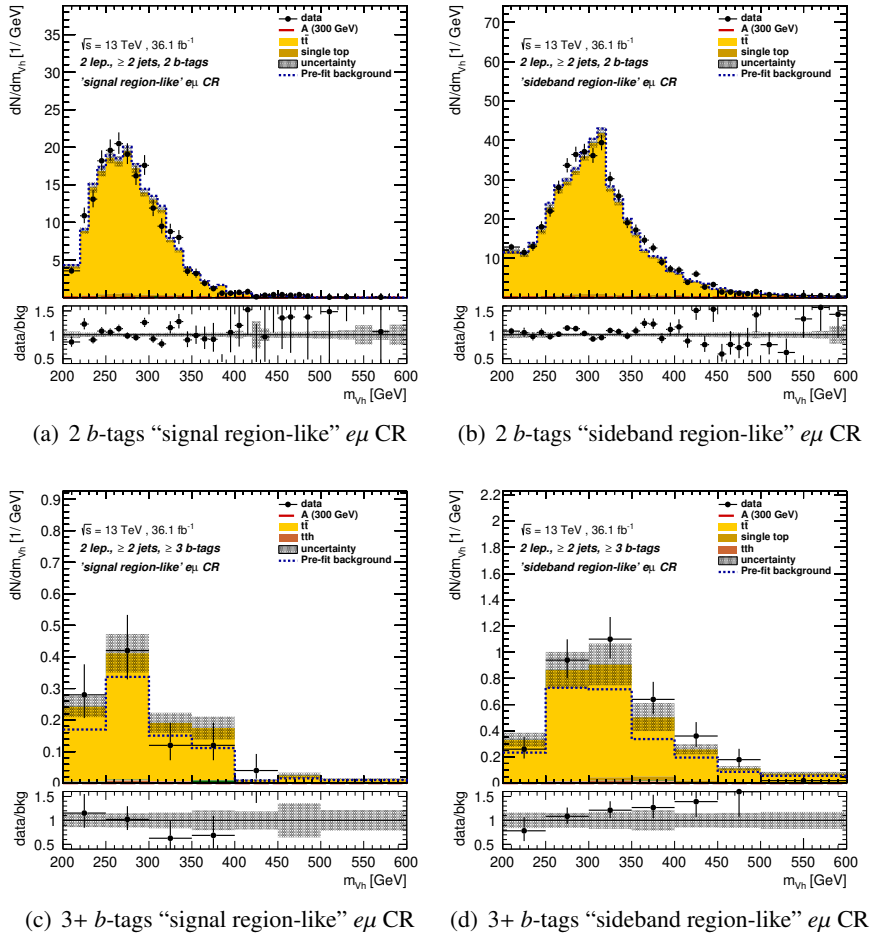


Figure 5.34: Postfit $m_{\nu h}$ distributions in the 2 b -tags (top) and 3+ b -tags (bottom) categories of the “signal region-like” (left) and “sideband region-like” (right) $e\mu$ validation regions, defined in the text. The $t\bar{t}$ -dominated background prediction is adjusted according to the postfit values of the nuisance parameters obtained in the nominal fit. The combined statistical and systematic uncertainties on the adjusted, total background distribution are shown as hatched band; no additional uncertainties accounting for acceptance differences with respect to the nominal $e\mu$ control region are considered. The ratio of the data and the fitted, total background distribution is shown in the lower panel.

Summary

Despite its complexity, the fit model described in Sec. 5.7.4, yields robust results. Any nuisance parameter constraints that appear are expected from the fits to the Asimov dataset; the same applies to the correlations. All pulls of nuisance parameters that occur (per definition) only in the fit to data seem justified and are supported by independent results where applicable. In general, the adjusted simulations show good agreement with the data; not only in the fit regions, but also in the sideband regions used to validate the results.

5.8 Results and Interpretations

In this section, the results of searching for the presence of a resonance compatible with an A boson with a mass between 220 GeV and 2 TeV in the transverse- and invariant-mass spectra of the Zh system in the 0- and 2-lepton channels, $m_{T,Vh}$ and m_{Vh} , are presented. The obtained upper limits on the cross section for A -boson production times the branching ratios for the decays $A \rightarrow Zh$ and $h \rightarrow bb$ are interpreted in the context of the four CP- and flavour-conserving 2HDMs, Type-I, Type-II, Lepton-specific and Flipped Model, that were introduced in Sec. 1.2; the constraints on the 2HDM parameters $\tan\beta$ and $\cos(\beta - \alpha)$ are discussed comprehensively.

Furthermore, also the results of searching for the presence of new heavy vector bosons, $V' = W', Z'$, with masses between 500 GeV and 5 TeV in their decays $W' \rightarrow Wh$ and $Z' \rightarrow Zh$ are presented. The general search strategy is very similar to the one for the A boson, and in particular the search for the Z' boson is conducted using a subset of the discussed 0- and 2-lepton analysis regions. In order to improve the sensitivity to a W' signal, the 0-lepton channel is combined with a 1-lepton channel, targeting the $\ell\nu bb$ final state. As the latter is not considered in the $A \rightarrow Zh$ search, it is not discussed in this thesis; details can be found in Ref. [6]. The results are presented in the context of the previously introduced HVT model (cf. Secs. 5.1 and 5.2).

Finally, the upper limits obtained in the $A \rightarrow Zh$ search are also interpreted in the context of the hMSSM, which is a concrete realisation of a Type-II 2HDM (cf. Secs. 1.2 and 5.2).

5.8.1 Results of the $A \rightarrow Zh$ Search

As described in detail in the previous section, in order to test for the presence of an A -boson signal in the $m_{T,Vh}$ and m_{Vh} distributions, each signal hypothesis is fit together with the different background processes to the data, simultaneously in all signal and control regions using a binned profile likelihood approach. Several signal hypotheses with masses ranging between 220 GeV and 2 TeV and different admixtures of the gluon-fusion and b -associated production mechanisms are tested.

Table 5.12 summarises the expected and observed number of events in the various signal regions. The background predictions are obtained by adjusting the simulations according to the values of the nuisance parameters from a conditional fit to the data assuming no signal to be present. The corresponding $m_{T,Vh}$ and m_{Vh} postfit distributions in the 0- and 2-lepton channels, respectively, are shown in double-logarithmic scale in Figs. 5.35 and 5.36. Expected distributions for hypothesised signals with masses of 500 GeV and 1.5 TeV and production cross-sections of 5 pb assuming pure b -associated production are overlaid for illustration.⁴² In the case of pure gluon-fusion production, no contributions in the 3+ b -tags (Figs. 5.35(c) and 5.36(c)) and 1+ add. b -tags regions (Figs. 5.35(f), (g) and 5.36(f)) are expected, and correspondingly higher contributions in the other regions; any admixture of both production modes leads to a result in between the extremes of pure production via either mode.

The level of disagreement of the data with the background-only hypothesis is quantified by the observed (local) p_0 -value, as discussed in Sec. 5.7.1. Figure 5.37 shows its distribution as function of the A -boson mass, m_A , separately for (a) pure gluon-fusion and pure (b) b -associated production. In addition to the nominal results obtained combining all regions, also the results considering only the 0- and 2-lepton regions, respectively, without any further changes to the nominal fit model are overlaid (cf. Sec. 5.7.4). The

⁴²Linear-scale plots, with restricted mass ranges in the resolved regime can be found in Figs. 5.28 and 5.29.

0 lepton	Resolved regime			Merged regime			
	1 b -tag	2 b -tags	3+ b -tags	1 b -tag 0 add. b -tags	2 b -tags 0 add. b -tags	1 b -tag 1+ add. b -tags	2 b -tags 1+ add. b -tags
$t\bar{t}$	20470 ± 970	5910 ± 160	1002 ± 34	1360 ± 100	62 ± 11	2110 ± 73	105 ± 11
single top	1860 ± 370	415 ± 86	26 ± 6	139 ± 51	8.6 ± 3.4	137 ± 51	5.5 ± 2.4
diboson	306 ± 39	43 ± 8	4.5 ± 1.1	175 ± 28	30 ± 4	12.8 ± 2.3	1.6 ± 0.4
$Z+l$	990 ± 370	7 ± 6	-	190 ± 110	0.32 ± 0.24	12 ± 8	0.11 ± 0.07
$Z+hl$	7460 ± 790	88 ± 30	5.3 ± 1.7	970 ± 170	7.1 ± 3.4	116 ± 26	0.57 ± 0.35
$Z+hf$	1260 ± 180	1220 ± 140	41 ± 8	222 ± 40	97 ± 16	17 ± 4	8.6 ± 2.3
$W+l$	1270 ± 370	7 ± 5	-	111 ± 69	1.1 ± 1.0	5 ± 4	0.02 ± 0.02
$W+hl$	4760 ± 910	66 ± 22	3.9 ± 2.4	640 ± 190	3.7 ± 2.7	65 ± 21	0.06 ± 0.12
$W+hf$	410 ± 110	359 ± 90	17 ± 5	89 ± 38	35 ± 14	10 ± 5	3.0 ± 1.6
SM Vh	39 ± 20	68 ± 35	1.1 ± 0.6	4.6 ± 2.4	2.8 ± 1.5	0.45 ± 0.24	0.07 ± 0.04
$t\bar{t}h$	9 ± 4	6.6 ± 3.1	6.4 ± 3.0	1.1 ± 0.5	0.16 ± 0.08	4.1 ± 2.0	0.63 ± 0.31
$t\bar{t}V$	87 ± 44	35 ± 18	9 ± 5	15 ± 8	1.4 ± 0.7	25 ± 13	1.9 ± 1.0
Total	38930 ± 210	8222 ± 88	1116 ± 33	3919 ± 74	250 ± 14	2515 ± 50	127 ± 11
Data	38920	8212	1125	3935	246	2516	127
2 lepton	1 b -tag	2 b -tags	3+ b -tags	1 b -tag 0 add. b -tags	2 b -tags 0 add. b -tags	1+2 b -tags 1+ add. b -tags	
$t\bar{t}$	2580 ± 110	1910 ± 85	58 ± 9	9 ± 4	0.70 ± 0.29	11 ± 5	
single top	176 ± 35	56 ± 12	1.5 ± 0.4	0.60 ± 0.24	0.22 ± 0.13	0.54 ± 0.35	
diboson	580 ± 75	166 ± 31	5.36 ± 1.32	34 ± 5	8.3 ± 1.3	4.6 ± 0.8	
$Z+l$	3800 ± 1600	58 ± 41	-	56 ± 30	0.9 ± 0.6	6.0 ± 3.5	
$Z+hl$	35600 ± 1500	228 ± 83	12 ± 5	270 ± 38	1.9 ± 1.0	54 ± 11	
$Z+hf$	7900 ± 770	6220 ± 190	151 ± 18	71 ± 11	34 ± 5	11.6 ± 2.6	
$W+l$	3.7 ± 1.5	-	-	0.04 ± 0.02	-	0.01 ± 0.01	
$W+hl$	32 ± 11	2.2 ± 1.4	-	0.52 ± 0.17	-	0.010 ± 0.001	
$W+hf$	5.1 ± 1.7	1.3 ± 0.4	0.03 ± 0.01	0.15 ± 0.07	0.02 ± 0.01	0.06 ± 0.05	
SM Vh	80 ± 41	103 ± 53	1.3 ± 0.7	1.1 ± 0.6	0.61 ± 0.32	0.20 ± 0.10	
$t\bar{t}h$	1.0 ± 0.5	1.7 ± 0.8	1.1 ± 0.5	0.05 ± 0.02	0.01 ± 0.01	0.15 ± 0.07	
$t\bar{t}V$	136 ± 69	55 ± 28	6.4 ± 3.3	9 ± 5	0.7 ± 0.4	12 ± 6	
Total	50870 ± 290	8810 ± 97	237 ± 15	451 ± 20	50 ± 5	101 ± 9	
Data	50880	8800	235	439	50	101	

Table 5.12: The predicted and observed number of events in the 0- and 2-lepton signal regions. The background yields are obtained from simulations where the values of the nuisance parameters are adjusted according to the results of a conditional background-only fit to the data. Statistical and systematic uncertainties are combined into the quoted uncertainties as obtained from the fit. “-” indicates that no events of a certain background component are left in the respective analysis region after the event selection. Similarly published in Ref. [6]; differences occur due to (i) the chosen fit model being the one for $A \rightarrow Zh$ everywhere, and (ii) the fit being here conditional background-only.

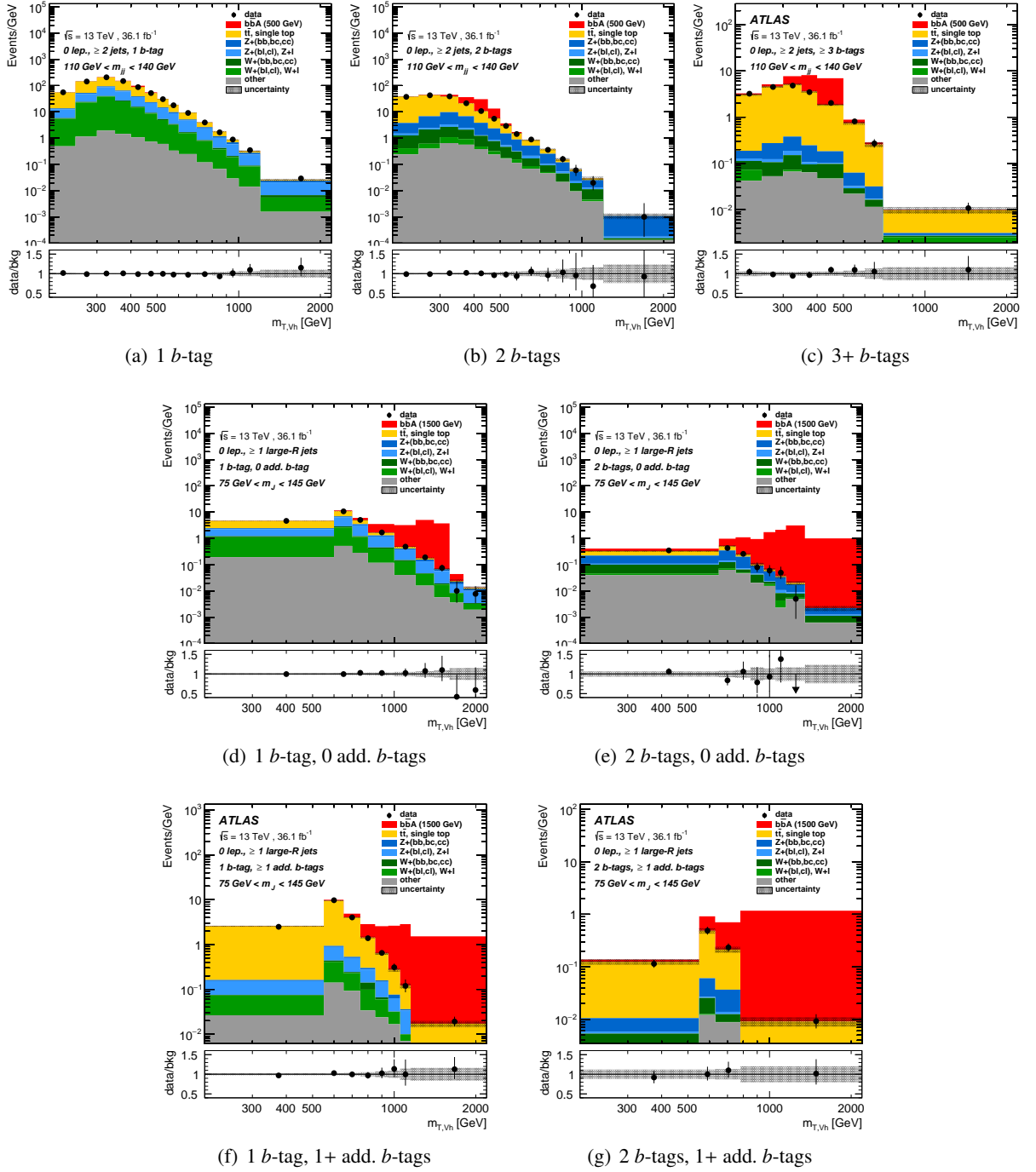


Figure 5.35: Postfit distributions of $m_{T,Vh}$ in the (a)-(c) resolved and (d)-(g) merged signal regions of the 0-lepton channel after a combined background-only fit to the data including the 2-lepton regions (cf. Fig. 5.36). The y-axis shows the number of events divided by the bin width in GeV. The various background components as obtained from the fit are drawn stacked as coloured, filled histograms. The combined statistical and systematic uncertainties on the fitted, total background distribution are shown as hatched band. The distribution expected for a hypothesised A boson with $m_A = 500$ GeV and $m_A = 1.5$ TeV produced purely in b -associated production with an assumed cross section of 5 pb is drawn as solid red histogram. The ratio of the data and the fitted, total background distribution is shown in the lower panel. Figures (c), (f) and (g) were previously published in Ref. [6].

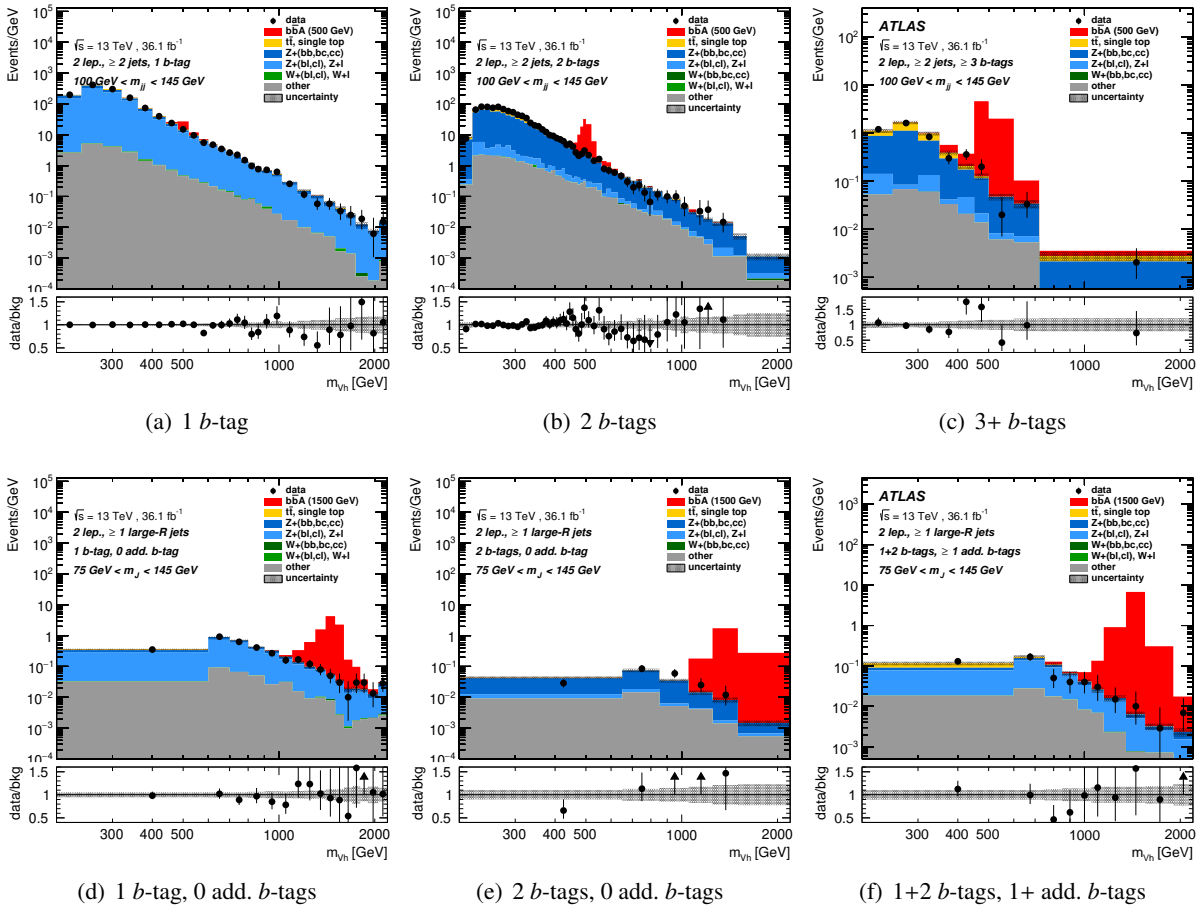


Figure 5.36: Postfit distributions of m_{Vh} in the (a)–(c) resolved and (d)–(f) merged signal regions of the 2-lepton channel after a combined background-only fit to the data including the 0-lepton regions (cf. Fig. 5.35). The y-axis shows the number of events divided by the bin width in GeV. The various background components as obtained from the fit are drawn stacked as coloured, filled histograms. The combined statistical and systematic uncertainties on the fitted, total background distribution are shown as hatched band. The distribution expected for a hypothesised A boson with $m_A = 500$ GeV and $m_A = 1.5$ TeV produced purely in b -associated production with an assumed cross section of 5 pb is drawn as solid red histogram. The ratio of the data and the fitted, total background distribution is shown in the lower panel. Figures (c) and (f) were previously published in Ref. [6].

strongest deviation from the background expectation is observed consistently for both production modes at $m_A = 440$ GeV, corresponding to significances of 2.48σ for pure gluon-fusion production (ggF) and 3.57σ for pure b -associated production (bbA). Considering the “look elsewhere” effect by computing the global p -value via Eq. 5.9, the significance of the latter is reduced to 2.46σ globally (with an uncertainty of $^{+0.23}_{-0.15}$).⁴³

Given the mass at which the excess is located, only the resolved regions are expected to contribute to its significance (cf. Sec. 5.7.6) and in particular the 2 b -tags and, in the case of bbA production, also the 3+ b -tags regions (cf. Figs. 5.35(b), (c) and 5.36(b), (c)). In fact, the rather large difference in significance for ggF and bbA production can be attributed to the 3+ b -tags signal regions. However, from Figure 5.37 it

⁴³The global significance is computed with $N = 4 \pm 2$ down-crossing at a reference significance of $Z_{ref} = 0\sigma$, read off Fig. 5.37(b).

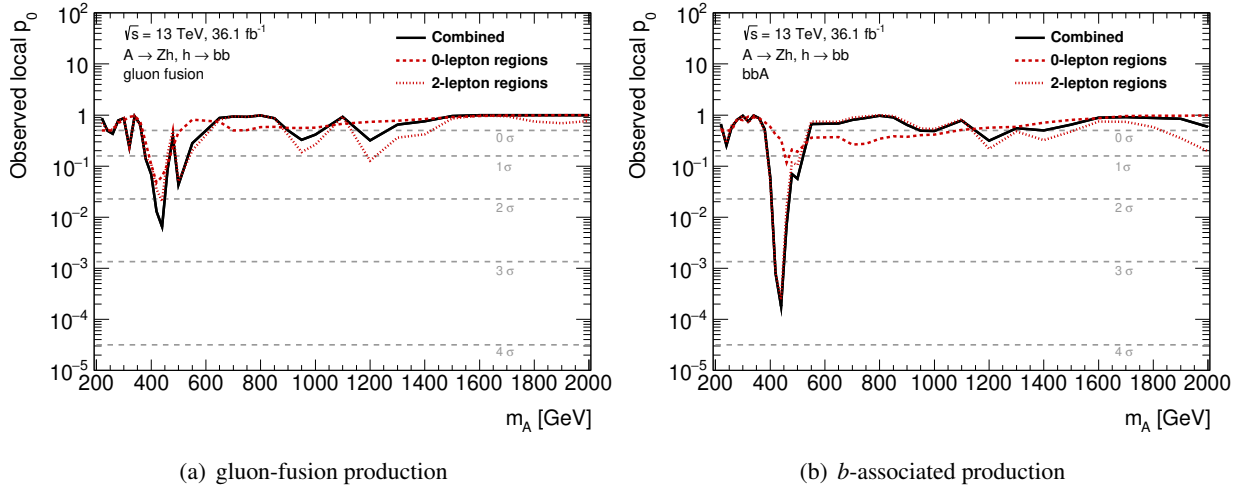


Figure 5.37: Observed local p_0 values as function of the mass of a hypothesised A boson both for the combination (solid) as well as the 0- and 2-lepton channels individually (dashed) assuming pure (a) gluon-fusion and (b) b -associated production. The results obtained for the various mass points are linearly interpolated in order to obtain the shown curves. The smallest p_0 values for both production modes are found at $m_A = 440$ GeV corresponding to a significance of (a) 2.48σ and (b) 3.57σ . Considering the “look-elsewhere” effect as described in the text the latter is reduced to 2.46σ global significance.

Setup	Local significance (in σ)					
	0 lepton		2 lepton		0+2 lepton	
	ggF	<i>bbA</i>	ggF	<i>bbA</i>	ggF	<i>bbA</i>
nominal	1.53	0.44	2.04	3.49	2.48	3.57
\hookrightarrow without 3+ <i>b</i> -tags regions	1.68	1.74	1.89	1.97	2.38	2.51
\hookrightarrow only 3+ <i>b</i> -tags regions	-	-1.31	-	2.85	-	2.55

Table 5.13: Local significances of the excess in the data over the background expectation for a hypothesised A boson with $m_A = 440$ GeV in standard deviations (σ). The results are given separately for pure gluon-fusion (ggF) and pure b -associated production (bbA). In addition to the results obtained with the nominal fit model, also the results are shown when omitting the 3+ b -tags regions and all regions *except* the 3+ b -tags regions, respectively, in order to assess the impact of the 3+ b -tags regions; as well as when considering only the 0- and 2-lepton regions, respectively.

can be seen that while in the case of ggF production the 0- and 2-lepton channels are both contributing to the observed significance, in the case of bbA production it is clearly driven by the 2-lepton channel. This suggests that (i) there are excesses in the 2 b -tags regions of both channels and (ii) there is an excess in the 3+ b -tags signal region of the 2-lepton channel.

In order to test this hypothesis, fits with two alternative setups are performed, where only a subset of the nominal regions are considered: (i) omitting the 3+ b -tags regions and (ii) exclusively considering the 3+ b -tags regions (without modifying the nominal fit model further).⁴⁴ In Table 5.13 the obtained significances of the excess for a signal with $m_A = 440$ GeV are compared to the nominal result for the two production

⁴⁴The 3+ b -tags category of $e\mu$ control region is omitted and considered, respectively, as well. However, the impact on the significance is only by means of providing constraints for certain nuisance parameters (cf. Sec. 5.7.7).

modes and for the two channels both separately and combined. As expected, in the case of (i) the results are similar for ggF and bbA production; the somewhat higher significance for the latter is explained by the relatively lower contribution to the 2 b -tags regions, thus requiring a higher μ value to fill the gap to the data. The significances in the 0-lepton channel are only slightly lower than in the 2-lepton channel; which is somewhat surprising given that it is expected to be less sensitive (cf. Sec. 5.7.6).

The comparison with (ii) reveals that overall the 3+ b -tags regions contribute similarly to the significance of the excess for bbA production as the 2 b -tags regions. The significance of the excess considering all the 3+ b -tags regions is smaller than when considering only the 3+ b -tags regions of the 2-lepton channel: there is a clear excess in data over the expected background contribution that can even be seen from Fig. 5.36(c). In contrast, in the 0-lepton channel the data is somewhat undershooting the background expectation at $m_{T,Vh}$ values around 350 GeV, where a potential signal with $m_A = 440$ GeV would be located (cf. Fig. 5.35(c)), leading to a negative significance value when considering only the 0-lepton 3+ b -tags region and reducing the significance of the excess in the 2-lepton channel when combined.

A number of tests have been performed on the 2-lepton 3+ b -tags region to rule out an underlying issue causing the somewhat stronger deviation in data from simulation than in the other regions. As the excess occurs in the tail of the background distribution, a simple underestimation or slight mismodelling of the latter can be ruled out; this was also confirmed by dedicated variations of the fit model testing the robustness of the results beyond what was already discussed in Sec. 5.7.7. At the same time, the excess in the data seems not to be particularly in agreement with what is expected from a hypothesised A boson, considering (i) also other sensitive distributions, such as the transverse momentum of the Z boson, p_T^V , and (ii) that it appears mainly in the muon channel.

In the meantime, the CMS collaboration conducted a similar search and presented a preliminary result [343]. It does not confirm the excess at $m_A = 440$ GeV, nor finds any other significant deviation from the background-only hypothesis in the searched mass range, up to $m_A = 1$ TeV.

Nonetheless, it is certainly worth to test this mass range again with an even larger dataset. Also because already the previous analysis presented by the ATLAS collaboration found a small excess at the same mass with a significance of about 2σ (cf. Sec. 5.2). It used only about 10% of the present dataset and preliminary calibrations; the 3+ b -tags regions were not considered and the event selection of the 2-lepton channel has not been optimised (in addition to several other, but comparably minor differences).

As no significant excesses of events in the data are observed compared to the background expectation, upper limits on the cross section for A -boson production times the branching fractions for the $A \rightarrow Zh$ and $h \rightarrow bb$ decays at the 95% confidence limit (CL) are set. Figure 5.38 shows the obtained expected and observed limits as function of m_A separately for assuming (a) pure gluon-fusion and (b) pure b -associated production. Except for around $m_A = 440$ GeV, where the observed limit is somewhat weaker than expected (due to the discussed excess), the observed limit tends to be somewhat stronger than expected, in particular towards higher values of m_A . This corresponds to a deficit in the data relative to the expected background contribution; examples can be seen in the last bins of the m_{Vh} and $m_{T,Vh}$ distributions in the sensitive 2 b -tags regions in Fig. 5.36(b) for the resolved regime and in Figs. 5.35(e) and 5.36(e) for the merged regime. The observed upper limits range between $1.9 \cdot 10^{-3}$ pb and $8.1 \cdot 10^{-1}$ pb for pure gluon-fusion production and between $3.4 \cdot 10^{-3}$ pb and $7.3 \cdot 10^{-1}$ pb for pure b -associated production for masses in the range of 220 GeV to 2 TeV.

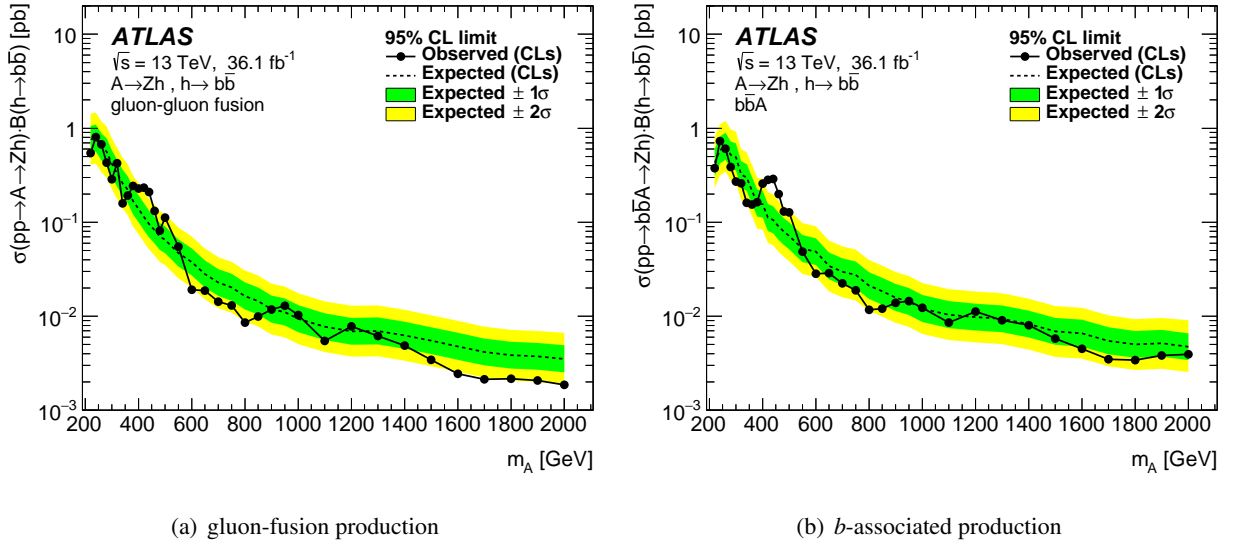


Figure 5.38: Observed and expected upper limits at the 95 % CL on the cross section for A -boson production times the branching ratios for the $A \rightarrow Zh$ and $h \rightarrow bb$ decays for (a) pure gluon-fusion and (b) pure b -associated production, as function of the A -boson mass. Previously published in Ref. [6].

5.8.2 2HDM Interpretation of the $A \rightarrow Zh$ Results

The upper limits presented in the previous section on the cross section for A -boson production times the branching fractions for the $A \rightarrow Zh$ and $h \rightarrow bb$ decays can also be interpreted as constraints on the 2HDM parameters $\tan\beta$ and $\cos(\beta - \alpha)$ in the four CP- and flavour-conserving 2HDMs, Type-I, Type-II, Lepton-specific and Flipped Model. For this purpose, the ratios of the efficiencies and predicted cross sections for the gluon-fusion and b -associated production are taken into account. The cross sections and branching ratios expected in the various 2HDMs are calculated as described in Sec. 5.3. It is furthermore considered that the width of the A boson varies as function of the 2HDM parameters and that it may be larger than the experimental mass resolution. Since this is done by employing the smearing procedure explained in Sec. 5.3, only relative widths up to $\Gamma_A/m_A = 10\%$ are considered.

Since also the A -boson mass is a free parameter, in order to present two-dimensional constraints one of the three parameters need to be fixed. Two sets of exclusion contours are discussed in the following with (i) $m_A = 300$ GeV and (ii) $\cos(\beta - \alpha) = 0.1$, allowing to compare the results to the ones obtained in Run 1 (cf. Fig. 5.3). To be able to explain the shape of the obtained contours, Figs. 1.4, 1.6 and 1.8 show the expected cross sections for A -boson production and the branching fractions for the $A \rightarrow Zh$ and $h \rightarrow bb$ decays in the $[\cos(\beta - \alpha), \tan\beta]$ plane (for $m_A = 300$ GeV); Fig. 1.7 the branching ratios of the dominant A -boson decays as function of m_A for $\cos(\beta - \alpha) = 0.1$ and two benchmark $\tan\beta$ values. They were previously discussed in Sec. 1.3.

Constraints in the $\cos(\beta - \alpha)$ - $\tan\beta$ plane

The observed and expected exclusion regions at the 95 % CL as function of $\cos(\beta - \alpha)$ and $\tan\beta$ for $m_A = 300$ GeV in the four 2HDMs are shown in Fig. 5.39. The narrow regions with no exclusion power at low

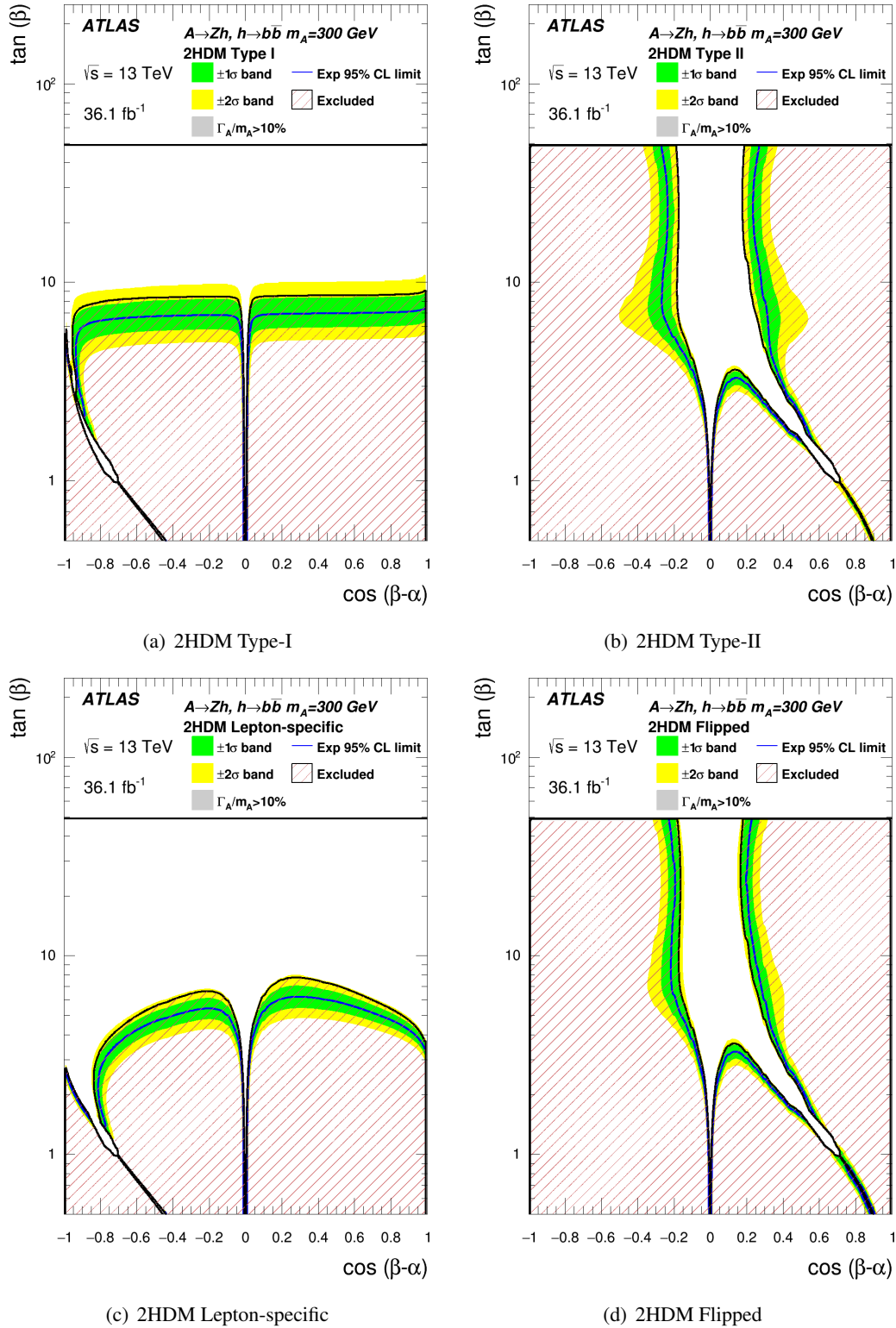


Figure 5.39: Observed and expected exclusion regions at the 95 % CL in the context of the various 2HDM types, namely (a) the Type I, (b) the Type II, (c) the Lepton-specific and (d) the Flipped Model, as function of the model parameters $\tan\beta$ and $\cos(\beta - \alpha)$ for $m_A = 300$ GeV. In the case of the Type-II and the Flipped models, both gluon-fusion and b -associated production are considered. The variation of the natural width in the parameter space is taken into account up to $\Gamma_A/m_A = 10\%$; regions with larger values are indicated by the grey solid area. Previously published in Ref. [6].

$\tan\beta$ and (i) at $\cos(\beta - \alpha) = 0$, in the alignment limit, as well as (ii) away from $\cos(\beta - \alpha) = 0$ are caused by the vanishing branching ratios of the decays $A \rightarrow Zh$ and $h \rightarrow bb$, respectively. While there is limited sensitivity towards high $\tan\beta$ values in the Type-I and Lepton-specific Model, this is not the case for the Type-II and the Flipped Model. The main reason is that the degradation in the cross-section for gluon-fusion production towards high $\tan\beta$ values, is compensated in those models with $\tan\beta$ -enhanced couplings to down-type quarks through the corresponding increase in the cross-section for b -associated production.⁴⁵ The exclusion power in the Lepton-specific Model is worse for high $\tan\beta$ values, and in particular towards large $\cos(\beta - \alpha)$ values, than in the Type-I Model, because the branching fraction of the $h \rightarrow bb$ decay is quickly dropping in the case of the former.

The Run-1 results show almost the opposite: the inclusion of a channel targeting the $A \rightarrow Zh \rightarrow \ell\ell\tau\tau$ decay mode allowed to extend the limit towards higher $\tan\beta$ values for large $\cos(\beta - \alpha)$ in the Lepton-specific Model, where the couplings of the Higgs boson to leptons is enhanced as well (cf. Table 1.3). The additional decay mode also compensates for the vanishing $h \rightarrow bb$ branching ratio at low $\tan\beta$ and far away from the alignment limit allowing to close the narrow regions with no exclusion power discussed before; not only in the Lepton-specific, but also in the Flipped Model, since in both models the couplings of the Higgs boson to down-type quarks and leptons are differently modified.

Restricting the comparison to the Run-1 results for the Lepton-specific and Flipped Model to the ones obtained by including only the $\nu b\bar{b}$ and $\ell\ell b\bar{b}$ final states,⁴⁶ reveals that the Run-2 analysis is able to improve the limits in all four models. In the Type-I and the Lepton-specific Model the observed exclusion region is extended towards higher $\tan\beta$ values, despite the rapid decrease of the cross section for A -boson production with increasing $\tan\beta$ values: close to the alignment limit, from about $\tan\beta \approx 6$ to ≈ 9 and $\tan\beta \approx 5$ to ≈ 8 , respectively. The improvements are somewhat stronger for the observed limit than for the expected one, due to a deficit in the data, especially in the 2 b -tags category of the 2-lepton channel, as can be seen from Fig. 5.36(b).

Significant improvements over the Run-1 results are observed in the high- $\tan\beta$ regions for the Type-II and the Flipped Model. Thanks to the inclusion of the analysis regions targeting the b -associated production mode, the allowed space is further restricted to values close to the alignment limit. For example, at $\tan\beta = 10$ the limit of excluded $\cos(\beta - \alpha)$ values is extended from about ± 0.4 to ± 0.2 in the Type-II Model and from ± 0.6 to ± 0.2 in the Flipped Model.

Constraints in the m_A - $\tan\beta$ plane

Figure 5.40 shows for all four 2HDMs the obtained constraints in the m_A - $\tan\beta$ plane for $\cos(\beta - \alpha) = 0.10$. It is particular interesting to study the constraints provided from direct searches at such values close to the alignment limit, given that the current coupling measurements of the observed SM-like Higgs boson to SM particles already exclude most of the parameter space (cf. Fig. 1.1).

At low $\tan\beta$ values, below ≈ 0.4 , and A -boson masses above 350 GeV the relative decay width exceeds 10%, i.e. the level where the exploited smearing method to account for the expected deviation from the zero natural-width assumption in simulation is valid (cf. Sec. 5.3). In those regions, indicated by the grey

⁴⁵The $\tan\beta$ -enhancement of the couplings to down-type quarks in the Type-II and the Flipped Models also results in an increased $h \rightarrow bb$ branching fraction at high $\tan\beta$ values, which compensates the drop in the branching ratio of the $A \rightarrow Zh$ decay (cf. Figs. 1.6(b) and 1.6(d) versus Figs. 1.8(b) and 1.8(d)).

⁴⁶In fact Ref. [344] provides some additional results for the Lepton-specific and Flipped Model on top of what is published in Ref. [283], where only the $\nu b\bar{b}$ and $\ell\ell b\bar{b}$ final states are considered.

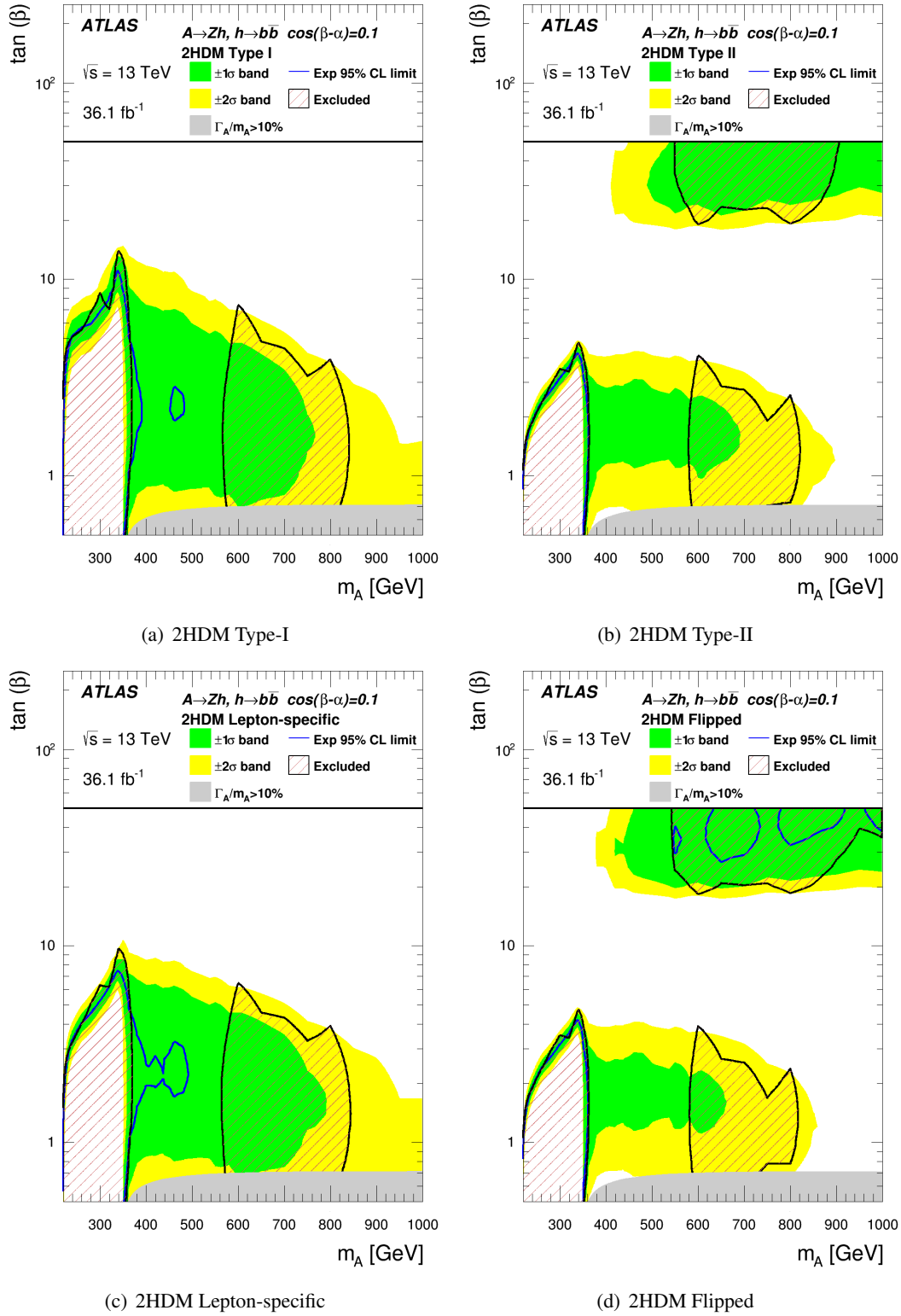


Figure 5.40: Observed and expected exclusion regions at the 95 % CL in the context of the various 2HDM types, namely (a) the Type I, (b) the Type II, (c) the Lepton-specific and (d) the Flipped Model, as function of the model parameters $\tan\beta$ and m_A for $\cos(\beta - \alpha) = 0.1$. In the case of the Type-II and the Flipped models, both gluon-fusion and b -associated production are considered. The variation of the natural width in the parameter space is taken into account up to $\Gamma_A/m_A = 10\%$; regions with larger values are indicated by the grey solid area. Previously published in Ref. [6].

solid areas, the exclusion power is expected to be lower than suggested by the obtained results. While they are therefore disregarded, the regions hardly overlap with those of exclusion power.

The regions with expected exclusion power are mainly at low $\tan\beta$ values and $m_A < 350$ GeV. However, there are also some small “islands” of excluded regions and stretched uncertainty bands, indicating that statistical fluctuations in the data might exclude a larger parameter space than expected, that extend to higher m_A values; also at high $\tan\beta$ values in the Type-II and Flipped Models. The observed exclusion regions deviate slightly from the expectation: (i) for $m_A < 350$ GeV they reach to slightly higher $\tan\beta$ values, (ii) in the Type-I and Lepton-specific Model, there is no exclusion at small $\tan\beta$ values between $m_A = 350 - 580$ GeV, (iii) for $\tan\beta < 10$ there are excluded regions between $m_A = 580 - 850$ GeV and (iv) in the Type-II and Flipped Model, there are excluded regions between $m_A = 550 - 900/1000$ GeV for $\tan\beta \geq 20$; i.e. the observed exclusion regions are generally larger than expected, with the exception of (ii) due to (expected) fluctuations in the data.

As before the exclusion contours can be understood from considering the expected cross sections for A -boson production and branching fractions for the A -boson and Higgs-boson decays as function of the 2HDM parameters.

At small $\tan\beta$ values, the branching ratio for the $A \rightarrow Zh$ decay rises steeply with increasing m_A until it reaches a maximum below $m_A = 350$ GeV, i.e. below the threshold, where the $A \rightarrow t\bar{t}$ decay becomes accessible. It is the dominant decay mode in the Type-I and the Lepton-specific Model and has a sizeable branching fraction in the Type-II and Flipped Model (cf. Fig. 1.7). Consequently, the exclusion regions for the former two models extend to larger values of $\tan\beta$.

After a sharp drop at $m_A = 350$ GeV, the branching fraction of $A \rightarrow Zh$ rises again slowly with increasing m_A , staying the subdominant decay mode after $A \rightarrow t\bar{t}$ (at small $\tan\beta$ values), which explains the observed exclusion regions (iii), i.e. at $m_A = 580 - 850$ GeV and $\tan\beta < 10$. Nonetheless, the exclusion power is reduced towards larger m_A , because of the decrease of the A -boson production cross-sections with increasing resonance mass (cf. Fig. 1.3(a)).

At large values of $\tan\beta$ (≥ 10), the branching ratio of the $A \rightarrow Zh$ decay is even dominant for $m_A \geq 400$ (800) GeV in the Type-I/Lepton-specific Model (Type-II/Flipped Model). However, only for the Type-II and Flipped Model corresponding exclusion regions are observed. The rapid decrease of the generally dominant gluon-fusion production cross-section with increasing $\tan\beta$ values is only compensated by the b -associated production in the models with $\tan\beta$ -enhanced couplings of the A boson to down-type quarks. The remaining lack of exclusion for $m_A \leq 800$ GeV is similarly caused by the $\tan\beta$ -enhancement: the $A \rightarrow bb$ decay clearly dominates (cf. Fig. 1.7).

The excluded regions for A -boson masses above 350 GeV constitute an important improvement over the Run-1 results shown in Figs. 5.3(e)-(h), which were limited to about $m_A < 360$ GeV. Despite significant extension towards higher m_A , the current exclusion is still restricted to a mass range, where the resolved regime dominates. Besides some analysis improvements, such as the optimised event selection in the 2-lepton channel and the inclusion of the regions targeting the b -associated production mode, especially the gain in the production cross-sections due to the increase of the beam energy from $\sqrt{s} = 8$ TeV to 13 TeV is responsible for the extension. With increasing luminosity, the additional acceptance provided by the merged regime will be crucial to further push the limits towards higher masses.

For $m_A < 350$ GeV, the improvements over the Run-1 results are smaller. In the Type-II and the Flipped Model, the excluded parameter space is almost the same; in the Type-I and the Lepton-specific

Model, the limits are only extended towards higher $\tan\beta$ values for $m_A > 300$ GeV: the maximal exclusion is reached at about $m_A = 340$ GeV, where the limits are pushed from $\tan\beta = 8$ to 15 and from $\tan\beta = 6$ to 10, respectively. In this low-mass region (i) the gain in parton luminosity due to the increase of the beam energy hardly benefits the signal cross-section over the main background processes and (ii) the sensitivity is limited by the uncertainties due to the limited size of the simulated background samples (cf. Table 5.10 and Fig. 5.26), which increased tremendously relative to Run 1. It was shown in a projection study, that even when considering about three times more data, the exclusion regions close to the alignment, where these results are determined, do not improve unless the current systematic uncertainties are reduced considerably.

5.8.3 Additional Results and Interpretations

Search for V' Bosons and their HVT Interpretation

Besides the search for $A \rightarrow Zh$, also a search for the presence of new heavy vector bosons, $V' = W', Z'$, with masses between 500 GeV and 5 TeV in their decays $W' \rightarrow Wh$ and $Z' \rightarrow Zh$ is conducted. The general search strategy is very similar to the one for the A boson, each signal hypothesis is fit together with the different background processes to the data, simultaneously in all signal and control regions using a binned profile likelihood approach.

In particular the search for the Z' boson is performed on subset of the discussed 0- and 2-lepton analysis regions (cf. Table 5.7); namely without the regions targeting the b -associated production mode, the 3+ b -tags regions in the resolved regime and the 1+ add. b -tags regions in the merged regime. Relative to the $A \rightarrow Zh$ search, the fit range in the m_{Vh} and $m_{T,Vh}$ distributions is extended to 6 TeV; however, only two to three extra bins are considered in the range beyond what is shown in Figs. 5.35 and 5.36. While also the binning in the rest of the distributions is somewhat adapted to the masses and resolutions of the tested Z' signals, the fit model is otherwise unchanged with respect to what is described in Sec. 5.7.4.

No significant excess over the background expectation is observed. Since only Z' signals with masses $m_{Z'} > 500$ GeV are considered, the region where the excess discussed in the context of the $A \rightarrow Zh$ search is not tested. The obtained expected and observed upper limits at the 95 % CL on the cross section for Z' production times the branching ratios for the $Z' \rightarrow Zh$ decay and the sum of the $h \rightarrow bb$ and $h \rightarrow cc$ decays, which is fixed to the SM expectation of 60.6 % [19], are shown as a function of $m_{Z'}$ in Fig. 5.41(a). It can be seen that Z' bosons with $m_{Z'} < 2.65$ (2.83) TeV are excluded for the HVT benchmark *Model A* (*Model B*) with coupling constant $g_V = 1$ ($g_V = 3$). This constitutes a significant extension of the mass range excluded by the previous search (cf. Sec. 5.2).

The sensitivity to a W' signal is predominantly coming from a 1-lepton channel, targeting the $\ell\nu b\bar{b}$ final state (with $\ell = e, \mu$ as in the 2-lepton channel).⁴⁷ Nonetheless, it is combined with the 0-lepton channel that also shows some acceptance for $W' \rightarrow Wh$ decays. Since in particular events with $W \rightarrow \tau\nu$ decays, where the τ -lepton decays hadronically, pass the 0-lepton selection, the veto on τ_{had} objects of the nominal event selection is dropped for the combination.

As no significant excess over the background expectation is observed, upper limits at the 95 % CL are set on the W' production cross-section times the branching fractions for $W' \rightarrow Wh$ and $h \rightarrow bb + h \rightarrow cc$ as function of $m_{W'}$. W' bosons with $m_{W'} < 2.67$ (2.82) TeV are excluded for the same HVT benchmark

⁴⁷Since this channel is not considered for the $A \rightarrow Zh$ search, it is not discussed in the context of this thesis focusing on the $A \rightarrow Zh$ search; instead the interested reader is referred to Ref. [286] for details.

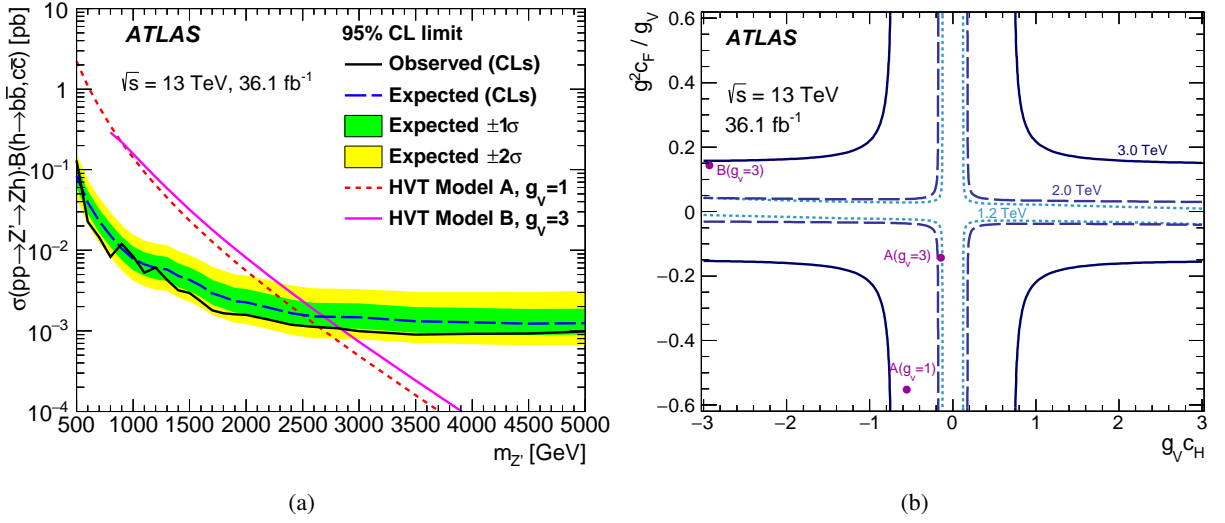


Figure 5.41: (a) Observed and expected upper limits at the 95% CL on the production cross-section for a Z' boson times the branching ratios for $Z' \rightarrow Zh$ and $h \rightarrow bb$ or $h \rightarrow cc$ as function of the resonance mass for the combined 0- and 2-lepton channels. (b) Observed exclusion regions at the 95% CL as function of the HVT parameters $g_V c_H$ and $(g^2/g_V)c_F$ for resonance masses of 1.2 TeV, 2.0 TeV and 3.0 TeV for the combined 0-, 1- and 2-lepton channels, taking into account the branching fractions to Wh and Zh from the HVT model prediction and assuming $m_{W'} = m_{Z'}$; excluded are the areas outside the curves towards increasing parameter values. The parameter values of the benchmark models *Model A* ($g_V = 1$), *Model A* ($g_V = 3$) and *Model B* ($g_V = 3$) are also indicated. Previously published in Ref. [6].

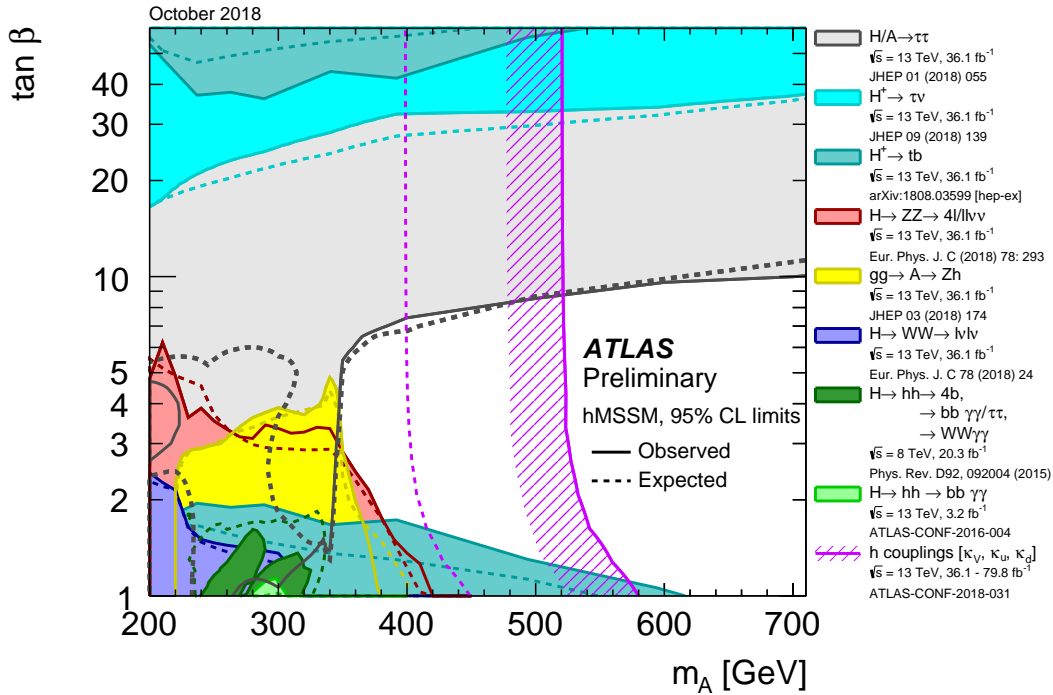
Model A (*Model B*) with $g_V = 1$ ($g_V = 3$), significantly extending the excluded mass range relative to the previous search.

Also the scenario, where $m_{W'} = m_{Z'}$, is tested by combining all three channels and setting limits on the V' production cross-section times the branching fractions for $Z' \rightarrow Zh/W' \rightarrow Wh$ and $h \rightarrow bb + h \rightarrow cc$ as function of $m_{V'}$. This allows to exclude V' bosons with $m_{V'} < 2.8$ (2.93) TeV at the 95% CL for *Model A* (*Model B*) with $g_V = 1$ ($g_V = 3$).

These results are further presented as exclusion contours in the HVT parameter space in Fig. 5.41(b) for three resonance masses, 1.2 TeV, 2.0 TeV and 3.0 TeV; for this, the branching ratios to Zh and Wh from the HVT model prediction are taken into account. The areas outside the curves, towards increasing values of $g_V c_H$ and $(g^2/g_V)c_F$, are excluded. In particular for resonance masses below 2 TeV, the allowed parameter space is strongly restricted to values close to zero. The excluded region is significantly extended relative to the previous result (cf. Sec. 5.2).

hMSSM Interpretation of the $A \rightarrow Zh$ Results

The upper limits obtained on the cross section for A -boson production times the branching ratios for the decays $A \rightarrow Zh$ and $h \rightarrow bb$ are also interpreted in the context of the hMSSM. As mentioned before, as a simplified version of the MSSM, where the lightest CP-even Higgs boson h is identified with the observed Higgs boson, the hMSSM is a concrete realisation of a Type-II 2HDM. In the hMSSM, the Higgs sector is parametrised such that α is not free, but determined by $\tan\beta$ and the masses of the Z and A bosons, i.e. the number of free parameters is reduced with respect to the general Type-II Model. Figure 5.42



(a)

Figure 5.42: Observed and expected exclusion regions at the 95 % CL in the context of the hMSSM model as function of m_A and $\tan\beta$ obtained from several direct searches for heavy Higgs bosons in both 8 TeV and 13 TeV data as well as fits to the measured production and decay rates of the observed Higgs boson using data at $\sqrt{s} = 13$ TeV. Also the results of the $A \rightarrow Zh \rightarrow \ell\ell(\nu\nu)bb$ search presented in this thesis are included. The results are derived following the same approach as for Fig. 5.4 detailed in Ref. [67]. Taken from Ref. [345].

shows the obtained exclusion region in the m_A versus $\tan\beta$ plane, together with results from various other direct searches for heavy Higgs bosons as well as indirect constraints from fits to the measured rates of the production and decay of the observed Higgs boson identified with the light CP-even scalar h .

The excluded region provided by the $A \rightarrow Zh$ search can be compared to the one in the general Type-II Model shown in Fig. 5.40(b). However, while in Fig. 5.40(b) $\cos(\beta - \alpha)$ is fixed to 0.1, in the present plot $\cos(\beta - \alpha)$ varies across the plane according to the hMSSM parametrisation. For $m_A < 400$ GeV, the exclusion regions resemble each other; although at very small values of $\tan\beta$ there are also some differences. At higher masses, $m_A > 550$ GeV, there are no “islands” of exclusion in the hMSSM that are present in the general Type-II. This can be explained by the fact that in the hMSSM, $\cos(\beta - \alpha)$ decreases with increasing m_A , and when the alignment limit is reached, the branching ratio of $A \rightarrow Zh$, and thus the sensitivity of the analysis, vanishes.

The comparison of Fig. 5.42 with the Run-1 version in Fig. 5.4 shows that the parameter space excluded by the present $A \rightarrow Zh$ search is only slightly increased. At low $\tan\beta$, the maximally excluded A -boson mass is shifted from $m_A \approx 360$ GeV to 380 GeV, while it was expected to exclude $m_A < 400$ GeV. For m_A between 220 GeV and 340 GeV, the excluded $\tan\beta$ range is pushed from $\tan\beta \approx 2 - 4$ to $\tan\beta \approx 3 - 5$.

Nonetheless, it is interesting to note that the presented exclusion region overlaps with parameter space excluded by several other searches for additional Higgs bosons, namely for the heavy CP-even scalar H

via the decays into $hh \rightarrow 4b/bb\gamma\gamma/bb\tau\tau/WW\gamma\gamma$ (based on Run-1 data), $hh \rightarrow bb\gamma\gamma$, $ZZ \rightarrow 4\ell/\ell\ell\nu\nu$ and $WW \rightarrow \ell\nu\ell\nu$, for the charged Higgs boson in its decay $H^\pm \rightarrow tb$ as well as for $A/H \rightarrow \tau\tau$. While this indicates the consistency of the results, this also demonstrates the relevance of the $A \rightarrow Zh$ search for exploring the m_A - $\tan\beta$ parameter space also in the hMSSM.

While the recent measurements of the couplings of the observed Higgs boson, identified with the CP-even scalar h , allow to consistently exclude $m_A \lesssim 540$ GeV for any $\tan\beta$ value - also covering an area in the mid- $\tan\beta$ range not excluded by any of the direct searches-, higher masses up to almost 2 (1)TeV are only excluded for $\tan\beta > 10$ (30) by the $A/H \rightarrow \tau\tau$ ($H^\pm \rightarrow \tau\nu$) search. Thus, large parts of the parameter space still need to be explored.

Conclusion

The discovery of a scalar particle in the year 2012 by the ATLAS and CMS collaborations at the Large Hadron Collider (LHC) at CERN, that is compatible with the Higgs boson predicted by the Standard Model (SM) of particle physics, seems to conclude an almost 50 years lasting search for this last missing piece and, as such, constitutes the culmination in the long history of successes of one of the most stringent tested scientific theories. Nonetheless, there is little doubt that the SM is a low-energy limit of a more fundamental theory that ultimately describes Nature: it only incorporates three of the four fundamental forces and it fails to explain various observed phenomena. While many possible candidates for such an ultimate theory have been proposed, experimental indications that either of them is actually realised in Nature are lacking. Probing the predictions of various theories beyond the SM (BSM) is the main goal of the LHC project and in particular of the two multipurpose experiments ATLAS and CMS.

Most BSM models suggest the existence of new heavy resonances that may be produced in the proton-proton (pp) collisions provided by the LHC. The combination of unprecedented centre-of-mass energies and luminosities, reached in particular in Run 2 of the LHC, allowed to extend the mass ranges accessible for searches beyond what was possible before. Identifying new signals from the reconstruction of their decay products over the dominant SM background, requires excellent understanding of the experimental devices as well as the performance of the algorithms exploited to translate the hits in the detector into physics objects. While both have been achieved with impressive precision already after a relatively short time of operation, as clearly demonstrated by the Higgs-boson discovery, the effort continues: as more data is collected the understanding of the detector is constantly improving and the increasing dataset both allows and requires new experimental strategies to be developed.

Since many BSM signatures involve b quarks, the identification of jets likely originating from b quarks by means of b -tagging, constitutes an important tool in many analyses of LHC data. Relying on a number of characteristic properties of the production and the decay of b hadrons, b -tagging algorithms at the ATLAS experiment use information provided by the inner tracking detectors to distinguish b jets from c jets and light jets. In order to exploit the information in physics analyses, not only the efficiency with which a b jet is identified as such, but also the efficiencies of mistakenly identifying c jets and light jets as b jets, need to be measured. The results, typically presented in the form of data-to-simulation scale factors, are then used to correct the corresponding efficiencies in simulations which constitute an important ingredient to physics analyses. In this thesis a novel method to calibrate the b -tagging efficiency for c jets has been presented.

Using data collected with the ATLAS experiment in pp collisions at a centre-of-mass energy of 7 TeV during the 2011 data-taking, the calibration was demonstrated for the MV1 tagging algorithm, the most commonly used b -tagging algorithm in ATLAS analyses in Run 1. It was applied for use in physics analyses for the first time in Run 2. It is based on a sample of c jets that is obtained from events, where a W boson is produced in association with a single c quark. The c jet is identified by a muon stemming

from the semileptonic decay of the c hadron that emerges in the hadronisation of the c quark; the W boson is reconstructed via its decay to an electron and a neutrino. Exploiting the charge correlation of the muon with the electron, the c -jet sample is extracted as the difference between the number of events with opposite-signed and same-signed lepton charges. This strategy has been used previously in several measurements of the $W+c$ production cross-section; also in the latest one, in whose context the calibration was performed. Presenting scale factors for c jets with a muon as ratios relative to the corresponding efficiencies in simulated $W+c$ events, concludes the first step of the calibration.

In a second step, the measured scale factors are extrapolated using a simulation-based and data-supported procedure in order to obtain scale factors appropriate for inclusive samples of c jets, to which they are usually applied. The scale factors obtained with uncertainties between 5 % and 13 %, increasing with the considered c -jet rejection, are systematically below unity. This result implies that the used reference simulation is overestimating the c -jet tagging efficiency relative to the one in the data, in particular for inclusive c -jet samples.

There are three main sources of uncertainties that contribute each by roughly the same amount: the statistical and systematic uncertainties on the measured scale factors for c jets containing a muon, and the systematic uncertainties due to the extrapolation procedure, which is dominated by the limited knowledge of the charged particle multiplicity of (hadronic) c -hadron decays. Thus, the required extrapolation poses quite a limitation of the presented method; one that the calibration method relying on the reconstruction of exclusive D^* decays, which adopted the extrapolation procedure, is afflicted with as well. Nonetheless, the $W+c$ calibration became one of the standard calibration methods used by the ATLAS collaboration in Run 2. It continues to provide an important alternative to the recently established method that measures the c -jet tagging efficiency directly on an inclusive sample of c jets selected in $t\bar{t}$ events.

Experimental evidence that any of the candidates for an ultimate theory, such as *Supersymmetry* or *String Theory*, is realised in Nature is still pending. Thus, one approach to search for BSM physics without having to make assumptions on the details of the underlying theory, is via models that build up on the well-established SM and modify only a particular aspect of it. One such modification that only affects the Higgs sector leads to the class of *Two-Higgs-Doublet Models* (2HDMs).

In the 2HDMs, the Brout-Englert-Higgs mechanism, which results in its simplest implementation to one Higgs boson - as in the SM -, is consistently extended by adding a second scalar isospin doublet. This leads, under the assumption of CP and lepton-flavour conservation, to the prediction of five Higgs bosons and four model types, the Type-I, Type-II, Lepton-specific and Flipped Model, which differ regarding the couplings of the Higgs bosons to the charged SM fermions. One of the Higgs bosons, the light CP-even scalar h , can be identified with the observed Higgs boson with a mass of roughly 125 GeV. While the couplings of the h boson to both fermions and bosons are generally predicted to deviate from the ones of the SM Higgs boson, the degree of the deviation is a priori not known: the modifying factors depend not only on the 2HDM type, but also on two free parameters, α and β . Since the couplings of the observed scalar are found to be in good agreement with the SM expectation, the allowed parameter space is already strongly constrained. However, the limited precision of the measurements of the order of 10 – 20 % still permits modifications of the couplings as suggested by the 2HDMs. Not only measuring the couplings with higher precision can help to elucidate whether the observed Higgs boson is part of an extended scalar sector, also the observation of one of the additional Higgs bosons expected in the 2HDMs would be a clear

indication for this scenario.

In this thesis the latter approach was pursued and a search for the CP-odd pseudoscalar Higgs boson A was presented, based on data collected with the ATLAS experiment from pp collisions at a centre-of-mass energy of 13 TeV in the years 2015 and 2016. Focusing on the A -boson decay into a Z boson and an h boson, the analysis uses the observed SM-like scalar as a probe for BSM physics.

The decay rate of $A \rightarrow Zh$ is large and even dominant for parts of the parameter space; in particular for A -boson masses, $m_A \leq 350$ GeV, i.e. below the threshold, where $A \rightarrow t\bar{t}$ decays become kinematically accessible and dominant. However, the branching ratio for $A \rightarrow Zh$ vanishes in the *alignment limit*, where the h boson becomes indistinguishable from the SM Higgs boson.

The analysis targets Z - and the h -boson decays into pairs of leptons (electrons/muons (ℓ) or neutrinos (ν)) and b quarks, respectively. Similarly to the SM prediction, the h boson at a mass of ~ 125 GeV decays in most of the parameter space predominantly into a pair of b quarks; in the Type-II and the Flipped Model the branching ratio can become especially large due to the $\tan\beta$ -enhanced couplings to down-type quarks. This decay mode allows to fully reconstruct the h -boson decay and to use the reconstructed invariant mass or, in the case of the $Z \rightarrow \nu\bar{\nu}$ decay, the transverse mass of the Zh system to search for A -boson signals with masses between 220 GeV and 2 TeV.

Extending the searched mass range beyond what was done in previous searches, did not only require pp collisions provided by the LHC with unprecedented centre-of-mass energy, but also dedicated reconstruction techniques for *boosted* topologies. With increasing A -boson mass, the Z and h bosons tend to acquire larger transverse momenta and their decay products become collimated. This poses a challenge in particular for the reconstruction of the h -boson candidate: the b quarks become too close to be reconstructed as two individual jets (with small radius), and instead the b -quark pair needs to be captured within one jet (with larger radius). Thus, the reconstruction strategy used for the h -boson candidate changes over the considered m_A range and reflects two kinematic regimes that are referred to as resolved and merged regimes, respectively. In an intermediate mass regime a transition region occurs, where both reconstruction techniques can be efficiently used. However, in order to obtain orthogonal analysis regions, events need to be exclusively assigned to either; priority is given to the resolved regime. In addition, an optimised event selection in the $\ell\bar{\ell}b\bar{b}$ channel accounts for the change in background contribution and composition across the targeted m_A range by using selection criteria that vary as a function of the reconstructed Zh invariant mass.

In both regimes, several analysis categories with varying sensitivities are defined using b -tagging information. While they primarily target the $h \rightarrow b\bar{b}$ decay signature, they are also designed to boost the sensitivity to A -boson production in association with b jets. The latter constitutes an important improvement with respect to previous versions of the analysis. In most of the parameter space of the four considered 2HDMs, the A boson is predominantly produced in gluon fusion via a top-quark loop. However, in the Type-II and the Flipped Model also the b -quark associated production contributes significantly and becomes even the dominant production mode at high $\tan\beta$, due to the enhanced couplings to down-type quarks.

With the aim to test for the presence of an A -boson signal in the invariant and transverse mass distributions of the Zh system, respectively, binned profile likelihood fits to the data are performed simultaneously in 15 signal and control regions. Several signal hypotheses with different masses and admixtures of the gluon-fusion and b -associated production mechanisms are probed. No particularly significant excess of

events over the background expectation is observed in the data. The strongest deviation from the background expectation is found for $m_A = 440$ GeV, corresponding to a local significance of 2.5σ for pure gluon-fusion production and 3.6σ for pure b -associated production. Considering the “look elsewhere” effect, the significance of the latter excess is reduced to a global significance of 2.5σ . Whereas both lepton channels are contributing almost equally to the significance of the excess of events in the case considering pure gluon-fusion production, it is driven by the $\ell\bar{\ell}b\bar{b}$ channel in the case of considering pure b -associated production. This difference can be explained by the different impact of the signal regions with additional b -tagged jets ($3+$ b -tags) for the two production modes: while they are quite sensitive to the b -associated production, they hardly affect the significance of the results for gluon-fusion production. Performed tests were not able to uncover an underlying issues that could explain the excess in data; at the same time, the observed excess seems not particularly compatible with the signal hypothesis, when studying its properties.

Following the publication of the analysis, the CMS collaboration conducted a similar search and presented a preliminary result. It does not confirm the excess, nor finds any other significant deviation from the background-only hypothesis in the searched mass range up to $m_A = 1$ TeV. Nonetheless, since the excess is found in several independent regions and was already visible with reduced significance in the previous version of the analysis (where no regions dedicated to b -associated production were considered), it is certainly worth to study this mass range further with an even larger dataset.

As no significant excess of events in the data is observed relative to the background expectation, upper limits at the 95 % confidence limit (CL) are set on the cross section for A -boson production times the branching ratios for the $A \rightarrow Zh$ and $h \rightarrow b\bar{b}$ decays, as a function of the A -boson mass. The observed upper limits range between $1.9 \cdot 10^{-3}$ pb and $8.1 \cdot 10^{-1}$ pb for pure gluon-fusion production and between $3.4 \cdot 10^{-3}$ pb and $7.3 \cdot 10^{-1}$ pb for pure b -associated production for m_A values between 220 GeV to 2 TeV. Except around the mass, where the discussed excess is located, the observed limits are somewhat stronger than expected, in particular towards higher masses. This corresponds to a deficit in the data relative to the expected background contribution.

The results are interpreted in the context of the four 2HDMs and presented as two-dimensional constraints in the $\tan\beta$ versus $\cos(\beta - \alpha)$ plane for a fixed $m_A = 300$ GeV, and in the m_A versus $\tan\beta$ plane for a fixed $\cos(\beta - \alpha) = 0.1$, i.e. close to the alignment limit. The efficiencies and the predicted cross-section ratios for the gluon-fusion and b -associated production are taken into account, as well as that the width of the A boson may take values larger than the experimental mass resolution. Compared to previous results, the limits are improved most notably (i) at high $\tan\beta$ values ($\tan\beta \gtrsim 4$) in the Type-II and the Flipped Models, thanks to the consideration of the regions with additional b -tagged jets, and (ii) for masses above the $t\bar{t}$ threshold. However, all limits are improved for $m_A \gtrsim 280$ GeV: below the $t\bar{t}$ threshold, $\cos(\beta - \alpha)$ values down to a few percent are excluded for $\tan\beta$ values up to 5-18, depending on the model type; the maximally excluded values are reached in any of the four models just below $m_A = 350$ GeV. Focusing at low- $\cos(\beta - \alpha)$ values and $m_A < 350$ GeV, the analysis is most sensitive to the Type-I model and excludes most of the parameter space that was still allowed by the coupling measurements of the observed Higgs boson performed in Run 1. However, values close to the alignment limit are still possible, leaving room for small deviations from the SM expectation.

While a future $A \rightarrow Zh$ search can still profit from the analysis of an even larger dataset for $m_A \gtrsim 300$ GeV, for masses below, it is already in its current version limited by systematic uncertainties. At such low masses, improving over the Run-1 limits requires in particular a reduction of the statistical uncertainty

due to the limited sizes of the simulated background samples. The next-leading systematic uncertainty related to the b -tagging of b jets has already been reduced significantly after the publication of this result.

A subset of the discussed analysis regions, namely without the regions targeting the b -associated production mode, was also used to conduct a search for a new, heavy vector boson Z' in its decay $Z' \rightarrow Zh$ in a mass range between 500 GeV and 5 TeV; and by combining the $\nu\bar{\nu}b\bar{b}$ channel with an additional channel targeting the $\ell\bar{\nu}b\bar{b}$ final state also for a W' boson in its decay $W' \rightarrow Wh$.

Since, no significant excess of events is observed in the data compared to the background expectation,⁴⁸ upper limits at the 95 % CL are set on the Z' (W') production cross-section times the branching ratios for the decays $Z' \rightarrow Zh$ ($W' \rightarrow Wh$) and $h \rightarrow b\bar{b}/c\bar{c}$, as a function of the resonance mass. Interpreting the results in the context of different benchmark models, allows to exclude Z' and W' bosons with $m_{Z'/W'} < 2.65 - 2.83$ TeV. The limits are slightly improved, by combining all the three lepton channels under the assumption that the new vector bosons are degenerate in mass: Z' and W' bosons with $m_{Z'} = m_{W'} < 2.8 - 2.93$ TeV are excluded at the 95 % CL for the same models. These results constitute a significant extension of the mass range excluded by previous searches. The combined results are further presented as two-dimensional exclusion regions in the parameter space of a simplified model. In particular for masses below 3 TeV, the allowed parameter space is strongly constrained.

The upper limits obtained on the cross section for A -boson production times the branching ratios for the decays $A \rightarrow Zh$ and $h \rightarrow b\bar{b}$ are also interpreted in the context of the hMSSM. As a simplified version of the Minimal Supersymmetric Standard Model (MSSM), where the lightest CP-even Higgs boson h is identified with the observed Higgs boson, it is a concrete realisation of a Type-II 2HDM. Its Higgs sector can be described by only two free parameters, $\tan\beta$ and m_A ; i.e. with respect to the general Type-II 2HDM the parameter α is not a free parameter, but determined by $\tan\beta$ and the masses of the Z and A bosons. For small A -boson masses the obtained exclusion region in the $\tan\beta$ - m_A plane resembles highly the one obtained for the Type-II 2HDM; however, there is no exclusion power at large A -boson masses (and high $\tan\beta$ values). This is because with increasing A -boson mass, α moves closer to the alignment limit, where the branching ratio for $A \rightarrow Zh$ vanishes. Relative to previous versions of the analysis the observed (expected) exclusion region is extended towards higher masses, up to $m_A \approx 380$ (400) GeV, and for $m_A > 260$ GeV towards higher $\tan\beta$, excluding values up to $\tan\beta \approx 5$. The presented exclusion region overlaps with the exclusion limits provided by several other searches for additional Higgs bosons, namely for the heavy CP-even scalar H via its decays $H \rightarrow hh/ZZ/W^+W^-$, in several final states, and $A/H \rightarrow \tau^+\tau^-$, as well as for the charged Higgs boson in $H^\pm \rightarrow tb$,⁴⁹ and by recent measurements of the couplings of the observed Higgs boson. Besides indicating the consistency of the results, this furthermore shows the relevance of the $A \rightarrow Zh$ search for exploring the m_A - $\tan\beta$ parameter space also in the hMSSM.

Although in various BSM models the excluded parameter space is constantly growing and no signs of new physics have been found so far, there is still room for small deviations from the SM. Many BSM searches mainly focusing on the high(er)-mass regime, such as the described one, can still profit from an increased dataset that is already available at the time of writing. At the end of the year 2018, the end

⁴⁸Since the search focuses on $m_{Z'} > 500$ GeV, the $m_{\nu h}$ range, where the excess discussed in the context of the $A \rightarrow Zh$ search is observed, is not tested.

⁴⁹Where $H^\pm \rightarrow tb$ stands for $H^+ \rightarrow t\bar{b}$ and $H^- \rightarrow \bar{t}b$.

of Run 2, the dataset is about a factor of four larger than what was analysed in the presented search. Also, future searches can benefit from the increased experience with boosted topologies gained during Run 2: several new reconstruction techniques are now available that promise significant improvements in particular in the TeV regime. Searches targeting (very) low-mass resonances start to be limited by systematic uncertainties and significant improvements become harder to achieve. They begin to share challenges with SM precision measurements that increasingly regain attention given that deviations from the SM are progressively confirmed to be small.

Bibliography

- [1] ATLAS Collaboration. “Measurement of the production of a W boson in association with a charm quark in pp collisions at $\sqrt{s} = 7$ TeV with the ATLAS detector”. In: *JHEP* 05 (2014), p. 068. doi: [10.1007/JHEP05\(2014\)068](https://doi.org/10.1007/JHEP05(2014)068). arXiv: [1402.6263](https://arxiv.org/abs/1402.6263) [[hep-ex](#)].
- [2] H. Arnold. “Messung des Wirkungsquerschnitts der assoziierten Produktion eines W-Bosons mit einem charm-Jet am ATLAS Experiment”. Diploma Thesis. Albert-Ludwigs-Universität Freiburg, 2012.
- [3] ATLAS Collaboration. *Calibration of the b -tagging efficiency for c jets with the ATLAS detector using events with a W boson produced in association with a single c quark*. ATLAS-CONF-2013-109. 2013.
- [4] ATLAS Collaboration. “Performance of b -jet identification in the ATLAS experiment”. In: *JINST* 11 (2016), P04008. doi: [10.1088/1748-0221/11/04/P04008](https://doi.org/10.1088/1748-0221/11/04/P04008). arXiv: [1512.01094](https://arxiv.org/abs/1512.01094) [[hep-ex](#)].
- [5] ATLAS Collaboration. *Search for a CP-odd Higgs boson decaying to Zh in pp collisions at $\sqrt{s} = 13$ TeV with the ATLAS detector*. ATLAS-CONF-2016-015. 2016.
- [6] ATLAS Collaboration. “Search for heavy resonances decaying into a W or Z boson and a Higgs boson in final states with leptons and b -jets in 36 fb^{-1} of $\sqrt{s} = 13$ TeV pp collisions with the ATLAS detector”. In: *JHEP* 03 (2018), p. 174. doi: [10.1007/JHEP03\(2018\)174](https://doi.org/10.1007/JHEP03(2018)174). arXiv: [1712.06518](https://arxiv.org/abs/1712.06518) [[hep-ex](#)]. Erratum: *JHEP* 11 (2018) 051.
- [7] ATLAS Collaboration. “Observation of a new particle in the search for the Standard Model Higgs boson with the ATLAS detector at the LHC”. In: *Phys. Lett. B* 716 (2012), p. 1. doi: [10.1016/j.physletb.2012.08.020](https://doi.org/10.1016/j.physletb.2012.08.020). arXiv: [1207.7214](https://arxiv.org/abs/1207.7214) [[hep-ex](#)].
- [8] CMS Collaboration. “Observation of a new boson at a mass of 125 GeV with the CMS experiment at the LHC”. In: *Phys. Lett. B* 716 (2012), p. 30. doi: [10.1016/j.physletb.2012.08.021](https://doi.org/10.1016/j.physletb.2012.08.021). arXiv: [1207.7235](https://arxiv.org/abs/1207.7235) [[hep-ex](#)].
- [9] A. D. Sakharov. “Violation of CP in variance, C asymmetry, and baryon asymmetry of the universe”. In: *Phys.-Uspekhi* 34.5 (1991), pp. 392–393. doi: [10.1070/PU1991v034n05ABEH002497](https://doi.org/10.1070/PU1991v034n05ABEH002497).
- [10] Planck Collaboration. “Planck 2013 results. XVI. Cosmological parameters”. In: *Astronomy & Astrophysics* 571 (2014), A16. doi: [10.1051/0004-6361/201321591](https://doi.org/10.1051/0004-6361/201321591). arXiv: [1303.5076](https://arxiv.org/abs/1303.5076) [[astro-ph.CO](#)].
- [11] Super-Kamiokande Collaboration. “Evidence for Oscillation of Atmospheric Neutrinos”. In: *Phys. Rev. Lett.* 81.8 (1998), pp. 1562–1567. doi: [10.1103/PhysRevLett.81.1562](https://doi.org/10.1103/PhysRevLett.81.1562). arXiv: [hep-ex/9807003](https://arxiv.org/abs/hep-ex/9807003) [[hep-ex](#)].

- [12] SNO Collaboration. “Direct Evidence for Neutrino Flavor Transformation from Neutral-Current Interactions in the Sudbury Neutrino Observatory”. In: *Phys. Rev. Lett.* 89.1 (2002), p. 011301. doi: [10.1103/PhysRevLett.89.011301](https://doi.org/10.1103/PhysRevLett.89.011301).
- [13] F. Halzen and A. D. Martin. *Quarks and Leptons: An Introductory Course in Modern Particle Physics*. New York, USA: Wiley, 1984.
- [14] D. Griffiths. *Introduction to Elementary Particles*. Ed. by D. Griffiths. 2nd, revis. Weinheim, Germany: Wiley-VCH Verlag GmbH, 1987. doi: [10.1002/9783527618460](https://doi.org/10.1002/9783527618460).
- [15] S. Dittmaier and M. Schumacher. “The Higgs boson in the standard model - From LEP to LHC: Expectations, searches, and discovery of a candidate”. In: *Prog. Part. Nucl. Phys.* Vol. 70. 2013, pp. 1–54. doi: [10.1016/j.pnpnp.2013.02.001](https://doi.org/10.1016/j.pnpnp.2013.02.001). arXiv: [1211.4828](https://arxiv.org/abs/1211.4828) [hep-ph].
- [16] G. C. Branco et al. “Theory and phenomenology of two-Higgs-doublet models”. In: *Phys. Rep.* 516.1-2 (2012), pp. 1–102. doi: [10.1016/j.physrep.2012.02.002](https://doi.org/10.1016/j.physrep.2012.02.002). arXiv: [1106.0034](https://arxiv.org/abs/1106.0034) [hep-ph].
- [17] L. Altenkamp. “Precise Predictions within the Two-Higgs-Doublet Model”. PhD Thesis. Albert-Ludwigs-Universität Freiburg, 2017.
- [18] A. Djouadi. “The anatomy of electroweak symmetry breaking: Tome I: The Higgs boson in the Standard Model”. In: *Phys. Rep.* 457.1-4 (2008), pp. 1–216. doi: [10.1016/j.physrep.2007.10.004](https://doi.org/10.1016/j.physrep.2007.10.004). arXiv: [hep-ph/0503172](https://arxiv.org/abs/hep-ph/0503172) [hep-ph].
- [19] LHC Higgs Cross Section Working Group. *Handbook of LHC Higgs Cross Sections: 3. Higgs Properties*. CERN-2013-004. 2013. doi: [10.5170/CERN-2013-004](https://doi.org/10.5170/CERN-2013-004). arXiv: [1307.1347](https://arxiv.org/abs/1307.1347) [hep-ph].
- [20] P. Skands. *QCD for Collider Physics*. ESHEP Proceedings. 2011, pp. 1–48. arXiv: [1104.2863](https://arxiv.org/abs/1104.2863) [hep-ph].
- [21] A. Buckley et al. “General-purpose event generators for LHC physics”. In: *Phys. Rep.* 504.5 (2011), pp. 145–233. doi: [10.1016/j.physrep.2011.03.005](https://doi.org/10.1016/j.physrep.2011.03.005). arXiv: [1101.2599](https://arxiv.org/abs/1101.2599) [hep-ph].
- [22] T. Sjöstrand, S. Mrenna, and P. Skands. “PYTHIA 6.4 physics and manual”. In: *JHEP* 2006.05 (2006), pp. 026–026. doi: [10.1088/1126-6708/2006/05/026](https://doi.org/10.1088/1126-6708/2006/05/026). arXiv: [hep-ph/0603175](https://arxiv.org/abs/hep-ph/0603175) [hep-ph].
- [23] J. M. Campbell, J. W. Huston, and W. J. Stirling. “Hard Interactions of Quarks and Gluons: a Primer for LHC Physics”. In: *Rep. Prog. Phys.* 70.1 (2006), pp. 89–193. doi: [10.1088/0034-4885/70/1/R02](https://doi.org/10.1088/0034-4885/70/1/R02). arXiv: [hep-ph/0611148](https://arxiv.org/abs/hep-ph/0611148) [hep-ph].
- [24] G. P. Salam. “Elements of QCD for hadron colliders”. In: *ESHEP Proceedings*. 2010. arXiv: [1011.5131](https://arxiv.org/abs/1011.5131) [hep-ph].
- [25] G. 't Hooft and M. Veltman. “Regularization and renormalization of gauge fields”. In: *Nucl. Phys. B* 44.1 (1972), pp. 189–213. doi: [10.1016/0550-3213\(72\)90279-9](https://doi.org/10.1016/0550-3213(72)90279-9).
- [26] B. W. Lee and J. Zinn-Justin. “Spontaneously Broken Gauge Symmetries. I. Preliminaries”. In: *Phys. Rev. D* 5.12 (1972), pp. 3121–3137. doi: [10.1103/PhysRevD.5.3121](https://doi.org/10.1103/PhysRevD.5.3121).
- [27] B. W. Lee and J. Zinn-Justin. “Spontaneously Broken Gauge Symmetries. II. Perturbation Theory and Renormalization”. In: *Phys. Rev. D* 5.12 (1972), pp. 3137–3155. doi: [10.1103/PhysRevD.5.3137](https://doi.org/10.1103/PhysRevD.5.3137).

- [28] B. W. Lee and J. Zinn-Justin. “Spontaneously Broken Gauge Symmetries. IV. General Gauge Formulation”. In: *Phys. Rev. D* 7.4 (1973), pp. 1049–1056. doi: [10.1103/PhysRevD.7.1049](https://doi.org/10.1103/PhysRevD.7.1049).
- [29] H. Fritzsch, M. Gell-Mann, and H. Leutwyler. “Advantages of the color octet gluon picture”. In: *Phys. Lett. B* 47.4 (1973), pp. 365–368. doi: [10.1016/0370-2693\(73\)90625-4](https://doi.org/10.1016/0370-2693(73)90625-4).
- [30] D. J. Gross and F. Wilczek. “Ultraviolet Behavior of Non-Abelian Gauge Theories”. In: *Phys. Rev. Lett.* 30.26 (1973), pp. 1343–1346. doi: [10.1103/PhysRevLett.30.1343](https://doi.org/10.1103/PhysRevLett.30.1343).
- [31] H. D. Politzer. “Reliable Perturbative Results for Strong Interactions?” In: *Phys. Rev. Lett.* 30.26 (1973), pp. 1346–1349. doi: [10.1103/PhysRevLett.30.1346](https://doi.org/10.1103/PhysRevLett.30.1346).
- [32] S. L. Glashow. “Partial-symmetries of weak interactions”. In: *Nucl. Phys.* 22.4 (1961), pp. 579–588. doi: [10.1016/0029-5582\(61\)90469-2](https://doi.org/10.1016/0029-5582(61)90469-2).
- [33] A. Salam and J. Ward. “Electromagnetic and weak interactions”. In: *Phys. Lett.* 13.2 (1964), pp. 168–171. doi: [10.1016/0031-9163\(64\)90711-5](https://doi.org/10.1016/0031-9163(64)90711-5).
- [34] S. Weinberg. “A Model of Leptons”. In: *Phys. Rev. Lett.* 19.21 (1967), pp. 1264–1266. doi: [10.1103/PhysRevLett.19.1264](https://doi.org/10.1103/PhysRevLett.19.1264).
- [35] T. Nakano and K. Nishijima. “Charge Independence for V -particles”. In: *Prog. Theor. Phys.* 10.5 (1953), pp. 581–582. doi: [10.1143/PTP.10.581](https://doi.org/10.1143/PTP.10.581).
- [36] M. Gell-Mann. “The interpretation of the new particles as displaced charge multiplets”. In: *Il Nuovo Cimento* 4.S2 (1956), pp. 848–866. doi: [10.1007/BF02748000](https://doi.org/10.1007/BF02748000).
- [37] M. Kobayashi and T. Maskawa. “CP-Violation in the Renormalizable Theory of Weak Interaction”. In: *Prog. Theor. Phys.* 49.2 (1973), pp. 652–657. doi: [10.1143/PTP.49.652](https://doi.org/10.1143/PTP.49.652).
- [38] N. Cabibbo. “Unitary Symmetry and Leptonic Decays”. In: *Phys. Rev. Lett.* 10.12 (1963), pp. 531–533. doi: [10.1103/PhysRevLett.10.531](https://doi.org/10.1103/PhysRevLett.10.531).
- [39] P. W. Higgs. “Broken Symmetries and the Masses of Gauge Bosons”. In: *Phys. Rev. Lett.* 13.16 (1964), pp. 508–509. doi: [10.1103/PhysRevLett.13.508](https://doi.org/10.1103/PhysRevLett.13.508).
- [40] G. S. Guralnik, C. R. Hagen, and T. W. B. Kibble. “Global Conservation Laws and Massless Particles”. In: *Phys. Rev. Lett.* 13.20 (1964), pp. 585–587. doi: [10.1103/PhysRevLett.13.585](https://doi.org/10.1103/PhysRevLett.13.585).
- [41] F. Englert and R. Brout. “Broken Symmetry and the Mass of Gauge Vector Mesons”. In: *Phys. Rev. Lett.* 13.9 (1964), pp. 321–323. doi: [10.1103/PhysRevLett.13.321](https://doi.org/10.1103/PhysRevLett.13.321).
- [42] Y. Nambu. “Axial Vector Current Conservation in Weak Interactions”. In: *Phys. Rev. Lett.* 4.7 (1960), pp. 380–382. doi: [10.1103/PhysRevLett.4.380](https://doi.org/10.1103/PhysRevLett.4.380).
- [43] J. Goldstone. “Field theories with « Superconductor » solutions”. In: *Il Nuovo Cimento* 19.1 (1961), pp. 154–164. doi: [10.1007/BF02812722](https://doi.org/10.1007/BF02812722).
- [44] J. Goldstone, A. Salam, and S. Weinberg. “Broken Symmetries”. In: *Phys. Rev.* 127.3 (1962), pp. 965–970. doi: [10.1103/PhysRev.127.965](https://doi.org/10.1103/PhysRev.127.965).
- [45] Particle Data Group. “Review of Particle Physics”. In: *Phys. Rev. D* 98 (2018), p. 030001. doi: [10.1103/PhysRevD.98.030001](https://doi.org/10.1103/PhysRevD.98.030001).
- [46] D. Ross and M. Veltman. “Neutral currents and the Higgs mechanism”. In: *Nucl. Phys. B* 95.1 (1975), pp. 135–147. doi: [10.1016/0550-3213\(75\)90485-X](https://doi.org/10.1016/0550-3213(75)90485-X).

- [47] P. Sikivie et al. “Isospin breaking in technicolor models”. In: *Nucl. Phys. B* 173.2 (1980), pp. 189–207. doi: [10.1016/0550-3213\(80\)90214-X](https://doi.org/10.1016/0550-3213(80)90214-X).
- [48] P. Langacker. “Grand unified theories and proton decay”. In: *Phys. Rep.* 72.4 (1981), pp. 185–385. doi: [10.1016/0370-1573\(81\)90059-4](https://doi.org/10.1016/0370-1573(81)90059-4).
- [49] T. D. Lee. “A Theory of Spontaneous \mathcal{T} Violation”. In: *Phys. Rev. D* 8.4 (1973), pp. 1226–1239. doi: [10.1103/PhysRevD.8.1226](https://doi.org/10.1103/PhysRevD.8.1226).
- [50] S. P. Martin. “A Supersymmetry Primer”. In: 1998, pp. 1–98. doi: [10.1142/9789812839657_0001](https://doi.org/10.1142/9789812839657_0001). arXiv: [hep-ph/9709356](https://arxiv.org/abs/hep-ph/9709356) [[hep-ph](#)].
- [51] R. D. Peccei and H. R. Quinn. “CP Conservation in the Presence of Pseudoparticles”. In: *Phys. Rev. Lett.* 38.25 (1977), pp. 1440–1443. doi: [10.1103/PhysRevLett.38.1440](https://doi.org/10.1103/PhysRevLett.38.1440).
- [52] R. D. Peccei and H. R. Quinn. “Constraints imposed by CP conservation in the presence of pseudoparticles”. In: *Phys. Rev. D* 16.6 (1977), pp. 1791–1797. doi: [10.1103/PhysRevD.16.1791](https://doi.org/10.1103/PhysRevD.16.1791).
- [53] J. F. Gunion and H. E. Haber. “Conditions for CP violation in the general two-Higgs-doublet model”. In: *Phys. Rev. D* 72.9 (2005), p. 095002. doi: [10.1103/PhysRevD.72.095002](https://doi.org/10.1103/PhysRevD.72.095002). arXiv: [hep-ph/0506227](https://arxiv.org/abs/hep-ph/0506227) [[hep-ph](#)].
- [54] J. F. Gunion and H. E. Haber. “CP -conserving two-Higgs-doublet model: The approach to the decoupling limit”. In: *Phys. Rev. D* 67.7 (2003), p. 075019. doi: [10.1103/PhysRevD.67.075019](https://doi.org/10.1103/PhysRevD.67.075019). arXiv: [hep-ph/0207010](https://arxiv.org/abs/hep-ph/0207010) [[hep-ph](#)].
- [55] M. Carena et al. “Impersonating the Standard Model Higgs boson: Alignment without decoupling”. In: *JHEP* 04 (2014), p. 015. doi: [10.1007/JHEP04\(2014\)015](https://doi.org/10.1007/JHEP04(2014)015). arXiv: [1310.2248](https://arxiv.org/abs/1310.2248) [[hep-ph](#)].
- [56] E. A. Paschos. “Diagonal neutral currents”. In: *Phys. Rev. D* 15.7 (1977), pp. 1966–1972. doi: [10.1103/PhysRevD.15.1966](https://doi.org/10.1103/PhysRevD.15.1966).
- [57] S. L. Glashow and S. Weinberg. “Natural conservation laws for neutral currents”. In: *Phys. Rev. D* 15.7 (1977), pp. 1958–1965. doi: [10.1103/PhysRevD.15.1958](https://doi.org/10.1103/PhysRevD.15.1958).
- [58] M. Aoki et al. “Models of Yukawa interaction in the two Higgs doublet model, and their collider phenomenology”. In: *Phys. Rev. D* 80.1 (2009). doi: [10.1103/PhysRevD.80.015017](https://doi.org/10.1103/PhysRevD.80.015017). arXiv: [0902.4665](https://arxiv.org/abs/0902.4665) [[hep-ph](#)].
- [59] ATLAS Collaboration. “Measurement of the Higgs boson mass from the $H \rightarrow \gamma\gamma$ and $H \rightarrow ZZ^* \rightarrow 4\ell$ channels in pp collisions at center-of-mass energies of 7 and 8 TeV with the ATLAS detector”. In: *Phys. Rev. D* 90 (2014), p. 052004. doi: [10.1103/PhysRevD.90.052004](https://doi.org/10.1103/PhysRevD.90.052004). arXiv: [1406.3827](https://arxiv.org/abs/1406.3827) [[hep-ex](#)].
- [60] CMS Collaboration. “Precise determination of the mass of the Higgs boson and tests of compatibility of its couplings with the standard model predictions using proton collisions at 7 and 8 TeV”. In: *Eur. Phys. J. C* 75 (2015), p. 212. doi: [10.1140/epjc/s10052-015-3351-7](https://doi.org/10.1140/epjc/s10052-015-3351-7). arXiv: [1412.8662](https://arxiv.org/abs/1412.8662) [[hep-ex](#)].
- [61] ATLAS and CMS Collaborations. “Combined Measurement of the Higgs Boson Mass in pp Collisions at $\sqrt{s} = 7$ and 8 TeV with the ATLAS and CMS Experiments”. In: *Phys. Rev. Lett.* 114 (2015), p. 191803. doi: [10.1103/PhysRevLett.114.191803](https://doi.org/10.1103/PhysRevLett.114.191803). arXiv: [1503.07589](https://arxiv.org/abs/1503.07589) [[hep-ex](#)].

- [62] ATLAS Collaboration. “Evidence for the spin-0 nature of the Higgs boson using ATLAS data”. In: *Phys. Lett. B* 726 (2013), p. 120. doi: [10.1016/j.physletb.2013.08.026](https://doi.org/10.1016/j.physletb.2013.08.026). arXiv: [1307.1432](https://arxiv.org/abs/1307.1432) [hep-ex].
- [63] CMS Collaboration. “Study of the Mass and Spin-Parity of the Higgs Boson Candidate Via Its Decays to Z Boson Pairs”. In: *Phys. Rev. Lett.* 110 (2013), p. 081803. doi: [10.1103/PhysRevLett.110.081803](https://doi.org/10.1103/PhysRevLett.110.081803). arXiv: [1212.6639](https://arxiv.org/abs/1212.6639) [hep-ex].
- [64] ATLAS Collaboration. “Study of the spin and parity of the Higgs boson in diboson decays with the ATLAS detector”. In: *Eur. Phys. J. C* 75 (2015), p. 476. doi: [10.1140/epjc/s10052-015-3685-1](https://doi.org/10.1140/epjc/s10052-015-3685-1). arXiv: [1506.05669](https://arxiv.org/abs/1506.05669) [hep-ex].
- [65] ATLAS Collaboration. “Measurements of the Higgs boson production and decay rates and coupling strengths using pp collision data at $\sqrt{s} = 7$ and 8 TeV in the ATLAS experiment”. In: *Eur. Phys. J. C* 76 (2016), p. 6. doi: [10.1140/epjc/s10052-015-3769-y](https://doi.org/10.1140/epjc/s10052-015-3769-y). arXiv: [1507.04548](https://arxiv.org/abs/1507.04548) [hep-ex].
- [66] ATLAS and CMS Collaborations. “Measurements of the Higgs boson production and decay rates and constraints on its couplings from a combined ATLAS and CMS analysis of the LHC pp collision data at $\sqrt{s} = 7$ and 8 TeV”. In: *JHEP* 08 (2016), p. 045. doi: [10.1007/JHEP08\(2016\)045](https://doi.org/10.1007/JHEP08(2016)045). arXiv: [1606.02266](https://arxiv.org/abs/1606.02266) [hep-ex].
- [67] ATLAS Collaboration. “Constraints on new phenomena via Higgs boson couplings and invisible decays with the ATLAS detector”. In: *JHEP* 11 (2015), p. 206. doi: [10.1007/JHEP11\(2015\)206](https://doi.org/10.1007/JHEP11(2015)206). arXiv: [1509.00672](https://arxiv.org/abs/1509.00672) [hep-ex].
- [68] D. Kominis. “The Phenomenology of the CP-odd Scalar of Two-Doublet Models”. In: (1994). doi: [10.1016/0550-3213\(94\)90641-6](https://doi.org/10.1016/0550-3213(94)90641-6). arXiv: [hep-ph/9402339](https://arxiv.org/abs/hep-ph/9402339) [hep-ph].
- [69] N. Craig, J. Galloway, and S. Thomas. *Searching for Signs of the Second Higgs Doublet*. 2013, p. 48. arXiv: [1305.2424](https://arxiv.org/abs/1305.2424) [hep-ph].
- [70] LHC Higgs Cross Section Working Group. *Handbook of LHC Higgs Cross Sections: 4. Deciphering the Nature of the Higgs Sector*. CYRM-2017-002. 2016. doi: [10.23731/CYRM-2017-002](https://doi.org/10.23731/CYRM-2017-002). arXiv: [1610.07922](https://arxiv.org/abs/1610.07922) [hep-ph].
- [71] R. V. Harlander, S. Liebler, and H. Mantler. “SusHi: A program for the calculation of Higgs production in gluon fusion and bottom-quark annihilation in the Standard Model and the MSSM”. In: *Comput. Phys. Commun.* 184.6 (2013), pp. 1605–1617. doi: [10.1016/j.cpc.2013.02.006](https://doi.org/10.1016/j.cpc.2013.02.006). arXiv: [1212.3249](https://arxiv.org/abs/1212.3249) [hep-ph].
- [72] R. V. Harlander and P. Kant. “Higgs production and decay: analytic results at next-to-leading order QCD”. In: *JHEP* 12 (2005), pp. 015–015. doi: [10.1088/1126-6708/2005/12/015](https://doi.org/10.1088/1126-6708/2005/12/015). arXiv: [hep-ph/0509189](https://arxiv.org/abs/hep-ph/0509189) [hep-ph].
- [73] R. V. Harlander and W. B. Kilgore. “Higgs boson production in bottom quark fusion at next-to-next-to-leading order”. In: *Phys. Rev. D* 68.1 (2003), p. 013001. doi: [10.1103/PhysRevD.68.013001](https://doi.org/10.1103/PhysRevD.68.013001). arXiv: [hep-ph/0304035](https://arxiv.org/abs/hep-ph/0304035) [hep-ph].
- [74] R. V. Harlander and W. B. Kilgore. “Next-to-next-to-leading order Higgs production at Hadron colliders”. In: *Phys. Rev. Lett.* 88.20 (2002), p. 2018011. doi: [10.1103/PhysRevLett.88.201801](https://doi.org/10.1103/PhysRevLett.88.201801). arXiv: [hep-ph/0201206](https://arxiv.org/abs/hep-ph/0201206) [hep-ph].

- [75] H. M. Georgi et al. “Higgs Bosons from Two-Gluon Annihilation in Proton-Proton Collisions”. In: *Phys. Rev. Lett.* 40.11 (1978), pp. 692–694. doi: [10.1103/PhysRevLett.40.692](https://doi.org/10.1103/PhysRevLett.40.692).
- [76] F. Wilczek. “Decays of Heavy Vector Mesons into Higgs Particles”. In: *Phys. Rev. Lett.* 39.21 (1977), pp. 1304–1306. doi: [10.1103/PhysRevLett.39.1304](https://doi.org/10.1103/PhysRevLett.39.1304).
- [77] ATLAS Collaboration. “Search for charged Higgs bosons in the $H^\pm \rightarrow tb$ decay channel in pp collisions at $\sqrt{s} = 8$ TeV using the ATLAS detector”. In: *JHEP* 03 (2016), p. 127. doi: [10.1007/JHEP03\(2016\)127](https://doi.org/10.1007/JHEP03(2016)127). arXiv: [1512.03704 \[hep-ex\]](https://arxiv.org/abs/1512.03704).
- [78] D. Eriksson, J. Rathsman, and O. Stål. “2HDMC - Two-Higgs-Doublet Model Calculator”. In: *Comput. Phys. Commun.* 181 (2010), p. 189. doi: [10.1016/j.cpc.2009.09.011](https://doi.org/10.1016/j.cpc.2009.09.011). arXiv: [0902.0851 \[hep-ph\]](https://arxiv.org/abs/0902.0851).
- [79] H. E. Haber and O. Stål. “New LHC benchmarks for the CP-conserving two-Higgs-doublet model”. In: *Eur. Phys. J. C* 75.10 (2015), p. 491. doi: [10.1140/epjc/s10052-015-3697-x](https://doi.org/10.1140/epjc/s10052-015-3697-x). arXiv: [1507.04281 \[hep-ph\]](https://arxiv.org/abs/1507.04281).
- [80] A. A. Bhatti and D. Lincoln. “Jet Physics at the Tevatron”. In: *Ann. Rev. Nucl. Part. Sci.* 60.1 (2010), pp. 267–297. doi: [10.1146/annurev.nucl.012809.104430](https://doi.org/10.1146/annurev.nucl.012809.104430). arXiv: [1002.1708 \[hep-ex\]](https://arxiv.org/abs/1002.1708).
- [81] G. Dissertori. “The Determination of the Strong Coupling Constant”. In: *A contribution to: The Standard Theory up to the Higgs discovery - 60 years of CERN*. 2015. doi: [10.1142/9789814733519_0006](https://doi.org/10.1142/9789814733519_0006). arXiv: [1506.05407 \[hep-ex\]](https://arxiv.org/abs/1506.05407).
- [82] D. J. Gross and F. Wilczek. “Ultraviolet Behavior of Non-Abelian Gauge Theories”. In: *Phys. Rev. Lett.* 30.26 (1973), pp. 1343–1346. doi: [10.1103/PhysRevLett.30.1343](https://doi.org/10.1103/PhysRevLett.30.1343). arXiv: [arXiv: 1011.1669v3](https://arxiv.org/abs/1011.1669v3).
- [83] S. D. Drell and T.-M. Yan. “Massive Lepton-Pair Production in Hadron-Hadron Collisions at High Energies”. In: *Phys. Rev. Lett.* 25.5 (1970), pp. 316–320. doi: [10.1103/PhysRevLett.25.316](https://doi.org/10.1103/PhysRevLett.25.316).
- [84] J. C. Collins and D. E. Soper. “The Theorems of Perturbative QCD”. In: *Ann. Rev. Nucl. Part. Sci.* 37.1 (1987), pp. 383–409. doi: [10.1146/annurev.ns.37.120187.002123](https://doi.org/10.1146/annurev.ns.37.120187.002123).
- [85] J. C. Collins, D. E. Soper, and G. Sterman. “Factorization of Hard Processes in QCD”. In: *Adv. Ser. Direct. High Energy Phys.* 5 (1989), pp. 1–91. doi: [10.1142/9789814503266_0001](https://doi.org/10.1142/9789814503266_0001). arXiv: [hep-ph/0409313 \[hep-ph\]](https://arxiv.org/abs/hep-ph/0409313).
- [86] W. Stirling. *Standard Model cross sections as a function of collider energy*. Private Communication. URL: http://www.hep.ph.ic.ac.uk/~wstirlin/plots/crosssections2012_v5.pdf (visited on 12/01/2018).
- [87] F. Bloch and A. Nordsieck. “Note on the Radiation Field of the Electron”. In: *Phys. Rev.* 52.2 (1937), pp. 54–59. doi: [10.1103/PhysRev.52.54](https://doi.org/10.1103/PhysRev.52.54).
- [88] T. Kinoshita. “Mass Singularities of Feynman Amplitudes”. In: *J. Math. Phys.* 3.4 (1962), pp. 650–677. doi: [10.1063/1.1724268](https://doi.org/10.1063/1.1724268).
- [89] T. D. Lee and M. Nauenberg. “Degenerate Systems and Mass Singularities”. In: *Phys. Rev.* 133.6B (1964), B1549–B1562. doi: [10.1103/PhysRev.133.B1549](https://doi.org/10.1103/PhysRev.133.B1549).

- [90] S. Catani and M. Seymour. “A general algorithm for calculating jet cross sections in NLO QCD”. In: *Nucl. Phys. B* 485.1-2 (1997), pp. 291–419. doi: [10.1016/S0550-3213\(96\)00589-5](https://doi.org/10.1016/S0550-3213(96)00589-5). arXiv: [hep-ph/9605323](https://arxiv.org/abs/hep-ph/9605323) [hep-ph].
- [91] V. Gribov and L. Lipatov. “Deep inelastic electron scattering in perturbation theory”. In: *Phys. Lett. B* 37.1 (1971), pp. 78–80. doi: [10.1016/0370-2693\(71\)90576-4](https://doi.org/10.1016/0370-2693(71)90576-4).
- [92] Y. L. Dokshitzer. “Calculation of the Structure Functions for Deep Inelastic Scattering and e^+e^- Anihilation by Perturbation Theory in Quantum Chromodynamics.” In: *Sov. Phys. JETP* 46 (1977), pp. 641–653.
- [93] G. Altarelli and G. Parisi. “Asymptotic freedom in parton language”. In: *Nucl. Phys. B* 126.2 (1977), pp. 298–318. doi: [10.1016/0550-3213\(77\)90384-4](https://doi.org/10.1016/0550-3213(77)90384-4).
- [94] T. Sjöstrand, S. Mrenna, and P. Skands. “A brief introduction to PYTHIA 8.1”. In: *Comput. Phys. Commun.* 178.11 (2008), pp. 852–867. doi: [10.1016/j.cpc.2008.01.036](https://doi.org/10.1016/j.cpc.2008.01.036). arXiv: [0710.3820](https://arxiv.org/abs/0710.3820) [hep-ph].
- [95] M. Bähr et al. “Herwig++ physics and manual”. In: *Eur. Phys. J. C* 58.4 (2008), pp. 639–707. doi: [10.1140/epjc/s10052-008-0798-9](https://doi.org/10.1140/epjc/s10052-008-0798-9). arXiv: [0803.0883](https://arxiv.org/abs/0803.0883) [hep-ph].
- [96] T. Gleisberg et al. “Event generation with SHERPA 1.1”. In: *JHEP* 0902 (2009), p. 007. doi: [10.1088/1126-6708/2009/02/007](https://doi.org/10.1088/1126-6708/2009/02/007). arXiv: [0811.4622](https://arxiv.org/abs/0811.4622) [hep-ph].
- [97] M. L.e. a. Mangano. “ALPGEN, a generator for hard multiparton processes in hadronic collisions”. In: *JHEP* 07 (2003), p. 1. doi: [10.1088/1126-6708/2003/07/001](https://doi.org/10.1088/1126-6708/2003/07/001). arXiv: [hep-ph/0206293](https://arxiv.org/abs/hep-ph/0206293) [hep-ph].
- [98] T. Gleisberg and S. Höche. “Comix, a new matrix element generator”. In: *JHEP* 2008.12 (2008), pp. 039–039. doi: [10.1088/1126-6708/2008/12/039](https://doi.org/10.1088/1126-6708/2008/12/039). arXiv: [0808.3674](https://arxiv.org/abs/0808.3674) [hep-ph].
- [99] T. Stelzer and W. Long. “Automatic generation of tree level helicity amplitudes”. In: *Comput. Phys. Commun.* 81.3 (1994), pp. 357–371. doi: [10.1016/0010-4655\(94\)90084-1](https://doi.org/10.1016/0010-4655(94)90084-1). arXiv: [hep-ph/9401258](https://arxiv.org/abs/hep-ph/9401258) [hep-ph].
- [100] F. Maltoni and T. Stelzer. “MadEvent: automatic event generation with MadGraph”. In: *JHEP* 2003.02 (2003), pp. 027–027. doi: [10.1088/1126-6708/2003/02/027](https://doi.org/10.1088/1126-6708/2003/02/027). arXiv: [hep-ph/0208156](https://arxiv.org/abs/hep-ph/0208156) [hep-ph].
- [101] J. Alwall et al. “The automated computation of tree-level and next-to-leading order differential cross sections, and their matching to parton shower simulations”. In: *JHEP* 7 (2014), p. 79. doi: [10.1007/JHEP07\(2014\)079](https://doi.org/10.1007/JHEP07(2014)079). arXiv: [1405.0301](https://arxiv.org/abs/1405.0301) [hep-ph].
- [102] P. Nason. “A New Method for Combining NLO QCD with Shower Monte Carlo Algorithms”. In: *JHEP* 11 (2004), pp. 040–040. doi: [10.1088/1126-6708/2004/11/040](https://doi.org/10.1088/1126-6708/2004/11/040). arXiv: [hep-ph/0409146](https://arxiv.org/abs/hep-ph/0409146) [hep-ph].
- [103] S. Frixione, P. Nason, and C. Oleari. “Matching NLO QCD computations with Parton Shower simulations: the POWHEG method”. In: *JHEP* 11 (2007), p. 070. doi: [10.1088/1126-6708/2007/11/070](https://doi.org/10.1088/1126-6708/2007/11/070). arXiv: [0709.2092](https://arxiv.org/abs/0709.2092) [hep-ph].

- [104] S. Frixione, G. Ridolfi, and P. Nason. “A positive-weight next-to-leading-order Monte Carlo for heavy flavour hadroproduction”. In: *JHEP* 09 (2007), pp. 126–126. doi: [10.1088/1126-6708/2007/09/126](https://doi.org/10.1088/1126-6708/2007/09/126). arXiv: [0707.3088](https://arxiv.org/abs/0707.3088) [[hep-ph](#)].
- [105] S. Alioli et al. “A general framework for implementing NLO calculations in shower Monte Carlo programs: The POWHEG BOX”. In: *JHEP* 6 (2010), p. 043. doi: [10.1007/JHEP06\(2010\)043](https://doi.org/10.1007/JHEP06(2010)043). arXiv: [1002.2581](https://arxiv.org/abs/1002.2581) [[hep-ph](#)].
- [106] C. F. Berger et al. “Automated implementation of on-shell methods for one-loop amplitudes”. In: *Phys. Rev. D* 78.3 (2008), p. 036003. doi: [10.1103/PhysRevD.78.036003](https://doi.org/10.1103/PhysRevD.78.036003). arXiv: [0803.4180](https://arxiv.org/abs/0803.4180) [[hep-ph](#)].
- [107] S. Frixione and B. R. Webber. “Matching NLO QCD computations and parton shower simulations”. In: *JHEP* 06 (2002), p. 029. arXiv: [hep-ph/0204244](https://arxiv.org/abs/hep-ph/0204244) [[hep-ph](#)].
- [108] S. Catani et al. “QCD Matrix Elements + Parton Showers”. In: *JHEP* 2001.11 (2001), pp. 063–063. doi: [10.1088/1126-6708/2001/11/063](https://doi.org/10.1088/1126-6708/2001/11/063). arXiv: [hep-ph/0109231](https://arxiv.org/abs/hep-ph/0109231) [[hep-ph](#)].
- [109] L. Lönnblad. “Correcting the Colour-Dipole Cascade Model with Fixed Order Matrix Elements”. In: *JHEP* 05 (2002), pp. 046–046. doi: [10.1088/1126-6708/2002/05/046](https://doi.org/10.1088/1126-6708/2002/05/046). arXiv: [hep-ph/0112284](https://arxiv.org/abs/hep-ph/0112284) [[hep-ph](#)].
- [110] K. Hamilton, P. Richardson, and J. Tully. “A modified CKKW matrix element merging approach to angular-ordered parton showers”. In: *JHEP* 11 (2009), pp. 038–038. doi: [10.1088/1126-6708/2009/11/038](https://doi.org/10.1088/1126-6708/2009/11/038). arXiv: [0905.3072](https://arxiv.org/abs/0905.3072) [[hep-ph](#)].
- [111] M. L. Mangano. *The so-called MLM prescription for ME/PS matching*. Talk presented at the Fermilab ME/MC Tuning Workshop. 2002.
- [112] F. Krauss. “Matrix Elements and Parton Showers in Hadronic Interactions”. In: *JHEP* 2002.08 (2002), pp. 015–015. doi: [10.1088/1126-6708/2002/08/015](https://doi.org/10.1088/1126-6708/2002/08/015). arXiv: [hep-ph/0205283](https://arxiv.org/abs/hep-ph/0205283) [[hep-ph](#)].
- [113] S. Höche et al. “QCD matrix elements and truncated showers”. In: *JHEP* 2009.05 (2009), pp. 053–053. doi: [10.1088/1126-6708/2009/05/053](https://doi.org/10.1088/1126-6708/2009/05/053). arXiv: [0903.1219](https://arxiv.org/abs/0903.1219) [[hep-ph](#)].
- [114] J. Alwall et al. “Comparative study of various algorithms for the merging of parton showers and matrix elements in hadronic collisions”. In: *Eur. Phys. J. C* 53.3 (2008), pp. 473–500. doi: [10.1140/epjc/s10052-007-0490-5](https://doi.org/10.1140/epjc/s10052-007-0490-5). arXiv: [0706.2569](https://arxiv.org/abs/0706.2569) [[hep-ph](#)].
- [115] K. Hamilton and P. Nason. “Improving NLO-parton shower matched simulations with higher order matrix elements”. In: *JHEP* 6 (2010), p. 39. doi: [10.1007/JHEP06\(2010\)039](https://doi.org/10.1007/JHEP06(2010)039). arXiv: [1004.1764](https://arxiv.org/abs/1004.1764) [[hep-ph](#)].
- [116] S. Höche et al. “NLO matrix elements and truncated showers”. In: *JHEP* 8 (2011), p. 123. doi: [10.1007/JHEP08\(2011\)123](https://doi.org/10.1007/JHEP08(2011)123). arXiv: [1009.1127](https://arxiv.org/abs/1009.1127).
- [117] T. Gehrmann et al. “NLO QCD matrix elements + parton showers in $e^+e^- \rightarrow$ hadrons”. In: *JHEP* 1 (2013), p. 144. doi: [10.1007/JHEP01\(2013\)144](https://doi.org/10.1007/JHEP01(2013)144).
- [118] S. Höche et al. “QCD matrix elements + parton showers. The NLO case”. In: *JHEP* 4 (2013), p. 27. doi: [10.1007/JHEP04\(2013\)027](https://doi.org/10.1007/JHEP04(2013)027). arXiv: [1207.5030](https://arxiv.org/abs/1207.5030) [[hep-ph](#)].

- [119] A. D. Martin et al. “Parton distributions for the LHC”. In: *Eur. Phys. J. C* 63.2 (2009), pp. 189–285. doi: [10.1140/epjc/s10052-009-1072-5](https://doi.org/10.1140/epjc/s10052-009-1072-5). arXiv: [0901.0002](https://arxiv.org/abs/0901.0002).
- [120] J. Rojo et al. “The PDF4LHC report on PDFs and LHC data: results from Run I and preparation for Run II”. In: *J. Phys. G* 42.10 (2015), p. 103103. doi: [10.1088/0954-3899/42/10/103103](https://doi.org/10.1088/0954-3899/42/10/103103). arXiv: [1507.00556](https://arxiv.org/abs/1507.00556) [[hep-ph](#)].
- [121] H. L. Lai et al. “New parton distributions for collider physics”. In: *Phys. Rev. D* 82.7 (2010), p. 074024. doi: [10.1103/PhysRevD.82.074024](https://doi.org/10.1103/PhysRevD.82.074024). arXiv: [1007.2241](https://arxiv.org/abs/1007.2241) [[hep-ph](#)].
- [122] A. D. Martin et al. “Parton distributions for the LHC”. In: *Eur. Phys. J. C* 63 (2009), pp. 189–285. doi: [10.1140/epjc/s10052-009-1072-5](https://doi.org/10.1140/epjc/s10052-009-1072-5). arXiv: [0901.0002](https://arxiv.org/abs/0901.0002) [[hep-ph](#)].
- [123] A. D. Martin et al. “Uncertainties on α_S in global PDF analyses and implications for predicted hadronic cross sections”. In: *Eur. Phys. J. C* 64.4 (2009), pp. 653–680. doi: [10.1140/epjc/s10052-009-1164-2](https://doi.org/10.1140/epjc/s10052-009-1164-2). arXiv: [0905.3531](https://arxiv.org/abs/0905.3531) [[hep-ph](#)].
- [124] NNPDF Collaboration. “Parton distributions for the LHC run II”. In: *JHEP* 4 (2015), p. 040. doi: [10.1007/JHEP04\(2015\)040](https://doi.org/10.1007/JHEP04(2015)040). arXiv: [1410.8849](https://arxiv.org/abs/1410.8849) [[hep-ph](#)].
- [125] A. Buckley et al. “LHAPDF6: parton density access in the LHC precision era”. In: *Eur. Phys. J. C* 75.3 (2015), p. 132. doi: [10.1140/epjc/s10052-015-3318-8](https://doi.org/10.1140/epjc/s10052-015-3318-8). arXiv: [1412.7420](https://arxiv.org/abs/1412.7420) [[hep-ph](#)].
- [126] T. Sjöstrand. *Monte Carlo Generators*. ESHEP Proceedings. 2006. arXiv: [hep-ph/0611247](https://arxiv.org/abs/hep-ph/0611247) [[hep-ph](#)].
- [127] B. Andersson et al. “Parton fragmentation and string dynamics”. In: *Phys. Rep.* 97.2-3 (1983), pp. 31–145. doi: [10.1016/0370-1573\(83\)90080-7](https://doi.org/10.1016/0370-1573(83)90080-7).
- [128] M. G. Bowler. “ e^+e^- - Production of heavy quarks in the string model”. In: *Z. Phys. C* 11.2 (1981), pp. 169–174. doi: [10.1007/BF01574001](https://doi.org/10.1007/BF01574001).
- [129] G. C. Fox and S. Wolfram. “A model for parton showers in QCD”. In: *Nucl. Phys. B* 168.2 (1980), pp. 285–295. doi: [10.1016/0550-3213\(80\)90111-X](https://doi.org/10.1016/0550-3213(80)90111-X).
- [130] R. D. Field and S. Wolfram. “A QCD model for e^+e^- annihilation”. In: *Nucl. Phys. B* 213.1 (1983), pp. 65–84. doi: [10.1016/0550-3213\(83\)90175-X](https://doi.org/10.1016/0550-3213(83)90175-X).
- [131] D. Amati and G. Veneziano. “Preconfinement as a property of perturbative QCD”. In: *Phys. Lett. B* 83.1 (1979), pp. 87–92. doi: [10.1016/0370-2693\(79\)90896-7](https://doi.org/10.1016/0370-2693(79)90896-7).
- [132] Y. I. Azimov et al. “Similarity of parton and hadron spectra in QCD jets”. In: *Z. Phys. C* 27.1 (1985), pp. 65–72. doi: [10.1007/BF01642482](https://doi.org/10.1007/BF01642482).
- [133] Y. I. Azimov et al. “Hump-backed QCD plateau in hadron spectra”. In: *Z. Phys. C* 31.2 (1986), pp. 213–218. doi: [10.1007/BF01479529](https://doi.org/10.1007/BF01479529).
- [134] B. Webber. “A QCD model for jet fragmentation including soft gluon interference”. In: *Nucl. Phys. B* 238.3 (1984), pp. 492–528. doi: [10.1016/0550-3213\(84\)90333-X](https://doi.org/10.1016/0550-3213(84)90333-X).
- [135] J.-C. Winter, F. Krauss, and G. Soff. “A modified cluster-hadronisation model”. In: *Eur. Phys. J. C* 36.3 (2004), pp. 381–395. doi: [10.1140/epjc/s2004-01960-8](https://doi.org/10.1140/epjc/s2004-01960-8). arXiv: [hep-ph/0311085](https://arxiv.org/abs/hep-ph/0311085) [[hep-ph](#)].

- [136] ATLAS Collaboration. “The ATLAS Experiment at the CERN Large Hadron Collider”. In: *JINST* 3 (2008), S08003. doi: [10.1088/1748-0221/3/08/S08003](https://doi.org/10.1088/1748-0221/3/08/S08003).
- [137] O. Bruning et al. *LHC Design Report Vol.1: The LHC Main Ring*. CERN-2004-003-V-1. 2004.
- [138] O. Buning et al. *LHC Design Report Vol.2. The LHC infrastructure and general services*. CERN-2004-003-V-2. 2004.
- [139] M. Benedikt et al. *LHC Design Report Vol.3 The LHC injector chain*. CERN-2004-003-V-3. 2004.
- [140] L. Evans and P. Bryant. “LHC Machine”. In: *JINST* 3.08 (2008), S08001–S08001. doi: [10.1088/1748-0221/3/08/S08001](https://doi.org/10.1088/1748-0221/3/08/S08001).
- [141] *LEP Design Report: Vol.2. The LEP Main Ring*. CERN-LEP-84-01. 1984.
- [142] CMS Collaboration. “The CMS experiment at the CERN LHC”. In: *JINST* 3 (2008), S08004. doi: [10.1088/1748-0221/3/08/S08004](https://doi.org/10.1088/1748-0221/3/08/S08004).
- [143] ALICE Collaboration. “The ALICE experiment at the CERN LHC”. In: *JINST* 3 (2008), S08002. doi: [10.1088/1748-0221/3/08/S08002](https://doi.org/10.1088/1748-0221/3/08/S08002).
- [144] LHCb Collaboration. “The LHCb Detector at the LHC”. In: *JINST* 3.08 (2008), S08005–S08005. doi: [10.1088/1748-0221/3/08/S08005](https://doi.org/10.1088/1748-0221/3/08/S08005).
- [145] LHCf Collaboration. “The LHCf detector at the CERN Large Hadron Collider”. In: *JINST* 3.08 (2008), S08006–S08006. doi: [10.1088/1748-0221/3/08/S08006](https://doi.org/10.1088/1748-0221/3/08/S08006).
- [146] TOTEM Collaboration. “The TOTEM Experiment at the CERN Large Hadron Collider”. In: *JINST* 3.08 (2008), S08007–S08007. doi: [10.1088/1748-0221/3/08/S08007](https://doi.org/10.1088/1748-0221/3/08/S08007).
- [147] J. Pinfold and Others. *Technical Design Report of the MoEDAL Experiment*. MoEDAL-TDR-001. 2009.
- [148] C. Lefèvre. *The CERN accelerator complex*. CERN-DI-0812015. 2008. URL: <https://cds.cern.ch/record/1260465>.
- [149] ATLAS Collaboration. *ATLAS Inner Detector Alignment Performance with February 2015 Cosmic Ray Data*. ATL-PHYS-PUB-2015-009. 2015.
- [150] ATLAS Collaboration. *ATLAS Insertable B-Layer Technical Design Report*. Tech. rep. 2010.
- [151] ATLAS Collaboration. “Production and integration of the ATLAS Insertable B-Layer”. In: *JINST* 13.05 (2018), T05008–T05008. doi: [10.1088/1748-0221/13/05/T05008](https://doi.org/10.1088/1748-0221/13/05/T05008). arXiv: [1803.00844](https://arxiv.org/abs/1803.00844) [[physics.ins-det](https://arxiv.org/abs/1803.00844)].
- [152] ATLAS Collaboration. “Performance of the ATLAS Transition Radiation Tracker in Run 1 of the LHC: Tracker properties”. In: *JINST* 12.5 (2017). doi: [10.1088/1748-0221/12/05/P05002](https://doi.org/10.1088/1748-0221/12/05/P05002).
- [153] ATLAS Collaboration. “Commissioning of the ATLAS Muon Spectrometer with cosmic rays”. In: *Eur. Phys. J. C* 70 (2010), p. 875. doi: [10.1140/epjc/s10052-010-1415-2](https://doi.org/10.1140/epjc/s10052-010-1415-2). arXiv: [1006.4384](https://arxiv.org/abs/1006.4384) [[hep-ex](https://arxiv.org/abs/1006.4384)].
- [154] ATLAS Collaboration. “Muon reconstruction performance of the ATLAS detector in proton–proton collision data at $\sqrt{s} = 13$ TeV”. In: *Eur. Phys. J. C* 76 (2016), p. 292. doi: [10.1140/epjc/s10052-016-4120-y](https://doi.org/10.1140/epjc/s10052-016-4120-y). arXiv: [1603.05598](https://arxiv.org/abs/1603.05598) [[hep-ex](https://arxiv.org/abs/1603.05598)].

- [155] ATLAS Collaboration. “Improved luminosity determination in pp collisions at $\sqrt{s} = 7$ TeV using the ATLAS detector at the LHC”. In: *Eur. Phys. J. C* 73 (2013), p. 2518. doi: [10.1140/epjc/s10052-013-2518-3](https://doi.org/10.1140/epjc/s10052-013-2518-3). arXiv: [1302.4393](https://arxiv.org/abs/1302.4393) [hep-ex].
- [156] G. Avoni et al. “The new LUCID-2 detector for luminosity measurement and monitoring in ATLAS”. In: *JINST* 13.07 (2018), P07017–P07017. doi: [10.1088/1748-0221/13/07/P07017](https://doi.org/10.1088/1748-0221/13/07/P07017).
- [157] ATLAS Collaboration. “Measurement of the total cross section from elastic scattering in pp collisions at $\sqrt{s} = 7$ TeV with the ATLAS detector”. In: *Nucl. Phys. B* 889 (2014), p. 486. doi: [10.1016/j.nuclphysb.2014.10.019](https://doi.org/10.1016/j.nuclphysb.2014.10.019). arXiv: [1408.5778](https://arxiv.org/abs/1408.5778) [hep-ex].
- [158] ATLAS Collaboration. “Measurement of the total cross section from elastic scattering in pp collisions at $\sqrt{s} = 8$ TeV with the ATLAS detector”. In: *Phys. Lett. B* 761 (2016), p. 158. doi: [10.1016/j.physletb.2016.08.020](https://doi.org/10.1016/j.physletb.2016.08.020). arXiv: [1607.06605](https://arxiv.org/abs/1607.06605) [hep-ex].
- [159] U. Amaldi et al. “The real part of the forward proton proton scattering amplitude measured at the CERN intersecting storage rings”. In: *Phys. Lett. B* 66.4 (1977), pp. 390–394. doi: [10.1016/0370-2693\(77\)90022-3](https://doi.org/10.1016/0370-2693(77)90022-3).
- [160] ATLAS Collaboration. *ATLAS Forward Proton Phase-I Upgrade Technical Design Report*. ATLAS-TDR-024. 2015, p. 206.
- [161] ATLAS Collaboration. *Proton tagging with the one arm AFP detector*. ATL-PHYS-PUB-2017-012. 2017.
- [162] ATLAS Collaboration. “Luminosity determination in pp collisions at $\sqrt{s} = 8$ TeV using the ATLAS detector at the LHC”. In: *Eur. Phys. J. C* 76 (2016), p. 653. doi: [10.1140/epjc/s10052-016-4466-1](https://doi.org/10.1140/epjc/s10052-016-4466-1). arXiv: [1608.03953](https://arxiv.org/abs/1608.03953) [hep-ex].
- [163] S. van der Meer. *Calibration of the Effective Beam Height in the ISR*. CERN-ISR-PO-68-31. 1968. URL: <https://cds.cern.ch/record/296752>.
- [164] C. Rubbia. *Measurement of the Luminosity of p anti- p Collider with a (Generalized) Van Der Meer Method*. CERN-p-anti-p-Note-38. 1977.
- [165] G. Anders et al. *LHC Bunch Current Normalisation for the April-May 2010 Luminosity Calibration Measurements*. CERN-ATS-Note-2011-004. 2011. URL: <https://cds.cern.ch/record/1325370>.
- [166] ATLAS Collaboration. “Performance of the ATLAS trigger system in 2015”. In: *Eur. Phys. J. C* 77 (2017), p. 317. doi: [10.1140/epjc/s10052-017-4852-3](https://doi.org/10.1140/epjc/s10052-017-4852-3). arXiv: [1611.09661](https://arxiv.org/abs/1611.09661) [hep-ex].
- [167] ATLAS Collaboration. *Performance of the ATLAS Electron and Photon Trigger in pp Collisions at $\sqrt{s} = 7$ TeV in 2011*. ATLAS-CONF-2012-048. 2012.
- [168] R. Achenbach et al. “The ATLAS Level-1 Calorimeter Trigger”. In: *JINST* 3.03 (2008), P03001.
- [169] ATLAS Collaboration. “The ATLAS Simulation Infrastructure”. In: *Eur. Phys. J. C* 70 (2010), p. 823. doi: [10.1140/epjc/s10052-010-1429-9](https://doi.org/10.1140/epjc/s10052-010-1429-9). arXiv: [1005.4568](https://arxiv.org/abs/1005.4568) [physics.ins-det].
- [170] ATLAS Collaboration. *ATLAS Computing Technical Design Report*. CERN-LHCC-2005-022. 2005, p. 248.

- [171] S. Agostinelli et al. “Geant4 – a simulation toolkit”. In: *Nucl. Inst. Meth. A* 506.3 (2003), pp. 250–303. doi: [10.1016/S0168-9002\(03\)01368-8](https://doi.org/10.1016/S0168-9002(03)01368-8).
- [172] ATLAS Collaboration. *The simulation principle and performance of the ATLAS fast calorimeter simulation FastCaloSim*. ATL-PHYS-PUB-2010-013. 2010.
- [173] ATLAS Collaboration. *Performance of the Fast ATLAS Tracking Simulation (FATRAS) and the ATLAS Fast Calorimeter Simulation (FastCaloSim) with single particles*. ATL-SOFT-PUB-2014-001. 2014.
- [174] ATLAS Collaboration. *Luminosity Public Results: Run 2*. URL: <https://twiki.cern.ch/twiki/bin/view/AtlasPublic/LuminosityPublicResultsRun2> (visited on 08/22/2018).
- [175] ATLAS Collaboration. *Data Quality Public Results: 2010 - 2018*. URL: <https://twiki.cern.ch/twiki/bin/view/AtlasPublic/RunStatsPublicResults2010> (visited on 08/22/2018).
- [176] T. Cornelissen et al. *Concepts, Design and Implementation of the ATLAS New Tracking (NEWT)*. ATL-SOFT-PUB-2007-007. 2007, pp. 1–25.
- [177] T. Cornelissen et al. “The new ATLAS track reconstruction (NEWT)”. In: *J. Phys. Conf. Ser.* 119.3 (2008). doi: [10.1088/1742-6596/119/3/032014](https://doi.org/10.1088/1742-6596/119/3/032014).
- [178] R. Frühwirth. “Application of Kalman filtering to track and vertex fitting”. In: *Nucl. Inst. Meth. A* 262.2-3 (1987), pp. 444–450. doi: [10.1016/0168-9002\(87\)90887-4](https://doi.org/10.1016/0168-9002(87)90887-4).
- [179] D. Wicke. *A New Algorithm for Solving Tracking Ambiguities*. LC-TOOL-1999-007-TESLA. 1999.
- [180] J. Illingworth and J. Kittler. “A survey of the hough transform”. In: *Computer Vision, Graphics, and Image Processing* 44.1 (1988), pp. 87–116. doi: [10.1016/S0734-189X\(88\)80033-1](https://doi.org/10.1016/S0734-189X(88)80033-1).
- [181] ATLAS Collaboration. *Performance of the ATLAS Inner Detector Track and Vertex Reconstruction in High Pile-Up LHC Environment*. ATLAS-CONF-2012-042. 2012.
- [182] ATLAS Collaboration. *Early Inner Detector Tracking Performance in the 2015 Data at $\sqrt{s} = 13$ TeV*. ATL-PHYS-PUB-2015-051. 2015.
- [183] ATLAS Collaboration. *The Optimization of ATLAS Track Reconstruction in Dense Environments*. ATL-PHYS-PUB-2015-006. 2015.
- [184] ATLAS Collaboration. *Performance of primary vertex reconstruction in proton–proton collisions at $\sqrt{s} = 7$ TeV in the ATLAS experiment*. ATLAS-CONF-2010-069. 2010.
- [185] ATLAS Collaboration. *Characterization of Interaction-Point Beam Parameters Using the pp Event-Vertex Distribution Reconstructed in the ATLAS Detector at the LHC*. ATLAS-CONF-2010-027. 2010.
- [186] W. Waltenberger, R. Frühwirth, and P. Vanlaer. “Adaptive vertex fitting”. In: *J. Phys. G* 34.12 (2007), N343–N356. doi: [10.1088/0954-3899/34/12/N01](https://doi.org/10.1088/0954-3899/34/12/N01).
- [187] ATLAS Collaboration. *Vertex Reconstruction Performance of the ATLAS Detector at $\sqrt{s} = 13$ TeV*. ATL-PHYS-PUB-2015-026. 2015.
- [188] ATLAS Collaboration. “Topological cell clustering in the ATLAS calorimeters and its performance in LHC Run 1”. In: *Eur. Phys. J. C* 77 (2017), p. 490. doi: [10.1140/epjc/s10052-017-5004-5](https://doi.org/10.1140/epjc/s10052-017-5004-5). arXiv: [1603.02934](https://arxiv.org/abs/1603.02934) [hep-ex].

- [189] W. Lampl et al. *Calorimeter Clustering Algorithms: Description and Performance*. ATL-LARG-PUB-2008-002. 2008.
- [190] G. P. Salam. “Towards jetography”. In: *Eur. Phys. J. C* 67.3-4 (2010), pp. 637–686. doi: [10.1140/epjc/s10052-010-1314-6](https://doi.org/10.1140/epjc/s10052-010-1314-6). arXiv: [0906.1833](https://arxiv.org/abs/0906.1833) [hep-ph].
- [191] M. Cacciari, G. P. Salam, and G. Soyez. “The anti- k_t jet clustering algorithm”. In: *JHEP* 04 (2008), p. 063. doi: [10.1088/1126-6708/2008/04/063](https://doi.org/10.1088/1126-6708/2008/04/063). arXiv: [0802.1189](https://arxiv.org/abs/0802.1189) [hep-ph].
- [192] M. Cacciari, G. P. Salam, and G. Soyez. “FastJet user manual”. In: *Eur. Phys. J. C* 72.3 (2012), p. 1896. doi: [10.1140/epjc/s10052-012-1896-2](https://doi.org/10.1140/epjc/s10052-012-1896-2). arXiv: [1111.6097](https://arxiv.org/abs/1111.6097) [hep-ph].
- [193] D. Krohn, J. Thaler, and L. T. Wang. “Jet trimming”. In: *JHEP* 2 (2010). doi: [10.1007/JHEP02\(2010\)084](https://doi.org/10.1007/JHEP02(2010)084). arXiv: [0912.1342](https://arxiv.org/abs/0912.1342) [hep-ph].
- [194] S. Catani et al. “Longitudinally-invariant k_{\perp} -clustering algorithms for hadron-hadron collisions”. In: *Nucl. Phys. B* 406.1-2 (1993), pp. 187–224. doi: [10.1016/0550-3213\(93\)90166-M](https://doi.org/10.1016/0550-3213(93)90166-M).
- [195] S. D. Ellis and D. E. Soper. “Successive combination jet algorithm for hadron collisions”. In: *Phys. Rev. D* 48.7 (1993), pp. 3160–3166. doi: [10.1103/PhysRevD.48.3160](https://doi.org/10.1103/PhysRevD.48.3160). arXiv: [hep-ph/9305266](https://arxiv.org/abs/hep-ph/9305266) [hep-ph].
- [196] M. Cacciari et al. “Quantifying the performance of jet definitions for kinematic reconstruction at the LHC”. In: *JHEP* 2008.12 (2008), pp. 032–032. doi: [10.1088/1126-6708/2008/12/032](https://doi.org/10.1088/1126-6708/2008/12/032). arXiv: [0810.1304](https://arxiv.org/abs/0810.1304) [hep-ph].
- [197] M. Cacciari, G. P. Salam, and G. Soyez. “The catchment area of jets”. In: *JHEP* 04 (2008), pp. 005–005. doi: [10.1088/1126-6708/2008/04/005](https://doi.org/10.1088/1126-6708/2008/04/005). arXiv: [0802.1188](https://arxiv.org/abs/0802.1188) [hep-ph].
- [198] ATLAS Collaboration. “Performance of jet substructure techniques for large- R jets in proton–proton collisions at $\sqrt{s} = 7$ TeV using the ATLAS detector”. In: *JHEP* 09 (2013), p. 076. doi: [10.1007/JHEP09\(2013\)076](https://doi.org/10.1007/JHEP09(2013)076). arXiv: [1306.4945](https://arxiv.org/abs/1306.4945) [hep-ex].
- [199] ATLAS Collaboration. “Identification of boosted, hadronically decaying W bosons and comparisons with ATLAS data taken at $\sqrt{s} = 8$ TeV”. In: *Eur. Phys. J. C* 76 (2016), p. 154. doi: [10.1140/epjc/s10052-016-3978-z](https://doi.org/10.1140/epjc/s10052-016-3978-z). arXiv: [1510.05821](https://arxiv.org/abs/1510.05821) [hep-ex].
- [200] ATLAS Collaboration. “Jet energy scale measurements and their systematic uncertainties in proton–proton collisions at $\sqrt{s} = 13$ TeV with the ATLAS detector”. In: *Phys. Rev. D* 96 (2017), p. 072002. doi: [10.1103/PhysRevD.96.072002](https://doi.org/10.1103/PhysRevD.96.072002). arXiv: [1703.09665](https://arxiv.org/abs/1703.09665) [hep-ex].
- [201] ATLAS Collaboration. “Performance of pile-up mitigation techniques for jets in pp collisions at $\sqrt{s} = 8$ TeV using the ATLAS detector”. In: *Eur. Phys. J. C* 76 (2016), p. 581. doi: [10.1140/epjc/s10052-016-4395-z](https://doi.org/10.1140/epjc/s10052-016-4395-z). arXiv: [1510.03823](https://arxiv.org/abs/1510.03823) [hep-ex].
- [202] M. Cacciari and G. P. Salam. “Pileup subtraction using jet areas”. In: *Phys. Lett. B* 659.1-2 (2008), pp. 119–126. doi: [10.1016/j.physletb.2007.09.077](https://doi.org/10.1016/j.physletb.2007.09.077). arXiv: [0707.1378](https://arxiv.org/abs/0707.1378) [hep-ph].
- [203] ATLAS Collaboration. “Jet energy measurement with the ATLAS detector in proton–proton collisions at $\sqrt{s} = 7$ TeV”. In: *Eur. Phys. J. C* 73 (2013), p. 2304. doi: [10.1140/epjc/s10052-013-2304-2](https://doi.org/10.1140/epjc/s10052-013-2304-2). arXiv: [1112.6426](https://arxiv.org/abs/1112.6426) [hep-ex].

- [204] ATLAS Collaboration. “Jet energy measurement and its systematic uncertainty in proton–proton collisions at $\sqrt{s} = 7$ TeV with the ATLAS detector”. In: *Eur. Phys. J. C* 75 (2015), p. 17. doi: [10.1140/epjc/s10052-014-3190-y](https://doi.org/10.1140/epjc/s10052-014-3190-y). arXiv: [1406.0076](https://arxiv.org/abs/1406.0076) [hep-ex].
- [205] ATLAS Collaboration. “Jet energy resolution in proton–proton collisions at $\sqrt{s} = 7$ TeV recorded in 2010 with the ATLAS detector”. In: *Eur. Phys. J. C* 73 (2013), p. 2306. doi: [10.1140/epjc/s10052-013-2306-0](https://doi.org/10.1140/epjc/s10052-013-2306-0). arXiv: [1210.6210](https://arxiv.org/abs/1210.6210) [hep-ex].
- [206] ATLAS Collaboration. *Monte Carlo Calibration and Combination of In-situ Measurements of Jet Energy Scale, Jet Energy Resolution and Jet Mass in ATLAS*. ATLAS-CONF-2015-037. 2015.
- [207] ATLAS Collaboration. *Data-driven determination of the energy scale and resolution of jets reconstructed in the ATLAS calorimeters using dijet and multijet events at $\sqrt{s} = 8$ TeV*. ATLAS-CONF-2015-017. 2015.
- [208] ATLAS Collaboration. *Determination of the jet energy scale and resolution at ATLAS using Z/ γ -jet events in data at $\sqrt{s} = 8$ TeV*. ATLAS-CONF-2015-057. 2015.
- [209] ATLAS Collaboration. *Jet mass reconstruction with the ATLAS Detector in early Run 2 data*. ATLAS-CONF-2016-035. 2016.
- [210] ATLAS Collaboration. “Jet mass and substructure of inclusive jets in $\sqrt{s} = 7$ TeV pp collisions with the ATLAS experiment”. In: *JHEP* 05 (2012), p. 128. doi: [10.1007/JHEP05\(2012\)128](https://doi.org/10.1007/JHEP05(2012)128). arXiv: [1203.4606](https://arxiv.org/abs/1203.4606) [hep-ex].
- [211] ATLAS Collaboration. *In-situ measurements of the ATLAS large-radius jet response in 13 TeV pp collisions*. ATLAS-CONF-2017-063. 2017.
- [212] ATLAS Collaboration. *Measurement of large radius jet mass reconstruction performance at $\sqrt{s} = 8$ TeV using the ATLAS detector*. ATLAS-CONF-2016-008. 2016.
- [213] ATLAS Collaboration. *Tagging and suppression of pileup jets with the ATLAS detector*. ATLAS-CONF-2014-018. 2014.
- [214] ATLAS Collaboration. “Characterisation and mitigation of beam-induced backgrounds observed in the ATLAS detector during the 2011 proton–proton run”. In: *JINST* 8 (2013), P07004. doi: [10.1088/1748-0221/8/07/P07004](https://doi.org/10.1088/1748-0221/8/07/P07004). arXiv: [1303.0223](https://arxiv.org/abs/1303.0223) [hep-ex].
- [215] ATLAS Collaboration. *Selection of jets produced in 13 TeV proton–proton collisions with the ATLAS detector*. ATLAS-CONF-2015-029. 2015.
- [216] ATLAS Collaboration. *Flavor Tagging with Track-Jets in Boosted Topologies with the ATLAS Detector*. ATL-PHYS-PUB-2014-013. 2014.
- [217] ATLAS Collaboration. “Measurements of b -jet tagging efficiency with the ATLAS detector using $t\bar{t}$ events at $\sqrt{s} = 13$ TeV”. In: *JHEP* 08 (2018), p. 089. doi: [10.1007/JHEP08\(2018\)089](https://doi.org/10.1007/JHEP08(2018)089). arXiv: [1805.01845](https://arxiv.org/abs/1805.01845) [hep-ex].
- [218] ATLAS Collaboration. *Performance of the ATLAS Secondary Vertex b -tagging Algorithm in 7 TeV Collision Data*. ATLAS-CONF-2010-042. 2010.
- [219] ATLAS Collaboration. *Expected performance of the ATLAS b -tagging algorithms in Run-2*. ATL-PHYS-PUB-2015-022. 2015.

- [220] ATLAS Collaboration. *Optimisation of the ATLAS b-tagging performance for the 2016 LHC Run*. ATL-PHYS-PUB-2016-012. 2016.
- [221] G. Piacquadio and C. Weiser. “A new inclusive secondary vertex algorithm for b-jet tagging in ATLAS”. In: *J. Phys. Conf. Ser.* Vol. 119. 3. 2008, p. 032032. doi: [10.1088/1742-6596/119/3/032032](https://doi.org/10.1088/1742-6596/119/3/032032).
- [222] D0 Collaboration. “b-Jet identification in the D0 experiment”. In: *Nucl. Inst. Meth. A* 620.2-3 (2010), pp. 490–517. doi: [10.1016/j.nima.2010.03.118](https://doi.org/10.1016/j.nima.2010.03.118). arXiv: [1002.4224](https://arxiv.org/abs/1002.4224) [hep-ex].
- [223] ATLAS Collaboration. *Measurement of b-tagging efficiency of c-jets in $t\bar{t}$ events using a likelihood approach with the ATLAS detector*. ATLAS-CONF-2018-001. 2018.
- [224] J. Erdmann et al. “A likelihood-based reconstruction algorithm for top-quark pairs and the KLFilter framework”. In: *Nucl. Inst. Meth. A* 748 (2014), pp. 18–25. doi: [10.1016/j.nima.2014.02.029](https://doi.org/10.1016/j.nima.2014.02.029). arXiv: [1312.5595](https://arxiv.org/abs/1312.5595) [hep-ex].
- [225] ATLAS Collaboration. *Calibration of light-flavour b-jet mistagging rates using ATLAS proton–proton collision data at $\sqrt{s} = 13$ TeV*. ATLAS-CONF-2018-006. 2018.
- [226] D. J. Lange. “The EvtGen particle decay simulation package”. In: *Nucl. Instrum. Meth. A* 462.1-2 (2001), pp. 152–155. doi: [10.1016/S0168-9002\(01\)00089-4](https://doi.org/10.1016/S0168-9002(01)00089-4).
- [227] ATLAS Collaboration. *Measurement of the top quark pair production cross section with ATLAS in pp collisions at $\sqrt{s} = 7$ TeV in the single-lepton channel using semileptonic b decays*. ATLAS-CONF-2012-131. 2012.
- [228] ATLAS Collaboration. “Electron reconstruction and identification efficiency measurements with the ATLAS detector using the 2011 LHC proton–proton collision data”. In: *Eur. Phys. J. C* 74 (2014), p. 2941. doi: [10.1140/epjc/s10052-014-2941-0](https://doi.org/10.1140/epjc/s10052-014-2941-0). arXiv: [1404.2240](https://arxiv.org/abs/1404.2240) [hep-ex].
- [229] ATLAS Collaboration. *Electron efficiency measurements with the ATLAS detector using the 2015 LHC proton–proton collision data*. ATLAS-CONF-2016-024. 2016.
- [230] ATLAS Collaboration. *Improved electron reconstruction in ATLAS using the Gaussian Sum Filter-based model for bremsstrahlung*. ATLAS-CONF-2012-047. 2012.
- [231] ATLAS Collaboration. “Electron efficiency measurements with the ATLAS detector using 2012 LHC proton–proton collision data”. In: *Eur. Phys. J. C* 77 (2017), p. 195. doi: [10.1140/epjc/s10052-017-4756-2](https://doi.org/10.1140/epjc/s10052-017-4756-2). arXiv: [1612.01456](https://arxiv.org/abs/1612.01456) [hep-ex].
- [232] CDF Collaboration. “First Measurements of Inclusive W and Z Cross Sections from Run II of the Tevatron Collider”. In: *Phys. Rev. Lett.* 94.9 (2004), p. 091803. doi: [10.1103/PhysRevLett.94.091803](https://doi.org/10.1103/PhysRevLett.94.091803). arXiv: [hep-ex/0406078](https://arxiv.org/abs/hep-ex/0406078) [hep-ex].
- [233] D0 Collaboration and V. Abazov. “Measurement of the shape of the boson rapidity distribution for $p\bar{p} \rightarrow Z/\gamma^* \rightarrow e^+e^- + X$ events produced at \sqrt{s} of 1.96 TeV”. In: *Phys. Rev. D* 76.1 (2007), p. 012003. doi: [10.1103/PhysRevD.76.012003](https://doi.org/10.1103/PhysRevD.76.012003). arXiv: [hep-ex/0702025](https://arxiv.org/abs/hep-ex/0702025) [hep-ex].
- [234] ATLAS Collaboration. *Electron Public Plots*. URL: <https://atlas.web.cern.ch/Atlas/GROUPS/PHYSICS/PLOTS/EGAM-2017-003/index.html> (visited on 08/22/2018).

- [235] ATLAS Collaboration. “Electron and photon energy calibration with the ATLAS detector using LHC Run 1 data”. In: *Eur. Phys. J. C* 74 (2014), p. 3071. doi: [10.1140/epjc/s10052-014-3071-4](https://doi.org/10.1140/epjc/s10052-014-3071-4). arXiv: [1407.5063](https://arxiv.org/abs/1407.5063) [hep-ex].
- [236] ATLAS Collaboration. “Muon reconstruction efficiency and momentum resolution of the ATLAS experiment in proton–proton collisions at $\sqrt{s} = 7$ TeV in 2010”. In: *Eur. Phys. J. C* 74 (2014), p. 3034. doi: [10.1140/epjc/s10052-014-3034-9](https://doi.org/10.1140/epjc/s10052-014-3034-9). arXiv: [1404.4562](https://arxiv.org/abs/1404.4562) [hep-ex].
- [237] ATLAS Collaboration. “Measurement of the muon reconstruction performance of the ATLAS detector using 2011 and 2012 LHC proton–proton collision data”. In: *Eur. Phys. J. C* 74 (2014), p. 3130. doi: [10.1140/epjc/s10052-014-3130-x](https://doi.org/10.1140/epjc/s10052-014-3130-x). arXiv: [1407.3935](https://arxiv.org/abs/1407.3935) [hep-ex].
- [238] S. Hassani et al. “A muon identification and combined reconstruction procedure for the ATLAS detector at the LHC using the (MUONBOY, STACO, MuTag) reconstruction packages”. In: *Nucl. Inst. Meth. A* 572.1 (2007), pp. 77–79. doi: [10.1016/j.nima.2006.10.340](https://doi.org/10.1016/j.nima.2006.10.340).
- [239] T. Lagouri et al. “A muon identification and combined reconstruction procedure for the ATLAS detector at the LHC at CERN”. In: *IEEE* 51.6 (2004), pp. 3030–3033. doi: [10.1109/TNS.2004.839102](https://doi.org/10.1109/TNS.2004.839102).
- [240] D. Adams et al. *Track reconstruction in the ATLAS Muon Spectrometer with MOORE 007*. ATL-SOFT-2003-007. 2003.
- [241] ATLAS Collaboration. “Identification and energy calibration of hadronically decaying tau leptons with the ATLAS experiment in pp collisions at $\sqrt{s} = 8$ TeV”. In: *Eur. Phys. J. C* 75 (2015), p. 303. doi: [10.1140/epjc/s10052-015-3500-z](https://doi.org/10.1140/epjc/s10052-015-3500-z). arXiv: [1412.7086](https://arxiv.org/abs/1412.7086) [hep-ex].
- [242] ATLAS Collaboration. *Reconstruction, Energy Calibration, and Identification of Hadronically Decaying Tau Leptons in the ATLAS Experiment for Run-2 of the LHC*. ATL-PHYS-PUB-2015-045. 2015.
- [243] ATLAS Collaboration. *Measurement of the tau lepton reconstruction and identification performance in the ATLAS experiment using pp collisions at $\sqrt{s} = 13$ TeV*. ATLAS-CONF-2017-029. 2017.
- [244] ATLAS Collaboration. “Performance of missing transverse momentum reconstruction in proton–proton collisions at $\sqrt{s} = 7$ TeV with ATLAS”. In: *Eur. Phys. J. C* 72 (2012), p. 1844. doi: [10.1140/epjc/s10052-011-1844-6](https://doi.org/10.1140/epjc/s10052-011-1844-6). arXiv: [1108.5602](https://arxiv.org/abs/1108.5602) [hep-ex].
- [245] ATLAS Collaboration. “Performance of missing transverse momentum reconstruction with the ATLAS detector using proton–proton collisions at $\sqrt{s} = 13$ TeV”. In: *Eur. Phys. J. C* 78.11 (2018), p. 903. doi: [10.1140/epjc/s10052-018-6288-9](https://doi.org/10.1140/epjc/s10052-018-6288-9). arXiv: [1802.08168](https://arxiv.org/abs/1802.08168) [hep-ex].
- [246] ATLAS Collaboration. *Expected performance of missing transverse momentum reconstruction for the ATLAS detector at $\sqrt{s} = 13$ TeV*. ATL-PHYS-PUB-2015-023. 2015.
- [247] ATLAS Collaboration. *Performance of Missing Transverse Momentum Reconstruction in ATLAS with 2011 Proton–Proton Collisions at $\sqrt{s} = 7$ TeV*. ATLAS-CONF-2012-101. 2012.
- [248] ATLAS Collaboration. “Evidence for the $H \rightarrow b\bar{b}$ decay with the ATLAS detector”. In: *JHEP* 12 (2017), p. 024. doi: [10.1007/JHEP12\(2017\)024](https://doi.org/10.1007/JHEP12(2017)024). arXiv: [1708.03299](https://arxiv.org/abs/1708.03299) [hep-ex].

- [249] CMS Collaboration. “Measurement of associated $W + \text{charm}$ production in pp collisions at $\sqrt{s} = 7 \text{ TeV}$ ”. In: *JHEP* 02 (2014), p. 013. doi: [10.1007/JHEP02\(2014\)013](https://doi.org/10.1007/JHEP02(2014)013). arXiv: [1310.1138](https://arxiv.org/abs/1310.1138) [[hep-ex](#)].
- [250] CDF Collaboration. “First Measurement of W Boson Production in Association with a Single Charm Quark in $p\bar{p}$ Collisions at $\sqrt{s} = 1.96 \text{ TeV}$ ”. In: *Phys. Rev. Lett.* 100.9 (2008), p. 091803. doi: [10.1103/PhysRevLett.100.091803](https://doi.org/10.1103/PhysRevLett.100.091803). arXiv: [0711.2901](https://arxiv.org/abs/0711.2901) [[hep-ex](#)].
- [251] CDF Collaboration. “Observation of the production of a W boson in association with a single charm quark”. In: *Phys. Rev. Lett.* 110.7 (2013), p. 071801. doi: [10.1103/PhysRevLett.110.071801](https://doi.org/10.1103/PhysRevLett.110.071801). arXiv: [1209.1921](https://arxiv.org/abs/1209.1921) [[hep-ex](#)].
- [252] D0 Collaboration. “Measurement of the ratio of the $p\bar{p} \rightarrow W + c - \text{jet}$ cross section to the inclusive $p\bar{p} \rightarrow W + \text{jet}$ cross section”. In: *Phys. Lett. B* 666.1 (2008), pp. 23–30. doi: [10.1016/j.physletb.2008.06.067](https://doi.org/10.1016/j.physletb.2008.06.067). arXiv: [0803.2259](https://arxiv.org/abs/0803.2259) [[hep-ex](#)].
- [253] ATLAS Collaboration. *b-jet tagging calibration on c-jets containing D^{*+} mesons*. ATLAS-CONF-2012-039. 2012.
- [254] G. Marchesini and B. Webber. “Simulation of QCD coherence in heavy quark production and decay”. In: *Nucl. Phys. B* 330.1 (1990), pp. 261–283. doi: [10.1016/0550-3213\(90\)90310-A](https://doi.org/10.1016/0550-3213(90)90310-A).
- [255] G. Corcella et al. *HERWIG 6.5 release note*. 2002. arXiv: [hep-ph/0210213](https://arxiv.org/abs/hep-ph/0210213) [[hep-ph](#)].
- [256] J. M. Butterworth, J. R. Forshaw, and M. H. Seymour. “Multiparton interactions in photoproduction at HERA”. In: *Z. Phys. C* 72 (1996), p. 637. doi: [10.1007/s002880050286](https://doi.org/10.1007/s002880050286). arXiv: [hep-ph/9601371](https://arxiv.org/abs/hep-ph/9601371) [[hep-ph](#)].
- [257] F. Caravaglios et al. “A new approach to multi-jet calculations in hadron collisions”. In: *Nucl. Phys. B* 539.1-2 (1999), pp. 215–232. doi: [10.1016/S0550-3213\(98\)00739-1](https://doi.org/10.1016/S0550-3213(98)00739-1). arXiv: [hep-ph/9807570](https://arxiv.org/abs/hep-ph/9807570) [[hep-ph](#)].
- [258] M. L. Mangano, M. Moretti, and R. Pittau. “Multijet matrix elements and shower evolution in hadronic collisions: $Wb\bar{b} + n \text{ jets}$ as a case study”. In: *Nucl. Phys. B* 632 (2002), pp. 343–362. doi: [10.1016/S0550-3213\(02\)00249-3](https://doi.org/10.1016/S0550-3213(02)00249-3). arXiv: [hep-ph/0108069](https://arxiv.org/abs/hep-ph/0108069) [[hep-ph](#)].
- [259] B. P. Kersevan and E. Richter-Was. “The Monte Carlo event generator AcerMC versions 2.0 to 3.8 with interfaces to PYTHIA 6.4, HERWIG 6.5 and ARIADNE 4.1”. In: *Comput. Phys. Commun.* 184 (2013), pp. 919–985. doi: [10.1016/j.cpc.2012.10.032](https://doi.org/10.1016/j.cpc.2012.10.032). arXiv: [hep-ph/0405247](https://arxiv.org/abs/hep-ph/0405247) [[hep-ph](#)].
- [260] J. Pumplin et al. “New Generation of Parton Distributions with Uncertainties from Global QCD Analysis”. In: *JHEP* 07 (2002), p. 12. doi: [10.1088/1126-6708/2002/07/012](https://doi.org/10.1088/1126-6708/2002/07/012). arXiv: [hep-ph/0201195](https://arxiv.org/abs/hep-ph/0201195) [[hep-ph](#)].
- [261] C. Anastasiou et al. “High precision QCD at hadron colliders: Electroweak gauge boson rapidity distributions at NNLO”. In: *Phys. Rev. D* 69 (2004), p. 94008. doi: [10.1103/PhysRevD.69.094008](https://doi.org/10.1103/PhysRevD.69.094008). arXiv: [hep-ph/0312266](https://arxiv.org/abs/hep-ph/0312266) [[hep-ph](#)].
- [262] M. Cacciari et al. “Top-pair production at hadron colliders with next-to-next-to-leading logarithmic soft-gluon resummation”. In: *Phys. Lett. B* 710.4–5 (2012), pp. 612–622. doi: [10.1016/j.physletb.2012.03.013](https://doi.org/10.1016/j.physletb.2012.03.013).

- [263] J. Campbell, R. K. Ellis, and F. Tramontano. “Single top-quark production and decay at next-to-leading order”. In: *Phys. Rev. D* 70.9 (2004), p. 94012. doi: [10.1103/PhysRevD.70.094012](https://doi.org/10.1103/PhysRevD.70.094012).
- [264] J. M. Campbell, R. K. Ellis, and C. Williams. “Vector boson pair production at the LHC”. In: *JHEP* 2011.7 (2011), p. 18. doi: [10.1007/JHEP07\(2011\)018](https://doi.org/10.1007/JHEP07(2011)018).
- [265] S. Jadach et al. “The τ decay library TAUOLA, version 2.4”. In: *Comput. Phys. Commun.* 76.3 (1993), pp. 361–380. doi: [10.1016/0010-4655\(93\)90061-G](https://doi.org/10.1016/0010-4655(93)90061-G).
- [266] P. Golonka and Z. Was. “PHOTOS Monte Carlo: a precision tool for QED corrections in Z and W decays”. In: *Eur. Phys. J. C - Particles and Fields* 45.1 (2006), pp. 97–107. doi: [10.1140/epjc/s2005-02396-4](https://doi.org/10.1140/epjc/s2005-02396-4).
- [267] J. Hartet. “Measurement of the $W \rightarrow e\nu$ and $Z/\gamma^* \rightarrow ee$ Production Cross-Sections in Proton-Proton Collisions at $\sqrt{s} = 7$ TeV with the ATLAS Experiment”. PhD thesis. Albert-Ludwigs-Universität Freiburg, 2011.
- [268] R. J. Barlow. “Extended maximum likelihood”. In: *Nucl. Instrum. Meth. A* 297 (1990), pp. 496–506. doi: [10.1016/0168-9002\(90\)91334-8](https://doi.org/10.1016/0168-9002(90)91334-8).
- [269] E. Lohrmann. *A Summary of Charm Hadron Production Fractions*. 2011. arXiv: [1112.3757](https://arxiv.org/abs/1112.3757) [[hep-ex](https://arxiv.org/abs/1112.3757)].
- [270] J. Beringer et al. “Review of Particle Physics”. In: *Phys. Rev. D* 86.1 (2012), p. 10001. doi: [10.1103/PhysRevD.86.010001](https://doi.org/10.1103/PhysRevD.86.010001).
- [271] ATLAS Collaboration. *Search for heavy resonances decaying to a W or Z boson and a Higgs boson in final states with leptons and b-jets in 36.1 fb⁻¹ of pp collision data at $\sqrt{s} = 13$ TeV with the ATLAS detector*. ATLAS-CONF-2017-055. 2017.
- [272] F. Sannino and K. Tuominen. “Orientifold theory dynamics and symmetry breaking”. In: *Phys. Rev. D* 71.5 (2005), p. 051901. doi: [10.1103/PhysRevD.71.051901](https://doi.org/10.1103/PhysRevD.71.051901). arXiv: [0405209](https://arxiv.org/abs/0405209) [[hep-ph](https://arxiv.org/abs/0405209)].
- [273] R. Foadi et al. “Minimal walking technicolor: Setup for collider physics”. In: *Phys. Rev. D* 76.5 (2007), p. 055005. doi: [10.1103/PhysRevD.76.055005](https://doi.org/10.1103/PhysRevD.76.055005). arXiv: [0706.1696](https://arxiv.org/abs/0706.1696) [[hep-ph](https://arxiv.org/abs/0706.1696)].
- [274] A. Belyaev et al. “Technicolor Walks at the LHC”. In: (2008). doi: [10.1103/physrevd.79.035006](https://doi.org/10.1103/physrevd.79.035006). arXiv: [0809.0793](https://arxiv.org/abs/0809.0793) [[hep-ph](https://arxiv.org/abs/0809.0793)].
- [275] M. J. Dugan, H. Georgi, and D. B. Kaplan. “Anatomy of a composite Higgs model”. In: *Nucl. Phys. B* 254 (1985), pp. 299–326. doi: [10.1016/0550-3213\(85\)90221-4](https://doi.org/10.1016/0550-3213(85)90221-4).
- [276] K. Agashe, R. Contino, and A. Pomarol. “The minimal composite Higgs model”. In: *Nucl. Phys. B* 719.1-2 (2005), pp. 165–187. doi: [10.1016/j.nuclphysb.2005.04.035](https://doi.org/10.1016/j.nuclphysb.2005.04.035). arXiv: [hep-ph/0412089](https://arxiv.org/abs/hep-ph/0412089) [[hep-ph](https://arxiv.org/abs/hep-ph/0412089)].
- [277] D. Pappadopulo et al. “Heavy vector triplets: bridging theory and data”. In: *JHEP* 09 (2014), p. 60. doi: [10.1007/JHEP09\(2014\)060](https://doi.org/10.1007/JHEP09(2014)060). arXiv: [1402.4431](https://arxiv.org/abs/1402.4431) [[hep-ph](https://arxiv.org/abs/1402.4431)].
- [278] J. de Blas, J. M. Lizana, and M. Pérez-Victoria. “Combining searches of Z' and W' bosons”. In: *JHEP* 01 (2013), p. 166. doi: [10.1007/JHEP01\(2013\)166](https://doi.org/10.1007/JHEP01(2013)166). arXiv: [1211.2229](https://arxiv.org/abs/1211.2229) [[hep-ph](https://arxiv.org/abs/1211.2229)].
- [279] ATLAS Collaboration. “Search for high-mass diboson resonances with boson-tagged jets in proton-proton collisions at $\sqrt{s} = 8$ TeV with the ATLAS detector”. In: *JHEP* 12 (2015), p. 055. doi: [10.1007/JHEP12\(2015\)055](https://doi.org/10.1007/JHEP12(2015)055). arXiv: [1506.00962](https://arxiv.org/abs/1506.00962) [[hep-ex](https://arxiv.org/abs/1506.00962)].

- [280] CMS Collaboration. “Search for massive WH resonances decaying into the $\ell\nu b\bar{b}$ final state at $\sqrt{s} = 8$ TeV”. In: *Eur. Phys. J. C* 76 (2016), p. 237. doi: [10.1140/epjc/s10052-016-4067-z](https://doi.org/10.1140/epjc/s10052-016-4067-z). arXiv: [1601.06431](https://arxiv.org/abs/1601.06431) [hep-ex].
- [281] A. Djouadi et al. “The post-Higgs MSSM scenario: habemus MSSM?” In: *Eur. Phys. J. C* 73.12 (2013), p. 2650. doi: [10.1140/epjc/s10052-013-2650-0](https://doi.org/10.1140/epjc/s10052-013-2650-0). arXiv: [1307.5205](https://arxiv.org/abs/1307.5205) [hep-ph].
- [282] A. Djouadi et al. “Fully covering the MSSM Higgs sector at the LHC”. In: *JHEP* 06 (2015), p. 168. doi: [10.1007/JHEP06\(2015\)168](https://doi.org/10.1007/JHEP06(2015)168). arXiv: [1502.05653](https://arxiv.org/abs/1502.05653) [hep-ph].
- [283] ATLAS Collaboration. “Search for a CP -odd Higgs boson decaying to Zh in pp collisions at $\sqrt{s} = 8$ TeV with the ATLAS detector”. In: *Phys. Lett. B* 744 (2015), p. 163. doi: [10.1016/j.physletb.2015.03.054](https://doi.org/10.1016/j.physletb.2015.03.054). arXiv: [1502.04478](https://arxiv.org/abs/1502.04478) [hep-ex].
- [284] CMS Collaboration. “Search for a pseudoscalar boson decaying into a Z boson and the 125 GeV Higgs boson in $\ell^+\ell^-b\bar{b}$ final states”. In: *Phys. Lett. B* 748 (2015), p. 221. doi: [10.1016/j.physletb.2015.07.010](https://doi.org/10.1016/j.physletb.2015.07.010). arXiv: [1504.04710](https://arxiv.org/abs/1504.04710) [hep-ex].
- [285] ATLAS Collaboration. “Search for neutral Higgs bosons of the minimal supersymmetric standard model in pp collisions at $\sqrt{s} = 8$ TeV with the ATLAS detector”. In: *JHEP* 11 (2014), p. 056. doi: [10.1007/JHEP11\(2014\)056](https://doi.org/10.1007/JHEP11(2014)056). arXiv: [1409.6064](https://arxiv.org/abs/1409.6064) [hep-ex].
- [286] ATLAS Collaboration. “Search for new resonances decaying to a W or Z boson and a Higgs boson in the $\ell^+\ell^-b\bar{b}$, $\ell\nu b\bar{b}$, and $\nu\bar{\nu}b\bar{b}$ channels with pp collisions at $\sqrt{s} = 13$ TeV with the ATLAS detector”. In: *Phys. Lett. B* 765 (2017), p. 32. doi: [10.1016/j.physletb.2016.11.045](https://doi.org/10.1016/j.physletb.2016.11.045). arXiv: [1607.05621](https://arxiv.org/abs/1607.05621) [hep-ex].
- [287] V. Barger, W. Y. Keung, and E. Ma. “A gauge model with light W and Z bosons”. In: *Phys. Rev. D* 22.3 (1980), pp. 727–737. doi: [10.1103/PhysRevD.22.727](https://doi.org/10.1103/PhysRevD.22.727).
- [288] R. Contino et al. “On the effect of resonances in composite Higgs phenomenology”. In: *JHEP* 10 (2011), p. 81. doi: [10.1007/JHEP10\(2011\)081](https://doi.org/10.1007/JHEP10(2011)081). arXiv: [1109.1570](https://arxiv.org/abs/1109.1570) [hep-ph].
- [289] ATLAS Collaboration. “Search for a new resonance decaying to a W or Z boson and a Higgs boson in the $\ell\ell/\ell\nu/\nu\nu + b\bar{b}$ final states with the ATLAS detector”. In: *Eur. Phys. J. C* 75 (2015), p. 263. doi: [10.1140/epjc/s10052-015-3474-x](https://doi.org/10.1140/epjc/s10052-015-3474-x). arXiv: [1503.08089](https://arxiv.org/abs/1503.08089) [hep-ex].
- [290] CMS Collaboration. “Search for heavy resonances decaying into a vector boson and a Higgs boson in final states with charged leptons, neutrinos, and b quarks”. In: *Phys. Lett. B* 768 (2017), p. 137. doi: [10.1016/j.physletb.2017.02.040](https://doi.org/10.1016/j.physletb.2017.02.040). arXiv: [1610.08066](https://arxiv.org/abs/1610.08066) [hep-ex].
- [291] CMS Collaboration. “Search for a massive resonance decaying into a Higgs boson and a W or Z boson in hadronic final states in proton–proton collisions at $\sqrt{s} = 8$ TeV”. In: *JHEP* 02 (2016), p. 145. doi: [10.1007/JHEP02\(2016\)145](https://doi.org/10.1007/JHEP02(2016)145). arXiv: [1506.01443](https://arxiv.org/abs/1506.01443) [hep-ex].
- [292] ATLAS Collaboration. “Search for heavy resonances decaying to a W or Z boson and a Higgs boson in the $q\bar{q}^{(\prime)}b\bar{b}$ final state in pp collisions at $\sqrt{s} = 13$ TeV with the ATLAS detector”. In: *Phys. Lett. B* 774 (2017), p. 494. doi: [10.1016/j.physletb.2017.09.066](https://doi.org/10.1016/j.physletb.2017.09.066). arXiv: [1707.06958](https://arxiv.org/abs/1707.06958) [hep-ex].

- [293] CMS Collaboration. “Searches for a heavy scalar boson H decaying to a pair of 125 GeV Higgs bosons hh or for a heavy pseudoscalar boson A decaying to Zh , in the final states with $h \rightarrow \tau\tau$ ”. In: *Phys. Lett. B* 755 (2016), p. 217. doi: [10.1016/j.physletb.2016.01.056](https://doi.org/10.1016/j.physletb.2016.01.056). arXiv: [1510.01181](https://arxiv.org/abs/1510.01181) [hep-ex].
- [294] CMS Collaboration. “Searches for heavy Higgs bosons in two-Higgs-doublet models and for $t \rightarrow ch$ decay using multilepton and diphoton final states in pp collisions at $\sqrt{s} = 8$ TeV”. In: *Phys. Rev. D* 90 (2014), p. 112013. doi: [10.1103/PhysRevD.90.112013](https://doi.org/10.1103/PhysRevD.90.112013). arXiv: [1410.2751](https://arxiv.org/abs/1410.2751) [hep-ex].
- [295] J. Alwall et al. “The automated computation of tree-level and next-to-leading order differential cross sections, and their matching to parton shower simulations”. In: *JHEP* 2014.7 (2014), p. 079. doi: [10.1007/JHEP07\(2014\)079](https://doi.org/10.1007/JHEP07(2014)079). arXiv: [1405.0301](https://arxiv.org/abs/1405.0301) [hep-ph].
- [296] R. D. Ball et al. “Impact of heavy quark masses on parton distributions and LHC phenomenology”. In: *Nucl. Phys. B* 849.2 (2011), pp. 296–363. doi: [10.1016/j.nuclphysb.2011.03.021](https://doi.org/10.1016/j.nuclphysb.2011.03.021). arXiv: [1101.1300](https://arxiv.org/abs/1101.1300) [hep-ph].
- [297] ATLAS Collaboration. *ATLAS Pythia 8 tunes to 7 TeV data*. ATL-PHYS-PUB-2014-021. 2014.
- [298] S. Dawson et al. “Exclusive Higgs boson production with bottom quarks at hadron colliders”. In: *Phys. Rev. D* 69 (2004), p. 074027. doi: [10.1103/PhysRevD.69.074027](https://doi.org/10.1103/PhysRevD.69.074027). arXiv: [0311067](https://arxiv.org/abs/0311067) [hep-ph].
- [299] S. Dittmaier, M. Krämer, and M. Spira. “Higgs radiation off bottom quarks at the Fermilab Tevatron and the CERN LHC”. In: *Phys. Rev. D* 70.7 (2004), p. 074010. doi: [10.1103/PhysRevD.70.074010](https://doi.org/10.1103/PhysRevD.70.074010). arXiv: [hep-ph/0309204](https://arxiv.org/abs/hep-ph/0309204) [hep-ph].
- [300] R. Harlander, M. Krämer, and M. Schumacher. *Bottom-quark associated Higgs-boson production: reconciling the four- and five-flavour scheme approach*. Tech. rep. 2011, pp. 1–8. arXiv: [1112.3478](https://arxiv.org/abs/1112.3478) [hep-ph].
- [301] F. Cascioli, P. Maierhöfer, and S. Pozzorini. “Scattering amplitudes with open loops”. In: *Phys. Rev. Lett.* 108.11 (2012), p. 111601. doi: [10.1103/PhysRevLett.108.111601](https://doi.org/10.1103/PhysRevLett.108.111601). arXiv: [1111.5206](https://arxiv.org/abs/1111.5206) [hep-ph].
- [302] S. Schumann and F. Krauss. “A parton shower algorithm based on Catani-Seymour dipole factorisation”. In: *JHEP* 03 (2008), pp. 038–038. doi: [10.1088/1126-6708/2008/03/038](https://doi.org/10.1088/1126-6708/2008/03/038). arXiv: [0709.1027](https://arxiv.org/abs/0709.1027) [hep-ph].
- [303] K. Melnikov and F. Petriello. “Electroweak gauge boson production at hadron colliders through $O(\alpha_s^2)$ ”. In: *Phys. Rev. D* 74.11 (2006), p. 114017. doi: [10.1103/PhysRevD.74.114017](https://doi.org/10.1103/PhysRevD.74.114017). arXiv: [hep-ph/0609070](https://arxiv.org/abs/hep-ph/0609070) [hep-ph].
- [304] P. Z. Skands. “Tuning Monte Carlo generators: The Perugia tunes”. In: *Phys. Rev. D* 82.7 (2010), p. 074018. doi: [10.1103/PhysRevD.82.074018](https://doi.org/10.1103/PhysRevD.82.074018). arXiv: [1005.3457](https://arxiv.org/abs/1005.3457) [hep-ph].
- [305] ATLAS Collaboration. *Comparison of Monte Carlo generator predictions to ATLAS measurements of top pair production at 7 TeV*. ATL-PHYS-PUB-2015-002. 2015.
- [306] M. Czakon, D. Heymes, and A. Mitov. “Dynamical scales for multi-TeV top-pair production at the LHC”. In: *JHEP* 04 (2017), p. 71. doi: [10.1007/JHEP04\(2017\)071](https://doi.org/10.1007/JHEP04(2017)071).

- [307] M. Czakon and A. Mitov. “Top++: A program for the calculation of the top-pair cross-section at hadron colliders”. In: *Comput. Phys. Commun.* 185.11 (2014), pp. 2930–2938. doi: [10.1016/j.cpc.2014.06.021](https://doi.org/10.1016/j.cpc.2014.06.021). arXiv: [1112.5675 \[hep-ph\]](https://arxiv.org/abs/1112.5675).
- [308] S. Gieseke, C. Rohr, and A. Siodmok. “Colour reconnections in Herwig++”. In: *Eur. Phys. J. C* 72 (2012), p. 2225. doi: [10.1140/epjc/s10052-012-2225-5](https://doi.org/10.1140/epjc/s10052-012-2225-5). arXiv: [1206.0041 \[hep-ph\]](https://arxiv.org/abs/1206.0041).
- [309] P. Artoisenet et al. “Automatic spin-entangled decays of heavy resonances in Monte Carlo simulations”. In: *JHEP* 3 (2013), p. 015. doi: [10.1007/JHEP03\(2013\)015](https://doi.org/10.1007/JHEP03(2013)015). arXiv: [1212.3460 \[hep-ph\]](https://arxiv.org/abs/1212.3460).
- [310] M. Aliev et al. “HATHOR - HAdronic Top and Heavy quarks crOss section calculator”. In: *Comput. Phys. Commun.* 182.4 (2011), pp. 1034–1046. doi: [10.1016/j.cpc.2010.12.040](https://doi.org/10.1016/j.cpc.2010.12.040). arXiv: [1007.1327 \[hep-ph\]](https://arxiv.org/abs/1007.1327).
- [311] P. Kant et al. “HatHor for single top-quark production: Updated predictions and uncertainty estimates for single top-quark production in hadronic collisions”. In: *Comput. Phys. Commun.* 191.1 (2015), pp. 74–89. doi: [10.1016/j.cpc.2015.02.001](https://doi.org/10.1016/j.cpc.2015.02.001). arXiv: [1406.4403 \[hep-ph\]](https://arxiv.org/abs/1406.4403).
- [312] N. Kidonakis. “Two-loop soft anomalous dimensions for single top quark associated production with a W- or H-”. In: *Phys. Rev. D* 82 (2010), p. 054018. doi: [10.1103/PhysRevD.82.054018](https://doi.org/10.1103/PhysRevD.82.054018). arXiv: [1005.4451 \[hep-ph\]](https://arxiv.org/abs/1005.4451).
- [313] N. Kidonakis. “Top Quark Production”. In: *Proceedings, Helmholtz International Summer School on Physics of Heavy Quarks and Hadrons (HQ 2013)*. 2014, pp. 139–168. arXiv: [1311.0283 \[hep-ph\]](https://arxiv.org/abs/1311.0283).
- [314] ATLAS Collaboration. “Measurement of the Z/γ^* boson transverse momentum distribution in pp collisions at $\sqrt{s} = 7$ TeV with the ATLAS detector”. In: *JHEP* 09 (2014), p. 145. doi: [10.1007/JHEP09\(2014\)145](https://doi.org/10.1007/JHEP09(2014)145). arXiv: [1406.3660 \[hep-ex\]](https://arxiv.org/abs/1406.3660).
- [315] ATLAS Collaboration. *Comparison of Monte Carlo generator predictions for bottom and charm hadrons in the decays of top quarks and the fragmentation of high p_T jets*. ATL-PHYS-PUB-2014-008. 2014.
- [316] ATLAS Collaboration. *Boosted Higgs ($\rightarrow b\bar{b}$) Boson Identification with the ATLAS Detector at $\sqrt{s} = 13$ TeV*. ATLAS-CONF-2016-039. 2016.
- [317] ATLAS Collaboration. *Expected Performance of Boosted Higgs ($\rightarrow b\bar{b}$) Boson Identification with the ATLAS Detector at $\sqrt{s} = 13$ TeV*. ATL-PHYS-PUB-2015-035. 2015.
- [318] ATLAS Collaboration. “Search for the $b\bar{b}$ decay of the Standard Model Higgs boson in associated $(W/Z)H$ production with the ATLAS detector”. In: *JHEP* 01 (2015), p. 069. doi: [10.1007/JHEP01\(2015\)069](https://doi.org/10.1007/JHEP01(2015)069). arXiv: [1409.6212 \[hep-ex\]](https://arxiv.org/abs/1409.6212).
- [319] A. Bukin. *Fitting function for asymmetric peaks*. 2007. arXiv: [0711.4449v2 \[physics.data-an\]](https://arxiv.org/abs/0711.4449v2).
- [320] B. Jäger. “Studien zum Zerfall eines pseudoskalaren Higgs-Bosons im Kanal $A \rightarrow Zh (h \rightarrow b\bar{b})$ mit dem ATLAS-Experiment”. Bachelor Thesis. Albert-Ludwigs-Universität Freiburg, 2014.

- [321] ATLAS Collaboration. “Search for Dark Matter Produced in Association with a Higgs Boson Decaying to $b\bar{b}$ using 36 fb^{-1} of pp collisions at $\sqrt{s} = 13 \text{ TeV}$ with the ATLAS Detector”. In: *Phys. Rev. Lett.* 119 (2017), p. 181804. doi: [10.1103/PhysRevLett.119.181804](https://doi.org/10.1103/PhysRevLett.119.181804). arXiv: [1707.01302](https://arxiv.org/abs/1707.01302) [hep-ex].
- [322] ATLAS Collaboration. “Measurement of the Inelastic Proton–Proton Cross Section at $\sqrt{s} = 13 \text{ TeV}$ with the ATLAS Detector at the LHC”. In: *Phys. Rev. Lett.* 117 (2016), p. 182002. doi: [10.1103/PhysRevLett.117.182002](https://doi.org/10.1103/PhysRevLett.117.182002). arXiv: [1606.02625](https://arxiv.org/abs/1606.02625) [hep-ex].
- [323] A. Buckley et al. “Rivet user manual”. In: *Comput. Phys. Commun.* 184.12 (2013), pp. 2803–2819. doi: [10.1016/j.cpc.2013.05.021](https://doi.org/10.1016/j.cpc.2013.05.021). arXiv: [1003.0694](https://arxiv.org/abs/1003.0694) [hep-ph].
- [324] ATLAS Collaboration. *Simulation of top-quark production for the ATLAS experiment at $\sqrt{s} = 13 \text{ TeV}$* . ATL-PHYS-PUB-2016-004. 2016.
- [325] J. M. Campbell and R. K. Ellis. “MCFM for the Tevatron and the LHC”. In: *Nucl. Phys. B - Proceedings Supplements* 205-206.C (2010), pp. 10–15. doi: [10.1016/j.nuclphysbps.2010.08.011](https://doi.org/10.1016/j.nuclphysbps.2010.08.011). arXiv: [1007.3492](https://arxiv.org/abs/1007.3492) [hep-ph].
- [326] K. Cranmer et al. *HistFactory: A tool for creating statistical models for use with RooFit and RooStats*. CERN-OPEN-2012-016. 2012.
- [327] W. Verkerke and D. Kirkby. *The RooFit toolkit for data modeling*. 2003. arXiv: [physics/0306116](https://arxiv.org/abs/physics/0306116) [physics].
- [328] L. Moneta et al. “The RooStats Project”. In: *Proceedings of the 13th International Workshop on Advanced Computing and Analysis Techniques in Physics Research.*, 2010, p. 11. arXiv: [1009.1003](https://arxiv.org/abs/1009.1003) [physics.data-an].
- [329] G. Cowan. “Statistics for Searches at the LHC”. In: *LHC Phenomenology*. September 2012. Cham: Springer International Publishing, 2015, pp. 321–355. doi: [10.1007/978-3-319-05362-2_9](https://doi.org/10.1007/978-3-319-05362-2_9). arXiv: [1307.2487](https://arxiv.org/abs/1307.2487) [physics.data-an].
- [330] W. Verkerke. *Guide to parameterized likelihood analyses (draft in preparation)*. Private Communication. 2012.
- [331] L. Lyons, Y. Perrin, and F. E. James, eds. *Workshop on Confidence Limits*. 2000. URL: <http://cds.cern.ch/record/411537>.
- [332] A. L. Read. “Presentation of search results: The CL(s) technique”. In: *J. Phys. G* 28 (2002), pp. 2693–2704. doi: [10.1088/0954-3899/28/10/313](https://doi.org/10.1088/0954-3899/28/10/313).
- [333] ATLAS Statistics Forum. *Frequentist Limit Recommendation*. Private Communication. 2011.
- [334] N. Metropolis and S. Ulam. “The Monte Carlo Method”. In: *J. Am. Stat. Assoc.* 44.247 (1949), pp. 335–341. doi: [10.1080/01621459.1949.10483310](https://doi.org/10.1080/01621459.1949.10483310).
- [335] G. Cowan et al. “Asymptotic formulae for likelihood-based tests of new physics”. In: *Eur. Phys. J. C* 71.2 (2011), p. 1554. doi: [10.1140/epjc/s10052-011-1554-0](https://doi.org/10.1140/epjc/s10052-011-1554-0). arXiv: [1007.1727](https://arxiv.org/abs/1007.1727) [hep-ex].
- [336] L. Lyons. “Open statistical issues in particle physics”. In: *Annals Appl. Stat.* 2.3 (2008), pp. 887–915. doi: [10.1214/08-AOAS163](https://doi.org/10.1214/08-AOAS163). arXiv: [0811.1663](https://arxiv.org/abs/0811.1663) [stat.AP].

- [337] E. Gross and O. Vitells. “Trial factors for the look elsewhere effect in high energy physics”. In: *Eur. Phys. J. C* 70.1 (2010), pp. 525–530. doi: [10.1140/epjc/s10052-010-1470-8](https://doi.org/10.1140/epjc/s10052-010-1470-8). arXiv: [1005.1891](https://arxiv.org/abs/1005.1891) [[physics.data-an](https://arxiv.org/archive/physics)].
- [338] ATLAS Collaboration. *Procedure for the LHC Higgs boson search combination in summer 2011*. ATL-PHYS-PUB-2011-011. 2011.
- [339] E. Gross. *Discussion on global significance computations using asymptotic formulae*. Private Communication. 2017.
- [340] R. Barlow and C. Beeston. “Fitting using finite Monte Carlo samples”. In: *Comput. Phys. Commun.* 77.2 (1993), pp. 219–228. doi: [10.1016/0010-4655\(93\)90005-W](https://doi.org/10.1016/0010-4655(93)90005-W).
- [341] ATLAS Collaboration. “Observation of Higgs boson production in association with a top quark pair at the LHC with the ATLAS detector”. In: *Phys. Lett. B* 784 (2018), p. 173. doi: [10.1016/j.physletb.2018.07.035](https://doi.org/10.1016/j.physletb.2018.07.035). arXiv: [1806.00425](https://arxiv.org/abs/1806.00425) [[hep-ex](https://arxiv.org/archive/hep)].
- [342] CMS Collaboration. “Observation of $t\bar{t}H$ Production”. In: *Phys. Rev. Lett.* 120 (2018), p. 231801. doi: [10.1103/PhysRevLett.120.231801](https://doi.org/10.1103/PhysRevLett.120.231801). arXiv: [1804.02610](https://arxiv.org/abs/1804.02610) [[hep-ex](https://arxiv.org/archive/hep)].
- [343] CMS Collaboration. *Search for a heavy pseudoscalar boson decaying to a Z boson and a Higgs boson at $\sqrt{s} = 13$ TeV*. CMS-PAS-HIG-18-005. 2018.
- [344] ATLAS Collaboration. *Search for a CP-odd Higgs boson decaying to Zh in pp collisions at $\sqrt{s} = 8$ TeV with the ATLAS detector*. Public Results. 2015. URL: <https://atlas.web.cern.ch/Atlas/GROUPS/PHYSICS/PAPERS/HIGG-2013-06/>.
- [345] ATLAS Collaboration. *Summary plots from the ATLAS Higgs physics group: BSM Higgs exclusion in the hMSSM*. URL: <https://atlas.web.cern.ch/Atlas/GROUPS/PHYSICS/CombinedSummaryPlots/HIGGS/> (visited on 12/01/2018).

Acknowledgements

It is almost to date, six years ago that I started to work on my Ph.D. project; more than one year ago I already started to work as a postdoc at Nikhef. During that whole period I faced many challenges, both related to work and to my private life. However, with the support of many people most challenges turned into opportunities. Opportunities to grow and develop, not only as a physicist, but also as a person. For this I am deeply grateful, and I want to take the opportunity to thank my supervisors, a few of my colleagues and friends - many are both-, as well as my family. Many that accompanied (part of) my way in the past years, and contributed to shape my work and myself as well, unfortunately, will remain unnamed. I hope that they are still aware of my appreciation and gratitude.

First of all, I want to thank Karl Jakobs for giving me the wonderful opportunity to continue with a Ph.D. project in his group after finishing my diploma. I appreciated every discussion that I had the chance to have with him, physics-related or otherwise, every valuable advice he gave me, and that he was always there to support me, when I needed it, despite his always too busy schedule. I admire his competence and determination; the passion with which he does everything, is a great inspiration.

I want to thank my supervisor Christian Weiser for giving me the freedom to develop and pursue my own ideas under his friendly guidance, for always being available for physics discussions and so willing to share his knowledge and experience with me. He keeps impressing me with his great knowledge and understanding of particle physics; not only, but in particular using $W+c$ events to calibrate the b -tagging efficiency of c jets was his idea. To earn his respect as a fellow researcher was (and still is) important for me.

Besides my official supervisors, I also want to thank in particular three amazing physicists and friends that tremendously contributed to me becoming the physicist that I am today. Lutz Fechner, who already believed in my (hidden) skills long before I did, for his patience and kindness with me during our studies, his generosity to share all his knowledge and understanding with me. Georges Aad, who continued to support me along the same lines during my diploma thesis and the early stages of my Ph.D. He taught me patiently all the basics of performing data analysis in ATLAS and enabled me to become an independent researcher. He challenged me, while providing all the support that I needed. I still appreciate his opinion and advice, both as a fellow researcher and a friend. Since he was a wonderful supervisor to me, I try to follow his good example with my own students today. Valerio Dao, who mainly accompanied me in the final stages of my Ph.D. project and supported me dependably both with his incredible experience in data analysis as well as with his friendship. It was a wonderful experience to co-work on the $A \rightarrow Zh$ analysis during our time together in Freiburg; although it was only for a while I learned a lot from him, in particular basically everything I know about building and validating a fit model. The carrot-and-stick approach he applied to support me preparing this document is unparalleled. I am very glad that I have the opportunity to continue working with him during my postdoc.

While it was a luxury to work on the $W+c$ calibration somewhat in solitary and detached from the ATLAS machinery, supported by Christian's and Georges' experience and knowledge, I enjoyed it a lot to work collaboratively with many different ATLAS members on the development and support of the CxAOD-Framework as well as on the two $A \rightarrow Zh$ analyses. In the context of the former, I want to thank especially my fellow (ex-)group members, Daniel Büscher and Karsten Könecke, as well as Nicolas Morange. I was very happy that after years of knowing Nicolas, I finally had the chance to work with him, not only on the CxAODFramework, but also on the early $A \rightarrow Zh$ analysis. I am very grateful for all the knowledge he willingly and reliably shared (and still shares) with me concerning many aspects of data analysis and in particular on statistical data analysis. Furthermore, I want to thank him for giving me advice and support as a friend, when I needed it. Not forgotten either are the dinners with friends and colleagues he always organised, when everyone gathered at CERN, - a tradition that he/we will hopefully keep up!

In the context of the $A \rightarrow Zh$ analysis, I furthermore want to thank especially Spyros Argyropoulos and Jeffrey Hetherly for the great collaboration. Jeff's polite and respectful way, his sympathy with other peoples (my) flaws and his good mood are exemplary to me. Thanks a lot also for the coffee breaks and all the nice things he said to me that made me feel good and appreciated.

I am grateful to Spyros for the very close, reliable and trustful collaboration from day one. I think during my time at CERN no day went by where we did not see each other and discuss our work and next steps, and it was always a pleasure. Thanks to him, our cross-institute collaboration can be called by name: Freiowa! A name that wonderfully describes the good connection between our institutes that existed already before us, one that I hope will stay. I am happy that also with my new affiliation I have the chance to continue working together.

I also want to thank all the conveners of the ATLAS Hbb and DBL groups I had (and currently have) the chance to (closely) work with. Some have already been mentioned (Nicolas, Valerio) and I would like to extend my explicit thank you to Paolo Francavilla, Yuji Enari, Tatsuya Masubuchi and Carl Gwilliam. It was and is a pleasure and an honour to work with everyone of them and to try and learn from their experience and individual excellence. I want to especially thank Carl for always backing-up my work and providing the necessary support for me to shape the final $A \rightarrow Zh$ analysis.

Furthermore, I want to thank everyone who was a member of the Freiburg group during my time and gave me the feeling of belonging and solidarity. Besides the ones I already mentioned, I especially want to thank my first office mates Evelyn Moser (formerly Schmidt), Matthias ("Matti") Werner and Susanne Kühn; for welcoming me so warmly and taking me under their wings, when I was still a shy and ignorant Diploma student. I will never forget their friendship, their patient and loving guidance and support. I am grateful to Susanne for her lasting close friendship, for being a mentor, for inspiring me with her never-ending energy and drive, and also for her great kindness to host me in her guestroom for far too long during the straining time trying to finish this document.

Thanks a lot also to all my other office mates and especially my friends Christian Lüttke, Julian Glatzer and Giulia Gonella - being at work was always more enjoyable, when they were there! Although not my office mate, but still spending a lot of time in my office, I want to also thank Vakhtang Tsiskaridze: for preventing me to starve when I stayed in the office late - much to his dislike -, for the flowers every May 1st, for his good heart and bear hugs.

I also want to say a special thank you to my fellow Ph.D. students Philip Sommer, Felix Bühner and

Dirk Sammel with whom I shared all the ups and downs of being a Ph.D. student. Thanks a lot for all the coffee breaks, pep talks, afterwork activities, for being good friends.

A warm thank you goes to Chris Skorek whose tireless support goes far beyond her job description, her organisational skills, power and kindness make her truly special to me. I also want to thank Ines Messmer for always taking care of us, e.g. organising our weekly exercises, for the many things she does to create a pleasant atmosphere at the work place. Thanks a lot also to Uli Parzefall another pillar of the group and maybe responsible for me ending up in particle physics; after all it was his support that made me become a summer student at CERN in 2009. Many thanks for the continuing support, e.g. for my applications, cheering me up with his light-spirited way and also the after work activities.

Not part of the Freiburg group, but still close to my work, I want to thank Stefan Fischer and Philippe Calfayan for the coffee breaks and long conversations on the bench in front of the institute and the R1 terrace, respectively. Stefan, I furthermore want to thank for the long and faithful friendship, continuing despite the long distance that is currently between us. Philippe, I want to also thank for teaching me wall-climbing, the lifts to the various spots and the late-night dinners during my time at CERN.

I am deeply grateful to my new group at Nikhef, especially to Tristan du Pree, Brian Moser and Marko Stamenkovic, for making the first year of my postdoc a wonderful experience. Their support and understanding helped me a lot to handle the challenge of dealing with finalising this thesis in addition to my postdoc duties. I very much appreciate the trust Tristan has in my work, the support he gives me to advance in my career and his patience regarding the time it took me to finally submit this document. I want to thank Marko and Brian for making it so enjoyable to work together. I consider myself extremely lucky to have the chance to follow the work and development of two such bright, diligent, reliable and lovely students and friends.

Finally, I want to thank all my friends and my family for bearing with me for so many years, for supporting me, for accepting how important my work is for me, leaving often little room for much else. Ich danke meinen Eltern und meiner Schwester für ihre bedingungslose Liebe, die ich aus tiefstem Herzen erwidere.